Karlsruhe Institute of Technology

Determination of Electromagnetic Fields and Tritium Column Density for Neutrino Mass Analysis with KATRIN

Zur Erlangung des akademischen Grades eines
Doktors der Naturwissenschaften (Dr. rer. nat.)
von der KIT-Fakultät für Physik des
Karlsruher Instituts für Technologie (KIT)
angenommene
Dissertation
von

M. Sc. Fabian Block

aus Bretten

Referentin:	Prof. Dr. Kathrin Valerius
	Institut für Astroteilchenphysik, KIT
Korreferent:	Prof. Dr. Guido Drexlin
	Institut für Experimentelle Teilchenphysik, KIT

Tag der mündlichen Prüfung: 10.12.2021

Dieses Werk ist lizenziert unter einer Creative Commons Namensnennung - Nicht-kommerziell - Weitergabe unter gleichen Bedingungen 4.0 International Lizenz (CC BY-NC-SA 4.0):
https://creativecommons.org/licenses/by-nc-sa/4.0/deed.de

Declaration of Authorship

Herewith I affirm that I wrote the current thesis on my own and without the usage of any other sources or tools than the cited ones and that this thesis has not been handed neither in this nor in equal form at any other official commission.

Erklärung der Selbstständigkeit

Hiermit versichere ich, die vorliegende Arbeit selbstständig angefertigt zu haben und keine Hilfsmittel jenseits der kenntlich gemachten verwendet zu haben. Weiterhin habe ich weder diese noch eine äquivalente Version dieser Arbeit bei einer anderen Prüfungskommission vorgelegt.

Walzbachtal, den 10.12.2021

Fabian Block

Contents

1. Introduction

Since the postulation of the neutrino by Wolfgang Pauli in 1930 [PKW64] and its discovery in 1956 by Cowan and Reines [Cow+56], the neutrino has become one of the most extensively studied particles of the Standard Model of particle physics. With the observation of neutrino flavor oscillation [Fuk+99; Ahm+01] proving their non-vanishing rest mass [Pon58; Pon68], neutrinos became of interest not only in particle physics, but also in other physics fields such as cosmology. Although their absolute rest mass is many orders of magnitude smaller than that of other massive particles in the Standard Model of particle physics [Zyl+20], they act as cosmic architects in the early universe due to their large abundance [FLS00]. Additionally, massive neutrinos imply physics beyond the Standard Model of particle physics, in which neutrinos are massless. The absolute neutrino mass scale is therefore one of the key features for a more in-depth understanding of the cosmological structure formation, as well as to physics beyond the Standard Model.

Neutrino oscillation experiments can not provide an absolute neutrino mass measurement. However, precision measurements conducted so far set a lower limit on the maximal neutrino mass of 50 meV, assuming normal hierarchy [Zyl+20]. Cosmological observations set a model-dependent upper limit on the sum of the three light neutrino mass eigenstates to 111 meV [Ala+20]. The search for neutrinoless double β decay also allows one to probe the neutrino mass scale. This method currently sets an upper limit on the effective Majorana mass of smaller than $61\,\text{meV} - 165\,\text{meV}$ [Zyl+20]. However, the obtained limit is only valid if neutrinos are Majorana particles. In contrast to the model-dependent approaches through cosmology and neutrinoless double β decay, the KArlsruhe TRItium Neutrino (KATRIN) experiment aims to model-independently probe the effective electron antineutrino mass by high-resolution spectroscopy of the β-decay spectrum close to the endpoint region. Based on the first two KATRIN neutrino mass measurement campaigns, the upper limit on the effective electron antineutrino mass could be set to 0.8 eV at 90 % confidence level [Ake+21a], more than a factor two improvement compared to predecessor experiments [Kra+05; Ase+11].

The design sensitivity of KATRIN on the effective electron neutrino mass is 200 meV at 90 % confidence level [KAT05]. To achieve this ambitious goal, the KATRIN experiment combines a high-luminosity Windowless Gaseous Tritium Source (WGTS) with a high-resolution Main Spectrometer for energy analysis based on the Magnetic Adiabatic Collimination with Electrostatic (MAC-E) filter technique. In the experimental setup, electrons stemming from the β decay of gaseous tritium in the WGTS are guided by magnetic fields of several Tesla strength towards the Main Spectrometer. In the Main Spectrometer, the electrons are either repelled back to the WGTS or transmitted to the detector, based on their kinetic energy. Strict requirements in precision and accuracy on the model used for data analysis have to be met to reach the targeted sensitivity on the neutrino mass. The experimental

response function, necessary to calculate the expected measured spectrum, describes the probability for a β-decay electron to overcome the Main Spectrometer and to reach the detector, taking into account energy-loss effects and the spectrometer's transmission function.

The main objectives of the thesis at hand are concerned with the characterization of contributions to the KATRIN response function, and with their systematic uncertainties impacting the neutrino mass analysis. In detail, this includes:

- Characterization of the WGTS magnet system and the pinch magnet in the completed KATRIN experimental setup, as their task goes beyond the mere guiding of β-decay electrons from source to detector. Indirect and direct measurement techniques are compared to simulations for better understanding of the field strength and the geometry of the solenoids in the experimental setup.
- Characterization of the electric and magnetic field strengths in the analyzing plane of the Main Spectrometer via complementary approaches as key parameters for the energy analysis. The field uncertainties are then quantified with respect to the systematic uncertainty contribution on the measured neutrino mass. This includes the field characterization of the configuration used in the first two neutrino mass measurement campaigns as well as a novel setting, the shifted analyzing plane, that is used from the third campaign onwards.
- Measurements with a photoelectron source to determine the tritium gas density in the WGTS as important parameter for energy-loss calculations of β-decay electrons leaving the WGTS. Simulations developed in former works are tested, as well as new methods to monitor the tritium gas density during neutrino mass measurement campaigns are presented.

Therefore, the thesis is structured as follows:

1. We give a brief summary on the history of neutrino physics in chapter 2 and put them into context to other elementary particles in the Standard Model of particle physics. Additionally, the neutrino flavor oscillation is introduced before we close the chapter with a presentation of possible neutrino mass generation mechanisms and complementary methods for experimental access to the absolute neutrino mass scale.
2. The MAC-E filter technique is presented in chapter 3 as central element for energy analysis in the KATRIN experiment. Subsequently, the individual hardware components of the 70 m-long experimental KATRIN setup are presented. As last part of this chapter, tools for neutrino mass analysis with KATRIN are introduced.
3. The pinch and WGTS magnetic field are characterized in chapter 4 via simulations and measurements. The obtained systematic uncertainty on the solenoid fields are put into context of the measured neutrino mass.
4. We investigate the electric and magnetic fields in the analyzing plane of the Main Spectrometer as used in the first two neutrino mass measurement campaigns in chapter 5. We identify contributions that do not fulfill the KATRIN sensitivity requirement and show measurement approaches for a more accurate model that can be used in neutrino mass analysis.

5. A novel Main Spectrometer electromagnetic configuration, namely the shifted analyzing plane, leads to a better signal to background ratio in subsequent neutrino mass measurement campaigns. A transmission characterization of this new mode via complementary measurements is given in chapter 6.

6. The contribution of the tritium gas density in the WGTS to the KATRIN response function is discussed in detail in chapter 7, before we present a method to directly measure the integrated gas density. Based on this measurement, monitoring methods are introduced to determine the gas density evolution during neutrino mass measurement campaigns. Furthermore, we employ the measurement method to test a prediction by gas model simulations that could cause a bias on the measured neutrino mass.

7. The findings of this thesis are summarized in chapter 8 and an outlook to future measurements is given.

2. Neutrino Physics

Since the first postulation of neutrinos in 1930 [PKW64] and their experimental discovery in 1956 [Cow+56], neutrino physics is a rapidly growing research field. The characteristic properties of neutrinos are their low interaction rate with matter, as they do only participate in the weak interaction. This property, which makes the study of neutrinos in laboratory experiments challenging, makes them interesting for other fields, for example they are used in astrophysics as messenger particles (see for example reference [Bra16]). The discovery of neutrino oscillations proved a non-zero rest mass of the neutrino in contradiction to the Standard Model of particle physics, leading to a key role of neutrinos in physics beyond the Standard Model.

The objective of the following chapter is to summarize the most-relevant aspects of neutrino physics for the thesis at hand and to emphasize the importance of determining the absolute neutrino mass scale by dedicated experiments like KATRIN. We therefore describe the most-important milestones in the theoretical prediction and the experimental discovery of the neutrino in section 2.1. Following, the neutrinos are put into the context of the Standard Model of particle physics in section 2.2. The theory of neutrino oscillation, pioneering experiments as well as the current research status and remaining open questions are discussed in section 2.3. Motivated by the experimental results of neutrino oscillations, possible extensions to the Standard Model to include a neutrino mass term are presented in section 2.4. Afterwards, three complementary approaches to experimentally determine the absolute neutrino mass scale are introduced in section 2.5.

2.1. The Postulation and Discovery of the Neutrino

The postulation of the neutrino is historically closely related to the discovery and investigation of radioactive decays. Towards the end of the 19th century, H. Becquerel discovered radioactivity [Bec96], which was further explored in the following years by M. and P. Curie [Cur10] and E. Rutherford [Rut05]. J. Chadwick investigated the β-decay spectrum in 1914, expecting a mono-energetic line of the electron similar to the already known mono-energetic, two-body α decay [Bra04]. However, Chadwick observed a continuous β-decay spectrum [Cha14], which was in contradiction to energy and angular momentum conservation of a two-body decay.
In 1930, W. Pauli postulated an electrically neutral, spin-$\frac{1}{2}$ particle involved in the β decay to explain how the continuous β spectrum could conserve energy and angular momentum [PKW64]. Pauli called this particle the "neutron", which had to have a significantly lower interaction rate compared to the other particles known at that time. The particle which we today know as the neutron was discovered two years after Pauli's postulation [Cha32]. Nonetheless, due to its large mass, it was clear that the neutron was not the particle postulated by Pauli.

In 1934, E. Fermi developed a theoretical description of the β decay, thereby introducing the word "neutrino" (ν) in the scientific terminology. In Fermi's theory, the neutron (n) decays to a proton (p), an electron (e^-), and an electron antineutrino ($\overline{\nu}_e$) in a point-like interaction

$$n \rightarrow p + e^- + \overline{\nu}_e \ . \tag{2.1}$$

Combining the expectation from his theory with data, Fermi concluded that the rest mass of the neutrino must be tiny compared to the electron mass, or even zero. The theory by Fermi was a milestone in neutrino physics, as it gave a solid theoretical basis for future experimental work. [Fer34]
Based on Fermi's theory, Bethe and Peierls suggested the inverse β decay

$$p + \overline{\nu}_e \rightarrow n + e^+ \tag{2.2}$$

to experimentally detect the neutrino. The cross-section for this process was expected to be below $10^{-44}\,\mathrm{cm}^2$, an experimental discovery of the neutrino seemed impossible. [BP34]

The usage of industrial nuclear power plants as high-intensity neutrino sources enabled the experimental discovery of the neutrino more than 20 years after its postulation. C. Cowan and F. Reines used the powerful fission reactor at the Savannah River Plant as antineutrino source in the "Poltergeist" experiment. A cadmium chloride solution in water formed the target for the antineutrinos. The water tanks were placed between scintillators to detect the reaction of antineutrinos with protons of the water according to equation 2.2, producing a neutron and a positron. The detection principle was a coincident measurement. The positron quickly annihilates with an electron, emitting two 511 keV photons that are detected by the scintillators. The neutron is moderated by the water and eventually captured on a cadmium nucleus. Thereby a gamma ray is released approximately 10 µs after the two 511 keV photons, which is also detected by the scintillators. [Cow+56; Zub12] This delayed coincidence signal gives a unique signature of a neutrino interaction and allows for an effective discrimination from background events. The measured neutrino flux yielded a significant signal rate of (36 ± 4) events/hour [RC59]. The cross-section for the inverse β decay was estimated to $(11 \pm 3) \times 10^{-44}\,\mathrm{cm}^2$ [RC59]. In 1995, Reines was awarded with the Nobel Prize for the experimental detection of the neutrino [The95].

In 1962, an experiment at the Brookhaven synchrotron proved the existence of a second type of neutrino, the muon neutrino ν_μ [Dan+62]. The discovery of the tau lepton in 1975 [Per+75] lead to the expectation of the associated tau neutrino ν_τ. In 1989, the Z^0-boson width was measured at the electron-positron collider LEP to investigate the number of light neutrino generations ($m_\nu < m_Z/2$). Within few months of data taking, the experiments ALEPH, DELPHI, L3, and Opal showed that the number of light neutrino generations has to be around three [Dec+90a; Aar+89; Ade+89; Dec+90b]. The full LEP dataset and further statistics from the electron-positron collider SLC allowed one to constrain the number of light neutrinos to 2.984 ± 0.008, assuming that the Z^0 decays only in Standard Model particles [Sch+06]. The DONUT experiment finally discovered the missing ν_τ neutrino in 2001 [Kod+01].

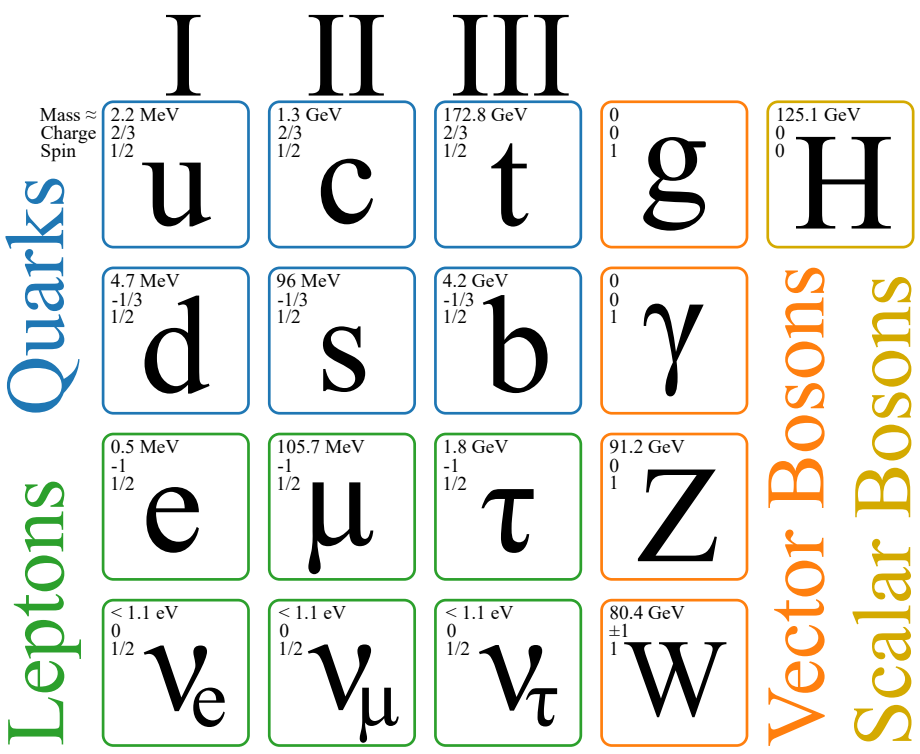

Figure 2.1.: **The Standard Model of particle physics.** The quarks (blue) and leptons (green) are grouped in three generations depending on their mass. The gauge bosons (orange) mediate the strong, electromagnetic, and weak forces. The scalar Higgs boson (yellow) is the excitation of the Higgs field, which generates the mass of the massive particles. Particle properties based on reference [Zyl+20].

2.2. Neutrinos in the Standard Model of Particle Physics

The Standard Model of particle physics describes the three fundamental forces (strong, electromagnetic, and weak force, omitting gravity) and classifies all known elementary particles (see figure 2.1) The three fundamental forces are mediated by the exchange of spin-1 vector bosons. The strong force is mediated via the massless gluon, the electromagnetic force via the photon. The Z^0- and $W^{\pm}$-bosons mediate the weak force. The known fundamental elementary particles are the twelve spin-$\frac{1}{2}$ fermions, that can be classified as quarks or leptons depending on the interactions they participate in. The Higgs boson is a spin-0 particle. It is the quantum excitation of the Higgs field that gives mass to the elementary particles. [Hig64; Pov+15] Six of the twelve fermions are quarks, characterized by their ability to carry color charge and to thus interact via the strong force. They are grouped in three generations with increasing mass and form weak isospin doublets. Each of the fermions has a corresponding antiparticle with same mass but opposite electric charge, color and opposite third component of the weak isospin. [Pov+15]
The remaining fermions are leptons, namely the electron, muon, and tauon, and one neutrino associated to each. Similar to the quarks, also the leptons are divided in three generations. In each generation, an electrically charged lepton and the associated neutrino form a weak isospin doublet that participates in the weak interaction.

The neutrinos are charge-less particles in the Standard Model and only undergo weak interactions, mediated via the $W^{\pm}$ and Z^0 bosons. The coupling to these bosons, and thus the interaction in the weak force, depends on the handedness of the particle. The handedness describes the spin orientation relative to the particle's momentum. The Wu experiment showed that the conservation of parity is violated in weak interaction [Wu+57] leading to the discovery that only left-handed (spin and momentum in same direction) particles and right-handed (spin and momentum in opposite direction) antiparticles participate in the weak force. Consequently, only left-handed weak isospin doublets exist. Right-handed particles do not participate in the weak interaction and thus form isospin singlets. M. Goldhaber et al. determined the neutrino to be left-handed by investigating the orbital electron capture of Eu^{152m} [GGS58]. A change of handedness is only allowed for massive particles via a coupling to the Higgs field. However, neutrinos are assumed to be massless in the Standard Model. It therefore allows the coupling of the weak interaction only to left-handed neutrinos and right-handed antineutrinos. Hypothetical right-handed neutrinos and left-handed antineutrinos would only interact gravitationally and not via the three fundamental forces of the Standard Model. [Pov+15]

Although the Standard Model has demonstrated huge success in providing experimental predictions, it cannot explain some phenomena. For example it does not incorporate the non-zero neutrino mass that is experimentally proven by discovering neutrino flavor oscillations. Consequently, neutrinos are a key to physics beyond the Standard Model. Detailed characterizations of their properties will have positive influence on related fields in particle physics.

2.3. Neutrino Flavor Oscillation

Mid of the 20th century, Pontecorvo formulated the theoretical possibility of neutrino-antineutrino oscillation [Pon57; Pon58; Pon68]. Based on Pontecorvo's theory, Maki, Nakagawa and Sakata proposed the flavour mixing of two generations of neutrinos in 1962 [MNS62]. The direct consequence of this flavor mixing is neutrino flavor oscillation. According to the theory, neutrino flavor oscillations can occur if the neutrino weak-interaction eigenstates are a superposition of the neutrino mass eigenstates, but they do not coincide [Zub12]. This phenomenon was previously already observed in the quark sector, where the weak and the mass eigenstates are connected by the CKM matrix [Zub12].

2.3.1. Theory of Neutrino Oscillation

The following description of the theory of neutrino oscillation is based on references [Zub12] and [Pov+15].
The fundamental assumption of neutrino oscillation is that the neutrino mass eigenstates $|\nu_i\rangle$ $(i = 1, 2, 3)$ do not coincide with the eigenstates of the weak interaction $|\nu_\alpha\rangle$ $(\alpha = e, \mu, \tau)$. Instead, the weak interaction eigenstates can be written as a

linear combinations of the mass states

$$\begin{pmatrix} |\nu_e\rangle \\ |\nu_\mu\rangle \\ |\nu_\tau\rangle \end{pmatrix} = \begin{pmatrix} U_{e1} & U_{e2} & U_{e3} \\ U_{\mu 1} & U_{\mu 2} & U_{\mu 3} \\ U_{\tau 1} & U_{\tau 2} & U_{\tau 3} \end{pmatrix} \cdot \begin{pmatrix} |\nu_1\rangle \\ |\nu_2\rangle \\ |\nu_3\rangle \end{pmatrix} ,$$

with U being the PMNS matrix. It is often parameterized as

$$U = \begin{pmatrix} 1 & 0 & 0 \\ 0 & \cos\theta_{23} & \sin\theta_{23} \\ 0 & -\sin\theta_{23} & \cos\theta_{23} \end{pmatrix} \begin{pmatrix} \cos\theta_{13} & 0 & \sin\theta_{13}e^{-i\delta} \\ 0 & 1 & 0 \\ -\sin\theta_{13}e^{i\delta} & 0 & \cos\theta_{13} \end{pmatrix} \begin{pmatrix} \cos\theta_{12} & \sin\theta_{12} & 0 \\ -\sin\theta_{12} & \cos\theta_{12} & 0 \\ 0 & 0 & 1 \end{pmatrix} \tag{2.3}$$

with θ_{ij} denoting the mixing angles, and δ being a CP-violating phase. If neutrinos are Majorana particles, i. e. their own antiparticles, the PMNS matrix must be extended by two Majorana phases $\alpha_{1,2}$. These phases can be included via an additional factor in equation 2.3

$$U_{\text{Majorana}} = \begin{pmatrix} 1 & 0 & 0 \\ 0 & e^{i\alpha_1/2} & 0 \\ 0 & 0 & e^{i\alpha_2/2} \end{pmatrix} .$$

A possible Majorana nature of neutrinos would give hint to the mass generation mechanism of neutrinos (see section 2.4). Many experiments try to deduce whether neutrinos are of Majorana or Dirac type by searching for the neutrinoless double β decay (see section 2.5.2). However, a possible existence of Majorana phases doesn't play a role in neutrino oscillations, therefore they are not considered in the following theoretical description. [Zub12; Pov+15]

A neutrino is produced and detected in a flavor state $|\nu_\alpha\rangle$ that is a coherent superposition of neutrino mass states $|\nu_i\rangle$. Between production and detection of the neutrino, its mass eigenstates propagate with different phase velocities leading to flavor oscillation. Consequently, the observed neutrino flavor at the point of detection depends on the distance between production and detection. [Zub12]
The time evolution of a neutrino with given flavor α at time $t = 0$ and at position $\vec{x}$ relative to the starting position can be written as

$$|\nu_\alpha(t, \vec{x})\rangle = \sum_i U_{\alpha i} e^{-i(E_i t - \vec{p}_i \vec{x})} |\nu_i\rangle \tag{2.4}$$

with $E_i = \sqrt{\vec{p}_i^{\,2} + m_i^2}$ and m_i being the mass of the mass eigenstate $|\nu_i\rangle$. Since E_i depends on the mass, the phase velocity of the propagation is different for the individual mass eigenstates. In the simplest approach the neutrino energy E_i is expanded relativistically

$$E_i = \sqrt{\vec{p}_i^{\,2} + m_i^2} \approx E_i + \frac{m_i^2}{2E} , \tag{2.5}$$

which is a good approximation due to the small mass. The probability of finding the neutrino in a different weak interaction eigenstate β at time t and position $\vec{x}$ is

$$P(\alpha \to \beta) = |\langle \nu_\beta | \nu_\alpha(t, \vec{x}) \rangle \ .|^2$$

Inserting approximation 2.5 and using $|\vec{x}| = L = ct$ with oscillation length L, the transition probability yields

$$P(\alpha \to \beta) = \sum_{i,j} U^*_{\alpha i} U_{\beta i} U_{\alpha j} U^*_{\beta j} \exp\left(-\mathrm{i}\frac{\Delta m^2_{ij} L}{2E}\right) \tag{2.6}$$

where $\Delta m^2_{ij} = \Delta m^2_i - m^2_j$ is the difference between the squared masses. Oscillatory behavior of neutrinos is thus possible as long as at least one neutrino mass eigenvalue is non-zero and if the weak flavor eigenstates do not coincide with the mass eigenstates. Furthermore, it is visible in equation 2.6 that measurements of the neutrino oscillation are not sensitive to the absolute mass scale of neutrinos, but only to the squared differences between the mass eigenstates. [Zub12; Pov+15]

For current high-precision neutrino oscillation experiments, the calculation of oscillation parameters in the three neutrino oscillation model is mandatory. Historically, the results of most neutrino oscillation experiments were interpreted assuming two neutrino states, which was a valid approximation for the targeted sensitivity. For two generation oscillation, equation 2.6 simplifies to

$$P(\alpha \to \beta) = \sin^2 2\theta \cdot \sin^2\left(\frac{\Delta m^2 L}{4E}\right)$$

where θ is the mixing angle between the two flavor states, and Δm^2 denotes the difference of squared masses. For fixed neutrino energy, the transition probability oscillates between zero and $\sin^2 2\theta$, depending on the oscillation length. The oscillation frequency is defined by the difference in squared masses between the two mass eigenstates. By measuring the transition probability at different oscillation lengths or different neutrino energies, the differences in squared masses and the mixing angle can be inferred. [Pov+15]

2.3.2. Pioneering Neutrino Oscillation Experiments

The first indications for neutrino flavor oscillations were found by results of experiments investigating the solar neutrino flux. The following section is mainly based on the historical overview given in [Pov+15] and the summary in [Zyl+20], unless stated otherwise.

Solar Neutrino Problem

The sun mostly produces energy via the proton-proton cycle as proposed by H. Bethe [BC38]. The net reaction of the cycle fuses protons to Helium according to

$$4\mathrm{p} + 2\mathrm{e}^- \to {}^4\mathrm{He}^{2+} + 2\nu_\mathrm{e} + 26.73\,\mathrm{MeV}$$

There are several intermediate steps involved in this fusion which produce electron neutrinos. The resulting neutrino electron spectrum consists of several different neutrino production processes with different spectra and percentage of the total flux [Pov+15]. The total mean flux of solar electron neutrinos at the earth sums up to $6 \times 10^{10}\,\mathrm{cm}^{-2}\mathrm{s}^{-1}$ with a mean energy of 0.3 MeV [Pov+15]. Davis et al. investigated the solar neutrino flux via the charged current reaction

$$\nu_e + {}^{37}\mathrm{Cl} \rightarrow {}^{37}\mathrm{Ar}^{+} + e^{-} \tag{2.7}$$

in the underground Homestake experiment. The charged current reaction is only sensitive to electron neutrinos and requires a neutrino energy of more than 0.81 MeV for the production of ^{37}Ar. The generated radioactive ^{37}Ar decays via electron capture with a half-life of 35 days. The thereby emitted Auger electron was detected. With this method, R. Davis et al. could prove the existence of solar neutrinos. R. Davis was recognized with the 2002 nobel prize in physics for this discovery [The02]. [DHH68]
However, the measured flux of solar neutrinos was found to be only 30 % of the expected flux [Cle+98]. Similar experiments with different energy thresholds, all solely sensitive to electron neutrinos, confirmed the reduced measured flux of the Homestake experiment [Kir+99; Abd+96]. This neutrino deficit became known as the solar neutrino problem, as it was not clear whether the standard solar model was correct and the measurements were faulty or vice versa.

Super-Kamiokande Experiment

The first experimental proof of neutrino oscillation and thus a possible solution to the solar neutrino problem was found by the Super-Kamiokande experiment in 1998. The Super-Kamiokande detector is an underground, 50 kt cylidrical water Cherenkov detector, instrumented with photomultiplier tubes. The most important measurement was performed with atmospheric neutrinos with energies of 100 MeV and higher. Atmospheric neutrinos are produced as a result of the scattering process of cosmic rays with the atmosphere a few kilometers above the earth's surface. The reaction mainly generates pions that cause a decay chain according to

$$\begin{aligned} \pi^{+} &\rightarrow \mu^{+} + \nu_\mu \Rightarrow \mu^{+} \rightarrow e^{+} + \overline{\nu}_\mu + \nu_e \ , \\ \pi^{-} &\rightarrow \mu^{-} + \overline{\nu}_\mu \Rightarrow \mu^{-} \rightarrow e^{-} + \overline{\nu}_e + \nu_\mu \ . \end{aligned}$$

Thus, the ratio of atmospheric muon neutrinos to electron neutrinos is approximately two. The atmospheric neutrinos scatter off the water molecules in the Super-Kamiokande detector according to

$$\begin{aligned} \nu_e + n &\rightarrow p + e^{-}, \\ \nu_\mu + n &\rightarrow p + \mu^{-}. \end{aligned}$$

The charged leptons form a Cherenkov cone as they are faster than the phase velocity of light in water for a short amount of time. The Cherenkov radiation is measured by the photomultiplier tubes. The shape of the Cherenkov cone differs for electrons and muons which allows the distinction of the flavor of the incident neutrino. Electrons produce a more diffuse ring than muons because of multiple

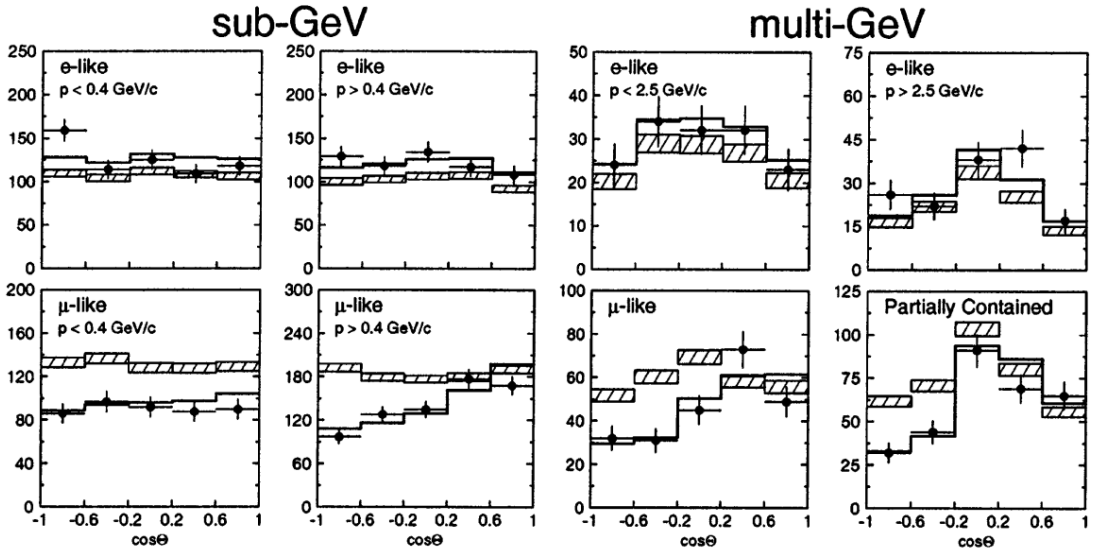

Figure 2.2.: **Measured e-like and μ-like events in the Super-Kamiokande experiment versus the cosine of the zenith angle Θ in the sub- and multi-GeV range.** Downwards going particles with a small travel distance ($\mathcal{O}(10\,\mathrm{km})$) between production and detection are located close to $\cos\Theta \approx 1$, while upwards going particles with long travel distance ($\mathcal{O}(10^4\,\mathrm{km})$) are located close to $\cos\Theta \approx -1$. The hatched region is the prediction for the expected flux if neutrinos do not change their flavors during propagation. The points with error bars are the measurement, the bold line is the best-fit model to describe the data allowing neutrino flavor oscillation. The flux of e-like events (upper panels) seems consistent with the model prediction of the non-oscillation hypothesis. μ-like events (lower panels) do show a clear flux deficit at long propagation length, that is well-described by assuming flavor oscillation of ν_μ to ν_τ. Figure reprinted with permission from reference [Fuk+98]. Copyright 1998 by the American Physical Society.

Coulomb scattering effects and electromagnetic cascades. For neutrinos with energies greater than 100 MeV the charged lepton produced by the incoming neutrino moves into the same direction as the incoming neutrino. This allows to reconstruct if the neutrino crossed the whole earth before entering the detector or whether the neutrino entered the detector from the top. [Fuk+98; Pov+15]
Since the earth is transparent for neutrinos with energies of 100 MeV or higher the expectation for the non-oscillation hypothesis was that the measured flux of neutrinos should be independent of the direction of the incoming neutrino. However, a deficit in the flux of factor of 2 was measured for muon neutrinos which crossed the earth (travel distance of about 10^4 km) compared to muon neutrinos with a flight distance of only a few kilometers (see figure 2.2). This data was inconsistent with the expectation of no flavor oscillations for atmospheric muon neutrinos in the energy range of 0.1 to 10 GeV. The deficit was later on also shown for muon neutrinos with approximately 100 GeV energy. Yet, the electron neutrinos did not show any deviation from the non-oscillation expectation. The conclusion was that electron neutrinos do not show any oscillation on the length scale of the radius of the earth for the investigated energy range. The deficit in the upward muon neutrino flux was

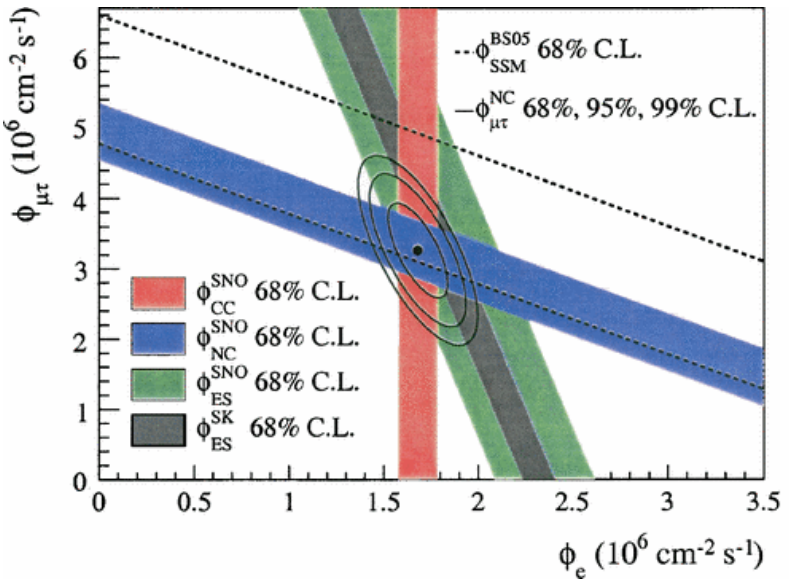

Figure 2.3.: **Flux of solar ^{8}B muon and tauon neutrinos $\phi_{\mu\tau}$ over flux of solar electron neutrinos ϕ_e.** The flux from charged current reactions ϕ^{SNO}_{CC} is shown in red, the neutral current reaction ϕ^{SNO}_{NC} in blue, and elastic scattering in green ϕ^{SNO}_{ES}. The result from Super-Kamiokande is shown as the grey band. The prediction of the standard solar model is visualized by the dashed lines. The black point indicates the solar neutrino flux composition of ϕ_e and $\phi_{\mu\tau}$ based on the fluxes ϕ^{SNO}_{CC} and ϕ^{SNO}_{NC}, and the solid lines represent the 1σ, 2σ, and 3σ contours. The total flux is in good agreement with the standard solar model prediction, the nonzero value of $\phi_{\mu\tau}$ indicates neutrino flavor transformation. Figure reprinted with permission from reference [Aha+05]. Copyright 2005 by the American Physical Society.

explained by an oscillation of muon neutrinos to tauon neutrinos, which could not be identified in the detector. The best fit of an oscillation model to the data lead to the neutrino mixing parameters of $\sin^2 2\theta_{23} > 0.4$ and a squared mass difference of $10^{-3} < \Delta m_{23} < 10^{-1}\,\mathrm{eV}^2$ at 90% confidence level. [Fuk+98; Fuk+99]

Sudbury Neutrino Observatory

The Sudbury Neutrino Observatory (SNO) resolved the solar neutrino problem by providing a direct evidence for the existence of a non-electron neutrino component in the solar neutrino flux [Ahm+01; Ahm+02]. SNO was an underground Cherenkov detector equipped with more than 9000 photomultipliers to detect solar neutrinos with energies of a few MeV. It used ultrapure heavy water as target material in the first measurement phase and heavy water plus 2000 kg of sodium chloride in the second phase. The second phase was especially sensitive to neutrinos from the ^{8}B production in the proton-proton cylce. Solar neutrinos were detected in the SNO experiment via the charged current (see equation 2.8), neutral current (see equation

2.9), and elastic scattering (see equation 2.10) reactions

$$\nu_e + d \rightarrow p + p + e^- , \tag{2.8}$$

$$\nu_{e,\mu,\tau} + d \rightarrow p + n + \nu_{e,\mu,\tau} , \tag{2.9}$$

$$\nu_{e,\mu,\tau} + e^- \rightarrow \nu_{e,\mu,\tau} + e^- , \tag{2.10}$$

with d being the deuterium nucleus in the heavy water target of SNO. The charged current reaction is only sensitive to electron neutrinos since the ^{8}B neutrinos do not have enough kinetic energy to produce a free muon or tauon. The neutral current and elastic scattering reactions are sensitive to all neutrino flavors. The combination of the three reactions allowed to test the solar neutrino flux with regard to all neutrino flavors and therefore probing the standard solar model. [Aha+05]
As shown in figure 2.3, the results of the SNO experiment contained two important discoveries. Firstly, the total neutrino flux is in good agreement with the prediction by the standard solar model. Secondly, the solar neutrino flux contains a non-vanishing muon and tauon neutrino flavor component, giving strong evidence for oscillation of solar electron neutrinos. [Aha+05]

Takaaki Kajita of the Super-Kamiokande collaboration and Arthur B. McDonald of the SNO collaboration were recognized with the physics nobel prize in 2015 for "the discovery of neutrino oscillations, which show that neutrinos have mass" [The15].

2.3.3. Current Research Status

The observation of neutrino oscillation and its implication of a non-zero neutrino mass highlights the role of neutrino physics as a key to physics beyond the Standard Model of elementary particle physics. Consequently, numerous subsequent neutrino oscillation experiments explored and still explore the parameter space of neutrino oscillation (an overview is given in [Zyl+20]). Global analyses of the obtained neutrino data try to form a consistent picture of the oscillation parameters. An overview of the best-fit estimates of one of these global analyses is given in table 2.1.
Two of the major open questions in current neutrino oscillation research are discussed in the following, namely the mass ordering of the neutrinos and the value of the CP-violating phase.

Neutrino Mass Ordering

As stated in table 2.1, oscillation results are inter alia parametrized with two differences of squared masses, namely $\left|\Delta m^2_{21}\right| \approx 7.4 \times 10^{-5}\,\mathrm{eV}^2$ and $\left|\Delta m^2_{32}\right| \approx 2.4 \times 10^{-3}\,\mathrm{eV}^2$. The sign of Δm^2_{21} was found with the oscillation results of solar neutrinos and the Mikheyev-Smirnov-Wolfenstein (MSW) effect [Sal+18].
Wolfenstein showed that coherent forward scattering must to be considered when discussing the oscillation of neutrinos propagating in matter [Wol78; Wol79]. Based on Wolfenstein's work Mikheyev and Smirnov calculated that neutrino mixing can resonantly be increased by a slow continuous decrease of the matter density [MS85]. Solar neutrinos produced in the core have to travel through the sun before reaching the sun's surface. Since the sun produces not only large amounts of electron

Table 2.1.: **Overview of neutrino oscillation parameters obtained from global analyses.** Shown are the best-fit results for the mixing angles θ_{ij}, the CP-violating phase δ, and the differences of the squared masses Δm^2_{ij} for normal and inverted mass ordering. Three neutrino generations are assumed in the model. Values taken from reference [Zyl+20].

Parameter	Normal ordering	Inverted ordering
$\theta_{12}\,(\mathrm{deg})$	$33.82^{+0.78}_{-0.76}$	$33.82^{+0.78}_{-0.76}$
$\theta_{23}\,(\mathrm{deg})$	$48.3^{+1.2}_{-1.9}$	$48.6^{+1.1}_{-1.5}$
$\theta_{13}\,(\mathrm{deg})$	$8.61^{+0.13}_{-0.13}$	$8.65^{+0.13}_{-0.12}$
$\delta\,(\mathrm{deg})$	222^{+38}_{-28}	285^{+24}_{-26}
$\Delta m^2_{21}\ \left(10^{-5}\,\mathrm{eV}^2\right)$	$7.39^{+0.21}_{-0.20}$	$7.39^{+0.21}_{-0.20}$
$\Delta m^2_{32}\ \left(10^{-3}\,\mathrm{eV}^2\right)$	$2.449^{+0.032}_{-0.030}$	$-2.509^{+0.032}_{-0.032}$

neutrinos but also lots of electrons, the electron neutrinos have to travel through matter with high-electron density. While muon and tauon neutrinos only interact via neutral current reactions with the surrounding electrons, electron neutrinos also perform charged current interactions with the electrons. The charged current interactions result in an increased effective mass of the electron neutrinos, which changes the oscillation properties. The comparison of data from solar neutrino experiments with the theoretical description of the MSW effect shows that the product $\Delta m^2_{21} \cdot \cos 2\theta_{12}$ needs to be greater than zero, leading to $\Delta m^2_{21} > 0$. [Sal+18]
The mass splitting Δm^2_{32} is mainly measured in experiments with neutrino oscillation in vacuum such that the oscillation depends only on the absolute value of Δm^2_{32}. Thus, there are two possibilities how the neutrino masses can be ordered. The case $\Delta m^2_{32} < 0$ is called "inverted ordering", whereas $\Delta m^2_{32} > 0$ is called "normal ordering" (see figure 2.4). To reach the necessary statistics to be sensitive on the sign of Δm^2_{32}, one currently needs to combine the data of several different neutrino oscillation experiments and in addition observations from cosmology [Sal+18]. These global analyses find that normal ordering is favored over inverted ordering at the 3σ level [Cap+18].

CP-Violating Phase

CP transformation is the combination of the parity transformation P (inversion of spatial coordinates) and the charge conjugation C (interchange of particle with antiparticle). A violation of the CP symmetry implies that the laws of physics are different for particles and antiparticles, for example the transition probability $P(\nu_\alpha \to \nu_\beta)$ differs from the probability for $P(\overline{\nu}_\alpha \to \overline{\nu}_\beta)$. CP violation is one of the Sakharov conditions to explain the dominance of matter over antimatter in today's universe [Sak91]. The first evidence for CP violation was found in the decay of neutral kaons, the discovery was recognized with the 1980's nobel prize in physics [The80]. Further CP violating decays were later found also for other mesons, for example the B meson. However, since the CP violation in the quark sector is too

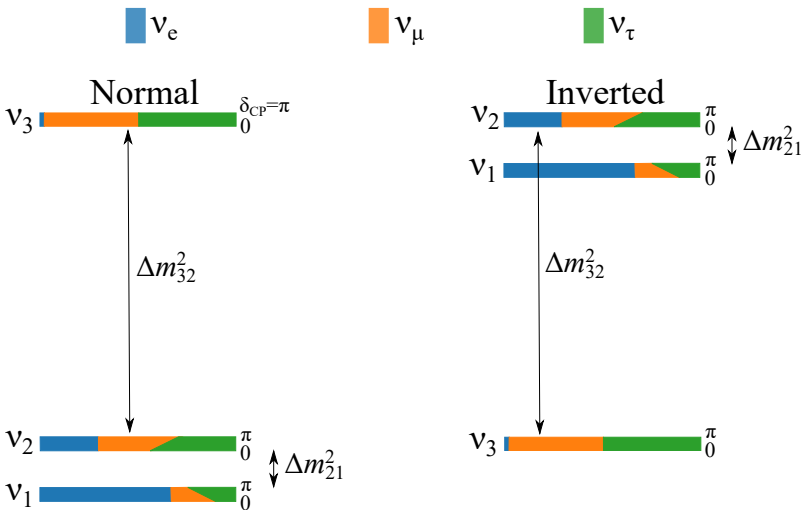

Figure 2.4.: **Possible neutrino mass orderings and flavor composition of mass eigenstates.** $\Delta m^2_{32} > 0$ is called normal mass ordering, whereas $\Delta m^2_{32} < 0$ is called inverted mass ordering. The color coding within one mass eigenstate give the probability to find a certain flavor in the mass eigenstate, depending on possible values of the CP violating phase δ. Schematic figure, not to scale.

small [Jar89] to explain the baryon asymmetry in the universe, a larger source of CP violation is necessary. Consequently, the measurement of the CP-violating phase δ in the PMNS matrix is of interest. [Pov+15]
Values for δ different from 0 or π indicate CP violation in neutrino oscillation. Precise determinations of δ are performed in long-baseline experiments. In these type of experiments neutrinos are produced by a proton beam colliding with a fixed target. Their oscillation behavior is observed in a near (few hundred meters) and a far detector (few hundred kilometers). By changing the selection mechanism in the production, one can either produce a neutrino or an antineutrino beam. Different oscillation behavior for neutrinos and antineutrinos gives direct information about the CP-violating phase. Global analyses indicate a nearly maximal CP-violating phase $|\sin\delta| \approx 1$ and further experiments are planned for high-precision measurements. [Abe+17; Ada+17; Cap+18; Zyl+20]

2.4. Neutrino Mass Generation

The phenomenon of neutrino oscillation shows that neutrinos must posses mass, which is in contradiction to the Standard Model of particle physics. In the following section, the mass generation for fermions in the Standard Model is described. In addition, two approaches are discussed how the Standard Model can be extended to include the neutrino mass.

In the Standard Model, all fermion particles obtain their masses through Yukawa coupling to the Higgs field ϕ after spontaneous symmetry breaking [Zyl+20]. For the electron, the Yukawa coupling is

$$-\mathcal{L}_{\text{Yukawa}} = \lambda_e \overline{L}_e \phi e_R + \text{h.c.}$$

with $L_e = \left(\nu_{e,L}, e_L\right)$ being the left-handed lepton doublet containing the left-handed electron neutrino and left-handed electron component, and e_R being the right-handed electron component. The free coupling constant λ_e has to be determined for each lepton experimentally and can strongly differ for the individual elementary particles. The notation "h.c." is an abbreviation for "Hermitian conjugate". Once the Higgs field acquires a vacuum expectation value v in the electroweak symmetry breaking [Zyl+20], the Yukawa coupling reads

$$-\mathcal{L}_{\text{Yukawa}} = m_e \left[\overline{e}_R e_L + \overline{e}_L e_R\right],$$

with the Dirac electron mass term

$$m_{\text{e}} = \lambda_{\text{e}} \frac{v}{\sqrt{2}}. \tag{2.11}$$

The vacuum expectation value of the Higgs field is determined to $v \approx 246\,\text{GeV}$, the free coupling constant λ has to be measured. For the top quark the coupling constant is close to one, while it is on the order of 10^{-6} for the electron. However, since the Standard Model does not contain right-handed neutrinos, and therefore no corresponding Yukawa interaction term, it describes neutrinos as massless. [Sch20c; Zyl+20]
In detail, there are three reasons why neutrinos are massless in the Standard model of particle physics:

- The Standard Model does not contain right-handed neutrinos to form a Dirac mass term.
- The lepton number is an accidental global symmetry in the Standard Model. Introducing Majorana mass terms would break lepton number conservation.
- The Standard Model Lagrangian shall only contain renormalizable terms.

At least one of these three principles needs to be violated to allow for neutrino masses in the Standard Model. In the following, we will focus on the first two items, how these principles can be violated, and what the consequences are. [Sch20c]

In principle it is possible to introduce right-handed neutrinos. However, they would not participate in any interaction with the fundamental forces of the Standard Model. If right-handed neutrinos are introduced in the Standard Model, the Dirac mass term for neutrinos would look similar to the one for the electron (see equation 2.11). The smallness of the neutrino mass would then be explained by a coupling constant of $\lambda_\nu \lesssim 10^{-11}$. [Sch20c; Zyl+20]

Another way to introduce neutrino masses into the Standard Model is via a combined approach of Dirac and Majorana mass terms [Zub12]. In the following derivation only one neutrino generation is considered.
Majorana mass terms can be introduced under the condition that particles are their own antiparticles, but the discrimination in left- and right-handed neutrinos still remains [Zub12]. The introduction of Majorana mass terms leads to two real masses m_L and m_R for two sterile neutrinos $\text{N}_{\text{L,R}}$ that do not participate in weak interactions, i.e. they do interact only gravitationally [Zub12]. The combination of Dirac

and Majorana masses yields [Zub12]

$$\begin{aligned}\mathcal{L} &= \frac{1}{2}\left(m_D\left(\overline{\nu}_{\mathrm{L}}\mathrm{N}_{\mathrm{R}} + \overline{\mathrm{N}}_{\mathrm{L}}\nu_{\mathrm{R}}^{C}\right) + m_{\mathrm{L}}\overline{\nu}_{\mathrm{L}}\nu_{\mathrm{R}}^{C} + m_{\mathrm{R}}\overline{\mathrm{N}}_{\mathrm{L}}^{C}\mathrm{N}_{\mathrm{R}}\right) + \mathrm{h.c.} \\ &= \frac{1}{2}\left(\overline{\nu}_{\mathrm{L}}, \overline{\mathrm{N}}_{\mathrm{L}}^{C}\right)\begin{pmatrix} m_{\mathrm{L}} & m_{\mathrm{D}} \\ m_{\mathrm{D}} & m_{\mathrm{R}} \end{pmatrix}\begin{pmatrix} \nu_{\mathrm{R}}^{C} \\ \mathrm{N}_{\mathrm{R}} \end{pmatrix} + \mathrm{h.c.}.\end{aligned}$$

The mass eigenvalues are the eigenvalues of the matrix, resulting in

$$\tilde{m}_{1,2} = \frac{1}{2}\left((m_{\mathrm{L}} + m_{\mathrm{R}}) \pm \sqrt{(m_{\mathrm{L}} - m_{\mathrm{R}})^2 + 4m_{\mathrm{D}}^2}\right).$$

Three cases are typically derived from this equation [Zub12; Zyl+20; Pov+15]:

1. Pure Dirac case: $m_{\mathrm{L}} = m_{\mathrm{R}} = 0$, leading to $\tilde{m}_{1,2} = m_{\mathrm{D}}$. In that case, the Dirac neutrino can be written as a pair of degenerated Majorana neutrinos.
2. Pure Majorana case: $m_{\mathrm{D}} = 0$, resulting in $\tilde{m}_{1,2} = m_{\mathrm{L,R}}$. The neutrinos have thus pure Majorana character.
3. Seesaw mechanism: $m_{\mathrm{R}} \gg m_{\mathrm{D}}$ and $m_{\mathrm{L}} = 0$, leading to two mass eigenvalues with $m_1 = \frac{m_D^2}{m_R}$ and $m_2 \approx m_R$. The mass m_1 is identified as the mass of the neutrino, that participates in the weak interaction, while m_2 is the mass of the sterile neutrino. Consequently, the mass of the active neutrino is assumed to be resulting from a Dirac mass, that is similar to the one of the other fermions, but this mass is suppressed by the mass of the sterile neutrino.

2.5. Experimental Determination of the Neutrino Mass Scale

Numerous theoretical approaches exist to give mass to the neutrinos as extensions to the Standard Model of particle physics. Due to the smallness of the neutrino mass, neutrino mass generations that deviate from the pure Yukawa coupling to the Higgs field are considered, for example the seesaw mechanism discussed in section 2.4. Possible neutrino mass generations can be categorized into a group leading to quasi-degenerate mass eigenstates, and another group leading to hierarchical eigenstates. A measurement of the neutrino mass scale comprises thus important information about the underlying neutrino mass generation. However, until now only upper limits on the neutrino mass scale could be provided. [Zyl+20]
In the following, three complementary approaches to determine the neutrino mass scale are presented

2.5.1. Cosmology

Neutrinos are the most abundant massive particles in the universe [FLS00]. The standard model of cosmology predicts neutrinos as a relic of the big bang with an abundance of 336 neutrinos/cm^3 comprising all flavors. Due to their high abundance

neutrinos contribute roughly 7 % to the total matter density of the universe. Thus, high-precision cosmological data allows to investigate neutrino properties. [Bil10]

The sum of the light neutrinos $\sum_i m_i$, with m_i below few eV, plays a role in the large scale structure formation of the universe. Due to their small interaction rate neutrinos can carry away energy out of clamped matter. Neutrinos therefore smear out structures smaller than their free streaming length. The neutrino's free streaming length depends on many parameters, inter alia the sum of the light neutrino mass eigenvalues. [Bil10; FdR21]
The influence of neutrino masses can mainly be seen in the power spectrum, which quantifies the density fluctuations in the universe, and in the temperature anisotropies of the cosmic microwave background radiation [Sch06]. The power spectrum is measured with the Baryon Oscillation Spectroscopic Survey by observing more than one million galaxies [Ala+20]. The cosmic microwave background is investigated by satellite measurements, for example the PLANCK satellite mission [Pla+20].
Using the neutrino oscillation parameters and assuming that the lightest neutrino mass eigenstate has zero mass constrains the sum of light neutrinos to $\sum_i m_i \geq 5.8 \times 10^{-2}\,\mathrm{eV}$ (normal ordering) or $\sum_i m_i \geq 9.9 \times 10^{-2}\,\mathrm{eV}$ (inverted ordering). A combined analysis of the cosmological data of structure formation, including the cosmic microwave background, yields

$$\sum_i m_i < 0.11\,\mathrm{eV}$$

at 95 % confidence level [Ala+20]. Next generation experiments aim to be sensitive to $\sum_i m_i \geq 2 \times 10^{-2}\,\mathrm{eV}$ (see for example reference [Aba+19]). If the expectations from oscillation parameters are met, these experiments should be able to measure a non-vanishing sum of light neutrino masses at the 3σ level. [FdR21]

Despite giving stringent boundaries on the sum of neutrino masses, the extraction of the neutrino mass from cosmological observations are model-dependent. The boundaries are vulnerable to modifications of the standard model of cosmology, for example the expansion rate of the universe or if neutrinos are unstable but with a large half-life. The stability of neutrinos can relax the boundaries by up to one order of magnitude. [Esc+20; FdR21]

2.5.2. Neutrinoless Double-Beta Decay

As shown in section 2.4, a Majorana nature of neutrinos is an elegant way to introduce mass terms for the neutrinos and to explain the small mass of the active neutrinos via the seesaw mechanism. If neutrinos are Majorana fermions, the lepton number is not a conserved quantity but can be violated in some rare processes. Searches for neutrinoless double-beta ($0\nu\beta\beta$) decay are a powerful tool to probe lepton-number conservation. [Pov+15]

Double-beta decay is a second-order weak decay with typical half-life of larger than 10^{19} years. Two neutrons in a nucleus are converted to two protons, to two electrons, and to two electron antineutrinos

$$(A, Z) \rightarrow (A, Z+2) + 2\mathrm{e}^- + 2\overline{\nu}_\mathrm{e}\ .$$

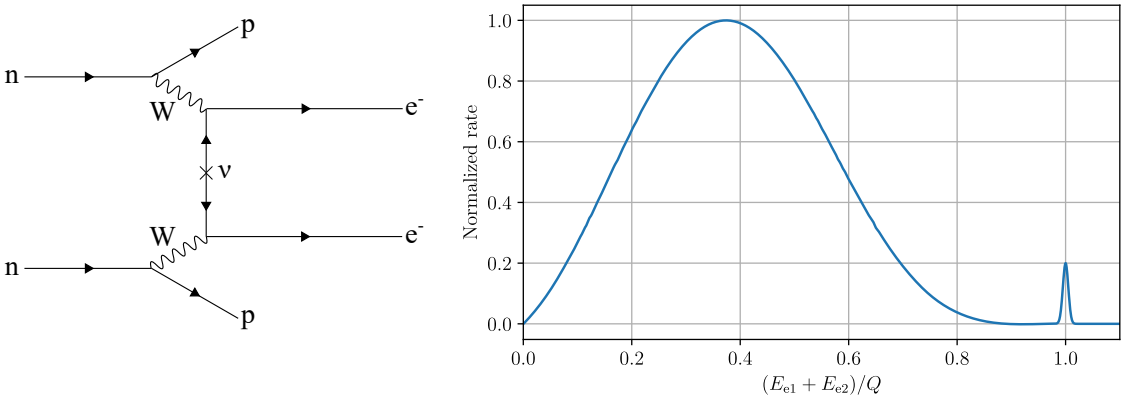

Figure 2.5.: **Feynman graph of the 0νββ and combined spectrum of the 2νββ and 0νββ decay.** The Feynman graph of the simultaneous decay of two neutrons into protons and electrons is shown on the left side. If the neutrino is a Majorana fermion, the neutrino produced in one decay can be absorbed at the other vertex, resulting in the 0νββ decay. The continuous spectrum of the 2νββ decay versus the total energy of both emitted electrons is shown in the plot on the right side. The 0νββ manifests itself as a peak at $(E_{e1} + E_{e1})/Q = 1.0$ at the endpoint of the continuous spectrum of the 2νββ. Note that the size of the peak is artificially increased here for better visibility.

The double-beta decay is allowed if the final nucleus has a larger binding energy than the original nucleus. It was first directly measured in 1987 in ^{82}Se [EHM87]. There are 35 naturally occurring isotopes that can undergo double-β decay [TZ02]. [Pov+15]

If neutrinos are of Majorana type, the 0νββ decay is an allowed process

$$(A, Z) \rightarrow (A, Z + 2) + 2e^{-} .$$

It violates the lepton number conservation by two units. The Feynman diagram of this process is shown in the left graph of figure 2.5. In an experiment, the electrons resulting from the 0νββ decay would be visible as a sharp peak above the endpoint of the 2νββ decay spectrum (see right plot of figure 2.5). [Zyl+20]
The half-life of the 0νββ is related to the effective Majorana neutrino mass

$$\langle m_{\beta\beta} \rangle = \left| |U_{e1}|^2 m_1 + |U_{e2}|^2 m_2 e^{i\alpha_1} + |U_{e3}|^2 m_3 e^{i\alpha_2} \right| ,$$

with U_{ei} being the entries of the PMNS matrix, m_i the mass eigenvalues of the neutrino mass eigenstates, and α_i the unknown CP-violating Majorana phases (see section 2.3.1) [GPM12]. The Majorana phases could cause cancellation of terms, so that $\langle m_{\beta\beta} \rangle$ is smaller than any of the eigenvalues of the mass eigenstates. Assuming that only 0νββ decay contributes to lepton number violations, its decay half-life $T_{1/2}^{0\nu\beta\beta}$ can be calculated to

$$T_{1/2}^{0\nu\beta\beta} = \left(\mathcal{G} \left| \mathcal{M} \right|^2 \langle m_{\beta\beta} \rangle^2 \right)^{-1} \approx 10^{27-28} \left(\frac{0.01\,\text{eV}}{\langle m_{\beta\beta} \rangle} \right) \text{ years},$$

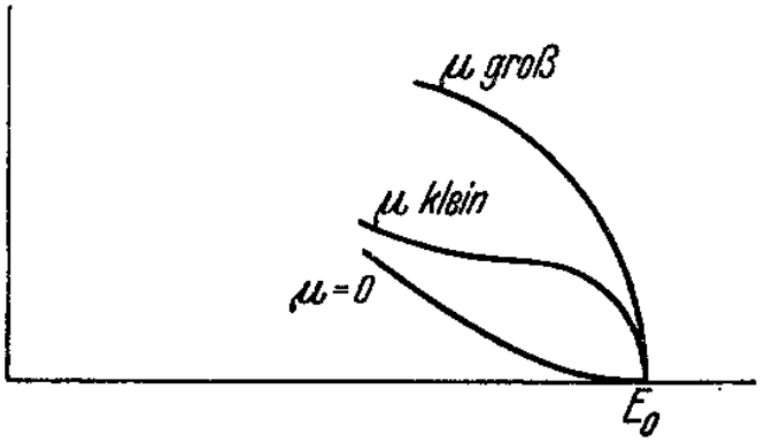

Figure 2.6.: **Neutrino mass influence on the shape of the β-decay spectrum near the endpoint as calculated by Fermi.** Three different sketches of the shape of the β-decay spectrum near the maximal electron energy E_0 are given in this plot, namely a large neutrino mass ("μ groß"), a small neutrino mass ("μ klein"), and a vanishing neutrino mass ("$\mu = 0$"). Reprinted by permission from Springer Nature from [Fer34].

with the phase-space factor $\mathcal{G}$ and the matrix element of the nuclear decay process $\mathcal{M}$. From this estimation of the decay half-life it is clear that huge amounts of source material are required to probe the $0\nu\beta\beta$ decay. [DPR19]
The KamLAND-Zen experiment currently gives one of the strongest boundaries on $\langle m_{\beta\beta} \rangle$, searching for the $0\nu\beta\beta$ decay in ^{136}Xe with roughly 13 tons of Xe-loaded liquid scintillator. The resulting lower boundary for the decay half-life is $T_{1/2}^{0\nu\beta\beta} > 1.07 \times 10^{26}$ years at 90 % confidence level, leading to an upper bound on the effective Majorana mass of $\langle m_{\beta\beta} \rangle < 0.06 - 0.16\,\text{eV}$. The range of the mass boundary is caused by different theoretical predictions of the nuclear matrix element $\mathcal{M}$. [Zyl+20] It should be noted that this neutrino mass boundary requires the Majorana nature of neutrinos.

2.5.3. Single-Beta Decay

The neutrino mass inference via the single-beta decay is purely based on kinematics and is therefore often referred to as "direct neutrino mass measurement". As shown in figure 2.6, Fermi suggested that the shape of the β-decay spectrum close to the kinematic endpoint can be used to determine the mass of the neutrino. By comparing his theoretical considerations with the measurements of the β-decay spectrum at that time, Fermi concluded that the neutrino mass must be zero or at least small compared to the electron's rest mass. [Fer34]
We will summarize the principle of direct neutrino mass measurements in the following paragraphs based on reference [FdR21], unless stated otherwise. For further details we refer the interested reader to reference [FdR21].

Beta-Decay Spectrum and Observable

Based on Fermi's Golden Rule, the β-decay spectrum can be derived as

$$\frac{\mathrm{d}\Gamma}{\mathrm{d}E} = C \cdot F(Z,E) \cdot p\,(E + m_\mathrm{e})\,(E_0 - E) \times \sum_{i=1,3} |U_{ei}|^2 \sqrt{(E_0 - E)^2 - m_i^2}\;\Theta\,(E_0 - E - m_i)\,, \tag{2.12}$$

with the Fermi function $F(Z,E)$ taking into account the interaction of the outgoing electron with the nuclear Coulomb field. The maximum kinetic energy of β electrons in the absence of the neutrino mass is denoted as E_0. The step function $\Theta\,(E_0 - E - m_i)$ ensures energy conversation. The factor C is a constant for super-allowed transitions and comprises inter alia the nuclear matrix elements. Near the endpoint of the β-decay spectrum several approximations can be made, for example the Fermi function can be assumed to be constant. In first-order approximation, this leads to

$$\frac{\mathrm{d}\Gamma}{\mathrm{d}E} \approx 3r_0\,(E_0 - E)\sqrt{(E_0 - E)^2 - \sum_{i=1,3} |U_{ei}|^2\, m_i^2} \times \Theta\left(E_0 - E - \sum_{i=1,3} |U_{ei}|^2\, m_i^2\right)\,, \tag{2.13}$$

with r_0 being a constant related to the total activity. Consequently, the experimental observable in direct neutrino mass measurements is the incoherent sum of the mass eigenvalues

$$m_\nu^2 = \sum_{i=1,3} |U_{ei}|^2\, m_i^2\;. \tag{2.14}$$

In contrast to the observable measured in the $0\nu\beta\beta$ decay, no cancellations due to possible Majorana phases of m_ν^2 can appear. The single beta-decay mass m_ν can be used to deduce the neutrino mass scale independent of the underlying neutrino nature. It does not require the neutrino to be a Majorana fermion. The direct neutrino mass inference basically relies on the well-understood β-decay model. [FdR21] As visible in equation 2.12 and 2.13, the effect of the neutrino mass on the β-decay rate is mostly pronounced close to the endpoint, where $E - E_0$ is close to zero. Thus, direct neutrino mass experiments follow Fermi's approach and investigate the endpoint region of the β-decay spectrum to search for the characteristics of a non-vanishing neutrino mass, which is shown in figure 2.7. According to equation 2.13, it is in principle possible to experimentally resolve the different neutrino mass eigenstates with high-resolution scans of the β-decay spectrum. However, no planned experiment has such an excellent energy resolution. Nevertheless, by measuring m_ν^2 it is possible to indirectly resolve the individual masses of the neutrino mass eigenstates by exploiting the precision measurements of the PMNS matrix. [FdR21]

Choice of Isotope

A fundamental decision that must be made for any direct neutrino mass experiment is the decision on the source isotope of the β-decay. Several aspects must be considered in the decision making:

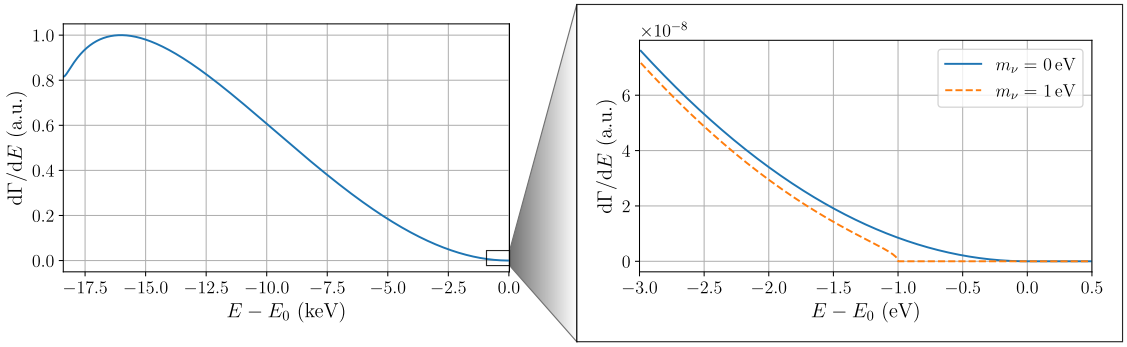

Figure 2.7.: **Single β-decay spectrum of tritium as function of the electron energy *E*.** The plot on the left shows the whole single β-decay spectrum of tritium. The plot on the right is a zoom of the β-decay spectrum into the last 3 eV below the endpoint. As visible, the shape of the spectrum differs for a non-zero neutrino mass, here exemplary for $m_\nu = 1\,\mathrm{eV}$ (orange line), from a spectrum with vanishing neutrino mass (blue line). Note that the rate in the endpoint region is significantly smaller than the maximum rate of the overall spectrum.

- Equation 2.13 shows that the β-decay spectrum rises quadratically for $E - E_0 \gg m_\nu^2$. The fraction of decays that produces electrons in the region m_ν near the endpoint scales thus with $(m_\nu/E_0)^3$. A low endpoint is thus advantageous to maximize the count rate in the signal region. Furthermore, a lower endpoint is also advantageous considering the experimental realization of the energy analysis of the β-decay electrons.

- The specific activity of the source material is of similar importance as the low endpoint. For example, tritium decays in helium via a superallowed β decay, which results in a specific activity of $3.6 \times 10^{14}\,\mathrm{Bq/g}$. In contrast, Cs-135 decays via a forbidden decay, resulting in a small specific activity of $1.5 \times 10^{6}\,\mathrm{Bq/g}$. An experiment using Cs-135 as source isotope of the β-decay would thus need much more source material compared to one employing tritium to obtain the same amount of β-decay electrons in the endpoint region. The significant lower endpoint of Cs-135 compared to tritium is outweighed by tritium's larger specific activity.

- Depending on the experimental set-up it is advantageous if the used isotope can be used in a gaseous state. This reduces solid states effects like energy losses of the β-decay electrons.

- A simple atomic structure is important as interactions of the decay electron with hull electrons smear out the energy distribution. As will be shown in section 3.3.1, the modeling of the spectrum must take into account the electronic final states of the daughter nucleaus. The theoretical prediction of the final states can be conducted with higher precision for simple atomic structures.

Despite its high endpoint of 18.6 keV, tritium is the isotope by choice for many neutrino mass experiments in the last years. Its superallowed decay results in a high specific activity and allows for several simplifications in the theoretical model. Additionally, tritium can be used in a gaseous source at temperatures larger than 30 K. Coulomb interactions of the decay electron with the single hull electron can

mostly be neglected. Additionally, the half-life of tritium of 12.3 years facilitates the experimental storage on a time scale of several years. [FdR21]

Direct Neutrino Mass Measurements

Most direct neutrino mass experiments employ tritium as source material due to its excellent properties as described in the previous paragraph. Since tritium decays via the β-minus decay it emits an electron together with an electron antineutrino (see equation 2.1). Consequently, direct neutrino mass experiments using tritium are sensitive to the effective mass of the electron antineutrino. In the present thesis, we assume that the antineutrino mass equals the neutrino mass ($m_{\overline{\nu}} = m_{\nu}$), as predicted by the CPT symmetry.

First attempts to determine the neutrino mass were already made by Curran et al. in 1948, employing tritium in a gaseous source. They could set an upper limit on the neutrino mass of 1.7 keV [CAC48]. The best limit on the neutrino mass from a direct neutrino mass measurement is currently set by the KATRIN experiment to

$$m_{\nu} = \sqrt{\sum_{i=1,3} |U_{ei}|^2 \, m_i^2} < 0.8\,\mathrm{eV}$$

at 90 % confidence level [Ake+21a]. KATRIN is the first direct neutrino mass experiment to ever set an upper limit on the neutrino mass in the sub-eV range. This limit is achieved by using molecular tritium in a windowless gaseous source (more details on the experimental setup are given in section 3.2). Compared to predecessor experiments, the upper limit on the neutrino mass is improved by more than a factor of two [Kra+05; Ase+11]. The projected KATRIN sensitivity is 200 meV at 90 % confidence level after three years of net measurement time [KAT05].
The "Project 8" experiment aims to reach sensitivities down to 40 meV on the neutrino mass by using atomic tritium and cyclotron radiation emission spectroscopy. This high-precision measurement would allow to directly probe the inverted neutrino mass ordering [Esf+17].

However, not all direct neutrino mass measurements rely on tritium as source material. Holmium-163 is also an interesting source material due to its low endpoint on the order of 2.8 keV. Holmium-163 decays via electron capture into Dysprosium-163 under the emission of an electron neutrino. The emitted radiation during the electron capture as well as the radiation emitted during de-excitation of the Dysprosium-163 allow neutrino mass measurements. Based on this method, the ECHo experiment is designed to achieve sub-eV sensitivity on the effective electron neutrino mass and could already set an upper limit of 150 eV (95 % C.L.). Further direct neutrino mass experiments based on the Holmium-163 decay are the HOLMES and the NuMECS experiments. [Vel+19; Bec+19; Cro+16]

3. The Karlsruhe Tritium Neutrino Experiment

The KArlsruhe TRItium Neutrino (KATRIN) experiment aims to directly and model-independently measure the effective electron antineutrino mass by investigating the β-decay spectrum shape near the endpoint. The projected sensitivity of KATRIN for a net measurement time of three years is 0.2 eV at 90 % confidence level [KAT05]. This corresponds to an improvement of factor ten in sensitivity compared to KATRIN's predecessor experiments in Mainz [Kra+05] and Troitsk [Ase+11].
The following chapter comprises three aspects. In section 3.1, we derive the MAC-E filter principle as key feature for the energy analysis of the β-decay electron in KATRIN. The KATRIN experimental setup is described in detail in section 3.2. As a last aspect, the model description, analysis, and software tools that are relevant for a successful neutrino mass determination with KATRIN and thus also for the thesis at hand are introduced in section 3.3.

3.1. MAC-E Filter Principle

The KATRIN experimental setup is centered around the Main Spectrometer, that analyzes the kinetic energy of the β-decay electrons. The energy analysis is based on the principle of Magnetic Adiabatic Collimation with Electrostatic (MAC-E) filtering, which was first proposed by Beamson et al. [BPT80]. KATRIN's predecessor experiments at Troitsk and Mainz used the MAC-E filter technique as well [Kra+05; Ase+11], albeit on a smaller scale.
The MAC-E filter technique features eV-scale energy resolution for energies around 18.6 keV, which corresponds to the kinematic endpoint of the tritium β-decay spectrum. Furthermore, it allows high luminosity for signal electrons, as it accepts electron angles up to nearly 2π. [KAT05] Consequently, it is an excellent choice for KATRIN, since a successful neutrino mass measurement requires large statistics and at the same time good energy resolution.
In total, the KATRIN experimental setup includes three MAC-E filter spectrometers, namely the Pre-, the Main and the Monitor Spectrometer. We will, focus on the Main Spectrometer in the following sections as it is a major component of the KATRIN experiment. The working principle of the Main Spectrometer can trivially be adopted for the Pre- and Monitor Spectrometer.
The following derivation of the MAC-E filter principle in the context of the KATRIN experiment is based on references [BPT80; Val09; Beh16; Kle+19]. We refer the interested reader to these works for further details.

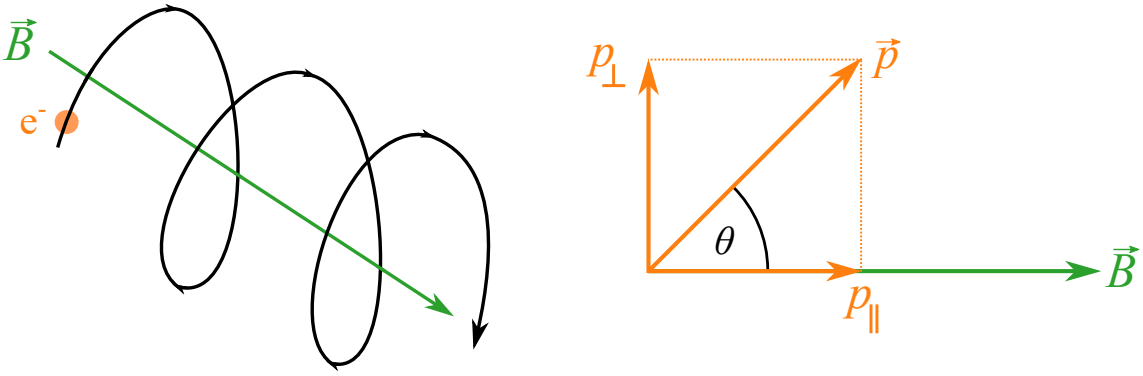

Figure 3.1.: **Schematic drawing of the cyclotron motion of an electron around a magnetic field line (left) and decomposition of the electron's momentum in parallel and transversal components (right).** As soon as the β-decay electron (drawn in orange) is produced, it follows the strong magnetic field $\vec{B}$ (green) in a cyclotron motion (black). Using the pitch angle θ, the electron's momentum $\vec{p}$ in the cyclotron motion can be written as a component $p_\parallel$ parallel to the magnetic field and a component $p_\perp$ perpendicular to it.

3.1.1. Measurement Principle of a MAC-E Filter

A MAC-E filter exploits the interplay of electric and magnetic fields to analyze an electron with regards to its kinetic energy. The β-decay electrons, that are investigated in KATRIN, are isotropically emitted in the gaseous tritium source. Strong magnetic fields confine the electrons in radial direction and guide them adiabatically towards the Main Spectrometer, where their energy is analyzed. The derivation of the MAC-E filter transmission function parameters is in the following discussed for the non-relativistic case. The β-decay electrons from tritium decay posses at maximum kinetic energies around 18.6 keV, leading to a Lorentz factor

$$\gamma_{\max} = \frac{1}{\sqrt{1-\beta^2}} < 1.04,$$

that justifies the non-relativistic approach.
As soon as the β-decay electron is generated, it follows the magnetic field lines in a cyclotron motion towards the MAC-E filter (see left graph of figure 3.1). The cyclotron motion is defined by the pitch angle θ between the electron momentum $\vec{p}$ and the magnetic field $\vec{B}$. As shown in the right graph of figure 3.1, the electron momentum can be rewritten with the pitch angle θ as a component $\vec{p}_\parallel$ parallel and a component $\vec{p}_\perp$ perpendicular to the magnetic field

$$|\vec{p}_\parallel| = |\vec{p}| \cos\theta,$$
$$|\vec{p}_\perp| = |\vec{p}| \sin\theta.$$

Similarly, the total kinetic energy E of the electron can be rewritten as a parallel $E_\parallel$ and a transversal $E_\perp$ energy contribution

$$\begin{aligned} E &= \frac{\vec{p}^2}{2m_\mathrm{e}} = \frac{\vec{p}_\parallel^2 + \vec{p}_\perp^2}{2m_\mathrm{e}} \\ &= \frac{|\vec{p}|^2 \cos^2\theta}{2m_\mathrm{e}} + \frac{|\vec{p}|^2 \sin^2\theta}{2m_\mathrm{e}} \\ &= E_\parallel + E_\perp, \end{aligned} \tag{3.1}$$

with m_e as the rest mass of the electron. In case an electric field parallel to the magnetic field is applied, the electron is repelled by the electrostatic barrier if

$$E_\parallel < qU_\mathrm{ret}$$

where q is the electric charge of the electron and U_ret the applied retarding voltage. The transversal energy component $E_\perp$ is not considered by the energy analysis of the electrostatic barrier. Since the β-decay electrons are isotropically emitted in KATRIN's tritium source, the analysis of only the longitudinal energy component would lead to a bad energy resolution, making an accurate and precise neutrino mass measurement impossible. However, the MAC-E filter technique enables a nearly full analysis of the whole kinetic energy. [BPT80; Val09; Beh16; Kle+19]
The MAC-E filter exploits the so-called "first adiabatic invariant" to transform the perpendicular energy component to contribute to the longitudinal energy. In the cyclotron motion, the electron defines a magnetic moment

$$\mu = |\vec{\mu}| = \frac{q}{2m_\mathrm{e}} \left|\vec{l}\right| = \frac{E_\perp}{\left|\vec{B}\right|},$$

with $\left|\vec{l}\right|$ being the absolute orbital angular momentum of the electron. The magnetic moment becomes invariant if the gradient $\mathrm{d}\vec{B}/\mathrm{d}t$ is sufficiently small during one cyclotron motion of the electron, fulfilling

$$\left| \frac{1}{\left|\vec{B}\right|} \frac{\mathrm{d}\vec{B}}{\mathrm{d}t} \right| \ll \frac{\omega_C}{2\pi} = \frac{q\left|\vec{B}\right|}{2\pi m_\mathrm{e}}, \tag{3.2}$$

where ω_C denotes the cyclotron frequency. If equation 3.2 is fulfilled, the transformation of the initial transversal kinetic energy component $E_{\perp,i}$ to the final transversal kinetic energy component $E_{\perp,f}$ can be written in dependence of the corresponding magnetic field strengths $\left|\vec{B}_i\right|$ and $\left|\vec{B}_f\right|$ to

$$E_{\perp,f} = E_{\perp,i} \frac{\left|\vec{B}_f\right|}{\left|\vec{B}_i\right|}. \tag{3.3}$$

By choosing $\left|\vec{B}_f\right| \ll \left|\vec{B}_i\right|$ and fulfilling equation 3.2, we can transform the transversal energy component into a longitudinal energy component, as the total kinetic electron energy E is conserved during the process. On the example of the KATRIN experiment, an electron starts with the transversal energy $E_{\perp,\mathrm{src}}$ in the source magnetic field B_src. Assuming no energy loss from the starting position of the electron up to

the MAC-E filter, this energy component transversal to the magnetic field translates to

$$E_{\perp,\mathrm{ana}} = E_{\perp,\mathrm{src}} \frac{B_{\mathrm{ana}}}{B_{\mathrm{src}}}$$

in the energy analysis. In the limit that the whole energy of the decay electron is stored in the transversal component at the start $E_{\perp,\mathrm{src}} = E$, we obtain the energy filter width ΔE of the MAC-E filter by calculating the non-analyzed transversal energy component

$$\Delta E = E_{\perp,\mathrm{ana}} = E \cdot \frac{B_{\mathrm{ana}}}{B_{\mathrm{src}}}. \tag{3.4}$$

The energy filter width is often also referred to as the energy resolution of the MAC-E filter. [BPT80; Val09; Beh16; Kle+19]
By exploiting equation 3.1 and 3.3, we can derive the transformation of pitch angles from the initial θ_i to the final θ_f state in MAC-E filters to

$$\sin^2 \theta_f = \sin^2 \theta_i \frac{\left|\vec{B}_f\right|}{\left|\vec{B}_i\right|}. \tag{3.5}$$

This allows us to write the non-analyzed transversal energy component at the point of energy analysis with the starting pitch angle θ_{src} and the electron's kinetic energy as

$$\begin{aligned} E_{\perp,\mathrm{ana}} &= E \cdot \sin^2 \theta_{\mathrm{ana}} \\ &= E \cdot \sin^2 \theta_{\mathrm{src}} \frac{B_{\mathrm{ana}}}{B_{\mathrm{src}}}. \end{aligned}$$

The electron's longitudinal energy component $E_{\parallel,\mathrm{ana}}$ for energy analysis is thus

$$\begin{aligned} E_{\parallel,\mathrm{ana}} &= E - E_{\perp,\mathrm{ana}} \\ &= E - E \cdot \sin^2 \theta_{\mathrm{src}} \frac{B_{\mathrm{ana}}}{B_{\mathrm{src}}}. \end{aligned}$$

Since the electron can overcome the electrostatic barrier if $E_{\parallel,\mathrm{ana}} > qU_{\mathrm{ret}}$, we can write down the MAC-E filter transmission function for an electron with total energy E, pitch angle θ_{src} in the source magnetic field B_{src}, applied MAC-E filter retarding potential qU_{ret}, and filter magnetic field B_{ana} to

$$\mathcal{T}(E, \theta_{\mathrm{src}}, U_{\mathrm{ret}}) = \begin{cases} 1, & \text{if } E - E\frac{B_{\mathrm{ana}}}{B_{\mathrm{src}}} \sin^2 \theta_{\mathrm{src}} \geq qU \\ 0, & \text{else} \end{cases}. \tag{3.6}$$

The transmission function shows that a MAC-E filter acts as an integrating high-pass filter. All electrons above the threshold energy are transmitted and those below are rejected.[Val09; Beh16; Kle+19]

3.1.2. Transmission Function of the Main Spectrometer

Due to the KATRIN source properties and the beamline magnetic field design, several modifications of the transmission function and the field evolution have to be considered, which are discussed in the following.

The first modification that we consider is that the β-decay electrons are emitted isotropically in the source. Electrons with pitch angles in the interval $[0°, 90°)$ in the source magnetic field are transported towards the Main Spectrometer. However, not all pitch angles can overcome the retarding potential due to the finite energy resolution of the Main Spectrometer. According to the transmission function derived in equation 3.6, an electron can only overcome the retarding potential, if

$$E - E\frac{B_{\text{ana}}}{B_{\text{src}}}\sin^2\theta_{\text{src}} - qU_{\text{ret}} \geq 0.$$

This leads to a maximally allowed pitch angle θ_{src} in the source to overcome the retarding potential qU_{ret} to

$$\theta_{\text{src}} \leq \theta_0 = \arcsin\left(\sqrt{\frac{E - qU_{\text{ret}}}{E}\frac{B_{\text{src}}}{B_{\text{ana}}}}\right), \tag{3.7}$$

if the total kinetic electron energy E is larger than qU_{ret}. The angle θ_0 defines a cone with solid angle $\Delta\Omega$, containing electrons that can be transmitted through the Main Spectrometer. The probability of electrons to be transmitted is thus $\Delta\Omega$ with respect to the full forward solid angle of 2π, leading to

$$\frac{\Delta\Omega}{2\pi} = 1 - \cos\theta_0\,. \tag{3.8}$$

By inserting equation 3.7 into equation 3.8 and exploiting the relation $\cos(\arcsin\sqrt{x}) = \sqrt{1-x}$, we obtain the transmission function $T(E,U)$ of a MAC-E filter with isotropic electron source to

$$T(E,U) = \begin{cases} 0, & \text{if } E \leq qU \\ 1 - \sqrt{1 - \frac{E-qU}{E}\frac{B_{\text{src}}}{B_{\text{ana}}}}, & \text{if } qU < E \leq qU + \Delta E\,, \\ 1, & \text{if } qU + \Delta E < E \end{cases} \tag{3.9}$$

where ΔE denotes the energy resolution of the MAC-E filter as given in equation 3.4. [Val09; Beh16; Kle+19]

Another effect that alters the transmission function is the beamline magnetic field design. In the KATRIN experiment, the magnetic field B_{src} in the gaseous tritium source is not equal the maximal magnetic field B_{max} along the beamline. The maximal magnetic field is located at the exit of the Main Spectrometer inside the Pinch magnet (PCH, see also chapter 4). This leads to a desired effect called "magnetic mirror", that reflects electrons with large pitch angles in the PCH. Electrons with large pitch angles have higher probability to loose energy in the tritium source due to scattering processes (see section 7.1.2) and also loose more energy via synchrotron radiation, compared to electrons with small pitch angles. To reduce the arising systematic uncertainty on the measured neutrino mass from these energy losses, the magnetic mirror reflects β-decay electrons above a certain pitch angle. In the absence of electric fields, which is a valid approximation for the grounded beam tubes at the exit of the Main Spectrometer and the tritium source, we calculate the maximum acceptance pitch angle θ_{max} with equation 3.5 to be

$$\theta_{\text{max}} = \arcsin\left(\sqrt{\frac{B_{\text{src}}}{B_{\text{pch}}}}\right). \tag{3.10}$$

The maximum acceptance angle, also called "cut-off angle", is $\theta_{\text{max}} = 50.5°$ for the nominal KATRIN setup with $B_{\text{src}} = 2.5\,\text{T}$ and $B_{\text{pch}} = 4.2\,\text{T}$. The absence of transmitted electrons with large pitch angles modifies the transmission function derived in equation 3.9 in two ways. Firstly, the energy resolution has to be modified compared to equation 3.4 to

$$\Delta E = E \cdot \frac{B_{\text{ana}}}{B_{\text{pch}}}. \tag{3.11}$$

Additionally, a normalization has to be included in the transmission function due to the missing β-decay electrons with large pitch angles, leading to

$$T(E,U) = \begin{cases} 0, & \text{if } E \leq qU \\ 1 - \sqrt{1 - \frac{E-qU}{E}\frac{B_{\text{src}}}{B_{\text{ana}}}}, & \text{if } qU < E \leq qU + \Delta E \\ 1 - \sqrt{1 - \frac{B_{\text{src}}}{B_{\text{pch}}}}, & \text{if } qU + \Delta E < E \end{cases}.$$

The transmission function calculated for the configuration used in KATRIN's first two neutrino mass measurement campaigns KNM1 and KNM2 for the case with and without magnetic reflection is shown in figure 3.2. The energy resolution with magnetic reflection is $\Delta E = 2.8\,\text{eV}$, the fraction of accepted electrons is approximately 36.4 %. [Val09; Beh16; Kle+19; Ake+21b]
For analyses carried out in the course of this thesis, it is necessary that the transmission function covers the range between zero and unity. We therefore apply a normalization, leading to

$$T(E,U) = \begin{cases} 0, & \text{if } E \leq qU \\ \frac{1-\sqrt{1-\frac{E-qU}{E}\frac{B_{\text{src}}}{B_{\text{ana}}}}}{1-\sqrt{1-\frac{B_{\text{src}}}{B_{\text{pch}}}}}, & \text{if } qU < E \leq qU + \Delta E \\ 1, & \text{if } qU + \Delta E < E \end{cases}. \tag{3.12}$$

The KATRIN-specific working principle of the MAC-E filter is visualized in figure 3.3. A schematic drawing of the Main Spectrometer vessel together with a sketch of the magnetic field lines and the retarding potential for electrons is presented in the upper graph. The Main Spectrometer is designed such, that the analyzing points for all electrons are located in a flat plane at the center of the Main Spectrometer, the so-called analyzing plane. The magnetic flux

$$\Phi = \int \vec{B} \cdot \mathrm{d}\vec{A}.$$

is a conserved quantity in KATRIN, which means that the flux tube radius significantly increases in the Main Spectrometer compared to the tritium source due to the decreasing magnetic field (shown in the second graph of figure 3.3). This puts requirements on the geometrical Main Spectrometer design (see also section 3.2.4). The applied electric retarding field in axial direction is shown in the lower graph of figure 3.3. The retarding potential has not only the task to produce the retarding potential at the analyzing point, it also must ensure that the magnetic collimation happens adiabatically in the Main Spectrometer. In the nominal configuration, as used in KNM1 and KNM2, the magnetic field strength drops by approximately a

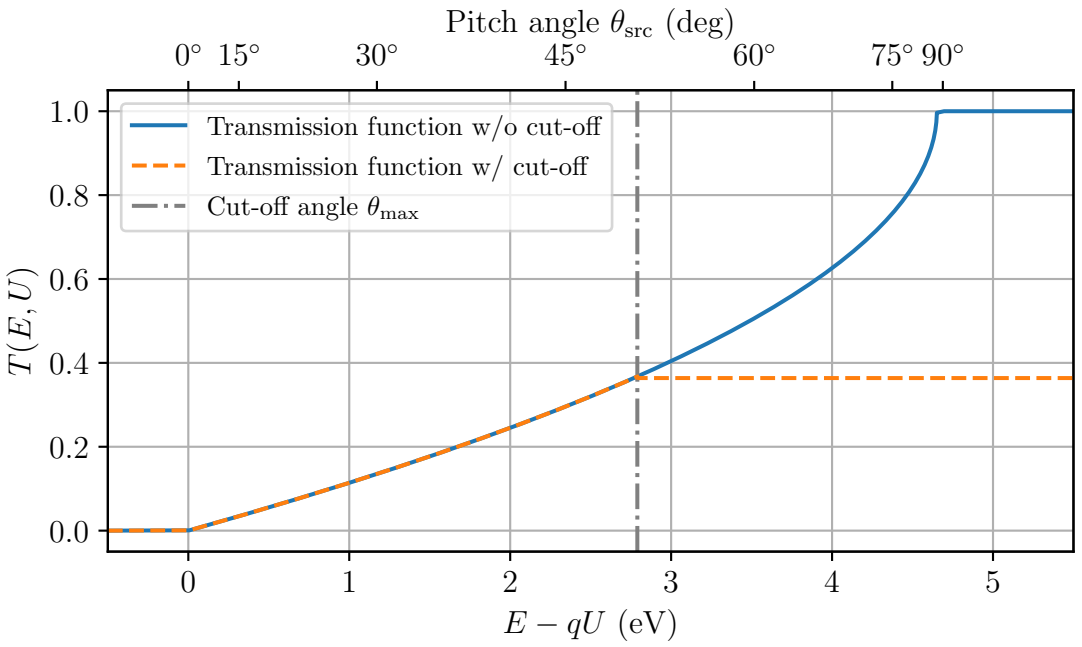

Figure 3.2.: **Transmission function $T(E,U)$ of the KATRIN Main Spectrometer for an isotropic source versus the surplus energy $E - qU$.** The transmission function indicates the fraction of transmitted electrons through the Main Spectrometer at certain surplus energy $E - qU$, according to the derived function in equation 3.12. The calculated transmission function uses a mean electron energy of 18.6 keV and the magnetic field configuration of KNM1 and KNM2. The transmission function for a scenario in which the maximal magnetic field in the beamline equals the source field is shown with the blue function. The KATRIN-specific scenario with the PCH as maximal magnetic field in the beamline, resulting in a magnetic mirror for pitch angles larger than 50.5° (gray vertical line), is presented with the orange function.

factor 5000 from Main Spectrometer entrance to the analyzing plane. Since the collimation of the electrons' pitch angles has to happen adiabatically for proper energy analysis, it is necessary to fulfill the requirement given in equation 3.2. The electric field therefore has the task to slow the electrons down, so that they experience a sufficiently small $\mathrm{d}\vec{B}/\mathrm{d}t$ gradient. The electrode design of the Main Spectrometer (see section 3.2.4) allows for fine-shaping of the electric field inside the spectrometer according to these requirements. [Val09; Ake+21b]

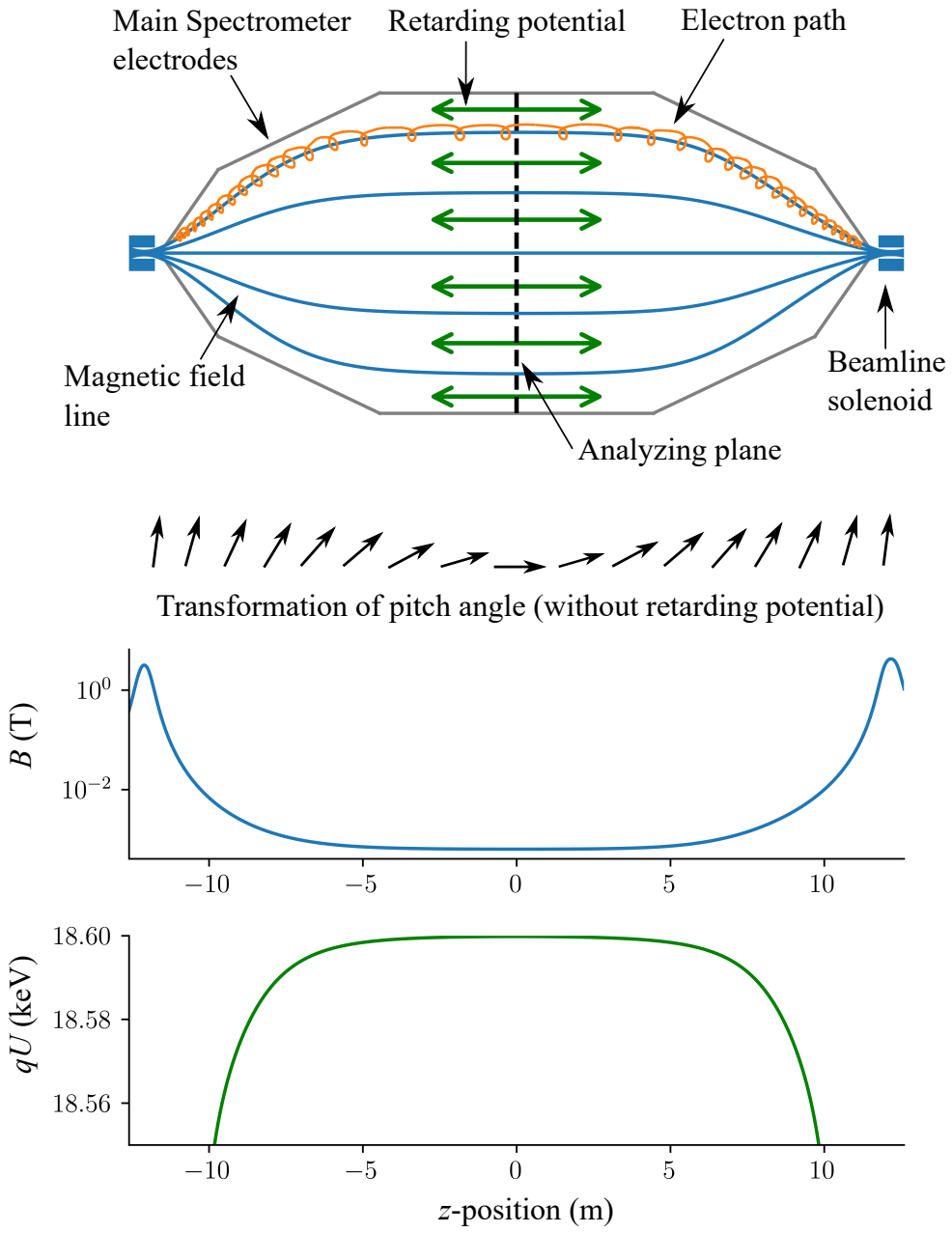

Figure 3.3.: **Sketch of the MAC-E filter principle on the example of the Main Spectrometer.** A schematic drawing of the Main Spectrometer electrodes (drawn in gray) together with the super-conducting beamline solenoids (drawn as blue boxes) at both ends of the Main Spectrometer are shown in the upper-most graph. The β-decay electrons follow the magnetic field lines (drawn in blue) in a cyclotron motion (visualized in orange), an electric retarding potential (indicated by the green arrows) is applied that reaches its maximum at the analyzing plane (black dashed line). The black arrows below the Main Spectrometer schematically indicate the magnetic adiabatic collimation of the pitch angle in the spectrometer, without taking the retarding potential into account. The collimation is caused by a reduction of the magnetic field by a factor of 5000 from the source towards the center of the Main Spectrometer, as shown in the third graph. The electric retarding potential analyzes the longitudinal kinetic energy component of the electron (shown in the lower graph).

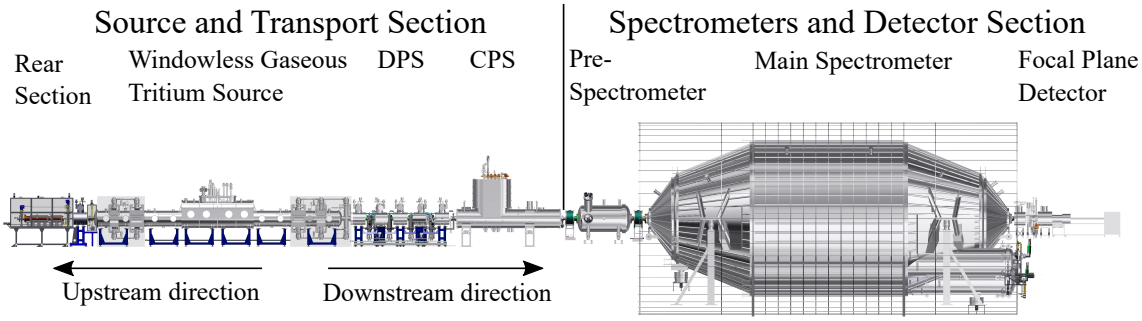

Figure 3.4.: **Overview of the KATRIN experimental setup.** The β-decay electrons, produced in the Windowless Gaseous Tritium Source are guided by magnetic fields towards the Main Spectrometer for energy analysis. The upstream and downstream directions in KATRIN are defined via the flux direction of the β-decay electrons from source to detector for energy analysis.

3.2. Experimental Setup

The 70 m-long experimental setup of KATRIN is shown in figure 3.4. It can be divided into two major sections. The Source and Transport Section (STS) comprises the Rear Section, the Windowless Gaseous Tritium Source (WGTS), the Differential Pumping System (DPS), as well as the Cryogenic Pumping System (CPS). The Pre-Spectrometer, Main Spectrometer, and Focal Plane Detector (FPD) system constitute the Spectrometers and Detector Section (SDS).
The β decay of gaseous molecular tritium in the WGTS produces decay electrons. If their momentum has a non-vanishing component in downstream direction, they are magnetically guided by super-conducting magnets towards the DPS and CPS. The task of the DPS and CPS is to reduce the number of tritium molecules and ions in the beam tube. The kinetic energy of the decay electrons is subsequently analyzed by the Pre- and Main Spectrometer utilizing the MAC-E filter technique. The β-decay electrons, that can overcome the Main Spectrometer retarding potential, are counted at the FPD. [KAT05]
In the following sections, we present the individual hardware components of the KATRIN experiment with the focus on the relevance for the thesis at hand.

3.2.1. Rear Section

The Rear Section is located at the upstream end of the KATRIN beamline and mostly contains calibration and activity monitoring tools. A technical drawing of the Rear Section is shown in figure 3.5. In the objective of the present thesis, the Rear Section has three key features. Firstly, a high resolution angular-selective photoelectron source is installed here. Secondly the rear wall separates the Rear Section from the WGTS, and thirdly two X-ray detectors monitor the tritium source activity.

The high-resolution angular-selective photoelectron source (“e-gun”) can emit a pencil electron beam of narrow energy and angular distribution towards the FPD to probe electromagnetic fields along the KATRIN beamline (see sections 5.3.3 and

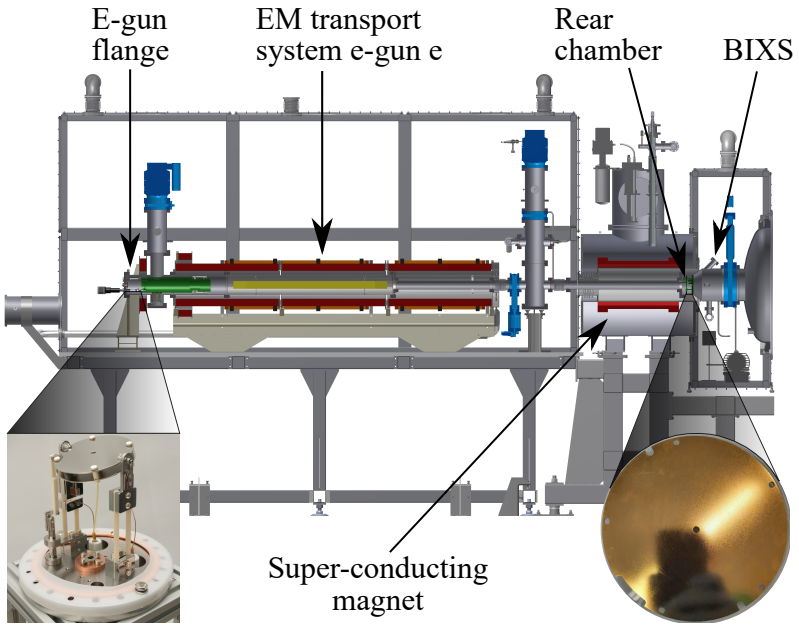

Figure 3.5.: **Experimental setup of the Rear Section.** The gold-coated rear wall is located in the rear chamber and separates the e-gun setup from the WGTS beam tube. The BIXS detector exploits the X-ray emission that the β-decay electrons cause when they collide with the rear wall to monitor the source activity. The Rear Section e-gun setup consists of the e-gun flange in which the photoelectrons are produced and firstly accelerated, aswell as the following electromagnetic transport system that guides and further accelerates the e-gun beam towards the WGTS. Photographs kindly provided by R. Sack.

6.2) or conduct calibration measurements (see section 7.3). For this purpose, the 3 m-long e-gun setup in the Rear Section consists of a metallic photocathode followed by an electrostatic acceleration system [Sch21]. An explanation on the e-gun working principle is given in section 5.3.3 or in detail in references [Sac20; Sch21].

The rear wall is a gold-coated stainless steel disk with a diameter of 14.5 cm that separates the Rear Section from the WGTS. A hole with a diameter of 0.5 cm is located at the center of the rear wall to allow the e-gun electron beam to enter the WGTS beam tube. The geometrical and magnetic design of the Rear Section is optimized that the magnetic flux tube of signal β-decay electrons is exactly mapped onto the rear wall. Besides the FPD, the rear wall is the only surface in the experimental setup, that is in contact with the flux tube. Due to this contact, the rear wall has a key role in defining the starting potential within the WGTS beam tube. A low-density plasma within the WGTS beam tube is formed as consequence of the β decay, as each single β-decay electron can ionize neutral gas molecules in the source leading to increasing numbers of free charges [Höt12]. The mobility of the ionized gas molecules is strongly limited in radial direction by the magnetic field, however, they can freely move in longitudinal direction, along the beam tube axis. This can lead to different plasma potentials along the beam tube axis, which defines the reference potential of β-decay electrons at the moment of their production relative to the Main Spectrometer. As the Main Spectrometer is not sensitive to the the ax-

ial place of origin of an individual decay electron, an unrecognized axial instability of the plasma in the WGTS can produce a bias on the measured neutrino mass. For the final KATRIN sensitivity, the spatial plasma instabilities have to be smaller than 10 mV [Kuc+18]. Since the vacuum potential is dominated by the electrical potential of the surface, the rear wall can tune the plasma potential in longitudinal direction by exploiting the mobility of free charge carriers along the beam tube axis. For this purpose, the rear wall's surface potential can be tuned with a bias voltage up to ±500 V. [Bab14; Kuc16; Fri20]

The Beta-Induced X-ray Spectroscopy (BIXS) detector is part of the Rear Section and is used for continuous activity monitoring of KATRIN's tritium source. Decay electrons, that are emitted in downstream direction in the WGTS are magnetically guided towards the rear wall. The total β-decay electron flux onto the rear wall amounts approximately to 10^{11} electrons/s. The decay electrons produce X-ray radiation during the adsorption process in the gold coating on the rear wall, that is monitored by two silicon drift detectors. The combined count rate of the two BIXS detector systems in the Rear Section allows activity stability monitoring on the 0.1 %-level within 100 s measurement time. [Ake+21d]

3.2.2. Windowless Gaseous Tritium Source

The ultra-luminous Windowless Gaseous Tritium Source (WGTS) provides the necessary activity of up to 10^{11} Bq to perform a high-statistics spectroscopy close to the β-decay endpoint region. In the following, we introduce the basic working principle of the WGTS. For a detailed technical description, please see reference [Ake+21d]. Additionally, a tool is presented to monitor the tritium gas purity in the WGTS beam tube.

The 16 m-long WGTS cryostat comprises inter alia several insulation layers, seven super-conducting magnets, over 800 sensors and valves [Hei18], as well as five beam tube elements with 90 mm diameter. A CAD drawing of the WGTS cryostat as well as a visualization of the WGTS working principle is given in figure 3.6. The central beam tube is 10 m long and contains in nominal operation mode more than 99 % of the gas amount in the whole KATRIN beamline. High-purity molecular tritium gas continuously flows through small orifices at the axial center of WGTS beam tube with an injection pressure of about 3 μbar. The tritium gas can decay inside the beam tube while flowing towards the WGTS front and rear end. A magnetic field of approximately 2.5 T, produced by the seven super-conducting magnets, magnetically guide the arising β-decay electrons towards both ends of the WGTS. Decay electrons emitted in downstream direction, and thus towards the front end, are used for neutrino mass measurements (also referred to as "signal electrons" in the following). The β-decay electrons emitted in upwards direction eventually collide with the rear wall and are thereby used for activity monitoring (see section 3.2.1). Both ends of the central beam tube are windowless to prevent energy loss of the β-decay electrons when leaving the source section. Since also gas molecules do stream through both ends of the central beam tube, a differential pumping section equipped with turbo-molecular pumps is attached on both ends ("DPS-1R/F"). Four smaller beam tubes with 1 m length connect the beamline to the neighboring pump port or to the rear wall (rear end) and transport section (front end). This pumping section removes

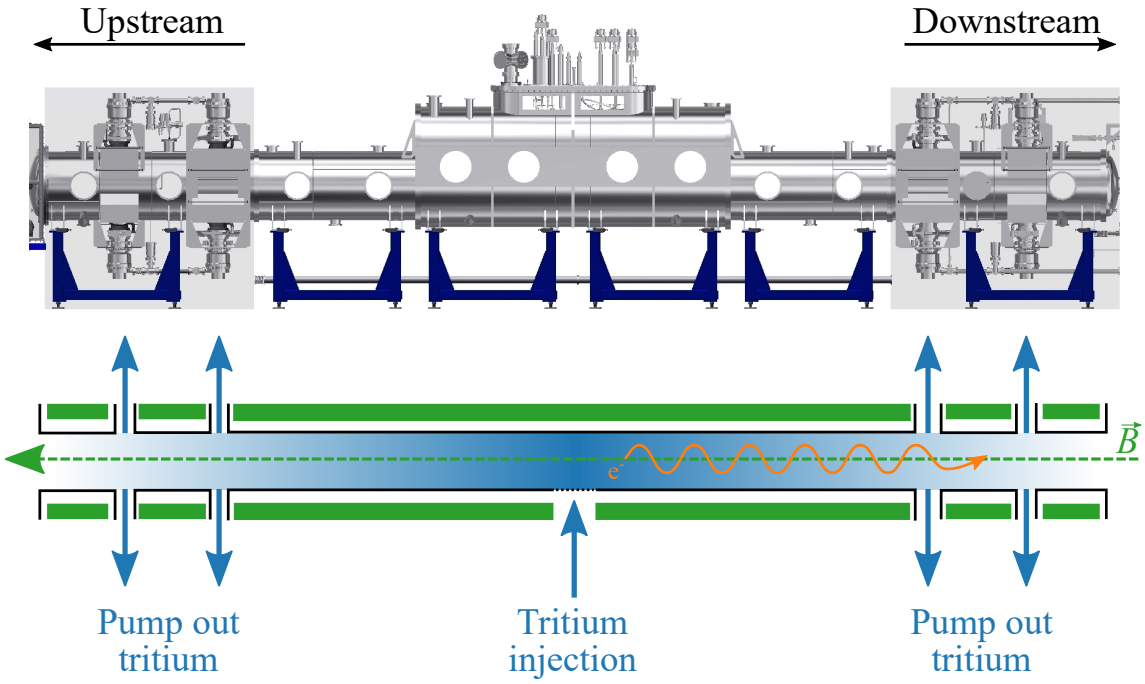

Figure 3.6.: **CAD drawing of the WGTS (upper part) and schematic working principle (lower part).** All five CPS beam tube elements (drawn in black) are located inside the warm bore of super-conducting magnets (drawn in green). Molecular tritium gas (drawn in blue) is injected at the axial center of the 10 m-long WGTS central beam tube, where it can freely stream towards both ends of the WGTS. Towards the rear and front end, the two differential pumping sections DPS-1R/F pump out tritium and feed it back to the inner loop. The β-decay electrons (drawn in orange) that are born in the WGTS are guided to the rear or front end by the magnetic field. Figure inspired by A. Marsteller [Mar20a].

roughly 99 % of the gas inside the beam tube, lowering the number of molecules inside the whole KATRIN beamline to avoid tritium contamination in vulnerable parts of the experiment's setup, for example in the spectrometers. The central requirement on the WGTS is to provide high and stable activity on a constant level over several measurement campaigns, leading to certain requirements on the applied technique. In the following, we therefore summarize the most-important aspects of the WGTS magnetic field stability, technical realization of the beam tube temperature cooling, and present the WGTS tritium loops system. [Kuc+18; Ake+21d]
The seven-superconducting magnets define the starting magnetic field of the β-decay electrons and shall magnetically guide the decay electrons towards both ends of the WGTS beam tube. Therefore, the seven super-conducting solenoids with warm bores are arranged in a straight line inside the WGTS cryostat, surrounding the five beam tube sections interconnected with four pump ports. The WGTS magnet system is described in more detail in section 4.2.2. The KATRIN requirement on the solenoids yields a stability of the magnetic field of better than 0.03 % per month, which is met by power supplies, that provide a current with greater stability than 10 ppm per 8 h. The experimental setup of the super-conducting magnets is designed for a total field strength of 3.6 T in the central WGTS beam tube. However, commissioning measurements of the whole KATRIN beamline show that the solenoid magnets should

operate at 70 % design magnetic field to suppress the risk of quenching [Are+18a; Are+18b]. Therefore, the central WGTS solenoids are operated at a nominal field of 2.5 T during neutrino mass measurements [Are+18b]. [Ake+21d]
The requests on the WGTS beam tube cooling is two-folded for successful neutrino mass measurements. Firstly, it is designed to deliver a beam tube temperature below 100 K to reduce the conductance of the beam tube. Only at these low temperatures, the tritium gas flow velocity inside the WGTS is small enough to keep the necessary amount of tritium in the central beam tube to enable decay activities on the order of 10^{11} Bq. Secondly, the temperature stability needs to be better than 0.1 % in the central beam tube to keep the tritium gas amount at a constant level during neutrino mass measurements. The requirements for the central beam tube cooling are met by a two-phase neon cooling system that doesn't require any mechanical pumping. Therefore, two tubes are brazed to both sides of the central beam tube and are filled with liquid and gaseous neon, both occupying about half of the cross section. The liquid neon evaporates due to heat input of the beam tube and diffuses at one end of the cooling pipe, where it is re-liquefied and re-injected [Gro+08; Gro09]. An exchange of coolants and adjusting the coolant's pressure allow to set and fine-tune the beam tube temperature to various absolute values. The neighboring beam tube parts are also cooled by a two-phase neon cooling system, while the two outer-most parts are only cooled with gaseous neon. Since the tritium gas amount at both WGTS ends is significantly lower compared to the central beam tube, the temperature requirements at the ends of the beam tubes are not as stringent. The temperature of the beam tube is monitored with in total 52 platinum wire-wound glass sensors of type Pt500 or Pt1000 [Gro+11], 24 of them installed at the central beam tube. [Ake+21d]
The WGTS requires a daily throughput of roughly 40 g tritium per day for operation at the design values [Hei18]. This can only be achieved by means of a closed gas loop system at the Tritium Laboratory Karlsruhe (TLK) [Dör+05]. The TLK loop system consists of the inner and the outer loop, that are connected. The primary task of the inner loop system is to provide a stable injection rate of tritium into the central WGTS beam tube. This is enabled by using a temperature- and pressure-stabilized buffer vessel, that is connected to the tritium injection chamber via a 5 m-long capillary. A uniform injection of tritium into the beam tube is ensured by 415 injection ports, arranged azimuthally homogeneous around the beam tube. Tritium gas that is pumped out at the DPS-1R/F is purified with a permeator, removing non-hydrogen-isotopologues. Subsequently, the gas is re-injected into the buffer vessel in the inner loop system, maintaining the circuit. Additionally, around 1 % of the polluted tritium is replaced by pure tritium from the outer loop, leading to a constant tritium purity level above 95 %. The tritium purity in the inner loop is monitored by the LARA system, that is presented in the following paragraph. The task of the outer loop is to supply the KATRIN experiment with pure tritium as well as to collect and recycle degraded tritium gas. The exhaust gas from the inner loop is reprocessed with respect to hydrogen isotope recovery and impurity removal in the TLK infrastructure. Commissioning measurements of the loop system with deuterium indicate a stable injection pressure on the relative 10^{-5} level, exceeding the KATRIN requirement of 0.1 % by nearly two orders of magnitude. [Kuc+18; Ake+21d]

The LARA system has the task to monitor the WGTS gas composition that is injected into the beam tube in real time. Its working principle is based on Laser Raman spectroscopy. We expect, that the WGTS tritium gas contains some impurities, mainly deuterium and hydrogen from the reservoir gas and due to outgassing. These impurities have a different final state distribution than tritium, which influences the kinetic energy of the β-decay electrons (see also section 3.3.1). An inaccurate gas composition in the model can lead to a neutrino mass bias in the analysis. The gas composition must thus be taken into account in the analysis. Furthermore, activity detectors (for example BIXS) can be used together with the gas composition information for precise monitoring of the gas amount inside the WGTS. [Ake+21d]
The LARA monitoring system can be implemented as a non-invasive and fast inline monitoring tool. Furthermore, Laser Raman spectroscopy is able to provides the necessary information on the tritium purity as well as the ratio of the most common impurities, HT to DT. We refer the interested reader to the references [Sch+13; Jam+13; Fis+11] for the explanation of the working principle of LARA. Commissioning measurements reveal a relative measurement precision of 3×10^{-4} on the gas composition, which is well within the KATRIN requirement. [Ake+21d]

3.2.3. Transport Section

The Transport Section is located between the WGTS and the SDS (see figure 3.4). It consists of the Differential Pumping System (DPS) and the Cryogenic Pumping System (CPS). Their primary task is to reduce the tritium flow rate into the SDS by at least 14 orders of magnitude, since already small amounts of tritium in the spectrometers can produce a large background rate that endangers KATRIN neutrino mass measurements [KAT05]. In addition, β-decay electrons have to be transported adiabatically to the spectrometers. In the following, we describe the working principle of the DPS and CPS. Furthermore, the forward beam monitor is also presented as an activity monitoring tool in the CPS.

The DPS is the upstream neighbor of the WGTS. It is the second upstream differential pumping stage after the DPS-1F, located in the WGTS cryostat (see section 3.2.2). The DPS adiabatically guides the electrons from the WGTS to the CPS, while reducing the neutral tritium flow rate, in combination with the DPS-1F, by at least seven orders of magnitude. Furthermore, tritium ions from the WGTS, that would also be magnetically guided towards the SDS, are blocked and removed. [KAT05]
To meet the requirements, the DPS is constructed as a chicane. The single beam tube elements in the DPS are horizontally tilted by 20° relative to each other (see figure 3.7). This geometry prevents a direct line of sight from the WGTS to the SDS. Charged particles, for example β-decay electrons, are adiabatically guided downstream through this setup by five super-conducting magnets operating at 4 T. Six pump ports are installed between the magnets, each one equipped with a turbomolecular pump. Electric neutral particles are not guided by the magnetic fields, leading to collisions with the beam tube walls, which increases their pumping probability. Tritium ions follow the magnetic field lines. However, electrostatic dipoles and ring-shaped electrodes induce an $\vec{E} \times \vec{B}$ drift of the ions towards the walls, where they are neutralized and pumped-out or reflected towards the source. [Fri+19; Ake+21d]

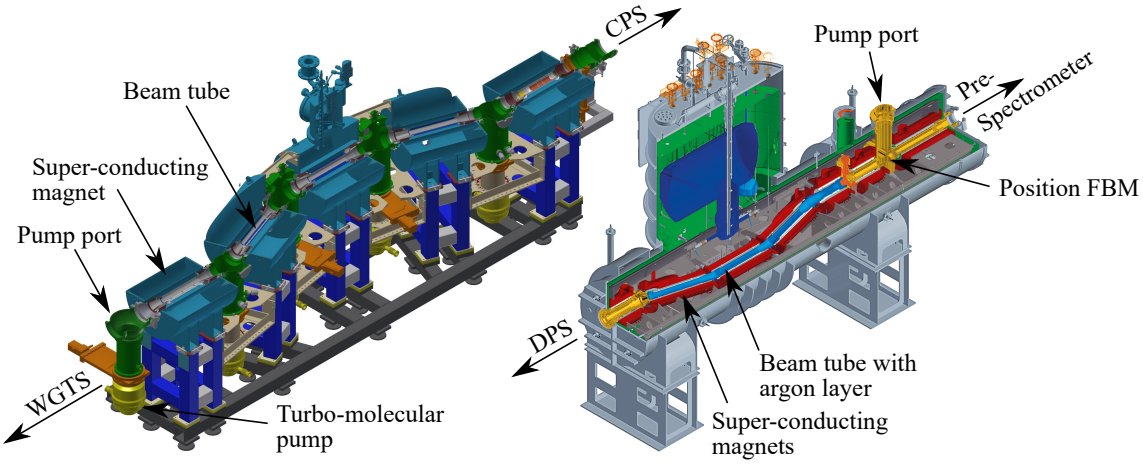

Figure 3.7.: **CAD drawing of the Differential (left) and the Cryogenic (right) Pumping System.** The electrons enter the DPS from the WGTS and are guided adiabatically through the chicane by the five super-conducting magnets. Neutral particles are likely to be pumped out by one of the six pump ports. Following the DPS, the β-decay electrons enter the CPS through which they are also adiabatically guided by super-conducting magnets towards the Pre-Spectrometer. A condensed argon layer on the beam tube walls forms a cold trap for neutral particles. The Forward Beam Monitor FBM can be inserted into the flux tube at the downstream end of the WGTS to monitor the activity of the WGTS. Figure adapted from [Fri+19], CC BY 4.0.

Based on the data of KNM1 and KNM2 with 98 % pure tritium, the combined reduction factor of the DPS-1F in the WGTS and the DPS is calculated to 9.6×10^7 [Mar+21], meeting the KATRIN requirement.

The CPS is located between the DPS and the Pre-Spectrometer. Similar to the DPS, the CPS adiabatically guides the β-decay electrons while further reducing the tritium flow rate coming from the DPS by at least seven orders of magnitude.
Following the DPS, the gas flow is in a regime where a reduction of the flow rate by another seven orders of magnitude is not achievable via additional turbo-molecular pumps. Therefore, a cryo-sorption pump with a condensed argon layer prepared on the gold-plated inner beam tube wall is chosen. Similar to the DPS, three of the seven CPS beam tube elements are tilted horizontally and arranged in a chicane to prevent a direct line of sight from entrance to exit (see figure 3.7). The tilting is implemented to increase the probability for electrically neutral particles to hit the inner beam tube wall. After hitting the inner beam tube wall, the neutral particles are eventually adsorbed by the cold trap of the condensed argon layer that is prepared on the 3 K-cold beam tube surface. The inner surface of the cold trap is enlarged by 90 circular fins to further increase the adsorption probability. In nominal measurement mode, the argon frost must be regenerated approximately every 60 days before accumulating too much tritium. To prepare a new frost layer, the CPS beam tube is heated up to 80 K and purged with helium. The β-decay electrons are adiabatically and magnetically guided by the fields from super-conducting magnets through the CPS chicane without collisions with the inner beam tube wall. [Fri+19; Ake+21d]
First CPS commissioning measurements show that the design beam tube tempera-

ture cannot be reached. Nevertheless, a limit on the reduction factor of better than 10^8 is measured with deuterium. This surpasses the KATRIN requirement by at least one order of magnitude. [Röt17; Röt19; Fri+19]

The Forward Beam Monitor (FBM) is an activity detector, that can be inserted in the beamline at the downstream end of the CPS (see figure 3.7) to directly measure the β-decay electron flux coming from the WGTS with large statistics. For this purpose, the FBM detector board can be shifted from the side into the beamline by a 2 m-long bellow. Two independent motion systems allow to move the detector board through the whole flux tube with 0.1 mm precision. During neutrino mass measurements, the detector board is located in the outer rim of the flux tube to avoid shadowing parts of the flux tube that are used for neutrino mass analysis. It is expected that the outer rim of the flux tube is representative for activity fluctuations. During KNM1, the FBM detector board is equipped with two silicon *p-i-n* diode detectors with an energy threshold of about 5 keV. Additionally, a Hall sensor is mounted on the detector board to measure the local magnetic field, which is around 0.84 T in the center of the flux tube. A PT-1000 sensor records the detector board temperature, as the *p-i-n* diode detectors as well as the Hall sensor are temperature dependent. [Beg+21; Ake+21d] After KNM1, the two *p-i-n* diode detectors are replaced by one seven pixel silicon drift detector to improve the energy resolution to roughly 200 eV and to test a novel detector design development [Urb19].

3.2.4. Pre-, Main and Monitor Spectrometer

The Pre-, the Main and the Monitor Spectrometers are all operated as MAC-E filters (see section 3.1). Thus, they house the same or similar technology. To avoid repetitions, we focus on the Main Spectrometer in the following as key component of energy analysis in KATRIN, and keep the description of the Pre- and Monitor Spectrometer rather short.
In all spectrometers, the electromagnetic fields have to be designed such that the magnetic adiabatic collimation is completed before applying the maximal retarding potential, to avoid for example early retardation (see references [Val09; Erh16]). A sophisticated high-precision high-voltage system together with an unique large-volume air-coil system fulfills these requirements for the Main Spectrometer. Additionally, the Main Spectrometer vacuum system is designed to reach pressures in the 10^{-11} mbar-regime to reduce background effects originating from inside the spectrometer, which is crucial to reach KATRIN's final sensitivity goal.

Magnetic Field System of the Main Spectrometer

The Main Spectrometer magnetic field system has the task to fulfill magnetic adiabatic collimation of the electron's momentum, before the longitudinal kinetic energy of the electron is analyzed by the applied electric retardation. Two geometrical requirements to the Main Spectrometer arise from this task.
Firstly, the magnetic field change along one cyclotron motion of the electrons has to be small (as defined in equation 3.2) to enforce the collimation process to happen adiabatically. Therefore, the Main Spectrometer has a total length of 23 m [Ake+21d].
Secondly, the design energy resolution of the Main Spectrometer is smaller than 1 eV.

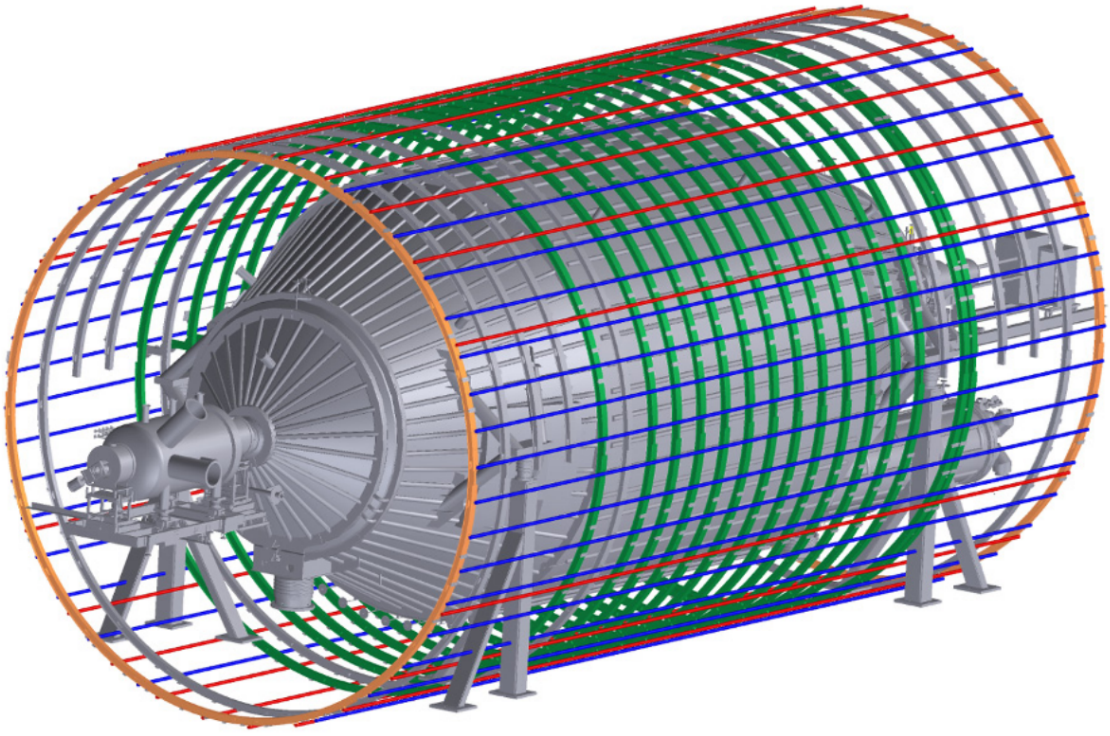

Figure 3.8.: **CAD drawing of the large-volume air-coil system around the Main Spectrometer vessel.** The vertical (visualized in blue) and horizontal (visualized in red) EMCS compensates the components of the earth magnetic field perpendicular to the beam axis. The LFCS, highlighted in green, fine-shapes the magnetic field inside the Main Spectrometer. EMCS and LFCS are both mounted on the same aluminum holding structure. For a visualization of the LFCS update eLFCS, see figure 5.4. Figure reprinted from [Glü+13], CC BY 3.0.

According to equation 3.11, the necessary magnetic field in the analyzing plane at the center of the Main Spectrometer has to be below 250 μT to achieve this energy resolution. The significantly smaller field in the Main Spectrometer with respect to the source field yields a strong increase of the flux tube radius, that guides the β-decay electrons through the experimental setup and is defined as

$$\Phi = \int \vec{B} \cdot \mathrm{d}\vec{A}.$$

With the current operational setting, the flux tube yields

$$\begin{aligned} \Phi &= B_{\mathrm{src}} \cdot A_{\mathrm{src}} \\ &\approx 133\,\mathrm{T} \cdot \mathrm{cm}^2 \end{aligned}$$

where B_{src} denotes the source magnetic field and A_{src} is the WGTS beam tube cross section. With a magnetic field at the center of the Main Spectrometer of 250 μT, the flux tube expands to a diameter of roughly 9 m, explaining the 10 m diameter of the Main Spectrometer. [KAT05; Ake+21d]

The magnetic field inside the Main Spectrometer is dominated by the stray fields of the super-conducting beam line magnets close to the Main Spectrometer and the

field of the large-volume air-coil system.
The three dominating super-conducting beamline magnets that influence the analyzing plane field are the solenoid at the entrance of the Main Spectrometer (PS2), the Pinch magnet (PCH) at the exit as well as the Detector solenoid (DET) that houses the detector. The PS2 magnet is normally operated at 3.1 T in driven operation mode and has a field stability better than 100 ppm per 8 h. The PCH contains a total magnetic field of 4.2 T in nominal neutrino mass measurements and is operated in persistent current mode, just like the DET. The DET magnetic field is set to 2.5 T and roughly matches the WGTS field. Both solenoids, the PCH and the DET, feature a relative magnetic field stability that is better than $3 \times 10^{-4}\,\mathrm{month}^{-1}$. [Ake+21d]
The large-volume air-coil system must provide optimal electron transport in the Main Spectrometer. In addition, it has to fine-shape the magnetic field to ensure correct magnetic adiabatic collimation inside the spectrometer. Therefore, the air-coil system contains the Low Field Correction System (LFCS) and the Earth Magnetic field Compensation System (EMCS, see also figure 3.8). The EMCS has the task to compensate the earth magnetic field perpendicular to the beam axis to avoid undesired collisions of the flux tube with the Main Spectrometer vessel. It comprises two sets of normal-conducting dipole coils installed horizontally around the Main Spectrometer vessel, mounted on an aluminum holding structure. The LFCS fine-shapes the magnetic field inside the Main Spectrometer to provide an optimal energy analysis. It consists of 14 normal-conducting air coils coaxially aligned with the spectrometer axis. The diameter of each coil is 12.6 m. They are mounted on the same aluminum holding structure as the EMCS. Each coil is individually regulated by a power supply, allowing great flexibility in field strength design along the spectrometer axis. In early 2020, the LFCS is modified to the eLFCS to allow a novel electromagnetic field configuration in the Main Spectrometer (see chapter 6). Five additional coils are added at the downstream side of the spectrometer vessel, as well as additional coil windings to nine of the already existing coils. [Glü+13; Erh+18; Thü20; Ake+21d]

High-Voltage System of the Main Spectrometer

The Main Spectrometer high-voltage system controls and monitors the high voltage, that is applied on the vessel and the inner electrodes. It consists of several voltage supplies, high-voltage dividers, and digital voltmeters.
The main part of the electric retardation is established by applying a negative high voltage to the spectrometer vessel. The applied voltage is on the order of -18.4 kV for neutrino mass measurements, but can be varied further down to -35 kV for special measurements, such as calibration measurements with $^{83\mathrm{m}}$Kr decay electrons. An active post-regulation system reduces high-frequency noise and AC fluctuations. The retarding potential is altered in nominal operation mode by adjusting the voltage on the vessel. For calibration measurements with the Rear Section e-gun, the vessel voltage can be distributed to the e-gun high voltage system. [Ake+21d]
The electric field is fine-shaped with an electrically isolated wire electrode system. It is divided in 15 rings that are grouped according to their position in steep cones, flat cones, and central part electrodes (see figure 3.9). An individual bias voltage can be applied on each ring, except for the five central rings in the cylindrical part of the Main Spectrometer. They are short-circuited to maintain a homogeneous

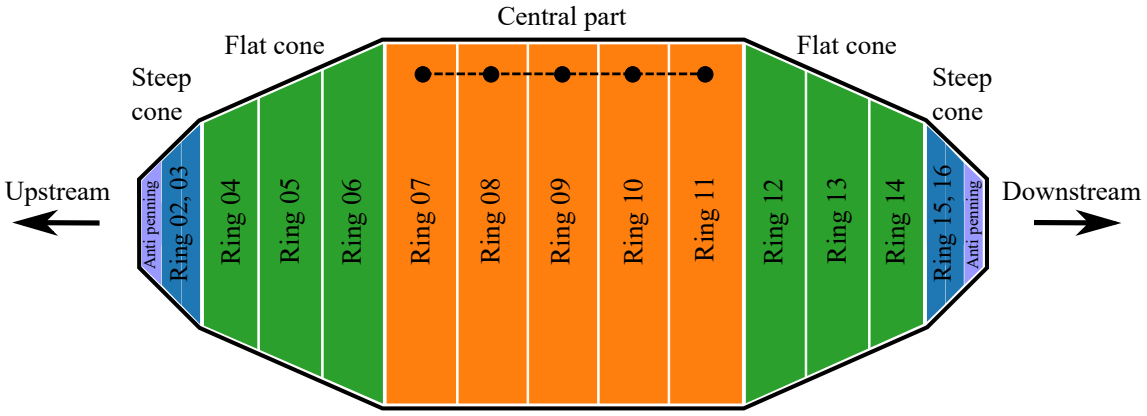

Figure 3.9.: **Schematic drawing of the location of the 15 rings of the Main Spectrometer inner electrode system.** Ring 02, 03 and 15, 16 constitute the steep cone inner electrode system (drawn in dark blue). The flat cone system comprises ring 04, 05, 06 and 12, 13, 14 (drawn in green). The central rings (drawn in orange) 07-11 are short-circuited (symbolized by dashed line) to sustain a homogeneous electric retardation close to the analyzing plane (at ring 09). Individual inner electrode settings, that are relevant for the present thesis, are stated in table B.3.

retarding potential. In the symmetric Main Spectrometer configuration, the central inner electrode rings are usually on an offset of -200 V with respect to the vessel to prevent background electrons from the Main Spectrometer vessel walls to enter the flux tube. The central inner electrodes at -200 V together with the -18.4 kV from the vessel result in an absolute retarding potential at the center of the Main Spectrometer of approximately 18.6 keV for the β-decay electrons. The applied bias voltages on the steep and flat cones ensure optimal interplay of the electric and magnetic field at the entrance and exit of the spectrometer, according to the electrons kinetic energy (see also table B.3). The maximum voltage offset that can be applied to the inner electrodes is -2 kV. [Val09; Ake+21d]
The applied high voltage on the Main Spectrometer vessel and inner electrode system is monitored by two ppm-precision high-voltage dividers in combination with precision digital voltmeters, that monitor the sum of inner electrode and vessel voltage [Ake+21d]. The high-voltage dividers only need to be calibrated a few times during their life time as they feature excellent long-term stability [Rod21a], the digital voltmeters are calibrated twice per week during neutrino mass measurements.

Vacuum System of the Main Spectrometer

The ultra-high vacuum system of the Main Spectrometer serves two purposes. Firstly, it is crucial that β-decay electrons cross the spectrometer without any collisions with residual gas. Secondly, the good vacuum directly prevents possible background production in the Main Spectrometer. According to these requirements, the vacuum system of the Main Spectrometer must reach a pressure in the 10^{-11} mbar regime during neutrino mass measurement campaigns. [KAT05; Ake+21d]
The Main Spectrometer vessel has a total volume of 1240 m^3 with an inner surface of 1222 m^2. To meet the vacuum requirements in this large volume, custom-made non-

evaporable getter pumps are installed in two of the three turbo-molecular pump ports with a diameter of 1.7 m and a length of 3 m, located at the downstream end of the Main Spectrometer. As the getter pumps cause radon-induced electron background in the Main Spectrometer (see also section 5.1.2), it was decided to not install the remaining getter pump in the third pump port. Additionally, the two pump ports that house the getter pumps also contain three turbo-molecular pumps each for the initial pump-down during commissioning and pumping of non-getterable gases in standard operation. A crucial role to achieve the pressure design goal is the baking of the Main Spectrometer, that fulfills two tasks. Firstly, the non-evaporable getter pumps have to be activated at temperatures around 200 °C. Secondly, the heating causes a desorption of water and hydrogen from all surfaces. This reduces the surface's out-gassing rate in nominal operation which is the limiting factor for the final pressure in the Main Spectrometer. The vacuum system of the Main Spectrometer contains two independent thermal cycles for the baking, with a total heating power of more than 440 kW, and a control system to set the temperature with a precision of better than 1 °C. After the bake-out in May 2017, the Main Spectrometer vacuum design goal is achieved with a vessel operation temperature of 9.5 °C. [Are+16; Ake+21d]

Pre-Spectrometer

The Pre-Spectrometer is located in between the CPS and the Main Spectrometer. Its design goal is to suppress the incoming β-decay electron flux from $10^{10}\,\mathrm{s}^{-1}$ to $10^{4}\,\mathrm{s}^{-1}$ before the Main Spectrometer. Additionally, it served as a prototype in the research and development phase for the Main Spectrometer design. In an alternative time-of-flight MAC-E mode, the Pre-Spectrometer can act as a fast switch. [KAT05] Since the Pre-Spectrometer's main task in nominal neutrino mass measurements is to act as a pre-filter, the energy resolution requirements are rather moderate. To reduce the flux by six orders of magnitude, it is normally set to 300 eV below the tritium endpoint. As a MAC-E filter energy resolution of 100 eV is sufficient, the dimensions of the Pre-Spectrometer are significantly smaller compared to the Main Spectrometer. The flux tube expands to only 1 m in the analyzing plane, the Pre-Spectrometer tank has thus a diameter of 1.7 m and a total length of 3.4 m. A dedicated air-coil system to fine-shape the magnetic field inside the vessel is not necessary, the two super-conducting magnets at the spectrometer entrance (PS1) and exit (PS2) provide the necessary field shape in the Pre-Spectrometer. The high-voltage system is similar to the one of the Main Spectrometer. The major part of the electric retardation is caused by a high-voltage on the vessel, an inner electrode system provides the fine-shaping. As the Pre-Spectrometer served as the prototype for the Main Spectrometer, also its vacuum system shows strong similarities to the one of the Main Spectrometer. The Pre-Spectrometer ultra-high vacuum is provided by a mixture of turbo-molecular and non-evaporable getter pumps. [KAT05; Ake+21d]

Monitor Spectrometer

The Monitor Spectrometer is located in a parallel beamline setup, in a building next to the Main Spectrometer hall. The primary task of the Monitor Spectrometer

during neutrino mass measurement campaigns is to monitor the high voltage of the Main Spectrometer. The Monitor Spectrometer is the former MAC-E filter of the Mainz experiment (see reference [Kra+05]) and can be powered by the same power supply as the Main Spectrometer high-voltage system. It continuously analyzes quasi-monoenergetic decay electrons of ^{83m}Kr (see also section 5.4.1) via the MAC-E filter technique. An instability of the Main Spectrometer high-voltage system would cause a shift of the decay electron line position that can be recognized. [Ake+21d]
The Monitor Spectrometer vessel has a length of 3 m and a diameter of 1 m. The necessary magnetic field is produced by super-conducting magnets at both ends of the spectrometer and an air-coil system consisting of four normal-conducting air coils and an earth field compensation system. The electric retardation is produced by a set of cylindrical and conical electrodes and wire electrodes. [Ake+21d] If the Monitor Spectrometer is not connected to the Main Spectrometer high-voltage system, it is a suitable tool for test and commissioning measurements, for example of a new e-gun flange (see for example references [Beh16; Sch23]).

3.2.5. Focal-Plane Detector System

The Focal-Plane Detector (FPD) system comprises a pixel-segmented silicon *p-i-n*-diode array, the PCH and the DET, readout electronics, data-acquisition system, calibration and monitoring devices, and an ultra-high vacuum system [Ake+21d]. A drawing of the focal plane detector system is shown in figure 3.10.
The task of the FPD is to count the number of β-decay electrons that overcome the Main Spectrometer retarding potential. The PCH and DET ensure adiabatic guiding of the electrons to the FPD. The post-acceleration electrode allows to accelerate the electrons before arriving at the FPD. With the addition of the post acceleration, the signal peak can be shifted into a region with low detector background and furthermore leading to a minimization of the backscattering probability. The FPD itself is a monolithic 148 pixel *p-i-n*-diode array in a dartboard design on a single silicon wafer (see figure 3.10). The pixels are arranged in a bulls-eye ring at the center housing four pixels and twelve rings containing twelve pixels each. Each pixel covers by design 44 mm^2 in surface area leading to a total sensitive area of 6512 mm^2, matching the dimensions of the flux tube in the DET magnetic field. For operational mode, the FPD as well as the electronics are cooled in order to reduce leakage current and noise. The energy scale of the FPD can be calibrated by moving an ^{241}Am γ source into the beamline in between the PCH and DET. The absolute FPD efficiency can be determined by a photoelectron source, that can also be installed in the beamline between the two super-conducting solenoids. Since the FPD system couples to the Main Spectrometer, it must fulfill the ultra-high vacuum requirements with a pressure of 10^{-9} mbar or below. [Ams+15; Ake+21d]

3.3. KATRIN Neutrino Mass Analysis

Having described the KATRIN hardware and working principle in the previous sections, we focus here on how to translate the measured electron count rates at various surplus energies into an estimation on the neutrino mass. In the following, we derive

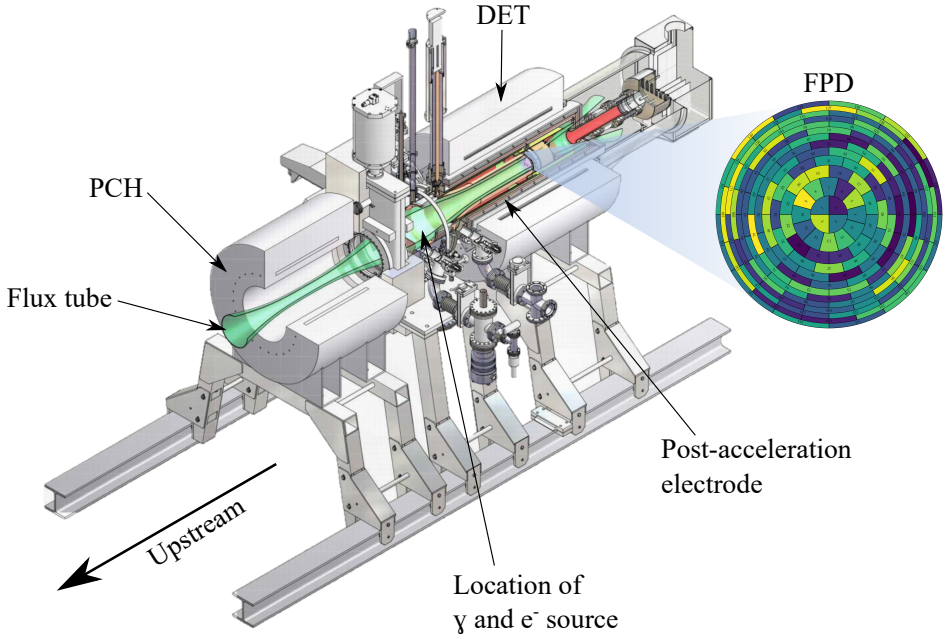

Figure 3.10.: **CAD drawing of the focal-plane detector system.** The PCH and DET guide the β-decay electron flux tube (shown in green) from the Main Spectrometer towards the Focal Plane Detector (FPD). The post-acceleration electrode allows to shift the signal peak to a low-background region. A γ and photoelectron source can be inserted between the PCH and the DET for FPD calibration. Figure adapted from [Ams+12].

the model for the integral spectrum, methods of parameter inference, how an integral tritium β scan is influenced by a non-vanishing neutrino mass, and the KATRIN sensitivity goal. Additional topics that are of special interest for the present thesis are outlined. These include the presentation of various approaches how to treat systematic uncertainties in parameter inference, different methods of data combination, the KATRIN analysis tools, the calculation of electric and magnetic fields, as well as a technical insight how measurement and simulation information is used in the neutrino mass analysis.

3.3.1. The Integral KATRIN Model

The integral KATRIN model describes the expected count rates of β-decay electrons at the FPD at certain retarding potential and is crucial to infer the neutrino mass from measurements. For an unbiased neutrino mass measurement, the integral model must comprise the theoretical description of the differential β-decay spectrum with the necessary corrections for molecular tritium as well as the the response function summarizing the characteristics of the experimental KATRIN setup.

Differential Beta-Decay Spectrum

We have introduced an approximate formulation for the differential β-decay spectrum $\mathrm{d}\Gamma/\mathrm{d}E$ in equation 2.13, based on reference [FdR21]. Nevertheless, fine corrections for molecular tritium and the finite structure of the decay daughter nuclei must be included in the theoretical description to reach the KATRIN sensitivity goal. For a detailed introduction and discussion of the individual effects, please see references [OW08; Kle+19]. Taking into account the necessary corrections, the differential β-decay spectrum can be written as

$$\begin{aligned}\frac{\mathrm{d}\Gamma}{\mathrm{d}E} = &\frac{G_\mathrm{F}\cos^2\Theta_\mathrm{C}}{2\pi^3}\left|M_\mathrm{nuc}\right|^2 F\cdot(E_0+m_\mathrm{e}-\epsilon)\cdot\sqrt{(E_0+m_\mathrm{e}-\epsilon)^2-m_\mathrm{e}^2}\\ &\times\sum_{i,j}\left|U_{\mathrm{e}i}\right|^2 P_j\cdot\left(\epsilon-V_j\right)\cdot\sqrt{\left(\epsilon-V_j\right)^2-m_i^2}\cdot\Theta\left(\epsilon-V_j-m_i^2\right)\end{aligned} \tag{3.13}$$

with G_F denoting the Fermi constant, Θ_C the Cabibbo angle, and M_nuc the nuclear matrix element. In this context, F represents the Fermi function, taking into account the Coulomb interaction of the outgoing electron with the nucleus. E_0 is the kinematic endpoint of the tritium spectrum, m_e is the electron mass, and the difference between electron energy E and kinematic endpoint E_0 is summarized in $\epsilon = E_0 - E$. The PMNS mixing matrix element that links the neutrino electron flavor with the mass eigenstates is denoted as $U_{\mathrm{e}i}$ (see also equation 2.3). P_j is the probability for a certain electronic final state j of the daughter nucleus with energy V_j. The squared neutrino mass of a certain mass eigenstate is denoted here as m_i^2. The step function $\Theta\left(\epsilon - V_j - m_i^2\right)$ confines the spectral components to the physical sector. The differential decay spectrum versus electron energy is shown in figure 2.7. [OW08]

Response Function

The response function $R(E,U)$ describes the probability for an electron starting in the WGTS with energy E to overcome the retarding potential qU of the Main Spectrometer and to reach the FPD. The response function includes the energy losses due to the electron scattering with tritium gas molecules in the WGTS, losses due to synchrotron radiation because of the transport in strong magnetic fields, and comprises also the transmission of electrons through the Main Spectrometer. [Ake+21a]
The energy-loss probability for β-decay electrons in scattering off tritium gas in the WGTS as well as the corresponding energy-loss model are discussed in detail in section 7.1.2 and section 7.1.3. We therefore skip the derivation of these energy-loss processes here and only present subsequently the impact on the response function.
The transmission function $T(E,U)$ describes the probability for an isotropically emitted electron with surplus energy $E - qU$ to overcome the MAC-E filter. An analytical formulation for the transmission function of the Main Spectrometer is derived in section 3.1.2, leading to equation 3.12. The synchrotron energy losses of the β-decay electrons are included as an analytical modification to the transmission function in the model, that we do not further discuss here.
The response function is calculated as the convolution of the transmission function

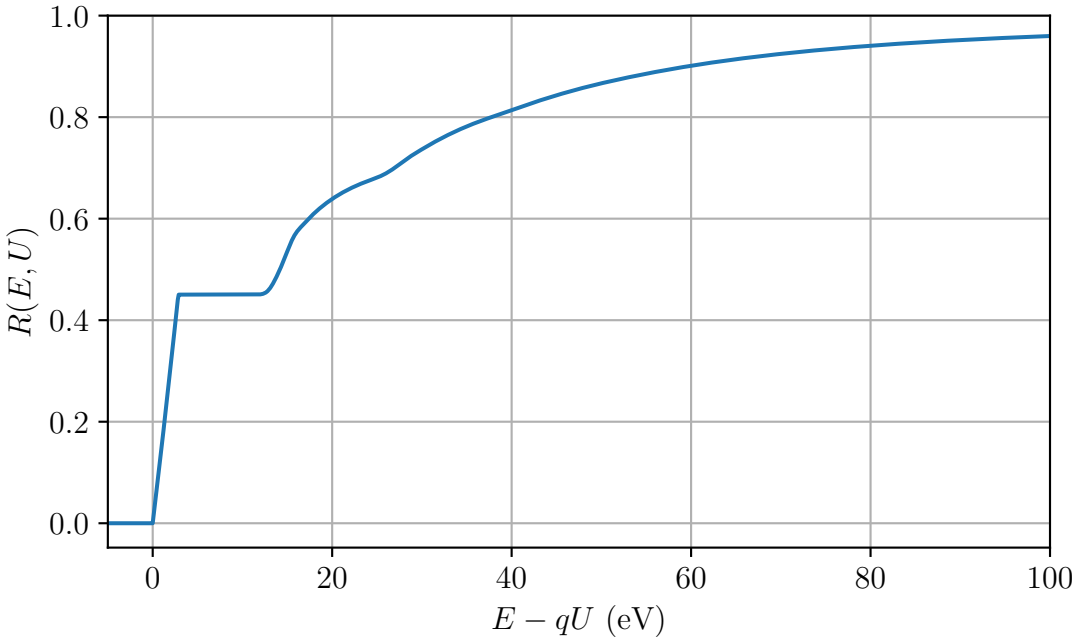

Figure 3.11.: **The KATRIN response function $R(E, U)$ versus the surplus energy $E - qU$.** It describes the probability for a β-decay electron produced in the WGTS to overcome the Main Spectrometer retarding potential. The response function is needed to calculate the integral β-decay spectrum, that is measured in KATRIN.

with the probability-weighted energy-loss models for i-fold scattering (for details, please see section 7.1.3). Figure 3.11 shows the calculated response function $R(E, U)$ versus the surplus energy $E - qU$ for β-decay electrons in a setting, that is similar to the one of KNM2 (see also table C.4). The response function shape below surplus energies of 11 eV is dominated by the transmission function, normalized to the probability for electrons to leave the WGTS without scattering off tritium molecules. For surplus energies larger than 11 eV, also scattered electrons can arrive at the detector. This is represented by a convolution of the transmission function with the energy-loss function, leading to the characteristic shape. [Kle+19]

Integral Spectrum

The rate $\dot{N}_{\text{theo}}(U)$ is the expected count rate of the integral spectrum at a certain retarding potential. It is calculated as the convolution of the differential β-decay spectrum with the response function

$$\dot{N}_{\text{theo}}(U) = \frac{1}{2} \cdot N_{\text{T}} \int_{qU}^{E_0} \frac{\mathrm{d}\Gamma}{\mathrm{d}E}(E_0, m_\nu^2) \cdot R(E, U)\ \mathrm{d}E. \tag{3.14}$$

The factor 1/2 incorporates that the response function only considers electrons emitted in downstream direction, N_{T} depicts the number of tritium nuclei in the source. [Kle+19] The expected integral spectrum close to the endpoint is shown in the upper graph of figure 3.12.

3.3.2. Parameter Inference

The goal of the KATRIN experiment is to measure the absolute neutrino mass by measuring count rates of the tritium β decay. We have to employ statistical methods to properly infer the neutrino mass from the measured count rates at several retarding potentials.

The likelihood $P(x|H)$ is the probability to measure the data x given the underlying hypothesis H. If the hypothesis H is defined by one or more parameters θ, then $L(\theta) = P(x|H)$ is called the likelihood function. When the data consists of independent and identically distributed values one has a set of n statistically independent values $x = (x_1, ..., x_n)$. If each component follows the same probability density function $f(x|\theta)$, the likelihood function is calculated according to

$$L(\theta) = \prod_{i=1}^{n} f(x_i|\theta).$$

The maximum likelihood estimator is a common tool to infer the hypothesis parameters that describe the data best. The maximum likelihood estimators $\hat{\theta}$ for the true hypothesis parameters θ are defined as the parameter set that gives the maximum of the likelihood function. These estimators $\hat{\theta}$ are efficient, asymptotically unbiased, and often have a Gaussian sampling distribution. Instead of maximizing the likelihood function $L(\theta)$, it is common in numerical approaches to exploit the properties of the logarithm and to minimize the negative logarithmic likelihood function

$$-\log L(\theta) = -\log \prod_{i=1}^{n} f(x_i|\theta) = -\sum_{i=0}^{n} \log f(x_i|\theta), \tag{3.15}$$

leading to the same estimators $\hat{\theta}$. [Zyl+20]

In the KATRIN experiment, the dataset $x = N_{\mathrm{obs}}$ consists of a set of measured electron counts $N_{\mathrm{obs},i}$ at several scan steps i with retarding potentials qU_i. The electron counts follow a Poissonian distribution with expectation value $N_{\mathrm{theo},i}(qU_i, \theta)$. The underlying hypothesis H for the expected counts in the KATRIN likelihood function is $N_{\mathrm{theo},i}(qU_i, \theta) = \dot{N}_{\mathrm{theo},i}(qU_i, \theta) \cdot t_i$ with the measurement time t_i and the expected count rate

$$\dot{N}_{\mathrm{theo},i}(qU_i, \theta) = A_s \cdot \int_{qU_i}^{E_0} \frac{\mathrm{d}\Gamma}{\mathrm{d}E}(E_0, m_\nu^2) \cdot R(E, qU_i)\ \mathrm{d}E + R_{\mathrm{bg}}. \tag{3.16}$$

The expected count rate is derived from the theoretical description of the integral spectrum (see section 3.3.1) with minor modifications. A_s denotes here a normalization, E_0 the molecular tritium endpoint, and R_{bg} the background rate. The incoherent sum of the neutrino mass eigenvalues (defined in equation 2.14), which is the experimental observable in direct neutrino mass measurements, is denoted as m_ν^2. The hypothesis parameters θ are thus the parameter of interest m_ν^2 and the nuisance parameters E_0, A_s, and R_{bg}, that are not sufficiently well known to be fixed in advance. Consequently, the KATRIN-specific likelihood function yields

$$L(m_\nu^2, E_0, A_s, R_{\mathrm{bg}}) = \prod_{i=1}^{n} f(N_{\mathrm{obs},i}|N_{\mathrm{theo},i}(qU_i, m_\nu^2, E_0, A_s, R_{\mathrm{bg}})), \tag{3.17}$$

with f being the Poissonian probability density function. The best-fit parameter for the squared neutrino mass can then be derived via the maximum likelihood estimator method. [Kle14]

For sufficiently high count rates the Poisson distribution $f(N_{\mathrm{obs},i})$ can be approximated by a normal distribution $\mathcal{N}(x, \mu, \sigma)$ with mean $\mu = N_{\mathrm{obs},i}$ and width $\sigma = \sqrt{N_{\mathrm{obs},i}}$. Inserting this probability density function into equation 3.17 leads to a concordance of the negative logarithmic likelihood function with the method of least squares, yielding

$$\chi^2(\theta) = -2 \log L(\theta) + \text{const.} = \sum_{i=0}^{n} \frac{\left(N_{\mathrm{theo},i}(\theta) - N_{\mathrm{obs},i}\right)^2}{N_{\mathrm{obs},i}}.$$

This term consists of a sum of n random normal distributed variables, that thus follow Pearson's χ^2 statistic. χ^2 is a suitable estimator for the goodness of fit when evaluated at the location of the maximum likelihood estimators $\hat{\theta}$. The expectation value for the χ^2 distribution is the number of degrees of freedom (ndof), which is the number of observations reduced by the number of free model parameters. This leads to the so-called normalized χ^2, that is calculated as $\chi^2\left(\hat{\theta}\right)/\text{ndof}$ with unity as expectation value. [Pla83; BL98; Zyl+20]
The method of least squares allows a rather straight-forward way of implementing correlations between the individual observations of the data in the best-fit parameter estimation. Taking into account the covariance matrix V, the least-squares estimator yields

$$\chi^2(\theta) = (\vec{y} - \vec{m}(\theta))^T V^{-1} (\vec{y} - \vec{m}(\theta))$$

with $\vec{y}$ denoting the vector of measurements and $\vec{m}(\theta)$ the model prediction. The uncertainties on the data and on the model, as well as the correlations, are comprised in the inverted covariance matrix V^{-1}. [BL98; Zyl+20]

3.3.3. Analysis of Beta Scan

A non-vanishing neutrino mass manifests itself in the spectrum shape close to the endpoint of the tritium β decay (see figure 2.7). In the first two neutrino mass measurement campaigns of KATRIN, the β-decay spectrum was analyzed in a range down to about 40 eV below the endpoint. The choice of the analysis window range is a trade-off between larger count rates further down below the endpoint, leading to smaller statistical uncertainties, and at the same time increasing systematic uncertainties. [KAT05; Ake+21a; Ake+21b] Sensitivity studies carried out in the course of this thesis use the 40 eV analysis window.

The integral β-decay spectrum $\dot{N}_{\mathrm{theo}}$, as defined in equation 3.16, is shown for the 40 eV analysis window in the upper graph of figure 3.12. Additionally, the impact of the four free fit parameter in the KATRIN neutrino mass analysis is also presented in the upper graph of figure 3.12. The operational KATRIN parameter for the integral spectrum calculation, such as tritium gas density in the WGTS, are chosen similar to the parameters of KNM2. The molecular tritium endpoint E_0 separates the β-decay spectrum region from the background region. Although the molecular

tritium endpoint is well-known from external measurements to be $E_0 = 18\,574\,\mathrm{eV}$ [Sei19], KATRIN will likely measure a different endpoint. The KATRIN-specific molecular tritium endpoint is modified with respect to the literature value by non-vanishing starting potentials in the WGTS for the β-decay electrons or the Main Spectrometer work function. As this KATRIN-specific endpoint is not accurately and precisely known a priori, it is introduced as nuisance parameter in the fit. The signal normalization A_s is a normalization factor applied to the integral spectrum. It absorbs effects such as the total number of tritium nuclei in the WGTS that can contribute to the decay rate, or an energy-independent FPD detection efficiency for electrons. The parameter R_bg describes the background electron rate, underlying the integral β-decay spectrum. The KATRIN parameter of interest, the squared neutrino mass m_ν^2, mostly affects the spectrum close to the endpoint, as shown in the middle graph of figure 3.12. The comparison of the integral β-decay spectrum with $m_\nu^2 = 1\,\mathrm{eV}^2$ with the one with vanishing neutrino mass yields a dip below the endpoint. In a typical KATRIN neutrino mass analysis, all four free fit parameters are estimated via the maximum likelihood method. [Ake+21b]
KATRIN investigates the integral β-decay spectrum by sequentially applying several, non-equidistant retarding potentials to the Main Spectrometer and measuring the β-decay electron rate with the FPD. These individual rate measurements at certain high-voltage set points and with defined measurement time are called scan steps. The choice of scan steps influences the sensitivity on the squared neutrino mass. The sequential application of all scan steps constitutes one tritium β-decay spectrum scan, that takes around four hours. The length of a β scan is chosen such, that the experimental environment (WGTS gas column density, magnetic fields, ...) guarantees good stability during one scan. However, the accumulated statistics within one scan is too small to extract any information on the squared neutrino mass. The single tritium β scans are repeated continuously in a measurement campaign to collect sufficient statistics. By applying a combination strategy (see section 3.3.6), the various β scans within a measurement campaign can be summarized as one high-statistics β scan. [Ake+21b] A toy measurement of one combined high-statistics tritium β scan with $m_\nu^2 = 1\,\mathrm{eV}^2$ in the 40 eV analysis window is shown in the upper graph of figure 3.12. The total net measuring time of the toy measurement is 60 days. The absolute value of the retarding potential of the individual scan steps and their measuring time are chosen similar to KNM2 [Ake+21a]. The measurement time distribution is visualized in the lower graph of figure 3.12. The measurement time is significantly increased in the region that is particularly sensitive to a non-vanishing neutrino mass. We recommend the interested reader to reference [Kle14] for the derivation of the measurement time distribution, that maximizes the KATRIN sensitivity on the neutrino mass.

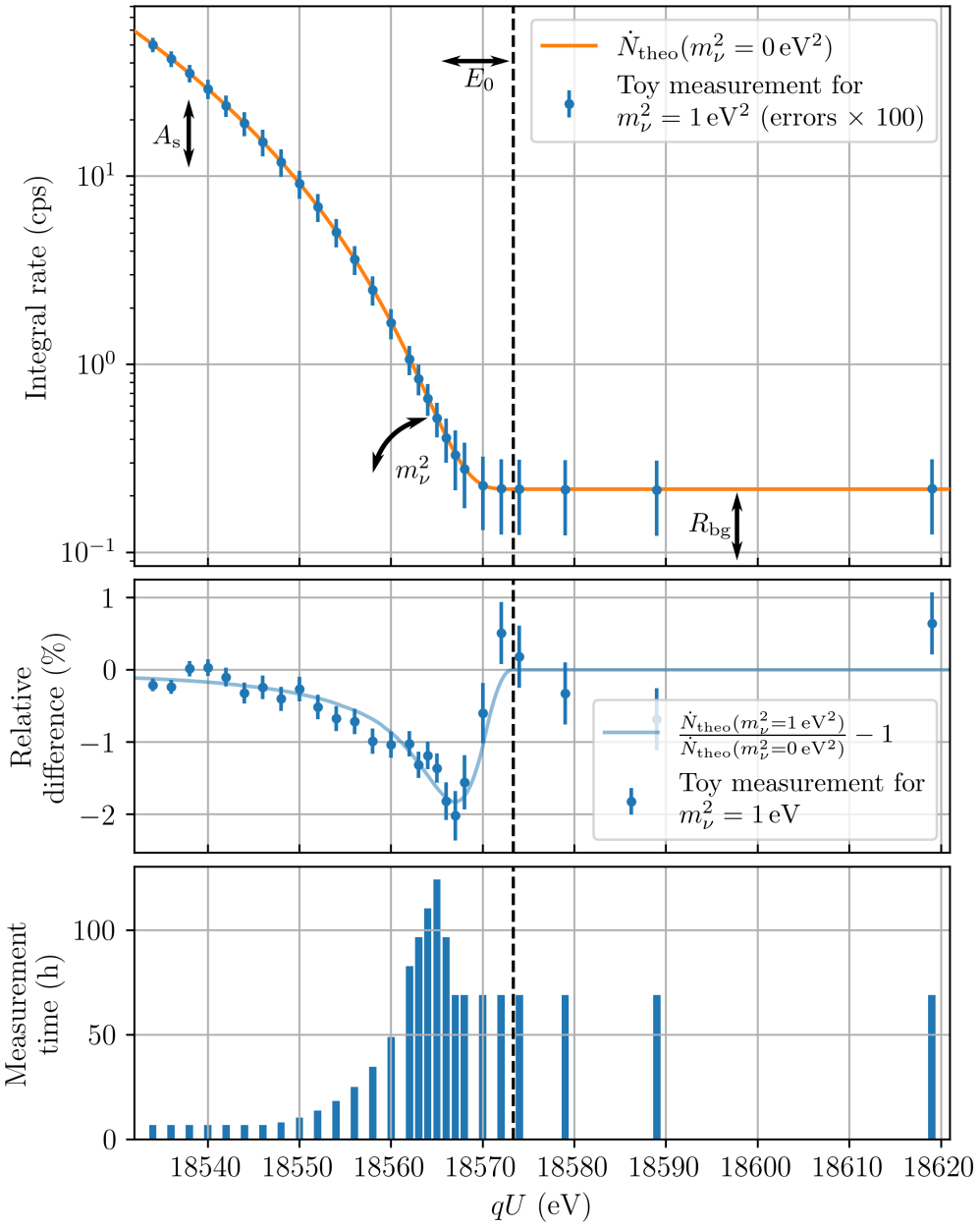

Figure 3.12.: **Integral β-decay spectrum in the last 40 eV below the tritium endpoint (upper graph), relative difference between integral spectrum with vanishing neutrino mass and one with $m_\nu^2 = 1\,\mathrm{eV}^2$ (central graph), and measurement time distribution, similar to the one used in KNM2 (lower graph).** The comparison of the integral spectrum with vanishing neutrino mass together with a toy measurement with simulation truth of $m_\nu^2 = 1\,\mathrm{eV}^2$ is shown in the upper graph. The impact of the free fit parameters on the integral spectrum are indicated by the black arrows. In the central graph, the impact of a non-vanishing neutrino mass on the integral spectrum is presented. The relative difference is maximal approximately 6 eV below the endpoint for the assumed signal-to-background ratio, in that region also the measurement time of the scan steps is significantly larger compared to the other steps (lower graph). Measurement time distribution and other input parameters chosen similar to the KNM2 configuration, figure inspired by M. Kleesiek [Kle+19].

3.3.4. KATRIN Sensitivity

The major KATRIN goal is to reach a sensitivity on the effective electron antineutrino mass of 0.2 eV at 90 % C.L. after three years of net measuring time. This corresponds to a discovery potential (five standard deviations) of 0.35 eV [KAT05]. KATRIN's definition of the sensitivity on the neutrino mass can be interpreted as follows: if the KATRIN neutrino mass measurement finds a best-fit neutrino mass $\hat{m}_\nu$ larger than the stated sensitivity, KATRIN can reject the null hypothesis of vanishing neutrino mass on the given confidence level. The stated KATRIN sensitivity limit comprises the statistical and systematic uncertainty contributions on the neutrino mass. [KAT05; Kle14]
The statistical uncertainty is inter alia given by the measurement time and its distribution, the β-decay rate in the WGTS, the background rate, and the chosen analysis window. The studies performed in the KATRIN technical design report [KAT05] employ a 30 eV analysis window and a background rate of 10 mcps. In the technical design report, the statistical uncertainty is determined via ensemble tests. A large number of KATRIN measurements is simulated, the squared neutrino mass is fixed to zero but fluctuations according to the statistical uncertainties are allowed. The estimated squared neutrino mass $\hat{m}_\nu^2$ is determined for each toy measurement via the maximum likelihood approach. The statistical uncertainty of m_ν^2 is then calculated by analyzing the distribution of all $\hat{m}_\nu^2$. The one standard deviation interval quantifies the statistical uncertainty on the squared neutrino mass to $\Delta m^2_{\nu,\mathrm{stat}} = 18 \times 10^{-3}\,\mathrm{eV}^2$. [KAT05; Kle14]
Possible systematic uncertainties are identified in the KATRIN design report. The squared sum of all anticipated contributions does not exceed a total systematic uncertainty on the squared neutrino mass of $10 \times 10^{-3}\,\mathrm{eV}^2$. All individual contributions are smaller than $7.5 \times 10^{-3}\,\mathrm{eV}^2$. To account for unidentified systematic effects, five major systematic uncertainties are allowed that each cause a systematic uncertainty of $7.5 \times 10^{-3}\,\mathrm{eV}^2$ on the squared neutrino mass. This leads to a systematic uncertainty budget of $\Delta m^2_{\nu,\mathrm{sys}} \leq 17 \times 10^{-3}\,\mathrm{eV}^2$, balancing the statistical uncertainty budget. [KAT05] A summary of the currently known systematic effects is given in reference [Sei19]. The maximally allowed systematic uncertainty for an individual contribution of $7.5 \times 10^{-3}\,\mathrm{eV}^2$ will be used as benchmark in the following chapters.
Assuming that m_ν^2 is Gaussian distributed, we can calculate the total uncertainty on the squared neutrino mass as

$$\Delta m^2_{\nu,\mathrm{tot}} = \sqrt{\left(\Delta m^2_{\nu,\mathrm{stat}}\right)^2 + \left(\Delta m^2_{\nu,\mathrm{sys}}\right)^2} = 25 \times 10^{-3}\,\mathrm{eV}^2.$$

The sensitivity on the neutrino mass for 90 % C.L. and five standard deviations can now be calculated as

$$S(90\,\%\ \mathrm{C.L.}) = \sqrt{1.645 \cdot \Delta m^2_{\nu,\mathrm{tot}}} = 0.2\,\mathrm{eV},$$
$$S(5\,\sigma) = \sqrt{5 \cdot \Delta m^2_{\nu,\mathrm{tot}}} = 0.35\,\mathrm{eV}.$$

The factor 1.645 translates a 68.3 % C.L. to a 90 % C.L. for Gaussian distributed quantities. [KAT05]

3.3.5. Treatment of Systematic Uncertainties

Several parameters have to be taken into account for a neutrino mass analysis, for example the gas amount in the WGTS. If this gas amount is estimated inaccurately, as a consequence, a wrong model assumption can lead to a shape distortion of the spectrum, eventually resulting in a possible bias of the neutrino mass. To account for the systematic uncertainty arising from these effects in the total neutrino mass uncertainty, the correct treatment of the systematic uncertainties in the KATRIN likelihood function is crucial.
Currently, three approaches to incorporate systematic uncertainties in the neutrino mass analysis are pursued in the KATRIN collaboration. These are the Monte-Carlo-propagation method, the pull-term method, and the covariance-matrix approach. All three methods result in the same or similar uncertainty estimations for the KATRIN systematic neutrino mass uncertainties [Ake+21a]. As only the latter two are relevant for the thesis at hand, we focus on these approaches in the following. For the Monte-Carlo-propagation method, see reference [Ake+21b]. For better readability, we show the incorporation of the two methods in the fit by example of the least squares, that coincidences with the likelihood function for Gaussian uncertainties.

Pull-Term Method

The least-squares term, that has to be minimized in the statistics-only fit of the neutrino mass to the n measured β-decay electron counts $N_{\mathrm{obs},i}$ at the individual scan steps yields

$$\chi^2\left(m_\nu^2, E_0, A_\mathrm{s}, R_\mathrm{bg}\right) = \sum_{i=0}^{n} \frac{\left(N_{\mathrm{theo},i}\left(m_\nu^2, E_0, A_\mathrm{s}, R_\mathrm{bg}\right) - N_{\mathrm{obs},i}\right)^2}{N_{\mathrm{obs},i}}, \tag{3.18}$$

with the model prediction $N_{\mathrm{theo},i}\left(m_\nu^2, E_0, A_\mathrm{s}, R_\mathrm{bg}\right)$. A Gaussian distributed systematic effect η with estimated uncertainty $\Delta\eta$ can be introduced in the pull-term approach into the KATRIN least-squares term as an additional free nuisance fit parameter, that is effectively constrained by the estimated uncertainty $\Delta\eta$. This leads with the best-estimation value $\hat{\eta}$ for the systematic to a correct implementation of the systematic effect in the least-squares term to

$$\chi^2\left(m_\nu^2, E_0, A_\mathrm{s}, R_\mathrm{bg}, \eta\right) = \sum_{i=0}^{n} \frac{\left(N_{\mathrm{theo},i}\left(m_\nu^2, E_0, A_\mathrm{s}, R_\mathrm{bg}\right) - N_{\mathrm{obs},i}\right)^2}{N_{\mathrm{obs},i}} + \frac{(\eta - \hat{\eta})^2}{\Delta\eta^2}. \tag{3.19}$$

The additional nuisance parameter can change the uncertainty intervals of the other fit parameters depending on their correlations. The advantage of the pull-term method is that it makes maximum use of the data, as the measured integral spectrum contains information to a certain degree about a systematic effect (see for example figure 4.6) that can be used in the parameter inference. [Kle14] One disadvantage is that only systematic effects can be incorporated if they can be parametrized. This is for example not the case for the uncertainties of the model for tritium molecular final state distribution, as used in KNM1 and KNM2 [Ake+21a]. Another disadvantage is that this approach can quickly become computationally expensive in the parameter

inference, as the number of free fit parameters increases with each added penalty term. In total, 34 additional fit parameters are introduced in the KNM2 analysis to incorporate systematic uncertainties. This can lead to problems in the combination of several KATRIN neutrino mass measurement campaigns with individual uncertainties.

In the following, we often want to quantify the systematic uncertainty contribution on the squared neutrino mass of a single effect and compare it to the benchmark of a maximally allowed uncertainty contribution of $7.5 \times 10^{-3}\,\mathrm{eV}^2$. For this investigation, we employ Asimov datasets [Cow+11] in combination with the pull-term method. The theoretical model is calculated with the estimated central value $\hat{\eta}$ for the systematic effect η. For the sake of simplicity, the neutrino mass is set to zero in the model calculation. The count rates at the individual scan steps of the pseudo-measurement are determined from the model without any statistical fluctuations. Afterwards, we investigate the toy measurement with a statistics-only fit according to equation 3.18 with fixed systematic η at the estimated central value $\hat{\eta}$. The inferred squared neutrino mass is necessarily at zero for a correct maximum likelihood estimation as all input parameters are the same as used for the model calculation and no statistical fluctuations are applied on the pseudo counts. The uncertainty estimation, given by the likelihood shape close to the maximum likelihood estimators, is solely given by the statistical uncertainty $\Delta m^2_{\nu,\mathrm{stat}}$. As next step, the fit procedure is repeated but now with the additional nuisance parameter η and the penalty term in the least-squares term (see equation 3.19). In case of a correct parameter inference, the central value of the squared neutrino mass is again vanishing but its estimated uncertainty comprises the statistical and systematic uncertainty $\Delta m^2_{\nu,\mathrm{tot}}$. This results in a broadened χ^2 profile of m^2_ν close to the minimum (see figure 3.13). The uncertainty contribution on the squared neutrino mass due to the single systematic can now be estimated with Gaussian uncertainty propagation to

$$\Delta m^2_{\nu,\mathrm{sys}} = \sqrt{\left(\Delta m^2_{\nu,\mathrm{tot}}\right)^2 - \left(\Delta m^2_{\nu,\mathrm{stat}}\right)^2}.$$

Covariance Matrix Approach

Although the covariance matrix is a different formalism to include systematic uncertainties in the neutrino mass analysis, the result is the same as obtained with the pull-term method [Fog+02]. As described in section 3.3.2, the least-squares method allows an elegant way of introducing correlations among the data points via the correlation matrix V to [BL98; Zyl+20]

$$\chi^2(\theta) = \left(\vec{y} - \vec{m}\left(m^2_\nu, E_0, A_\mathrm{s}, R_\mathrm{bg}\right)\right)^T V^{-1} \left(\vec{y} - \vec{m}\left(m^2_\nu, E_0, A_\mathrm{s}, R_\mathrm{bg}\right)\right)$$

where $\vec{y}$ denotes the vector of measured counts at the individual scan steps and $\vec{m}\left(m^2_\nu, E_0, A_\mathrm{s}, R_\mathrm{bg}\right)$ the model predictions for the scan steps. In the analysis, the covariance matrix comprises the statistical and systematic uncertainties. The diagonal entries contain uncorrelated uncertainties, for example the statistical uncertainties, while the off-diagonal terms describe the correlated uncertainties between the data points. The covariance matrix of a single systematic effect η is derived by calculating a large number $\mathcal{O}\left(10^4\right)$ of integral β-decay spectra with randomized values of η

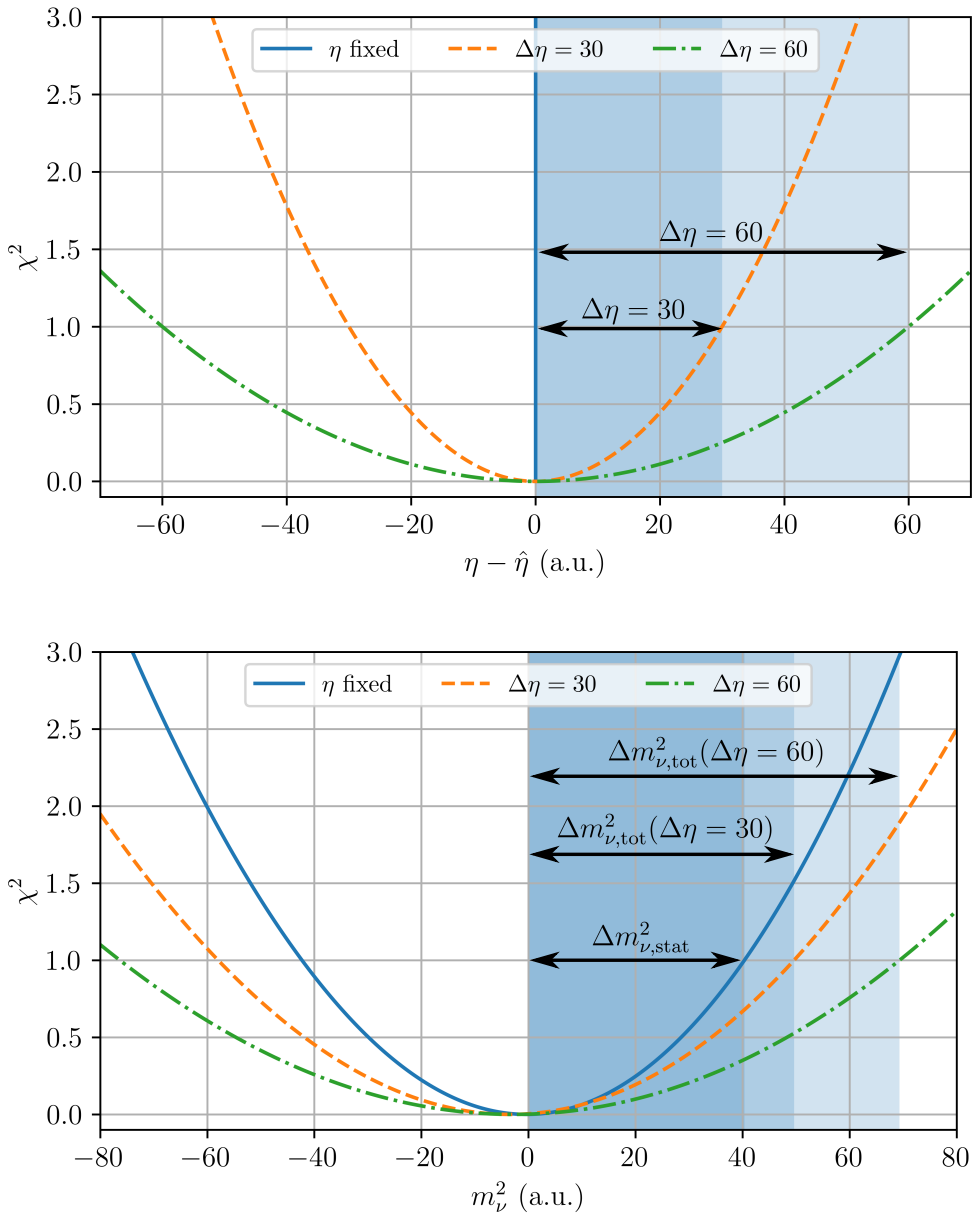

Figure 3.13.: **Visualization of the pull-term method on the χ^2 profile of m_ν^2 close to the best-fit minimum.** Three pull terms with different uncertainties $\Delta\eta$ on the systematic effect η with mean value $\hat{\eta}$ are shown in the upper plot ("$\Delta\eta$ fixed" corresponds to $\Delta\eta = 0$). In the lower graph, it is shown that the broadening of the χ^2 profile of m_ν^2 close to the best-fit minimum increases with $\Delta\eta$, and thus also the uncertainty $\Delta m^2_{\nu,\mathrm{tot}}$ on the determined neutrino mass. The fit with η fixed corresponds to the nominal four-parameter fit.

according to the estimated uncertainty. Based on the calculated spectra, the rates at the individual scan steps are calculated as well as their covariance

$$\mathrm{Cov}(x, y) = \frac{\sum_{i=0}^{N} (x_i - \overline{x})\,(y_i - \overline{y})}{N - 1},$$

with x and y being the count rate at two scan steps, and N is the number of total calculated samples. The count rate in a single spectrum with randomized η is denoted as x_i, and the expected count rate with $\hat{\eta}$ as input as $\overline{x}$ [Sch19]. To incorporate all systematic and statistical uncertainties, a single matrix has to be computed based on the randomized spectra sample that incorporates the fluctuation of all sources of uncertainties in a sufficiently large number. However, a modification has to be applied for neutrino mass analysis, since the signal normalization is a free fit parameter. The covariance matrices of all systematic effects, that solely translate into an uncertainty on the signal normalization, have to be eliminated. Therefore, a normalization on the covariance matrix must be applied, leading to the so-called shape-only covariance matrix. [Ake+21b]
The advantage of this method is that the fit itself is computationally fast, as it remains a four-parameter fit with the parameters describing the squared neutrino mass, endpoint, signal normalization, and background rate. However, the large number of spectra needs to be calculated before the minimization, yielding additional computational costs. Another disadvantage is that the obtained shape-only covariance matrix has to be inverted for the calculation of the least-squares term. This can lead to problems for large number of data points, for example in the combination of several measurement campaigns.

3.3.6. Data Combination

One measurement campaign consists of a few hundred individual β scans, that again comprise several scan steps at various retarding potentials. Furthermore, we also have to take into account that the FPD is segmented into 148 pixels to account, inter alia, for spatial variations of the Main Spectrometer electromagnetic fields. The electron counts, measured in various scan steps within several β scans and at different FPD pixels, have to be combined for a robust neutrino mass analysis. The combination must be carried out without loss of information or introducing a bias on the determined neutrino mass that endangers the KATRIN sensitivity goal.

Pixel Combination

The segmentation of the FPD into 148 independent pixel allows to resolve spatial effects in radial and azimuthal direction and account for them in the analysis. The β-decay electrons arriving for example at one certain pixel have to overcome a different Main Spectrometer retarding potential than electrons at another pixel. As also the same holds for the magnetic field in the analyzing plane and the PCH field, we can conclude that each pixel measures a statistically independent integrated β-decay spectrum with its own transmission function. This has to be considered when the measured counts on the individual pixels shall be combined for the neutrino mass analysis. [Ake+21b]
The first approach that we want to present here is the uniform pixel combination. This combination method is suitable, if the spatial effects are expected to be small. For the electromagnetic field configuration in the Main Spectrometer during KNM1 and KNM2, the magnetic field in the analyzing plane varies radially by approximately 2 μT, the electric retardation by 140 mV. In the uniform approach, the

pixel-wise spectra are combined into a single effective pixel, by adding the counts of all pixels at the individual scan steps. The transmission function for the effective pixel is calculated as the average of the pixel-wise transmission functions. The averaging of the pixel-wise transmission functions causes a negligible broadening on the effective measured spectrum and a small neutrino mass bias on the order of $10^{-3}\,\mathrm{eV}^2$ for the KNM1 setting. [Ake+21b] The advantage of this approach is that it does not increase the number of free fit parameters, as effectively only one β-decay spectrum is analyzed.

In the analysis of the KNM2 data, a different approach is pursued. Since the WGTS gas density is in KNM2 more than a factor three larger compared to KNM1, there is the possibility of forming radially dependent starting potentials in the WGTS plasma leading to a radially dependent effective endpoint. As the deviation level of possible radial starting potentials is not known a priori, it must be taken into account in the analysis as free fit parameter. Therefore, the 117 active pixels during KNM2 are grouped into twelve concentric rings. The pixel counts in one ring at a specific scan step are summed and constitute the counts of the respective ring. In the analysis, all ring-wise counts are simultaneously analyzed with a model that allows for ring-wise endpoints, signal normalizations, background rates, and one common neutrino mass. [Ake+21a] The total number of free fit parameters in this analysis yields $12{\cdot}3{+}1 = 37$ for a statistics-only fit. This method is called multi-ring analysis. Consequently, a multi-pixel neutrino mass analysis treats the endpoint, signal normalization, and background rate separately for each pixel with a common free neutrino mass fit parameter. For 117 active pixels, the number of free parameters in a statistics-only multi-pixel fit is 352. The same principle holds for the multi-patch analysis that simultaneously analyzes a group of pixel patches. The advantage of the multi-ring, -pixel, or -patch method is that it can take into account spatial inhomogeneities without producing any bias on the inferred parameters. However, the calculated number of free fit parameters shows that the computational costs for this type of analysis grow significantly with finer spatial resolution.

The last analysis strategy, presented in the following, is not used for neutrino mass analysis and mostly only relevant for the thesis at hand. This strategy is applied if the uniform approach is not appropriate due to strong spatial inhomogeneities and a multi-pixel fit is not feasible due to the computational costs. If the total uncertainty of the dataset, that shall be analyzed, is dominated by statistical uncertainty, we can perform a pixel-wise analysis. This means that each pixel is analyzed with its own parameter set and independently of the neighboring pixels. The same principle holds for a ring- or patch-wise analysis. The advantage of this strategy is the small computation time. The main disadvantage is that not all accumulated statistics are fully propagated onto the parameter of interest and that correlations among the pixels are not taken into account.

Scan Combination

Two methods that are pursued for neutrino mass analyses are important for the thesis at hand. The first one is the stacking approach, the second one is the multi-period method.

The stacking approach relies on good temporal stability and reproducibility of the slow-control parameters [Ake+21b]. This includes for example stability of tritium gas in the source, or the ppm-level high-voltage reproducibility for the time period over which the scans are combined. This is normally the case for the selected scans within one measurement campaign, that pass the quality criteria.
The measured electrons at like scan steps of the various β scans are added and the applied high-voltage values of the specific scan step of all scans are averaged. This results in one high-statistics integral β scan with the same number of scan steps as an individual tritium β scan. Implicitly, not only the scan-wise high-voltage values are averaged in the stacking approach but also all other slow-control parameters. The averaging of the slow-control parameters can introduce a bias on the neutrino mass. Dedicated studies based on Monte-Carlo spectra, that incorporate the slow-control parameter fluctuation as determined in the individual scans, investigate the expected bias due to the stacking procedure that is afterwards included in the analysis. [Ake+21a; Ake+21b]
The main advantage of the stacking procedure is its low computational cost. One disadvantage is that the procedure itself can introduce a bias on the determined neutrino mass, however, this can be corrected for if all fluctuations of the individual slow-control parameters are relatively small and correctly included in the Monte-Carlo studies.

The second approach to combine several runs or measurement campaigns is a multi-period fit. This approach is computationally expensive, and has so far been tested by example of the combination of KNM1 and KNM2 data [HK21]. The advantage of the multi-period fit is that it does not have to rely on the same slow-control parameter settings between the two measurement campaigns or the same absolute values for the scan steps. For example, the KNM1 measurement campaign has a smaller column density by a factor of more than three compared to KNM2. Furthermore, also the scan-wise high-voltage set points differ. The combination of these two campaigns via the stacking procedure is thus not possible, as the slow-control parameters differ too much, resulting in a large neutrino mass bias.
The multi-period fit approach extracts the neutrino mass information by analyzing both campaigns with their individual models, however, both models share one common squared neutrino mass parameter. For a statistical-only, uniform multi-period fit for KNM1 and KNM2, the least-squares term looks like

$$\chi^2 = \chi_1^2\left(m_\nu^2, E_0^1, A_\mathrm{s}^1, R_\mathrm{bg}^1\right) + \chi_2^2\left(m_\nu^2, E_0^2, A_\mathrm{s}^2, R_\mathrm{bg}^2\right).$$

The term χ_1^2 denotes here the least-squares term for the stacked, high-statistics β scan of KNM1, while χ_2^2 is the one for KNM2. The nuisance parameters like endpoint, signal normalization, and background rate are treated in the multi-period analysis for each campaign individually, for example E_0^1 is the spectrum endpoint for KNM1 and E_0^2 the one for KNM2. The squared neutrino mass m_ν^2 as parameter of interest is a shared parameter and links the individual least-squares term with each other. [HK21]
The main advantage of this method is that it allows an unbiased neutrino mass inference, even for parameter sets that show significant differences for the individual slow-control parameters. The major disadvantage is its computational intensity due to the large number of free fit parameters. The example above is only for the combination of two parameter sets and for uniform, statistics-only fit. For each

additional neutrino mass campaign included in the analysis, the number of free nuisance parameters grows as they are normally treated period-wise. Additionally, if the pull-term method is used for the treatment of systematic uncertainties, the number of fit parameters again significantly increases as also the pull-terms are usually individual for each campaign.

3.3.7. KATRIN Databases and Software Tools

To enable the analysis of the measured integral spectrum with respect to the neutrino mass, several successive data layers have to process the flood of data produced by the several detectors and sensors in the large-scale KATRIN experiment. Therefore, a run control and data acquisition software is used together with a sophisticated database infrastructure. Afterwards, the acquired data can either be extracted via web frontends or the Kasper package allows user-defined analysis.

Databases

M. Kleesiek presents a detailed and technical insight into the design of the KATRIN software architecture in reference [Kle14]. Subsequently, we will only give a brief overview over the relevant aspects for the thesis at hand.

The Orca software [How+04] is used in KATRIN for run control and data acquisition of the FPD system as well as operation of crucial experimental parameters. For example, FPD measurements can automatically be started and stopped with dedicated runlists, the eLFCS coil currents can be altered, or the Rear Section e-gun can be switched on. The data acquired via Orca, especially the measured FPD counts in the individual runs, are saved in a dedicated storage.

The values of more than 15,000 KATRIN slow-control channels [Sei19], comprising the read-back of various types of sensors, are saved to a dedicated slow-control database. The Advanced Data Extraction Infrastructure ADEI with a web-based frontend allows to monitor the data from the sensors in real time. Additionally, slow-control data can be extracted for further use or user-defined time ranges can be investigated. Note that only raw values, without any sensor calibration, are displayed in ADEI. [Chi+10]

The KATRIN Data Base KDB server is the central connection to all KATRIN data. Contrary to ADEI, KDB can access in addition to the slow-control database the calibration of the individual sensors or their geometry and location. Furthermore, it retrieves also data from the Orca storage, allowing the processing of FPD data. Besides the web frontend, KDB can also corporate with the Kasper software package for refined analysis. [Kle14]

The Kasper Software Package

Kasper is a global analysis and simulation package for the KATRIN experiment, which comprises more than ten semi-independent packages for simulation and analysis. We present in the following the packages relevant for the present thesis, based on the descriptions given in references [Kle14; Beh16; Hei18].

- Kommon: Core module that provides basic features for other packages, for example definitions of physics constants or mathematical utilities.
- KGeoBag: Contains geometry definitions and shapes that can be accessed by other modules, for example Kassiopeia.
- KEMField: Comprises algorithms to compute electric and magnetic fields from a given geometry (see also section 3.3.8). It is one of the Kassiopeia core modules where electromagnetic field simulations are used as input.
- Kassiopeia: Module for particle tracking Monte-Carlo simulation. Allows to simulate charged particles in electromagnetic field and complex geometries [Fur+17]. As the KGeoBag and KEMField modules are basic packages for Kassiopeia, we use the term "Kassiopeia" as umbrella term for all three packages.
- KaLi: Library that accesses measurement and slow-control data from the KDB through a web service layer. This module is used inter alia by the BEANS package.
- BEANS: Elements to build an analysis sequence to analyze raw data from the FPD or raw slow-control data.
- KSC: Module that contains KATRIN-specific code, for example for run summary generation (see section 3.3.9), to make Kassiopeia usable for other experiments.
- Peaberry: Post-analysis framework as extension to BEANS that provides the pre-processed input data. Contains methods to apply fits with various algorithms and an e-gun transmission function model (see section 5.3.1).
- SSC: Source and spectrum calculation for differential and integral tritium and krypton spectra. For the calculation of the response function, SSC can model gas dynamical properties of the WGTS (see section 7.2) and determine the transmission function of the MAC-E filters.
- KaFit: Translates SSC expectation for the calculated spectra into FPD count rates. Contains statistical tools for spectrum analysis to infer best-fit parameters, using SSC prediction as underlying hypothesis.

3.3.8. Field Calculation Methods

The energy analysis principle with the MAC-E filter technique used in KATRIN relies on optimized interplay of electric and magnetic fields. A correct simulation of the electromagnetic fields for an accurate transmission function modeling or for further optimizations of KATRIN's operational parameters (for example the shifted analyzing plane in chapter 6) is thus crucial.
The methods for the electromagnetic field calculation is part of the field solver module KEMField [Cor14; Bar17] of Kasper. In the context of the present thesis, the calculation of electromagnetic fields takes only place for KATRIN-specific geometry, that are defined in the Kasper module KGeoBag. The central module that links the computation of electromagnetic fields with the KATRIN geometry is Kassiopeia.

Magnetic Field Calculation

KEMField differentiates for the calculation of magnetic fields between non-axially and axially symmetric sources, as different field solvers can be applied. The geometry of the source from which the magnetic field is to be derived is passed from KGeoBag via Kassiopeia to KEMField. [Beh16]

Non-axially symmetric sources can be calculated using the law of Biot-Savart. The magnetic field $\mathrm{d}\vec{B}$ at location $\vec{r}$, that is generated by a current I running though a line segment $\mathrm{d}\vec{s}$, yields

$$\mathrm{d}\vec{B} = -\frac{\mu_0}{4\pi} \cdot \frac{I \cdot \vec{r} \times \mathrm{d}\vec{s}}{r^3}$$

with μ_0 as magnetic permeability constant [Gri14]. The magnetic field of a body with complex shape can be modeled as a field superposition of n finite small line segments. The resulting field is then calculated as

$$\vec{B}_{\mathrm{tot}} = \sum_{i=1}^{n} \mathrm{d}\vec{B}_i.$$

A better accuracy of the calculated magnetic field can be achieved by increasing the number of line segments in the calculation at the expense of a slower computational speed. [Gro15; Beh16]

As the discretization of complex bodies leads to considerably larger calculation time, we try to avoid it in the magnetic field calculation of axially symmetric bodies, for example beamline solenoids. Two methods are introduced for the field calculation of symmetric bodies, namely the elliptic integration method and the zonal harmonic expansion approach.
The elliptic integration method exploits that the Biot-Savart's law can be expressed for a thin coil with the elliptic integrals of first (equation 3.20) and second kind (see equation 3.21)

$$K(k) = \int_0^{\pi/2} \frac{\mathrm{d}\theta}{1 - k^2 \sin^2\theta}, \tag{3.20}$$

$$E(k) = \int_0^{\pi/2} \sqrt{1 - k^2 \sin^2\theta}\, \mathrm{d}\theta. \tag{3.21}$$

For a realistic coil with finite thickness R and length Z, the elliptic integral of third kind is also necessary to reduce the calculation to a one-dimensional problem in radial direction

$$\Pi(n,k) = \int_0^{\pi/2} \left(\left(1 - n^2 \sin^2\theta\right)\sqrt{1 - k^2 \sin^2\theta}\right)^{-1} \mathrm{d}\theta.$$

The axial B_z and radial B_r magnetic field components can then be calculated as

$$B_z = \hat{B}_z(Z_{\mathrm{max}}) - \hat{B}_z(Z_{\mathrm{min}}),$$
$$B_r = \hat{B}_r(Z_{\mathrm{max}}) - \hat{B}_r(Z_{\mathrm{min}}),$$

with

$$\hat{B}_z = -\frac{\mu_0 \lambda}{\pi} \frac{(z-Z)R}{(r+R)S} \left(K(k) + \frac{R-r}{2R} (\Pi(n,k) - K(k)) \right),$$
$$\hat{B}_r = -\frac{\mu_0 \lambda}{\pi} \frac{R}{S} \left(2\frac{E(k) - K(k)}{k^2} + K(k) \right),$$

with the abbreviations

$$S = \sqrt{(r+R)^2 + (z-Z)^2},$$
$$k = \frac{4rR}{S^2},$$
$$n^2 = \frac{4rR}{(r+R)^2}.$$

The elliptic integral method allows to calculate the magnetic field at any position without the need for discretization. However, due to the large number of necessary integrations, this approach is still rather computationally expensive. [Wan13; Gro15; Beh16]

The zonal harmonic expansion approach [Gar51; Glü11] provides a significantly faster way to compute the magnetic field of an axially symmetric body. The method exploits that for this geometry, the magnetic field at an arbitrary off-axis point can be expressed in terms of the Legendre polynomial expansion and its derivative at a source point on the symmetry axis. If the point p, for which the magnetic field shall be calculated, is located within the convergence radius ρ_{cen} of the closest source point z_0, the magnetic field is computed with the central expansion to

$$B_z = \sum_{n=0}^{\infty} B_n^{\text{cen}} \cdot \left(\frac{\rho}{\rho_{\text{cen}}} \right) \cdot P_n(\cos\theta),$$
$$B_r = -\sin\theta \cdot \sum_{n=1}^{\infty} \frac{B_n^{\text{cen}}}{n+1} \left(\frac{\rho}{\rho_{\text{cen}}} \right) \cdot P_n'(\cos\theta)$$

with ρ as the distance of p and z_0. B_n^{cen} are the source point coefficients, that have to be computed beforehand. The Legendre polynomials of grade n and their derivatives are denoted as $P_n(\cos\theta)$ and $P_n'(\cos\theta)$. The zonal harmonic expansion converges fast for smaller ρ/ρ_{cen}. A large number of source points on the symmetry axis is thus advantageous, however, for each source point a number of coefficients has to be calculated beforehand. To reduce the necessary recalculations, KEMField saves the calculated coefficients to a cache to re-load them for calculations with the same field configuration. If the point p is located outside the convergence radius $\rho > \rho_{\text{cen}}$, the magnetic field can be calculated with the remote expansion to

$$B_z = \sum_{n=2}^{\infty} B_n^{\text{rem}} \cdot \left(\frac{\rho_{\text{rem}}}{\rho} \right)^{n+1} \cdot P_n(\cos\theta),$$
$$B_r = -\sin\theta \cdot \sum_{n=2}^{\infty} \frac{B_n^{\text{rem}}}{n} \left(\frac{\rho_{\text{rem}}}{\rho} \right) \cdot P_n'(\cos\theta).$$

ρ_{rem} is the maximum distance between source point z_0 and the source, B_n^{rem} are the remote source coefficients, that also have to be computed beforehand. The expansion converges faster for smaller ratios ρ_{rem}/ρ. [Glü11; Wan13; Gro15; Beh16]

The zonal harmonic expansion calculates the magnetic field of axially symmetric bodies several orders of magnitude faster than the approach using elliptic integrals. However, the zonal harmonic method is not able to accurately determine the magnetic field close to the coils due to a mismatch of ρ_{rem} and ρ_{cen}. KEMField uses mostly the zonal harmonic expansion to calculate the magnetic fields in KATRIN due to its fast computational speed and falls back to the slower elliptic integration method if the zonal harmonic estimation is not valid. [Gro15; Beh16]

Electric Field Calculation

Similar to the magnetic field computation, also the calculation of the electric field can be divided into non-axially and axially symmetric problems. Also here, the electric fields can be calculated via integration (non-axially symmetric bodies) or exploiting approximate methods like the zonal harmonic expansion (axially symmetric bodies) [Glü11; Cor14; Beh16].

KEMField uses the boundary element method for the calculation of non-axially symmetric bodies. The electrode geometry is split into a large number n of finitely small elements, the charge density is assumed to be homogeneously distributed on the element. As a first step to calculate the electric field, the charge densities σ_j for each element has to be calculated via

$$U_i = \sum_{j=1}^{n} C_{ij}\sigma_j. \tag{3.22}$$

The electric potential applied to electrode i is labeled U_i here. $C_{ij} = C_j(\vec{r}_i)$ denotes the elements of the Coulomb matrix, that accounts for that the individual electrodes influence each other. The matrix elements are calculated as

$$C_j(\vec{r}_i) = \frac{1}{4\pi\epsilon_0}\int_{S_j}\frac{\mathrm{d}^2\vec{r}_S}{|\vec{r}_i - \vec{r}_S|}$$

with S_j being the individual elements of body S, and ϵ_0 is the vacuum permittivity. The charge densities are then determined by solving equation 3.22 using for example the iterative solver Robin Hood [For+11]. Also here, the calculated charge densities for a specific geometry are stored in a cache in KEMField for fast reevaluation of the same geometry. The potential Φ at a specific location can finally be calculated with an integration over all elements to

$$\Phi(\vec{r}_i) = \frac{1}{4\pi\epsilon_0}\int_S \frac{\sigma(\vec{r}_S)}{|\vec{r}_i - \vec{r}_S|}\mathrm{d}^2\vec{r}_S.$$

The necessary calculation time scales with n^2 and is therefore not fast for large numbers of elements n to describe all electrodes. [Wan13; Gro15]

The electric field of axially symmetric bodies can be evaluated using either elliptic integrals or zonal harmonics expansion. Both methods work the same as for the magnetic fields with all the disadvantages and advantages. In contrast to the magnetic field calculation, the number of electrode segments in KATRIN and thus the number of source points for the zonal harmonic expansion is quite large, resulting in long computation time for the coefficients. Nevertheless, once the coefficients have been calculated, the field evaluation is quite fast which is useful if a simulation needs several field evaluations. [Wan13; Beh16]

3.3.9. Implementation of Input Parameters for Data Analysis

SSC and KaFit require several input parameters to analyze an integral β-decay measurement with respect to the neutrino mass. For example, SSC needs the information on the tritium gas density in the WGTS and the applied electromagnetic fields to calculate the integral spectrum. Technically, the relevant information to analyze a (toy-)measurement is stored in two files, that are called run and period summary.

Run Summary

In case of neutrino mass analysis, the run summary describes an individual β scan. If the run summary describes a real measurement, it is computed in near-real time for every measured β scan in a measurement campaign. Its most-important information are the measured counts at the FPD pixels in the region of interest at the individual scan steps, the applied Main Spectrometer high voltage, and the measurement time of the scan steps. Additionally, it contains relevant slow-control values for integral spectrum calculation during the measurement, for example the gas amount in the WGTS at each scan step or the tritium concentration in the source. The only relevant slow-control parameter that is not part of the run summary is the magnetic field, however, this is covered by the period summary.
A run summary is not only processed for every β scan, but can be computed for all kinds of rate measurements with the FPD, taking into account special requirements relevant for the subsequent analysis. A special run summary can be produced for ^{83m}Kr measurements, as decay electrons from ^{83m}Kr are often used in KATRIN for calibration purpose (see section 5.4.1).
An overview of the computing procedure and the currently available run summary versions are given in reference [KAT21].

Period Summary

The period summary contains information on the electric retardation for a certain applied voltage on the high-voltage system of the Main Spectrometer as well as information on the magnetic field at relevant positions in the spectrometer and the beamline. The period summary gives individual values on the electric and the magnetic fields for each FPD pixel to enable a pixel-wise analysis. In case of the magnetic fields, this means that an electron arriving at a certain pixel has to be transmitted through a certain magnetic field in the analyzing plane and a certain PCH field. In contrast to the run summary, there is normally only one period summary per measurement campaign, as the fields feature sufficiently high stability throughout one campaign. For the analysis of the first two neutrino mass measurement campaigns, the period summary is completely derived from simulations including the best knowledge on the actual experimental setup. Nevertheless, it can also be obtained with dedicated measurements, as proposed in chapter 5 and 6.
The derivation of the period summary for the magnetic field in the analyzing plane for the symmetric Main Spectrometer configuration is visualized in figure 3.14. As a first step, not shown in figure 3.14, detailed Kassiopeia simulations test whether the electrons' analyzing points are sufficiently close to the axial center of the Main

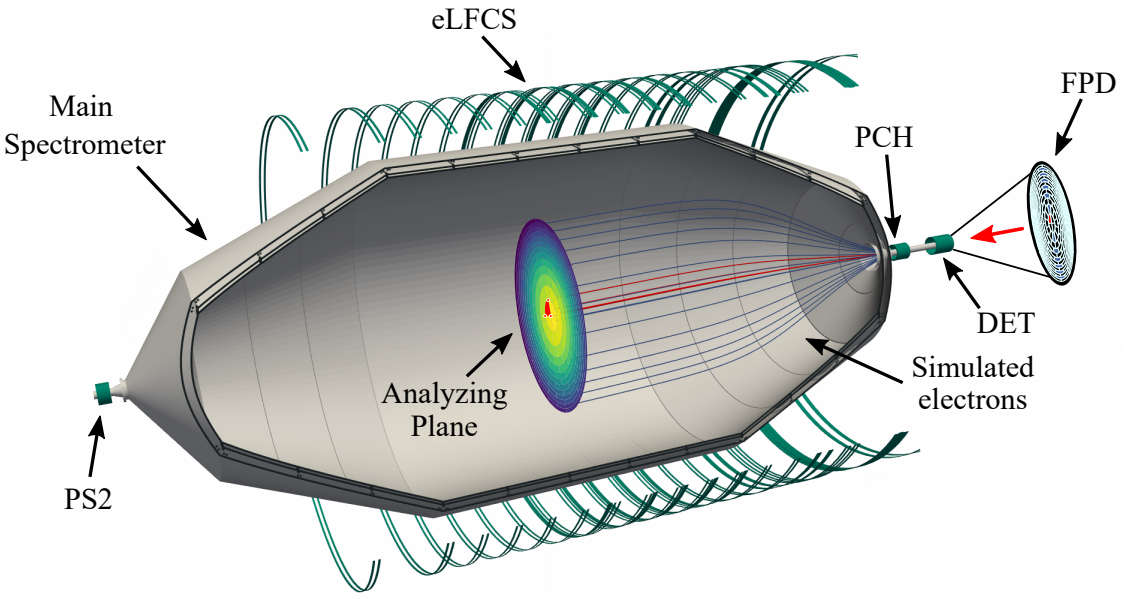

Figure 3.14.: **Sketch of the calculation of the period summary for the magnetic field in the analyzing plane.** The magnetic field in the analyzing plane shall be computed for electrons that arrive at the red-shaded pixel at the FPD. Therefore, pseudo-electrons are started in upstream direction at the pixel boundary and its center and tracked into the analyzing plane (red lines). In the analyzing plane, the magnetic field for the effective area of the pixel projection is calculated (red-shaded pixel). Figure adapted from [BB20].

Spectrometer for all positions in the magnetic flux tube ($z = 0\,\mathrm{m}$ in the KATRIN coordinate system). If this is fulfilled, we can approximate that all electrons are analyzed with respect to their kinetic energy in the Main Spectrometer at the plane that is perpendicular to the beam axis and located at $z = 0\,\mathrm{m}$. In this plane, the magnetic field is calculated with Kassiopeia on more than 7000 discrete points, constituting a fine-grained magnetic field map. Each FPD pixel maps to a specific area on the analyzing plane. The area is determined by field line tracking, which means that pseudo-electrons with large surplus energy and pitch angle zero are started at the FPD in upstream direction. These pseudo-electrons start at each FPD pixel corner and in the center of each pixel. The area in the analyzing plane is then estimated by the position of these pseudo-electrons at $z = 0\,\mathrm{m}$. The central magnetic field value in the analyzing plane for a specific pixel is then determined by calculating the median of the magnetic field map points within the projected area of this pixel. The inhomogeneity is calculated via the spread of the points. The described procedure is for example repeated for the electric retardation in the analyzing plane or the PCH magnetic field. [BB20]

4. Characterization of Pinch and WGTS Magnetic Field

The WGTS magnet system as well as the Pinch magnet (PCH) are part of the KATRIN beamline magnets. As discussed in section 3.1.2, their task goes beyond the mere magnetic guidance of the β-decay electrons from the source to the FPD. These two magnetic field strengths, together with the magnetic field strength of the analyzing plane, define the MAC-E filter transmission properties. Consequently, we need to determine the absolute strength of the two magnetic fields, and also their spatial homogeneity, to prevent biased analysis results of the neutrino mass. The requirements on the PCH magnetic field, a characterization via simulations, and a method to determine the coil alignment in the experimental KATRIN setup are discussed in section 4.1. Subsequently, the source magnetic field is investigated via simulations and measurements inside the beamline in section 4.2.

4.1. Pinch Magnetic Field

The PCH magnetic field is the strongest magnetic field in the KATRIN beamline and thus forms a magnetic mirror for the β-decay electrons. A β-decay electron with pitch angle in the source larger than

$$\theta_{\mathrm{max}} = \arcsin\left(\sqrt{\frac{B_{\mathrm{src}}}{B_{\mathrm{pch}}}}\right)$$

is magnetically reflected in the PCH. B_{src} denotes the magnetic field in the source, at the location of the tritium decay. By reflecting electrons with large pitch angles, the PCH field has an impact on the Main Spectrometer energy resolution ΔE with

$$\Delta E = E \cdot \frac{B_{\mathrm{ana}}}{B_{\mathrm{pch}}}$$

where B_{ana} is the magnetic field in the analyzing plane and E is the total kinetic electron energy. [Kle+19] It is therefore crucial for an accurate description of the Main Spectrometer transmission function, and thus for successful neutrino mass analysis, to accurately and precisely characterize the PCH magnetic field.
The PCH was originally planned to be operated at 6 T magnetic field during neutrino mass measurements [KAT05]. Due to the 70 % global magnetic field setting to reduce the risk of quenching, its adapted value during neutrino mass measurements is 4.2 T.

4.1.1. Pinch Magnetic Field in Neutrino Mass Analysis

We rely on magnetic field simulations of the PCH field strength as input for neutrino mass analysis mainly due to two reasons.
Firstly, direct time-consuming magnetic field measurements inside the solenoid can only be performed as long as it is operated in standalone mode, without being integrated in the global KATRIN beamline. A direct PCH field measurement inside the coil has only been performed once as part of commissioning measurements in 2015 (see reference [Sch15]).
Secondly, simulations allow one to numerically estimate the magnetic field with a fine spatial resolution inside the beam tube which is not possible with measurements. As discussed in section 3.3.9, it is necessary to describe which FPD pixel "sees" which PCH field in neutrino mass analyses, to draw conclusions about the properties of the incoming β-decay electrons at that specific pixel. The pixels' PCH field is calculated by a projection of the FPD into the PCH, upstream along the magnetic flux tube that guides the decay electrons from source to FPD (see section 3.3.9). As we suffer from small misalignments between the beamline components, for example PCH and DET, the projection cannot be accessed via direct measurements, as the location of a specific FPD pixel projection in the PCH is unknown without magnetic field simulations. Furthermore, these direct measurements, which are only possible in standalone mode, would have to be repeated every time the beamline setup is modified (for example exchange of detector wafer).
We employ the zonal harmonic field solver as part of KEMField and Kassiopeia for the calculation of the field inside the PCH, due to its fast calculation time and robust results (see section 3.3.8). The simulation must meet certain requirements in accuracy and precision to avoid a bias or large systematic uncertainties in neutrino mass analysis.

An inaccurate estimation of the absolute PCH magnetic field strength causes a bias on the determined neutrino mass. We investigate this resulting systematic uncertainty on the neutrino mass as a function of the model uncertainty ΔB_{pch} of the PCH magnetic field strength. The systematic uncertainty is calculated with the pull-term method (see section 3.3.5). Therefore, a typical KATRIN Asimov dataset is produced using the SSC software package. The dataset is based on the calculated PCH magnetic field assuming perfect temporal stability, which is a valid approximation over one neutrino mass measurement campaign. The neutrino mass is set to zero for the calculation of the Asimov dataset. Typical operational parameters are chosen for the nuisance parameters necessary for spectrum calculation, for example the magnetic field in the analyzing plane. Instead of the nominal four-parameter fit with neutrino mass m_ν^2, spectrum endpoint E_0, normalization A_s, and background R_bg, the PCH field B_pch is added as fifth fit parameter constrained by a penalty term. The penalty term in the likelihood is Gaussian-shaped with mean B_pch and width ΔB_pch, chosen according to the investigated uncertainty. The systematic uncertainty on the squared neutrino mass $\Delta m^2_{\nu,\mathrm{sys}}$ caused by the uncertainty of the PCH magnetic field is calculated using the total uncertainty on the neutrino mass $\Delta m^2_{\nu,\mathrm{tot}}$ and the statistical uncertainty $\Delta m^2_{\nu,\mathrm{stat}}$. $\Delta m^2_{\nu,\mathrm{stat}}$ is determined by calculating the uncertainty on m_ν^2 in the four parameter fit of m_ν^2, E_0, A_s, and R_bg to the Asimov dataset. The total uncertainty $\Delta m^2_{\nu,\mathrm{tot}}$ is given by the uncertainty on m_ν^2 in the five parameter fit with B_pch as fit parameter, only constrained by the penalty

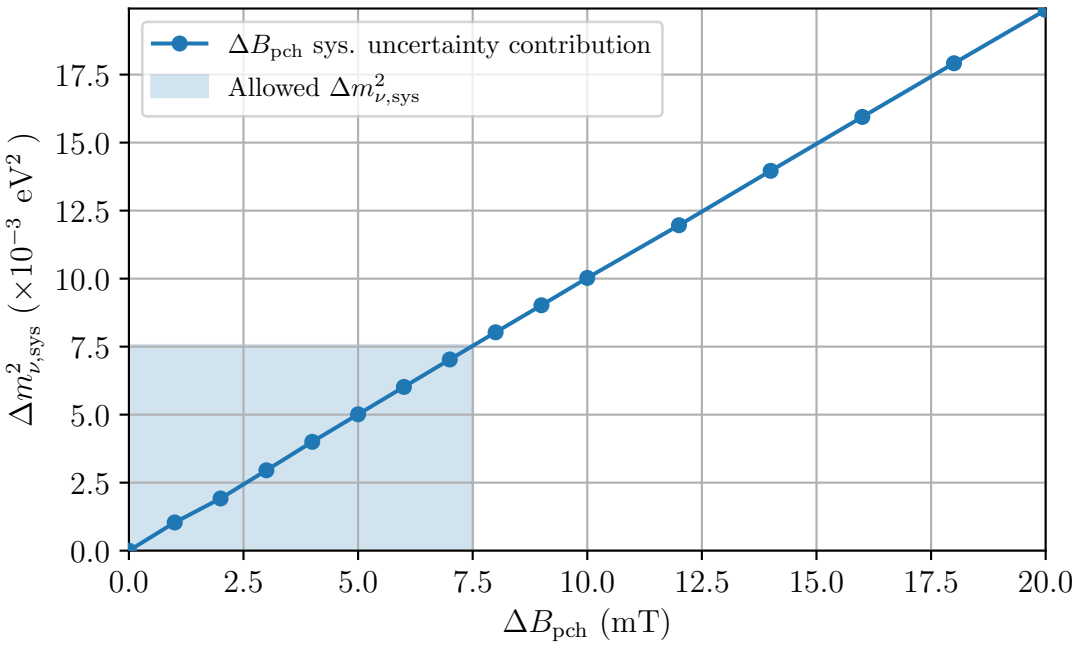

Figure 4.1.: **Impact of the PCH magnetic field uncertainty ΔB_{pch} on the systematic neutrino mass uncertainty $\Delta m^2_{\nu,\mathrm{sys}}$.** The systematic neutrino mass uncertainty increases proportionally to the PCH field uncertainty. The maximally allowed uncertainty on the PCH field is 7.5 mT in order to fulfill the KATRIN requirement on a single systematic uncertainty contribution of $\Delta m^2_{\nu,\mathrm{sys}} \leq 7.5 \times 10^{-3}\,\mathrm{eV}^2$.

term. The pure systematic contribution due to the source magnetic field uncertainty is then approximated by

$$\Delta m^2_{\nu,\mathrm{sys}} = \sqrt{\left(\Delta m^2_{\nu,\mathrm{tot}}\right)^2 - \left(\Delta m^2_{\nu,\mathrm{stat}}\right)^2},$$

according to Gaussian uncertainty propagation.
The results of the sensitivity study for PCH field uncertainties $\Delta B_{\mathrm{pch}} \in [0, 10]\,\mathrm{mT}$ are presented in figure 4.1. The systematic neutrino mass uncertainty is proportional with the PCH field uncertainty in the investigated range. The maximally allowed contribution of a single systematic effect is $\Delta m^2_{\nu,\mathrm{sys}} \leq 7.5 \times 10^{-3}\,\mathrm{eV}^2$. This translates with the performed sensitivity study to the maximally allowed uncertainty $\Delta B_{\mathrm{pch}} = 7.4\,\mathrm{mT}$ on the PCH field, which must be undercut to meet the KATRIN requirements.

The uncertainty estimation on the absolute simulated PCH field, used in neutrino mass measurements, is two-fold. The first part of the uncertainty estimation is given by the comparison of simulation and direct magnetic field measurement inside the PCH. The second part comprises uncertainties stemming from a possible inaccurate projection of the FPD into the PCH due to non-considered misalignment in the geometry model.
The direct magnetic field measurement used as comparison to the simulation was performed in 2015. The PCH was not yet part of the beamline at that time, allowing detailed magnetic field measurements in its warm bore. C. Schönfeld performed

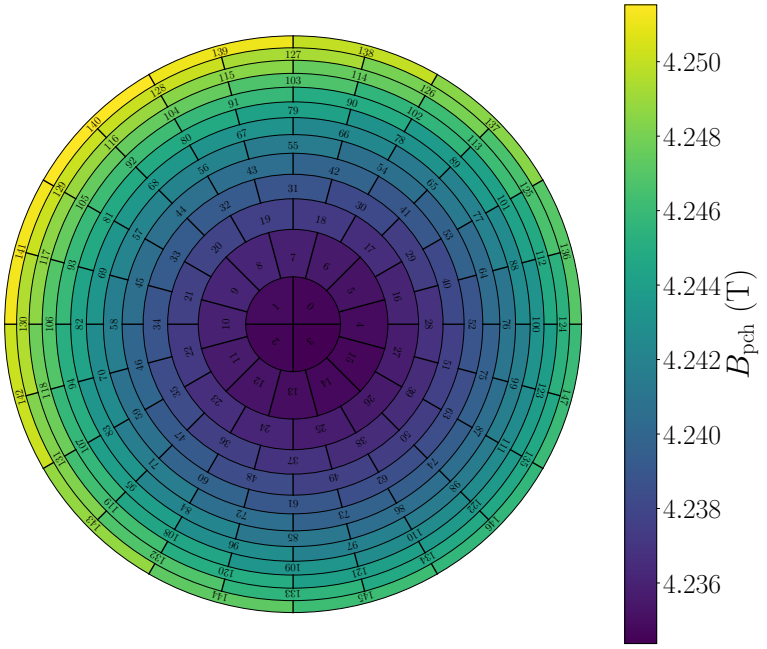

Figure 4.2.: **The simulated PCH magnetic field B_{pch} for each FPD pixel.** The PCH field is minimal for the central FPD pixels at 4.235 T and increases by 0.4 % towards the outer-most rings. The small azimuthal asymmetry is caused by misalignment between the FPD and the PCH. Simulation data extracted from period summary, produced by J. Behrens.

the measurement with a mean PCH field of 6 T, as this was the planned nominal field. The field in the center of the solenoid, measured with an NMR precision teslameter, amounted to (6.0099 ± 0.00003) T. [Sch15] Using the PCH field model as implemented in Kassiopeia, we calculate the magnetic field to (6.011 ± 0.004) T for the PCH current setting used during the measurement. The simulation uncertainty stems from the experimental error on the positioning of the NMR probe within the PCH during the measurement, that we conservatively estimate to ± 1 cm. The uncertainty on the simulated magnetic field in this first part of the uncertainty estimation is given by the deviation between measurement and simulation, and the uncertainty on the measurement as well as on the simulation. All contributions are added in quadrature, leading to a relative uncertainty of 0.06 %.
The PCH field features radial magnetic field variations in the beamline due to the solenoid's geometrical design. The outer-most pixels have 0.4 % larger field strength compared to the bulls-eye pixels in the projection of the FPD into the center of the PCH (see figure 4.2). Misalignment between FPD wafer and PCH, for example coil tilts, which are not correctly taken into account in the simulation, can shift the calculated position of the FPD projection in the PCH compared to the true position. This leads to inaccurate magnetic field estimations for the individual FPD pixels. Simulations in combination with dedicated measurements indicate that the projection of the FPD in the PCH could vary in the millimeter range due to misalignment (see also section 4.1.2), resulting in a maximum uncertainty on the pixel-wise calculated PCH magnetic field of 0.08 %.
The uncertainty on the PCH field simulation is given via error propagation by the squared sum of both contributions, leading to a total relative uncertainty on the PCH

magnetic field of 0.1 %. This translates to a systematic uncertainty contribution on the neutrino mass of $\Delta m^2_{\nu,\mathrm{sys}} = 3 \times 10^{-3}\,\mathrm{eV}^2$, meeting the KATRIN requirements of a maximal single systematic contribution of less than $7.5 \times 10^{-3}\,\mathrm{eV}^2$.

Misalignment of the PCH relative to the FPD and the DET does not only affect the calculated PCH field, but also the simulated projection of the FPD into the Main Spectrometer. If the misalignment is not correctly included in the Kassiopeia model, the consequences are inaccurate magnetic field and electric potential calculations for the analyzing plane. To improve the understanding of the spatial evolution of the FPD projection into the analyzing plane, it is necessary as first step to investigate the alignment of the PCH and DET compared to one another.

4.1.2. Alignment Measurements with Hall Probe

The alignment parameters that are important for magnetic field calculations of an individual beamline solenoid are divided into two categories. The first category describes the alignment of the cryostat with five parameters. Three of the five parameters are the position in the KATRIN analysis coordinate system, in which the center of the Main Spectrometer is the reference. Two parameters are Euler angles, indicating the tilt of the cryostat relative to the coordinate system axes. The second category expresses the orientation of the coil that generates the magnetic field within the cryostat system. Three parameters describe the shift of the coil in the cryostat, and two angles take tilts of the coil in the cryostat into account.
The alignment of the cryostat with respect to the global KATRIN coordinate system is determined with dedicated FaroARM® measurements. These measurements are performed on a regular basis after maintenance breaks to measure any changes in the geometrical hardware setup.
The alignment of the coil in the cryostat in operational mode cannot trivially be measured due to the closed system. A possibility to estimate these alignment parameters is the comparison of simulations with magnetic field measurements at various, well-known positions around the cryostat. Initial efforts with this type of alignment measurement have already been performed with the PCH magnet (see reference [Mül14; Sch15]). In the thesis at hand, a refined method based on these approaches is developed in cooperation with Marco Deffert. The refined method is presented in the following.

Measurement Procedure and Analysis

A custom-built holding structure allows a Hall probe to be mounted in multiple positions outside the solenoid cryostat being investigated. The measurement positions are located at the lateral surface of the cryostat near the two end caps, as visualized in figure 4.3. The measurement positions cover the azimuth angle range in steps of 10°, leading to 36 measurement positions per side.
The coordinates of the measurement positions, as well as of the cryostats in the global KATRIN coordinate system, are determined with FaroARM® measurements with an accuracy of better than 0.5 mm [Mül21]. Due to the beamline setup around the PCH and DET, it is not possible to reach every measurement position with the FaroARM®, therefore not all positions can be used for the analysis.

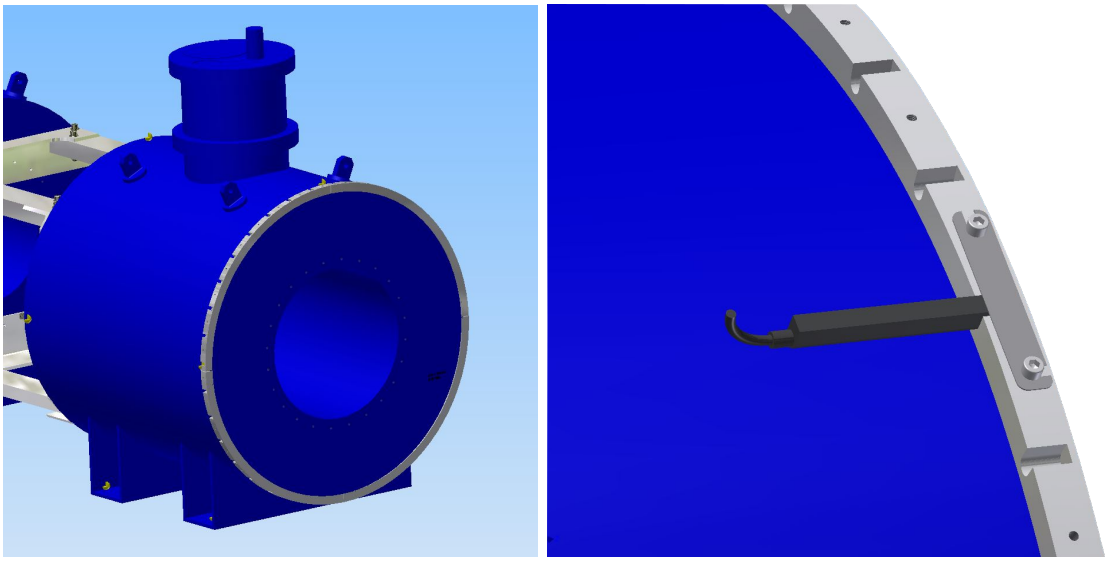

Figure 4.3.: **CAD drawing of the Hall probe holding structure for the PCH and DET alignment measurements.** The Hall probe holding structure (silver-colored) on the downstream side of the DET cryostat (blue) is shown in the left drawing. In the described measurement, the holding structure is installed at both ends of the cryostat. The Hall probe (black) position in the holding structure for a magnetic field measurement is visualized in the right drawing. Drawings provided by K. Müller.

We measured the stray field of the beamline magnets with two THM1176 three-axis Hall magnetometers [Met20] in December 2020. The Hall magnetometers were chosen for their ease of use in combination with laptop computers, which allow magnetic field measurements without long preparation time and without the need for additional external data acquisition systems. The magnetic field measurement with three axes simplifies the analysis considerably, since the total magnetic field can be obtained in the data analysis, regardless of the orientation that changes with the measurement positions.

The analysis is based on the comparison of Kassiopeia magnetic field calculations at the measurement positions with the measured field. The five parameters of interest in an individual measurement, describing the coil alignment and tilts within the cryostat, are obtained from a χ^2 minimization. We do not have to take into account the cryostat orientation in the analysis, as the measurement positions as determined by the FaroARM® are defined in the local cryostat system.
Reliable parameter inference requires accurate uncertainty estimation of the measured data and model prediction. The dominating uncertainty on an individual field measurement is given by the Hall probe uncertainty on a single measurement. Both Hall probes were calibrated with an NMR teslameter before the measurement, leading to a relative uncertainty of 0.3 % on the absolute measured field for the magnetic field strength of interest. Furthermore, it must be taken into account that the uncertainty is correlated with other measurements made with the same probe. We therefore decide to take this uncertainty into account via the pull-term method. A calibration factor for each sensor is introduced and applied to the measured data taken with the respective probe. The calibration factors are fit parameters in the χ^2 minimization, however they are constrained by a Gaussian-shaped penalty term

with a mean of 1 and a width of 0.3 %. Another source of measurement uncertainty stems from the reproducibility of the Hall sensor, taking into account time-dependent drifts of the measurement due to, for example, temperature fluctuations of the sensor. We estimate the magnitude of this effect by making several field measurements at constant position at different times, leading to a relative uncertainty of 0.2 %. The third uncertainty, that is taken into account in the analysis, is given by the measurement position reconstruction. Each measurement position is determined by the FaroARM® with 0.5 mm accuracy. This causes an uncertainty on the magnetic field simulation as the exact position that should be used for the comparison between simulation and measurement is not known. Calculations carried out at the determined measurement positions with a tolerance of ±0.5 mm yield a relative uncertainty of 0.16 % on the field simulation for the comparison.
We perform the χ^2 minimization, and obtain the parameters and their uncertainty estimation, with a minimization algorithm using the Trust Region Reflective method as implemented in the LMFIT package [New+14].

We start with the analysis of the PCH measurement. All beamline magnets, except for the PCH, were switched off during the measurement. The PCH was operated at its nominal magnetic field of 4.2 T. Out of the 72 possible measurement positions, 50 can be used for the analysis. The minimization term S contains in total seven fit parameters

$$\begin{aligned} S(\delta x, \delta y, \delta z, \alpha, \beta, A_1, A_2) = &\sum_i \frac{\left(A_1 \cdot D_i - M_i(\delta x, \delta y, \delta z, \alpha, \beta)\right)^2}{\sigma_i^2} \\ &+ \sum_j \frac{\Big(A_2 \cdot D_j - M_j(\delta x, \delta y, \delta z, \alpha, \beta)\Big)^2}{\sigma_i^2} \\ &+ \frac{(A_1 - 1)^2}{0.003^2} + \frac{(A_2 - 1)^2}{0.003^2} \end{aligned}$$

where D_i denotes the data that is measured with Hall probe number one, while D_j is the data taken with Hall probe two. The models M_i and M_j describing the measured data depend on the alignment parameters of the coil within the cryostat, namely the position shifts δx, δy, and δz, as well as the horizontal and vertical tilts α and β. The σ term is the estimated uncertainty on the individual measurement, given by the uncertainty on the position reconstruction and the reproducibility of the Hall probe. The 0.3 % calibration uncertainty on both Hall probes is included via the pull-term method by introducing the amplitudes A_1 and A_2 as nuisance parameters in the minimization, which are constrained by the pull-terms. The minimization of S yields a normalized $\chi^2 \approx 0.85$, indicating that the model describes the data well within its uncertainties.
The measured data and the best-fit model calculations versus the azimuth angle are shown in figure 4.4. The total magnetic field measured on the upstream side is significantly larger compared to the downstream side. This indicates that the coil inside the cryostat is shifted towards the upstream side. The data in each graph has a sinusoidal structure over the azimuth angle, which is a typical sign of radial coil shifts or tilts. The best-fit parameters for the alignment of the PCH, found in the χ^2 minimization, are printed in the middle column of table 4.1. The assumption of a downwards shifted coil inside the cryostat is confirmed by the best-fit parameter with $\delta z = (-4.1 \pm 0.2)$ mm. The best-fit estimators also indicate significant radial

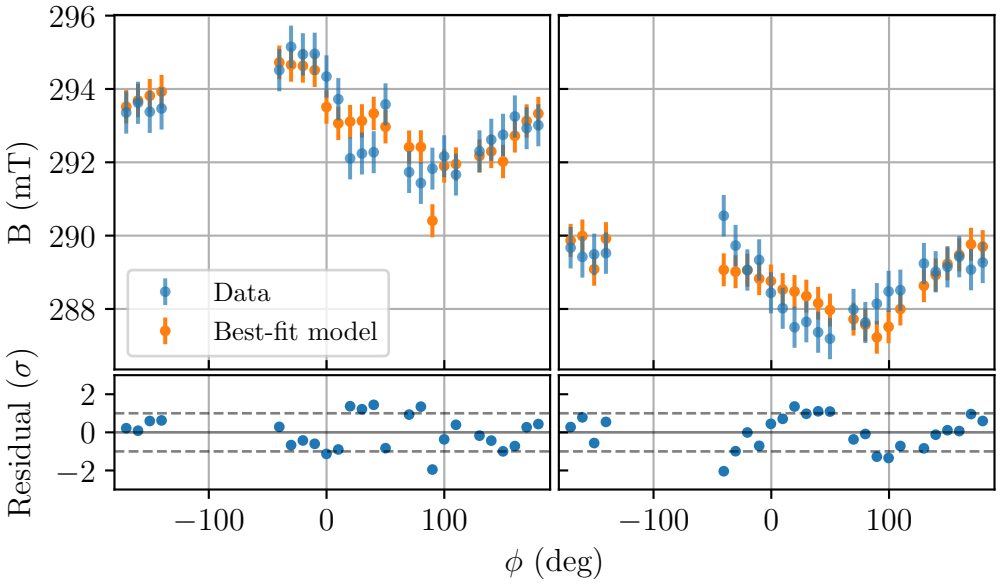

Figure 4.4.: **PCH coil alignment measurements relative to the PCH cryostat with stray field measurements.** The plots in the left column refer to the measurement performed at the upstream end of the PCH cryostat, and the right side to the downstream end. The comparison of the measured magnetic field and best-fit model versus the measurement position, given by the azimuth angle ϕ, is shown in the upper panels. The best-fit model is obtained by a χ^2 minimization with respect to the alignment parameters. The residuals between measurement and best-fit model in units of the uncertainty are presented in the graphs in the lower panels.

shifts (see PCH δx and δy in table 4.1) and tilts (PCH α, β) of the coil relative to the cryostat.
The comparison of the best-fit model with the measurement, shown by the residuals in figure 4.4, indicates a possible analysis problem. The residuals are not randomly distributed but have a structure, especially the residuals on the downstream side (right graph in figure 4.4). Possible reasons for this residual structure are unaccounted magnetic field contributions or unknown drifts in the Hall probe. In the data pre-processing for the analysis described above, a correction for magnetic background fields at the PCH is included. Consequently, unaccounted magnetic field contributions can be excluded as the cause of the residual structure. Drifts in the measured magnetic field can be caused for example by temperature drifts in the Hall probe. If these drifts are not corrected for, they can lead to structures in the residuals and also to biases of the best-fit parameters. Therefore, the results obtained in the analysis have to be taken cautiously. To avoid this problem in future measurements, we recommend to measure the magnetic stray field twice, once clockwise and once counterclockwise, to effectively cancel out time-dependent drifts with a linear shape.

We perform the same measurement and analysis with the DET magnet. All beamline magnets were switched off in the measurement, except for the DET which operated

Table 4.1.: **Best-fit parameters and uncertainties of the PCH and DET coil alignment inside their respective cryostats.** The spatial shift parameters of the coil relative to the cryostats are labeled as δx, δy, and δz. The angle α is the horizontal coil tilt relative to the cryostat, β is the vertical tilt. The measurement results when only one solenoid is in operational mode are presented in the column "Individual measurement". The combined analysis result with both magnets at nominal magnetic field are shown in the column "Combined measurement".

Parameter	Individual measurement	Combined measurement
PCH δx (mm)	-0.69 ± 0.07	-0.72 ± 0.07
PCH δy (mm)	-0.8 ± 0.1	-0.9 ± 0.1
PCH δz (mm)	-4.1 ± 0.2	-4.9 ± 0.2
PCH α (deg)	0.11 ± 0.02	0.19 ± 0.02
PCH β (deg)	-0.01 ± 0.03	0.02 ± 0.03
DET δx (mm)	-0.22 ± 0.1	0.11 ± 0.07
DET δy (mm)	-1.25 ± 0.1	-1.36 ± 0.09
DET δz (mm)	-0.58 ± 0.2	-2.8 ± 0.1
DET α (deg)	-0.39 ± 0.02	-0.26 ± 0.02
DET β (deg)	0.01 ± 0.03	0.01 ± 0.02

at nominal field. The analysis has 55 degrees of freedom with a normalized $\chi^2 \approx 1.4$. The best-fit parameters are also shown in table 4.1. Similar to the PCH analysis, the best-fit residuals of the DET measurement also have some structure.

The PCH is less than 1 m away from the DET and both feature strong magnetic fields in nominal operation mode. It is therefore possible that the coil alignment within the cryostat changes due to the magnetic force between both magnets. We therefore repeated the above-described measurement procedure with both solenoids switched on. We measure on all possible positions at both cryostats. The analysis procedure is similar to described above, however, the number of free alignment parameters increases in the minimization.
The best-fit model has a normalized $\chi^2 \approx 0.75$. The structure in the residuals is not as pronounced as in the individual measurement analyses, however, it is still present. Therefore these results should also be taken with caution. The derived best-fit parameters are shown in the right column of table 4.1. The coil shifts in radial direction within the cryostat do not change significantly. This is expected, as the magnetic force mostly acts in axial direction. The distance between the two coils decreases in the global coordinate system as expected, however, we would expect PCH δz to increase instead of decrease. The tilts of the coils are significantly changed in the combined analysis compared to the individual measurements. Although the alignment parameters change between the individual and the combined analysis, the change of alignment parameters is not fully in agreement with the expectation of an axially attracting force.

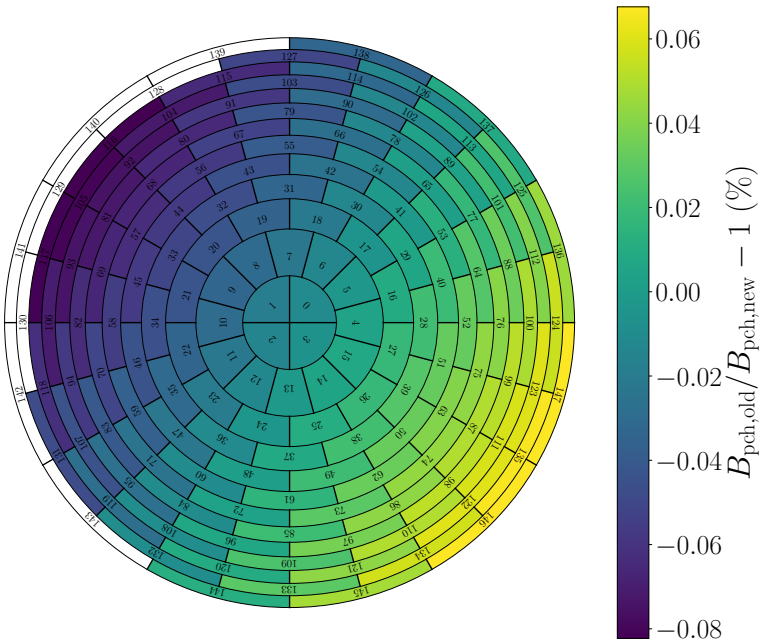

Figure 4.5.: **Change in PCH field simulation when including the obtained coil alignment data in the beamline geometry.** $B_{\mathrm{pch,old}}$ is the calculated magnetic field without assumptions on the coil alignment inside the cryostat, $B_{\mathrm{pch,new}}$ includes the newly-obtained alignment values. The magnetic field in the PCH for an individual FPD pixel changes due to the modified alignment by up to 0.08 % for pixels in the outer-most ring. The pixels in white are excluded from the analysis due to collisions of the beamline with the flux tube. Simulation taken from period summaries, provided by J. Behrens.

Impact of Updated Alignment on Calculated PCH Magnetic Field

We now use the results of the PCH and DET alignment study to re-calculate the PCH field for the individual FPD pixels. The simulated position of the FPD projection in the PCH changes by 0.5 mm in radial direction with the above-derived coil shifts and tilts relative to the simulated position neglecting the tilts and shifts. The position change also leads to a change in the pixel-wise calculated PCH magnetic field, as shown in figure 4.5. The field change due to the updated coil alignment is at maximum 0.08 %. The white pixels in figure 4.5 are neglected due to collisions of the flux tube with the inner electrode system of the Main Spectrometer in the simulation with the obtained coil parameters. SDS-only characterization measurements show that flux tube collisions with the Main Spectrometer vessel hull do not occur in reality for the simulated setting [Frä21]. There are in principle two possible reasons for the false collisions in the simulation. Either the above derived coil tilts are not correct, or the position of the FPD wafer is not correctly included in the simulation.
The above-derived position and tilts of the coils inside the cryostats can be biased by time-dependent effect of the Hall probe, as discussed above. We therefore cross-check the alignment results by comparing the non-alignment corrected simulation and the corrected simulation with additional PCH and DET stray field measurements. Dur-

ing the measurement, both solenoids have their nominal fields, all other magnets are switched off. Nine low-field three-axis fluxgate magnetometers, mounted at the Main Spectrometer vessel with well-known location, measure the magnetic stray field with 0.5 % relative accuracy [SEN20] (more details given in section 5.2.1). The distance between the solenoids and the magnetometers is more than 7 m. We correct the measured stray field for constant magnetic background fields in the Main Spectrometer hall, for example the earth magnetic field, by subtracting the data of a background measurement with all magnets switched off. This processed data is then compared to the Kassiopeia simulation. The simulation with the above-found coil alignment slightly improves the accordance of measurement and simulation compared to the simulation without the new coil alignment. The PCH and DET magnetic fields at the location of the low-field magnetometers amounts to approximately 185 μT. The deviation between simulation and measurement with the old PCH and DET alignment is between 0.3 μT and 1.3 μT, depending on the magnetometer. With the newly-found alignment, the comparison yields 0.1 μT to 0.9 μT. However, it has to be noted that the uncertainty on the magnetic field measurement is on the order of 0.9 μT. Nevertheless, the small improvement in the comparison indicates that the new coil parameters are reasonable.
Another possible reason for the false collisions in the simulation can be an inaccurate position of the FPD in the Kassiopeia geometry model. The position of the FPD wafer in the geometry model is the basis for calculating the period summary, as the pseudo-electrons start in upstream direction at the pixel boundaries to derive the magnetic field at the position of interest, in that case in the Main Spectrometer (see section 3.3.9). A shift of the FPD wafer in radial direction directly propagates to a radial shift of the FPD projection in the Main Spectrometer. Consequently, the false collisions of the flux tube with the inner electrode system can be explained by a radial shift of the FPD between geometry model and reality. In the visualization of figure 4.5, this radial FPD shift must be aligned to the lower right side to avoid the collisions on the upper left side. The challenge in the determination of the FPD wafer position is that it is located inside a vacuum chamber and can thus not be directly accessed with FaroARM® measurements. The position of the FPD wafer in reference to the chamber can be measured in an indirect measurement, as shown by M. Deffert in reference [Def17]. For this purpose, a radioactive source is installed at five different positions in front of the wafer and the alignment of the wafer relative to the chamber is then estimated via geometrical methods [Def17]. However, this method is only feasible in standalone mode. The system has to be moved afterwards to be integrated in the global beamline. As soon as the detector system is connected to the beamline, there is no reliable method to test the final alignment. Additionally, the post-acceleration electrode surrounding the wafer has to be cooled down for operational mode. The cooling is inhomogeneous, leading to a deformation of the electrode that could cause a further shift of the wafer position [Def17].

In summary, including the derived alignment parameters in the simulation leads to a shifted position of the FPD projection in the PCH. Furthermore, collisions of the flux tube with the Main Spectrometer vessel appear in the simulation, which are not observed in measurements. The reason for the unrealistic flux tube collision cannot clearly be identified. The comparison of magnetic stray field measurements at the Main Spectrometer vessel with the updated alignment simulations shows a slightly better agreement of measurement and simulation. The newly-obtained alignment

parameters are thus unlikely to be the reason for the false collision. We cannot exclude the FPD alignment as cause of the unrealistic collision in the simulation, since we cannot make any statement about the final FPD alignment in the beamline due to a lack of methods to estimate it. It is therefore possible that a small unknown FPD wafer misalignment causes the unrealistic collision in the simulation. As we cannot draw any conclusions here, we stick to simulations with the non-corrected coil alignment for further magnetic field studies in the following chapters. Nevertheless, further investigations are necessary to find a solution for the FPD alignment, as small misalignment in the detector system results in an unrecognized shift on the FPD projection in the analyzing plane of the Main Spectrometer of up to 0.5 m. Further discussion on the FPD alignment takes place in section 5.5.1 by using results from dedicated e-gun measurements.

4.2. Source Magnetic Field

The source magnetic field B_{src} guides the β-decay electrons from their origin to the front and rear end of the WGTS. The magnetic flux tube, that guides the electrons through the KATRIN setup from the source towards the FPD, is given by

$$\Phi = \int \vec{B} \cdot \mathrm{d}\vec{A}.$$

Since gas dynamics considerations of the tritium gas in the WGTS prefer a small cross section of the beam tube, a strong source magnetic field is required for optimal electron transport [Hei18].

The source magnetic field strength, together with the PCH field strength, defines the fraction of β-decay electrons reflected by the magnetic mirror in the PCH as the strongest magnetic field in the KATRIN beamline. A stronger source magnetic field results in less reflected β-decay electrons by the PCH and thus more electrons at the FPD which can contribute to neutrino mass measurements. Considering the probability for inelastic scattering of tritium gas by electron impact in the WGTS (see section 7.1.3) and increasing systematic uncertainties due to the scattering leads to the KATRIN operational parameters of $B_{\mathrm{src}}/B_{\mathrm{max}} \approx 0.6$. [KAT05]
Additionally, the intensity of the source magnetic field at the location of the β decay defines, together with the electron's pitch angle, its pitch angle in every other location of the KATRIN beamline. Accurate knowledge of the source magnetic field is therefore crucial for transmission function calculations in the Main Spectrometer and also for the estimation of the energy loss due to synchrotron radiation [Gro15]. The central WGTS beam tube contains 99 % of the molecular tritium gas in the KATRIN beamline [Kuc+18], thus also the majority of β-decay electrons is generated there. Therefore, the strength of the source magnetic field in the central WGTS beam tube is of particular interest.

4.2.1. Source Magnetic Field in Neutrino Mass Analysis

Having presented the most relevant physical processes for KATRIN that depend on the source magnetic field, it is important to quantify the impact of uncertainties in

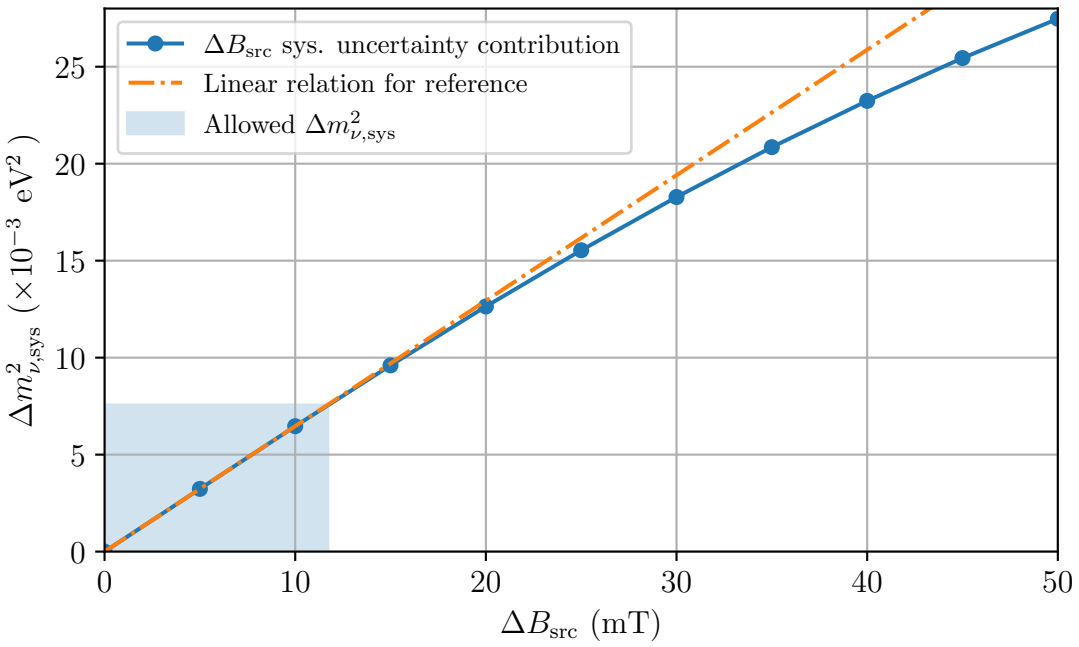

Figure 4.6.: **Impact of source magnetic field uncertainty ΔB_{src} on the systematic neutrino mass uncertainty $\Delta m^2_{\nu,\mathrm{sys}}$.** The source magnetic field uncertainty has to be smaller than 12 mT in order to not exceed the KATRIN systematic uncertainty requirement on a single contribution of $\Delta m^2_{\nu,\mathrm{sys}} \leq 7.5 \times 10^{-3}\,\mathrm{eV}^2$.

the description of the source magnetic field in neutrino mass measurements. Neutrino mass measurements are conducted with a source magnetic field of 2.5 T in the global 70 % scaling of the magnetic fields. The sensitivity studies performed in the following are thus carried out with the same setting.
We investigate the impact of uncertainties ΔB_{src} on the absolute source magnetic field strength on the systematic neutrino mass uncertainty with the pull-term method, similar to the study in section 4.1.1. We add the mean source magnetic field as additional free fit parameter to the nominal four-parameter neutrino mass analysis. The width of the applied penalty term in the likelihood, representing the source magnetic field uncertainty, is varied in the range of $\Delta B_{\mathrm{src}} \in [0, 50]$ mT. The resulting estimated systematic uncertainties on the neutrino mass due to uncertainties on the source magnetic field are shown in figure 4.6.
The main result of this study is that the uncertainty on the source magnetic field strength should be smaller than 12 mT in order to not exceed the allowed single systematic contribution of $7.5 \times 10^{-3}\,\mathrm{eV}^2$. Another remarkable result of this study is an interesting non-linearity of the relationship. We would expect a linear model describing the relation between source magnetic field and neutrino mass uncertainty, provided the fit does not learn about the source magnetic field from the data (see for example figure 4.1). Nevertheless, we see a deviation from this expectation for magnetic field uncertainties larger than 20 mT, indicating that the fit can extract information about the source magnetic field from the measured spectrum.

The challenging goal of less than 0.5 % relative uncertainty on the source magnetic field needs a comprehensive characterization and understanding of all components

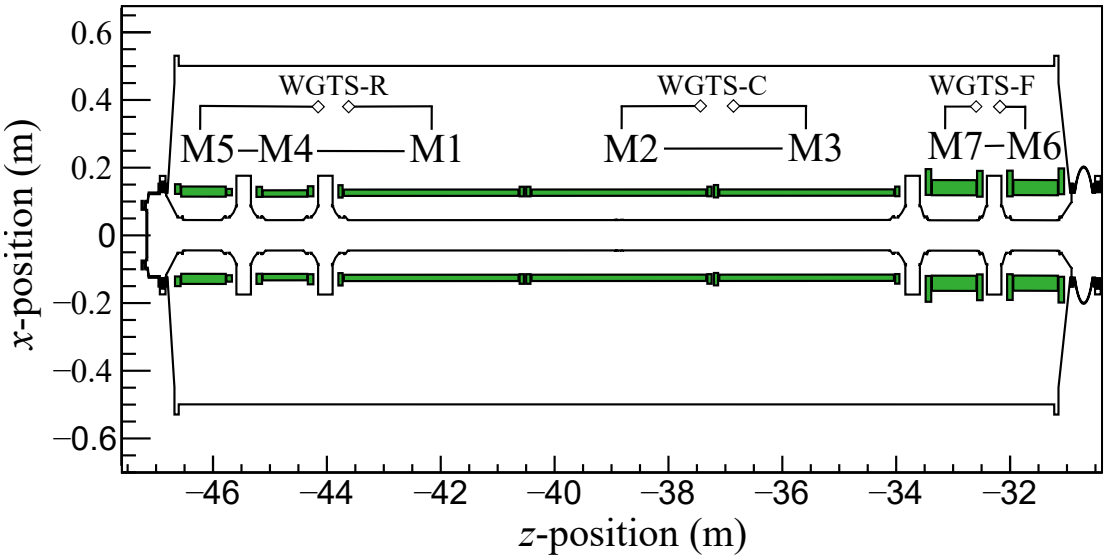

Figure 4.7.: **Schematic layout of the WGTS magnet system, produced with Kassiopeia.** The solenoid modules M5 and M4 surround the rear end of the WGTS, the DPS-1R, while the magnets M7 and M6 surround the downstream end, the DPS-1F. The central WGTS beamtube is embedded in the M1, M2, and M3 module. To reduce the stored energy, the WGTS magnet system is divided in three electrical circuits (WGTS-R/C/F) instead of one circuit.

involved. We therefore start in the following with a brief overview of the hardware setup of the WGTS magnets. Subsequently, simulation and measurement methods are presented to precisely and accurately determine the source magnetic field.

4.2.2. WGTS Magnet System

The source magnetic field itself has to fulfill two main requirements. Firstly, it has to be as homogeneous as possible in the central, 10 m-long WGTS beam tube to provide the same starting environment for each electron. Additionally, the effective path length of the electrons defining the scattering probabilities with tritium gas, as well as the synchrotron losses, depend on the source magnetic field. A homogeneous magnetic field simplifies the modeling of these effects for calculation of the expected measured spectrum at the FPD. Secondly, the magnetic field has to have good time stability to ensure constant measurement conditions within one neutrino mass measurement campaign. The maximally allowed field drift is 0.03 % per month [Are+18b; Ake+21d].

The requirements are addressed by a complex hardware setup consisting of seven super-conducting solenoids located in the 16 m-long WGTS cryostat (see figure 4.7). The solenoids with warm bores are placed in a straight line, surrounding the five WGTS beam tube sections interconnected with four pump ports. Each module has two compensation coils at both ends, in addition to the main coil, to optimize the magnetic field homogeneity by reducing stray fields. Three 3.3 m-long solenoids (M1, M2, and M3) surround the central 10 m-long beam tube section that hosts over 99 %

of the tritium gas. Consequently, these central solenoids are the main components that define the source magnetic field. Two 1 m-long solenoids are installed at the rear (M5, M4) and front end (M7, M6) of the WGTS, surrounding the beam tube sections between the DPS-1R/F pump ports. In addition, two dipole coil pairs are installed at the rear end module M5 and two further at the front end module M6. These dipole coils allow steering of the electron's guiding magnetic field in radial and azimuthal direction for calibration and systematic measurements (for example e-gun measurements as described in section 5.3.3). [Are+18b; Ake+21d]
During operation, the super-conducting coils of the WGTS are cooled in a liquid helium bath at 4.5 K. The solenoid modules are grouped in three electrical circuits, each with its own power supply unit, to reduce the magnetic stored energy in each circuit. The rear solenoids M4 and M5, together with the central M1 solenoid, form the electrical circuit WGTS-R. The two remaining central coils M2 and M3 are grouped in the circuit WGTS-C, while the front end solenoids are connected to the WGTS-F circuit. The magnets are operated in driven mode, the current stability is monitored via a closed-loop flux gate sensor in the WGTS-R and WGTS-C circuit and a precision resistor in WGTS-F. [Ake+21d] The current read-backs show excellent time stability over multiple neutrino mass measurement campaigns, surpassing the KATRIN requirement on the magnetic field stability by more than one order of magnitude.

4.2.3. Simulation and Stray Field Measurements of the Source Magnetic Field

We need to know the source magnetic field at all positions in the WGTS beam tube because electrons starting at all locations in the beam tube contribute to the measured β-decay spectrum. Direct field measurements with a magnetic field sensor inside the beam tube are not possible, as the WGTS is a closed system that is difficult to access with objects that have dimensions of the typical magnetic field sensor [Hei18]. Furthermore, the accurate positioning of the sensor inside the beam tube is necessary for the development of a detailed magnetic field model. This is not possible in this challenging tritium-contaminated experimental environment.
Only simulations can describe the source magnetic field at all positions inside the WGTS. Therefore, the simulated source magnetic field is used in neutrino mass analyses. However, we need to measure the source magnetic field to verify the WGTS field calculation and to quantify the accuracy of the simulation, leading to the estimated uncertainty on the source magnetic field for neutrino mass analyses.
In the following, we first discuss the main properties of the WGTS magnetic field calculation, as it is the input for further analyses. Afterwards, we present an indirect measurement approach by F. Heizmann [Hei18] and W. Gil [Gil20b] to verify the field calculations.

WGTS Magnetic Field Calculation

The best knowledge on the alignment and orientation of the individual WGTS magnets, stemming from alignment measurements, is taken into account in the calculation of the source magnetic field. Additionally, a cooling factor is included in the

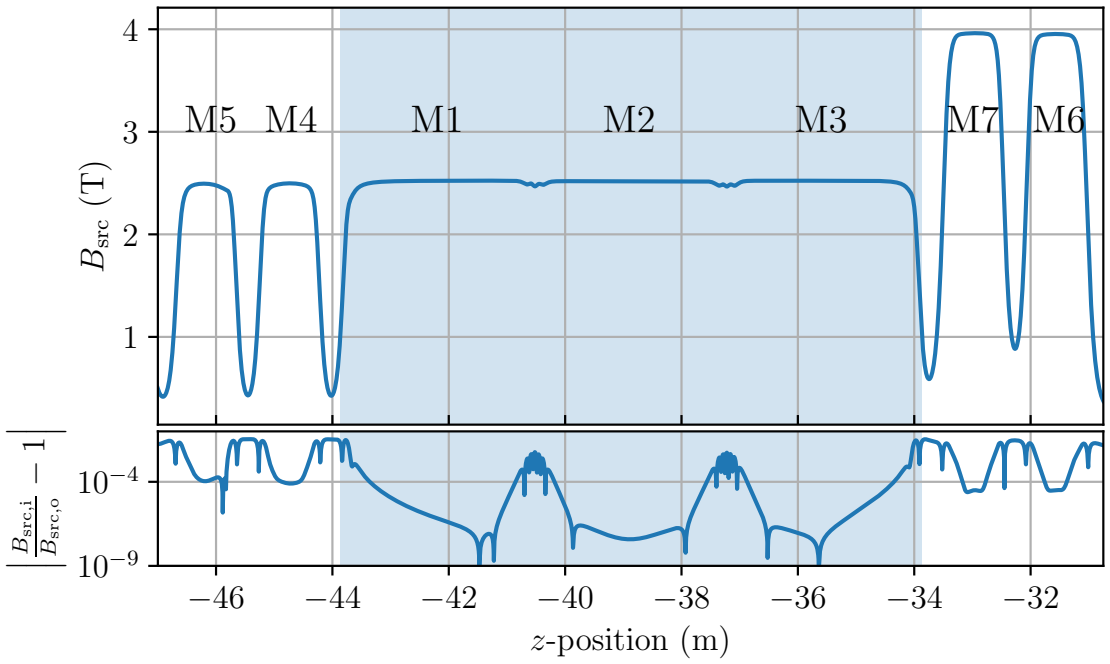

Figure 4.8.: **Simulated source magnetic field in axial direction.** The blue shaded area represents the axial position of the central WGTS beam tube. The simulated magnetic field along the beam axis in the radial center of the WGTS beam tube is shown in the upper graph. The magnetic field features a great longitudinal homogeneity in the central part, that is important for isotropic starting conditions for all β-decay electrons. The radial inhomogeneity is visualized in the lower plot by calculating the ratio of the simulated field in the radial center $B_{\mathrm{src,i}}$ and at large radius in the WGTS beam tube $B_{\mathrm{src,o}}$. The isotropic magnetic field starting conditions for the decay electrons are also met by a good radial homogeneity in the central WGTS beam tube.

calculation [Hei18]. This factor corrects for shrinking of the solenoids due to the cool-down to 4.5 K, compared to room temperature at which the alignment measurement is performed. We exploit the axial symmetry of the solenoids by using the zonal harmonics field solver in Kassiopeia for the field calculation.

The simulated source magnetic field with nominal operational parameters is shown in the upper graph of figure 4.8. The magnetic field at the longitudinal and radial center of the WGTS ($z = -38.8\,\mathrm{m}$, $r = 0\,\mathrm{m}$) in the solenoid module M2 is $B_{\mathrm{src}} = 2.519\,\mathrm{T}$. It slightly increases towards the two neighboring central modules to 2.522 T. The compensation coils at the end of each module suppress the unavoidable drop in magnetic field between the central modules to less than 0.06 T. The magnetic field decreases before and after the central beam tube due to the necessary gap in the line of magnetic modules for the first DPS-1R/F pump ports. Similarly, a second drop is caused by the second pump port in the DPS-1. The field strength between the two pump ports in the DPS-1R amounts to 2.5 T and to 3.9 T in the DPS-1F. The radial magnetic field inhomogeneity is shown in the lower graph of figure 4.8 by the ratio of calculated field at zero radius over the field near the beam tube walls with radius of 4.1 cm. The field has excellent radial homogeneity on the 10^{-3} to the

10^{-9}-level in most parts of the central WGTS beam tube. The radial homogeneity is given by the geometry design of the solenoids. As an indicator, we can compare the length-to-radius ratio of the magnets. The M4 magnet has a length-to-radius ratio of 6.8 and provides a homogeneity on the 10^{-4} level. The M2 magnet has a length-to-radius ratio of 26.3 and has a radial homogeneity of 10^{-7} at the center.

In summary, the simulation of the source magnetic field shows that the technical implementation of the WGTS magnet system enables strong magnetic fields with good homogeneity along the beam axis in the central WGTS beam tube. Additionally, the radial homogeneity in this part of the WGTS is better than 10^{-3}. As a next step, it is necessary to verify the magnetic field simulations and to quantify their accuracy.

Measurement of the Magnetic Stray Field

Due to the lack of measurement possibilities with a magnetic field sensor inside the WGTS beam tube, stray field measurements outside the WGTS cryostat are a promising approach to verify and quantify the accuracy of the magnetic field calculations. F. Heizmann therefore developed and built a magnetic field sensor system to measure the WGTS stray fields with the goal to achieve an accuracy of better than 0.5 % when comparing measurement and simulation [Hei18].

The following section summarizes the efforts by F. Heizmann to develop this magnetic field sensor system. For details on the experimental setup see reference [Hei18]. The developed sensor system consists of two slides on rails, each one housing a magnetic field sensor. The rails are installed at the west side of the WGTS cryostat, the slides move parallel to the WGTS beam tube in the longitudinal direction. The rails are arranged such that one slide covers the stray field region of the M6, M7, and M3 magnets, and the other the region parallel to the M1 and M2 solenoids. The goal of 0.5 % accuracy leads to stringent requirements on the measurement position as well as on the absolute measured magnetic field. [Hei18]
A three axis Hall probe [SEN21], mounted together with its data acquisition system on the slide, measures the magnetic field. The estimated accuracy on the measured magnetic field is 0.2 mT with a resolution of 0.02 mT and thus meets the requirements for the 0.5 % accuracy goal in comparison of measurement and simulation. Additionally, the location of the sensitive volume in the Hall probe is well known. This property is necessary to accurately determine the measurement position. [Hei18]
The necessary precision on the measurement position needs to be on the sub-millimeter level so as to not endanger the 0.5 % accuracy goal. This results in two further requirements, namely the absolute positioning of the sensor system with respect to the WGTS, and the position monitoring of the slide within the system. The longitudinal position of the slide on the rail is the only degree of freedom within the sensor system. Consequently, a rope sensor monitors with 0.1 mm uncertainty the movement of the slide fulfilling the requirement on the position monitoring of the slide within the system. The uncertainty on the absolute position of the rail system relative to the WGTS is on the order of 2 cm and thus exceeds the allowed uncertainty budget. Although dedicated alignment measurements with a laser tracker performed later-on reduced the uncertainty on the absolute rail position [Gil20b], the necessary precision on the sub-millimeter level for the individual measurement position was not achieved. [Hei18]

W. Gil used the sensor system to perform the comparison of measured stray field of the WGTS magnetic field with simulations during the second neutrino mass measurement campaign. The simulated magnetic field, used for the comparison to measured data, was based on calculations with the RADIA application [ECC97; CEC98], which takes into account the impact of the magnetic shielding material located on the turbo-molecular pumps. W. Gil found that the measured magnetic field is 1.7 % higher on average compared to the simulation expectation [Gil20b].
The described measurement procedure is vulnerable to two main aspects. Firstly, a possible inaccuracy in the measurement position reconstruction with respect to the WGTS can introduce an artificial offset between measured and expected magnetic field that the observer would interpret as inaccuracy of the simulation. Secondly, background magnetic fields can disturb the stray field measurement but do not significantly affect the magnetic field inside the WGTS. An example for background fields is the remnant magnetic field caused by magnetized material close to the WGTS cryostat.
Nevertheless, we can use the 1.7 % difference between measured and expected magnetic field as first estimate of the uncertainty on the source field simulation. The 1.7 % relative error on the field translates to 43 mT absolute magnetic field uncertainty in the WGTS beam tube. Based on the study performed in section 4.2.1, this simulation uncertainty yields a systematic neutrino mass uncertainty of $\Delta m^2_{\nu,\mathrm{sys}} = 2.4 \times 10^{-2}\,\mathrm{eV}^2$, exceeding the overall KATRIN systematic uncertainty budget. Consequently, an alternative, more robust approach is necessary to test the source magnetic field calculations with higher precision and accuracy.

4.2.4. Magnetic Field Determination Inside WGTS Beam Tube

In the present thesis, we develop a novel measurement technique to determine the magnetic field strength inside the WGTS beam tube by using electrons as probes. Thereby we exploit the transmission condition of electrons to the detector, and in particular the magnetic mirror effect. The measurement principle is inspired by an idea described by F. Heizmann in reference [Hei18]. The novel measurement principle leads to direct conclusions on the source magnetic field inside the beam tube as experienced by the electrons, and is therefore a good test for the magnetic field calculations. The measurement principle, shown below by example of the source magnetic field, can be transferred to the determination of further solenoids' magnetic fields with strengths on the order of few Tesla in the KATRIN beamline.

Measurement Principle

We begin by discussing the magnetic mirror effect as a fundamental element of the measurement principle. The WGTS is evacuated for the following considerations. As introduced in section 3.1.2, an electron starting in a magnetic field B_0 is magnetically reflected by a stronger magnetic field B_s if their pitch angle θ in the starting magnetic field is larger than the angle θ_max, which is calculated to

$$\theta_\mathrm{max} = \arcsin\left(\sqrt{\frac{B_0}{B_\mathrm{s}}}\right),$$

Table 4.2.: **Measurement configuration for the magnetic field setup of the KATRIN beamline solenoids for the source field determination.** All solenoids are at non-nominal field at the beginning of the measurement, except for the WGTS-M2M3 which define large parts of the central WGTS beam tube field. The solenoid with the maximum magnetic field contains the magnetic mirror. The magnetic mirror for the activity electrons from the rear wall is in this special setup in the WGTS-M2M3.

Solenoid	Nominal field (T)	Measurement setup (T)
Rear section	4.0	3.0
WGTS-M5M4M1	2.5	2.0
WGTS-M2M3	2.5	2.5
WGTS-M6M7	3.9	2.0
DPS	4.0	2.0
CPS	4.0	2.0
PS1	3.1	2.0
PS2	3.1	2.0
PCH	4.2	2.3
DET	2.5	2.0

assuming magnetic adiabatic transformation. We can exploit this effect to determine the maximal WGTS source magnetic field B_{src} relative to a well-known reference field.
Therefore, we switch from the nominal solenoid operational parameters to a special configuration, as shown in table 4.2. In this special configuration, all solenoids downstream from the rear wall have a magnetic field of less than 2.5 T. The maximum magnetic field in the downstream part is located in the central beam tube of the WGTS, that is surrounded by the M2 and M3 module. Electrons starting at the rear end of the WGTS in downstream direction are thus sensitive to the cut-off angle θ_{max} defined by the maximal magnetic field in the M2 and M3 module as the strongest magnetic field on the way to the FPD. With an exact knowledge on the absolute emitted electron rate, the angular distribution, and the starting magnetic field, we could in principle determine the maximal magnetic field in the WGTS beam tube in this special configuration. However, no electron source at the rear end of the WGTS meets the accuracy requirements of known absolute electron rates and known starting magnetic field. Therefore we adapt the measurement principle by switching to a relative measurement.

The relative measurement approach requires a well-characterized reference field. The PCH magnetic field has only 0.1 % relative uncertainty on the applied field (see section 4.1.1) and is therefore the reference of choice. The PCH magnetic field in the special setting is chosen to be 2.3 T at the beginning of the measurement. If we perform a sweep with the PCH magnetic field from 2.3 T to roughly 2.7 T in this setting, and monitor in parallel the rate of electrons arriving at the FPD, we see a

useful relation of the rate evolution versus PCH field strength.
The simulated rate trend with increasing PCH magnetic field in the range from 2.3 T to 2.7 T is shown in figure 4.9. The PCH measurement range is chosen as narrow as possible, so that the variation of the PCH magnetic field does not significantly alter the transmission conditions of the analyzing plane throughout the measurement. We assume for this simulation an isotropic electron source at the rear end of the WGTS with a starting magnetic field of $B_0 = 1.2\,\mathrm{T}$. The source magnetic field is fixed to $B_{\mathrm{src}} = 2.5\,\mathrm{T}$. The electron rate is expected to be constant, as long as the PCH magnetic field is smaller than the maximal source magnetic field. Electrons with pitch angle larger than the cut-off angle are magnetically reflected in the WGTS. In the beginning of the PCH field up-sweep, we do not change anything in this process, as the PCH field variations do not significantly affect the analyzing plane and source magnetic field. However, as soon as the PCH magnetic field becomes stronger than the maximal source field, the electron rate at the FPD starts to decrease. The strongest magnetic field for the electrons in the beam line towards the FPD is now located in the PCH. The PCH field is larger than the source magnetic field, leading to smaller acceptance angles and thus to more magnetically reflected electrons. By further increasing the PCH magnetic field, the cut-off angle decreases and thus also the rate.
In summary, the expected electron rate at the FPD is divided in two regimes. In the first regime, the source magnetic field is stronger than the PCH field and the rate stays constant with varying PCH magnetic field. In the second regime, the PCH field is stronger than the source field, leading to decreasing rate with increasing PCH field. Exactly at the transition of the two regimes, the PCH field and the maximal source magnetic field are equal. Since we accurately know the PCH magnetic field, we then also know the maximal source magnetic field. The analysis challenge is thus to find the transition point. This task is facilitated by a good choice of the electron source in the measurement.

The electrons, that are used for the measurement, have to start at the rear end of the WGTS in downstream direction, so that they experience the magnetic field in the central WGTS beam tube as well as in the PCH magnet. The electron source must have good rate stability over time. Decreasing rate with time results in an additional rate slope in both regimes, which can complicate the transition point determination. Additionally, it is advantageous if the source provides high electron rate at large pitch angles. The rate decrease due to the PCH magnetic field being greater than the source field is more pronounced with more electrons at high pitch angle, allowing a clear separation of the two regimes. The last requirement on the electron source is that its intensity should be high to keep the statistical uncertainty at minimum in a given measurement time.
A possible electron source is the Rear Section e-gun. It has a good electron rate stability and an overall high intensity with more than 1 kcps. To produce electrons at large pitch angle, we have to tilt the e-gun plates. However, in this setting the overall e-gun rate is reduced by factor two (see section 6.2.2), probably due to geometric cut-off of the electron beam in the Rear Section. Additionally, the e-gun illuminates only one FPD pixel. If the radial homogeneity of the source magnetic field shall be tested, it is necessary to repeat this measurement several times at various pixels.
Another electron source is the tritium implanted in the rear wall surface. A fraction of tritium molecules and ions which stream towards the rear end of the WGTS

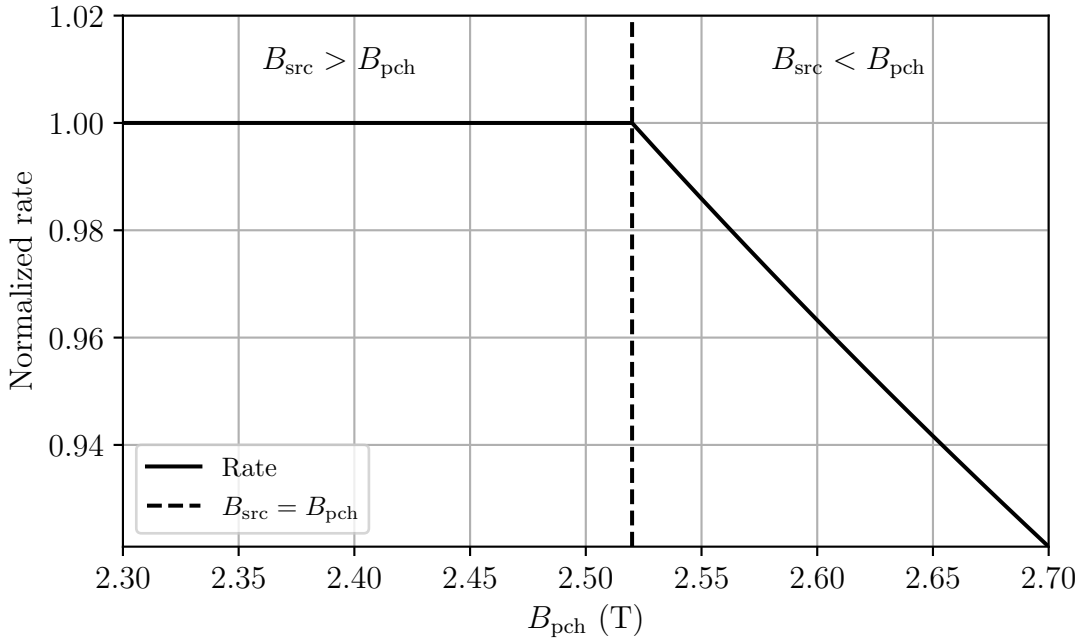

Figure 4.9.: **Simulation of the expected electron rate versus PCH field in the special measurement configuration according to table 4.2.** On the left side of the dashed line, the source magnetic field is the maximal field in the beamline and defines the magnetic mirror. The changing PCH field does not affect the rear wall rate measured at the FPD. On the right side of the dashed line, the PCH field is larger than the source field. The magnetic mirror is now located in the PCH. Increasing the PCH field strength leads to more reflected electrons by the magnetic mirror in that regime and therefore to a rate decrease.

collides with the rear wall and gets implanted in the gold-coated surface. The implanted tritium eventually decays and emits β-decay electrons, leading to a tritium β-decay spectrum from the rear wall. Dedicated rear wall measurements indicate that the angular distribution of emitted electrons is approximately isotropic. The overall implanted activity is estimated to 90 MBq at the time of the measurement [Ake20]. The rear wall is completely mapped to the detector, thus all FPD pixels are illuminated by the rear wall electrons. We can adjust the overall electron rate at the FPD by altering the retarding potential in the Main Spectrometer, since the emitted energy spectrum is a tritium β-decay spectrum. The rear wall activity decreases with increasing measurement time, as the WGTS must be evacuated during the measurement and thus no more tritium is implanted. However, this rate decrease is negligibly small at 20 ppm per hour. Implanted tritium on the rear wall surface is thus an appropriate electron source for the WGTS magnetic field measurement, as the angular electron distribution comprises all pitch angles, illuminates all FPD pixels simultaneously, and features a sufficiently stable and high rate. We therefore performed the WGTS magnetic field measurement using the decay electrons emitted by the rear wall.

Measurement Procedure and Data Analysis

The solenoid operational parameters are set according to table 4.2 at the beginning of the measurement. Two approaches are possible to measure the FPD rate evolution versus the PCH field.
The first approach is to measure at discrete, pre-defined PCH currents. The advantage of this method is that the PCH field is stable during the rate measurement. The disadvantage is that the power supply of the PCH magnet automatically reduces the current ramping speed near the set point to precisely reach the field stabilization at the set point. The necessary waiting time to stabilize the current in the magnet is approximately 20 minutes per measurement. If we want to resolve the rate evolution versus PCH field with six measurements to determine the transition region, we would lose more than two hours of measurement time only to current stabilization.
The second measurement approach bypasses this problem by performing a continuous sweep of the current in the PCH magnet. The magnetic field is continuously ramped up from 2.3 T to 2.7 T and the electron rate at the FPD is monitored in parallel. In this approach, the complete measurement time can be used for the analysis. The disadvantage is that it needs a more sophisticated analysis chain.
We decided to use the second method for the measurement due to its significantly larger efficiency.

The ramping speed of the PCH current was chosen to be 3 mA/s, which translates to approximately 0.2 mT/s. The total measurement time for one sweep amounted to 50 minutes. We performed one up-sweep from 2.3 T to 2.7 T and directly afterwards one down-sweep from 2.7 T to 2.3 T. This allows one to test and correct time shifts as an artifact of the current ramp in the analysis.
The measured FPD rate was averaged over one second measurement time in the data acquisition system for smarter data processing. Thus, the smallest possible time resolution in the analysis is one second, which is sufficient due to the low ramping speed of the PCH current.
We set the filter energy in the Main Spectrometer to 16 keV during the measurement, more than 2.5 keV below the tritium endpoint. This resulted in an β-decay electron rate from the rear wall of more than 3 kcps per pixel in the bulls-eye of the FPD. The filter energy in the Main Spectrometer could have been in principle even smaller, leading to higher count rate at the detector, but this would have led to severe pile-up effects of the measured rate.

The measured FPD rate at pixel zero versus the PCH current, as given by the readback of the power supply, is shown in figure 4.10. The two regions of constant and decreasing rate are visible by eye. The relative rate decrease due to the changing cut-off angle is approximately 7.5 % and thus in good agreement with the calculated rate evolution shown in figure 4.9, indicating that the assumptions made in the simulation are correct to first-order approximation.
Although the rate decrease follows the relation $(1-\cos\theta_{\max})$, it is well approximated by a first-order polynomial in the narrow region investigated in this measurement (see also figure 4.9). The description of the constant-rate region with a first-order polynomial in the model allows us to compensate for time-dependent drifts in the emitted rear wall activity. The edge position is a free parameter in the model, since the transition between the two regimes, and therefore also between the two first-order polynomials, has to be continuous. The best-fit parameters of the model

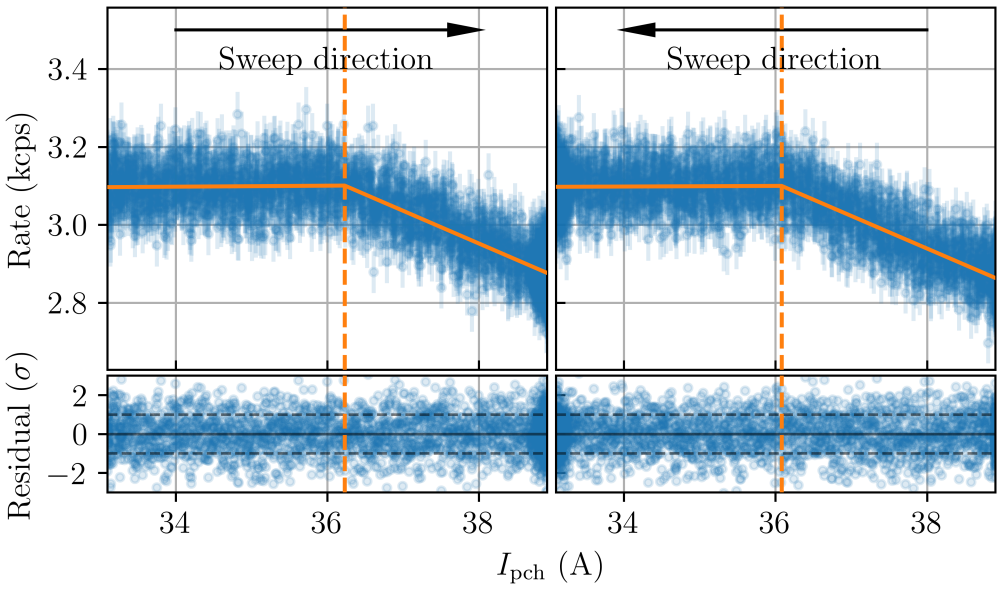

Figure 4.10.: **Activity rate measurement of the rear wall at FPD pixel 0 versus the read-back current of the PCH.** The FPD rate evolution versus the PCH current is shown in the graphs in the upper panels. The solid orange line represents the best-fit model to the rate, the dashed orange line is the best-fit edge position. The up-sweep measurement is shown in the left plot (as indicated by the arrow), the PCH current is continuously increased from 33.1 to 38.9 A during the measurement. The right plot is the down-sweep measurement. The calculated residuals between measured rate and best-fit model, normalized to the statistical uncertainty, are shown in the plots in the lower panels. The best-fit model describes the measured rate evolution without any residual structure.

to describe the measured data are found from a χ^2 minimization. The measured data at FPD pixel zero is well-described by the model, indicated by the normalized $\chi^2 = 1.02$ for the up-sweep and $\chi^2 = 0.99$ for the down-sweep. Measurements and fits at other FPD pixels look similar.
The best-fit edge at pixel zero for the up-sweep edge position is (36.23 ± 0.05) A, the one for the down-sweep is (36.08 ± 0.05) A. The discrepancy between the two edge positions is slightly larger than two standard deviations, although the shapes of the best-fit models match for both measurements. The comparison of this edge discrepancy at pixel zero to the analyses performed with the data measured at other FPD pixels shows that the up-sweep has in general larger edge positions compared to the down-sweeps (see left graph in figure 4.11). This behavior is expected due to inductance effects in the PCH solenoid [Gil20a]. The increasing current induces a voltage in the coil to resist the current change. The effective current in the coil, that produces the PCH magnetic field, is therefore smaller during the up-sweep than the power supply read-back current that is used for the analysis. This consequently results in a time delay Δt between effective current in the coil and the one in the power supply. The current difference between the two during the up-sweep

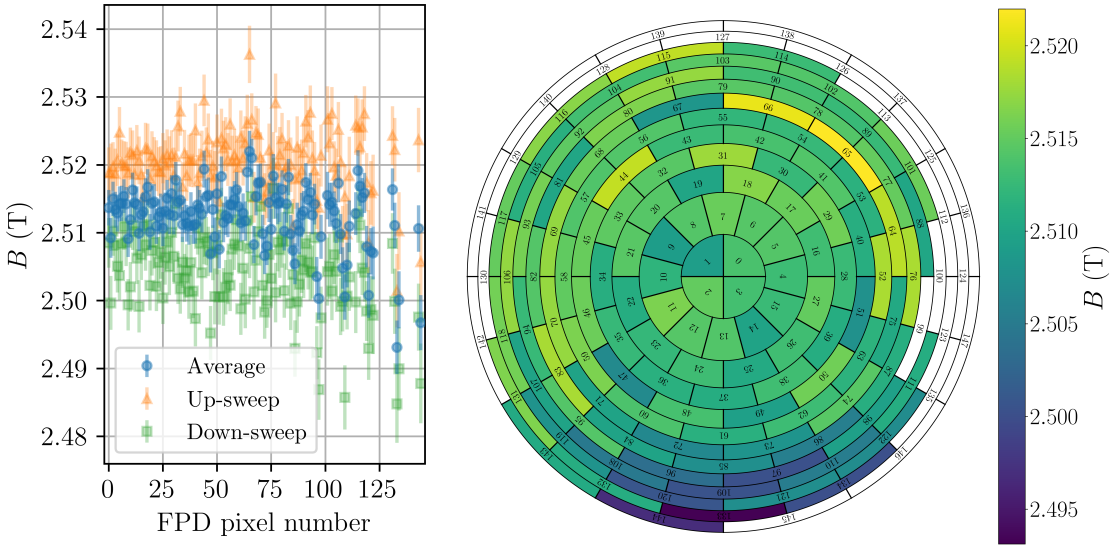

Figure 4.11.: **Measured edge positions for all active FPD pixels in the measurement of the source magnetic field.** All measured currents are translated to magnetic field values with the Kassiopeia PCH simulation. The measured edge positions in the up-sweep and down-sweep measurements, as well as the averaged position, versus the pixel numbers are shown in the left plot. The error bars represent the statistical uncertainty of the measurement. The plot on the right shows the averaged edge positions in the FPD projection.

is approximately $\Delta I = \dot{I} \cdot \Delta t$ with the ramping speed $\dot{I} = 3\,\mathrm{mA/s}$. The sensor data of low-field magnetometers on the Main Spectrometer vessel at 7 m distance to the PCH magnet show that the change of measured magnetic field is delayed in comparison to the PCH current read-back of the power supply by $\Delta t = (25 \pm 5)\,\mathrm{s}$, leading to $\Delta I \approx 75\,\mathrm{mA}$. The effect of delayed current reverses in the down-sweep, the effective current in the PCH coil is larger than the power supply read-back. As the ramping speed is the same as in the up-sweep, we expect the current delay now to be $\Delta I \approx -75\,\mathrm{mA}$. Taking this current delay into account leads to a consistent edge position of up- and down-sweeps to 36.15 A for FPD pixel zero. However, the determination of the current time delay via magnetic field sensor reading is a rather approximate method. We therefore take the mean of up- and down-sweep edge position to effectively cancel out the impact of the time delay, assuming that it is exactly the same for up- and down-sweep due to the same current ramping speed.

The Kassiopeia magnetic field calculation for the PCH enables the translation of the determined current edge positions to magnetic field. The individual FPD pixels are tracked into the PCH detector and the mean magnetic field is calculated for every pixel. This calculation is performed in several steps for PCH currents from 35.6 T to 36.4 T, which allows us to translate each measured current edge position on the individual pixels to an edge position in the magnetic field. At this stage, we do not yet take into account the systematic uncertainty of the simulation due to the translation from current to magnetic field. The resulting magnetic field estimation for each pixel of the 125 analyzed FPD pixels is shown in figure 4.11. The remaining 23 FPD pixels are excluded from the analysis due to shadowing by the beamline or

by the FBM.
The estimated averaged magnetic field for the individual pixels is rather homogeneous (see left graph in figure 4.11), particularly for the first 45 FPD pixels, located at or near the detector's center. Towards higher pixel numbers, the fluctuation is larger than the expectation from statistical uncertainty. The measured magnetic fields as a projection to the FPD are shown in the right plot in figure 4.11. It seems as if the magnetic field decreases towards the lower side. However, this does not mean that the measurement contradicts the calculated radial homogeneity of the source magnetic field (see section 4.2.3). Positions at large radius in the flux tube, corresponding to FPD pixels at large radii, are more vulnerable to non-adiabatic effects in the energy analysis of electrons, resulting in biased analysis results for the current edge position. This effect can further be investigated in the future with dedicated e-gun measurements. The e-gun allows us to measure at individual pixels and with an acceptable rate at small surplus energies. Another source for this behavior could be due to small unknown shifts in the experimental alignment of FPD to PCH, that are not taken into account in the model. This can lead to inaccurate magnetic field calculations compared to the true magnetic field. The effect is more pronounced for the outer rings compared to the central ones, as shown in figure 4.5. As we expect the central pixels to be less biased in this magnetic field measurement compared to the ones at larger radii, we only use the two inner detector rings for the determination of the final magnetic field result. The statistics of these pixels are combined by calculating the error-weighted average and its uncertainties. The systematic uncertainty of the translation from current to magnetic field, based on the simulation, has not yet been considered to this point. According to section 4.1.1, the relative uncertainty on the calculated PCH magnetic field is 0.1 %. Consequently, the final result for the measured maximal magnetic field in the WGTS is

$$B_{\text{meas}} = 2.5133 \pm 0.0007\ (\text{stat.}) \pm 0.0025\ (\text{sys.})\,\text{T}.$$

Resulting Neutrino Mass Uncertainty

The calculated magnetic field for this special measurement configuration inside the WGTS beam tubes is shown in figure 4.12. The maximum calculated magnetic field is located at the rear end of the M3 model, towards the M2 module. Although the M2 and M3 solenoids do have the same currents in their coils and are geometrically identical, the field inside M3 is larger due to 1 ‰ more coil windings. The maximum calculated magnetic field strength is $B_{\text{sim}} = 2.518\,\text{T}$. The measured maximal field with the PCH as reference yields $B_{\text{meas}} = (2.513 \pm 0.003)\,\text{T}$. The difference between measurement and simulation is less than two standard deviations, which is an acceptable deviation.

We use the comparison between measurement and simulation for the maximum source magnetic field in this special configuration as benchmark for the general uncertainty on the calculated source magnetic field in the nominal configuration. As mentioned above, the magnetic field in the central WGTS beam tube is more important for neutrino mass measurements compared to the one in the DPS-1R/F. The magnetic field in this region is defined by the solenoids M1, M2, and M3, that all come from the same manufacturer and have the same geometrical design. It is therefore reasonable to assume that if the magnetic field calculation accurately describes

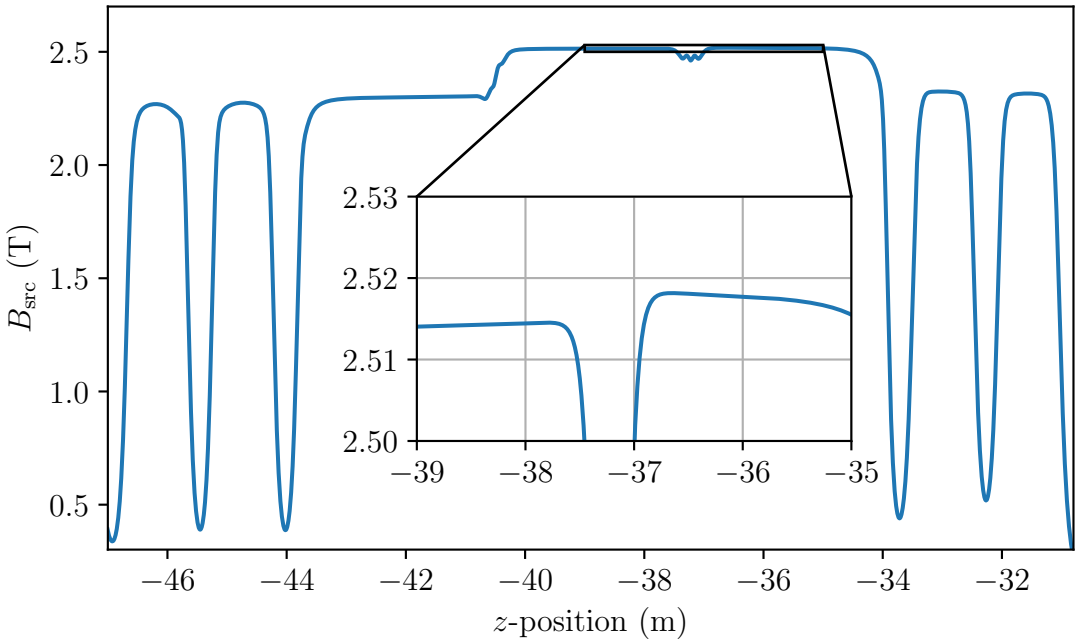

Figure 4.12.: **Simulated source magnetic field for the special field configuration during the performed measurement.** The maximum source magnetic field, measured with the rear wall electrons, is located in the WGTS-M3 magnet and is 2.518 T, according to the simulation.

the measured field in M3, it also describes the field in the M1 and M2 modules with the same accuracy. Based on the measured and simulated magnetic field, we calculate a conservative uncertainty on the simulated source magnetic field. The conservative uncertainty estimate takes into account the error of the measurement ΔB_{meas}, as well as the difference between simulation and measurement. This results in the total uncertainty of

$$\begin{aligned}\Delta B_{\mathrm{src}} &= \sqrt{\Delta B_{\mathrm{meas}}^2 + \left(B_{\mathrm{sim}} - B_{\mathrm{meas}}\right)^2} \\ &= \sqrt{\left(0.003\,\mathrm{T}\right)^2 + \left(2.518\,\mathrm{T} - 2.513\,\mathrm{T}\right)^2} \\ &= 5.8 \times 10^{-3}\,\mathrm{T}.\end{aligned}$$

According to the neutrino mass sensitivity study performed in section 4.2.1, the uncertainty ΔB_{src} translates to a systematic neutrino mass uncertainty of $\Delta m^2_{\nu,\mathrm{sys}} = 4 \times 10^{-3}\,\mathrm{eV}^2$. The size of the uncertainty consequently meets the KATRIN requirement for a single systematic uncertainty contribution to be below $7.5 \times 10^{-3}\,\mathrm{eV}^2$. The remaining open question to be answered in this thesis with respect to the source magnetic field is the central value used for neutrino mass analysis.

4.2.5. Source Magnetic Field for Neutrino Mass Analysis

Two different approaches are pursued in KATRIN neutrino mass analyses to take into account source related effects in the expected β-decay spectrum at the FPD (see also section 7.1.2). The first approach is to segment the WGTS into slices in the

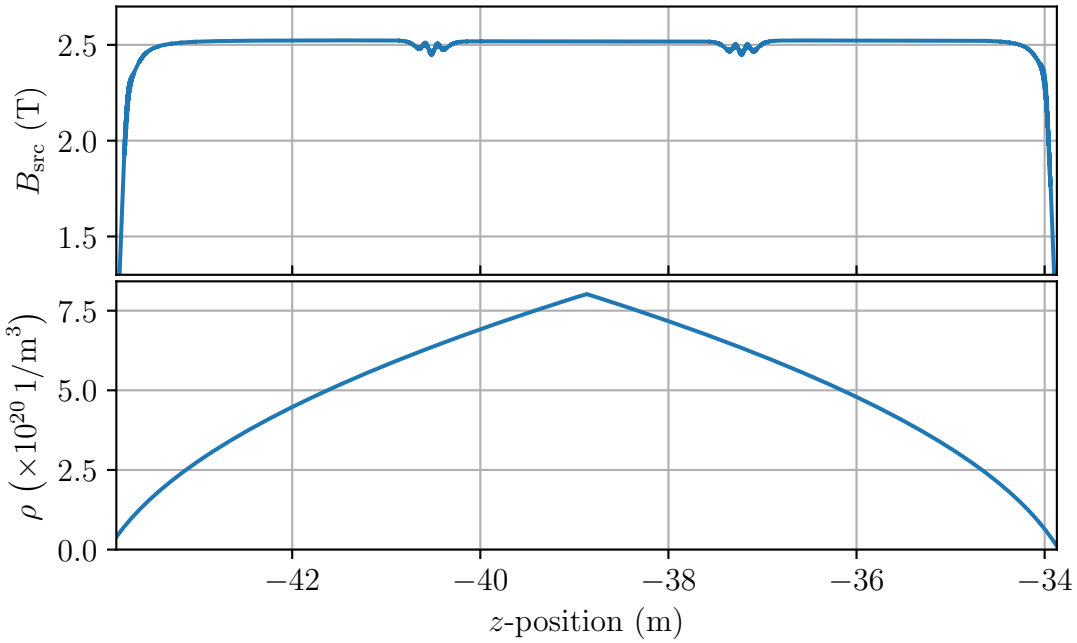

Figure 4.13.: **Simulated source magnetic field B_{src} and tritium gas density profile ρ versus z-position.** The calculated source magnetic field is shown in the upper graph, the simulated density profile of the tritium gas in the central WGTS beam tube in the lower graph. The central value for the source magnetic field, that should be used for neutrino mass analysis, is the weighted average of gas density profile and source magnetic field.

model and calculate the properties of each slice individually, for example the cut-off angle due to magnetic field inhomogeneity. This approach is computationally expensive, as the properties of each slice need to be reevaluated in each step of the likelihood optimization. The favored, second approach is to average the source properties and choose the input parameters accordingly so that a neutrino mass bias is avoided in the analysis. This approach is currently used in the analysis due to is significantly faster calculation. Consequently, we have to determine the central source magnetic field for neutrino mass analysis in the following. Additionally, the impact of longitudinal magnetic field inhomogeneity on the neutrino mass has to be quantified in the thesis at hand.

The magnetic field in which the β-decay electrons are created determines to large extent their physical properties, for example whether they are reflected in the PCH. More β-decay electrons are generated at the region of higher gas density compared to the one with lower density. Consequently, the magnetic field at this point is of greater importance for the effective β-decay spectrum. Detailed gas dynamics simulations (see section 7.2) are able to precisely calculate the tritium gas profile inside the WGTS. The calculated source magnetic field for nominal operational parameters, as well as the tritium gas density profile in the central WGTS beam tube, are shown in figure 4.13. The gas density is maximal at the tritium injection capillary at the longitudinal center of the WGTS, consequently the magnetic field at this location has the most significant impact on the measured β-decay spectrum. To account for this, we determine the central source magnetic field value for neutrino

mass analysis by calculating the weighted average of magnetic field with gas density at the individual longitudinal positions. The recommended input value for the source magnetic field in neutrino mass analysis is therefore $\langle B_{\mathrm{src}} \rangle = 2.51\,\mathrm{T}$. The weighted standard deviation, quantifying the longitudinal field inhomogeneity, is 157 mT and thus more than a factor 25 larger than the uncertainty on the absolute field of 6 mT. Sensitivity studies are thus required to investigate the influence of this longitudinal inhomogeneity on the measured neutrino mass.

We generate an Asimov dataset with the most-precise model we have using source slicing and fit the dataset with the averaged model and the above-determined input parameters to estimate the effect of the averaging on the measured neutrino mass.
To describe the source magnetic field with its longitudinal inhomogeneity in the model, we use the source segmentation method. We use 10^3 segments for the central WGTS beam tube to resolve all field variations along the longitudinal direction. The neutrino mass is set to zero in the model. A self-fit of the model to the Asimov dataset yields $m_\nu^2 = (0 \pm 55) \times 10^{-3}\,\mathrm{eV}^2$.
Afterwards, the Asimov dataset is fit with the averaging approach. We use the above-derived mean source magnetic field $\langle B_{\mathrm{src}} \rangle = 2.51\,\mathrm{T}$ as a fixed input parameter for the fit. The neutrino mass determined by the fit is $m_\nu^2 = (-0.3 \pm 55) \times 10^{-3}\,\mathrm{eV}^2$. The first result of this study is that the averaging approach causes a small bias on the measured neutrino mass due to the averaging of the magnetic field. However, this bias is significantly smaller compared to the individual KATRIN systematic contributions and can easily be corrected for in the analysis. The bias thus does not endanger the targeted neutrino mass sensitivity. Additionally, the uncertainty on the determined neutrino mass is the same for the averaging approach and the self-fit. Consequently, the averaging approach of the axial magnetic field variations in the WGTS does not broaden the KATRIN likelihood and therefore does not affect the measurement uncertainty. In summary, we recommend to use

$$B_{\mathrm{src}} = (2.510 \pm 0.006)\,\mathrm{T}$$

as input parameter for the source magnetic field in neutrino mass analyses, when the beamline solenoid's currents are set to the nominal configuration (see table B.1).

4.3. Summary

The WGTS source and PCH magnetic fields both influence the measured β-decay spectrum at the FPD, mainly with their contribution to the magnetic mirror. The PCH field is 4.2 T in nominal operation mode, while the WGTS source field is 2.5 T. In the present thesis, we have shown that it is necessary to characterize both field strengths with sub-percent accuracy (see section 4.1.1 and 4.2.1) to achieve the final KATRIN sensitivity goal. Magnetic field simulations are the only tools that meet all requirements in terms of flexibility and spatial resolution for neutrino mass analysis with KATRIN. The main goal of the field characterization in this section is therefore to experimentally cross-check the simulations and quantify their accuracy.

The absolute uncertainty on the simulated PCH field strength consists of two uncertainty components. The first component comprises the comparison of simulation

and direct high-precision field measurements inside the cryostat, the second one uncertainties stemming from possible misalignment between FPD and PCH. We have shown that the components add up to 0.1 % relative uncertainty on the PCH field strength, leading to an acceptable systematic neutrino mass uncertainty contribution of $\Delta m^2_{\nu,\mathrm{sys}} = 3 \times 10^{-3}\,\mathrm{eV}^2$ (see section 4.1.1). The magnetic field strength in the PCH is thus sufficiently well understood and characterized for neutrino mass analysis with KATRIN.
To avoid biased magnetic field calculations for the individual FPD pixels in the PCH and analyzing plane, it is crucial to understand the alignment between FPD and analyzing plane. The first step to improve this understanding is to investigate the alignment of the PCH and DET magnet, and in particular their coil positioning inside the cryostat. A high-precision measurement to investigate the coil alignment inside the cryostat by measuring the solenoid's stray field with a Hall probe at well-known measurement positions is developed and conducted in this work (see section 4.1.2). The inclusion of the obtained alignment results in the Kassiopeia geometry model indicates an additional unknown misalignment, which is most likely the FPD wafer positioning in the KATRIN coordinate system. The alignment discussion is continued in section 5.5.1 by taking into account results from e-gun measurements.

The source magnetic field meets the KATRIN requirements in terms of stability during a neutrino mass measurement campaign (see section 4.2.2) and in field homogeneity, according to the field simulation (see section 4.2.3).
Similar to the PCH field simulation, the source field simulation also needs to be validated and its accuracy must be quantified. However, the source magnetic field is not trivially accessible via direct field measurements inside the beam tube due to the experimental environment. The stray field measurement approach by Heizmann and Gil suffers from systematic uncertainties and is vulnerable to background fields. Therefore, this method does not allow characterization of the source field strength with sub-percent accuracy (see section 4.2.3). In the thesis at hand, we devise a novel, more direct measurement approach to determine the source magnetic field strength (see section 4.2.4). β-decay electrons from the rear wall are used as probes for the maximal source field in a special measurement configuration, the PCH field serves as well-defined reference magnetic field in the analysis. This approach enables an absolute source field measurement with 5.8 mT uncertainty, leading to a systematic neutrino mass contribution of only $\Delta m^2_{\nu,\mathrm{sys}} = 4 \times 10^{-3}\,\mathrm{eV}^2$. Future follow-up measurements with the e-gun are proposed to resolve small deviations found in the analysis that are currently assumed to be caused by non-adiabatic effects.
We investigate the impact of the variations of the source magnetic field strength along the beam axis on the neutrino mass measurement in section 4.2.5, using the typical KATRIN analysis chain. Taking into account the density profile of the tritium gas in the source leads to an averaged source magnetic field strength of $B_{\mathrm{src}} = (2.510 \pm 0.006)\,\mathrm{T}$, which reduces the measurement bias on the neutrino mass to the $10^{-4}\,\mathrm{eV}^2$ level. This value for the source magnetic field strength is recommended for future neutrino mass analyses.
Consequently, the methods devised in this work enabled the determination of the source magnetic field strength with a precision and accuracy that meets the final KATRIN requirement for systematic uncertainties.

5. Characterization of the Nominal Analyzing Plane

The analyzing point of an electron in the Main Spectrometer is defined as the point of minimal kinetic energy in longitudinal direction of the β-decay electron. If magnetic-adiabatic conversion of transversal energy into longitudinal energy is performed correctly in the Main Spectrometer, the analyzing point is at the location where the electric retardation is maximal. Simultaneously, the magnetic field is either minimal at the analyzing point to achieve the best-possible energy resolution or it has a local maximum to ensure optimal field homogeneity in the Main Spectrometer. The locations of the analyzing points of all β-decay electrons in the magnetic flux tube then define a plane, the so-called analyzing plane. The electromagnetic fields of the Main Spectrometer are designed such that, in the symmetric setting, the analyzing plane is a flat surface perpendicular to the beam axis, close to the axial center of the Main Spectrometer (see also figure 3.14) [Erh16; Ake+21d; KAT05]. The analyzing plane is one of the key features of the KATRIN experiment due to its impact on the Main Spectrometer energy resolution. The objective of the following chapter is the characterization of the analyzing plane in the symmetric Main Spectrometer setting, the so-called nominal analyzing plane.
General remarks on the properties of the nominal analyzing plane and sensitivity studies on the requirements for neutrino mass measurements are given at the beginning of this chapter in section 5.1. Subsequently, a first characterization of the magnetic fields in the analyzing plane based on Kassiopeia simulations is performed in section 5.2. In the following section 5.3, we discuss and apply methods to characterize the analyzing plane fields with the Rear Section e-gun. Quasi mono-energetic internal conversion electrons stemming from the ^{83m}Kr γ decay are a powerful tool to measure the electric retardation as well as the magnetic field in the analyzing plane of the Main Spectrometer, as shown in section 5.4. The three characterization approaches of simulation, e-gun, and ^{83m}Kr measurements are compared in section 5.5 and necessary follow-up investigations are identified.

5.1. Analyzing Plane Properties

The analyzing plane has two crucial ingredients that need to be well-investigated in a comprehensive characterization. Firstly, the retarding potential that arises in the analyzing plane for β-decay electrons, when high voltage is applied on the spectrometer vessel. Secondly, the magnetic field in the analyzing plane that defines the energy resolution at the point of kinetic energy analysis.

5.1.1. Retarding Potential

The effective retarding potential for electrons originating from β-decay in the WGTS is the difference of the electric potential at the point of decay and the electric potential, which the electrons experience in the Main Spectrometer. The WGTS beam tube therefore acts as common reference ground in KATRIN to compensate to a certain level for the starting potential of the β-decay electrons in the WGTS.
The retarding potential in the Main Spectrometer is produced by the Main Spectrometer vessel and the inner electrode system, comprising steep cones, flat cones, and the central cylindrical part. An overview on the high-voltage system of the Main Spectrometer is given in section 3.2.4. The potential on the central part of the inner electrode system defines together with the vessel potential the homogeneous retarding potential at the axial center of the Main Spectrometer. The more positive steep and flat cone settings of the inner electrode system compared to the central part (see also table B.3) allow to fine-shape the electric field close to the entry and exit of the Main Spectrometer to optimize the transmission conditions. [Ake+21d]
The electric retardation at each point of the analyzing plane is a superposition of the potential of the vessel, the inner electrode system, and the grounded beam tubes at both ends of the Main Spectrometer. The voltage difference between the central inner electrodes and the vessel results in an approximately constant, positive offset of the retarding voltage in the analyzing plane relative to the applied voltage at the Main Spectrometer electrodes. The grounded beam tubes, as well as the steep and flat cones, cause a radial inhomogeneity of the retarding voltage in the analyzing plane. As a consequence of these two effects, the retarding voltage is more positive at the center of the analyzing plane compared to the outer rim (see figure 5.1), resulting in a smaller Main Spectrometer potential qU_{ret} for β-decay electrons close to the radial center of the spectrometer. Further inhomogeneities arise from deformations of the Main Spectrometer vessel [Cor14]. All above-described effects, that either cause a deviation from homogeneity in the electric field or that result in an offset relative to the applied voltage, effectively result in a smaller retarding potential at the center of the analyzing plane compared to the outer rim. Furthermore, the superposition of these effects cause a smaller total potential than the applied potentials at the Main Spectrometer electrodes. Therefore, these effects are summarized in the term "potential depression" in the thesis at hand.
In summary, the retarding voltage in the analyzing plane is given by $U_{\mathrm{ret}} = U_{\mathrm{v}} + U_{\mathrm{ie}} + U_{\mathrm{pd}}$, with the vessel voltage $U_{\mathrm{v}} < 0\,\mathrm{V}$, the central inner electrode offset $U_{\mathrm{ie}} < 0\,\mathrm{V}$, and potential depression $U_{\mathrm{pd}} > 0\,\mathrm{V}$. The simulated retarding voltage in the analyzing plane as used in KNM1 and KNM2 (see also table B.3) is shown in figure 5.1.

5.1.2. Magnetic Field Settings and Interplay with Main Spectrometer Background

The magnetic field in the analyzing plane is together with the source magnetic field responsible for the magnetic-adiabatic collimation in the Main Spectrometer and plays a key role in the MAC-E filter's energy resolution (see equation 3.11). As described in the following paragraphs, a sophisticated air-coil system allows to tune

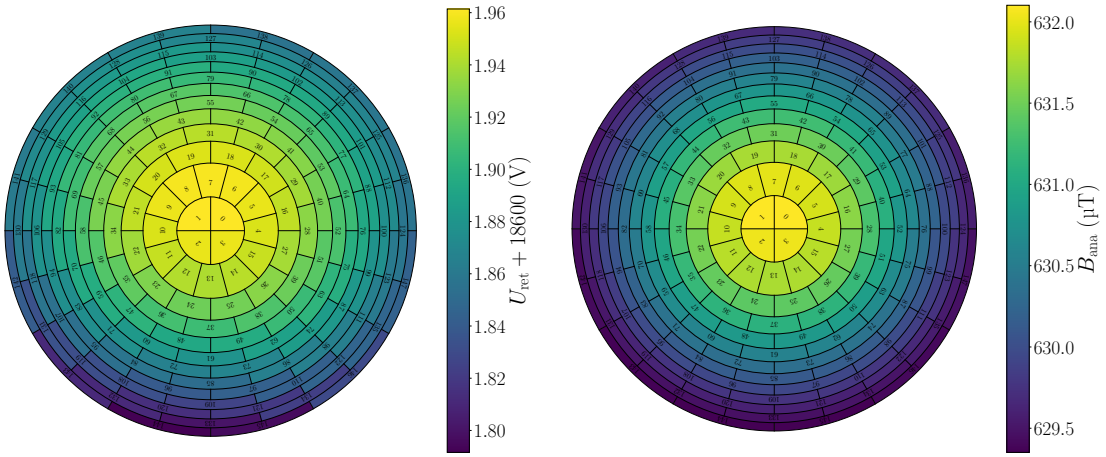

Figure 5.1.: **Simulated retarding voltage U_{ret} (left plot) and magnetic field B_{ana} (right plot) in the analyzing plane for the setting of KNM1 and KNM2, visualized in the FPD projection.** The potential depression causes an offset of 1.96 V on the retarding voltage at the center of the analyzing plane for $U_{\mathrm{v}} = -18.4\,\mathrm{kV}$ and $U_{\mathrm{ie}} = -200\,\mathrm{V}$, that decreases to 1.8 V with increasing radius in the Main Spectrometer. The 6 G magnetic field setting in the analyzing plane, used in KNM1 and KNM2, also reaches its maximum at the radial center of the analyzing plane. It features a good field homogeneity with peak-to-peak amplitude of 2.8 μT. Simulation taken from period summaries, provided by J. Behrens.

the field setting in the Main Spectrometer to meet certain requirements, based on the measurement goal.

Strength and Shape of the Magnetic Field in the Analyzing Plane

The magnetic field in the analyzing plane is a superposition of the beam line solenoids' fields, background fields like the earth magnetic field, and as dominating contribution the field by the large-volume air-coil system.
The large-volume air-coil system (see figure 5.4) consists of the Low Field Correction System (LFCS) and the Earth Magnetic Field Compensation System (EMCS). The basic principle, technical realization, and the dimensions of the LFCS as well as the EMCS described in the following paragraph is based on reference [Erh+18].
The goal of the EMCS is to compensate contributions of the earth magnetic field perpendicular to the beam axis to avoid collisions of the magnetic flux tube with the Main Spectrometer vessel. It is designed as a cylindrical geometry surrounding the Main Spectrometer vessel with length of approximately 23 m and diameter 12.6 m [Glü+13]. It is mounted on an aluminum holding structure. Several layers of wire loops along the vertical and horizontal axis with adjustable current constitute the EMCS. Each wire loop is made up of two current segments parallel to the spectrometer that are connected at the EMCS endrings. The wire loops are arranged according to a $\cos\theta$-distribution, the applied current on the EMCS thus causes a homogeneous magnetic field inside the Main Spectrometer. The vertical earth magnetic field component is compensated by the horizontal loops, and the horizontal component by the vertical loops. [Erh+18]

The goals of the LFCS is to fine-shape the magnetic field inside the Main Spectrometer to provide optimal magnetic-adiabatic collimation for β-decay electrons as well as to reduce the spectrometer's background via magnetic shielding [Ake+21d]. During KNM1 and KNM2, the LFCS comprised 14 air coils, that are coaxially aligned with the spectrometer axis [Ake+21d]. The air coils are mounted on ring-shaped aluminum support frames [Ake+21d]. In the first quarter of 2020, before the third neutrino mass measurement campaign KNM3, the LFCS was modified to enable an additional operational mode, namely the shifted analyzing plane (see chapter 6). Therefore, six additional coils were added to the LFCS and further windings were attached to some of the existing coils. This updated system is called Extended Low Field Correction System (eLFCS). We will mainly focus on the characterization of the analyzing plane with the eLFCS in the following, as it is the relevant one for future neutrino mass campaigns. Each of the 20 air coils has a diameter of approximately 12.6 m and can be controlled via its own power supply. This allows to precisely set the magnetic field strength and shape in the Main Spectrometer to fulfill the requirements on magnetic-adiabatic collimation. The largest possible magnetic field strength that can be maintained at the center of the Main Spectrometer with the eLFCS is approximately 2 mT.

Small magnetic fields in the analyzing plane are in principle desirable for neutrino mass measurements, as they result in a better energy resolution (see equation 3.11). The dimension of the Main Spectrometer vessel sets a lower boundary on the minimal possible magnetic field strength in the analyzing plane. The magnetic flux, guiding the β-decay electrons from the source to the spectrometer, is

$$\begin{aligned} \Phi &= B_{\mathrm{src}} \cdot A_{\mathrm{src}} \\ &\approx 133\,\mathrm{T} \cdot \mathrm{cm}^2 \end{aligned} \tag{5.1}$$

in the current operational setting. The maximal inner radius at the center of the Main Spectrometer is given by the radius of the Main Spectrometer vessel minus the offset of the inner electrode system to 4.85 m. The minimal possible magnetic field in the analyzing plane, that transports the complete flux tube through the Main Spectrometer, is therefore 1.8×10^{-4} T. This calculation unrealistically assumes that the magnetic flux tube is perfectly aligned with the Main Spectrometer vessel. That is not the case, as discussed in section 4.1.2. In reality, the minimal magnetic field, that transports the whole flux tube through the Main Spectrometer, is roughly 2.7×10^{-4} T in the current setup. In the following, we follow the KATRIN terminology to name the setting of the magnetic field in the analyzing plane in the unit Gauss ($1\,\mathrm{G} = 10^{-4}\,\mathrm{T}$).
The magnetic field settings, that are of interest for the thesis at hand, are the 6 G, 2.7 G, and 1 G settings. The shape of the flux tube in the Main Spectrometer and the transmission function for the respective settings is visualized in figure 5.2. Although the 1 G setting features high energy resolution, as shown by the transmission function, it cannot be used for neutrino mass measurements as large parts of the β-decay electrons in the flux tube collide with the Main Spectrometer vessel before reaching the FPD. Only that part of the flux tube that corresponds to the four inner-most pixel rings of the FPD is transmitted through the spectrometer. Consequently, the 1 G setting can only be considered for measurements in which an excellent energy resolution is favored over the guidance of the whole flux tube to the FPD. The 6 G and the 2.7 G setting can both in principle be used for neutrino mass

measurements. The 2.7 G setting is favorable due to the better energy resolution of 1.2 eV, in comparison to the 2.8 eV resolution of the 6 G setting for an isotropic source. However, the 6 G setting has one significant advantage relevant for neutrino mass measurements in comparison to the 2.7 G setting, as discussed in the following paragraphs.

Main Spectrometer Background

The final KATRIN sensitivity goal of $m_\nu = 0.2\,\text{eV}$ (90 % C.L.) is derived by assuming a background rate on the order of $R_{\text{bg}} = 10\,\text{mcps}$ during neutrino mass measurements [KAT05]. Commissioning measurements in 2013 and 2014 yield a total Main Spectrometer background rate of $(565 \pm 8)\,\text{mcps}$, making it the dominant background contribution in neutrino mass measurements [Har15; Ake+21b]. This more than a factor 50 increased background rate is a limiting factor for the KATRIN neutrino mass sensitivity and needs to be reduced. In the following, we briefly review the two dominant Main Spectrometer background components to provide a basis for discussing the interplay of the spectrometer background rate, measured by the FPD, with the magnetic field setting in the analyzing plane.

The first main background component originates from α decays of ^{219}Rn, as found and described inter alia in references [Frä+11; Har15; Ake+21b]. The non-evaporable getter pumps used in the Main Spectrometer emanate single ^{219}Rn atoms in the spectrometer volume, where the α decay generates several electrons. If the decay happens to be in the magnetic flux tube, these primary electrons are usually stored in the Main Spectrometer due to the magnetic mirror effect, caused by the strong magnetic fields of the PCH and PS2, in combination with the electrons' kinetic energy up to the keV scale. The trapped primary electrons scatter off residual gas in a cool-down process, until they lose enough energy to escape the magnetic trap. During the scattering processes, secondary electrons are produced. Both, the primary as well as the secondary electrons, contribute to the Main Spectrometer background. The electrons stemming from ^{219}Rn decays are correlated and therefore non-Poissonian distributed [Mer+13]. Consequently, a systematic uncertainty on the neutrino mass arises [Ake+21a; Mer+13]. Liquid nitrogen cooled copper baffles are installed as a countermeasure in the Main Spectrometer pump ports to prevent a direct line of sight from the getter pumps to the spectrometer's volume to suppress the number of ^{219}Rn decays in the Main Spectrometer. [Har15] The background component related to radon decay can further be reduced by a radical change of the Main Spectrometer storing conditions, for example via the shifted analyzing plane (see section 6.1.2).

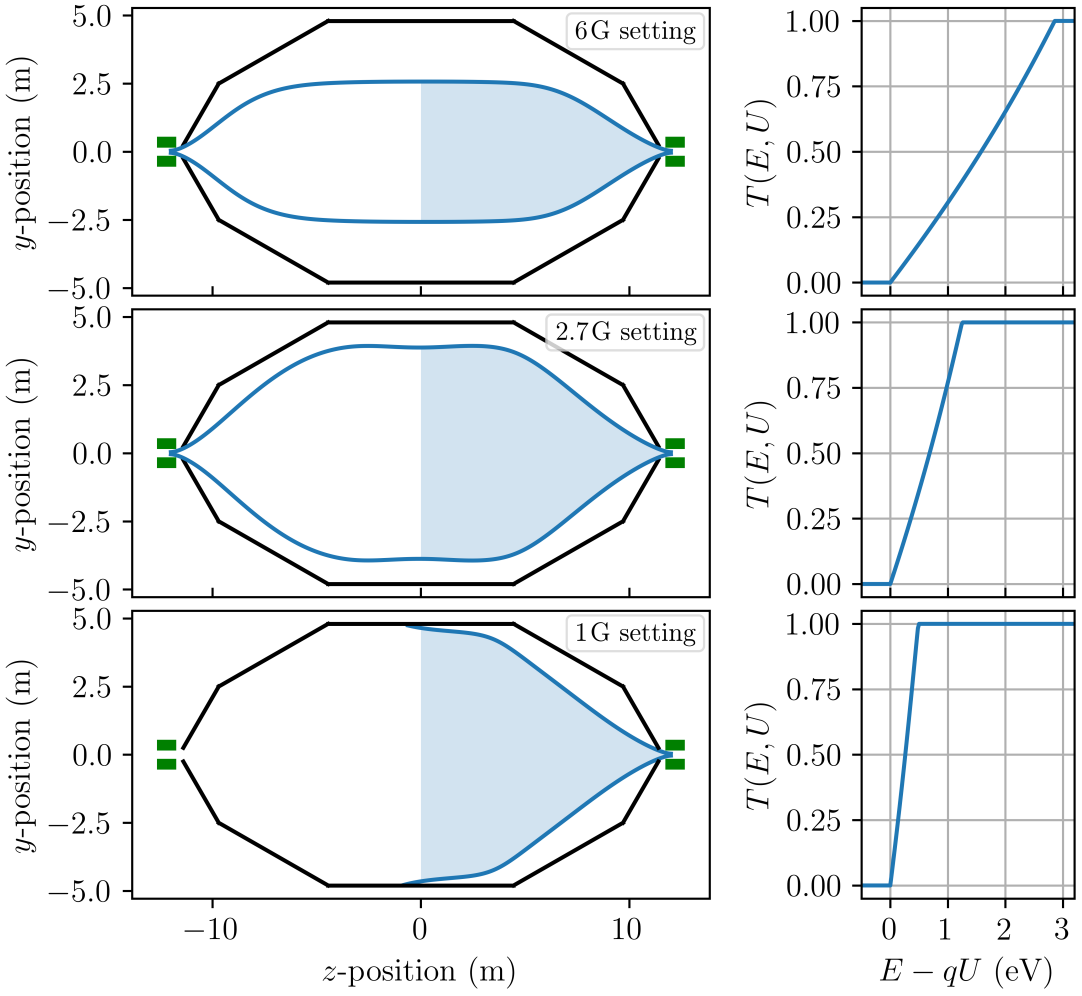

Figure 5.2.: **Simulated spatial evolution of the 6 G, 2.7 G, and 1 G magnetic field setting in the analyzing plane of the Main Spectrometer (left column) and calculated transmission function $T(E, U)$ for the respective setting for β-decay electrons near the tritium endpoint (right column).** The analyzing plane is located at $z = 0$ m for all settings. The top graph shows the 6 G setting. The β-decay flux tube expands to approximately 5 m diameter in the analyzing plane. The blue-shaded area represents the volume that contributes to the Main Spectrometer background seen by the FPD. The plot in the right column shows the transmission function, the spectrometer energy resolution for the 6 G setting is approximately 2.8 eV. The graphs in the middle panels present the same features for the 2.7 G configuration. The flux tube expands to a diameter of nearly 8 m in the analyzing plane, the energy resolution increases to 1.2 eV due to the lower magnetic field strength. The spatial evolution of the 1 G setting causes a collision of the outer part of the flux tube with the Main Spectrometer vessel, the transmission function is narrower compared to the other two settings due to the excellent energy resolution. The eLFCS currents for the individual settings are stated in table B.2, the simulation input parameters for the beamline magnets are given in table B.1.

The second main background source is an ionization process of hydrogen Rydberg atoms in the Main Spectrometer volume. The following description is based on the work by Fränkle et al., for details see reference [Frä+20].
The Main Spectrometer is exposed to ambient air during the five year installation period of the inner electrode system in the Main Spectrometer vessel. Thereby, its surface comes in contact with ^{222}Rn as part of ambient air, starting a decay chain at the inner surface. The half-lives of following decay products are at maximum on the orders of several minutes up to the long-lived daughter product ^{210}Pb with half-life 22.3 years. As the decay chain from ^{222}Rn to ^{210}Pb contains several α decays, the isotope ^{210}Pb is implanted in the Main Spectrometer surface by recoil energies. The total activity due to ^{210}Pb on the Main Spectrometer surface is estimated to $1\,\mathrm{Bq/m^2}$. Subsequently, ^{210}Po arises via the intermediate ^{210}Bi in the decay chain of ^{210}Pb. ^{210}Po decays via α decay into the stable ^{206}Pb. Due to its high nuclear recoil energy, ^{206}Pb can sputter off hydrogen atoms from the Main Spectrometer surface and cause excitation of the atoms to Rydberg states. Neutral Rydberg atoms are not directly affected by the electric and magnetic shielding of the Main Spectrometer and can thus propagate into the spectrometer volume and the magnetic flux tube. Due to their low ionization energy in the range of meV to eV, black body radiation of the spectrometer can stimulate photo-emission of the Rydberg atoms, leading to low-energetic background electrons ($E < 2\,\mathrm{eV}$) in the Main Spectrometer volume [Sch20a]. Since β-decay electrons are decelerated in the MAC-E filter by the retarding potential, the background electrons from Rydberg atoms as well as the β-decay electrons have similar kinetic energies in the analyzing plane. As both categories of electrons, the transmitted ones from β decay as well as the background electrons, are accelerated after the analyzing plane towards the FPD, it is not possible to kinematically distinguish between the signal and background electrons at the FPD. [Frä+20]
The electric potential barrier at the analyzing plane is an insurmountable obstacle for the low-energetic electrons stemming from Rydberg ionization. Thus, only those background electrons are measured at the FPD, that are created at the downstream side of the analyzing plane in the magnetic flux tube, in the so-called downstream volume (marked in blue in figure 5.2). Consequently, the background rate originating from Rydberg ionization can be reduced by decreasing the volume of the flux tube between analyzing plane and FPD.

Magnetic Field Configuration in the Analyzing Plane for Neutrino Mass Measurements

The larger background rate compared to the design report due to Rydberg electrons increases the statistical uncertainty at constant measurement time. As the total background rate at the FPD is volume dependent due to the Rydberg electron component, it can be reduced by reducing the downstream flux tube volume in the Main Spectrometer. One approach to lower the downstream volume is to increase the magnetic field strength in the analyzing plane and thereby reducing the radial expansion of the flux tube, according to equation 5.1 and as visualized in figure 5.2. The downstream volume of the 2.7 G setting yields approximately $320\,\mathrm{m^3}$, while the 6 G volume only amounts to $160\,\mathrm{m^3}$. The disadvantage of this procedure is that the Main Spectrometer resolution becomes worse (see equation 3.11). Additionally, an

increase of the magnetic field strength in the analyzing plane comes at the necessity to better know the magnetic field to keep the systematic uncertainty at constant level (as investigated in section 5.1.3).
Dedicated magnetic field measurements allow to estimate the accuracy of the field model in the analyzing plane for a certain setting (as presented in section 5.2.3). Based on a model for the volume-dependent background [Tro19] and magnetic field measurements before KNM1 [BBG18], an optimization between statistical and systematic uncertainty contributions is performed. This study leads to an optimal magnetic field setting of 6 G for KATRIN neutrino mass measurements. The 6 G setting was used in KNM1 and KNM2, and also partially in KNM3 (see table C.4). The simulated 6 G magnetic field setting is visualized in the FPD projection in figure 5.1.

5.1.3. Requirements for Neutrino Mass Measurements

The electric retardation and the magnetic field in the Main Spectrometer vessel as important quantities of the analyzing plane cannot directly be accessed via model-independent field measurements due to the experimental environment (see also reference [Erh16]). It is therefore necessary to rely on simulations or model-dependent measurements for neutrino mass analysis with KATRIN. The following paragraphs investigate the allowed model uncertainties on the electric retardation and the magnetic field that simultaneously also set stringent requirements on the hardware, producing these fields.

Requirement on Retarding Voltage Hardware and Model

The requirements on the retarding voltage hardware and model in the KATRIN experiment was extensively discussed by Kašpar et al. in reference [Kaš+04]. We briefly summarize in the following the main effects from the electric retardation on the neutrino mass based on this article and add another effect that is not taken into account in the work by Kašpar et al.
The systematic contributions on the neutrino mass discussed in the following are time instabilities, a constant offset between simulation and reality, and deviations in the shape of the analyzing plane potential between simulation and reality.

Time instabilities of the electric retardation can either occur as short-term fluctuations within one scan step as well as long-term drifts over a whole measurement campaign.
Kašpar et al. investigated the short-term fluctuations by blurring the energy scale with a Gaussian kernel. The systematic neutrino mass shifts due to the fluctuations seem to be independent of the measurement time but depend on the width σ of the applied Gaussian probability function for blurring. The systematic neutrino mass shift $\delta m^2_{\nu,\mathrm{sys}}$ follows the approximate equality $\delta m^2_{\nu,\mathrm{sys}} \approx -2\sigma^2$ [RK88], hence the width of short-term retarding voltage fluctuations should be on the order or below 50 mV for the final KATRIN sensitivity [Kaš+04]. This stability is accomplished by inter alia the high-voltage post-regulation [Ake+21d].
Possible long-term drifts in a whole measurement campaign are examined as sudden unrecognized changes of the calibration during the campaign as well as continuously

changing calibrations. The performed studies show that a retardation monitoring on the ppm-level is necessary to achieve the final neutrino mass uncertainty. Additionally, calibrations should be performed on a regular basis to exclude the possibility of unrecognized time variations in the calibration line. [Kaš+04] The requirements are met with the two high voltage dividers and the regular calibrations of the digital voltmeters [Ake+21d].

Kašpar et al. examined also the effect of a retardation offset between calculation and reality. It is thereby assumed that the offset is constant for all pixels in the FPD projection into the analyzing plane. The shape of the retarding voltage is thus the same in simulation and reality. Since the tritium endpoint as well as the signal normalization are free fit parameters in the KATRIN neutrino mass analysis, they absorb a constantly biased energy scale. Consequently, a constant offset does not cause any systematic bias on the measured neutrino mass. [Kaš+04]

Another possible effect that can bias the neutrino mass measurement is the shape deviation of modeled retarding potential versus the real shape. S. Groh investigated the impact of a radial potential inhomogeneity on the measured neutrino mass in reference [Gro15]. In the following, we focus on the study of another possible effect, namely shape deviations due to misalignment that is not correctly included in the Kassiopeia model (see also section 5.5.1). Unrecognized misalignment, especially of the PCH magnet or the FPD wafer, leads to a different true position of the FPD projection in the analyzing plane compared to simulation expectation. This again results in imperfections of the estimated electric retardation for the individual pixel projections.
In the following study we investigate the effect of potential shape deviations on the neutrino mass due to unrecognized misalignment. We therefore simulate an Asimov dataset with vanishing neutrino mass based on a period summary, that is exactly centered at the Main Spectrometer. Additionally, further period summaries are produced for which the center of the FPD projection in the Main Spectrometer is shifted for the calculation of the electric field in the analyzing plane. This causes a sinusoidal-shaped difference in the shifted period summary potential relative to the potential of the production period summary on the FPD. The magnetic field in the analyzing plane is artificially kept constant despite the shift, so that the procedure is only sensitive to deviations in the retarding potential. The Asimov dataset is then analyzed in a uniform fit by using the shifted period summaries, representing possible unrecognized shifts. A determined neutrino mass that deviates from zero directly indicates the systematic shift due to the potential shape deviation. We test unrecognized displacements of up to 1.5 m in the 6 G setting. Such large shifts are rather unrealistic but useful as an upper limit.
Although the energy imperfection amounts up to $\sigma = 65\,\mathrm{meV}$, the neutrino mass shift determined in a uniform fit is $\delta m^2_{\nu,\mathrm{sys}} < 10^{-5}\,\mathrm{eV}^2$ for all tested shifts, and therefore negligible for the targeted neutrino mass sensitivity of KATRIN. The free endpoint parameter absorbs most of the bias by deviating from the Monte Carlo truth by up to 20 meV. In summary, the neutrino mass measurements are not sensitive to potential shape deviations due to unrecognized misalignment. Nonetheless, further systematic studies relevant for the success of KATRIN need an accurate description of the potential shape in the analyzing plane (see for example reference [Mac21]).

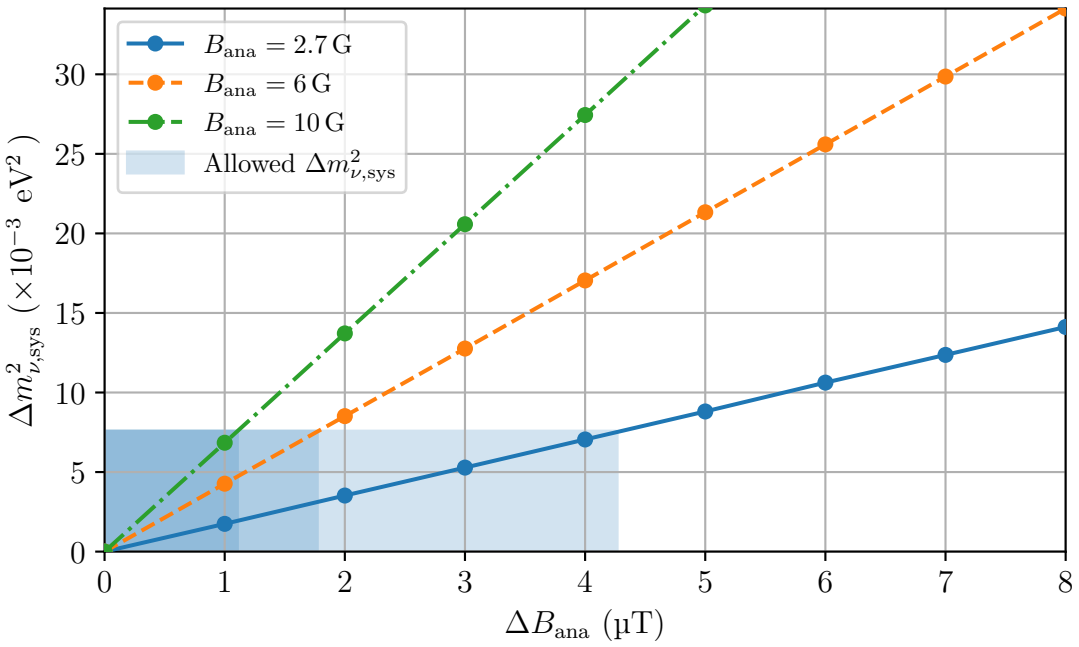

Figure 5.3.: **Systematic uncertainty contribution $\Delta m^2_{\nu,\mathrm{sys}}$ to the measured neutrino mass due to uncertainties on the magnetic field ΔB_{ana} in the analyzing plane.** The systematic uncertainty contribution is investigated with the pull-term method for three field configurations, that can be used for neutrino mass measurements. The blue-shaded area represents the KATRIN requirement on the systematic uncertainty contribution of $\Delta m^2_{\nu,\mathrm{sys}} \leq 7.5 \times 10^{-3}\,\mathrm{eV}^2$ by a single systematic uncertainty.

Requirement on Magnetic Field Hardware and Model

In this works, the requirements on the magnetic field strength in the analyzing plane have to be investigated for multiple mean magnetic field configurations, as the magnetic field setting can be subject to change, depending on the Main Spectrometer background. Therefore, three settings are analyzed with regard to the systematic neutrino mass uncertainty. We decide to investigate the 2.7 G setting as the one with the best energy resolution that still transports the complete flux tube through the Main Spectrometer. In addition, the 6 G setting as the KNM1 and KNM2 default configuration is analyzed as well as a hypothetical 10 G setting. The 10 G setting would, compared to the 6 G configuration, further reduce the downstream volume and consequently the background rate.
The systematic uncertainty study is performed with the pull-term method. The magnetic field strength in the analyzing plane is therefore added as a fifth fit parameter to the nominal four-parameter fit of the neutrino mass analysis. The fit parameter describing the magnetic field is constrained by a Gauss-shaped penalty term in the likelihood function with the analyzed field strength as mean value and investigated uncertainty ΔB_{ana} as width. The systematic contribution to the neutrino mass uncertainty is then obtained by the comparison of the neutrino mass uncertainty in the four- and five-parameter fit.
The results of the sensitivity study are shown in figure 5.3. The uncertainty on the

squared neutrino mass is plotted over the uncertainty of the magnetic field model. The study shows that the squared neutrino mass uncertainty due to a fixed field uncertainty is larger at stronger magnetic fields in the analyzing plane. As example, we report the maximally allowed model uncertainty on the magnetic field in order to satisfy the KATRIN requirement for a single systematic uncertainty contribution of less than $7.5 \times 10^{-3}\,\mathrm{eV}^2$. To fulfill the requirement, the field uncertainty on the 2.7 G model is not allowed to exceed $\Delta B_{\mathrm{ana}} \leq 4.2\,\mu\mathrm{T}$. In the 6 G setting, the field uncertainty in the analyzing plane has to be below $\Delta B_{\mathrm{ana}} \leq 1.7\,\mu\mathrm{T}$, for the 10 G setting even below $\Delta B_{\mathrm{ana}} \leq 1.1\,\mu\mathrm{T}$.
Consequently, we need a thorough characterization of the magnetic field in the analyzing plane to achieve the ambitious goal of percent or even permill relative precision.

In order to avoid significant biases on the measured neutrino mass, it is crucial that the magnetic field in the analyzing plane is stable to the μT level or better over a measurement campaign. This sets stringent requirements on the time stability of the KATRIN magnets. Measurements with low-field magnetometers at the Main Spectrometer vessel close to the analyzing plane (see section 5.2.1) show a field stability of better than the permill-level for the 6 G setting during a neutrino mass measurement campaign, satisfying the requirement on a stable field.

5.2. Magnetic Field Characterization with Simulations and Sensor Measurements

As shown in the sensitivity studies above, the allowed tolerances on the electric retardation model in the analyzing plane are rather large. Additionally, the simulations on electric retardation produced by the Main Spectrometer have thoroughly been investigated in the course of several works, see for example references [Cor14; Gro15; Hil16; Bar17]. The critical part in terms of neutrino mass systematic uncertainties is the monitoring and stability of the applied high voltage at the inner electrodes and the Main Spectrometer vessel, for which we refer the interested reader to references [Res+19; Ake+21d; Rod22].
We therefore focus in this section on the model for the magnetic field in the analyzing plane based on simulations, and whether it is possible to reach with simulations the sub-percent accuracy on the total magnetic field strength for neutrino mass measurements. The goodness of the magnetic field simulation is quantified by comparison to field measurements with low-field magnetometers close to the analyzing plane.

5.2.1. Magnetic Field Monitoring System

Due to the experimental environment, it is not possible to perform direct measurements of the magnetic field inside the Main Spectrometer vessel. The monitoring system for the magnetic field in the analyzing plane is therefore mounted outside of the Main Spectrometer vessel (see figure 5.4). It consists of several sub-systems. Some of the systems were installed in the course of previous works and are modified as part of this work to provide the sensitivity necessary to test the magnetic field

models at the level required for neutrino mass measurements. Additional systems are added in the course of this thesis to allow a more detailed insight on individual contributions and to address the modifications in operational parameters of KATRIN (for example the shifted analyzing plane). We report in the following on the final monitoring system setup as tool to quantify the goodness of magnetic field simulations.
The monitoring system of the magnetic field near the nominal analyzing plane is split up in two categories, the stationary monitoring system and the mobile monitoring system.

The mobile monitoring system comprises robots with magnetometers, that move automatically around the Main Spectrometer. This system allows measurements of the environmental magnetic field over a larger area close to the Main Spectrometer. The magnetic field monitoring can only be performed at specific times, a continuous monitoring is currently not possible. In total, eight robots form the mobile monitoring system. Four units are part of the Radial Magnetic Monitoring System (RMMS), the remaining four units form the Vertical Magnetic Monitoring System (VMMS).
The four units of the RMMS are called Mobile Sensor Units (MobSU). Each MobSU is a "T"-shaped robot, that moves on the inner side of the eLFCS aluminum holding structure, perpendicular to the beam axis (see figure 5.4). Toothed-gear wheels and a toothed belt on the inner side of the aluminum structure allows the MobSU to navigate mechanical discontinuities. Each wing of the "T"-shaped robot contains a low-field flux gate sensor to measure the magnetic field. Each MobSU measures the magnetic field at 144 predefined sampling positions with a step size of 2.5° in azimuthal direction close to the Main Spectrometer surface during one sweep around the spectrometer's vessel. A sophisticated inclinometer system allows the transformation of the measurement positions to the global KATRIN coordinate system [Gar17]. The four MobSU are mounted on the eLFCS holding structures that are closest to the nominal analyzing plane. [Let+18; Let19; Ake+21d]
The VMMS measures the magnetic fields near the walls of the Main Spectrometer hall, parallel to the beam axis. The walls' and some of the pillars' concrete in the Main Spectrometer hall contain normal steel that is magnetized by the beamline fields and thus produces a background magnetic field. The VMMS is designed to measure remnant and induced magnetization effects from the steel in the concrete, influencing the magnetic field in the analyzing plane (see section 5.2.2) [Erh16; Rei13]. Similar to the RMMS, the VMMS is based on a movable construction that is mounted on the hall pillars. Each VMMS unit carries a flux gate magnetometer. The four units can measure the magnetic field at nearly the complete wall surface in the area of the Main Spectrometer vessel in a measurement grid of 20 cm × 20 cm. [Let+18; Ake+21d] Measurements with the VMMS carried out during this thesis show that the motor moving the unit is too close to the magnetometer, resulting in distorted magnetic field measurements [Bou19]. Measurements conducted with the VMMS are therefore not analyzed within the scope of this work.

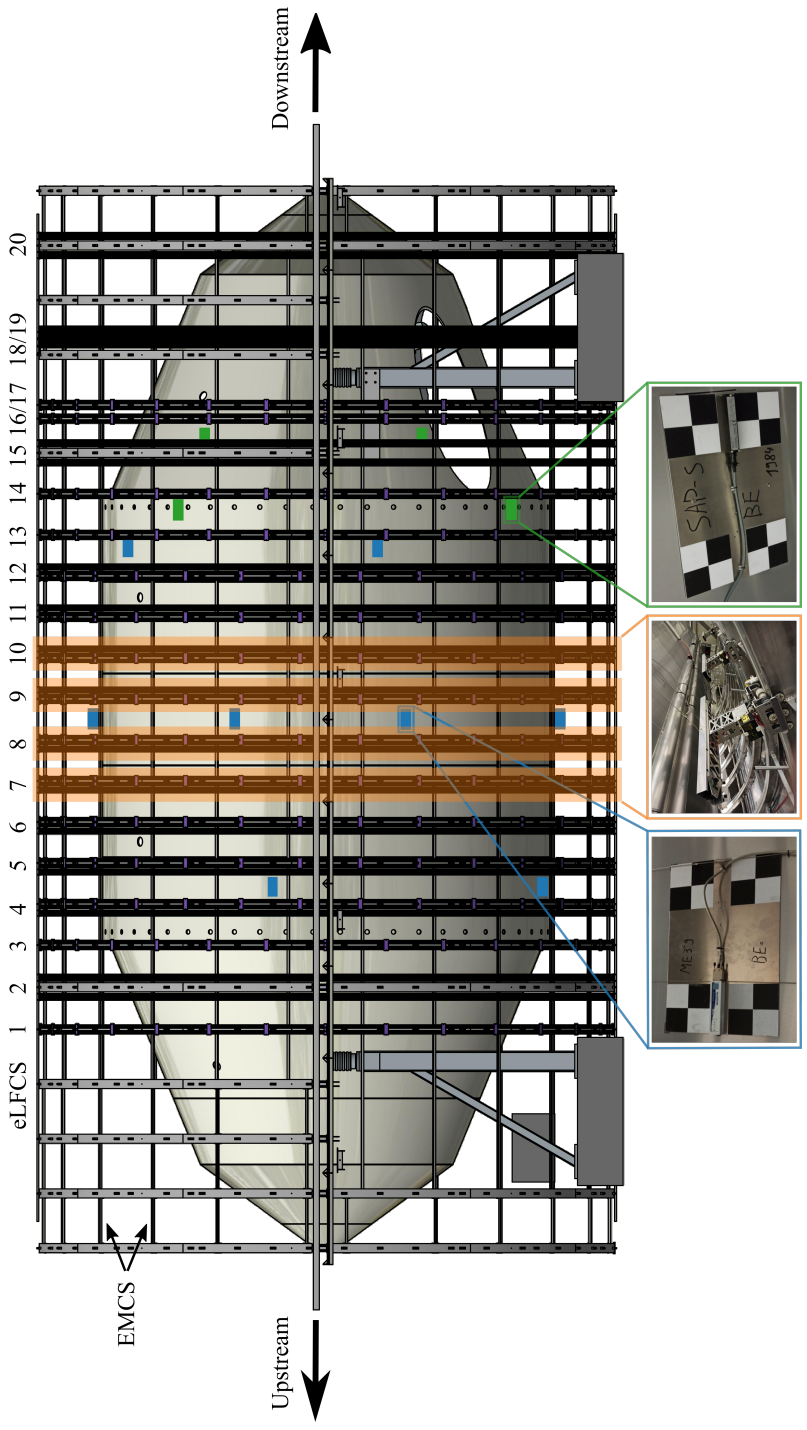

Figure 5.4.: **Lateral schematic drawing of the Main Spectrometer vessel, the large-volume air-coil system, and the high-precision magnetometer system at or in close vicinity to the spectrometer.** The coils of the eLFCS are visualized as black vertical lines, the holding structure for the EMCS is drawn with horizontal black lines. The Bartington® magnetometer system is visualized by the blue boxes, the monitoring system for the shifted analyzing plane field is shown in green. The checkerboard pattern, that are displayed in the two photos of the sensor units of the stationary sensor systems, enable a precise and accurate positioning measurement of the magnetometer. The four MobSU are mounted on the inner side of the eLFCS holding structure of coil 7, 8, 9 and 10 (marked in orange). The nominal analyzing plane is located in axial direction between eLFCS coil 8 and 9. Drawing of Main Spectrometer and large-volume air-coil system provided by R. Rinderspacher, figure inspired by M. Erhard [Erh16].

The stationary magnetic monitoring system enables continuous monitoring of the magnetic field, either directly on the Main Spectrometer vessel, as close as possible to the flux tube, or at the walls of the Main Spectrometer hall. The stationary magnetic monitoring system comprises in total four different sub-systems.
The first sub-system is formed by 24 magneto-resistance magnetic field sensors. The sensor units are distributed on three rings, sharing the same axial position but differ in azimuthal position. The magneto-resistance sensors can measure the magnetic flux with 5 % relative systematic uncertainty. [Ake+21d] Compared to the necessary permill-level accuracy on the magnetic field in the analyzing plane for neutrino mass measurements, these sensors are not sensitive enough to test the magnetic field simulations. Consequently, the sensors are not used for analysis in the following sections and are mentioned here only for completeness.
The second sub-system consists of 14 Bartington® three-axis fluxgate magnetic field sensors with measurement range ±1 mT [Bar11]. The sensor units are mounted at the outer vessel hull of the Main Spectrometer and arranged in three rings (see figure 5.4). Similar to the first sensor sub-system, magnetometers mounted on one ring share the same axial position but differ in azimuthal position. The rings are located at $z \approx -4.5\,\mathrm{m}$, $z \approx 0\,\mathrm{m}$ and $z \approx +4.5\,\mathrm{m}$ [Ake+21d]. The sensor network is commissioned and aligned by M. Antoni [Ant13]. As part of the present thesis, the alignment routine of the sensor units with respect to the global KATRIN alignment is improved by adapting the sensor units to enable precise Faro® Laser Tracker measurements. Additionally, the systematic uncertainty of the Bartington® sensors is improved from 0.5 % relative uncertainty [Bar11] to 0.2 % by applying a calibration routine. Therefore, the Bartington® sensors are calibrated with a magnetometer that was calibrated to 0.13 % relative precision at the "Physikalisch-Technische Bundesanstalt", the German metrology institute. In addition, we also calibrate the data acquisition system, which also reduces the systematic uncertainty of the measured magnetic field.
The magnetic field system dedicated for magnetic monitoring near the shifted analyzing plane (see chapter 6) comprises nine sensor units. Each unit houses one SENSYS three-axis fluxgate magnetometer with measurement range ±1 mT [SEN20]. The nine units are split on two rings, one at z-position 5.2 m and one at 6.4 m (see figure 5.4). The exact position is determined, similar to the Bartington® units, with Faro® Laser Tracker measurements. The relative measurement uncertainty on the magnetic field yields 0.5 % with these magnetometers.
The fifth stationary magnetic monitoring system is a tool to compensate the outage of the VMMS to certain extent. It is meant to measure the remnant and induced magnetic field from the steel bars in the concrete of the Main Spectrometer hall. The five magnetic field sensors are therefore mounted at the eastern wall of the Main Spectrometer hall at different axial positions and also at different absolute distances to the Main Spectrometer vessel. The used magnetometers are the same as employed for the monitoring system of the shifted analyzing plane.

5.2.2. Impact of the Earth Magnetic Field and Beamline Magnets

The calculated magnetic field contributions from the beamline solenoids and the earth magnetic field at the center of the Main Spectrometer, as approximate center

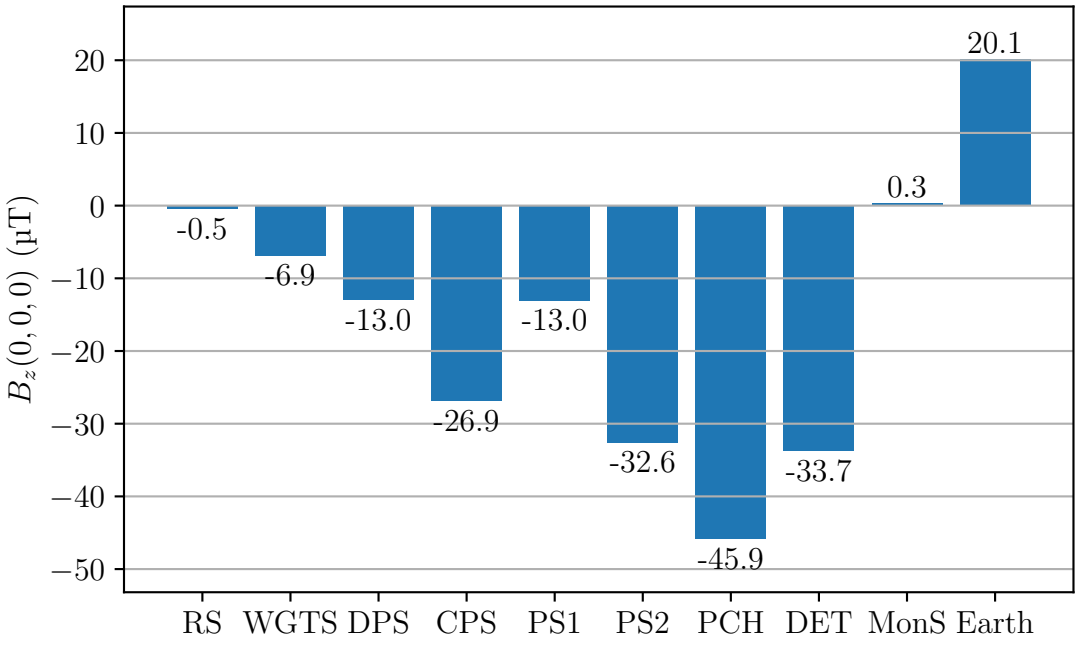

Figure 5.5.: **Simulated contribution of the beamline solenoids and the earth magnetic field to the axial field component B_z of the magnetic field at the approximate center of the nominal analyzing plane.** Note that the main magnetic field component B_z is oriented antiparallel to the flight direction of the β-decay electrons and therefore antiparallel to the KATRIN coordinate z-axis. The dominating contributions from the beamline solenoids to the magnetic field in the analyzing plane are given by the three SDS magnets PS2, PCH, and DET.

of the analyzing plane, is shown in figure 5.5. The field contributions are calculated for the z-component, along the beam axis, since this is the leading component in the field setting used for neutrino mass measurements. The leading field contributions are the SDS solenoids due to their comparably small distance of less than 13 m to the Main Spectrometer's center. It is evident that all contributions need to be correctly included in the simulation to reach a model accuracy on the μT-level.
The individual contributions are evaluated in the following paragraphs by comparison of measurement and simulation in the light of the allowed model uncertainty for neutrino mass measurements. Similar efforts have been made by M. Erhard in 2016 (see reference [Erh16]). However, the beamline was not yet in full operational mode in 2016 and the alignment was different compared to today. In the present thesis, we therefore reevaluate the contribution of the individual components in the final setup with the configuration used for neutrino mass measurements. Due to a lack of measurement data, it is not possible to investigate all contributions shown in figure 5.5.

Earth Magnetic Field

The earth magnetic field has a total intensity of 24 μT to 64 μT at the earth's surface [Thé+15], depending on the measurement position. As input for the magnetic field

model, we estimate the earth magnetic field at KATRIN with the field calculator by the "National Centers for Environmental Information"[1], using the geographic coordinates of the KATRIN experiment. Additionally, the tilt of the coordinate system versus the geographic North Pole by 15.4° is taken into account. This leads to an expected earth magnetic field of $\vec{B}_{\text{earth}} = (4.6, -43.9, 20.1)\,\mu\text{T}$ in the KATRIN coordinate system[2], that can be compared to measurements.

The comparison of expected intensity of the earth magnetic field with measurements is performed by using three different sensor networks. Firstly, the Bartington® magnetometers at the Main Spectrometer vessel near the analyzing plane are used as precise and accurate tools. Secondly, measurements with the MobSU allow a fine spatial resolution around the vessel. As third system, the magnetometers mounted at the eastern wall of the Main Spectrometer hall are employed. All magnetometer systems have in common that the z-axis of the sensors is well aligned with the z-axis of the coordinate system, in contrast to the x- and y-axis. We therefore split the analysis in a radial component, that comprises the x- and y-axis, and into the z-component, to avoid a bias in the comparison due to insufficient alignment reconstruction of the individual sensors. The magnetic field difference δB for the axial and the radial component is then calculated according to

$$\delta B = B_{\text{meas}} - B_{\text{sim}}$$

where B_{meas} denotes the measured and B_{sim} the simulated magnetic field.
All magnets were switched of during the performed measurement, we therefore expect to measure solely the earth magnetic field. The magnetic field difference for the radial and axial component over the azimuth angle is shown in figure 5.6. The data used for the plot was measured by MobSU-8 and MobSU-9 as units that are closest to the analyzing plane, as well as by the Bartington® system.
Both difference components show significant deviations between measured and simulated magnetic field. The difference in radial direction is between 3 µT and 6 µT, depending on the measurement position. The measurements with the Bartington® sensors show a more constant field difference than the MobSU measurements. The shape difference between Bartington® and MobSU measurements can be explained by the different measurement positions, as the MobSU measure at larger radius compared to the Bartington® sensors, and thus closer to sources of possible field distortions (as discussed below). The comparison of the expected z-component with the measurement yields an absolute difference of between −0.5 µT and up to 1.3 µT for the Bartington® sensors, depending on the location. The deviation measured with the MobSU is slightly larger, similar to the radial comparison.
The five magnetic field sensors, mounted at the eastern wall of the Main Spectrometer hall, confirm the deviation shown in figure 5.6. A sensor mounted at the front side of the gallery, and therefore only at few meter distance to the Bartington® sensor located at azimuth angle $\phi \approx -145°$, measures $\delta B_{\text{rad}} = -6.5\,\mu\text{T}$ and $\delta B_z = -2.7\,\mu\text{T}$. Another sensor mounted directly at the wall of the Main Spectrometer hall shows even further increased deviations.

The measured deviation from the expected intensity of the earth magnetic field is a known feature in the KATRIN Main Spectrometer hall. Several investigations that

[1] https://www.ngdc.noaa.gov/geomag/calculators/magcalc.shtml
[2] These values are obtained with the earth magnetic field model "WMM2015" at reference date 01.03.2019.

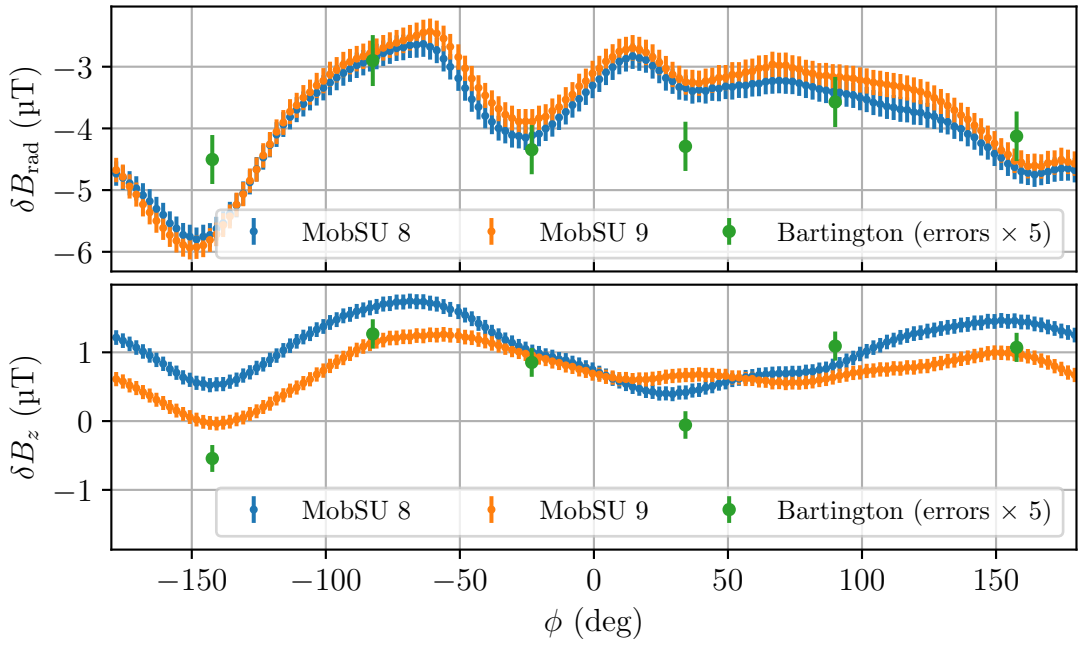

Figure 5.6.: **Deviation between simulated and measured magnetic field in radial δB_{rad} and axial δB_z direction over the azimuth angle ϕ.** Both components are investigated with MobSU measurements and Bartington® magnetometers close to the analyzing plane. The radial component shows deviations between simulation and measurement of 3 µT up to 6 µT, the axial component up to 1.3 µT.

are either summarized or carried out in reference [Erh16] prove that the reasons for this deviation are two-fold. The following section, reporting on effects that cause the measured deviation, is based on reference [Erh16].
The first contribution comprises effects from auxiliary devices installed in the Main Spectrometer hall that generate magnetic fields, which causes a local distortions of the field. However, a significant disturbance from these local field distortions inside the analyzing plane can be excluded [Bar+14].
The second and major contribution to the deviation is the magnetization of steel rods in the concrete of the Main Spectrometer hall. This background field due to the ferromagnetic material was already expected during the KATRIN design phase, but could not be avoided due to financial constraints. Normal steel is used in the walls of the Main Spectrometer hall parallel to the beam axis. The orientation of this ferromagnetic material in the y-z-plane gives the orientation of the remnant magnetic field. The construction of a model to describe the resulting remnant magnetic field in the Main Spectrometer hall is complex and would need more than 2000 measurement positions [Rei13; Ada15], that is not feasible without the VMMS. An industrial demagnetization was performed in 2014 to reduce the remnant field contributions [Wol16]. Although the demagnetization was successful [Ada16; Erh16], several measurement campaigns with magnetic field ramps before and after the campaign have been conducted since then. It is therefore likely that the effects from the demagnetization vanish with time. Erhard presents indications that the remnant magnetic field contribution can change over the course of several measurement cam-

paigns by comparing field measurements over a one year long time period [Erh16]. The remnant magnetic field due to the steel rods explains why the magnetometers mounted close to the walls of the Main Spectrometer hall see a larger deviation compared to the MobSU and Bartington® measurement. However, we would also expect to see a sinusoidal structure in figure 5.6. The floor of the Main Spectrometer hall does only contain stainless steel and the roof is made out of wood, while the concrete of the sidewalls is reinforced with normal steel. We therefore would expect large deviations at $\Phi = 0^\circ, 180^\circ$ (east, west side), and only little to no deviation at $\Phi = 90^\circ, 270^\circ$ (top, bottom). As this behavior is not shown, we have to conclude that either the used model of the earth magnetic field as global model is not accurate enough or that local distortions due to for example electrical devices locally overlay the effects from the magnetization of the steel rods.

An additional effect, that does not contribute to this special setup here but is connected to the remnant background field, is the induced magnetization by the ferromagnetism in the Main Spectrometer walls. The induced magnetization causes an additional background field contribution that depends on the external magnetic field strength at the position of the walls of the Main Spectrometer hall. Consequently, it cannot directly be accessed in measurements but only in the comparison of simulation and measurement (see also section 5.2.3).

STS Beamline Solenoids

The STS contains the Rear Section magnet, the WGTS solenoids, the DPS, and CPS, as well as the PS1 magnet. The necessary maintenance between measurement campaigns and the measurement schedule is optimized in the way that the STS magnetic fields are rarely changed, as a ramp of the field is time-consuming. The only exception to this is the CPS magnet system, that has to be ramped to zero before the Argon frost layer can be exchanged. This routine is performed every 40 to 80 days during neutrino mass measurement campaigns.
We are interested in the comparison of the pure magnetic field contribution to the simulation, especially in the analyzing plane. The Bartington® sensors mounted near $z = 0\,\mathrm{m}$ are therefore used for the comparison. To avoid a bias due to the remnant magnetic field or its time-dependent changes, a relative measurement principle is used. Therefore, the field before the ramp $\vec{B}_{\mathrm{off}}$ and after the ramp of the investigated solenoid to nominal field $\vec{B}_{\mathrm{on}}$ is measured. If all other KATRIN magnetic field sources stay constant, the difference $\vec{B}_{\mathrm{meas}}$

$$\vec{B}_{\mathrm{meas}} = \vec{B}_{\mathrm{on}} - \vec{B}_{\mathrm{off}}$$

represents the measured pure contribution of the individual solenoid and can be compared to simulation. However, this additionally assumes that the induced magnetization from the walls of the Main Spectrometer halls does not change significantly by switching on an individual solenoid. This assumption is fulfilled to first-order approximation, as the magnetic field change by an individual STS solenoid at the wall of the hall is small due to the large distance of the solenoid.
Since the STS magnetic field is only rarely changed, it is therefore also seldom that the requirement for the relative measurement method is met, namely that all other controlled magnetic field sources are constant before and after the ramp of the individual solenoid. The relative measurement is performed with the WGTS magnet

system, the CPS solenoids, and the PS1. The uncertainty on the measured fields is not stated for each analysis in the following for better readability, however, it is smaller than 0.07 µT for all measurements.

The pure field contribution by the WGTS was measured at the end of KNM5, it was ramped down after the measurement campaign for maintenance. As described above, the field was measured before and after the ramp of the WGTS magnet system. The measured difference with and without the WGTS magnetic field at the central Bartington® sensors is in average 1.5 µT in radial and −6.8 µT in z-direction. The simulation mostly agrees with the measured values, the difference between simulation and measurement is $\delta B_{\mathrm{rad}} \in [-0.1, 0.5]$ µT for the radial and $\delta B_z \in [-0.6, 0.1]$ µT for the z-component. As the deviation between measurement and simulation is on the sub-µT level, we conclude that inaccuracies in the WGTS field simulation do not significantly bias the calculated magnetic field strength in the analyzing plane and therefore also not the measured neutrino mass.

The CPS magnetic field could not directly be investigated due to the lack of suitable data. The measurement time during CPS regeneration is usually used for Main Spectrometer background measurements that differ in the magnetic field setting from the setting before ramping down the CPS. The relative method can therefore not easily be applied. However, we can use the data of an incident that occurred towards the end of the KNM5 measurement campaign. An alarm triggered the WGTS and CPS magnets to shut down simultaneously. This incident provides the necessary data for the relative measurement as the other solenoids show stable conditions before and afterwards. By subtracting the WGTS contributions as measured above, we correct for the effect by the WGTS field and enable a comparison of the pure CPS field to simulations. The deviations between measurement and simulation are in radial direction $\delta B_{\mathrm{rad}} \in [-1.4, 0.0]$ µT and for the axial component $\delta B_z \in [2.1, 3.1]$ µT. The comparably large difference between CPS measurement and simulation in z-direction can significantly bias the determined neutrino mass, if the field offset is the same in the analyzing plane. This would lead in a 6 G setting to a systematic uncertainty on the order of $\Delta m^2_{\nu,\mathrm{sys}} = 10^{-2}\,\mathrm{eV}^2$.
One reason for this discrepancy between simulation and measurement could be that the CPS position is not correctly included in the simulation. The z-component difference shows in azimuthal direction a sinusoidal-shaped structure with larger field differences at the east side and smaller differences at the west side. A sinusoidal-shaped structure in the difference between simulation and measurement is typically a sign of inaccurate geometry in the model (see also section 4.1.2). A shift analysis similar to the one performed in section 4.1.2 yields that the z-component difference could be resolved by an effective CPS cryostat shift of approximately 80 cm. Although such a large unrecognized shift between the Kassiopeia geometry model and reality is rather unrealistic, it is recommended to perform a dedicated FaroARM® measurement of the CPS cryostat to cross-check the real CPS alignment in the current beamline setup. Another explanation for the z-component difference could be an induced magnetic field that is not included in the Kassiopeia simulation. The concrete of the floor below the CPS contains steel rods, an induced magnetic field by the CPS stray field is thus possible. The hypothesis that the axial δB_z difference is caused by this induced magnetic field can be tested in a dedicated measurement. Therefore we recommend to measure the magnetic field at well-defined locations below the CPS with all other beamline magnets switched off. Close to the floor below

the CPS, the induced magnetic field must be few hundred mT to produce a deviation of $\delta B_z \approx 2.6\,\mu\text{T}$ at the Main Spectrometer. If the z-component difference at the Main Spectrometer is produced by an induced magnetic field, a field deviation of few hundred mT should be visible in the comparison of simulation to measurement close to floor below the CPS.

The last STS solenoid that could be investigated with the relative method is the PS1 magnet. The PS1 causes a mean magnetic field of $5.0\,\mu\text{T}$ in radial and $-10.0\,\mu\text{T}$ in z-direction at the location of the Bartington® sensors. The simulation agrees with the measured field change to the range of $[-0.3, 0.8]\,\mu\text{T}$ for the radial and $[-0.7, -0.1]\,\mu\text{T}$ for the z-component. Due to the small deviation in axial direction, the simulation of the PS1 field does not cause a significant neutrino mass bias.

SDS Beamline Solenoids

The SDS beamline solenoids PS2, PCH, and DET are the main contributors of the beamline solenoid to the analyzing plane, as shown in figure 5.5. Their contribution is investigated in the following with the same principle of relative measurements as for the STS magnets. The advantage of the SDS solenoids over the STS magnets in the aspect of these stray field measurements are that they are normally ramped in each maintenance break, leading to enough data for the comparison of measurement and simulation.

The PS2 magnet contributes to the Main Spectrometer field with $14.1\,\mu\text{T}$ in radial direction and $-19.3\,\mu\text{T}$ in z-direction at the location of the field sensors. The measurement mostly meets the expectation from simulation, the difference in radial direction is $\delta B_{\text{rad}} \in [-0.8, 1.3]\,\mu\text{T}$ and in axial direction $\delta B_z \in [-0.3, 0.3]\,\mu\text{T}$. The difference in axial direction as leading component in neutrino mass measurements is on the sub-μT level and thus does not significantly bias the simulation of the magnetic field.

The PCH contains the strongest beamline field in KATRIN. Due to the combination of strong field with relatively small distance to the analyzing plane, it is the leading solenoid contribution. A proper description of the PCH field in the analyzing plane is thus crucial. The measured magnetic field contributions of $19.7\,\mu\text{T}$ for the radial component and $-26.7\,\mu\text{T}$ in axial direction are reproduced by the simulation to the μT level. The comparison yields $\delta B_{\text{rad}} \in [-1.6, 1.4]\,\mu\text{T}$ and $\delta B_z \in [-0.1, 1.1]\,\mu\text{T}$. The difference between measurement and simulation is acceptable for neutrino mass measurements, as the maximally allowed magnetic field uncertainty for the 6 G setting is $1.7\,\mu\text{T}$ and for the 2.7 G configuration even $4.2\,\mu\text{T}$. Nevertheless, we recommend to further investigate this deviation and to pursue an improvement.

The DET is the last beamline magnet of KATRIN in downstream direction. The comparison of the simulated and measured field contributions at the Bartington® sensors show similar results to the PCH analysis. The radial component differs by $\delta B_{\text{rad}} \in [-1.0, 1.0]\,\mu\text{T}$, the axial by $\delta B_z \in [-0.2, 0.5]\,\mu\text{T}$.

Overview

A summary of the analyses performed above is given in table 5.1. The magnetic field of six beamline solenoid systems are measured and compared to simulations. The

Table 5.1.: **Overview of the deviation between measured contributions by the beamline solenoids and earth magnetic field to the respective simulations close to the analyzing plane.** Due to the lack of data, a comparison of the Rear Section, the DPS, and Monitor Spectrometer magnetic fields to simulation can not take place. The columns "$B_{\mathrm{rad,meas}}$" and "$B_{z,\mathrm{meas}}$" present the measured contribution in the respective direction. δB_{rad} and δB_z show the lower and upper deviation between measurement and simulation, as measured by the six Bartington® magnetometers close to the analyzing plane. Note that the row labeled as "Earth" contains all background fields, including contributions from remnant magnetization.

Field	$B_{\mathrm{rad,meas}}$ (μT)	δB_{rad} (μT)	$B_{z,\mathrm{meas}}$ (μT)	δB_z (μT)
WGTS	1.5	[−0.1, 0.5]	−6.8	[−0.6, 0.1]
CPS	8.4	[−1.4, 0.0]	−19.2	[2.1, 3.1]
PS1	5.0	[−0.3, 0.8]	−10.1	[−0.7, −0.1]
PS2	14.1	[−0.8, 1.3]	−19.3	[−0.3, 0.3]
PCH	19.7	[−1.6, 1.4]	−26.7	[−0.1, 1.1]
DET	13.7	[−1.0, 1.0]	−22.0	[−0.2, 0.5]
Earth	40.2	[−4.5, −2.9]	20.7	[−0.5, 1.3]

missing components are the Rear Section and the Monitor Spectrometer that have vanishing contribution to the magnetic field in the analyzing plane, as well as the DPS. It is recommended to perform a dedicated DPS measurement the next time the STS field is ramped.

The comparison of measurement to simulation leads to significant differences for almost all sensors. The largest difference in radial direction exists if all magnets are switched off, i.e. if we expect that only the earth magnetic field is measured. The remnant magnetic field by the steel rods in the walls of the Main Spectrometer hall is the most likely source of this deviation. The comparison of the CPS measurement with simulation shows the largest difference in z-direction, the deviation is more than a factor two larger than other differences. A possible explanation for this discrepancy between measurement and simulation could be misalignment of the CPS cryostat in the Kassiopeia model, or a strong induced magnetic field by the steel rods in the floor below the CPS.

As the z-component is the leading magnetic field contribution in neutrino mass measurements, we focus on this component in the following brief discussion. The systematic KATRIN requirement demands for the magnetic field model of the 6 G configuration, as used in KNM1 and KNM2, a precision and accuracy in magnetic field strength of better than 1.7 μT in the analyzing plane. This requirement is fulfilled for the individual deviations, except for the CPS. It must be taken into account that all beamline magnets are switched on for neutrino mass measurements, leading to the superposition of all deviations between simulation and measurement and thus surpassing the allowed KATRIN uncertainty. The simulation cannot easily be improved, since either extremely detailed models and measurements (for descrip-

tion of the remnant magnetic field) or time-consuming alignment measurements with the FaroARM® and Hall probes (similar to section 4.1.2) are required. This is not feasible in parallel to neutrino mass measurement campaigns, indicating that methods must be tested to directly measure the magnetic field strength in the analyzing plane (see section 5.3.2 and 5.4.3).

5.2.3. Impact of Low-Field Correction System

The LFCS dominates the magnetic field strength in the analyzing plane. The mechanical layout and the geometry of the LFCS was accurately measured [GL13] and implemented in the Kassiopeia framework [Erh16]. Due to the upgrade from the LFCS to the eLFCS, the layout of the system was slightly changed in terms of additional coils and windings since the investigation by Erhard in 2016. However, we do not expect significant magnetic field deviations due to this upgrade for the nominal analyzing plane, since the individual eLFCS coil currents are scaled accordingly to the increased number of coil windings.

Difference Between Measurement and Simulation for Various Settings

A measurement with various magnetic field strengths in the analyzing plane, and therefore with different eLFCS currents, enables the comparison of the eLFCS simulation to measurement. Furthermore, this also allows the estimation of possible effects by induced magnetization from the Main Spectrometer hall [Erh16]. The measurement is conducted with all beamline solenoids at nominal magnetic field after KNM3. Magnetic field measurements with the Bartington® sensors were performed with four different settings, the 0 G, 1 G, 2.7 G, and 6 G setting. The 0 G configuration indicates in that context, that the eLFCS is turned off and only the contributions from EMCS, the beamline magnets, and background fields are measured.

The deviation between measurement and simulation in z-direction as function of the absolute magnetic field strength at the magnetometers is shown in figure 5.7. The difference increases with increasing field strength, pointing towards effects of induced magnetization or inaccurate eLFCS field simulations. Of course, a combination of both effects is also possible.
Based on the idea by M. Erhard [Erh16], we effectively describe this behavior by a linear model of the shape

$$\delta B_z = \alpha \cdot B + B_0.$$

The slope α represents effects from inaccurate eLFCS simulations or from induced magnetization. The offset B_0 estimates remnant and constant background magnetic fields. It is thus also affected by inaccurate stray field simulations from beamline magnets or induced magnetic fields by the beamline solenoids. The best fit estimates the free model parameters to

$$\alpha = (6 \pm 2) \times 10^{-3},$$
$$B_0 = (2.0 \pm 0.3)\,\mu\mathrm{T}.$$

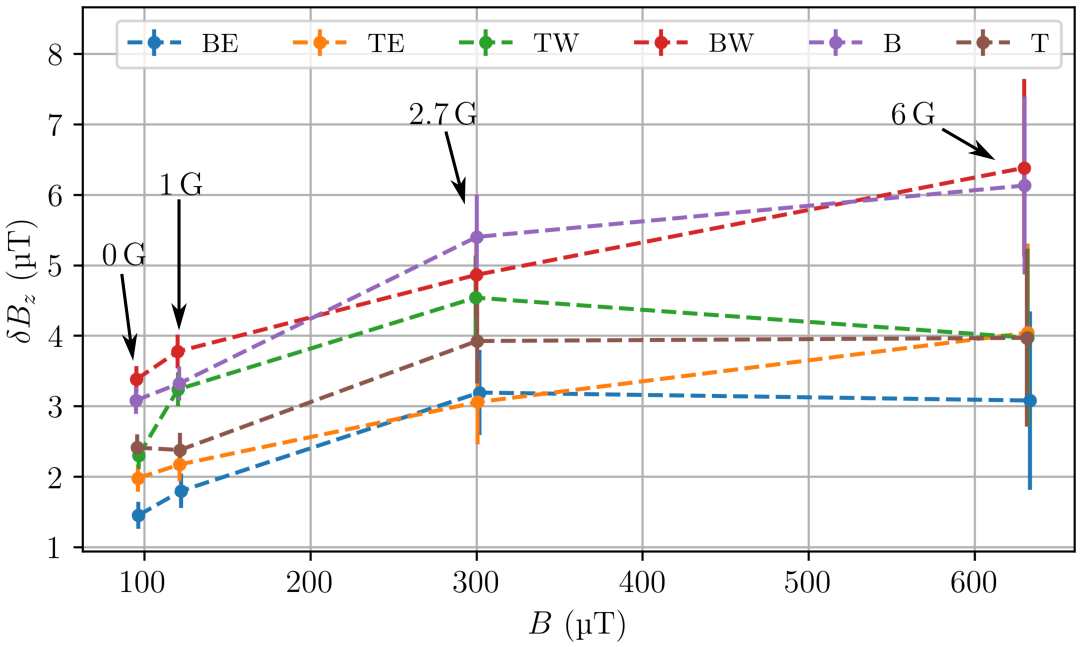

Figure 5.7.: **Deviation in axial direction δB_z between measurement and simulation as function of the absolute measured field strength B at the Main Spectrometer vessel by the Bartington® magnetometers.** The investigated settings are eLFCS switched off (labelled as "0 G"), 1 G, 2.7 G, and 6 G. The colors corresponds to specific magnetometers, for example the blue "BE" corresponds to the bottom east, while the green "TW" is the top west magnetometer.

The found slope is consistent with the slope of $\alpha = (3.9 \pm 0.3) \times 10^{-3}$ found by Erhard in [Erh16], even though the central value is higher in the recent measurement. A discussion on the difficulty to disentangle the effects of possible inaccurate eLFCS simulations and induced magnetization is given in the section below. The observed offset of $B_0 = (2.0 \pm 0.3)\,\mu\text{T}$ should agree with the field strength of the remnant magnetic field and further background fields, if the simulation of the beamline solenoids and eLFCS is accurate, and if the beamline solenoids do not cause any induced magnetization. However, the measurements with all magnets switched off yields a background field strength of less than 1.3 µT at the measurement position of the Bartington® magnetometers (see section 5.2.2). With this method we can conclude that at least 0.7 µT of the deviation in figure 5.7 is caused by inaccurate stray field simulations of the beamline solenoids or by non-considered induced magnetization by the beamline magnets.

A similar measurement with various eLFCS settings but all beamline magnets switched off enables us to investigate the impact of the beamline solenoids on the deviation. The deviation of simulation and measurement for the z-component decreases by roughly 2 µT in the measurement without beamline field compared to the measurement with beamline field for all eLFCS configurations. The fitted slope yields $\alpha = (8 \pm 4) \times 10^{-3}$ in this measurement configuration. It is consistent with the measurement with beamline solenoids at nominal field. This underlines the hypothesis that the eLFCS either causes an induced magnetic field or that the deviation

is caused by inaccurate eLFCS simulations. The fitted offset $B_0 = (0.2 \pm 0.3)\,\mu\mathrm{T}$ is in good agreement with the earth magnetic field measurement performed in 5.2.2. This shows that a non-negligible part of $2\,\mu\mathrm{T}$ of the observed difference between measurement and simulation in figure 5.7 exists only when the beamline magnets are switched on. The difference can be caused by deviations between the Kassiopeia model alignment and the true alignment for the beamline magnets, induced magnetization by the beamline fields, or both effects combined.

Another topic that needs to be discussed in this context is the reproducibility of the measurement results after a certain elapsed time. Erhard presented a time-dependent component of the remnant magnetic field in his work [Erh16]. This time dependence could introduce time-dependent changes in the above-shown difference plot. We thus compare measurements performed before KNM3 to the above-analyzed data, measured after KNM3. The time difference between both measurements is three months with different applied eLFCS field settings, especially with the shifted analyzing plane setting that yields comparably large field values at the walls with steel rods. In the measurement before KNM3, the difference between simulation and measurement for the 2.7 G setting is $\delta B_z \in [3.5, 5.2]\,\mu\mathrm{T}$, compared to $\delta B_z \in [3.1, 5.4]\,\mu\mathrm{T}$ in the post-KNM3 measurement. This difference is in agreement with fluctuations by the magnetometer. A similar picture is drawn for the comparison of the 6 G configuration. The pre-KNM3 measurement yields $\delta B_z \in [3.8, 5.8]\,\mu\mathrm{T}$ versus the post-KNM3 measurement of $\delta B_z \in [3.1, 6.4]\,\mu\mathrm{T}$. Consequently, the magnetic field strength in the analyzing plane and the deviations between measurement and simulation appear to stay constant within one measurement campaign, despite several field changes in between the magnetic field measurements.

Disentanglement of Induced Magnetization and Inaccurate eLFCS Simulation

The remnant magnetic field of an individual steel rod at position $\vec{r}$ relative to the observer can be written as

$$\vec{B}(\vec{r}) = \frac{\mu_0}{4\pi} \frac{3\vec{r}(\vec{m}\vec{r}) - \vec{m}r^2}{r^5}$$

with the magnetic dipole moment $\vec{m}$. For the ensemble of several steel rods it is necessary to calculate the total magnetization in a volume V to

$$\vec{M} = \frac{\sum \vec{m}_i}{V}.$$

The total magnetization comprises the dependence on an external applied magnetic field, leading to the induced magnetization. An external magnetic field $\vec{B}_{\mathrm{ext}}$ in the steel rod influences the magnetization as

$$\vec{M} = \frac{\chi}{\mu_0(1+\chi)} \vec{B}_{\mathrm{ext}},$$

with the susceptibility $\chi = \mu_r - 1$ and the relative permeability μ_r. [Erh16] Consequently, the induced magnetization by the steel rods is in first-order proportional to the external magnetic field at the location of the steel rods.
Simulations with artificially introduced misalignment of the eLFCS versus the magnetometers show that misalignment causes a deviation between measurement and

simulation that also increases to first-order approximation linearly with the applied field strength by the eLFCS.
Both effects, induced field as well as misalignment, have thus the same imprint on the difference between measurement and simulation. Both effects cause a linear increase with increasing eLFCS field strength.

One approach to disentangle the imprints of misalignment and induced magnetization would be to compare two field settings, that are expected to produce the same field strength on one of the magnetometers but differ in field strength at the Main Spectrometer walls. However, the finding of these two settings depends on simulations and is therefore again vulnerable to inaccurate simulations or incorrect alignment in the simulation.
Another approach is only possible with several thousand measurement positions. By measuring the magnetic field at various distances to the eLFCS and the Main Spectrometer walls in several eLFCS configurations it could in principle be possible to disentangle the individual effects. In the analysis of the data, the alignment parameters of the magnets in the Kassiopeia model could be treated as free parameters in an optimization problem. Similarly, the positions and the magnetization of the steel rods would be treated as free fit parameters. However, the necessary measurement infrastructure does not exist in the Main Spectrometer hall.
With the available methods it is thus currently not possible to disentangle the effects of induced magnetization from inaccurate Kassiopeia simulations.

5.2.4. Conclusions for Neutrino Mass Measurements

The analyses presented in the sections above show that the Kassiopeia field simulations provide good estimations of the magnetic field in the analyzing plane with accuracy on the few μT level. The deviation between measurement and simulation for the z-component of the magnetic field as function of the applied eLFCS setting can be parameterized by a linear model, with the overall field strength as variable. The determined slope is $(6 \pm 2) \times 10^{-3}$, the offset $(2.0 \pm 0.3)\,\mu\mathrm{T}$. It is shown that the offset is significantly reduced when beamline magnets are switched off. The offset is therefore assumed to be mostly caused by either inaccurate magnetic field simulations of the beamline solenoids, or that the solenoids induce a magnetic field. The cause of the slope is likely related to inaccurate eLFCS simulations or to induced magnetization in the Main Spectrometer hall. A correction or extension of the field simulation and model is currently not possible, since the sources of the deviations are not yet identified.

The maximal deviation between measurement by the Bartington® magnetometers near the analyzing plane and simulation can be used as uncertainty estimation if the Kassiopeia simulation is used for neutrino mass analysis. In the case of a 2.7 G setting, the measured absolute field strength is at maximum 5.5 μT smaller than the expected total field, leading to a systematic uncertainty contribution on the neutrino mass measurement of $\Delta m^2_{\nu,\mathrm{sys}} = 9.9 \times 10^{-3}\,\mathrm{eV}^2$. This is slightly larger than the maximally allowed single contribution of $7.5 \times 10^{-3}\,\mathrm{eV}^2$. The uncertainty estimation for the 6 G setting conservatively yields $\Delta B_{\mathrm{ana}} = 6\,\mu\mathrm{T}$ and causes a systematic uncertainty contribution of $\Delta m^2_{\nu,\mathrm{sys}} = 2.6 \times 10^{-2}\,\mathrm{eV}^2$, surpassing the overall KATRIN systematic uncertainty budget.

The comparison of magnetic field simulation and measurement shows, that the simulation provides reasonable field estimations. It can thus be used for neutrino mass analysis at the cost of systematic uncertainty contributions that do not meet the final KATRIN sensitivity requirements. The simulated 6 G magnetic field in the analyzing plane is used for the analysis of KNM1 and KNM2. Although the systematic uncertainty caused by the inaccuracy of the simulated magnetic field in the analyzing plane is relatively large, the simulation is still acceptable for the analysis of KNM1 and KNM2 due to the vast magnitude of statistical uncertainty in these campaigns [Ake+21b; Ake+21a]. Nevertheless, to meet the final KATRIN sensitivity requirements we strongly recommend to measure the magnetic field in the analyzing plane inside the Main Spectrometer vessel. Possible tools for a model-dependent measurement inside the vessel are either the e-gun or the conversion electrons of krypton-83m, as discussed in the following sections.

5.3. Characterization with the Rear Section E-Gun

The Rear Section e-gun is implemented in the KATRIN setup for systematic investigations, such as column density measurements (see section 7.3.1), but also for high-precision measurements of the electric retardation and magnetic field in the analyzing plane. A brief summary of the e-gun working principle and the theoretical description of the e-gun transmission function is given in the following sections. Afterwards, a method to measure magnetic fields in the analyzing plane is presented. In the final part of this section, detailed analyses of measurements in the 6 G and 2.7 G setting are performed to characterize the retarding potential in the analyzing plane.

5.3.1. E-Gun Working Principle and Model

As basis for the following sections, it is necessary to firstly derive the e-gun working principle and the kinetic energy of the produced electrons. This is done based on the work by L. Schimpf [Sch21] and R. Sack [Sac20]. Subsequently, the e-gun transmission model as implemented in Kasper is introduced.

E-Gun Working Principle

The working principle of the e-gun is schematically visualized in figure 5.8. The central element of the e-gun setup is a plate capacitor, made of stainless steel. An optical fibre with a goal-coated end produces the photoelectrons. The emission electrode is formed by the back plate of the capacitor, in which the optical fiber is embedded. The back plate is set to a negative potential and thereby defines the starting potential of the photoelectrons. The front plate of the capacitor is set to 4 kV more positive potential, causing a collimation of the electrons' pitch angles to a narrow angular distribution. The collimated electrons leave the capacitor through a hole in the front plate towards the post-acceleration system. The post-acceleration system consists of three cylinder electrodes, which are connected via voltage dividers to the front plate potential. The design of the post-acceleration system is optimized

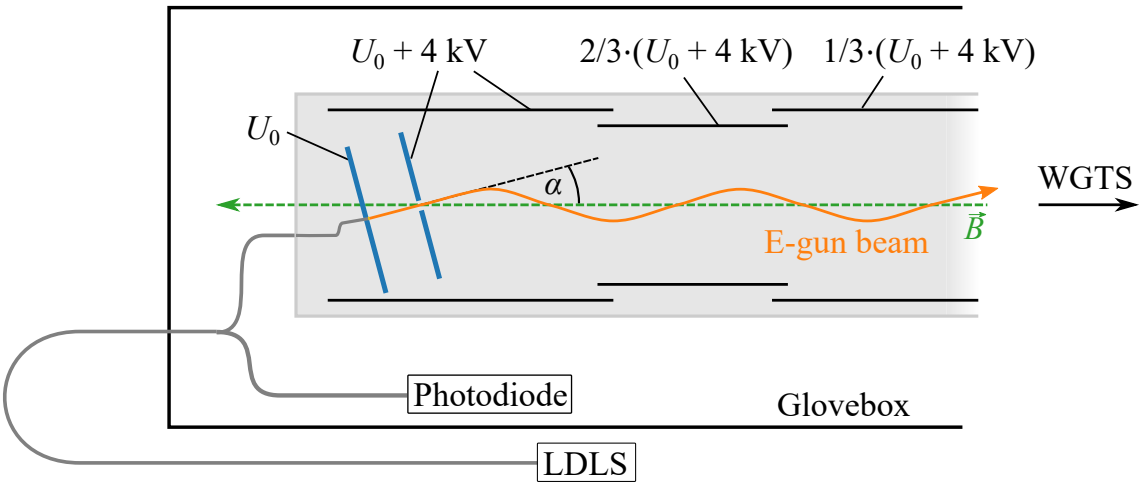

Figure 5.8.: **Sketch of the experimental e-gun setup.** The light produced by the LDLS is guided via optical fibres towards a photodiode to monitor the light intensity and towards the back plate of the e-gun capacitor (drawn in blue) inside the beamline. The gold-coated end of the optical fibre is embedded in the back plate of the e-gun capacitor that is set to a negative voltage U_0. The emerging electrons (orange) are accelerated by a 4 kV potential difference towards a hole in the front plate and afterwards magnetically guided to the WGTS. The post-acceleration system (black) produces an homogeneous electric field inside the setup. The e-gun capacitor can be tilted by angle α with a stepper motor to set the mean pitch angle of the e-gun electrons.

to feature good electric field homogeneity to ensure keeping the collimated state and simultaneously enable adiabatic acceleration of the electron beam towards the WGTS. The e-gun plate capacitor can be tilted by up to $\pm 15^\circ$ around an axis at the front plate with a stepper motor, allowing to adjust the mean pitch angle of the e-gun electrons with respect to the magnetic field lines. [Sch21] In the zero-angle setting, the electric field in the plate capacitor is parallel to the magnetic field lines. This setting is the default configuration for the measurements described below. Measurements with non-vanishing plate angle allow us for example to determine the magnetic fields in the analyzing plane (see section 5.3.2). For a non-zero plate angle, the electric field in the capacitor is not parallel to the magnetic field lines therefore a worse collimation is expected, resulting in a wider angular distribution of the e-gun electrons [Beh21]. The tilting range of the e-gun of $\pm 15^\circ$ allows probing the full pitch angle space in KATRIN up to more than 90° in the PCH [Sch21].
The primary voltage source of the e-gun high-voltage system is the Main Spectrometer vessel [Sch21]. The advantage of this connection is that no high-voltage differences between vessel and e-gun potential exists and thus the surplus energy of the electron beam in the Main Spectrometer is independent of vessel voltage fluctuations or drifts. The starting energy E_s relative to the grounded beam tube is thus approximately given by the vessel voltage U_v of the Main Spectrometer and a tunable offset U_{em} to [Sac20; Sch21]

$$E_s = q(U_v + U_{em}).$$

As shown in section 5.1.1, the retarding voltage U_{ret} of the Main Spectrometer is

given by the vessel voltage U_v, the inner electrode offset U_ie, and the potential depression U_pd to

$$U_\mathrm{ret} = U_\mathrm{v} + U_\mathrm{ie} + U_\mathrm{pd}.$$

The surplus energy for e-gun electrons is therefore approximately given by the difference of the starting energy E_s and the retarding voltage U_ret of the Main Spectrometer. As the vessel voltage is distributed to the back plate, the surplus energy is defined mostly by the difference of inner electrode voltage offset U_ie and emission electrode voltage U_em. The emission electrode voltage is limited by the power supply unit to $|U_\mathrm{em}| \leq 500\,\mathrm{V}$. Taking into account the inner electrode offset of $U_\mathrm{ie} = -200\,\mathrm{V}$ in nominal configuration, the maximal possible surplus energy of the e-gun beam is approximately 300 eV in the Main Spectrometer. The voltage stability of the e-gun setup is shown to be better than 10 mV. [Sac20; Sch21]
Besides the difference of inner electrode offset and emission electrode voltage, the surplus energy depends on three further effects each one with few eV size. The potential depression U_pd causes a positive offset on the retarding voltage of the Main Spectrometer, that is on the order of 1.96 eV at the center of the analyzing plane (see figure 5.1). Additionally, the starting potential of the e-gun electron depends on a work function, introduced by the golden photocathode. The e-gun work function $\Phi_\text{e-gun}$ can be thought of as the minimum energy required to move an electron from inside the metal to the vacuum. R. Sack measured this value to $\Phi_\text{e-gun} = (4.43 \pm 0.01)\,\mathrm{eV}$, but it should be noted that it can change with varying environmental parameters, especially changing vacuum conditions [Sac20]. Similar to the e-gun work function, the work function of the Main Spectrometer surface causes a modification of the retarding potential and was estimated to $\Phi_\mathrm{ms} = 3.87\,\mathrm{eV}$ in 2016 [Beh16; Beh21]. The estimated value depends on potential simulations in the Main Spectrometer, its absolute value cannot be measured model-independently [Beh21]. Additionally, the work function has a time dependence of few hundred meV, as it varies due to surface- and vacuum-changing processes, for example out-baking of the Main Spectrometer [Beh16; Beh21]. The absolute work function of the Main Spectrometer is currently not known precisely, but it is estimated to be on the order of $\Phi_\mathrm{ms} \approx 4\,\mathrm{eV}$ [Beh21]. Simulations indicate that the work function of the Main Spectrometer causes a constant potential offset for all positions in the analyzing plane on the sensitivity limit of the e-gun measurement [Beh21]. The calculated radial variations are on the order of few hundred µeV [Beh21]. Summarizing all these effects, the surplus energy of the e-gun electron beam relative to the Main Spectrometer is [Sch21]

$$E_\mathrm{surplus} = q\left(U_\mathrm{em} - U_\mathrm{ie} - U_\mathrm{pd}\right) + \Phi_\text{e-gun} - \Phi_\mathrm{ms}. \tag{5.2}$$

During measurements with the e-gun, we obtain a readback value of the emission electrode voltage U_em and of the inner electrode offset U_ie. The remaining terms in equation 5.2 are not known precisely (work function of the Main Spectrometer), depend on external measurements (e-gun work function), or can only be accessed in simulations (potential depression, work function of Main Spectrometer). These three terms are therefore summarized in the so-called potential edge term in the following

$$\Phi_\mathrm{pe} = -qU_\mathrm{pd} + \Phi_\text{e-gun} - \Phi_\mathrm{ms}. \tag{5.3}$$

The potential edge is different for individual positions in the analyzing plane due to the spatial dependence of the potential depression.

E-Gun Transmission Function

The transmission function of an ideal e-gun in the Main Spectrometer would be a step function. The term "perfect e-gun" in this context indicates an e-gun that only emits mono-energetic and mono-angular electrons. However, the KATRIN e-gun has several characteristics, that cause a deviation of this step-like behavior. A model describing the realistic e-gun transmission function was thoroughly developed in several works. In the following, a summary of the model for the transmission function of the KATRIN e-gun is given, based on references [Erh16; Beh16; Beh+17].
A transmission function measurement with the e-gun in KATRIN at the FPD comprises e-gun properties, such as the electron's starting energy, as well as MAC-E filter properties, for example the electromagnetic fields in the analyzing plane. In section 3.1 the transmission function for the KATRIN Main Spectrometer is derived for an angular isotropic source. However, the e-gun is not an angular isotropic source, the angular distribution $\omega(\theta)$ of emitted electrons by the e-gun is more Gaussian shaped. Additionally, broadening from the photoelectric effect occurs, leading to an initial kinetic energy distribution $\eta(E)$ of the electrons. Taking these properties into account, we can derive the theoretical description for the measured transmission function T as function of the electron starting potential E and the electric retardation U_{ret} in the analyzing plane as

$$T\left(E, U_{\mathrm{ret}}\right) = A_{\text{e-gun}} \cdot \int_{E}^{\infty} \eta(E') \int_{0}^{\theta_{\max}\left(E', U_{\mathrm{ret}}\right)} \omega(\theta) \mathrm{d}\theta \mathrm{d}E' + A_{\mathrm{Bkg}}, \tag{5.4}$$

with $A_{\text{e-gun}}$ being the total electron rate emitted by the e-gun, and A_{Bkg} being a constant background rate. The term $\theta_{\max}$ denotes the largest pitch angle that can surpass the retarding potential of the Main Spectrometer for given electron energy and retarding potential (see equation 3.7). The analytical description $T\left(E, U_{\mathrm{ret}}\right)$ summarizes the relevant KATRIN principles for e-gun electrons, for example the pitch angle transformation due to magnetic-adiabatic collimation. Furthermore, it allows us to determine $\eta(E)$ and $\omega(\theta)$ from transmission function measurements with the e-gun, if we have an empirical model for these distributions. [Erh16; Beh16; Beh+17]

The single electron is emitted with individual surplus energy from the e-gun photocathode, that is defined by its individual binding energy in the conduction band of the metallic cathode [Sch21]. The resulting initial kinetic energy distribution $\eta(E)$ for all emitted electrons can be described by a generalized normal distribution

$$\eta(E) = \frac{1}{\sqrt{2\pi}} \cdot \begin{cases} \frac{1}{\alpha_E} \cdot \exp\left(-\frac{1}{2} \frac{\left(E-\hat{E}\right)^2}{\alpha_E^2}\right), & \text{if } \kappa = 0 \\ \frac{1}{\alpha_E - \kappa(E-\hat{E})} \cdot \exp\left(-\frac{1}{2\kappa^2} \ln\left(1 - \kappa \frac{E-\hat{E}}{\alpha_E}\right)^2\right), & \text{if } \kappa \neq 0 \end{cases}$$

with the mean energy $\hat{E}$, energy width α_E and skewness κ. The energy distribution is a symmetric normal distribution for $\kappa = 0$. It is evaluated for the analysis of transmission function measurements in the range $E = [0,\ \infty)$. [Beh+17]
The angular distribution $\omega(\theta)$ describes the frequency of e-gun electrons emitted with certain pitch angle relative to the magnetic field. The model describes this

distribution as the sum of two normal distributions

$$\omega(\theta) = \frac{1}{\sqrt{2\pi\sigma_\theta^2}} \left(\exp\left(-\frac{\left(\theta - \hat{\theta}\right)^2}{2\sigma_\theta^2} \right) + \exp\left(-\frac{\left(\theta + \hat{\theta}\right)^2}{2\sigma_\theta^2} \right) \right), \tag{5.5}$$

with mean pitch angle $\hat{\theta}$ and angular spread σ_θ. The sum of the two normal distribution accounts for the deformation in the case of $\hat{\theta} < \sigma_\theta$, since the pitch angle is only defined for $\theta > 0$. [Beh+17]

The model of the e-gun transmission function is implemented in the post-analysis framework Peaberry [Beh16]. Each e-gun transmission function is in total described by ten parameters. Three parameters describe the initial kinetic energy distribution, two parameters characterize the angular distribution. Two further parameters are necessary to describe the magnetic field configuration in KATRIN to include the MAC-E filter properties. The total e-gun electron rate $A_{\text{e-gun}}$ is a free parameter, as well as the background rate A_{bg}. The remaining parameter is the potential edge Φ_{pe}, as defined in equation 5.3.
The individual imprints of the e-gun angular and energy distribution on the e-gun transmission function are shown in figure 5.9 as a function of the surplus energy of the e-gun beam. For simplicity, the e-gun work function is set equal to the Main Spectrometer work function in this example, the potential edge is thus located at $\Phi_{\text{pe}} = 0\,\text{eV}$ in this representation. The plots a.1) and a.2) in figure 5.9 illustrate the impact of three angular distributions for a vanishing initial kinetic energy of the e-gun electrons after emission. Angular distributions with mean pitch angle $\hat{\theta} = 0°$ affect the transmission function as a smoothing of the upper edge of the step-shaped transmission function for the ideal e-gun. A non-vanishing mean pitch angle results in a shift of the whole transmission function above the potential edge. Both effects are caused by the finite energy resolution of the Main Spectrometer since electrons with larger pitch angles are not analyzed with respect to their full kinetic energy. A non-vanishing angular distribution of the e-gun electrons consequently affects the transmission function above the potential edge, in contrast to non-vanishing initial kinetic energy distribution. The initial kinetic energy distribution influences the area below the potential edge, as shown in the graphs b.1) and b.2) of figure 5.9. For these exemplary calculations, we set the e-gun angular distribution to only produce electrons with pitch angle $\hat{\theta} = 0°$. Consequently, the finite energy resolution of the Main Spectrometer does not affect the transmission function measurement. A non-vanishing e-gun angular distribution produces electrons with larger kinetic energy in the Main Spectrometer than the expectation from the starting potential of the e-gun back plate. The electrons therefore can overcome the applied electric retardation at lower starting potentials than expected, consequently the area below the potential edge is affected in the scenario of non-vanishing initial energy distribution. The plot c) of figure 5.9 presents an e-gun transmission function if angular and initial energy distribution are both not vanishing, as it is the case for the KATRIN e-gun. It is not possible to discriminate by eye between effects of the energy and angular distribution, thus also the potential edge is difficult to estimate by eye.

To infer a robust estimate on the potential edge, it is consequently necessary to employ the model summarized in equation 5.4 to describe all relevant effects of the e-gun and the experimental KATRIN setup. However, using the model to estimate

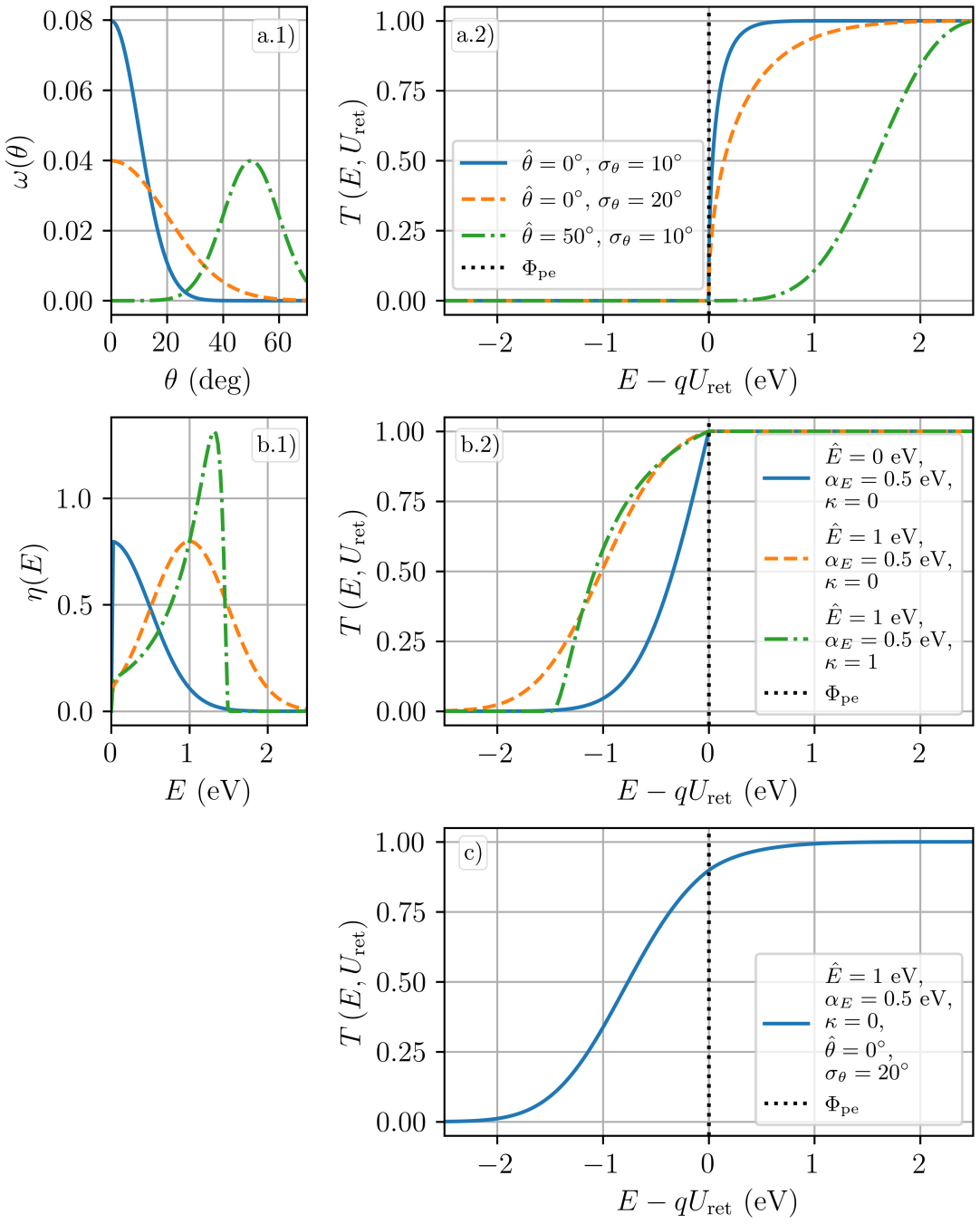

Figure 5.9.: **Calculated e-gun transmission functions $T(E, U_{\mathrm{ret}})$ over the surplus energy $E - qU_{\mathrm{ret}}$ of the e-gun beam in the Main Spectrometer.** a.1) Non-vanishing e-gun angular distributions $\omega(\theta)$. a.2) Effect of non-vanishing angular distribution on transmission function, calculated with Peaberry. b.1) Non-vanishing starting energy distributions $\eta(E)$ of the e-gun electrons, b.2) impact of these distributions on the e-gun transmission function. c) Combined effect of non-vanishing angular and starting energy distribution on the transmission function. The potential edge Φ_{pe} is fixed to zero for all calculations (dotted vertical line).

the ten free transmission parameters from a single transmission function measurement leads to ambiguous results, since the parameters show strong correlations to each other. One opportunity to break these correlations is to combine several transmission function measurements, each with slightly different properties (see section 5.3.3).

5.3.2. Magnetic Field Measurements

The e-gun allows one to determine the magnetic field strength of the analyzing plane in the Main Spectrometer, as described in reference [Erh16]. The e-gun key feature for magnetic field measurements in the analyzing plane is the possibility to set the mean pitch angle of the electron beam relative to the magnetic field.
The Main Spectrometer as MAC-E filter analyzes only the electron energy component parallel to the magnetic field lines $E_\parallel$ in the analyzing plane. According to section 3.1.1, this longitudinal energy component can be written as

$$\begin{aligned} E_\parallel &= E - E_\perp \\ &= E - E\sin^2\theta, \end{aligned} \tag{5.6}$$

with θ being the pitch angle of the electron in the cyclotron motion. Assuming magnetic-adiabatic transformation, the transformation of pitch angles due to different magnetic field strengths is

$$\frac{\sin^2\theta_0}{\sin^2\theta_1} = \frac{B_0}{B_1}. \tag{5.7}$$

Combining equation 5.6 and 5.7, we can derive the longitudinal energy component of an electron in the analyzing plane to

$$\begin{aligned} E_\parallel &= E\left(1 - \sin^2\theta_{\text{ana}}\right) \\ &= E\left(1 - \sin^2\theta_{\text{src}} \cdot \frac{B_{\text{ana}}}{B_{\text{src}}}\right) \end{aligned} \tag{5.8}$$

where θ_{src} denotes the electron's pitch angle in the source. The principle of magnetic field measurements in the analyzing plane with the e-gun becomes visible by comparing the longitudinal energy component for two different mean pitch angles θ_0 and θ_1 in the source. Exploiting equation 5.8, the difference δE in necessary energy for transmission of e-gun electrons starting with pitch angle θ_0 and θ_1 yields

$$\begin{aligned} \delta E &= E_{\parallel,0} - E_{\parallel,1} \\ &= E \cdot \frac{B_{\text{ana}}}{B_{\text{src}}}\left(\sin^2\theta_1 - \sin^2\theta_0\right). \end{aligned} \tag{5.9}$$

Measuring the shift of necessary electron energy for transmission at two different angles allows us to infer the magnetic field strength in the analyzing plane. [Erh16] However, it must be noted that equation 5.9 is only valid for mono-energetic and mono-angular electron beams. For magnetic field measurements with the KATRIN e-gun, the relation needs to be adapted for non-zero energy and angular electron beams. This is numerically included in the Peaberry model. For simplified discussions in the following, we stick to the relation as described in equation 5.9.

The electron energy, source magnetic field, and the two pitch angles as nuisance parameters in equation 5.9 must be determined beforehand to obtain precise and accurate results on the magnetic field in the analyzing plane. The energy shift δE is given by the shift between the two measured transmission functions and is thus the experimental observable. The electron starting energy E is mostly defined by the e-gun back plate potential. The two pitch angles θ_0 and θ_1 are defined in the context of the source magnetic field in equation 5.9. However, due to magnetic-adiabatic collimation we can use any magnetic field as reference as long as the pitch angles are transformed correctly, as shown in equation 5.7. We therefore propose to use the PCH magnetic field B_{pch} as currently best-known magnetic field (see section 4.1.1). The knowledge on the mean pitch angles in the measurements is crucial for the determination of the magnetic field in the analyzing plane with the e-gun. Deviations between assumption and reality result in a biased measured magnetic field strength. The different pitch angles, necessary for this type of measurement, are mechanically produced at the e-gun by tilting the e-gun capacitor with the stepper motor. The translation of motor step positions to pitch angles is not trivial. J. Behrens proposes a translation model from motor step positions to pitch angles in reference [Beh16], however, reproducibility problems of the motor positions (see reference [Sac20]) prevent the model's application. Without the possibility to accurately determine the pitch angle of the e-gun electrons, an accurate and precise measurement of the magnetic field strength in the analyzing plane with the e-gun is not possible for the nominal analyzing plane.
Nevertheless, by using the nominal analyzing plane as reference, it is still possible to perform measurements of the magnetic field strength with the e-gun. This measurement principle is demonstrated for the shifted analyzing plane in section 6.2.2. Additionally, there are plans to exchange the e-gun in the future. The new e-gun currently performs commissioning measurements at the Monitor Spectrometer and seems to provide reproducible motor positions (see reference [Sch23]).

5.3.3. Retarding Potential Measurements

In this work, we will show that transmission function measurements with the e-gun enable potential edge determinations that allow us to cross-check the simulated electric retarding potential. However, a test of the absolute applied electric retardation inside the Main Spectrometer is not possible due to the not precisely known work function of the Main Spectrometer. Nevertheless, a cross-check of the shape of the simulated potential depression is possible with the experimental results.
The measurement procedure and data pre-processing for potential edge determination with the e-gun is described in the following paragraphs. Subsequently, the analysis chain and experimental results are presented by example of measurements with a 6 G and a 2.7 G setting in the analyzing plane of the Main Spectrometer. The eLFCS currents for these magnetic field configurations are given in table B.2.

Measurement Procedure and Data Pre-Processing

Transmission function measurements using the e-gun are performed with evacuated WGTS since otherwise inelastic scattering processes of the e-gun electron beam with

tritium reduce the electron rate at the FPD. The measurements are performed with mean electron energies of 18.6 keV and thus above the tritium endpoint to avoid energy-dependent background from residual tritium in the WGTS, especially from the rear wall.
An incorrect assumption on the mean pitch angle in the analysis causes a bias on the determined potential edge since the mean pitch angle can shift the transmission function (see equation 5.9). The method proposed by R. Sack allows to accurately set the mean zero pitch angle with 0.5° uncertainty [Sac20] despite the reproducibility problems of the stepper motor. We therefore measure the e-gun transmission function at mean zero pitch angle.
We decide to use the LDLS as light source for transmission function measurements, although it produces a significantly smaller e-gun rate of approximately 1.5 kcps compared to the pulsed laser with more than 5 kcps. The reason for using the LDLS is two-fold. Firstly, the LDLS features a better rate stability [Sac20], that is important as one transmission function measurement takes around 40 minutes. Secondly, the pile-up correction for the pulsed laser is not fully understood [Sch21] which leads to systematic uncertainties on the determined potential edge.
The rear WGTS dipole magnets can shift the the e-gun electron beam to different FPD pixels. This enables the measurement of the potential edge at several FPD pixels and thus at several positions in the analyzing plane. The exact position of the 0.12 mm-thick electron beam [Sac20] at the individual FPD pixel is not known for the measurements presented below.
The Main Spectrometer retarding voltage is kept constant at $U_\mathrm{v} = -18.4\,\mathrm{kV}$ and $U_\mathrm{ie} = -0.2\,\mathrm{kV}$ during transmission function measurements with the e-gun. The e-gun electron energy, and thus the beam surplus energy, is varied with the emission electrode voltage of the e-gun. The surplus energy of the e-gun beam is only varied in a narrow few eV range for transmission function measurements.

Using equation 5.2 and 5.3, we derive the surplus energy of the e-gun electron beam to be

$$E_\mathrm{surplus} = q\,(U_\mathrm{em} - U_\mathrm{ie}) + \Phi_\mathrm{pe} \tag{5.10}$$

in the analyzing plane. The potential edge Φ_pe is the parameter of interest in retarding potential measurements. As stated in equation 5.3, the potential edge comprises the sum of potential depression, e-gun work function, and work function of the Main Spectrometer. As the last one is not precisely known, it is not possible to make conclusions on the absolute value of the potential depression and to compare it to simulations. Consequently, the e-gun potential measurements cannot be used for absolute comparison. Instead, these measurements can be used as a cross-check of the potential shape by measuring the potential at several pixels.

The measured e-gun rates at the FPD have to be pre-processed and all possible sources of uncertainties have to be taken into account to obtain a robust estimate of the potential edges with accurately calculated uncertainties. The major uncertainties are given by the uncertainty on the electron surplus energy, the statistical uncertainty, uncertainties caused by drifts of the beam intensity, and FPD pile-up corrections. These contributions are discussed in detail in the following.
It is crucial to measure the difference between emission voltage and inner electrode voltage offset as this defines the surplus energy of the electron beam. The voltage of the emission electrode and inner electrode during measurement either be obtained

by high-precision and high-accuracy digital voltmeters or by the voltage readback of the power supplies. Of course, the values of the digital voltmeters are the method by choice. Unfortunately, they are not always available during the performed measurements, in that case the readback of the power supply is used. We take the same voltage measurement devices if measurements at various pixels are combined or compared. The uncertainty estimation for the difference $U_{\mathrm{em}} - U_{\mathrm{ie}}$ comprises in theory two contributions. The first contribution is the absolute calibration of the used readback voltages. According to equation 5.10, incorrect calibrations give a bias on the determined potential edge. As discussed above, e-gun potential measurements in the analyzing plane are used to cross-check the potential shape, and are not suitable to determine the absolute retarding potential. As incorrect absolute calibrations of the voltmeter influence the measurements at different pixels in the same way, and bias thus the determined potential edge the same manner, we do not have to consider these uncertainties in the analysis. The second source of uncertainty is the stability of the emission electrode voltage of the e-gun and the stability of the inner electrode system in the Main Spectrometer. Fluctuations of both voltage readbacks at constant set point are taken into account in the analysis, as voltage fluctuations influence the measured rates at the individual scan steps. For the sake of readability, we change the notation for the following paragraphs. The emission electrode voltage of the e-gun defines the energy of the e-gun electron beam, therefore we will label the product of electron charge and emission electrode voltage as the electron energy E. The voltage offset of the central inner electrodes in the Main Spectrometer produces the retarding potential for the e-gun electron beam, and is therefore labeled as qU in the following.

The uncertainty on the measured rate would be given by Poissonian uncertainty estimation in case of an ideal photoelectron source. However, the KATRIN e-gun suffers from short- and long-term rate drifts, leading to increased uncertainties. We can correct to a certain level for these e-gun rate fluctuations in the analysis by normalizing the measured rates to the measured light intensity of the LDLS. Remaining rate fluctuations are quantified with a non-Poisson factor, which increases the uncertainty on the measured rate. The size of the non-Poisson factor was determined in dedicated measurements. The e-gun rate with the LDLS as light source is measured for 8 hours with evacuated WGTS at constant surplus energy in full transmission. The resulting rate distribution is described in one analysis by a Poisson density function, in another analysis by a Gauss function. In the absence of any rate drifts or fluctuations, we would expect that the widths of the Poisson and Gauss distributions are consistent. The experimental result yields that the width of the Gauss function is larger by 1 % compared to the width of the Poisson function, indicating rate fluctuations and drift. The resulting non-Poisson factor of 1.01 is therefore used in the following analyses as correction factor on the Poissonian uncertainty estimation.

The e-gun causes a rate of more than 1 kcps on one pixel in full transmission. This results in pile-up effects, which need to be corrected for. Based on a two-fold random coincidence model assuming incident electrons with Poissonian random time distribution, S. Enomoto develops a pile-up correction model [Eno19]. This pile-up correction model is applied in the data pre-processing. The relative uncertainty on the correction is quantified to 18 % [Eno19], and is rather small compared to the total statistical uncertainty.

Potential Measurement in 6 G Setting

We performed an e-gun potential measurement in mid-2019, during KNM1. At the time of the measurement, not all e-gun characteristics were as known as today, especially the reproducibility problem of the e-gun stepper motor to tilt the e-gun relative to the magnetic field lines was unknown. Additionally, a special ramping configuration of the rear WGTS dipole magnets triggered an interlock, causing the beamline valves to close. Therefore, we could only perform transmission function measurements at 14 FPD pixels.

The measurement and data pre-processing is performed as described above. As mentioned in section 5.3.1, it is not possible to extract robust information on the potential edge by fitting a single transmission function measurement due to strong correlations of the Peaberry parameters with each other. In an attempt to break these correlations, we describe the data of all 14 transmission function measurements with one multi-pixel model. The multi-pixel model comprises global parameters (same for all transmission function measurements) and local parameters (individual for a single measurement). The best-fit parameters are determined in a minimization of the negative likelihood function of the model to the measured data.
The initial energy distribution is a global feature of the e-gun and therefore influences all transmission function measurements at the various pixels the same way. We therefore treat the three parameters describing this distribution as global parameters.
The same holds in principle for the two parameters of the angular distribution. Unfortunately, the stepper motor is moved between measurements at the several pixels. Due to the reproducibility problems of the motor, it is consequently unclear whether the same mean pitch angle is set for all pixels. We therefore decide to treat the mean pitch angle as local fit parameter, that can vary for the individual transmission function measurements. Nevertheless, to avoid unrealistic large fluctuations of the mean pitch angle due to statistical fluctuations of the measured e-gun rate, we introduce a penalty term on all mean angles in the likelihood function with a conservative width of 5° and mean 0°. The angular width depends on the mean pitch angle due to the changing electromagnetic field configuration inside the plate capacitor, however, this dependence can be neglected in the region close to the zero pitch angle. Consequently, the width of the angular distribution of the e-gun beam is treated globally in the model.
Another global fit parameter in the model is a scaling factor to the PCH magnetic field to account for systematic uncertainties. The simulation of the PCH magnetic field is used as input parameter for the MAC-E filter setting. The systematic uncertainty on the PCH field simulation is estimated to 0.2 % at the time of the measurement [Ake+21b]. We introduce this systematic uncertainty with the pull-term method leading to one global fit parameter that is constrained by a penalty term in the likelihood.
The normalization of the e-gun rate as well as the background can be different for individual pixels and are therefore locally treated in the analysis.
The necessary information on the magnetic field in the analyzing plane is obtained from simulations. The simulations are accompanied by uncertainties on the order of 6 µT (see section 5.2.3). As the uncertainties cannot be interpreted as an unknown and common scaling factor to all pixels, it is necessary to treat the uncertainties

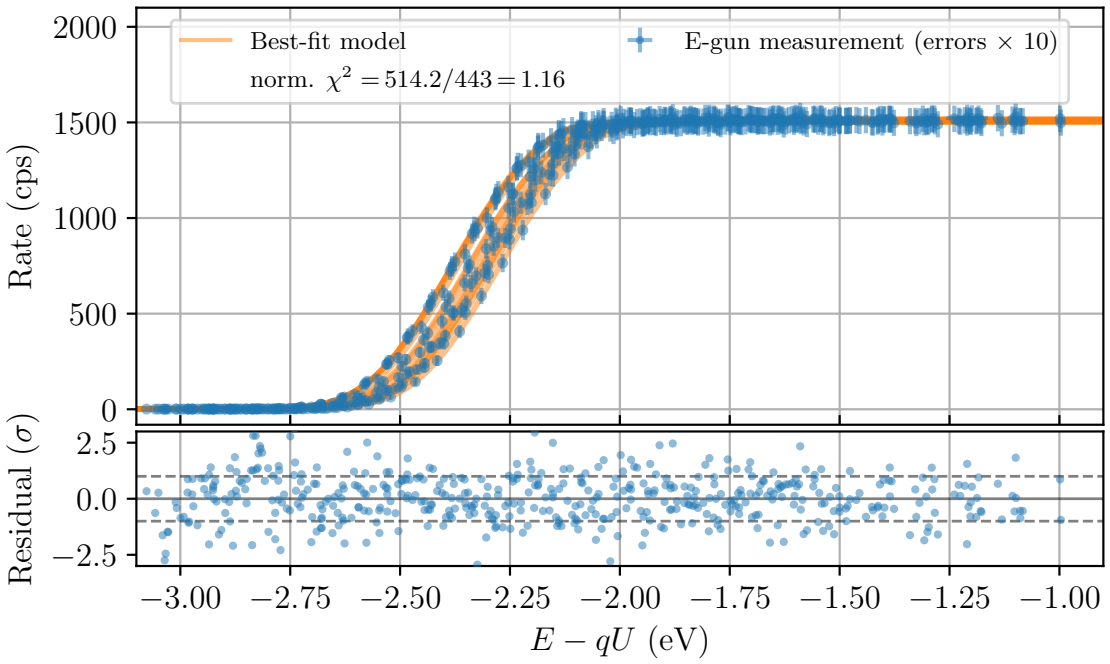

Figure 5.10.: **E-Gun transmission functions at 14 different FPD pixels in the 6 G setting to investigate the retarding potential in the analyzing plane of the Main Spectrometer.** The upper graph shows the measured e-gun rate in blue versus the surplus energy, as well as the best-fit model based on a multi-pixel analysis. The lower graph presents the fit residuals between measurement and best-fit model.

for each pixel individually, leading in the pull-term approach to additional local fit parameters for each pixel.
The parameter of interest in this analysis is of course the potential edge, which is also pixel-dependent and thus treated locally.

The 14 transmission function measurements comprise in total 518 scan steps at various electron surplus energies and at various FPD pixels. The number of free fit parameters is 75. The first minimization of the negative logarithmic likelihood function is performed with an algorithm using the Trust Region Reflective method as implemented in the LMFIT package [New+14]. For detailed correlation and uncertainty analysis, we use as a follow-up a Markov Chain Monte Carlo algorithm (MCMC) to sample from the likelihood probability distribution. The affine-invariant ensemble sampler emcee [For+13] is used for this part of the analysis due to its excellent performance. The walkers of the emcee sampler are initialized with the best-fit estimates from the Trust Region Reflective method and their uncertainties.
The measured e-gun rate and the best-fit model for the multi-pixel analysis of the 14 transmission function measurements is shown in figure 5.10. The normalized $\chi^2 = 1.16$ is reasonable, yet it indicates that the known uncertainties could slightly be underestimated or it indicates the existence of systematic uncertainties that are not considered in the analysis. A breakdown of the normalized χ^2 to the individual transmission function measurements dos not show any significant deviation from the expectation value 1.0 . The overall structure of the fit residuals looks fine, implying that the measured rate is well-described by the Peaberry model.

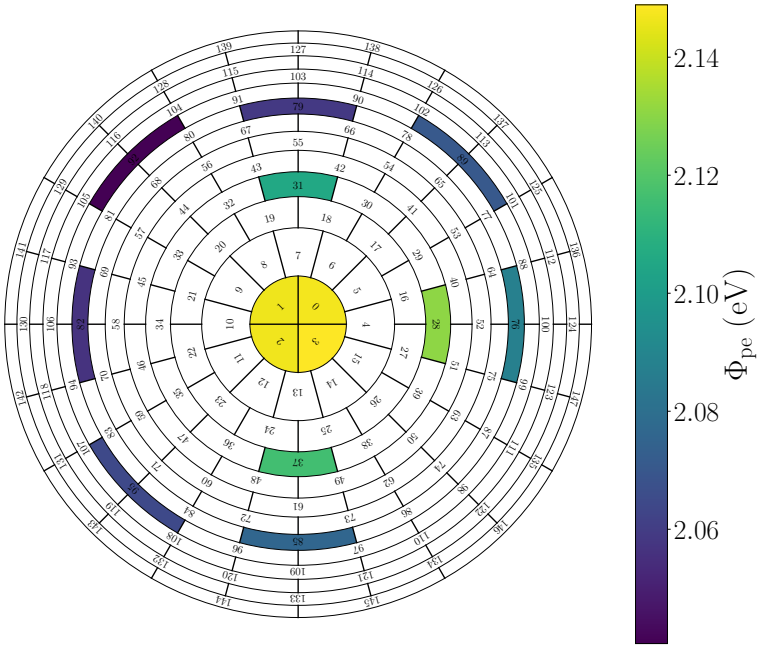

Figure 5.11.: **Measured potential edge Φ_{pe} by the e-gun for the 6 G setting in the FPD projection.** The uncertainty on the individual determined potential edge is 7 meV. The measured potential edge is by eye in good agreement with the expectation from simulation, it is maximal at the center and decreases towards larger radius.

The determined potential edges for all transmission function measurements are visualized in the FPD projection in figure 5.11. The uncertainty on an individual potential edge is on the order of 7 meV. The determined potential edge comprises the sum of potential depression, e-gun work function, and work function of the Main Spectrometer (see equation 5.3). As the latter two are approximately radially constant, we expect that the measured potential edge follows the potential depression. The potential depression simulation predicts the most positive values at the center of the analyzing plane and decreases towards larger radii (see section 5.1.1). This expectation on the shape is met by the e-gun measurement. A detailed comparison of the e-gun measurement to the simulation, and also to the analysis of $^{83\mathrm{m}}$Kr conversion line positions, is given in section 5.5.1.

The emcee sampler is used to investigate the correlations and uncertainties of the fit parameters. The distribution of sampled emcee steps near the best-fit result is shown in figure 5.12 for the fit parameters related to the central FPD pixel 1.
The two-dimensional sample plots indicate the correlations among the fit parameters. The approach with a multi-pixel model is mostly successful in breaking the correlations among the Peaberry parameters by splitting up the parameters in global and local parameter sets. Most parameters show only weak (absolute correlation coefficient below 0.3 [Rat09]) or moderate correlations (absolute correlation coefficient below 0.7 [Rat09]) to other fit parameters. The only correlation stronger than 0.7 is the correlation between the mean of the e-gun energy distribution $\hat{E}$ and the potential edge Φ_{pe} with correlation coefficient $\rho = -0.94$.
The histogram at the top of each column in figure 5.12 represents the projection of the sampler steps in one dimension and therefore allows us to estimate the cen-

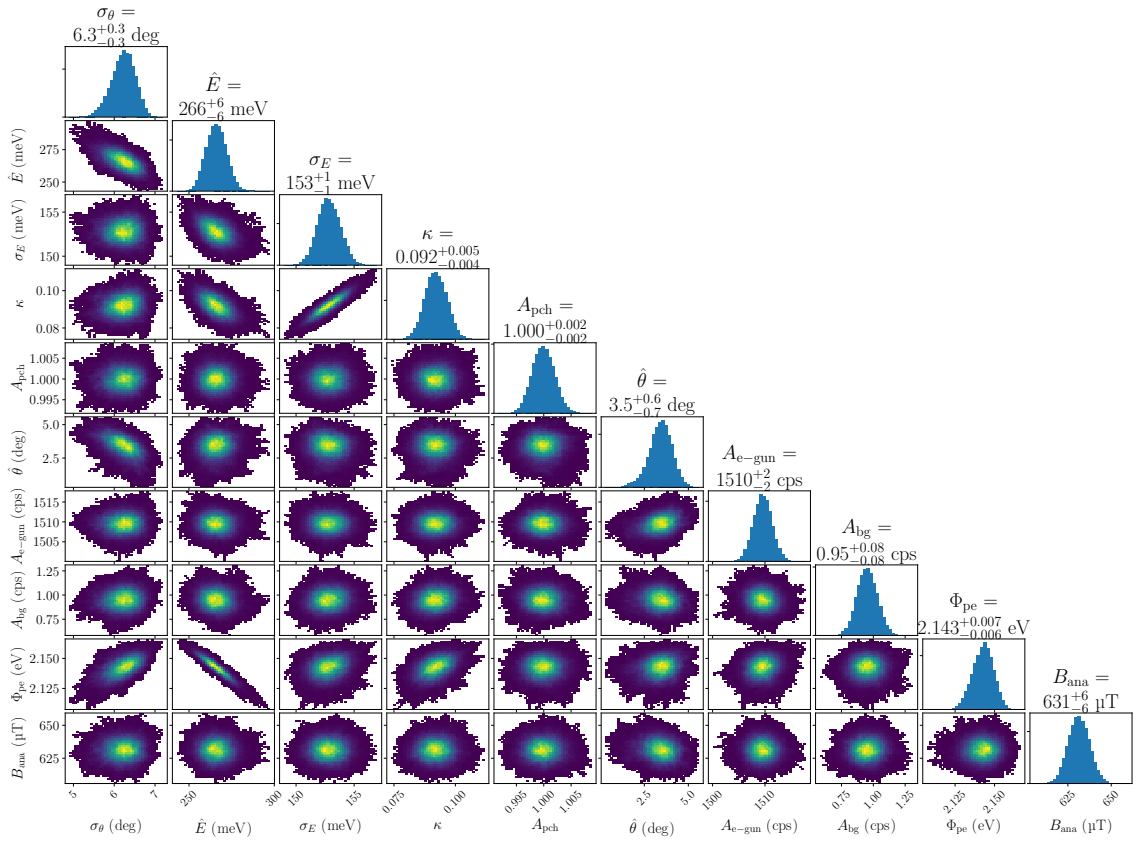

Figure 5.12.: **Distribution of six million emcee sampler steps close to the best-fit result of the e-gun potential edge analysis.** Shown are the parameter distributions related to the measurement at FPD pixel 1. The first five columns of the corner plot show the distribution of the global fit parameters in the analysis, namely the angular width, the three parameters of the starting energy distribution, and the normalization applied to the PCH magnetic field. The remaining four columns present the pixel-specific local fit parameters: the e-gun mean angle, the total e-gun electron rate, the background amplitude, the potential edge as parameter of interest, and the magnetic field in the analyzing plane.

tral value as well as the uncertainty on the fit parameter. The uncertainty on the potential edge as parameter of interest yields 7 meV at pixel 1 .

Besides the pure investigation of the potential in the analyzing plane, this analysis also enables a deeper understanding of the e-gun characteristics.
The angular distribution is an important parameter in e-gun column density measurements of the tritium gas in the WGTS, as outlined in section 7.3.1. The best-fit value for the angular width close to the zero pitch angle in the PCH field yields $\sigma_\theta = (6.3 \pm 0.3)^\circ$. This result is used as input for the column density measurements. The e-gun angular width is assumed to be constant over time.
The energy distribution describes the distribution of initial starting energy of the e-gun electrons. The best fit for the mean electron energy yields $\hat{E} = (266 \pm 7)$ meV, the width of the distribution is $\sigma_E = (153 \pm 1)$ meV. The energy skewness is close to zero, consequently the shape of the energy distribution is similar to a Gaussian probability distribution. The energy distribution depends on the electrons' binding

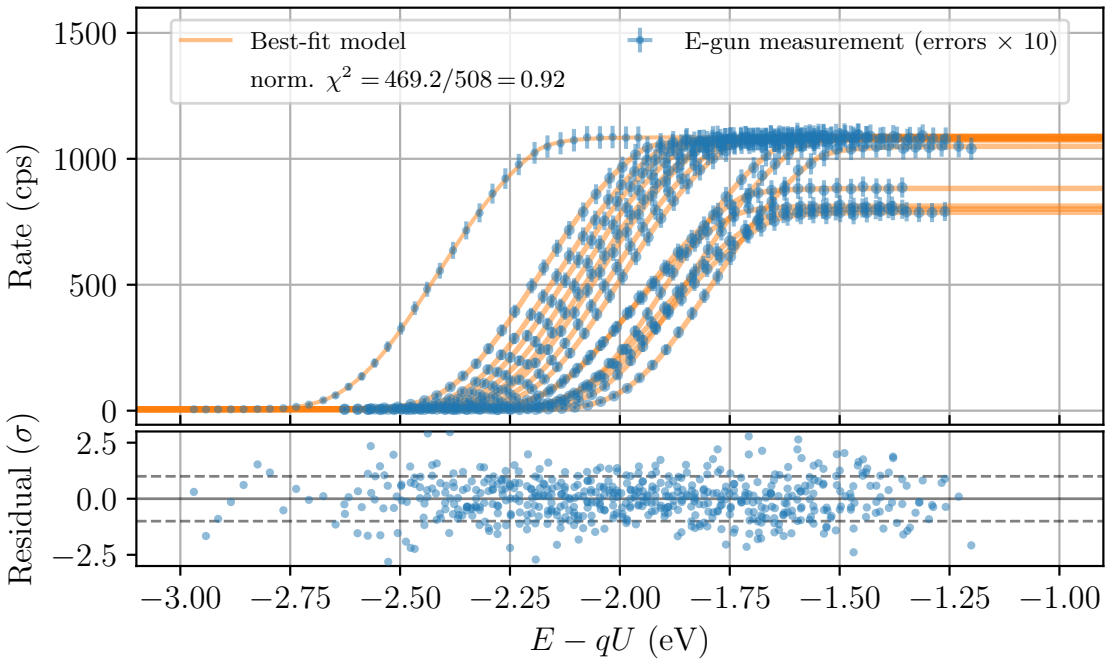

Figure 5.13.: **E-Gun transmission functions measured in the 2.7 G setting at 16 different FPD pixels.** In the upper graph, the measured e-gun rate is shown in blue over the surplus energy together with the multi-pixel best-fit model in orange. The fit residuals are shown in the lower graph. The amplitude of the measured transmission function decreases for measurements at larger surplus energies, this is related to a geometrical cut-off of the e-gun electron beam at pixels with large radius in the analyzing plane.

energy in the conduction band of the metallic cathode and the absolute value on the e-gun work function. As this can change due to changes of the experimental environment over time, a time-dependence of the starting energy distribution of the e-gun on long time scales is possible.
We cannot draw any conclusions on the magnetic field in the analyzing plane from e-gun measurements at only one angle, as shown by the fit result in figure 5.12. The best-fit value follows mostly the input from the pull-term. The width of the best-fit estimate for the magnetic field in the analyzing plane is exactly the same as the width of the pull-term, the fit thus does not gain additional information from data.

Potential Measurement in 2.7 G Setting

The preparation for KNM3 included an extensive commissioning phase. In that context, the retarding potential in the analyzing plane was measured in the 2.7 G setting. The 2.7 G setting is regularly used for commissioning measurements with ^{83m}Kr conversion electrons. The e-gun potential measurement enables a cross-check of certain effects appearing in the analysis of ^{83m}Kr conversion electrons. These measurements help to disentangle if unexpected ^{83m}Kr analysis results are caused by the electromagnetic field of the analyzing plane or by source effects (see also section 5.5.1).

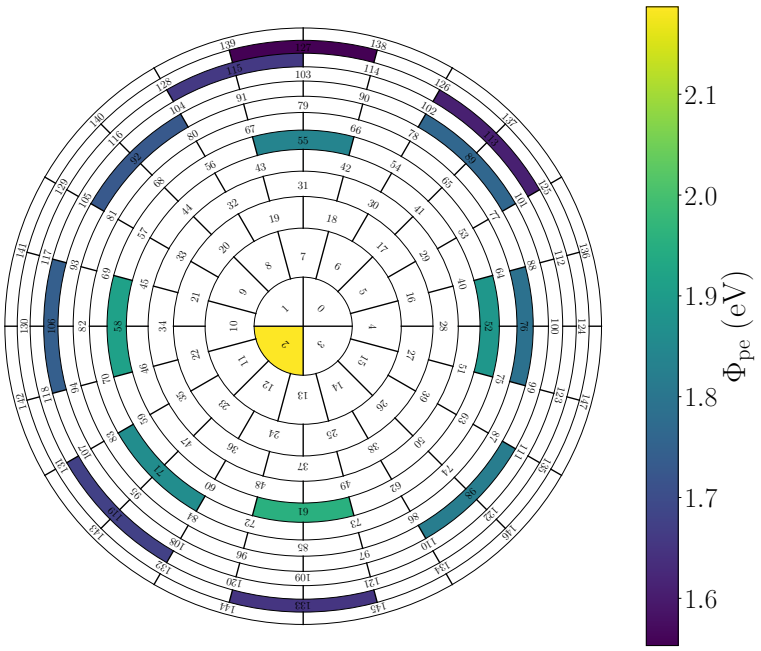

Figure 5.14.: **Analysis result of the potential edge Φ_{pe} measurement with the e-gun in the 2.7 G setting, visualized in the FPD projection.** The uncertainty on the individual determined potential edge is on the order of 3 meV. The determined potential edge is maximal at the center and decreases towards larger radius, as expected from electrostatic simulations.

In total 16 transmission functions with the e-gun at different FPD pixels are measured. The gained knowledge on the e-gun properties in the above-described KNM1 measurement permits an optimized execution of the KNM3 measurement, for example the e-gun plate angle is set to a mean pitch angle of zero degree and not moved throughout the whole measurement. A modification of the WGTS hardware enables the WGTS dipole magnets to steer the e-gun electron beam over the whole flux tube without triggering an interlock, allowing also transmission function measurements at the lower right quarter of the FPD.
The data pre-processing is performed as described in the sections above, as we again use the LDLS as light source and no major e-gun hardware modification is performed between KNM1 and KNM3. To break the ambiguity between the Peaberry model parameters for individual transmission function measurements, we again perform a multi-pixel analysis with global and local parameter sets. The major differences to the KNM1 analysis are the different input values from the simulation for the 2.7 G $^{83\mathrm{m}}$Kr setting and that the mean pitch angle of the e-gun is treated as a global parameter in the fit, since it remains unchanged during the measurement. The uncertainties on the used simulation input for the magnetic fields are again included via the pull-term method, the rate fluctuations of the e-gun are included via the non-Poisson factor.

The e-gun data and the best-fit model of the multi-pixel analysis for the 2.7 G potential measurement is shown in figure 5.13. The normalized $\chi^2 = 0.92$ of the best-fit result indicates good agreement between measured data and applied model. The fit residuals do not show any structure, emphasizing the good description of the e-gun

measurement by the model.
The uncertainty and the correlations among the fit parameters are investigated with the emcee sampler. Due to a modified measurement time distribution compared to the KNM1 measurement, the uncertainty on the measured e-gun potential edge is reduced to 3 meV. The measured potential edge positions for the individual pixels are shown in the FPD projection in figure 5.14. Similar to the KNM1 analysis, the potential edge parameter anti-correlates strongly with the e-gun energy distribution mean $\hat{E}$ with correlation coefficient $\rho = -0.8$. The overall correlation strength to other fit parameters is reduced in the KNM3 2.7 G analysis compared to the KNM1 6 G analysis, given by two reasons. Firstly, the measurement time is larger in the 2.7 G setting in KNM3, reducing the statistical uncertainty, which allows the fit to better disentangle the individual effects due to their shape impact on the transmission function. Secondly, the 2.7 G setting has a larger potential inhomogeneity in the analyzing plane compared to the 6 G setting due to its larger radial extent. The larger differences in potential edges between the pixels lead to a clearer separation of the global parameters of the energy distribution and the local parameters for the potential edges.
A comparison of the determined potential edges to simulations and ^{83m}Kr results takes place in section 5.5.1.

5.4. Characterization with Krypton-83m

Krypton-83m (^{83m}Kr) decays by γ emission or internal conversion into the stable ^{83}Kr. In case of internal conversion, free electrons are emitted. According to the subshell from which the electrons are emitted, they form several quasi mono-energetic conversion lines in the range of 7 keV to 32 keV. ^{83m}Kr features a short half-life of 1.8 hours. It is regularly used for characterizations of an experimental setup, for example in neutrino mass experiments (see for example reference [Wil+87]), high-energy physics (see for example reference [Dec+90c]), as well as in Dark Matter experiments (see for example reference [Kas+09]).

5.4.1. Krypton-83m in KATRIN

^{83m}Kr is an excellent tool to characterize the KATRIN setup. Its energy scale is comparable to the tritium endpoint. The short half-life combined with the stable daughter isotope allows us to perform measurements with ^{83m}Kr without any danger of long-term contamination. Based on the individual measurement goal, we can choose between several conversion lines that feature electron energy widths in the range from several eV to the few meV range [Vén+18b].
The KATRIN beamline can host three ^{83m}Kr sources in different places. Firstly, ^{83m}Kr can be injected in a gaseous state into the WGTS. Secondly, the CPS allows us to install a condensed source in the flux tube, and thirdly an implanted source can be used for measurements at the Monitor Spectrometer. We focus in the following on the gaseous ^{83m}Kr source due to its importance for the thesis at hand.
The basic idea of the gaseous ^{83m}Kr source is to inject ^{83m}Kr into the WGTS similar to tritium gas during neutrino mass measurements. Therefore, the parent radionuclide of ^{83m}Kr, rubidium-83 (^{83}Rb), is deposited in zeolite and stored in a dedicated

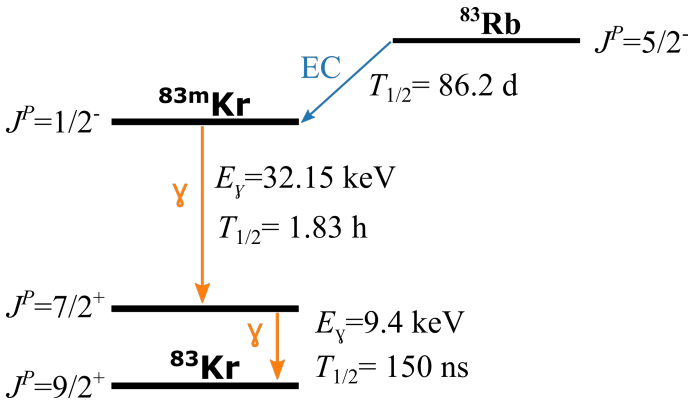

Figure 5.15.: **Schematic decay scheme of ^{83}Rb into the isomeric ^{83m}Kr and its subsequent decay into the stable ground state ^{83}Kr via an intermediate state.** The decay of ^{83}Rb takes place via electron capture (EC), the transition of ^{83m}Kr into ^{83}Kr via two γ transitions. The transition of interest for the following investigations is the 32 kev transition from $J^P = 1/2^-$ to $J^P = 7/2^+$. Values taken from [Vén+18b].

generator setup. ^{83}Rb decays with a half-life of 86.2 days and thus ensures continuous ^{83m}Kr supply for a measurement phase over several weeks. [Alt+20] A carrier gas transports the produced ^{83m}Kr into the WGTS, while ^{83}Rb is trapped inside the generator. The WGTS is operated at 80 K beam tube temperature during ^{83m}Kr measurements to avoid freeze-out of the gaseous ^{83m}Kr in the source pipes. As carrier gas of ^{83m}Kr to the beamline, we use a non-radioactive gas mixture consisting of hydrogen, methane, and air, that outgasses from the turbo molecular pumps in the WGTS [Mar20b]. The overall column density in this measurement configuration is estimated via a pressure sensor in the loop system to be on the order of 5 % nominal column density [Mar20b].

To understand how decay electrons from ^{83m}Kr can help to characterize electromagnetic fields in the analyzing plane of the Main Spectrometer, it is necessary to discuss the production mechanism of the decay electrons and the resulting shape of the spectrum.
^{83}Rb decays via electron capture to the isomeric ^{83m}Kr (see figure 5.15). Subsequently, it deexcitates to the 41 keV lower ground state via a cascade of two γ transitions. The decay energy splits up in a $E^{32}_{\text{exc}} \approx 32.15\,\text{keV}$ and a $E^{9.4}_{\text{exc}} \approx 9.4\,\text{keV}$ transition. The decay occurs either via direct γ emission or by internal conversion, in which the decay energy E^t_{exc} is transferred to a shell electron via Coulomb interaction. If the binding energy E^s_{b} of the electron in shell s is smaller than the transferred energy, the electron is emitted with a net kinetic energy of

$$E^{t,s}_{\text{kin}} = E^t_{\text{exc}} - E^s_{\text{b}}\,,$$

neglecting the recoil energies of γ and electron emission. Resulting from this behavior, line groups corresponding to the respective transition with energies according to the electrons' emission shell form the ^{83m}Kr decay spectrum. [Vén+18b; Mac21] The typical terminology is $\text{Shell}_{\text{subshell}}$-Transition, for example L_1-9.4.
The 9.4 keV transition is energetically significantly below the tritium endpoint, residual tritium contamination in the WGTS leads therefore to large background rates during the measurements. We thus focus on the 32 keV transition in the following

scope of the work. For better readability, we skip the transition in the line terminology from now on, for example the K-32 conversion line is simply denoted as K conversion line in the following.

The differential line shape of the conversion electrons is a Lorentzian energy distribution

$$L(E, A, E_0, \Gamma) = \frac{A}{\pi} \frac{\Gamma/2}{(E - E_0)^2 + \Gamma^2/4},$$

with normalization A, line position E_0 and line width Γ [Alt+20]. To account for distortion or inhomogeneities of the energy scale, for example the thermal Doppler broadening, the Lorentzian can be convolved with a Gaussian kernel G with width σ_g and centroid of zero [Alt+20; Mac21]

$$G(E, \sigma_\mathrm{g}) = \frac{1}{\sqrt{2\pi\sigma_\mathrm{g}^2}} e^{-\frac{E^2}{2\sigma_\mathrm{g}^2}}.$$

The resulting line shape is a so-called Voigt profile $V(E, A, E_0, \Gamma)$ [Alt+20]. The integral $^{83\mathrm{m}}$Kr spectrum of a single conversion line at the FPD is calculated as the convolution of the transmission function $T(E, qU)$ of the Main Spectrometer (see equation 3.9) with the Voigt profile, leading to [Alt+20]

$$I(qU, A, E_0, \Gamma) = \int_{qU}^{\infty} V(E, A, E_0, \Gamma) \cdot T(E, qU)\, \mathrm{d}E. \tag{5.11}$$

All following $^{83\mathrm{m}}$Kr analyses are based on the $^{83\mathrm{m}}$Kr implementation in the SSC software package as described in references [Mac16; Mac21]. The calculated differential and integral line shape of the K line is shown in figure 5.16. The input line parameters for the calculation are the line position $E_0 = 17\,821.2\,\mathrm{eV}$ and line width $\Gamma = 2.71\,\mathrm{eV}$, based on the values stated in reference [Vén+18b]. We choose the beam line magnets to be at nominal field, the magnetic field in the analyzing plane to $B_\mathrm{ana} = 200\,\mu\mathrm{T}$, and included the thermal Doppler broadening via the Gaussian kernel with width 41 meV (according to the formula stated in reference [Alt+20]) for the calculation of the integral spectrum.

In the thesis at hand, we use the properties of the $^{83\mathrm{m}}$Kr conversion electron lines in combination with the $^{83\mathrm{m}}$Kr SSC implementation to measure the retarding potential shape and the magnetic field in the analyzing plane.

5.4.2. Retarding Potential Measurements

Using the applied Main Spectrometer vessel voltage $qU = q(U_\mathrm{v} + U_\mathrm{ie})$ as energy scale, the measured $^{83\mathrm{m}}$Kr line position is

$$E_0 = E_\mathrm{kin}^{t,s} + (\Phi_\mathrm{src} + V_\mathrm{start} - \Phi_\mathrm{ms}) - qU_\mathrm{pd}, \tag{5.12}$$

with the source and Main Spectrometer work functions Φ_src and Φ_ms, the electron starting potential V_start in the source, and the potential depression qU_pd.
The density of non-radioactive carrier gas inside the WGTS beam tube during the

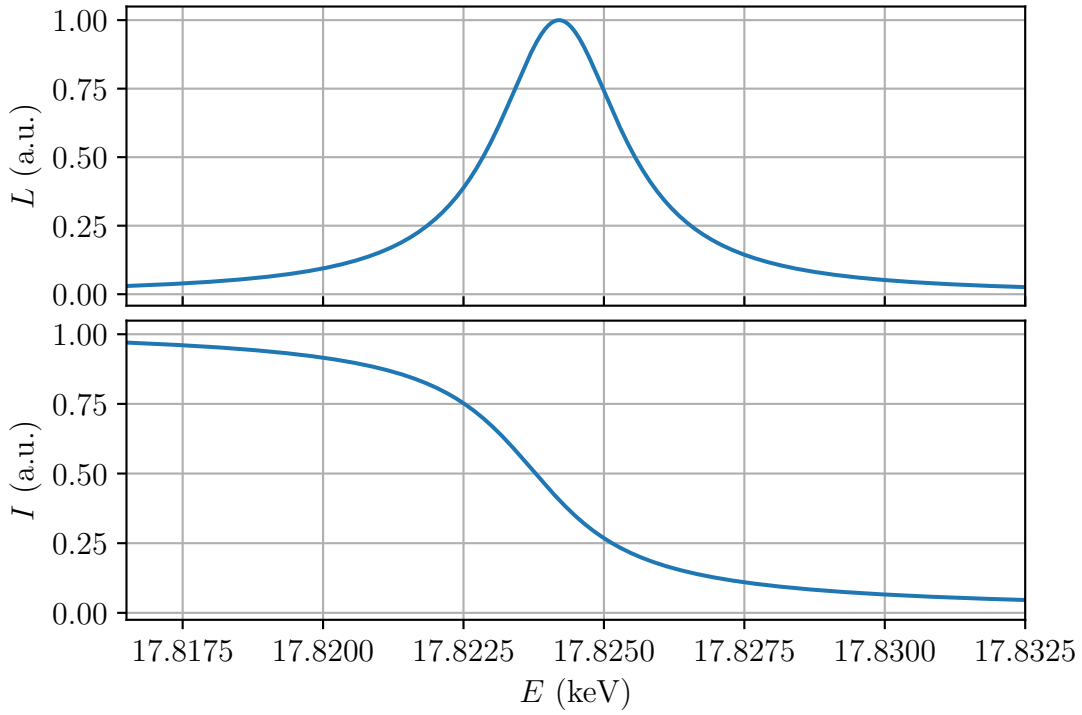

Figure 5.16.: **Differential ^{83m}Kr K line spectrum L (upper graph) and integral spectrum I (lower graph) over the electron energy E.** The calculation for the differential spectrum uses as line position $E_0 = 17.824\,\text{keV}$, and for the natural line width $\Gamma = 2.7\,\text{eV}$. For the calculation of the integral spectrum, a Gaussian energy smearing according to the expected thermal Doppler broadening and a magnetic field in the analyzing plane of 200 µT are assumed.

measurement was only 5 % of nominal tritium density in neutrino mass measurements. As the column density of the carrier gas was comparably small, also the overall ^{83m}Kr decay activity was small in the WGTS beam tube. The nominal configuration for neutrino mass measurements leads to a tritium decay activity on the order of 10^{11} Bq, during the ^{83m}Kr measurement the activity was limited to $(2.3 \pm 0.3) \times 10^5$ Bq [Mar20b]. By the choice of gas mixture and the limited activity in the beam tube, we reduced the risk of WGTS starting potential inhomogeneities due to plasma effects, as the amount of ions and electrons in the WGTS beam tube was rather small. We therefore expect, that the the electron starting potential is to first-order approximation radially constant.
The work function of the Main Spectrometer has the same impact for all positions in the analyzing plane on the sensitivity level that is reached with ^{83m}Kr measurements (see section 5.3.1). Similarly, we also expect that the impact of the source work function on the potential inside the WGTS is homogeneous for all positions on the given sensitivity level.
The absolute values of both work functions at the time of the measurements as well as the electron starting potential are not precisely known. Similar to the e-gun potential measurements, ^{83m}Kr measurements can consequently only provide a cross-check of the shape of the retarding potential in the analyzing plane. A determination

of the absolute retarding potential is thus not possible with ^{83m}Kr measurements. We choose to use the ^{83m}Kr K conversion line for retarding potential measurements, as it features strong intensity and therefore enables a pixel-wise analysis. Additionally, it is located only 750 eV below the tritium endpoint which is obviously the energy range of interest. A measurement of the magnetic field strength in the analyzing plane is not trivially possible with K line decay electrons, as the line width of $\Gamma \approx 2.7$ eV is similar to the energy resolution of the Main Spectrometer of 1 eV or larger. Without exact knowledge on the line width, we cannot draw conclusions on the magnetic field strength. As the line width as measured at the FPD depends on several experimental properties that are not precisely known for the WGTS conditions, we cannot just use the literature value as stated for example in reference [Vén+18b] as input for the analysis.

The retarding potential was varied in the range from 17819 eV to 17850 eV for the retarding potential measurement in the analyzing plane with the K line. The scan steps near the line position were 0.5 eV apart. Further away from the line position, the distance increased up to 1 eV. Additionally, one scan step with 10 eV distance to the next step was added at larger retarding potential for energy-dependent background investigations (see also figure 5.17). Although the integral spectrum was also measured at energies smaller than 17819 eV, they are excluded from the analysis due to the appearance of satellite lines [Mac21].
We do not take any scattering of ^{83m}Kr conversion electrons with carrier gas into account in the following analysis. Measurements with the e-gun [Rod20] indicate, that roughly 90 % of the ^{83m}Kr conversion electrons leave the source without undergoing inelastic scattering. Inelastically scattered electrons lose at least 8 eV energy [Rod20] and consequently do not contribute to the investigated analysis window.
The beamline magnets operate at nominal field during the ^{83m}Kr measurement. The Main Spectrometer is configured to a magnetic field in the analyzing plane of $B_{\text{ana}} = 270\,\mu\text{T}$, as this setting features the best energy resolution of possible field setups that guide the complete magnetic flux tube through the spectrometer without collisions. The elevated Main Spectrometer background due to the chosen setting is of no concern in this measurement, as the gaseous ^{83m}Kr source produces high rates per pixel. Furthermore, the β-decay electrons from the rear wall are as background many orders of magnitude larger than the spectrometer background.
To calculate the integral ^{83m}Kr spectrum, the magnetic field settings relevant for the MAC-E filter properties need to be considered in the calculation. As input, we use the simulated fields as stated in the period summary, knowing that they are subject to uncertainties. We therefore include the parameters for analyzing plane, PCH, and source magnetic field in the fit with the pull-term method to account for their uncertainties. The width of the penalty term for the magnetic field in the analyzing plane is 5 μT according to section 5.2.3, the one for the PCH field is 4 mT (see section 4.1.1), and the one for the source field 6 mT (see section 4.2.5). As consequence of the pull-term method, the transmission function depends now on the magnetic fields as fit parameters $T(E,U) \rightarrow T'(E,U,B_{\text{ana}},B_{\text{pch}},B_{\text{src}})$. Consequently, also the integral spectrum changes to $I(qU,A,E_0,\Gamma) \rightarrow I'(qU,A,E_0,\Gamma,B_{\text{ana}},B_{\text{pch}},B_{\text{src}})$.
As the ^{83m}Kr measurement takes place below the tritium endpoint, we face energy-dependent background by the β-decay electrons from the rear wall. Therefore, an energy-dependent background $R_{\text{bg}}(E)$ is included in the fit model. Dedicated measurements without ^{83m}Kr in the source show that the energy dependence of the

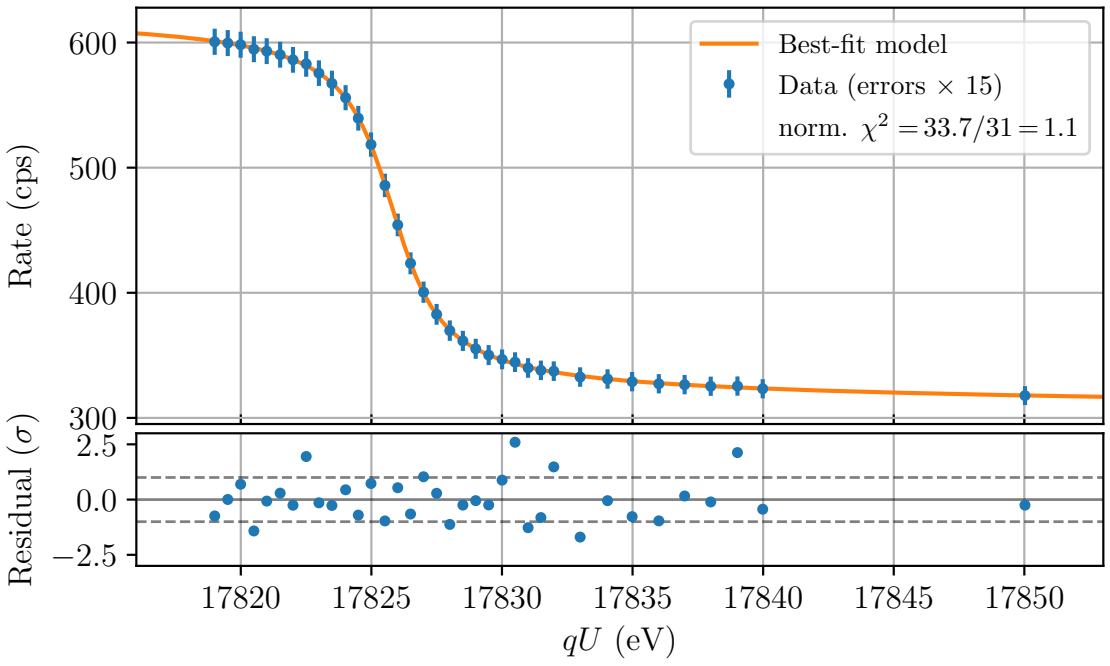

Figure 5.17.: **Measured integral spectrum (blue) of the ^{83m}Kr K line and the best-fit model (orange) over the applied retarding potential qU.** The best-fit residuals are shown in the lower graph. The shown spectrum is recorded at a central bulls-eye pixel, the total net-measurement time is 12 hours.

background at $E = 17.8\,\text{keV}$ is well described with a linear model for the 30 eV-wide analysis window. The slope of the background model as well as the constant offset are treated as free fit parameters in the likelihood optimization.
The uncertainty on the measured rate in each scan step is estimated by assuming that the count rates follow a normal distribution. We perform a pixel-wise analysis for each of the 125 active FPD pixels which means that the data measured on each pixel is analyzed independently of the other pixels. The calculated potential depression from the period summary is not included into the analysis to facilitate the direct comparison to the simulation. The presented measured line positions in the following therefore correspond to the line position as defined in equation 5.12.

The measured count rates and the best-fit model for a central FPD pixel is shown in figure 5.17. The normalized $\chi^2 = 1.1$ corresponds to a good p-value of 33.7 %, the best-fit model describes the measured rate without residual structure. The line position is determined to $E_0 = (17\,826.43 \pm 0.01)\,\text{eV}$.
The same fit is repeated for each of the active 125 FPD pixels. The overall fit statistic seems to be good. Only six of the 125 performed fits show a p-value of less than 5 %, indicating that the model generally describes well the data at the present uncertainty level. The measured K line positions for all active FPD pixels are visualized in figure 5.18 in the FPD projection. The uncertainty on the determined line position is on the order of 12 meV for an individual pixel. The line position varies over the whole FPD by 0.5 eV. The measured line position is larger at the center of the detector. This indicates a stronger potential depression at the Main Spectrometer center compared to larger flux tube radii, assuming a radially constant source work function (see

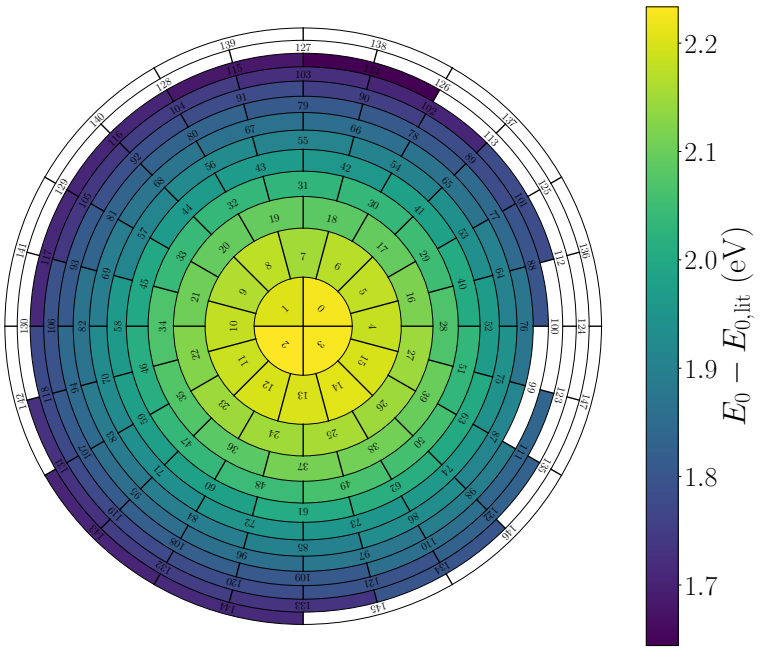

Figure 5.18.: **Measured K line position E_0 minus the literature value $E_{0,\mathrm{lit}}$ at the 125 active FPD pixels, shown in the FPD projection.** We use as literature value $E_{0,\mathrm{lit}} = 17\,824.2\,\mathrm{eV}$ [Vén+18b], the uncertainty on the measured line position is 12 meV. The measured line positions nicely reproduce the expected shape from the simulation for the retarding potential in the analyzing plane.

equation 5.12). A detailed comparison and discussion of the line position shape to e-gun measurements and Kassiopeia simulations is given in section 5.5.1.

5.4.3. Magnetic Field Measurements

The N shell is the outer-most occupied shell in the electric configuration of neutral $^{83\mathrm{m}}$Kr atoms. The vacancy caused by electron emission from the N shell can therefore only be resolved by neutralization via scattering processes. As the gas density in the WGTS is small, the process of electron N line emission in combination with a scattering process is not likely. We therefore expect the vacancy of the N shell to be long-lived, leading to a narrow natural line width. In the analysis of former KATRIN characterization measurements, it was sufficient to approximate the N conversion line by a δ-function. [Alt+20]
This narrow natural line width makes the line doublet $N_{2,3}$ an excellent tool for magnetic field investigations. As shown in figure 5.19, the width of the integral spectrum is dominated by the spectrometer resolution, given by the magnetic field strength in the analyzing plane. Additionally, further effects can easily be investigated with the line doublet, for example the energy scale smearing, as it smears out the sharp transmission function (also shown in figure 5.19). In this work, we therefore use measurements with conversion electrons of the $N_{2,3}$ line doublet to investigate the magnetic field strength in the analyzing plane.
One disadvantage of $N_{2,3}$ line doublet measurements is their line position of around 32 keV. The line position is significantly larger than the tritium endpoint, the re-

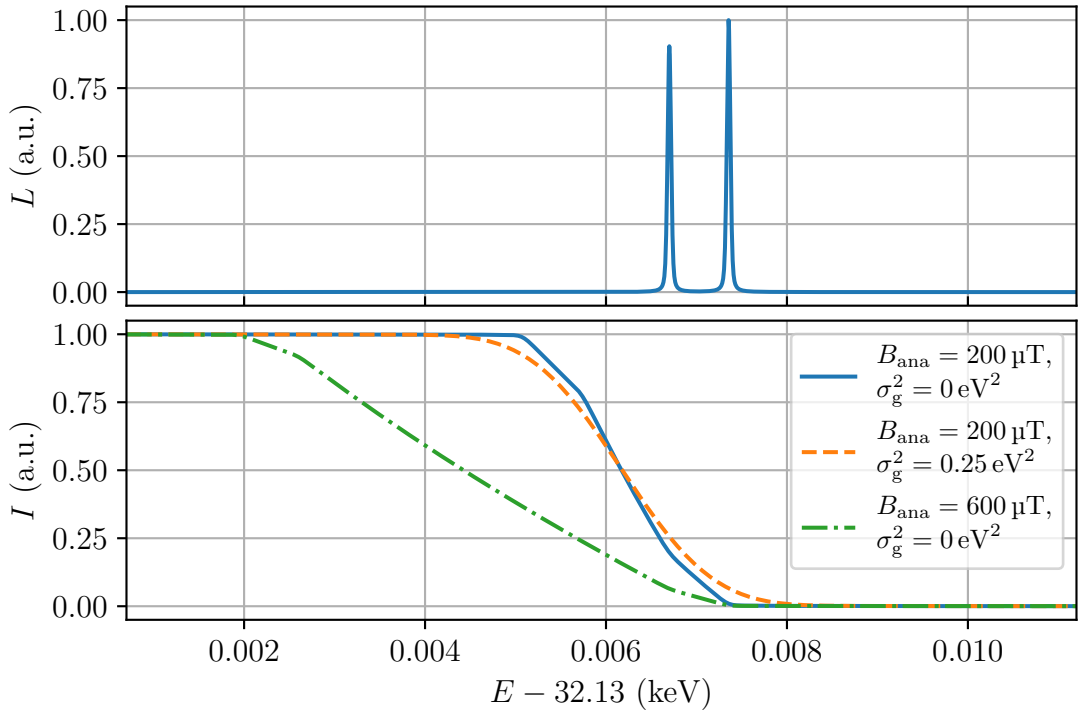

Figure 5.19.: **Calculated differential $N_{2,3}$ line double spectrum L (upper graph) and integral spectrum I (lower graph) over the electron energy E.** As shown by the calculations for the integral spectrum with different settings, it is evident that the width of the integral spectrum is dominated by the magnetic field strength B_{ana} in the analyzing plane and the shape by the energy broadening σ_g.

tarding potential in the Main Spectrometer therefore also needs to be significantly stronger than in neutrino mass measurements. Effects that are not that precisely investigated for this energy scale, for example non-adiabatic transport in the Main Spectrometer, could hinder the direct comparison of the potential shape measured in the $N_{2,3}$ analysis to the retarding potential shape applied in neutrino mass measurements. Another disadvantage is the small line intensity, given by the fact that the N shell is the outer-most shell. Internal conversion with subsequent electron emission from the K shell happens 30 times more frequently than the emission from the N_2 or N_3 line [Vén+18b]. Therefore, N line measurements either require a strong $^{83\mathrm{m}}$Kr source or a longer measurement time.

However, the intensity of the $^{83\mathrm{m}}$Kr source for the following study did not significantly differ from the above-described K line measurements to investigate the shape of the retarding potential. The measurement time was limited to eight hours for this measurement. A pixel-wise fit is therefore not possible, due to the small acquired statistics. A. Lokhov and C. Weinheimer propose to combine the data via a stacking approach. The 125 active FPD pixels are grouped in segments, so-called patches. All pixels in a patch feature similar transmission function properties [LW20], for example the same retarding potential in the Main Spectrometer. In a perfectly aligned KATRIN experiment, the patches would be equal to the concentric FPD wafer rings. Due to the realistic complex alignment of the experiment, the FPD pixels are sorted

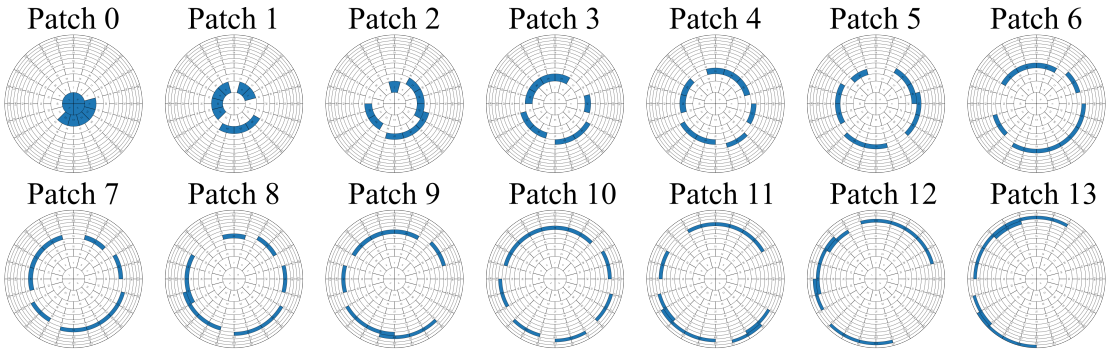

Figure 5.20.: **Grouping of the active 125 FPD pixels into 14 patches for the $N_{2,3}$ line doublet analysis, based on similar transmission properties measured with the ^{83m}Kr K line.** The patches 0 to 12 contain nine pixels each, patch 13 contains eight pixels. Patch 0 is located at the center of the FPD.

according to the fitted K line position (see figure 5.18), assuming that there are no radial starting potentials in the source for the ^{83m}Kr conversion electrons.
The 125 active pixels are grouped in 14 patches, each patch containing eight to nine pixels. The locations of the individual patches on the FPD are shown in figure 5.20. The K line position spread within one patch as indicator for the patch-wise potential spread is between 11 and 30 meV for the 2.7 G setting.

A new strategy was tested for the $N_{2,3}$ line doublet measurement to reduce the dead time during high voltage changes. In the nominal operational mode of KATRIN, the high voltage in the Main Spectrometer is changed by adapting the vessel voltage, while keeping the potential difference between inner electrodes and vessel constant. However, the vessel power supply needs several seconds to accurately set and stabilize the voltage after a change. This causes up to 40 % dead time in ^{83m}Kr measurements. An idea to bypass this problem is to use the inner electrode system to adapt the retarding potential. The difference between the electrodes and the vessel is fixed at 200 V in the nominal setting. ^{83m}Kr measurements normally require only a narrow energy range on the order of ten eV. The inner electrodes can also produce this potential change, while the vessel voltage stays constant. To further maximize the live time in the measurement, the typical scan steps in the measurements are replaced by a continuous ramp. The inner electrodes continuously change their potential with a ramping speed of 0.03 V/s in the range from 195 to 205 V during the measurement analyzed in the following. The continuous ramp is then binned for the analysis in bins of one second acquisition time. [Rod21b] The applied retarding potential, as well as the measured rate, is averaged over this one second and translated into a pseudo scan step-wise run summary for analysis [Eno21b]. This procedure enables nearly 100 % live time during the measurement. The inner electrode ramping introduces systematic effects that differ from the ones of the nominal vessel-ramping mode, as discussed in the following. Although we correct for the systematic effects, it is possible that unknown systematic effects bias the measurement results. Therefore, the following results should be understood as a test of principle until they are confirmed by measurements with the vessel ramping mode. Measurements of the $N_{2,3}$ line doublet with the vessel ramping mode have been conducted in the second half of 2021, first analysis results of these measurements are expected for early 2022.

The continuously changing inner electrode offset continuously alters the potential depression in the Main Spectrometer during the measurement [Fen21]. This is not the case for the nominal vessel ramping, in that case the potential depression stays constant. An unrecognized potential depression change leads to an effective stretching of the energy axis between true and assumed retarding potential in the Main Spectrometer. Unrecognized stretching effects of the energy axis are in particular for this analysis dangerous, as the measurement goal is to determine the width of the integral spectrum for the analysis of the magnetic field in the analyzing plane. To investigate the effect of the changing potential depression, three period summaries are calculated [Beh21]. The vessel voltage is fixed at $-31\,938\,\mathrm{V}$ for the calculation, the retarding potential in the analyzing plane is calculated for 195 V, 200 V, and 205 V difference between inner electrode and vessel. The simulation predicts a change of 4.96 eV in the retarding potential if the inner electrode potential is varied by 5 V. This change is constant for all pixels to first-order approximation. We therefore scale the energy axis to correct for this value with respect to the central inner electrode offset of 200 V by using the linear model as implemented in the KaFit framework by M. Machatschek.

The model to describe the measured data in each patch comprises two Lorentzian distributions, an energy smearing, the magnetic field strengths as part of the transmission function and a constant background.
The two Lorentzian distributions describe the differential shape of the two N lines. The limited measurement statistics in combination with the finite Main Spectrometer resolution does not allow extracting the N line widths from the fit. Therefore, a penalty term, based on our best knowledge, is applied in the likelihood. Vénos et al. state, that the N_2 and N_3 line widths are 30 meV [Vén+18b], based on measurements of the $M_{4,5}N_{2,3}$ Auger spectrum of ^{83m}Kr [Aks+77]. However, the conversion line width of the $N_{2,3}$ line doublet is influenced by the deexcitation mechanism of the ionized ^{83m}Kr atom, and thus by the atom's surroundings. Since the ^{83m}Kr is in a gaseous state and very dilute during the measurement, deexcitation of the atom is infrequent. We therefore expect smaller line widths than 30 meV, leading to a conservative Gaussian-shaped penalty term with mean and width of 15 meV in the likelihood function. Performed studies indicate that the chosen penalty term does not significantly influence the determined magnetic field strength in the analyzing plane as parameter of interest in this study. The normalization and position of the Lorentzian describing the N_3 conversion line are expressed in the model relative to the N_2 Lorentzian to facilitate the comparison to external measurements, for example the one from optical spectroscopy [Vén+18a].
Several effects disturb the energy scale in this measurement, on which the N line is sensitive due to its small line width. By summarizing several pixels into patches, an energy broadening of up to 30 meV is introduced due to the potential inhomogeneity in the Main Spectrometer. The thermal Doppler broadening is expected to be on the order of 55 meV for the N line and 80 K source temperature [Alt+20]. Additionally, a time synchronization problem between the detector and the high-voltage system caused a time delay on the second-level between the timestamps of the measured rate and the timestamps of the voltage readback of the inner electrode system [Rod21b]. This leads to a slightly shifted energy scale for up-scans with respect to down-scans in the continuous ramping mode. By applying the stacking procedure to combine the up- and down-scans, the time delay causes another energy smearing. Due to the

several effects that can only roughly be estimated, we decide to treat the width of the Gaussian kernel σ_g^2 as free fit parameter in the study.
The three magnetic fields in the transmission function are the one in the analyzing plane, the source, and the PCH field. The source and PCH magnetic field are well-known from simulations, we therefore include them with the pull-term method as systematic uncertainties in the fit. The magnetic field in the analyzing plane is as parameter of interest a free fit parameter. The eLFCS is set to the 2.7 G configuration for this measurement, since one of the measurement's goals is a high-resolution spectroscopy of the $N_{2,3}$ line doublet without collision of the flux tube with the Main Spectrometer vessel.
The model comprises in addition to the integral line spectrum a constant background. It is motivated by the Main Spectrometer background as well as the rare direct ^{83m}Kr decay directly to the ground state, without the intermediate state. This direct decay produces electrons with energies of around 41 keV.

The model fit to the measured data in the likelihood optimization comprises in total eleven free fit parameters, four of them are constrained by a penalty term. The fit is performed individually for each patch. Due to the low count rate in the individual scan steps in the background region, we assume that the observed number of counts follows a Poisson distribution. Similar to the ^{83m}Kr potential measurements, it is not necessary to consider the scattering of ^{83m}Kr conversion electrons off carrier gas in the WGTS in the analysis due to the small WGTS column density and the narrow analysis window.
The first minimization is performed with Minuit2 as implemented in the KaFit framework. Afterwards, we use the MCMC affine-invariant ensemble sampler emcee for detailed uncertainty and correlation analysis.

The data of the $N_{2,3}$ measurement as well as the best-fit model for patch 0 is shown in figure 5.21. Patch 0 is located at the center of the analyzing plane. The best-fit model describes well the measured rates at the individual scan steps, as indicated by the decent normalized $\chi^2 = 1.1$ and no visible structure in the residual plot.
The best-fit estimates on the line widths are approximately (15 ± 15) meV and thus do follow the penalty term. The measured line position distance between N_2 and N_3 is (0.65 ± 0.01) eV and in agreement with the results from optical spectroscopy measurements, that determined a line distance of (0.6701 ± 0.0001) eV [Vén+18a]. The best-fit energy broadening yields $\sigma_g = (129 \pm 13)$ meV and is larger than the thermal broadening or the stacking procedure of pixels into patches. The energy broadening is significantly reduced if only up- or down-scans are analyzed, in that case the analysis results in (69 ± 9) meV. This estimate is consistent with the expected broadening due to the thermal Doppler effect and potential variations in the analyzing plane within one patch. The major part of the energy broadening in the stacked analysis is consequently caused by stacking the up- and down-scans with the shifted energy scales due to the time synchronization problems of the high-voltage system.
The best-fit model yields for the parameter of interest, the magnetic field strength in the analyzing plane, a precise result of $B_{ana} = (262 \pm 1)$ μT in patch 0. The obtained uncertainty is dominated by the limited statistics, the systematic contributions due to source and PCH magnetic field are minor. However, the fit uncertainty does not yet contain an uncertainty estimation on the changing potential depression due to the non-constant inner electrode offset. The effect, that stretches the energy scale, is

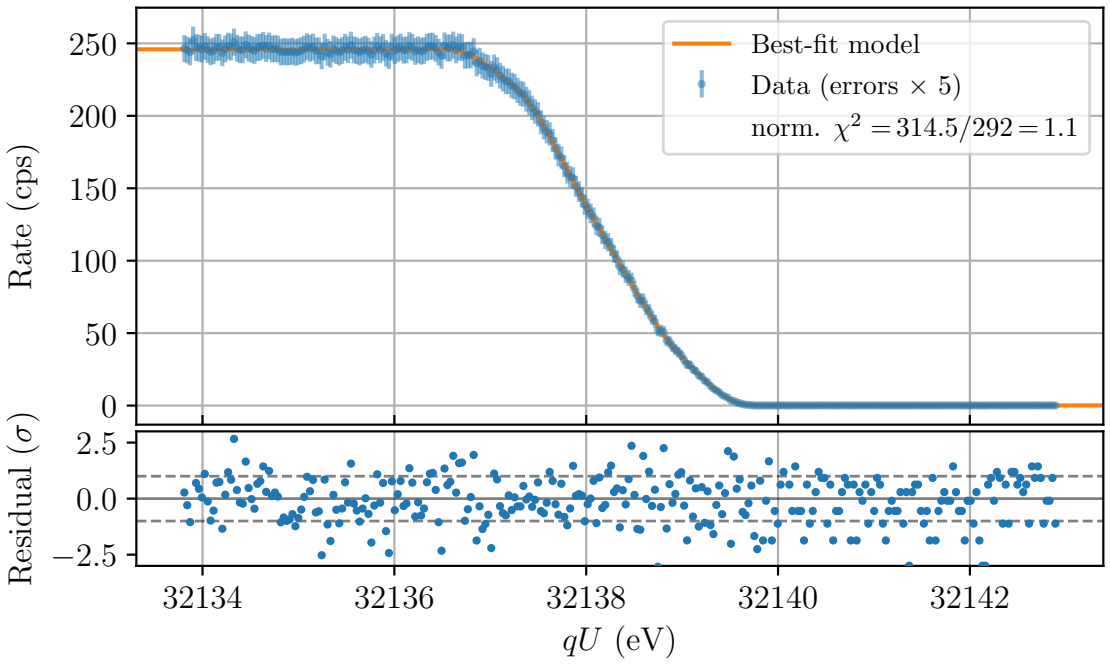

Figure 5.21.: **Measured integral spectrum of the ^{83m}Kr $N_{2,3}$ line doublet and the best-fit model as function of the applied retarding potential qU.** Shown is the measured spectrum at the central patch 0. Results of best fit and discussion of findings given in main text.

estimated by simulations to 80 meV for the whole analysis range. We conservatively estimate the error on this effect by assuming a 10 % systematic uncertainty. The impact on the uncertainty of the magnetic field strength in the analyzing plane is then calculated by employing the equation for the energy resolution of the MAC-E filter

$$\Delta E = \frac{B_{\text{ana}}}{B_{\text{pch}}} \cdot E, \tag{5.13}$$

with ΔE being the energy resolution and E the kinetic energy of the decay electrons. The 80 meV uncertainty on the energy scale is interpreted as an uncertainty on the energy resolution. By transforming equation 5.13, this uncertainty can be propagated to the analyzing plane, leading to $\Delta B_{\text{ana,sys}} = 1\,\mu\text{T}$. Consequently, the experimental result for the magnetic field in the analyzing plane for patch 0 is $B_{\text{ana}} = (262 \pm 2)\,\mu\text{T}$.
The correlation matrix of the free fit parameters in the $N_{2,3}$ analysis is shown for patch 0 in figure 5.22. The correlation between the magnetic field in the analyzing plane and the source as well as the PCH field is weak with $|\rho| < 0.3$ as correlation coefficient. The correlation of the magnetic field with the squared energy broadening yields $\rho = -0.25$ and is therefore also rather weak. The only fit parameters that have a strong correlation with the magnetic field in the analyzing plane are the position of the N_2 line and the distance between N_2 and N_3.

An overview of the relevant fit results for all patches in the 2.7 G measurement is given in the upper part of table 5.2. The normalized χ^2 for each minimization

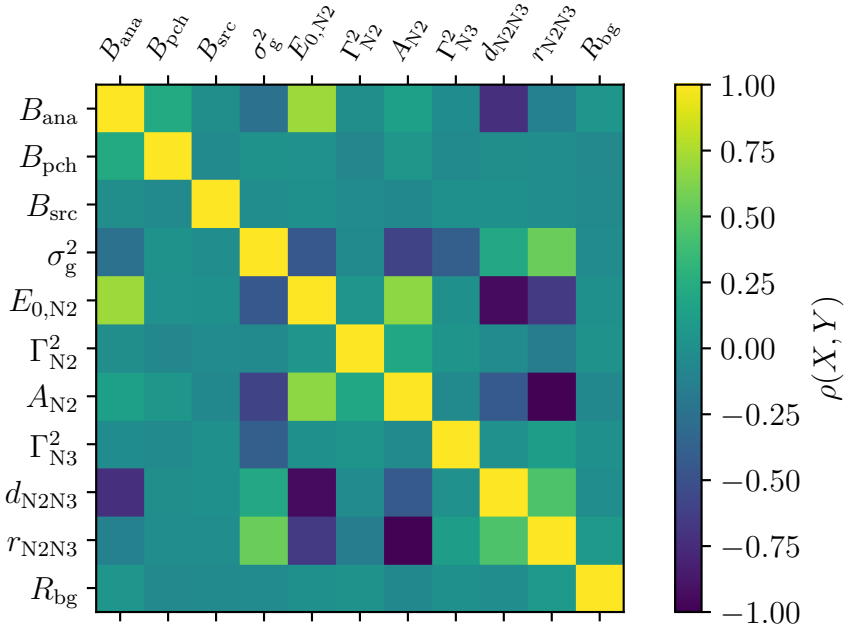

Figure 5.22.: **Correlation matrix of the $N_{2,3}$ line doublet analysis for patch 0, as found by the emcee sampler.** The magnetic field in the analyzing plane as parameter of interest shows only little absolute correlations to the other fit parameters, except for the absolute N_2 line position $E_{0,\mathrm{N2}}$ and the distance d_{N2N3} between N_2 and N_3 line.

is well distributed around the expectation value 1, indicating a good agreement between data and best-fit model. The fit results for the magnetic field strength in the analyzing plane show precise values with uncertainties on the 2 µT level. If these results were used for neutrino mass analyses in a 2.7 G setting, the resulting systematic neutrino mass uncertainty contribution due to the uncertainty on the magnetic field in the analyzing plane was $\Delta m^2_{\nu,\mathrm{sys}} = 4 \times 10^{-3}\,\mathrm{eV}^2$. The spatial evolution of the field indicates a larger field at the central patch 0, that decreases towards patch 5 and then increases again to the outer-most patch 14. A detailed comparison to the simulated magnetic field takes place in section 5.5.2. The fit result for the squared energy broadening seems to be rather constant with a slight increase towards the outer patches. We expect the behavior to be constant because the energy broadening is dominated by the stacking of the up- and down scans. The measured line position decreases from the inner- to the outer-most patch by approximately 450 meV. This decrease is expected as it follows the shape of the potential depression in the analyzing plane, that is not corrected for in the analysis.

The measurement of the $N_{2,3}$ line doublet is repeated with the 1 G configuration of the magnetic field in the analyzing plane, which features an even better energy resolution than the 2.7 G configuration. As the analysis procedure is exactly the same as for the 2.7 G measurement, we directly discuss the results. The 1 G setting only allows us to analyze the four inner-most patches, as the outer part of the magnetic flux tube collides in this setting with the Main Spectrometer vessel, leading to a shadowing of the outer FPD pixels. The relevant best-fit parameters of the 1 G analysis are summarized in the lower part of table 5.2. The normalized χ^2 of the

Table 5.2.: **Best-fit results for the $N_{2,3}$ line doublet measurements in the 2.7 G and 1 G settings.** In the 2.7 G setting, the whole cross section of the flux tube of decay electrons is transported to the FPD and therefore all 14 patches are illuminated. Due to collisions of the flux tube with the vessel as consequence of the radial expansion in the 1 G setting, only the four inner-most patches can be used for the analysis of ^{83m}Kr conversion electrons.

Setting	Patch	norm. χ^2	B_{ana} (μT)	σ_{g}^2 $\left(\times 10^{-3}\,\text{eV}^2\right)$	$E_{0,\text{N2}}$ (eV)
2.7 G	0	1.08	262 ± 2	17 ± 1	32138.87 ± 0.02
	1	1.01	261 ± 2	13 ± 1	32138.81 ± 0.02
	2	1.03	259 ± 2	15 ± 1	32138.77 ± 0.02
	3	1.06	260 ± 2	16 ± 1	32138.75 ± 0.02
	4	1.18	258 ± 2	16 ± 1	32138.69 ± 0.02
	5	0.92	255 ± 2	18 ± 1	32138.63 ± 0.02
	6	1.03	261 ± 2	15 ± 1	32138.64 ± 0.02
	7	0.87	259 ± 2	17 ± 1	32138.59 ± 0.02
	8	1.03	260 ± 2	17 ± 2	32138.57 ± 0.02
	9	0.97	260 ± 2	15 ± 2	32138.54 ± 0.02
	10	1.03	263 ± 2	18 ± 2	32138.54 ± 0.02
	11	1.05	263 ± 1	20 ± 2	32138.48 ± 0.02
	12	1.07	262 ± 2	23 ± 2	32138.45 ± 0.02
	13	1.08	265 ± 1	19 ± 2	32138.41 ± 0.02
1 G	0	1.07	98 ± 2	15 ± 1	32138.823 ± 0.007
	1	0.89	96 ± 2	16 ± 1	32138.705 ± 0.007
	2	1.04	92 ± 2	20 ± 1	32138.584 ± 0.006
	3	1.04	96 ± 2	18 ± 1	32138.514 ± 0.007

fits is distributed around the expectation value of 1, and the fit residuals do not show any structure indicating good agreement between model and data. Similarly to the 2.7 G measurement, also the 1 G analysis yields a precise estimate on the magnetic field strength in the analyzing plane with uncertainties on the 2 μT-level. This uncertainty comprises the statistical uncertainty from the fit result as well as the systematic contribution from the ramping mode from the inner electrode system. A detailed comparison of the measured magnetic field in the analyzing plane to the simulation expectation for the 1 G setting is stated in 5.5.2. We expect the energy broadening to be constant and similar to the 2.7 G result, as it is dominated by the stacking of the up- and down scans with the time synchronization problem of the high-voltage readback. The expectations are met, the broadening is on the same level and it tends to increase towards the outer patches, similar to the 2.7 G result. The

best-fit for the N_2 line position features a significantly smaller uncertainty compared to the 2.7 G measurement. This is related to the improved energy resolution of the 1 G setting compared to the 2.7 G setting. The line position decreases from the central to the outer patch because of the shape of the potential depression in the analyzing plane.

In summary, a high-precision measurement of the magnetic field strength in the analyzing plane of the 1 G and the 2.7 G setting was achieved in this thesis using decay electrons from the $N_{2,3}$ line doublet. Furthermore, the results can be considered to be robust, since correlations to other free fit parameters in the analysis are moderate. Measurements with a high-intensity ^{83m}Kr source have been performed in the second half of 2021, first analysis results are expected in early 2022. These measurements will enable us a pixel-wise determination of the magnetic field strength of the 1 G, 2.7 G, and 6 G setting. Additionally, these measurements have been performed with the nominal vessel ramping mode to avoid the high-voltage time synchronization problem as well as further unknown systematic effects of the ramping mode with the inner electrode system. It is expect that these measurements significantly reduce the systematic neutrino mass uncertainty due to the uncertainty of the magnetic field in the analyzing plane on the 6 G setting.

5.5. Comparison and Summary

In this thesis, we have characterized the electromagnetic fields of the nominal analyzing plane via three complementary approaches: via numerical simulations as default input for neutrino mass analyses, with the e-gun, and with ^{83m}Kr measurements. Each of the three methods is influenced by different systematic uncertainties. The following sections contain a comparison of the methods' results with regard to the retarding potential and the magnetic field.

5.5.1. Retarding Potential

The retarding potential simulation qU_{sim} with Kassiopeia takes into account the vessel voltage, inner electrode offset, as well as the potential depression

$$qU_{\mathrm{sim}} = q(U_{\mathrm{v}} + U_{\mathrm{ie}} + U_{\mathrm{pd}}). \tag{5.14}$$

The work function Φ_{ms} of the Main Spectrometer is not taken into account in the simulation, as its absolute value and its time evolution are not precisely known. It is important to add that the simulation depends on the accuracy of the magnetic field simulation and the global alignment of beamline elements between FPD and analyzing plane, since the FPD projection into the analyzing plane depends on these parameters.
The potential edge Φ_{pe} measured in transmission function measurements with the e-gun comprises the potential depression, the work function of the Main Spectrometer, and the e-gun work function $\Phi_{\text{e-gun}}$

$$\Phi_{\mathrm{pe}} = -qU_{\mathrm{pd}} + \Phi_{\text{e-gun}} - \Phi_{\mathrm{ms}}. \tag{5.15}$$

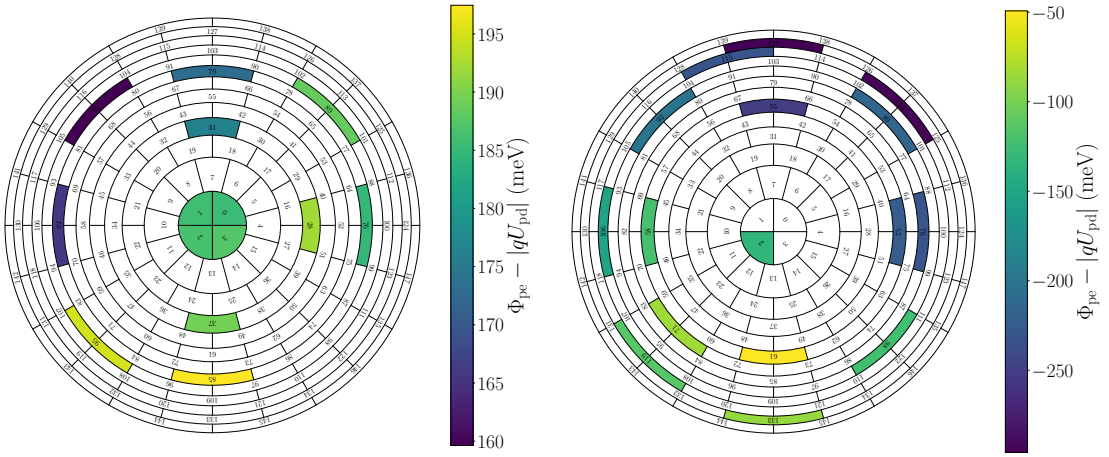

Figure 5.23.: **Comparison of the measured e-gun potential edge Φ_{pe} with the simulated potential depression qU_{pd}.** The comparison for the 6 G measurement is shown in the left plot, the comparison for the measurement in the 2.7 G configuration in the right plot. The uncertainty on the comparison is 7 meV (central pixels) to 8 meV (outer pixels) for the 6 G measurement and 10 meV to 20 meV for the 2.7 G.

Similarly, the ^{83m}Kr line position measurement E_0 is also sensitive on the potential depression and the Main Spectrometer work function, but also to the source work function Φ_{src} and the starting potential V_{start} in the WGTS

$$E_0 = E_{kin}^{t,s} + (\Phi_{src} + V_{start} - \Phi_{ms}) - qU_{pd}, \tag{5.16}$$

with $E_{kin}^{t,s}$ being the constant offset given by the net kinetic energy of the electron after the emission in the ^{83m}Kr decay.

Despite the sensitivity to different quantities of the three approaches, we try to put them into context in the following section.

Comparison of Simulation, E-Gun, and Krypton K Line Measurements

As a first step, we compare the simulated potential depression with the measured potential edge by the e-gun. The e-gun work function is independent of the location in the analyzing plane and therefore also independent of the FPD pixel at which the transmission function is measured. R. Sack measured the absolute value of the e-gun work function to $\Phi_{e\text{-gun}} = (4.43 \pm 0.01)$ eV [Sac20]. The Main Spectrometer work function was estimated to $\Phi_{ms} \approx 4$ eV [Beh21], and is also the same for all detector pixels. However, it has to be noted that the absolute determination of the work function of the Main Spectrometer is strongly dependent on potential simulations [Beh16]. Based on these assumptions, a subtraction of the simulated potential depression from the measured potential edges at the individual FPD pixels should result in a constant offset, if the potential depression in the analyzing plane is calculated correctly for each pixel. The constant offset should then be on the order of $\Phi_{e\text{-gun}} - \Phi_{ms} \approx 0.4$ eV.
The comparison of the 6 G and 2.7 G potential edge measurement with the e-gun (see section 5.3.3) to the simulation is shown in figure 5.23, visualized in the FPD

projection. Two components constitute the total uncertainty of the comparison. The first component is given by the uncertainty of the e-gun measurement, comprising the statistical uncertainty as well as the systematic uncertainty stemming, inter alia, from the uncertainty on the mean pitch angle of the e-gun electrons. The second component is given by the simulated potential variation over the investigated pixel in the analyzing plane, as the exact position of the e-gun electron beam within the pixel is not known in the measurement. This results in a total uncertainty of 7 meV for the central pixels and 8 meV for the outer-most measured pixels in the 6 G setting, the uncertainty from the e-gun measurement is the dominant error. For the comparison in the 2.7 G setting, the uncertainty from intra-pixel inhomogeneity is dominant due to the large radius of the analyzing plane in the Main Spectrometer. The statistical uncertainty on the measured potential edge is only 3 meV, the intra-pixel variations of the potential are between 9 meV for the central pixels up to 20 meV for the outer-most pixels. The total uncertainty in the comparison of e-gun measurement to simulation in the 2.7 G setting is thus in the range of 10 meV to 20 meV, depending on the investigated pixel.

The first remarkable property revealed in the comparison of simulation to measurement is that neither the 6 G nor the 2.7 G measurement have a constant offset to the simulation. The spread of the determined differences between simulation and potential edge for the 14 measured transmission functions in the 6 G setting are 11 meV. This is larger than expected for the estimated uncertainty of 7 meV. This discrepancy is even more pronounced for the 2.7 G measurement. The spread for the 16 determined potential edges is 74 meV, while the spread expectation value is 10 meV to 20 meV. Comparing the FPD projection of both settings, it becomes evident that the difference between simulation and potential edge is not randomly distributed over the detector, as we would expect it from statistical fluctuations. Moreover, both settings tend to show a more positive difference on the lower half of the detector compared to the upper half. We can therefore conclude that the difference between simulated potential depression and measured e-gun edge position is not constant, but hints at a pattern that is not expected for an accurate simulation of the potential depression.

The second remarkable feature in the comparison is the mean offset between simulated potential depression and e-gun edge position. The difference is in average +183 meV for the 6 G measurement, compared to −175 meV for the 2.7 G configuration. Firstly, both measurements deviate from the expectation value of 0.4 eV, pointing towards complications in the model-dependent estimation of the work function of the Main Spectrometer. Secondly, the averaged difference significantly deviates between both measurements. The time difference in between the two measurements is roughly one year. The 6 G measurements were performed during KNM1 in June 2019, while the 2.7 G measurements were conducted before the start of KNM3 in May 2020. Considering the definition of the e-gun potential edge (see equation 5.15), the e-gun work function and the work function of the Main Spectrometer are possible sources for the unequal average difference. The e-gun work function is regularly investigated in dedicated measurements and shows time-dependent effects of less than 50 meV [Sac20; Sac21a]. Thus, the major change is likely related to changes in the work function of the Main Spectrometer. Commissioning measurements indicated that a change in the work function of the Main Spectrometer on the order of few hundred meV is possible due to changing vacuum conditions [Beh16]. During the 6 G measurement the pressure in the vacuum pump port 1 was 1.0×10^{-11} mbar, com-

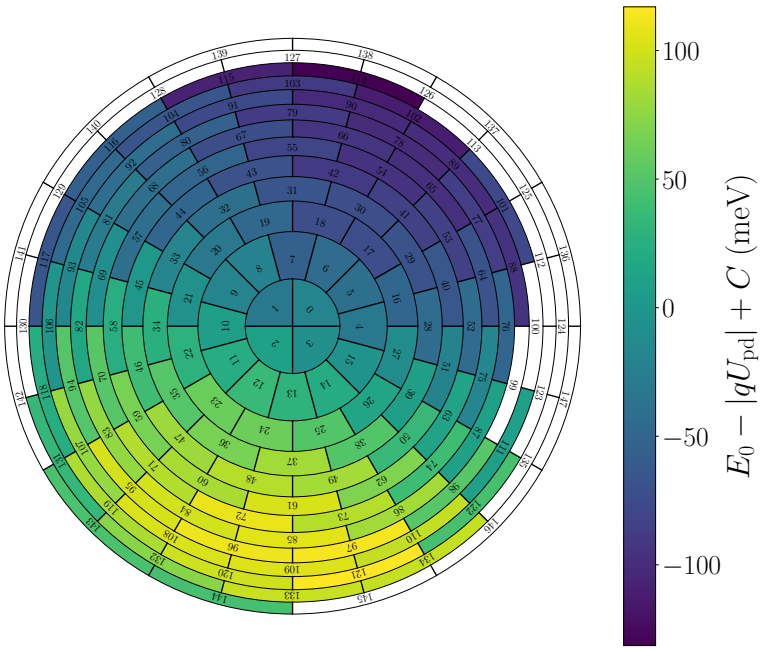

Figure 5.24.: **Comparison of the measured line position E_0 to the simulated potential depression qU_{pd} plus a constant offset C.** The constant offset comprises $C = E_{\mathrm{kin}}^{t,s} + \Phi_{\mathrm{src}} - \Phi_{\mathrm{ms}} = 17\,824.1\,\mathrm{keV}$ and is close to the literature value for the K line position of $(17\,824.2 \pm 0.1)\,\mathrm{keV}$ [Vén+18b]. The uncertainty on the comparison is 12 meV on an individual pixel.

pared to 7.1×10^{-11} mbar during the 2.7 G measurement. Additionally, the Main Spectrometer was baked-out between both measurements, causing a desorption of hydrogen from the inner walls of the Main Spectrometer and thus a change of the surface properties. Consequently, the different pressures and deviating surface properties between both measurements are likely reasons to cause the discrepancy in the mean difference between the two measurements. Another reason for the discrepancy in the averaged differences could be an inaccuracy in the potential simulation. The 6 G measurement was performed with the goal to investigate the neutrino mass configuration. Therefore, the offset of the steep cones of the inner electrode system near the entrance and exit of the Main Spectrometer was set to +40 V (see also table B.3). The goal of the 2.7 G measurement was to validate the simulation input for $^{83\mathrm{m}}$Kr measurements, the offset of the steep cones was consequently set to the $^{83\mathrm{m}}$Kr value of +130 V during the measurement. The steep cones influence the retarding potential in the analyzing plane on the order of 400 meV. An inaccurate consideration of the steep cones in the simulation could partly contribute to the discrepancy in the averaged differences of the 2.7 G and 6 G comparison.

$^{83\mathrm{m}}$Kr conversion line position measurements enable a comparison of the measured to the simulated potential with high spatial resolution, since all FPD pixels are illuminated at once. The K line is an appropriate tool for this comparison, due to its kinetic energy of 17.8 keV close to the molecular tritium endpoint. As shown in the pixel-wise analysis in section 5.4.2, the uncertainty on the measured line position in an individual pixel is 12 meV if all systematic uncertainties are taken into account. The line position on the pixels in the analyzing plane depends on the work function of the Main Spectrometer (see equation 5.16). A constant offset for all pixels is

introduced relative to the simulated potential by the net kinetic energy $E_{\mathrm{kin}}^{t,s}$ of the electrons after the emission in the $^{83\mathrm{m}}$Kr decay. We expect that the impact of the source work function is constant over the whole cross section of the flux tube, similar to the work function of the Main Spectrometer. Additionally, we assume that the electron starting potential in the WGTS is also homogeneous in radial direction at the $^{83\mathrm{m}}$Kr sensitivity level due to the choice of non-radioactive carrier gas for $^{83\mathrm{m}}$Kr (see section 5.4.2.) Based on these assumptions, the simulated retarding potential can be compared to the $^{83\mathrm{m}}$Kr measurements.
The comparison of the simulated retarding potential and the pixel-wise $^{83\mathrm{m}}$Kr K line is shown in figure 5.24. The uncertainty of this comparison is solely given by the 12 meV uncertainty on the line position from the measurement. The uncertainty by inner-pixel potential variations does not need to be considered in this comparison. The $^{83\mathrm{m}}$Kr conversion electrons traverse the entire cross section of the area in the analyzing plane corresponding to a certain FPD pixel and therefore average the variations. The comparison of the line position to simulation indicates a dipole-like structure in the FPD visualization with a significant peak-to-peak amplitude of more than 200 meV. Pixels in the lower left quarter have a more positive reconstructed line position compared to the ones in the upper right quarter. Source-related effects, for example a radially and azimuthally dependent source work function or source starting potential can be excluded as causes of this effect, as the e-gun 2.7 G potential edge measurement reveals a similar dipole-like structure with a comparable peak-to-peak amplitude. The most likely reason for this dipole-like structure is a misaligned projection of the FPD in the analyzing plane in the Kassiopeia simulation compared to reality, as discussed in the following section.

Implications for Kassiopeia Geometry Model

Simulations can reproduce a dipole-like structure, as found in the comparison of measured $^{83\mathrm{m}}$Kr K line positions to simulated retarding potential in the analyzing plane, by shifting the center of the analyzing plane in the Main Spectrometer versus the simulation truth. As the dipole structure is shown by two complementary measurement tools, namely e-gun and $^{83\mathrm{m}}$Kr measurements, it is likely that the found dipole structure is caused by an inaccurate geometry in the Kassiopeia model. We therefore attempt to use the results of the $^{83\mathrm{m}}$Kr and e-gun measurements to get a hint on the source and size of the inaccurate misalignment in the Kassiopeia geometry.
The calculation of the FPD projection in the analyzing plane depends basically on the alignment of all beamline elements between the Main Spectrometer and the FPD. Of course, the absolute position of the FPD is elementary for the correct geometry. Tilts and misalignments of the PCH and DET cryostats and coils as guiding magnets can shift the FPD projection in radial direction. The Main Spectrometer vessel produces the retarding potential, a radial misalignment of the spectrometer with respect to the PCH, DET, and FPD can consequently also alter the calculated retarding potential for the FPD projection.
The following analysis introduces a shift in radial direction on the position of the simulated FPD projection in the Main Spectrometer to reduce the dipole structure in the comparison of simulation to e-gun and $^{83\mathrm{m}}$Kr measurement. For this analysis, we use the results of the K line as well as of the 2.7 G e-gun measurement, as they

were taken with the same hardware setup. The 6 G measurement is not comparable due to major hardware changes after KNM1 that affect the alignment, for example the exchange of the FPD wafer. Additionally, the high-precision alignment result from the Hall probe measurements of the PCH and DET alignment are used here (see section 4.1.2), since it provides the best knowledge on these two crucial beamline elements.

As a first step of the analysis, the retarding potential is simulated on more than 7000 positions in the analyzing plane, leading to a fine-grained potential map of the analyzing plane [Beh21]. Exploring the FPD projection simulation (see section 3.3.9), the central positions of the FPD pixels measured with the e-gun are determined in the analyzing plane. Via linear interpolation of the potential map, we can calculate the simulation expectation and compare it to the result of the e-gun potential edge. This leads to a similar behavior as shown in the right plot of figure 5.23. We now employ the potential map to introduce shifts in horizontal and vertical direction to reduce the dipole structure.
We perform a χ^2 minimization

$$S(\delta x, \delta y, C) = \sum_i \frac{(D_i - M_i(\delta x, \delta y, C))^2}{\sigma_i^2}$$

to infer the optimal shift of the potential map to suppress the dipole-like structure. The results of the potential edge measurement with the e-gun is denoted as D_i. The model $M_i(\delta x, \delta y, C)$ is given by the interpolation of the potential map to the simulated location of the e-gun electron beam in the analyzing plane. The uncertainty σ_i for the comparison is given by the uncertainty of the e-gun potential edge measurement and the inner-pixel potential variations. The model contains as free fit parameter a shift in horizontal direction δx, in vertical direction δy, and a constant offset C that represents the difference between e-gun work function and work function of the Main Spectrometer. The minimization of $S(\delta x, \delta y, C)$ leads to the best-fit values for the shifts

$$\begin{aligned} \delta x &= (-66 \pm 4)\,\text{cm}, \\ \delta y &= (-22 \pm 3)\,\text{cm}. \end{aligned} \tag{5.17}$$

According to the comparison of the potential map with the potential edge measurement by the e-gun, the real FPD projection is shifted by 22 cm in horizontal and 66 cm in vertical direction compared to the Kassiopeia simulation.
The same method can be repeated for the comparison of the ^{83m}Kr K line positions with the simulated potential map in the Main Spectrometer. This leads to consistent results of the FPD projection shift in the analyzing plane of

$$\begin{aligned} \delta x &= (-60 \pm 1)\,\text{cm}, \\ \delta y &= (-22.5 \pm 0.9)\,\text{cm}. \end{aligned}$$

To avoid circular arguments, we use in the following the central shift values from the e-gun results, since the alignment correction shall be applied in future ^{83m}Kr measurements. Another approach would be of course to derive the effective shift parameters in a global analysis of ^{83m}Kr and e-gun data, assuming that the effective shift is caused in both approaches by the same effect.

Based on the effective shift parameters derived with the e-gun (see equation 5.17), a new period summary for the retarding potential and magnetic field strength in the analyzing plane is calculated. This new period summary is compared to the e-gun potential and ^{83m}Kr K line measurements in figure 5.25. Both plots indicate that the peak-to-peak amplitude of the difference is markedly reduced with respect to figures 5.23 and 5.24. In the e-gun comparison (see left graph in figure 5.25), the spread of the difference is reduced by more than a factor of two, from 74 meV to 30 meV, with an average difference of −179 meV. Nevertheless, the spread is still larger than the expectation value for statistical fluctuations in the range from 10 meV to 20 meV. The dipole-like structure vanishes in the e-gun plot. Instead two pixels in the upper right quarter of the projection with close spacial vicinity show largely different values. This effect could be a residue of the difference analysis, in which it is assumed that the e-gun beam strikes the pixel in the center. However, it is possible that the e-gun beam strikes in individual measurements the pixel not at the center but at deviating position. The probability for this effect to happen increases towards larger radii in the analyzing plane, as the pixels become more narrow in radial direction with increasing radius. If the effect occurs that two pixels at large radii with close vicinity are not struck in the center by the e-gun, an imprint similar to the one observed is possible.
The dipole structure is also significantly reduced in the comparison of the ^{83m}Kr K line position with the potential simulation based on the shifted period summary (see right graph in figure 5.25). The overall difference spread is reduced from 67 meV in the non-shifted simulations to 16 meV, and thus still slightly larger than the expectation value of 12 meV from statistical fluctuations. A small dipole structure remains with positive differences on the right side of the FPD and negative differences on the left side. However, so far we have not yet taken into account the uncertainties on the effective shift parameters from the e-gun. To demonstrate the impact of the uncertainties on the difference distribution on the FPD, the shift procedure is also repeated for the ^{83m}Kr shift parameters that are compatible with the e-gun parameters within the uncertainties. With the period summary based on the ^{83m}Kr measurement, the dipole structure in the ^{83m}Kr K line position on the FPD completely vanishes. The spread of line positions is with 13 meV in agreement with the assumption of statistical fluctuations of 12 meV. We therefore recommend to repeat the 2.7 G e-gun measurement with more measurement points to reduce the uncertainty on the effective shift parameters. Another option would be the already mentioned combined analysis of ^{83m}Kr and e-gun measurements to improve the precision, assuming that the reason for the effective shift is the same in both measurements.
Nevertheless, we can conclude that the dipole structure is mostly caused by a shift of the simulated FPD projection versus the true position in the Main Spectrometer. After an effective correction, the dipole structure vanishes or is significantly suppressed in both comparisons of simulated retarding potential to e-gun as well as ^{83m}Kr measurements. As a next step, it is important to assign this effective shift, which is only valid for a 2.7 G setting in the analyzing plane, to the beamline element that is most likely causing it.

As mentioned above, a shift of the simulated FPD projection versus the real position in the analyzing plane can be caused by an inaccurate FPD position in the model. Further sources for the simulation shift can be unrecognized shifts or tilts of the

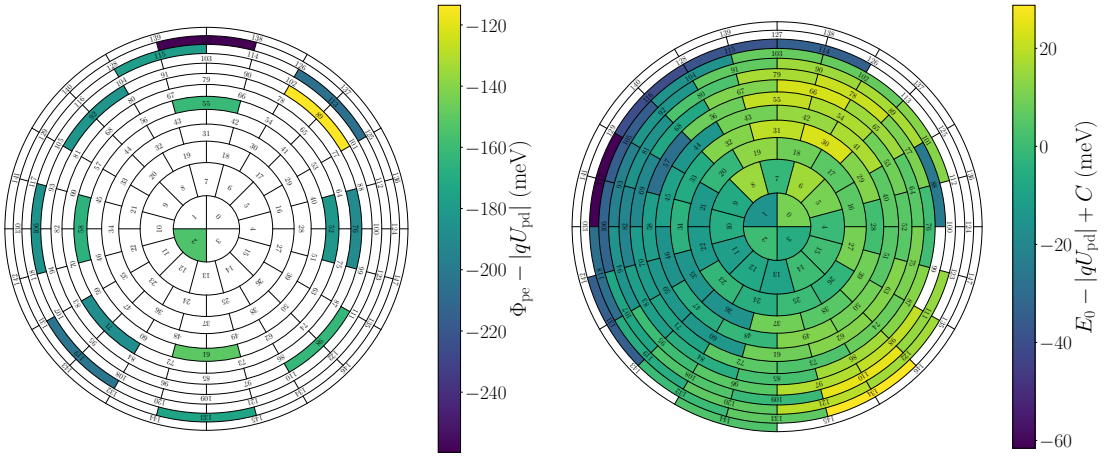

Figure 5.25.: **Comparison of e-gun potential edge Φ_{pe} and ^{83m}Kr K line position E_0 to the simulated potential depression qU_{pd}, after including the effective shift in the Kassiopeia simulation.** The dipole structure vanishes for the e-gun comparison and is significantly reduced for the ^{83m}Kr comparison due to the applied effective shift on the simulation. Nevertheless, deviations from the expected homogeneity remain.

PCH and DET cryostats and coils, as well as the position of the Main Spectrometer vessel in the Kassiopeia geometry model.
The Main Spectrometer vessel is per definition well aligned with the KATRIN coordinate system, as its center is the coordinate origin. A shift of the simulated retarding potential versus the vessel is not realistic, as the well-known spectrometer vessel produces the potential, and all vessel deformations are taken into account in the simulation (see also reference [Cor14]). A non-accounted Main Spectrometer misalignment in the simulation can therefore be excluded as reason for an inaccurate simulated position of the FPD projection in the Main Spectrometer.
The alignment of the PCH and DET cryostat relative to the coordinate system is thoroughly investigated with FaroARM® measurements. Additionally, the coil alignments within the cryostats are precisely measured with the Hall probe method (see section 4.1.2). We therefore expect, that the PCH and DET cryostat are correctly included in the Kassiopeia geometry model.
As discussed in section 4.1.2 based on the work by M. Deffert [Def17], the FPD wafer position is the most-likely source for inaccurate alignment in the Kassiopeia geometry model. Currently, there are no tools to precisely and accurately investigate the FPD wafer position, as soon as the wafer is integrated into the beamline. Additionally, further misalignment can come from the inhomogeneous cooling of the post-acceleration electrode surrounding the wafer [Def17]. A translation of the determined effective shift in equation 5.17 in the analyzing plane translates to an effective shift at the FPD of approximately 6.5 mm, as investigated by J. Behrens [BBM21]. A non-recognized misalignment on this order of magnitude is realistic for the FPD wafer position in the final beamline setup. We therefore draw as a conclusion, that the absolute FPD wafer position is the most-likely source of this wrong FPD projection position in the analyzing plane.

Based on a period summary in which the corrected FPD wafer position is included, an analysis of ^{83m}Kr measurements in the 6 G setting is performed. The dipole structure in the line position vanishes with the updated 6 G period summary [BBM21]. This indicates that the correction of the FPD position in the simulation is correct, as we can apply the 2.7 G-specific effective shift from equation 5.17 to a 6 G measurement. Nevertheless, it is necessary to find methods to directly review the FPD wafer position in the final beamline setup to test the findings of this alignment study.

Summary

In this thesis, we have shown that the complementary methods of e-gun potential edge and ^{83m}Kr K line measurements to investigate the retarding potential in the analyzing plane yield consistent results in the comparison to the Kassiopeia simulation. Both methods show a dipole-like structure in the shape comparison in contrast to the expectation of a constant offset.
We did find that the dipole-shaped structure can mostly be resolved by applying an effective shift in radial direction on the simulated position of the FPD projection in the analyzing plane. This indicates that the dipole structure is likely related to an inaccurate geometry model used for Kassiopeia simulations. By combining results of the work at hand, the effective shift can be traced back to the most-likely case of an inaccurate FPD wafer position in the geometry model, leading to an improved understanding of the alignment in the KATRIN beamline. However, further methods have to be applied to test the wafer alignment in the final KATRIN setup, independently of the e-gun and ^{83m}Kr measurement.
Having applied the effective correction in the simulation, the mean offset between simulated potential depression and measured e-gun edge yields -179 meV, which does not agree with the expected difference of 400 meV due to the differences in e-gun and Main Spectrometer work function. The deviation between the measured and expected offset is likely related to the absolute determination of the work function of the Main Spectrometer, since this depends on electrostatic simulations. Further studies with the updated FPD position are recommended to test the impact of this new geometry model on the estimated absolute value of the work function.

5.5.2. Magnetic Field

We presented in this chapter three tools that allow in principle to access the magnetic field strength in the analyzing plane inside the Main Spectrometer, namely Kassiopeia simulations, the e-gun, and the ^{83m}Kr $N_{2,3}$ line doublet. The e-gun cannot be used in the current setup due to the non-reproducibility of the motor stepper positions (see section 5.3.2), we therefore compare the findings of the ^{83m}Kr measurements with the Kassiopeia simulation in the following. An additional possibility to cross-check the Kassiopeia simulation is given by the comparison of simulation to measurements with magnetic field sensors close to the analyzing plane.

Measurements of the absolute magnetic field strength with the ^{83m}Kr $N_{2,3}$ line doublet are performed for the 1 G and 2.7 G configuration in this work. The analysis procedure is stated in section 5.4.3.
Due to the short measurement time of only few hours and the low intensity of the

^{83m}Kr $N_{2,3}$ line doublet, a pixel-wise analysis of the magnetic field strength in the analyzing plane is not possible. The statistics are therefore combined by summarizing the active FPD pixels in 14 segments based on similar transmission properties, the so-called patches. With this analysis strategy, high-precision results of the magnetic field strength in the analyzing plane with uncertainties on the order of 2 μT are achieved in the thesis at hand, improving the understanding of the Main Spectrometer transmission function.

The Kassiopeia simulation results for the analyzing plane are introduced and compared to measurements with magnetic field sensors at the Main Spectrometer vessel close to the analyzing plane in section 5.2.
As shown in section 5.2.3, the simulations deviate from the magnetic field measurements. The source for this deviation is mainly caused by single inaccurately aligned beamline solenoids in the Kassiopeia model (see section 5.2.2), non-accounted background fields, or possible misalignment of the large eLFCS coils (see section 5.2). As discussed in section 5.2.4, we use as uncertainty estimation for the simulated magnetic field strength in the analyzing plane the maximal deviation between measured absolute field by the magnetometers at the vessel and simulated absolute field. For the 1 G setting, this uncertainty estimation yields 4.5 μT, for the 2.7 G configuration 5.5 μT. It has to be noted that for both settings the measured absolute magnetic field at all six low-field magnetometers near the analyzing plane is smaller than the expectation from simulation.
Due to the patch-wise analysis of the ^{83m}Kr $N_{2,3}$ line doublet measurement, it is necessary to provide the simulated magnetic field strength for each patch for the following comparison. By exploiting the simulated pixel-wise period summary for the respective setting, we calculate the mean magnetic field in the analyzing plane of each patch by averaging over the pixels that form the respective patch.

The comparison of measured and simulated magnetic field for the 1 G (upper graph) and 2.7 G setting (lower graph) is shown in figure 5.26.
The simulated magnetic field in the analyzing plane and the ^{83m}Kr measurements agree within their uncertainties for the 1 G setting. The deviation between measurement and simulation is for all patches smaller than twice the combined uncertainty of both methods. The measured magnetic field is in average 4.7 μT smaller than the simulated field. This deviations is consistent with the comparison of simulated field and magnetometer measurements on the Main Spectrometer vessel. The difference between magnetic field simulation and measurement with ^{83m}Kr seems to be constant for all patches at the current sensitivity. If the deviation between measurement and simulation is mostly caused by remnant and induced magnetization from magnetic material in the Main Spectrometer hall (see section 5.2.2), we expect that the deviation increases from the central patch 0 to the outer patch 4 due to the decreasing distance to the possible sources.
The comparison of simulation and measurement for the 2.7 G configuration yields similar results as the analysis of the 1 G setting. The absolute measured magnetic field is smaller for all patches than the expectation from simulation, although both methods agree within their uncertainties. The measured magnetic field is on average 5.8 μT smaller than the simulation prediction for all patches. Similar to the 1 G comparison, this indicates that the method of comparing magnetometer measurements on the vessel to simulation is a valid approach to estimate the uncertainty on the simulated magnetic field inside the vessel. The difference of 5.5 μT, found in

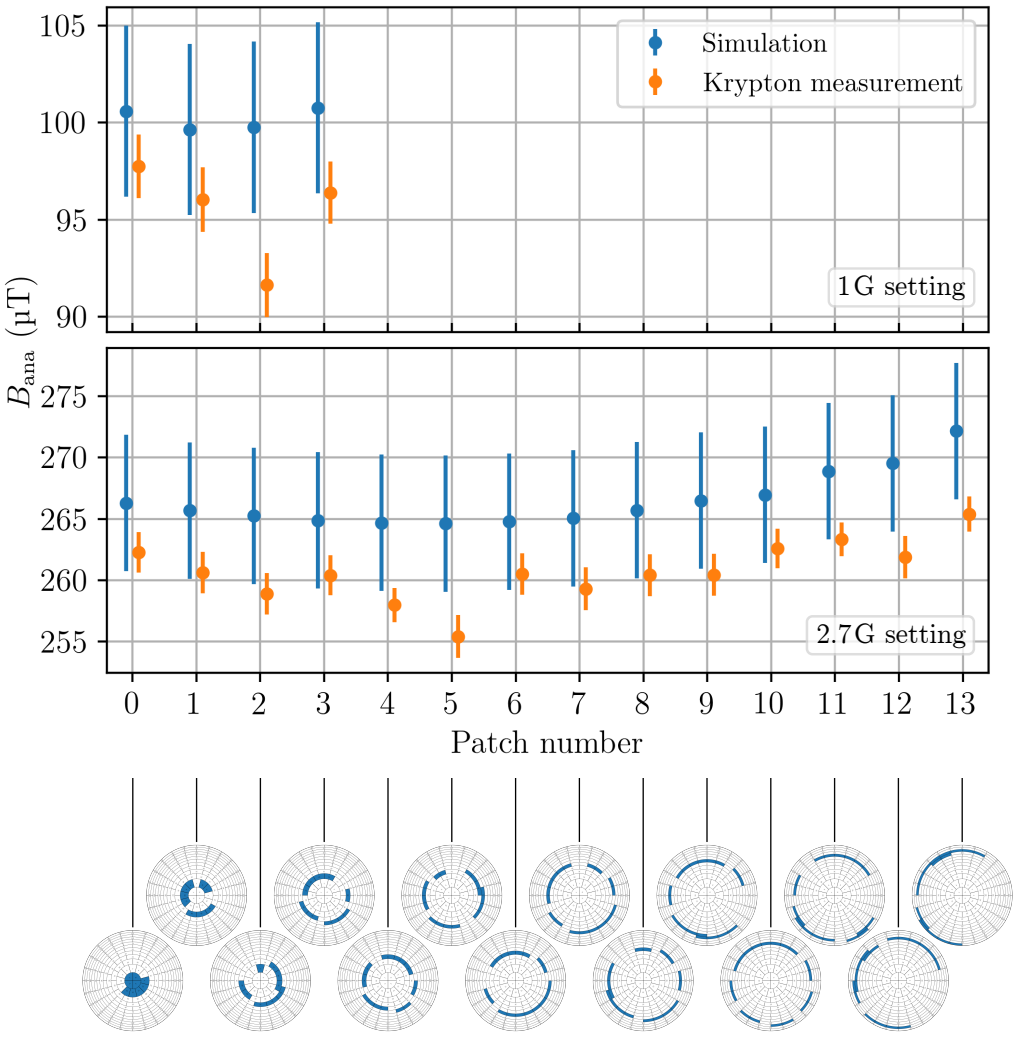

Figure 5.26.: **Comparison of simulated magnetic field strength in the analyzing plane with the results of ^{83m}Kr $N_{2,3}$ line doublet measurements for the 1 G setting (upper graph) and 2.7 G setting (lower graph) as function of the patch number.** Simulation and measurement are consistent within their uncertainties. The simulation tends to overestimate the magnetic field compared to the ^{83m}Kr results, as also indicated by the comparison of simulation with magnetometer measurements.

the comparison of magnetometer measurement with simulation, is consistent with the average difference of 5.8 μT. Also in the 2.7 G comparison, the difference between simulated magnetic field and ^{83m}Kr measurement seems to be constant over the patch number at the current sensitivity level. Due to the absence of this trend in the 1 G and 2.7 G comparison, we can therefore conclude that the deviation between simulation and measurement does not seem to be influenced by remnant and induced magnetization in the Main Spectrometer hall.

In summary, the comparison of magnetic field measurements in the analyzing plane and simulations show consistent results, within their uncertainties. The simulation tends to overestimate the absolute magnetic field strength close to the Main Spectrometer (see section 5.2.3). This behavior is confirmed for the magnetic field inside

the Main Spectrometer by high-precision ^{83m}Kr measurements, improving the understanding of the Main Spectrometer transmission function as consequence of the thesis at hand. Measurements with a high-intensity ^{83m}Kr source have been conducted in the second half of 2021, and their analysis is not yet complete. These measurements allow us to pixel-wise measure the magnetic field strength in the analyzing plane in various settings, including the 6 G setting, that can be used as input for neutrino mass analyses. Furthermore, these measurements enable one to refine the Kassiopeia simulations for the analyzing plane, in combination with the measurements of the low-field magnetometers at the Main Spectrometer vessel.

6. Characterization of the Shifted Analyzing Plane

In the neutrino mass measurement campaigns conducted with the 6 G setting, the background rate is 0.22 cps [Ake+21a], mainly caused by the volume-dependent Main Spectrometer contribution. As this background rate is a factor 20 larger than that planned for the final sensitivity [KAT05], a reduction of the Main Spectrometer background is crucial to achieve the KATRIN sensitivity goal with the same measurement time. A promising approach for strong background reduction is the Shifted Analyzing Plane (SAP, see also section 5.1.2). To benefit from the reduced background of the Main Spectrometer in neutrino mass sensitivity, it is necessary to precisely and accurately characterize the SAP transmission function properties to avoid large SAP-related systematic uncertainties. The goal of this chapter is therefore to characterize the SAP transmission function to a precision and accuracy that meets the final KATRIN requirement on a single systematic uncertainty contribution of $\Delta m^2_{\nu,\mathrm{sys}} \leq 7.5 \times 10^{-3}\,\mathrm{eV}^2$.
In section 6.1, we introduce the working principle of the SAP, present first background measurements, and discuss expected characteristics from simulations. Subsequently, e-gun measurements are employed to perform a first characterization of the potential depression and the magnetic field in the SAP on selected FPD pixels in section 6.2. In section 6.3.3, the transmission properties of the whole SAP are characterized by analyzing measurements of the $^{83\mathrm{m}}$Kr K line. In the following section 6.4, a similar procedure is repeated by measuring the integral shape of the $^{83\mathrm{m}}$Kr $N_{2,3}$ line doublet. In section 6.5, the SAP transmission function properties determined through the various methods are compared and analyzed with respect to the systematic uncertainty contributions to the neutrino mass analysis.

6.1. Basic Idea

As described in section 5.1.2, a large part of the Main Spectrometer background component stems from the ionization of Rydberg atoms in the flux tube volume between analyzing plane and the FPD. A reduction of this volume leads to a reduced background rate at the FPD. One approach, shown in section 5.1.2, makes use of the fact that an increase of the magnetic field strength in the Main Spectrometer reduces the radial extent of the flux tube. However, this approach worsens the spectrometer energy resolution. The SAP principle, based on an idea by C. Weinheimer, is to shift the analyzing plane closer to the FPD (see figure 6.1). This reduces the volume between analyzing plane and the FPD, and thus the background rate, without loss of energy resolution [Dyb19; Sch20a]. An additional advantage of shifting the analyzing plane closer to the FPD is a significant change of the storage conditions for

background electrons from ^{219}Rn decays (see section 5.1.2), leading to non-adiabatic losses of stored electrons [Bie20]. In the symmetric Nominal Analyzing Plane (NAP) configuration, used in KNM1 and KNM2, stored background electrons from ^{219}Rn decays cause a non-Poissonian background component [Ake+21a; Ake+21b]. This results in a major systematic uncertainty contribution of $\Delta m^2_{\nu,\mathrm{sys}} = 0.11\,\mathrm{eV}^2$ in KNM2 [Ake+21a]. It is expected that this systematic uncertainty contribution vanishes, or is at least significantly reduced, in the SAP setting due to unfavorable storage conditions [Kir20].

6.1.1. Design of the Shifted Analyzing Plane

Two aspects need to be considered for an optimal design of the SAP, namely the MAC-E filter principle as well as hardware limitations.
As described in section 3.1.1, the magnetic field change along one cyclotron motion has to become sufficiently small to achieve an adiabatic transformation of transversal to longitudinal energy, allowing for proper energy analysis of electrons with large incident angles. Lower magnetic fields in the analyzing plane are in principle preferred due to better energy resolution, however, the extent of the flux tube in the Main Spectrometer has to be considered. The radial extension of the SAP, and thus also the minimally allowed magnetic field in the analyzing plane, is limited by the available space at the cone-shaped downstream end of the Main Spectrometer. For further details on the magnetic field design of the SAP, see reference [Bie20].
The high-voltage setup of the Main Spectrometer is optimized for electron energy analysis in the NAP. Its retarding potential is mainly given by the applied voltage on the vessel as well as the configuration of the inner electrode system. Since the inner electrode setup cannot be easily modified, it is necessary to find a possibility to produce a retarding potential maximum at the downstream end of the Main Spectrometer in the existing system. Simulations show that the upstream flat cones (ring 12-14, see figure 3.9) of the inner electron system can be employed to produce a potential barrier around the axial position of $z \in [5, 7]\,\mathrm{m}$ (see table B.3) [Dyb19]. To avoid effects of early or late retardation, the interplay of magnetic and electric field has to be optimized. In particular, the minimum of the magnetic field strength and the maximum of the retarding potential should be at the same axial position for optimal electron energy resolution. However, simulations show that the LFCS is not able to produce a magnetic field minimum at the position of maximum retarding potential [Dyb19]. As consequence, the LFCS was modified to the extended LFCS (eLFCS). The eLFCS has a larger number of windings for nine LFCS coils [Thü20], leading to stronger sustainable magnetic fields in the Main Spectrometer. Additionally, five new coils were added mostly at the downstream side of the Main Spectrometer, allowing for more dedicated fine-shaping of the SAP magnetic field [Thü20].

With the new electric and magnetic field configuration, the analysis points of the SAP form a surface in the shape of an elliptical paraboloid (see upper graph of figure 6.1). In contrast to the NAP, the SAP is thus not a flat plane. The analyzing points for β-decay electrons are located at $z \approx 5.2\,\mathrm{m}$ at the SAP radial center and around $z \approx 6.6\,\mathrm{m}$ for electrons at the outer rim, according to the Kassiopeia simulation. In the NAP configuration, all electrons are analyzed at $z \approx 0\,\mathrm{m}$. The strong axial shift

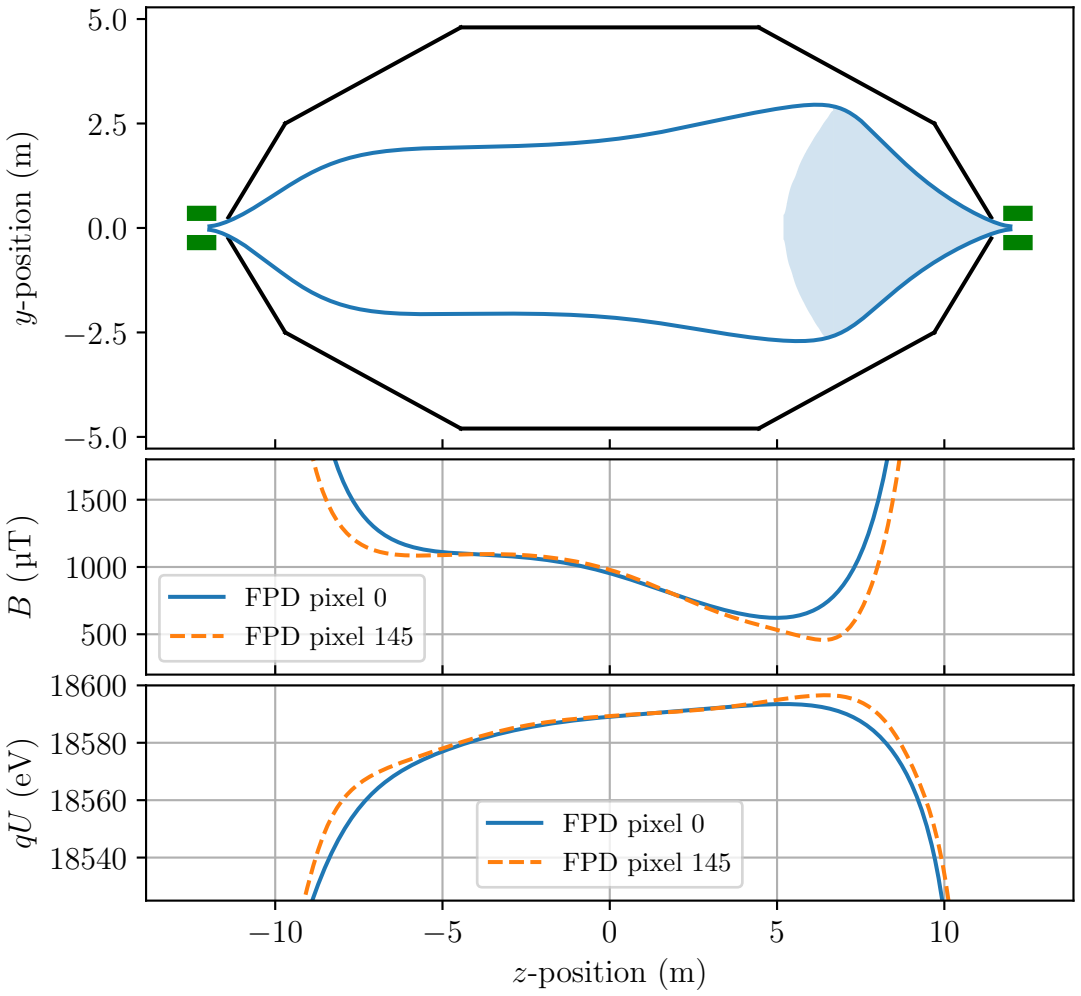

Figure 6.1.: **Simulated spatial coordinates of the flux tube in the SAP setting (upper graph), the axial strength of the magnetic field (central graph), and the retarding potential (lower graph) in the Main Spectrometer.** The volume between analyzing plane and FPD, that contributes to the Main Spectrometer background rate on the FPD, is visualized in the upper graph as blue-shaded area. The central graph presents the magnetic field in the Main Spectrometer for the central FPD pixel 0 and the outer pixel 145. A large radial dependence close to the analyzing point at $z \approx 6\,\mathrm{m}$ is visible. The simulated retarding potential is shown in the lower graph. Also here, a large radial dependence of few eV exists between the central and the outer FPD pixel close to the analyzing point. Used settings for the simulation given in tables B.2 and B.3.

of the SAP analyzing points, in combination with the location in the area of the conical spectrometer segments, introduces severe retarding potential and magnetic field inhomogeneities within the analyzing plane that need to be considered in the analysis.

6.1.2. SAP Background Measurements and Simulations

Various background measurements were performed after the LFCS hardware modifications to the eLFCS in April 2020 to characterize the individual background components in the Main Spectrometer SAP configuration.
Measurements with warm copper baffles reveal the impact of different storage conditions of background electrons stemming from ^{219}Rn decays [Har15] in SAP and NAP on the overall background rate. The nominal 6 G analyzing plane yielded a Main Spectrometer background rate of 0.445 cps at the 117 active FPD pixels, while the SAP showed a background rate of only 0.156 cps [LB20; Hin22]. The overall rate reduction of nearly a factor of three in the SAP setup confirms the simulation expectation of unfavorable storage conditions for background electrons in this configuration [Kir20]. We can therefore expect that the non-Poisson background component, caused by the electrons from ^{219}Rn decays, decreases, leading to better sensitivity on the neutrino mass.
Measurements with cold baffles reproduce the experimental setup of tritium β scans. The Main Spectrometer background rate was 190 mcps in the 6 G setting for the 117 active FPD pixels in April 2020 [LB20]. The change to SAP configuration reduced the background by a factor of two to 95 mcps [LB20; Hin22]. This improvement directly affects the statistical neutrino mass uncertainty (see also reference [Kle14]).

The Main Spectrometer in the NAP configuration has good axial and radial homogeneity for the electromagnetic fields close to the analyzing plane. This avoids significant systematic biases if simulations with minor inaccuracies in the geometry model are used as input for neutrino mass analysis. Additionally, the retarding potential and magnetic field can be assumed to be constant within one pixel or even over the whole FPD projection [Ake+21b]. The peak-to-peak variation over the FPD projection in the 6 G NAP configuration is on the order of $\delta B_{\mathrm{ana}} = 2.7\,\mu\mathrm{T}$ for the magnetic field strength, and on the order of $\delta qU_{\mathrm{ret}} = 169\,\mathrm{meV}$ for the retarding potential, according to the Kassiopeia simulations. The areas with maximal difference in electromagnetic field strengths within the NAP thereby have a distance of 2.7 m.
The homogeneity conditions are fundamentally different for the SAP. The Kassiopeia simulation yields an inhomogeneity of $\delta B_{\mathrm{ana}} = 273.3\,\mu\mathrm{T}$ for the SAP magnetic field strength (see right graph of figure 6.2), a factor 100 larger than the NAP. The difference of the magnetic field shape close to the SAP between two pixels is shown in the central graph of figure 6.1, the spatial distance between the analyzing points of these two pixel projections is 3.9 m. Similarly, the retarding potential inhomogeneity of the SAP is a factor 25 larger compared to the nominal 6 G setting, namely $\delta qU_{\mathrm{ret}} = 4.76\,\mathrm{eV}$ (see left graph of figure 6.2). Consequently, the electric and magnetic field spread within one FPD pixel projection into the SAP can be larger than for the whole FPD projection to the NAP. This needs to be considered in the neutrino mass analysis, as discussed further below. Additionally, the comparably large electromagnetic field inhomogeneity also influences the usage of Kassiopeia field simulations as accurate input for neutrino mass analysis. Sensitivity studies indicate that the SAP magnetic field needs to be known to the 1 % level or better in order to not counteract the smaller SAP statistical neutrino mass uncertainty with additional systematic uncertainties [Sch20a]. As shown in section 5.5.1, Kassiopeia model misalignment on the mm-scale is possible. In the SAP configuration, this

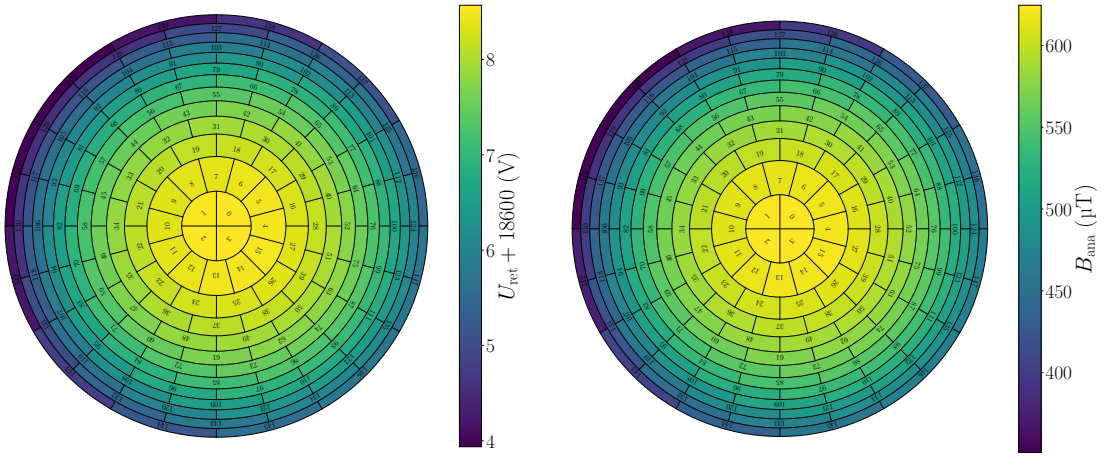

Figure 6.2.: **Simulated retarding voltage U_{ret} (left plot) and magnetic field B_{ana} (right plot) in the SAP.** According to the simulation, the potential depression causes an offset at the center of the analyzing plane of 8.6 V, which decreases at larger radii to 3.9 eV. Similarly, the magnetic field strength in the analyzing plane reaches its maximum at the center of the analyzing plane with estimated 625 μT and decreases down to 351 μT at the outer-most FPD ring. Simulation taken from period summaries, provided by J. Behrens.

inaccurate alignment can cause magnetic field biases on the order of 10 μT or larger due to the field inhomogeneity, especially at the outer FPD pixels. This possible bias in simulated fields exceeds the 1 % accuracy requirement, consequently it is not appropriate to use simulated electromagnetic fields as input for neutrino mass analysis. We therefore do not discuss SAP field simulation results in detail in the following, but only mention it as comparison.

The goal of the following sections is thus to experimentally determine the SAP transmission properties. A. Schaller presents first test measurements of the transmission function of a preliminary SAP setting in reference [Sch20a]. In the thesis at hand, we focus on the detailed SAP characterization with comparably high-statistics $^{83\mathrm{m}}$Kr measurements in the SAP configuration which is used for neutrino mass β scans. Additionally, electric and magnetic field measurements with the e-gun are performed in this work and compared to $^{83\mathrm{m}}$Kr results to cross-check for possible biases in the $^{83\mathrm{m}}$Kr analysis.

6.2. E-Gun Characterization Measurements

The e-gun working and measurement principle, as well as the analysis tools to investigate the analyzing plane fields, are described in detail in section 5.3. Here, we focus on the discussion of results and the SAP-specific properties that must be taken into account when putting the findings in context.
It is important to mention that the cross section of the e-gun beam is significantly smaller than the area of an FPD pixel projection in the analyzing plane. Based on the characterization measurements of the e-gun beam in reference [Sac20], we estimate the extent of the e-gun beam in the SAP. The mean beam radius is expected

to be smaller than 4.6 mm leading to a cross section of smaller than $6.6 \times 10^{-5}\,\mathrm{m}^2$. The maximal cyclotron radius for electrons that are not reflected by the magnetic mirror in the PCH is roughly 10.5 mm. The projected area of a bulls-eye pixel to the SAP is $0.16\,\mathrm{m}^2$ with an estimated distance of pixel center to boundary of 0.45 m [Beh21]. The size of the e-gun beam in the SAP is vanishingly small compared to the dimension of a pixel projection. The transmission function measurement with the e-gun thus describes only a narrow part of the overall pixel's transmission function. This is not a problem in NAP characterization measurements, but this property must be considered in the comparison of the measurement results to other methods due to the larger intra-pixel variations of the SAP electromagnetic fields.
In the following, we report on the analysis results of e-gun potential measurements in section 6.2.1. Subsequently, measurements of the SAP magnetic field with the e-gun are discussed in section 6.2.2. In both sections, we will directly compare the measurement results to expectations from simulation.

6.2.1. Retarding Potential Measurements

We measured the e-gun potential edge at several pixels. The measurement setup, procedure, and pre-processing of the data is the same as described in section 5.3.3. To enable, in principle, a detailed comparison of e-gun measurement results with simulations despite the larger intra-pixel field inhomogeneity, we attempted to measure the e-gun transmission at well-defined locations in each pixel. The on-axis pixels were measured at the pixels' center, the off-axis pixels close to boundaries to neighboring pixels. The determination of the exact e-gun beam position on the pixel was time consuming, as the WGTS magnetic dipoles to steer the e-gun beam in azimuthal and radial direction need several minutes to change the magnetic field. Additionally, they are slightly misaligned with respect to the horizontal and vertical axis of the FPD. It was therefore, especially for the off-diagonal pixels, cumbersome to find the best measurement position at each pixel. During a nominal measurement day of 8 hours, it was only possible to find the best measurement position at five to seven off-diagonal pixels. In total, transmission functions at 28 different FPD pixels in the SAP configuration were measured.
We try to break the strong correlations between the parameters of the Peaberry e-gun model by describing all transmission function measurements with one multi-pixel model with global and local fit parameters, similar to section 5.3.3. The separation in local and global parameters is the same as for the analysis of the 2.7 G setting measurement in section 5.3.3. As first step of the minimization process, the minimization of the negative logarithmic likelihood function is performed with an algorithm using the Trust Region Reflective method [New+14], before the uncertainties and correlations are investigated by the emcee sampler.

All transmission function measurements comprise 1010 rate measurements with the e-gun. The Peaberry model describing the measured data has 118 free fit parameters. The best-fit model to the data is shown in figure 6.3. The overall normalized $\chi^2 = 1.05$ is in good agreement with the expectation from statistical fluctuations of the measured rates. The residuals do not show any structure, which indicates that the Peaberry model correctly describes the measured data.
The measured SAP potential edge positions in the FPD projection are shown in the

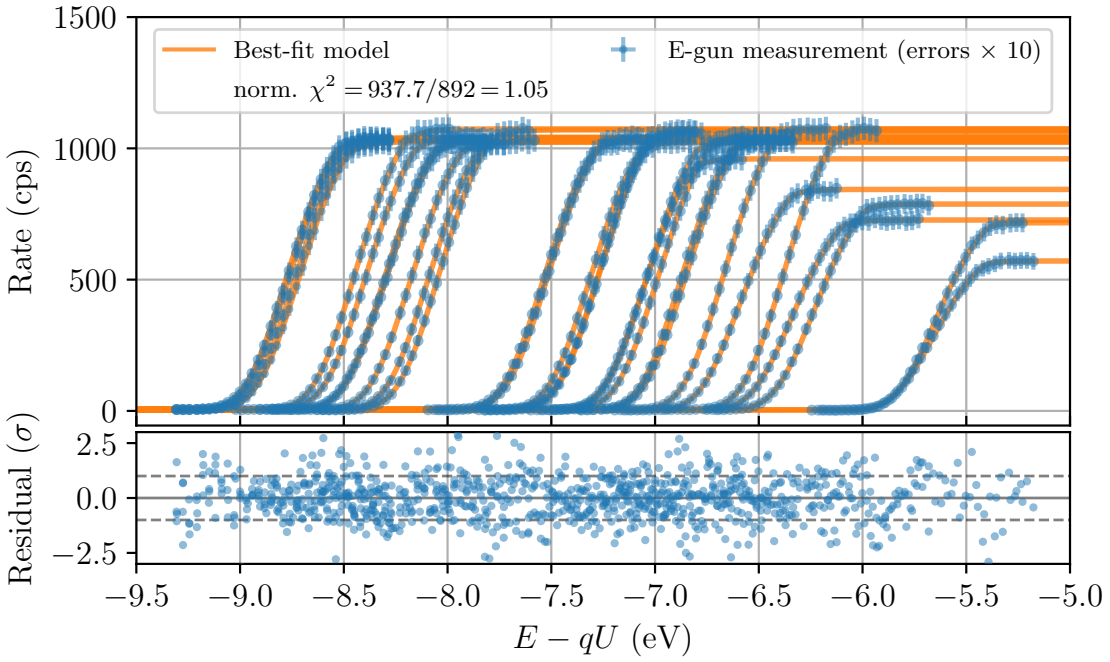

Figure 6.3.: **E-gun transmission function measurements at 28 FPD pixels in the SAP configuration to investigate the retarding potential shape.** The measured e-gun rate (blue) is shown as a function of the electron's surplus energy, the best-fit multi-pixel model (orange) is also shown in the upper panel. The amplitudes of the transmission functions decrease for pixels at larger radii in the analyzing plane (measurements at $E - qU > -6.5\,\text{eV}$) due to a geometrical cut-off of the e-gun electron beam in the rear section. The fit residuals are shown in the lower panel.

left plot of figure 6.4. The uncertainty on the individual potential edge measurement is on the order of 3 meV. The shape of the edge positions on the individual pixels is as expected. The maximum potential edge is measured at the center of the analyzing plane, as expected from the simulation of the potential depression (see figure 6.2). The central potential edge is situated approximately 3 eV higher than the one at the outer rim of the flux tube, this also agrees with simulation results.
The difference between measured edge position and simulated potential depression is presented in the right plot of figure 6.4. Similar to the findings in section 5.5.1, the comparison of e-gun measurement and simulation has a dipole-shaped structure. The difference is positive on the left side and negative one on the right side of the detector. The peak-to-peak fluctuation is greater than 600 meV, the most-likely reason for the dipole structure is inaccurate Kassiopeia model alignment.

6.2.2. Magnetic Field Measurements

The principle of magnetic field measurements in the analyzing plane with the e-gun is explained in section 5.3.2. A transmission function measurement with tilted e-gun plate angle θ_1 leads to a shifted transmission function δE relative to measurement

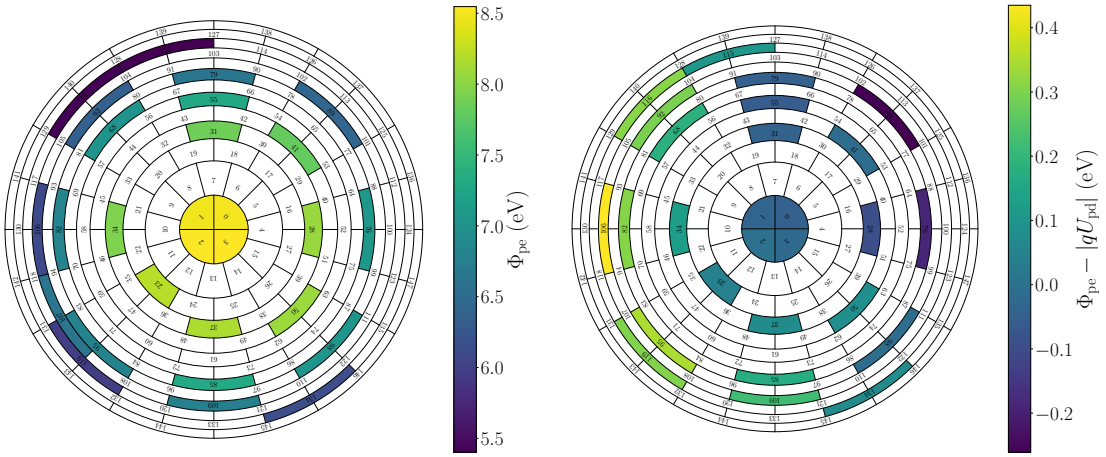

Figure 6.4.: **Results of the potential edge Φ_{pe} measurement with the e-gun (left plot) and comparison of analysis result to simulation (right plot), visualized in the FPD projection.** The uncertainty on the measured potential edge is approximately 3 meV. The decreasing edge position from roughly 8.5 to 5.5 eV from center to outer pixels in the left plot reflects the potential depression variation over the SAP. The comparison of the measured potential edge to the simulated potential depression yields a dipole-like structure with more positive differences on the left side and negative ones on the right side of the detector. The measured potential edge at FPD pixel 107 is not used for the comparison of simulation to measurement.

with non-tilted plate angle θ_0 of

$$\delta E = E \cdot \frac{B_{\mathrm{ana}}}{B_{\mathrm{ref}}} \left(\sin^2 \theta_1 - \sin^2 \theta_0 \right)$$

with E being the electron energy, and B_{ana} the magnetic field in the analyzing plane. The reference magnetic field for the electron pitch angles is denoted as B_{ref}. This measurement principle requires good knowledge of the mean pitch angle set at the e-gun to obtain accurate and precise results on the magnetic field in the analyzing plane. Due to reproducibility problems of the e-gun plate angle, this measurement could not be performed for the NAP. Nevertheless, we can perform magnetic field measurements with the e-gun in the SAP in a relative measurement approach by employing the NAP as reference.
In a first step of the relative measurement approach, transmission function measurements were performed at one central bulls-eye pixel in the NAP configuration and mean zero pitch angle θ_0. Afterwards, we performed transmission function measurements with the same pitch angle θ_0 at several pixels of interest in the SAP configuration. As next step, the e-gun plates was tilted once with the stepper motor to a not-accurately known higher pitch angle θ_1. The measurement procedure was repeated with this pitch angle θ_1. Transmission function measurements were performed at the central bulls-eye pixel in the NAP configuration and afterwards at the pixels of interest in the SAP setting. This procedure bypasses the reproducibility problem of the stepper motor, as it does not need to be moved for each transmission function measurement. The good knowledge on the NAP allows determination of both pitch angles from the transmission function measurements in the NAP config-

uration. The results on the pitch angles are then used as input parameters for the SAP analysis.

Reference Measurement

The goal of the reference transmission function measurement is to determine the angular distribution parameters for the zero and elevated pitch angle as input for the SAP analysis. Therefore, the transmission function at each pitch angle is measured twice, once in the 1 G setting and once in the 6 G setting. The 1 G configuration has excellent energy resolution and is therefore sensitive to the initial electron energy distribution. The energy resolution of the 6 G setting is worse compared to that of the 1 G setting. The measurement in the 6 G configuration is thus more sensitive to the combined effects of electron angular and energy distribution. By evaluating the measurements at different settings, we try to break the strong correlations between magnetic field and angular distribution.

Similar to the e-gun edge potential analysis above, we also use a multi-pixel model to describe all four transmission functions at once to reach the best sensitivity and to break the correlations. The parameters of the initial electron energy distribution are treated globally, they are common for all four transmission functions. The mean angle and angular width are shared parameters among the measurements at the same pitch angle. Background and e-gun rate can be different for each transmission function measurement and are thus introduced as local parameters. Simulated magnetic fields are used as input parameters for the model calculation, their systematic uncertainties are included via the pull-term method. We use as reference for the mean angle and angular width the PCH magnetic field, as it is the best-known field in KATRIN beamline. According to section 4.1.1, we assume 0.1 % relative uncertainty on the simulated PCH field. The errors on the 1 G and 6 G NAP magnetic field are estimated to $\Delta B_{\mathrm{ana,1G}} = 4.5\,\mu\mathrm{T}$ and $\Delta B_{\mathrm{ana,6G}} = 6\,\mu\mathrm{T}$, based on the principle described in section 5.2.3. We additionally apply a penalty term on the zero pitch angle θ_0, as it is determined to be the mean zero pitch angle with the method described in reference [Sac20]. The uncertainty on this method is conservatively assumed to be 1°. Since we have chosen the PCH field as reference field, the best-fit results of the angular distribution parameters are given relative to the PCH field strength.
Prior to the analysis, the measured data is pre-processed as described in section 5.3.3. Selected scan steps at large electron surplus energy have to be excluded from analysis due to a geometric cut-off of the electron beam in the e-gun setup, leading to significant e-gun rate drops at the FPD. Transmission functions at large pitch angle suffer in general from geometric cut-off effects, leading to smaller electron rate in full transmission.
Similar to former optimization problems involving the Peaberry model, the likelihood optimization is performed in two steps. First, an algorithm based on the Trust Region Reflective method minimizes the negative logarithmic likelihood function, before the ensemble sampler emcee investigates the parameters' uncertainties and correlations.

The reference measurement as well as the best-fit model are shown in figure 6.5. The blue data points are the measurements performed in the 6 G configuration, the

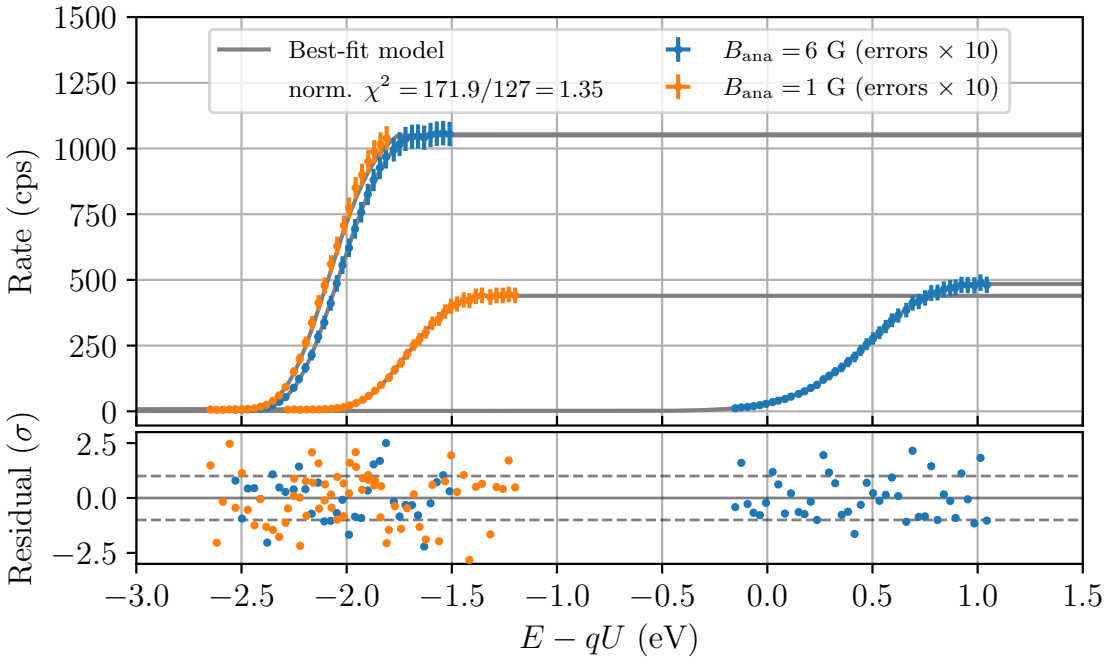

Figure 6.5.: **Reference measurement in the NAP configuration to determine the elevated pitch angle of the e-gun for magnetic field measurements in the analyzing plane.** The orange data points are the measured rate in the 1 G NAP setting at zero and elevated pitch angle, the blue ones are those in the 6 G configuration. The best-fit model describing all four transmission function parameters is drawn in gray. The orange transmission function measurement at $E - qU \approx -2\,\mathrm{eV}$ is conducted at zero mean angle, the shifted one at $E - qU \approx -1.7\,\mathrm{eV}$ at elevated mean angle. The same principle holds for the 6 G measurement.

orange ones the 1 G setting. The transmission function shift within one measurement configuration is given by the two different pitch angles θ_0 and θ_1, according to equation 5.9. A small shift between the two e-gun measurements conducted at θ_0 (orange and blue measurement at $E - qU \approx -2\,\mathrm{eV}$) exists, this is due to the non-vanishing e-gun angular width and the difference in NAP magnetic field settings. The gray lines represent the combined best-fit model with partially shared parameters. The Peaberry model describes the measured data well, indicated by the normalized $\chi^2 = 1.35$ and the well-distributed fit residuals.
The emcee sampler steps close to the best-fit minimum for the parameters of interest as well as for the parameters describing the NAP magnetic fields are presented in figure 6.6. The mean angle $\hat{\theta}_0$ fulfills the expectation of zero pitch angle, the scatter histograms indicating the correlations with the other free fit parameters show vanishing correlation, confirmed by the numerical result of the correlation coefficient. The fit does not extract new significant information from the data in terms of the mean angle $\hat{\theta}_0$, it is dominated by the penalty term introduced in the likelihood function. The angular width at zero pitch angle is $\sigma_{\theta,0} = (6.1 \pm 0.5)^\circ$, which is in good agreement with the results obtained in section 5.3.3. The best fit for elevated pitch angle is $\hat{\theta}_1 = (71.4 \pm 0.6)^\circ$. The fit result is strongly correlated to the angular width at this angle with correlation coefficient $\rho = 0.95$. The angular width at elevated pitch angle is estimated to be $\sigma_{\theta,1} = (7.2 \pm 0.3)^\circ$ based on the likelihood

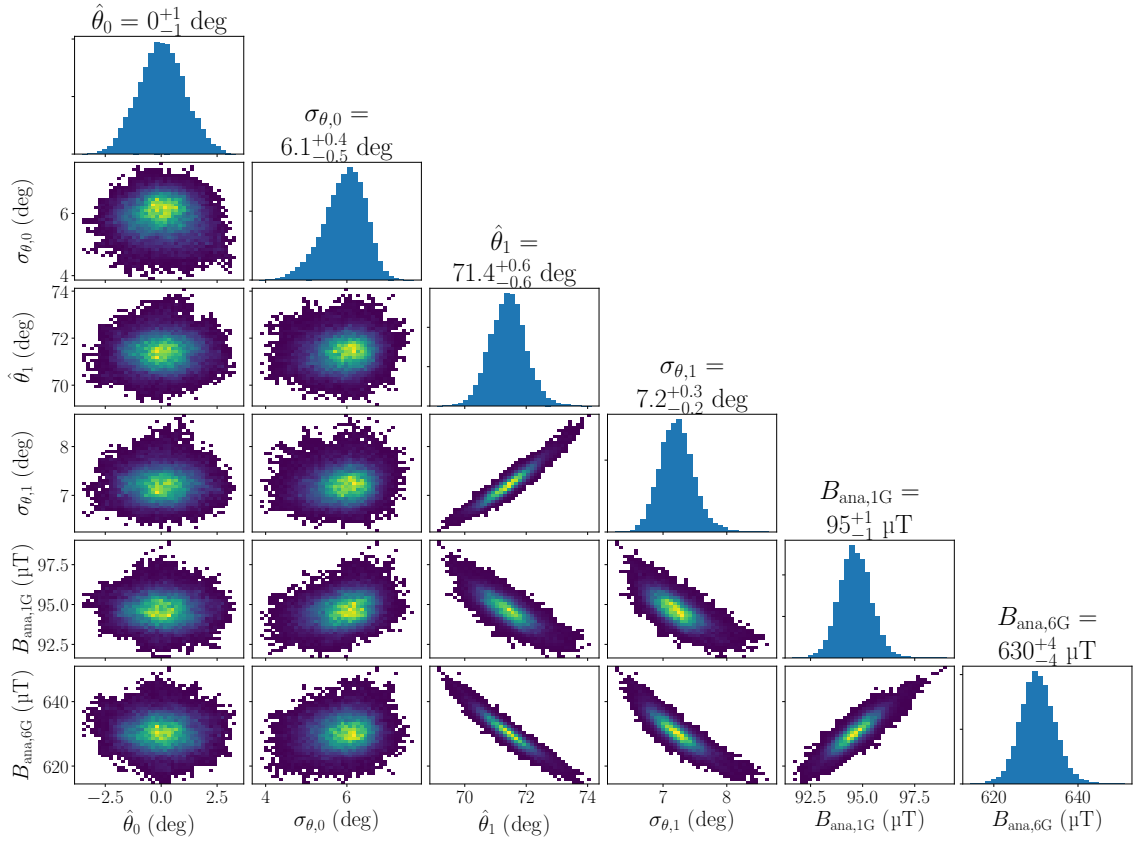

Figure 6.6.: **Emcee sampler steps in the best-fit minimum for the NAP reference measurement to determine the elevated e-gun pitch angle.** The elevated pitch angle is determined to be $\hat{\theta}_1 = (71.4 \pm 0.6)^\circ$ and strongly correlates with its angular width of $\sigma_{\theta,1} = (7.2 \pm 0.3)^\circ$. Both parameters also show strong correlations to the 6 G NAP magnetic field. The parameters' distributions to estimate the uncertainties and correlations are based on 2×10^5 emcee evaluations of the likelihood function.

optimization. The slightly larger angular width compared to the zero pitch width meets the expectations from former e-gun commissioning measurements. Both angular parameters at elevated pitch angle show strong or moderate anti-correlations to the NAP magnetic fields. For future measurements it is recommended to introduce transmission function measurements at one additional configuration, for example in the 2.7 G setting. This would further break the correlations and lead to larger robustness of the fit result.
The parameters that are introduced in the following SAP analysis as penalty terms in the likelihood function, are thus

$$\begin{aligned} \hat{\theta}_0 &= (0 \pm 1)^\circ, \\ \sigma_{\theta,0} &= (6.1 \pm 0.5)^\circ, \\ \hat{\theta}_1 &= (71.4 \pm 0.6)^\circ, \\ \sigma_{\theta,1} &= (7.2 \pm 0.3)^\circ. \end{aligned} \tag{6.1}$$

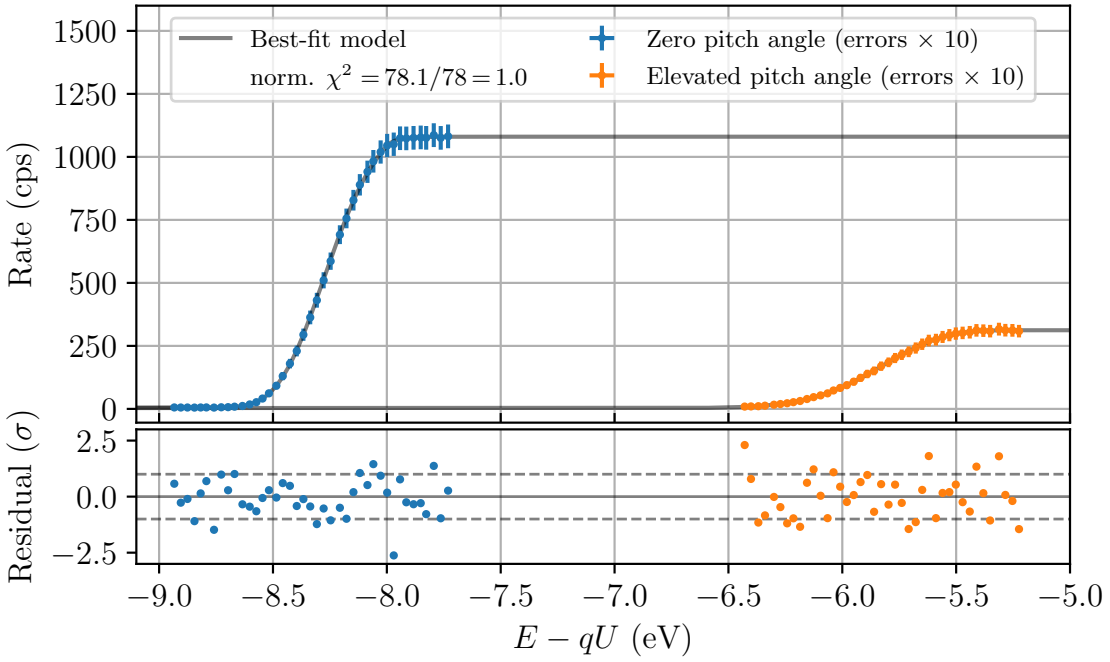

Figure 6.7.: **SAP magnetic field measurement with the e-gun at pixel 28.** The blue data points in the upper graph are the transmission function measurements at zero pitch angle, the orange ones at elevated pitch angle. The best-fit model to describe the measurement is shown in gray, the magnetic field in the analyzing plane is estimated to be $B_{\text{ana}} = (610 \pm 3)\,\mu\text{T}$. The fit residuals, shown in the lower graph, do not show any structure.

Magnetic Field Measurement in the SAP

The e-gun SAP magnetic field measurement is performed at ten pixels. We perform a pixel-wise analysis. Each pixel is analyzed individually, independent of the analysis result of other pixels.
The transmission function is measured at both pitch angles for each pixel. Within one pixel-wise analysis, the two measured transmission functions share the same potential edge, the same magnetic field settings, and the same energy distribution. The absolute e-gun rate, the background as well as the angular distribution are individual fit parameters of the transmission functions. The results of the reference measurement on the angular distributions (see equation 6.1) as well as their correlations are included as penalty terms in the likelihood function.
The measured data of the magnetic field measurement and the best-fit model is shown for FPD pixel 28 in figure 6.7. The normalized $\chi^2 = 1.0$ indicates good compatibility of the data with the model. The shift between the two transmission functions due to the pitch angle change provides information about the magnetic field in the analyzing plane, according to equation 5.9. The magnetic field in the analyzing plane at pixel 28 is estimated to be $B_{\text{ana}} = (610 \pm 3)\,\mu\text{T}$. This is a good result in terms of precision for the systematic KATRIN uncertainty. The fit parameter describing the magnetic field has strong anti-correlations to the value of the elevated pitch angle ($\rho = -0.94$), and the angular width at elevated pitch angle ($\rho = -0.72$). This underlines the necessity of additional information about the angular distribution from reference measurements. In future measurements, this

Table 6.1.: **Measured SAP magnetic field with the e-gun at ten investigated pixels.** The normalized χ^2 is acceptable for all measurements. The magnetic field measurement has uncertainties of 3 µT to 4 µT. Compared to the measurement, the simulated magnetic field on the investigated pixels tends to an average of 16 µT smaller field strengths for all pixels.

Pixel	χ^2/ndof	Measured B_{ana} (µT)	Simulated B_{ana} (µT)
1	101.8/79	638 ± 4	622 ± 2
3	75.4/61	637 ± 4	625 ± 2
28	78.1/78	610 ± 3	601 ± 9
50	78.7/73	603 ± 3	592 ± 11
55	98.1/78	566 ± 3	555 ± 13
85	83.7/73	552 ± 2	545 ± 18
89	130.1/69	523 ± 3	521 ± 20
92	135.9/73	520 ± 4	482 ± 20
106	119.4/73	498 ± 3	461 ± 23
109	78.1/68	523 ± 2	512 ± 23
Mean difference:		16 µT	

strong correlation could be tackled by adding a second elevated pitch angle in the SAP measurements to break the correlations and to foster the method's robustness. Further correlations of the SAP magnetic field to other fit parameters are negligibly small with $|\rho| < 0.35$.

The results of the SAP magnetic field measurements with the e-gun for all ten investigated pixels are summarized in table 6.1. The normalized χ^2 varies between 1.0 and 1.9 for the individual fits. This is slightly larger than the expectation value, however, the best-fit residuals are well-distributed, without any pattern. We therefore expect that the analysis results for the SAP magnetic field are unbiased and that the increased normalized χ^2 stems from an underestimated systematic uncertainty in the e-gun measurement. The expected magnetic fields from the Kassiopeia simulation are also printed in table 6.1 as reference.
The e-gun measurements show excellent precision on the measured magnetic fields in the analyzing plane with uncertainties at or below 4 µT for all ten investigated pixels. The simulation uncertainty is between 2 µT to 23 µT. It is obtained by an interpolation approach to estimate the intra-pixel variations of the SAP magnetic field. We decide to state this quantity as uncertainty on the simulation, as the exact e-gun beam position in radial and azimuthal direction on the pixel is unknown. The comparison of measurement and simulation indicates stronger measured magnetic fields than expected from simulations for all investigated pixels. This difference is significant for the inner-most pixels. Towards the outer rings, the simulation and measurement agree within their uncertainties, as the simulation uncertainty grows from the center to the outer rings. The discrepancy between simulation and mea-

surement emphasizes the importance of direct magnetic field measurements to enable unbiased neutrino mass analysis in the SAP configuration.

Conclusion

We have shown that the e-gun enables high-precision magnetic field and electric potential measurements of the SAP. Nevertheless, the e-gun measurements have two disadvantages.
Firstly, the cross section of the e-gun electron beam is significantly smaller compared to the dimension of one FPD pixel in the analyzing plane. Thus, e-gun measurements represent the transmission function properties only at a narrow part of the pixel. This would not be a problem in the NAP configuration, however, the SAP configuration has non-negligible intra-pixel magnetic and electric field variations. To account for this problem, several e-gun measurements must be performed at one pixel to describe the averaged transmission parameters of one pixel, leading to the second disadvantage.
E-gun measurements at several pixels require time-consuming operator-based preparations that cannot be trivially automatized. The necessary time for the SAP magnetic field measurement including preparation time is roughly two days for ten pixels, with one magnetic field measurement per pixel. Several e-gun measurements per pixel on all 148 FPD pixels are not feasible without significant loss of measurement time for tritium β scans.
Consequently, SAP electromagnetic field measurements with the e-gun cannot describe all SAP properties. However, the high-precision measurement results show that the e-gun is a powerful tool to provide a pixel-wise cross-check for other determination methods of the SAP transmission function, for example ^{83m}Kr measurements.

6.3. Characterization with Krypton-83m K-32 Conversion Line

As shown in section 5.4, ^{83m}Kr conversion electrons are suitable probes to investigate the transmission properties of the Main Spectrometer. The decay electrons from gaseous ^{83m}Kr in the WGTS illuminate the FPD pixels in the same way β-decay electrons do. This is a huge advantage especially for the SAP characterization, as intra-pixel variations of the electromagnetic fields in the analyzing plane are automatically correctly considered. This bypasses the necessity of performing several measurements on the same pixel, as it is necessary with the e-gun. Similar to chapter 5.4, we employ the ^{83m}Kr K and $N_{2,3}$ conversion lines for the characterization of the SAP properties. The K line is chosen due to its vicinity to the tritium endpoint and thus the natural measurement range of KATRIN, the $N_{2,3}$ line doublet due to its narrow line widths leading to excellent sensitivity on the analyzing plane fields. In this section we focus on the characterization measurements with the K conversion line, the $N_{2,3}$ measurements are discussed in section 6.4.
In the following section 6.3.1, the parameters of interest to describe the SAP transmission function, as well as the measurement and analysis principle to extract them, are introduced. The experimental results of the ^{83m}Kr measurements and analyses

are presented in the sections 6.3.2 and 6.3.3. Finally, in in section 6.3.4, we calculate the parameters of interest for the SAP characterization based on the analyses results obtained in sections 6.3.2 and 6.3.3.

6.3.1. Procedure

The parameters that need to be extracted from the ^{83m}Kr measurements to describe the transmission functions of the Main Spectrometer are the central values for the SAP magnetic and electric fields that each FPD pixel projection experiences, as well as the energy broadening that accounts for the electromagnetic field variations within the individual pixels. The energy broadening parameter is introduced in the SAP neutrino mass analysis of tritium data as a broadening of the transmission function. For the ^{83m}Kr data analysis in the following, the energy broadening is included in the model as the width of the Gaussian kernel σ_g that is used for the convolution of the differential decay spectrum before the calculation of the integral spectrum (see chapter 5.4 and figure 5.19).
The SAP magnetic field and the energy broadening define, together with the source and PCH magnetic field, the shape of the transmission function. The retarding potential depression links the applied high voltage on the Main Spectrometer vessel and inner electrode system with the true retarding potential in the analyzing plane. All three parameters, SAP magnetic field B_{ana}, squared energy broadening σ_g^2, and retarding potential depression $qU_{\text{pd,SAP}}$, can be extracted from ^{83m}Kr K line measurements via a relative method, based on an idea by A. Fulst, A. Lokhov, and C. Weinheimer (see also reference [Ful20]).

As discussed in section 5.4.2, it is not possible to directly derive the magnetic field or the absolute electric retardation in the analyzing plane from K line measurements. However, we can employ a relative measurement, similar to the above-described e-gun magnetic field measurements. Also here, ^{83m}Kr K line measurements in the NAP Main Spectrometer setting are used as reference measurements, the analysis results are used as input for the analysis of measurements in the SAP configuration [Ful20]. In the following, we explain the analysis procedure by example of a pixel-wise analysis. A schematic visualization of the procedure is shown in figure 6.8. The underlying idea of the relative measurement is that a certain flux tube part in the WGTS is, to first-order approximation, always mapped onto the same FPD pixel, despite the electromagnetic field configuration in the Main Spectrometer.

The K line position is an indicator for the electric retardation in the analyzing plane. As derived in section 5.4.2, the measured ^{83m}Kr line position E_0 is

$$E_0 = E_{\text{kin}}^{t,s} + (\Phi_{\text{src}} + V_{\text{start}} - \Phi_{\text{ms}}) - qU_{\text{pd}}.$$

The source and Main Spectrometer work functions are denoted as Φ_{src} and Φ_{ms}, V_{start} is the electron starting potential in the WGTS. The potential depression is labeled as qU_{pd}, the net kinetic emission energy of the ^{83m}Kr conversion electron is $E_{\text{kin}}^{t,s}$. The comparison of the measured line position at a certain pixel in the NAP setting $E_{0,\text{NAP}}$ with the one in the SAP-configuration $E_{0,\text{SAP}}$ consequently yields

$$\begin{aligned}\delta E_0 &= E_{0,\text{NAP}} - E_{0,\text{SAP}} \\ &= qU_{\text{pd,SAP}} - qU_{\text{pd,NAP}}\end{aligned}$$

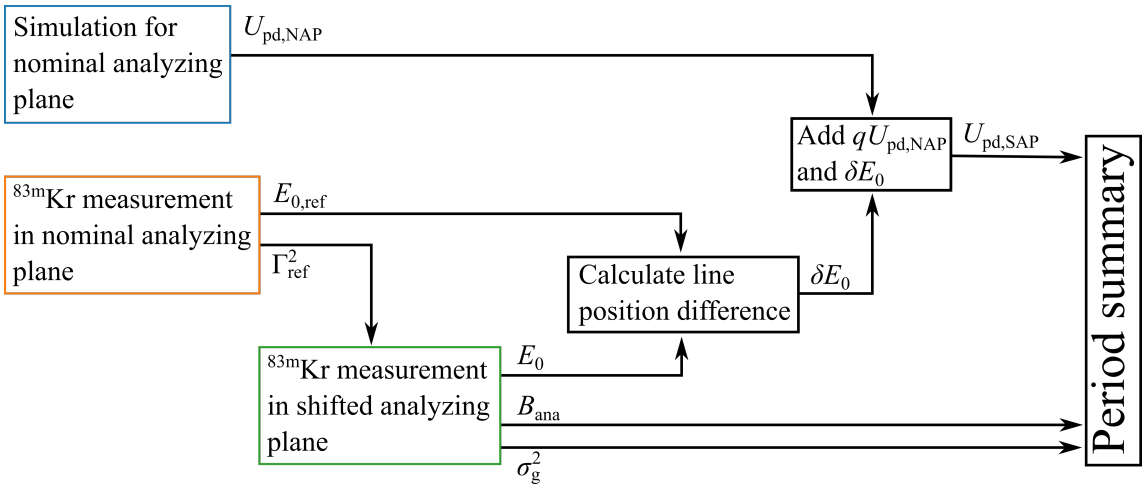

Figure 6.8.: **Schematic visualization of the relative measurement method to derive the SAP transmission function parameters from $^{83\mathrm{m}}$Kr K line measurements.** The reference squared K line width Γ^2_{ref} is estimated by measurements in the NAP and introduced as penalty-term in the SAP analysis. Afterwards, the magnetic field B_{ana} in the analyzing plane and the squared energy broadening σ^2_{g} are directly extracted from the SAP analysis. The SAP potential depression $U_{\mathrm{pd,SAP}}$ is calculated by comparing the K line positions in the NAP and SAP measurements, taking into account the simulated NAP potential depression $U_{\mathrm{pd,NAP}}$.

where $qU_{\mathrm{pd,NAP}}$ is the setting-specific potential depression for the NAP and $qU_{\mathrm{pd,SAP}}$ for the SAP configuration. The source work function as well as the electron starting potential cancel due to the assumption that the same flux tube part in the WGTS is always mapped to the same FPD pixel, independent of the NAP or SAP setting in the Main Spectrometer. Additionally, we implicitly assume that the Main Spectrometer work function is the same at the location of the NAP and SAP. Simulations estimate the work function difference of NAP to SAP to be below $\mathcal{O}(10\,\mathrm{meV})$ [Beh21], it is therefore expected to be smaller than the $^{83\mathrm{m}}$Kr sensitivity. The potential depression in the SAP setting is thus

$$qU_{\mathrm{pd,SAP}} = \delta E_0 + qU_{\mathrm{pd,NAP}}$$

and therefore independent of any possible radial impacts of the source or Main Spectrometer work functions as well as possible radial starting potentials. By using the NAP electric field simulation, we can obtain the potential depression for the NAP setting and thus determine the one for the SAP. However, $^{83\mathrm{m}}$Kr and e-gun measurements in the NAP configuration showed, that the NAP electric field simulation is accurate to a few hundred mV, but suffers from inaccurate model alignment (see section 5.5.1). To avoid this problem, we use only one $^{83\mathrm{m}}$Kr line measurement at one central pixel as reference measurement for the calculation of δE_0 and the derivation of the simulated potential depression. Using a central pixel has an advantage over using a pixel at larger radii in the analyzing plane because its simulated potential depression is more robust against model misalignment due to the elliptic paraboloid shape of the potential depression. The SAP potential depression at FPD

pixel i is consequently calculated as

$$\begin{aligned} qU_{\mathrm{pd,SAP,i}} &= E_{0,\mathrm{ref}} - E_{0,\mathrm{SAP,i}} + qU_{\mathrm{pd,ref}} \\ &= \delta E_{0,i} + qU_{\mathrm{pd,ref}}, \end{aligned}$$

with the reference line position measured at a central pixel $E_{0,\mathrm{ref}}$ and the simulated potential depression $qU_{\mathrm{pd,ref}}$ for this pixel in the NAP configuration. For this approach, we have to implicitly assume that the source and Main Spectrometer work functions have a radially constant impact on the potential in the $^{83\mathrm{m}}$Kr sensitivity limit to a few tens of meV. Additionally, the source starting potential also has to be constant in the radial direction on a similar level. Simulations [Beh21] and measurements indicate that these assumptions are valid to the necessary sensitivity.
The magnetic field strength B_{ana} in the SAP as well as the squared energy broadening σ_{g}^2 are simultaneously determined by the fit of the integral $^{83\mathrm{m}}$Kr spectrum to the SAP K line measurement. As the relatively large natural K line width of $\Gamma \approx 2.71\,\mathrm{eV}$ has a similar impact on the measured spectrum as the magnetic field in the analyzing plane, it is necessary to disentangle both effects for the SAP analysis [Ful20]. Therefore, a reference line width Γ_{ref} is measured in the NAP setting [Ful20], similar to the reference line position for potential depression calculation. The uncertainties on the NAP fields have to be taken into account in the determination of the reference line width, contributing to an uncertainty on the width $\Delta\Gamma_{\mathrm{ref}}$, given by the statistical and systematic uncertainty. The reference line width and its uncertainty are then introduced as a penalty term in the SAP analysis, allowing us to disentangle the impact of the magnetic fields on the integral spectrum from the line width. Due to the non-negligible natural K line width, the integral $^{83\mathrm{m}}$Kr spectrum has a rather smeared shape, compared to the sharp one of the $\mathrm{N}_{2,3}$ line doublet (see also figure 5.16 and 5.19). The shape effects of the expected pixel-wise energy broadenings are tiny on the integral K line spectrum and strongly correlated to the parameter describing the magnetic field in the analyzing plane. To get robust fit results on the energy broadening, it is thus necessary to artificially increase the measurement statistics in the analysis, as the measured rates on a single pixel are too small to disentangle the SAP magnetic field from energy broadening.
Lokhov and Weinheimer therefore propose to summarize the 125 pixels in 14 groups of pixels [LW20], the so-called patches, as presented in section 5.4.3 (see figure 5.20). Eight to nine pixels with similar transmission function properties, as determined in pixel-wise K line analyses, form one patch (see figure 5.20). Each patch is then analyzed with respect to its SAP transmission function properties, given by potential depression, magnetic field, and energy broadening. The grouping of the pixels into patches introduces an additional energy broadening, however, it is kept at minimum as pixels with similar transmission functions are within one patch. The main advantage of the patch-wise analysis is of course the increased statistics within one patch compared to a single pixel that allows extracting the energy broadening from the fit. Additionally, the calculation time is significantly shorter compared to the pixel-wise analysis, as only 14 spectra instead of 125 have to be analyzed. Nevertheless, the period summary that summarizes the field setting in tritium measurements, and is used as input for neutrino mass analysis, requires the field to be estimated for each pixel individually. This is not feasible with the patch-wise determination of the transmission function measurements. However, as it is planned to perform the neutrino mass analysis with SAP setting also in the patch-wise approach, it is

sufficient to determine the potential depression, the magnetic field, and the energy broadening for each patch.

Those systematic uncertainty contributions that are common between the analysis of the reference and the SAP measurement do not have to be considered in the relative method, as they cancel out. These uncertainties are separately included in subsequent neutrino mass analysis, an inclusion here would lead to a double consideration of these uncertainties. Systematic uncertainty contributions of this kind are the source and the PCH magnetic fields, for example.

6.3.2. Reference Measurement in Nominal Analyzing Plane

The measurement data used for the reference analysis is the same as used for the investigation of the potential depression in the NAP setting (see section 5.4.2). The fit model applied to describe the data is also similar to the analysis performed in section 5.4.2, but rather than a pixel-wise analysis we perform a patch-wise analysis in the following. The parameters of interest in the analysis here are the line position for the calculation of the SAP potential depression, and the line width as input for the SAP analysis.
The ^{83m}Kr K line was measured with a 2.7 G magnetic field setting in the analyzing plane over several scan steps of the retarding potential in the range from 17819 eV to 17850 eV. The beamline magnetic fields were at nominal operational field strength. The total measurement time amounted to roughly 12.5 hours, distributed over several scans. The data of the individual scans are combined with the stacking approach (see also section 3.3.6). Specifically, the rates measured at the same scan steps of all ^{83m}Kr scans are added and the voltage reading for that scan step is averaged over all scans.
The model fit to the data is the integral spectrum as calculated with the SSC software package. A linear, energy-dependent background model (see also section 5.4.2) is included since the measurement takes place below the tritium endpoint and is thus influenced by β-decay electrons of residual tritium from the rear wall. Similar to section 5.4.2, we use the simulated magnetic field strength of the analyzing plane for each patch as input of the integral spectrum calculation. The same holds for the source and the PCH magnetic fields. In the relative method, it is necessary to only include the uncertainty on the analyzing plane field in the analysis of the reference measurement, as it differs from the one in the SAP measurement. The uncertainty on the analyzing plane field is considered with the pull-term method in the fit of the model to the data. The mean of the Gauss-shaped penalty term in the likelihood is the patch-wise simulated field, the width is 5 μT as derived in section 5.2.3. Scattering of ^{83m}Kr conversion electron scattering off gas in the WGTS is not considered in the analysis as the scattered electrons do not contribute to the rate in the analysis window (see also section 5.4.2). Due to the large count rates in each patch, we assume the count rates to be following a Gaussian.

Patch-Wise Analysis

The model described above is fit with the KaFit framework to the measured rates for each of the 14 patches individually. The normalized χ^2 for all the fits is distributed

around the expectation value of one, indicating good agreement of model and data within the measurement uncertainties. The averaged squared line width is $\Gamma^2 \approx 7.31\,\mathrm{eV}^2$, and the uncertainty on the individual value for one patch is on the order of $\Delta\Gamma^2 \approx 0.04\,\mathrm{eV}^2$. The measured line widths do not show any patch-dependent structure. The distribution of the 14 measured line widths is in good agreement with statistical fluctuations and thus with a constant line width over all patches.
The patch-wise analysis has the advantage that it is computationally fast and can easily be parallelized, since the patch-wise fits are independent. On the downside, the patch-wise fits allow the magnetic field in the analyzing to assume unrealistic values, as discussed in the following. The comparison between $^{83\mathrm{m}}$Kr magnetic field measurements and simulations in the NAP configuration show that the simulation overestimates the field strength for all patches for the 2.7 G setting (see section 5.5.2). However, the implementation in the patch-wise analysis allows the magnetic field in the analyzing plane to be below the simulation in one patch and above in the neighboring patch, which is not in agreement with the comparison result. In a multi-patch analysis, we have the possibility to fix the offset in magnetic field strength between neighboring patches while at the same time allowing for a global shift in magnetic field strength for all patches.

Multi-Patch Analysis

The multi-patch analysis comprises a model that contains global fit parameters which are shared for all patches, and local parameters which are treated individually for each patch. The best-fit values for the parameters are then simultaneously determined in a global likelihood optimization.
The normalization of the $^{83\mathrm{m}}$Kr spectrum, the line position, and the background model parameters are introduced as local variables in the likelihood optimization, they are independent from the neighboring pixels. The K line width is a central input parameter for the SAP analysis below. As described in the previous paragraph, the estimated line width is constant over all patches. To reach the best sensitivity on the line width, we thus decide to implement it as a global fit parameter. The NAP magnetic field used in the fit shall now incorporate the behavior that the simulation tends to overestimate the field strength for all patches by a constant offset (see figure 5.26). We therefore define the NAP field used in the fit for a certain patch as the sum of the simulation for that patch plus an offset, which is the same for all patches. This definition enforces that the shape of the magnetic field in the analyzing plane stays as calculated by the simulations, while the overall field strength can still be varied. To avoid an unrealistically large global field offset, it is constrained by a Gauss-shaped penalty term in the likelihood with zero mean and width 5 μT (derived from section 5.2.3).

The comparison of measured spectrum to the best-fit multi-patch model is shown in figure 6.9. The normalized $\chi^2 = 1.01$ is close to the expectation value and thus indicates good agreement of data and model at the current level of sensitivity. The fit residuals, also presented in figure 6.9, are mostly randomly distributed, confirming the good agreement of model and measurement. The fit residuals tend to positive values for the smallest retarding potential scan step, this is likely caused by high-energetic tails of low-intensity satellite lines that are not included in the fit model.
The best-fit estimate for the global offset of the NAP magnetic field is $(-5 \pm 3)\,\mu\mathrm{T}$,

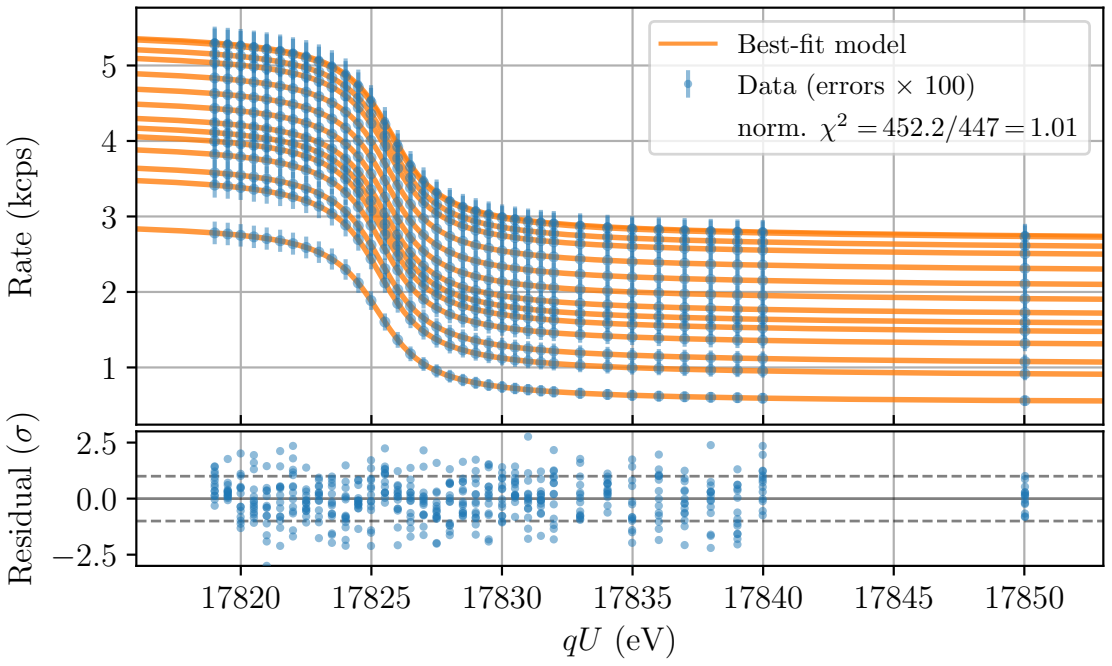

Figure 6.9.: **Multi-patch analysis of the NAP K line measurement to derive precise results on the squared line width.** The measured K line data at the 14 patches is shown in blue, and the best-fit model in orange in the upper graph. The lower graph shows the fit residuals which are randomly distributed, with the exception of a tendency at the smallest retarding potential scan step to positive values.

the likelihood optimization consequently prefers an NAP magnetic field that is approximately 5 µT smaller than the simulated field strength. This result is consistent with the comparison of simulation and $N_{2,3}$ line doublet measurements, where the offset is estimated to roughly 5.8 µT (see section 5.2.3). The best-fit model yields a squared line width of

$$\Gamma^2_{\text{ref}} = (7.33 \pm 0.02)\,\text{eV}^2.$$

This precise fit result is used as input for the SAP analysis performed below. Taking the square root of the fit parameter, we obtain a width of $\Gamma_{\text{ref}} = (2.705 \pm 0.004)$ eV. This is in good agreement with the values stated in reference [Vén+18b], indicating good accuracy of the analysis. The line position of patch 0 is also of interest, since we use it for the calculation of the SAP potential depression as a reference line position. The line position is determined to be

$$E_{0,\text{ref}} = (17\,826.395 \pm 0.008)\,\text{eV}.$$

Taking into account the simulated potential depression for patch 0 of $qU_{\text{pd,ref}} = -2.306$ eV leads to $E_0 = (17\,824.089 \pm 0.008)$ eV, 0.16 eV smaller than the value in reference [Vén+18b]. The offset can be explained by differences in the absolute WGTS starting potential and the impact of the Main Spectrometer work function. However, the offset is not a problem in the derivation of the SAP retarding potential, as it is expected to cancel in the relative measurement approach.

6.3.3. Measurement in Shifted Analyzing Plane

The K line was measured twice in the SAP configuration. It was first measured before the start of the third neutrino mass measurement campaign KNM3, in May 2020. The second measurement took place two months later, after KNM3. As both measurements were performed with the same ^{83m}Kr source generator and with similar column density of the carrier gas in the WGTS, the post-KNM3 measurement had 20 % less electron rate due to the decay of the mother isotope ^{83}Rb during KNM3. The net measurement time for the pre-KNM3 scans is 36 hours, and for the post-KNM3 scans 42 hours.
The reference squared line width, obtained from the measurements in the NAP configuration is $\Gamma^2_{\text{ref}} = (7.33 \pm 0.02)\,\text{eV}^2$. Including this as a penalty term in the likelihood allows us to directly determine the energy broadening and the magnetic field in the SAP by fitting the model for the integral spectrum to the data. The model that is used for the fit to the data is similar to the one used for the analysis of the patch-wise reference measurement in section 6.3.2, however, the magnetic field in the analyzing plane is now treated as free fit parameter and a non-vanishing energy broadening is taken into account.

Investigation of Inter-Patch Correlations

The reference line width is obtained by the multi-patch fit over all patches. It is necessary to consider that an uncertainty on the magnetic field in the NAP configurations affects all pixels or patches the same way, leading to a correlation of the best-fit parameters between various patches. A. Schwemmer discusses the impact of correlations between the patches on the systematic neutrino mass uncertainty for the SAP setting in reference [Sch20b]. The systematic uncertainty contributions due to uncertainties of the SAP magnetic field and energy broadening are significantly larger for maximal intra-patch correlations [Sch20b]. It is therefore necessary to investigate and quantify these inter-patch correlations carefully.

The model that is used for the analysis of the inter-patch correlations has to be a global, multi-patch model for all 14 patches in order to investigate the correlations among the patches. The only global parameter in the model is the squared line width, constrained by the penalty term from the reference measurement. All other parameters describing the integral spectrum are local fit parameters, inter alia the SAP magnetic field and the energy broadening. This leads to a total of 85 free fit parameters for 14 patches.
In the following, we analyze the pre-KNM3 SAP measurement with the global model with respect to the inter-patch correlations. A combined inter-patch analysis of the pre- and post-KNM3 measurement is computationally currently not feasible, as this would lead to 141 free fit parameters in the likelihood and significantly longer computational optimization time. The Minuit2 algorithm, used in the KaFit framework, has difficulty properly resolving the correlations among the parameters of the ^{83m}Kr spectrum, especially between the SAP magnetic field strength and the energy broadening. The inter-patch correlation study is thus performed with the KaFit emcee binding to properly investigate the correlations and uncertainties. The necessary time for emcee to converge and to explore the likelihood optimum takes more than 2×10^4 CPU hours.

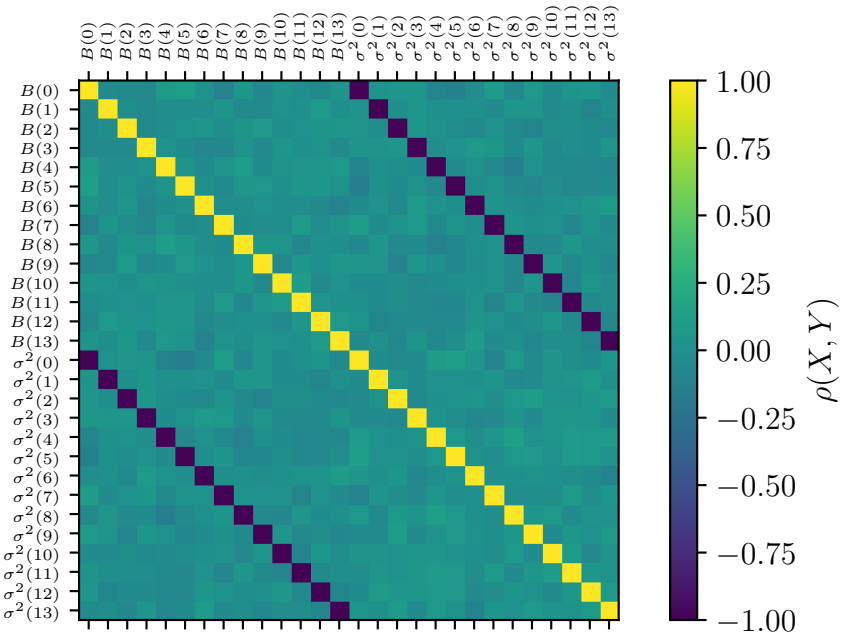

Figure 6.10.: **Correlation matrix of the SAP magnetic field B(PatchNumber) and the squared energy broadening σ^2(PatchNumber) parameters in the analysis of the SAP K line measurement.** The correlation matrix is calculated using 5×10^5 emcee sample steps per parameter close to the best-fit results. As expected, a strong anti-correlation between magnetic field and energy broadening is shown within one patch. The inter-patch correlations are weak and can be neglected in neutrino mass analysis.

The determined best-fit parameters for the model result in a normalized $\chi^2 = 1.2$, which is slightly larger than the expectation value from statistical fluctuations. One reason for this deviation could again be the negligence of the satellite lines at the lower end of the integral spectrum. The correlation matrix for the 14 patch-wise SAP magnetic fields and the 14 squared energy broadenings as determined by the emcee sampler close to the likelihood optimum is shown in figure 6.10. The fit parameter describing the SAP magnetic field strength $B_{\mathrm{ana},i}$ within a certain patch has a strong anti-correlation to the energy broadening parameter $\sigma^2_{\mathrm{g},i}$ of the same patch. This behavior is expected as both parameters have similar impact on the transmission function shape. The strong anti-correlation is also observed in a patch-wise analysis of the pre-KNM3 measurement, similar to the one performed in reference [Sch20b]. The determined correlation strength of the patch-wise analysis agrees with the estimated one from this multi-patch analysis. Inter-patch correlations of type $\rho\left(B_{\mathrm{ana},i}, B_{\mathrm{ana},j}\right)$, $\rho\left(B_{\mathrm{ana},i}, \sigma^2_{\mathrm{g},j}\right)$, or $\rho\left(\sigma^2_{\mathrm{g},i}, \sigma^2_{\mathrm{g},j}\right)$ with $i \neq j$ are weak with absolute values of $|\rho| < 0.15$. Since the impact of the small inter-patch correlations on the systematic neutrino mass uncertainty are negligible, they are currently not included in the neutrino mass analysis.
As a final test that the inter-patch correlations do not significantly affect the determined SAP transmission function properties, we compare the central values of the multi-patch analysis with the patch-wise analysis of the same data, in which

the patches are analyzed independently. The line positions, SAP magnetic field strengths, and energy broadening parameters obtained by the multi-patch analysis are consistent with the patch-wise approach. We therefore use the computationally fast patch-wise approach in the following, as it allows us to combine the pre- and post-KNM3 measurements to increase the sensitivity on the fit parameters of interest.

Multi-Period Patch-Wise Analysis

The K line was measured twice in the SAP configuration, once before and once after KNM3. The time distance between these measurements was roughly two months. The SAP magnetometers (see also section 5.2.1) show the same magnetic field at the vessel close to the SAP in both measurements, the deviations are on the order of less than 0.6 μT. We can therefore approximate that the SAP magnetic field and energy broadening is the same in both measurements. Consequently, the combination of the data of the two measurements in one analysis is possible, leading to a more precise result compared to a single analysis of only the pre- or post-KNM3 data.
In principle it should be possible to combine the data via the stacking approach, as we do not expect changes of the integral ^{83m}Kr spectrum shape before and after KNM3 besides the normalization and the magnitude of the energy-dependent background. However, there is an effect of apparently different K line positions in the pre- and post-KNM3 measurements that forbids the stacking approach. The calibration factor of the K35 voltage divider, used for the high-voltage monitoring of central inner electrodes and vessel, is determined with a novel method with higher precision directly before KNM3, resulting in a slightly different absolute high-voltage calibration factor between pre- and post-KNM3 measurements [Rod21a; Rod21c]. At the time of the data analysis, the calibration factor before KNM3 is not yet adjusted to the precise one after the campaign, leading to different high-voltage read-backs and thus seemingly different K line positions. The expected shift between the pre- and post-KNM3 measurement is roughly 117 meV [Rod21a]. A stacking of the two measurements would therefore result in an additional energy broadening, that we would wrongly classify as an SAP transmission property.

A work-around for this problem is the multi-period, patch-wise analysis. Each patch group is investigated individually from neighboring patches, as the inter-patch correlations are weak and the patch-wise optimization is computationally faster. Multi-period analysis in this context means that measurements taken at different points in time are analyzed using one model with common global and individual local parameters (see section 3.3.6). The global parameters in the analysis here are the K line width, the SAP magnetic field, and the energy broadening. Local parameters, that are individual in each measurement period, are the integral spectrum normalization, the line position, and the background model parameters. This amounts to a total of eleven free fit parameters for one patch-wise analysis.
The minimization of the negative logarithmic likelihood function is performed in two steps. Firstly, the data is minimized using the Minuit2 implementation of the KaFit framework. However, the fit parameters correlations within one patch are important for the uncertainty estimation on the measured SAP transmission function. We therefore use the KaFit emcee binding to investigate the parameter correlations around the likelihood optimum.

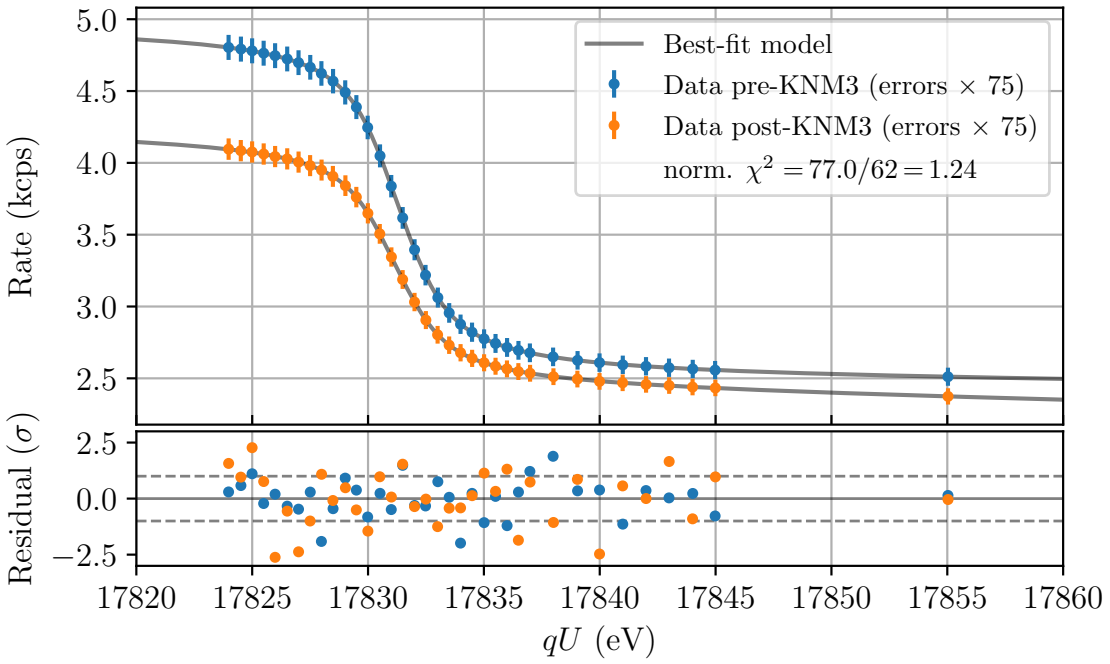

Figure 6.11.: **Multi-period analysis of the SAP K line measurement at patch 0 before and after KNM3.** The blue data is the measurement before KNM3, the orange one after KNM3. The difference in absolute ^{83m}Kr electron rate is caused by the decay of the mother isotope ^{83}Rb of ^{83m}Kr in between those two measurements.

The normalized χ^2 is distributed between 0.7 and 1.5 for all 14 multi-period, patch-wise analyses, indicating good agreement between model and measurement. The data obtained at patch 0 in the two measurements, as well as the best-fit model, is shown in figure 6.11. The normalized $\chi^2 = 1.24$ is reasonable. The fit residuals do not show any structure besides the familiar tendency to positive values at the low-energetic end of the spectrum due to the negligence of the satellite lines in the analysis.
The fit parameter correlations and uncertainties are investigated with the emcee sampler. The uncertainty estimations and the correlations among the fit parameters of interest for the analysis at patch 0 are shown in figure 6.12. The best fit for the SAP magnetic field and the energy broadening is

$$B_{\text{ana}} = (601 \pm 11)\,\mu\text{T},$$
$$\sigma_{\text{g}}^2 = (43 \pm 25) \times 10^{-3}\,\text{eV}^2.$$

Both uncertainties are statistically dominated. The fit parameters are strongly anti-correlated with a correlation coefficient of $\rho\left(B_{\text{ana}}, \sigma_{\text{g}}^2\right) = -0.97$. The determined line positions are

$$E_{0,\text{pre}} = (17\,832.67 \pm 0.03)\,\text{eV},$$
$$E_{0,\text{post}} = (17\,832.55 \pm 0.03)\,\text{eV}.$$

The distance between the two line positions is $(122 \pm 37)\,\text{meV}$ and thus in good agreement with the expectation of 117 meV due to the different high-voltage calibration factors. Both line positions are strongly correlated to the fit parameter

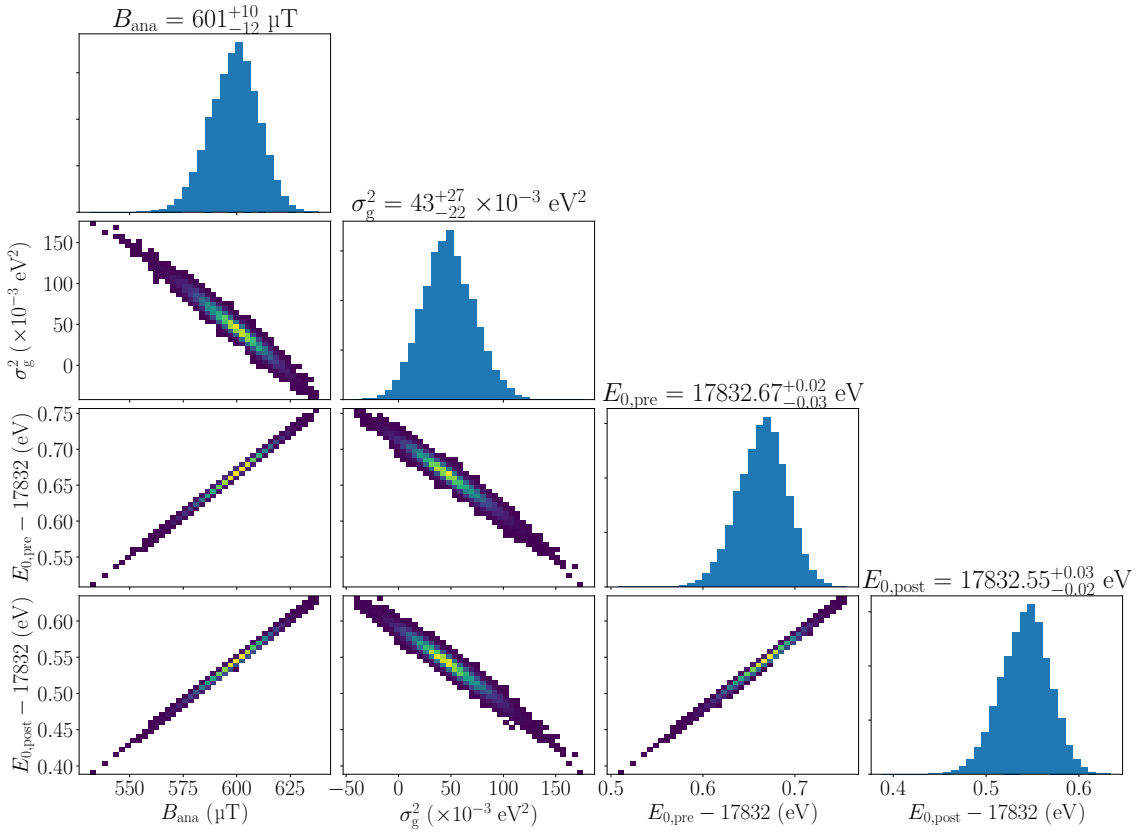

Figure 6.12.: **Corner plot of the emcee sampler steps for the parameters of interest in the multi-period fit of the data measured at patch 0.** The parameters of interest show strong correlations. The shown distributions summarize 8×10^4 sampler steps per parameter.

describing the SAP magnetic field with correlation coefficients $\rho\,(B_{\mathrm{ana}}, E_0) > 0.99$. The obtained best-fit parameters are used to extract the measured transmission function properties for the SAP. For the calculation of the SAP potential depression, we employ the measured line position of the pre-KNM3 measurement, as it is analyzed with the same calibration factor as the reference measurement.

6.3.4. Extraction of Transmission Function Properties

To obtain the parameters that describe the SAP transmission function properties, we follow the relative procedure as introduced in section 6.3.1.

The reference K line position is determined to be $E_{0,\mathrm{ref}} = (17\,826.395 \pm 0.008)$ eV (see section 6.3.2), the simulated NAP potential depression is $qU_{\mathrm{pd,ref}} = -2.306$ eV. With the patch-wise SAP line positions $E_{0,\mathrm{SAP,i}}$ (see section 6.3.3), we can thus calculate the patch-wise SAP potential depression from

$$qU_{\mathrm{pd,SAP,i}} = E_{0,\mathrm{ref}} - E_{0,\mathrm{SAP,i}} + qU_{\mathrm{pd,ref}}.$$

For patch 0, this gives an SAP potential depression of

$$qU_{\mathrm{pd,SAP,0}} = (-8.58 \pm 0.03)\,\mathrm{eV}.$$

The calculated SAP potential depressions are summarized for all patches in table 6.2. As expected, the potential depression decreases with increasing patch number. The difference between the central patch 0 and the outer-most patch 13 is nearly 3 eV, a consistent pattern is also found in the e-gun SAP potential analysis (see figure 6.4).

The SAP magnetic field and the energy smearing define the shape difference of the SAP transmission function with respect to the one of the NAP. The values, that are used for the calculation of the transmission function, as well as the correlation between these two, come directly from the likelihood optimization of the multi-period patch-wise analysis of the SAP K line measurement. The overview table 6.2 summarizes the obtained parameters for all patches. The SAP magnetic field strength decreases with increasing patch number by roughly 140 μT between the inner- and outer-most patch. For the energy broadening, we would expect an increasing broadening with patch number due to the elliptic paraboloid shape of the electromagnetic fields in the SAP. Pixels located at the outer part of the flux tube are therefore expected to have larger intra-pixel potential and magnetic field inhomogeneity compared to central pixels. However, we cannot make any statement about the shape of the energy broadening, as the uncertainties are comparably large with respect to the absolute values. The best-fit estimates for the energy broadenings are negative for few patches, but compatible with zero within their uncertainties. To allow for these statistical fluctuations into the negative regime, a continuation using the method of reference [Bel+08] is implemented in SSC [Mac16]. The anti-correlation between SAP magnetic field and the energy broadening, given by the correlation coefficient, is for all patches stronger than -0.97 .

A detailed comparison of the SAP transmission function parameters, measured with the K line, with e-gun, and further ^{83m}Kr measurements is given in section 6.5. The systematic uncertainty contributions to the measured neutrino mass analysis are also discussed.

6.4. Characterization with Krypton-83m $N_{2,3}$-32 Conversion Line Doublet

The parameters that are necessary to characterize the SAP transmission function are strongly correlated when derived from ^{83m}Kr K line measurements due to the non-vanishing intrinsic line width of the K line (see figure 6.12 and table 6.2). The $N_{2,3}$ line doublet enables us to perform a robust analysis of the necessary parameters due to the small natural line widths. The small line widths cause a sharp integral spectrum, leading to comparably small correlations between the free fit parameters (see section 5.4.3 and figure 5.22). In the following, we present an approach to determine the SAP transmission function parameters by investigating the integral spectrum of the $N_{2,3}$ line doublet.
The measurements analyzed in the following to derive the SAP transmission properties are performed with the continuous ramping mode of the inner electrode potential (see section 5.4.3). Although we correct for known systematic effects of this special ramping mode it is still possible that unknown systematic effects bias the analysis.

Table 6.2.: **SAP transmission function properties for all 14 patches, derived by analyzing the K line measurement.** The parameters of interest are the potential depression $qU_{\mathrm{pd,SAP}}$, the magnetic field B_{ana} in the analyzing plane, the squared energy broadening σ_{g}^2, and the correlation coefficient ρ between the last two parameters.

Patch	$qU_{\mathrm{pd,SAP}}$	B_{ana} (μT)	σ_{g}^2 $\left(\times 10^{-3}\,\mathrm{eV}^2\right)$	$\rho\left(B_{\mathrm{ana}}, \sigma_{\mathrm{g}}^2\right)$
0	-8.58 ± 0.03	601 ± 11	43 ± 25	-0.977
1	-8.42 ± 0.03	579 ± 14	82 ± 29	-0.982
2	-8.34 ± 0.03	598 ± 12	23 ± 26	-0.980
3	-8.21 ± 0.03	596 ± 12	14 ± 26	-0.978
4	-8.07 ± 0.03	600 ± 11	-16 ± 24	-0.975
5	-7.83 ± 0.03	562 ± 14	44 ± 29	-0.983
6	-7.68 ± 0.03	562 ± 13	16 ± 27	-0.980
7	-7.43 ± 0.03	537 ± 15	43 ± 29	-0.984
8	-7.29 ± 0.03	552 ± 13	-4 ± 25	-0.981
9	-7.03 ± 0.03	531 ± 14	18 ± 27	-0.983
10	-6.74 ± 0.04	502 ± 17	43 ± 30	-0.987
11	-6.42 ± 0.05	482 ± 19	58 ± 33	-0.989
12	-6.19 ± 0.04	500 ± 15	6 ± 27	-0.985
13	-5.68 ± 0.05	462 ± 20	23 ± 32	-0.990

Therefore, the following results should be understood as a test of principle. High-statistics measurements with the nominal vessel ramping mode as cross-check of the following results have been conducted in the second half of 2021, with the analysis still on-going.

6.4.1. Procedure

In the analysis a relative method is used, similar to the one described in section 6.3.1. The SAP potential depression is again calculated by the comparison of a reference line position, measured in the NAP, with the patch-wise measured line positions in the SAP configuration. This avoids the problem of imprecisely known source and Main Spectrometer work functions as well as starting potentials inside the source beam tube.

The integral spectrum of the $N_{2,3}$ line doublet allows us to directly measure the SAP magnetic field and the energy broadening due to its sharp form (see section 5.4.3). Compared to the K line measurements, the vanishingly small natural $N_{2,3}$ line widths do not impede the SAP magnetic field determination. We therefore do not use the line widths from NAP measurements as a reference for the SAP analysis.

Instead, the analysis described in section 5.4.3 shows that the magnetic field and the energy broadening have comparably large absolute correlations to the distance between the N_2 and N_3 lines (see figure 5.22). This distance must be the same in the NAP as well as the SAP setting. By measuring the distance in the NAP, we can include additional information into the SAP analysis to achieve a more robust and precise result.
The direct determination of the magnetic field and energy broadening in the NAP integral measurement has an additional aspect that was so far not yet explicitly considered in the K line analysis. We expect in the NAP measurement to suffer from energy broadening effects, for example thermal Doppler or the grouping of pixels into patches. Additionally, the continuous ramping mode of the inner electrodes combined with the time-synchronization problem of the high-voltage system leads to a further energy broadening in the stacked analysis of the $N_{2,3}$ measurement (see section 5.4.3). In the K line measurement, the NAP broadening is mostly absorbed by the reference line width and negligibly small compared to the sensitivity of the measurement. However, in the $N_{2,3}$ measurement we can directly measure it. By correcting the obtained energy broadening in the SAP analysis for the one determined in the NAP measurement, we get an accurate result on the pure SAP energy broadening.

6.4.2. Reference Measurement in Nominal Analyzing Plane

The reference measurement uses the same data, as that analyzed for the measurement of the 2.7 G NAP magnetic field. It was performed after KNM3, in August 2020. For details on the measurement, see section 5.4.3. The total live time of the reference measurement was 8 hours. Due to low statics and faster calculation time, we also perform a patch-wise analysis. Inter-patch correlations are not considered in the following due to the necessary computation time which we estimate to be larger than 10^5 CPU hours. However, we expect inter-patch correlations to be negligible small, similarly to section 6.3.3.

The model used for the analysis in the following is the same as described in section 5.4.3, except that we do not have to include the uncertainties on the source and PCH magnetic field due to the relative measurement principle. The model comprises two Lorentzian distributions, an energy smearing, the NAP magnetic field as part of the transmission function, and a constant background. As discussed in section 5.4.3, we apply a penalty term on the N_2 and N_3 lines width in the likelihood function. The mean as well as the width of the Gauss-shaped penalty term is 15 meV. The parameters of interest for this analysis are the N_2 line position of patch 0, used as reference line position, the energy broadening of all patches, and the line position distance between the N_2 and N_3 conversion lines.

The obtained best-fit estimates agree with the results of the characterization measurement of the 2.7 G NAP field (see upper half of table 5.2). The normalized χ^2 is between 0.8 and 1.2 for all 14 patch-wise analyses. The average energy broadening yields $17 \times 10^{-3}\,\mathrm{eV}^2$, the uncertainty on the patch-wise broadening is on the order of $10^{-3}\,\mathrm{eV}^2$. The mean distance between N_2 and N_3 lines is $(0.664 \pm 0.003)\,\mathrm{eV}$ and thus in agreement with the results from optical spectroscopy measurements

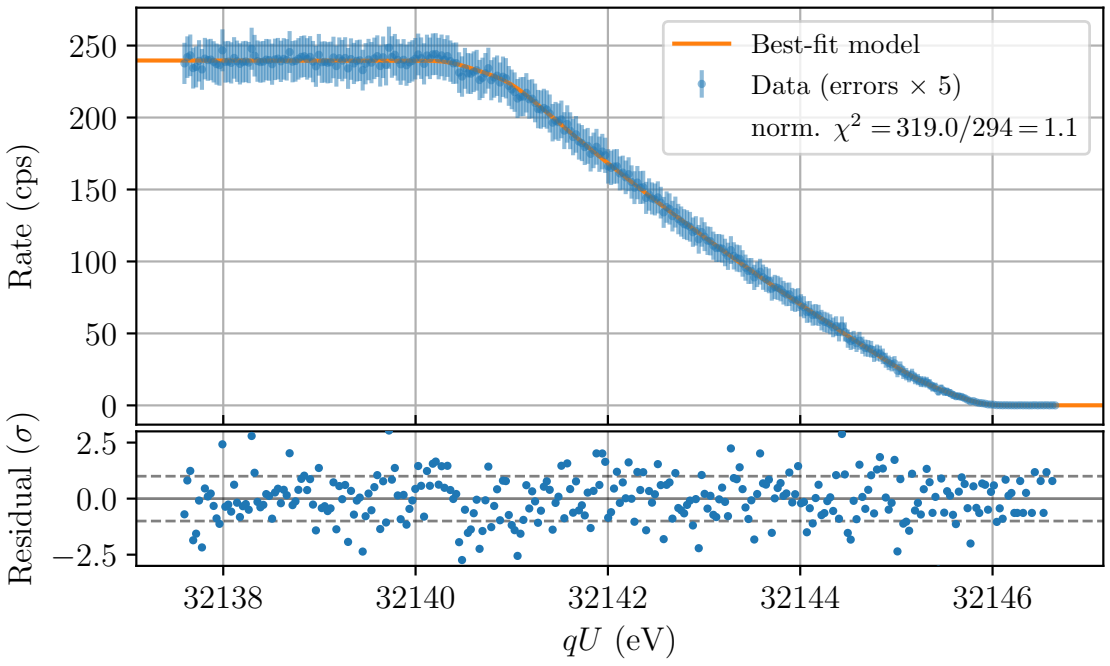

Figure 6.13.: **Measurement and best-fit model of the $N_{2,3}$ line doublet at patch 0 in the SAP configuration.** The measured rate of the integral ^{83m}Kr $N_{2,3}$ line doublet spectrum (blue), as well as the best-fit model (orange), are shown in the upper graph. The well-distributed best-fit residuals are shown in the lower graph.

(0.6701 ± 0.0001) eV [Vén+18a]. The N_2 line position is measured to be $E_{0,\mathrm{ref}} = (32\,138.87 \pm 0.02)$ eV at patch 0.

6.4.3. Measurement in Shifted Analyzing Plane

The $N_{2,3}$ line doublet measurement in the SAP configuration was also performed after KNM3, in August 2020. The measurement time was only 2.5 hours. The uncertainties of the analysis results presented in the following are statistically dominated. The SAP measurements are also conducted with the inner electrode ramping mode instead of the nominal vessel ramping.

The model used to describe the data is the same as that used in the reference measurement in section 6.4.2. The patch-wise information on the distance between the N_2 and the N_3 lines obtained from the reference measurements is included as a penalty term in the likelihood optimization.

The normalized χ^2 is distributed between 0.9 and 1.2 for all patch-wise fits and thus around the expectation value. The measured integral spectrum and the best-fit model for patch 0 is shown in figure 6.13. The normalized $\chi^2 = 1.1$ is in agreement with statistical fluctuations, the residuals do not show any structure. These features indicate a good agreement between measurement and model.
The correlations among the parameters of interest as well as their uncertainties are estimated using the KaFit emcee python binding. The uncertainty and correlations

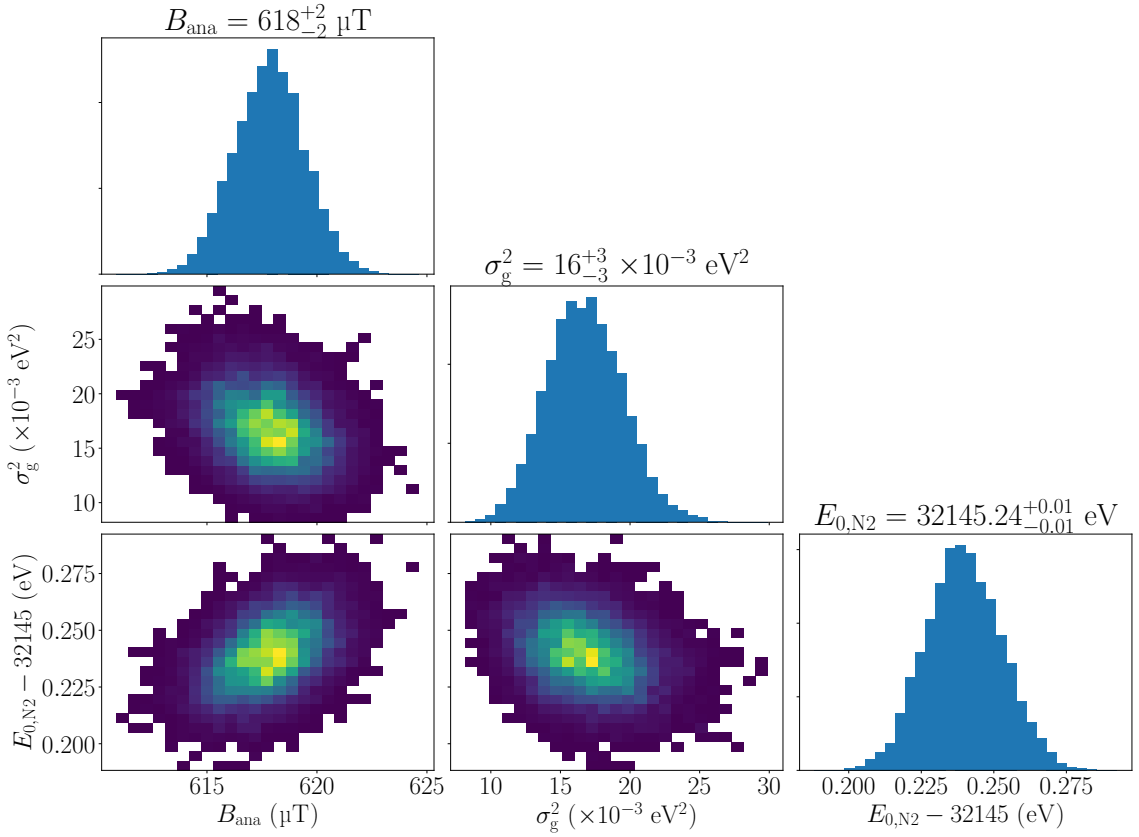

Figure 6.14.: **Emcee sampler steps for the SAP analysis of the $^{83\mathrm{m}}$Kr $\mathrm{N}_{2,3}$ line doublet measurement at patch 0 for the parameters of interest.** The parameters of interest show only weak or moderate absolute correlations. The distributions are obtained with 8×10^4 emcee function evaluations close to the best-fit minima.

are shown for patch 0 as an example in figure 6.14. It is obvious that the correlations are significantly smaller compared to the K line analysis (see figure 6.12). The correlation between SAP magnetic field and energy broadening is reduced by a factor of three compared to the K line analysis, the correlation coefficient is now $\rho\left(B_{\mathrm{ana}}, \sigma_{\mathrm{g}}^2\right) = -0.29$. Similarly, the correlation coefficient between the line position and the magnetic field in the $\mathrm{N}_{2,3}$ analysis is $\rho\left(B_{\mathrm{ana}}, E_{0,\mathrm{N2}}\right) = 0.43$ and thus reduced by more than a factor two. The uncertainties on the parameters of interest are also reduced in comparison to the K line analysis. The magnetic field uncertainty improves by a factor of five, the energy broadening a factor of seven, and the line position a factor of two for fit results of patch 0.

We did not take into account the likely negligible additional uncertainty arising from the inner electrode ramping mode associated with a change of the potential depression (see section 5.4.3). We correct for this effect based on the simulated potential depression. However, the necessary Monte-Carlo study to properly investigate the arising additional uncertainty is currently not feasible within a reasonable computational time due to the comparably long calculation time of the model evaluation.

6.4.4. Extraction of Transmission Function Properties

Similar to section 6.3.4, we now make use of the ^{83m}Kr $N_{2,3}$ measurement results to extract the parameters of interest to describe the SAP transmission function properties.

The SAP potential depression $qU_{\mathrm{pd,SAP}}$ is calculated with the reference N_2 line position $E_{0,\mathrm{ref}} = (32\,138.87 \pm 0.02)\,\mathrm{eV}$ in the NAP configuration, the simulated NAP potential depression $qU_{\mathrm{pd,ref}} = -2.32\,\mathrm{eV}$, and the patch-wise determined N_2 line positions $E_{0,\mathrm{SAP,i}}$. For patch 0, this yields

$$\begin{aligned} qU_{\mathrm{pd,SAP,0}} &= E_{0,\mathrm{ref}} - E_{0,\mathrm{SAP,0}} + qU_{\mathrm{pd,ref}} \\ &= (32\,138.87 \pm 0.02)\,\mathrm{eV} - (32\,145.24 \pm 0.01)\,\mathrm{eV} - 2.32\,\mathrm{eV} \\ &= (-8.69 \pm 0.02)\,\mathrm{eV}. \end{aligned}$$

Table 6.3 presents the calculated potential depressions for all patches. As expected, the absolute potential depression decreases from central patch 0 to the outer-most patches by roughly 3 eV.

The SAP magnetic field is directly extracted from the analysis of the $N_{2,3}$ measurement conducted in the SAP configuration. Also here, the shape of the magnetic field follows the expectation and decreases from the center to larger radii by 160 µT (see table 6.3). The mean uncertainty on the magnetic field is only 2 µT for all patches. The energy broadening σ_{g}^2 due to the SAP configuration is calculated by comparing the measured energy broadening in the NAP, $\sigma_{\mathrm{g,NAP}}^2$, and in the SAP, $\sigma_{\mathrm{g,SAP}}^2$, configuration. With this method, any effects that do not arise from the SAP configuration itself are removed. For patch 0, this yields

$$\begin{aligned} \sigma_{\mathrm{g}}^2 &= \sigma_{\mathrm{g,SAP}}^2 - \sigma_{\mathrm{g,NAP}}^2 \\ &= (16 \pm 3) \times 10^{-3}\,\mathrm{eV}^2 - (16 \pm 1) \times 10^{-3}\,\mathrm{eV}^2 \\ &= (0 \pm 3) \times 10^{-3}\,\mathrm{eV}^2. \end{aligned}$$

The expectation for the energy broadening is that it increases with increasing patch number. Pixels at the outer-most part of the flux tube contain stronger intra-pixel potential and magnetic field variations compared to the central pixels. The expectations are met: the energy broadening significantly increases starting from patch 9 onwards with increasing patch number (see table 6.3).
The correlation between SAP magnetic field and energy broadening is estimated with the emcee sampler steps near the likelihood optimum. Generally, the correlations are rather weak with a correlation coefficient on the order of $\rho \in [-0.2, -0.4]$ (see table 6.3).

6.5. Comparison and Summary

We have presented in this chapter three complementary methods to investigate the SAP transmission properties, namely by simulations, by e-gun measurements, and by ^{83m}Kr conversion electrons measurements. The simulations are introduced only as reference, as they are vulnerable in the SAP configuration to inaccurate model

Table 6.3.: **SAP transmission function properties for all 14 patches, derived by analyzing the $N_{2,3}$ line doublet measurement.** The parameters of interest are the potential depression $qU_{\mathrm{pd,SAP}}$, the magnetic field B_{ana} in the analyzing plane, the squared energy broadening σ_{g}^2, and the correlation coefficient ρ between the last two parameters.

Patch	$qU_{\mathrm{pd,SAP}}$	B_{ana} (μT)	$\sigma_{\mathrm{g}}^2 \left(\times 10^{-3}\,\mathrm{eV}^2\right)$	$\rho\left(B_{\mathrm{ana}}, \sigma_{\mathrm{g}}^2\right)$
0	-8.69 ± 0.02	618 ± 2	0 ± 3	-0.297
1	-8.56 ± 0.02	613 ± 2	1 ± 3	-0.268
2	-8.43 ± 0.02	603 ± 2	4 ± 3	-0.219
3	-8.29 ± 0.02	596 ± 2	4 ± 3	-0.281
4	-8.12 ± 0.02	588 ± 2	1 ± 3	-0.208
5	-7.94 ± 0.02	577 ± 2	4 ± 3	-0.287
6	-7.79 ± 0.02	571 ± 2	6 ± 3	-0.323
7	-7.57 ± 0.02	556 ± 2	5 ± 3	-0.321
8	-7.37 ± 0.02	544 ± 2	11 ± 3	-0.331
9	-7.15 ± 0.02	533 ± 2	11 ± 3	-0.270
10	-6.89 ± 0.02	517 ± 2	16 ± 3	-0.338
11	-6.58 ± 0.02	501 ± 2	23 ± 3	-0.308
12	-6.25 ± 0.02	485 ± 2	39 ± 3	-0.416
13	-5.77 ± 0.02	458 ± 2	47 ± 3	-0.355

alignment. Nevertheless, they are mentioned in the following comparisons for completeness. In this work, the e-gun characterization is only performed on individual pixels (see section 6.2) since these measurements are time-consuming, a full characterization of the SAP with the e-gun is not possible on measurement time-scales of less than a week. The results from e-gun measurements are therefore also used as a cross-check to the other methods. The only approach that accurately characterizes the whole SAP cross section at once is measurements with $^{83\mathrm{m}}$Kr conversion electrons. Measurement results of the K and $N_{2,3}$ lines are presented in chapter 6.3 and 6.4. The focus of the following sections is the comparison of the K and $N_{2,3}$ line results.

6.5.1. Retarding Potential

The electric retardation in the analyzing plane is mostly given by the applied voltage on the Main Spectrometer vessel and the inner electrode system. Additionally, the grounded beam tubes as well as the steep cones cause a deviation from homogeneity, summarized in the potential depression term. In this work, the SAP potential depression, $qU_{\mathrm{pd,SAP}}$, is determined with $^{83\mathrm{m}}$Kr conversion electrons in the relative method by the difference of line positions δE_0 and the simulated potential

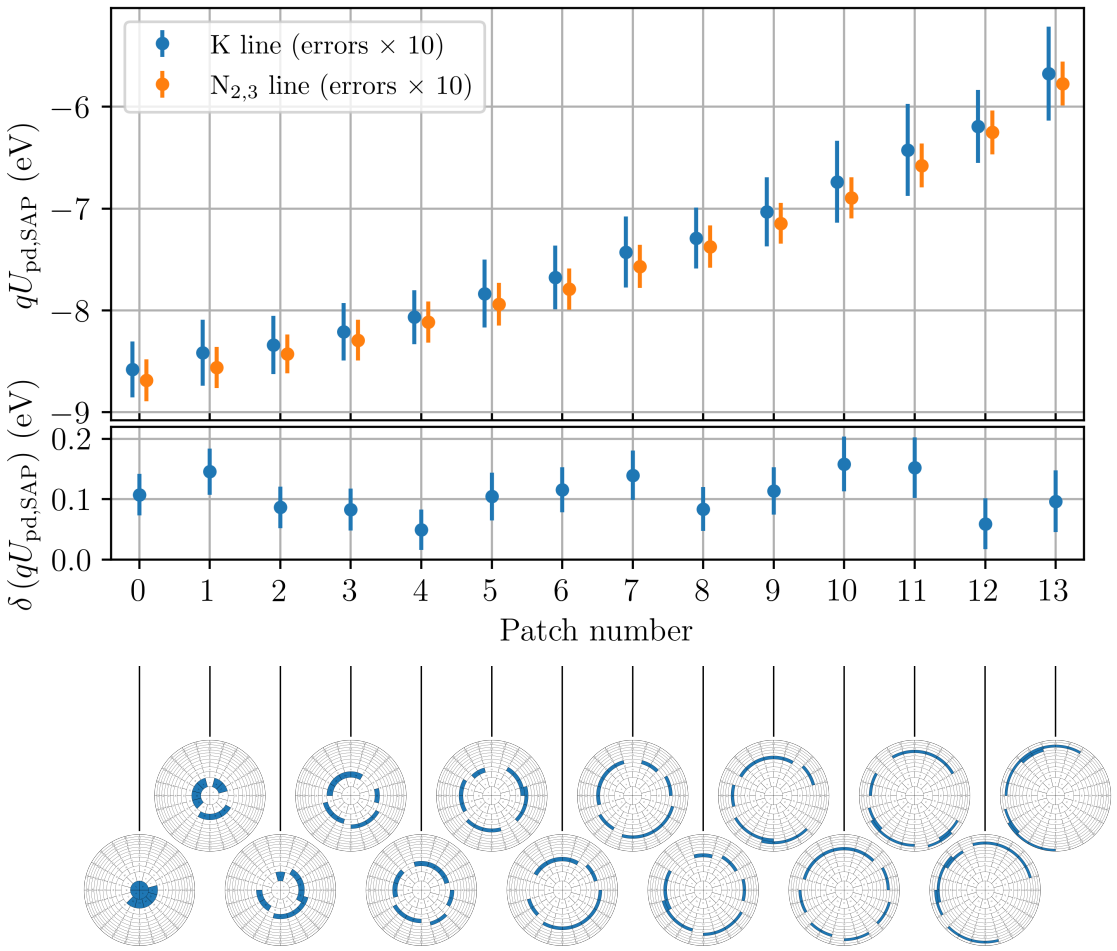

Figure 6.15.: **Comparison of the calculated potential depression determined with the ^{83m}Kr K line measurement to the one determined with the $N_{2,3}$ line doublet measurement.** The upper graph shows the measured evolution of SAP potential depression $qU_{\mathrm{pd,SAP}}$ over patch number. Note that in this graph, the error bars of both methods are increased by a factor ten for better visualization. The lower graph shows the difference $\delta\left(qU_{\mathrm{pd,SAP}}\right)$ of the determined potential depressions between the two methods for each patch, this is consistent with a constant offset of $(102 \pm 8)\,\mathrm{meV}$.

depression, $qU_{\mathrm{pd,NAP}}$, in the NAP configuration

$$qU_{\mathrm{pd,SAP}} = \delta E_0 + qU_{\mathrm{pd,NAP}}. \tag{6.2}$$

The SAP potential depressions for each patch, measured with the ^{83m}Kr K and $N_{2,3}$ lines, are shown in figure 6.15. Both ^{83m}Kr methods agree well on the measured shape, with a constant difference for all patches of

$$\delta\left(qU_{\mathrm{pd,SAP}}\right) = (102 \pm 8)\,\mathrm{meV}.$$

The constant offset between the ^{83m}Kr K and $N_{2,3}$ line measurements can either be caused by the line position difference term δE_0 or by the simulated potential depression in the NAP configuration $qU_{\mathrm{pd,NAP}}$ (see equation 6.2). To calculate the SAP potential depression based on the K line analysis, the NAP potential depression

needs to be simulated for −17.8 kV vessel voltage, for the $N_{2,3}$ analysis for −31.8 kV. If the different vessel voltages are not accurately simulated, a small discrepancy is possible, although an inaccuracy of 0.1 V is unrealistic. The second possible reason for the offset lies in the δE_0 measurement. Drifts of the Main Spectrometer or the source work function, as well as of the source starting potential, can in principle introduce an offset in δE_0. However, these effects are rather unlikely, since the NAP and the SAP measurements are conducted in direct succession for both methods. Energy-dependent effects, for example non-adiabaticity, are not expected to shift the line position in the SAP compared to the NAP setting. The reason for this constant offset in the determined SAP potential depression remains unknown.
The e-gun is a suitable tool to investigate the δE_0 term with a complementary measurement method close to the tritium endpoint energy. An e-gun potential edge measurement allows us to test whether the K line δE_0 term or the $N_{2,3}$ line doublet δE_0 term deviate significantly from the one determined with the e-gun. The measured potential edge in the 2.7 G measurement (see section 5.3.3) is therefore compared with the potential edge of the SAP measurement (see section 6.4). We decide to compare the measured potential edges of FPD pixel 2, as motivated in the following. The e-gun measurement takes only place at one pixel while the ^{83m}Kr data is analyzed patch-wise. Pixel 2 belongs to the central patch 0, which possesses the smallest potential variation within the patch due to the elliptical parabolic shape of the SAP electromagnetic fields. The comparison of pixel- to patch-wise analysis is thus more accurate here than for the outer patches. The measured difference in the potential edge on pixel 2 is (-6.346 ± 0.004) eV. Taking into account the simulated 2.7 G potential depression leads to (-8.652 ± 0.004) eV. This is slightly closer to the $N_{2,3}$ line doublet measurement with (-8.69 ± 0.02) eV than to the result of the K line measurement with (-8.58 ± 0.03) eV. Both ^{83m}Kr results differ by roughly two standard deviations from the e-gun result, thus a conclusion is not possible with the current sensitivity.

The constant offset does not cause any systematic bias on the measured neutrino mass, since the tritium endpoint is a free fit parameter in the neutrino mass analysis which absorbs possible offsets without biasing the neutrino mass (see section 5.1.3) [Kaš+04]. Consequently, the knowledge on the retarding potential in the SAP derived with ^{83m}Kr measurements in this thesis is sufficient for neutrino mass analysis. Nevertheless, it is interesting to compare the measured tritium endpoint to external measurements (see reference [Sac20]). We therefore recommend further investigation into the reason for the constant offset in the estimated SAP retarding potential depression by the two ^{83m}Kr results.

6.5.2. Transmission Function Shape

The transmission function shape in a certain patch is inter alia given by the SAP magnetic field and the energy broadening. As the PCH and source magnetic fields are independent of the Main Spectrometer SAP or NAP configuration, we focus on the influence of the SAP magnetic field and the energy broadening on the transmission function. Additionally, the impact of the parameters' uncertainties on the systematic neutrino mass error is estimated.

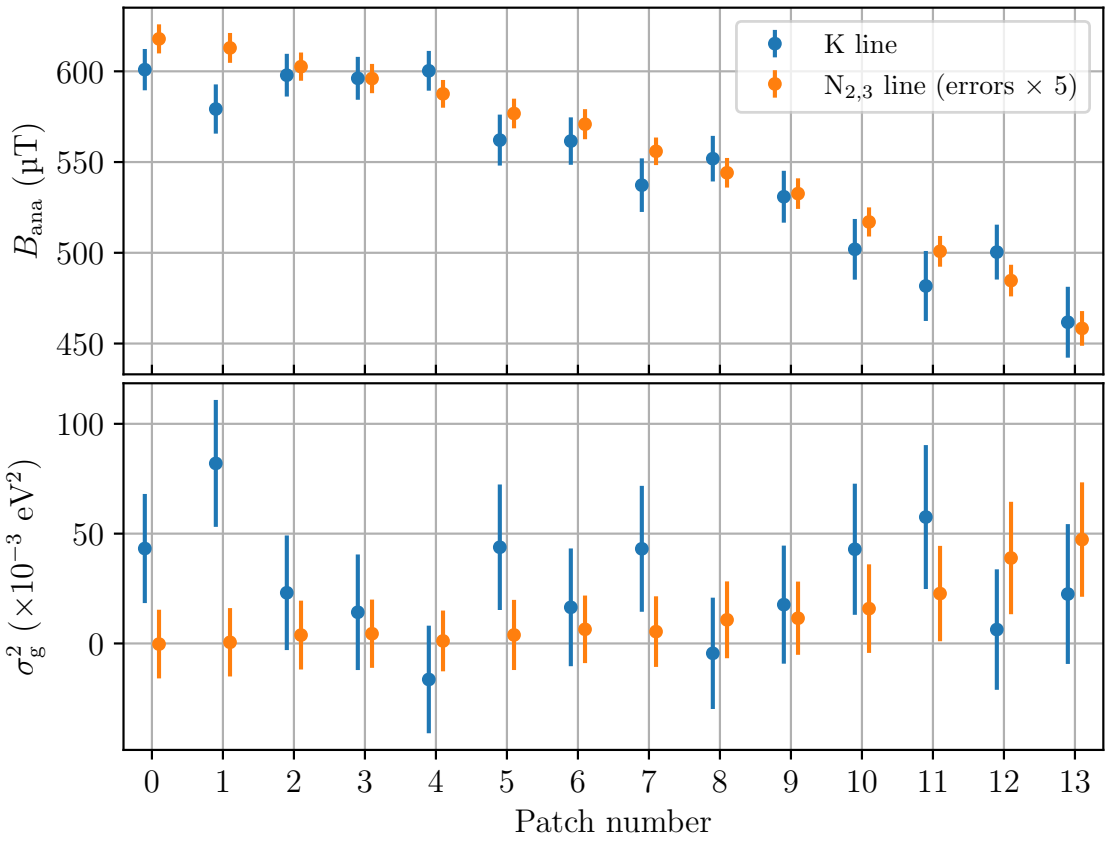

Figure 6.16.: **SAP magnetic field B_{ana} and the energy broadening σ_g^2 versus patch number, as measured with the $^{83\mathrm{m}}$Kr K and $N_{2,3}$ line measurement.** Please note that in both graphs the error bars of the $N_{2,3}$ analysis results (drawn in orange) are increased by a factor five for better visibility, while the error bars of the K line measurements (drawn in blue) reflect the true uncertainty.

The shape expectation for the SAP magnetic field is a continuously decreasing field strength from the central patch 0 to the outer-most patch 14. We expect the energy broadening to have an opposite shape due to the elliptical parabolic shape of the SAP electromagnetic fields with a minimum at patch 0 and increasing broadening with patch number. The measured SAP magnetic field and the energy broadening with the K and $N_{2,3}$ line doublet are shown in figure 6.16.
The expectation for the SAP magnetic field is met by both $^{83\mathrm{m}}$Kr measurements. The two methods agree with each other within their uncertainties, the largest difference is found in patch 1 with a difference of 2.5 standard deviations. In this patch, the magnetic field estimated by the K line is smaller than what we would expect and also smaller compared to the $N_{2,3}$ measurement. This smaller magnetic field determined with the K line is partially absorbed by a larger energy broadening than expected due to the strong anti-correlation between the two parameters in the K line determination. In general, the magnetic field results obtained by the $N_{2,3}$ analysis clearly follow the expectation while the K line results show stronger fluctuations around the expectation, compatible with their significantly larger error bars. The simulated magnetic field for the SAP is in good agreement with the $N_{2,3}$ line measurement for patches 0 to 6 with a deviation of less than 3.5 µT. Towards

the outer-most patches, the deviation increases to a maximum of 25 μT, which is too inaccurate to be used as input for neutrino mass analysis. A comparison of the pixel-wise e-gun magnetic field measurement of the SAP to patch-wise ^{83m}Kr results is not possible at the necessary accuracy level due to the strong intra-patch magnetic field inhomogeneity and the small number of investigated pixels with the e-gun. To enable a comparison of the SAP magnetic field measured with the e-gun to ^{83m}Kr results, it is either necessary to probe the magnetic field with the e-gun at each pixel within a patch, or to significantly increase the statistics of the $N_{2,3}$ measurement allowing a pixel-wise analysis.
The energy broadening, estimated by the K line measurement, has relatively large uncertainties on the order of $27 \times 10^{-3}\,\mathrm{eV}^2$. Based on these measurements, the shape expectation can neither be confirmed nor rejected. The $N_{2,3}$ line analysis has uncertainties of only $3 \times 10^{-3}\,\mathrm{eV}^2$. The determined energy broadenings follow the shape with zero-compatible broadenings in the first eight patches and a significant increase towards the larger patch numbers. The feature to calculate the expected potential spread within pixels or patches is currently not yet implemented in the Kassiopeia field simulation.

The $N_{2,3}$ line doublet measurements deliver high-precision estimations of the SAP magnetic field and the energy broadening with weak correlations among these two parameters. Compared to the $N_{2,3}$ line doublet results, the analysis of the K line measurements leads to large uncertainties on the broadening and the magnetic field with a strong anti-correlation between these two parameters. In the following, we quantify the impact of these measurement results on the systematic neutrino mass error by using the pull-term method (see section 3.3.5). The systematic uncertainties on the squared neutrino mass, stated in the following, are based on Monte Carlo data of β scans. The quoted numbers give a first estimate of the impact of the SAP transmission function uncertainties on the systematic neutrino mass uncertainty. However, they can differ in the final neutrino mass analysis on real data.
A simulated β-scan Asimov dataset with vanishing neutrino mass is produced based on the period summary derived from the $N_{2,3}$ line doublet analysis. Afterwards, this dataset is analyzed in a self-fit with the same period summary as used for the Asimov generation in the typical 40 eV analysis window. We perform a multi-patch fit, as this is also the procedure for neutrino mass analysis in the SAP configuration. The statistics-only multi-patch fit comprises one global fit parameter describing the squared neutrino mass, 14 endpoints (one for each patch), 14 signal normalizations, and 14 background rates. In the pull-term approach, the 14 parameters for the magnetic field in the SAP as well as the 14 broadening parameters are also included as free fit parameters, constrained by the penalty terms that are chosen corresponding to their uncertainties. The correlations between the SAP magnetic field and energy broadening within one patch are included via the penalty terms. The broadening of the likelihood function close to the minimum in the pull-term fit compared to the statistics-only fit quantifies the systematic uncertainty on the neutrino mass due to the SAP magnetic field and energy broadening uncertainties. The resulting systematic uncertainty contribution on the squared neutrino mass is

$$\Delta m^2_{\nu,\mathrm{sys}} = 2 \times 10^{-3}\,\mathrm{eV}^2. \tag{6.3}$$

Consequently, the SAP magnetic field and the energy broadening uncertainties, as determined with the $N_{2,3}$ line doublet measurements in the thesis at hand, fulfill the

final KATRIN requirement of less than $7.5 \times 10^{-3}\,\mathrm{eV}^2$ for an individual systematic uncertainty contribution.
The same procedure is repeated with the SAP electromagnetic field results of the K line measurement. The simulated β-scan Asimov dataset is produced based on the period summary derived from the K line analysis and afterwards analyzed in the self-fit, multi-patch approach. The resulting systematic uncertainty contribution on the neutrino mass is

$$\Delta m^2_{\nu,\mathrm{sys}} = 3 \times 10^{-3}\,\mathrm{eV}^2 \tag{6.4}$$

and thus slightly larger than the uncertainty contributions based on the $N_{2,3}$ measurement, but still comparable. This might sound unexpected, since the $N_{2,3}$ line uncertainties are a factor of five smaller for the SAP magnetic field, and a factor of seven better for the energy broadening compared to the K line measurement. However, the significant difference between both methods with large impact on the neutrino mass uncertainty is the correlation between magnetic field and broadening. The field and the broadening have only a weak correlation coefficient of $\rho \approx -0.3$ in the $N_{2,3}$ line doublet analysis, while it is $\rho \approx -0.98$ for the K line. Neglecting the strong correlation between energy broadening and magnetic field in the K-line based fit of the Asimov dataset leads to significantly larger systematic neutrino mass uncertainties around $\Delta m^2_{\nu,\mathrm{sys}} \approx 20 \times 10^{-3}\,\mathrm{eV}^2$.

Consequently, the uncertainties on the K- and N-line based transmission functions lead to similar uncertainties on the neutrino mass, which both meet the final KATRIN requirements. The next question, that needs to be answered for neutrino mass measurement analysis is whether the transmission functions themselves agree within their uncertainties. If they do agree, it does not matter which of the two derived transmission function parameter sets is used for neutrino mass analysis, as they have similar impact on the neutrino mass uncertainty.
We first start with quantifying the transmission function shape difference. In the upper graph in figure 6.17, the K-line based transmission function and the one based on $N_{2,3}$ measurements are shown together with their uncertainties for patch 0. The error band is derived by Monte-Carlo propagation of the magnetic field and energy broadening uncertainties, taking into account the correlation between these two parameters. For better comparison, the transmission functions are shifted on the energy axis such that the middle of transmission $T = 0.5$ is located at 0 eV. The difference between the two transmission functions, normalized to their uncertainties, is shown in the lower graph of figure 6.17. The difference shows a bumpy structure in the transition between the steep part of the transmission function and the constant parts, at roughly $E - C = -1.1\,\mathrm{eV}$ and 0.8 eV. This region is dominated by the energy broadening, where the K-line and N-line based parameters differ strongly in central values (see lower graph of figure 6.16). The central part of the transmission function is mostly affected by the estimated SAP magnetic field as it influences the slope (see equation 3.12). The estimated magnetic fields manifest themselves in two approximately constant regions in the difference structure around 0 eV. In general, the difference is mostly larger than one standard deviation. As a next step, the impact on the measured neutrino mass due to the shape difference of the two transmission functions is estimated.
To quantify the impact of the shape difference on the measured neutrino mass, we generate a simulated β-scan Asimov dataset based on the period summary derived from the $N_{2,3}$ line doublet measurement. The neutrino mass is set to 0 eV

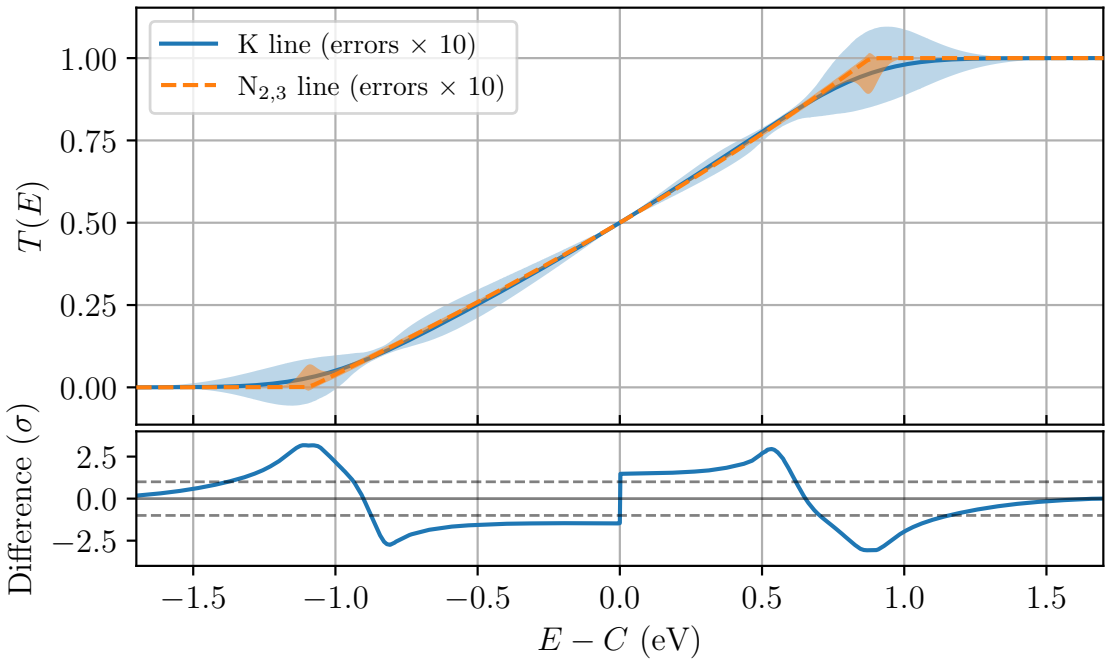

Figure 6.17.: **Comparison of the transmission function shape at patch 0 as determined by the K (blue) and by the $N_{2,3}$ (orange) line measurements.** The upper graph shows both measured transmission functions versus the energy E as well as their uncertainties, multiplied by a factor of five. These are calculated via Monte-Carlo propagation, taking into account the correlations between SAP magnetic field and squared energy broadening. The parameter C is a constant offset on the energy axis for each transmission function, which shifts the middle of transmission with $T = 0.5$ to $E - C = 0\,\mathrm{eV}$. The lower graph shows the difference between the transmission functions, normalized to their uncertainties.

in this study. The generated data is analyzed in a multi-patch approach using the transmission function properties derived from the K line measurement. The best-fit estimation for the neutrino mass is not located at 0 eV anymore but shows a measurement bias, that is caused by the shape difference of the transmission function. The measurement bias δm_ν^2 for the squared neutrino mass yields

$$\delta m_\nu^2 = 6 \times 10^{-3}\,\mathrm{eV}^2.$$

This is a factor of 1.5 larger than the systematic uncertainty estimations of both method combined (see equation 6.3 and 6.4). The direct transmission function comparison (see figure 6.17) predicts a bias that is slightly larger than the one from the systematic uncertainty estimation, because the difference between the transmission functions is mostly larger than one standard deviation. However, since the possible bias is consistent with the estimated systematic uncertainty of both methods, it is decided to not take the possible bias into account in the calculation of the systematic SAP uncertainty.
Nevertheless, it is necessary to decide on the more accurate period summary for the analysis to avoid a biased result of the neutrino mass. We recommend use of a period summary based on $N_{2,3}$ line doublet measurements for future analyses. The uncertainties on the patch-wise estimated magnetic field strengths and the energy

broadenings are significantly smaller compared to the K line analysis. Additionally, the correlation between these two parameters is only weak in the $N_{2,3}$ measurement, leading to a robust determination of each parameter of interest in contrast to the K line analysis.

6.5.3. Summary and Outlook

The SAP is a configuration which significantly reduces the dominating background component in neutrino mass measurements, namely the one from the Main Spectrometer. In addition, also the non-Poisson component of the Main Spectrometer background is suppressed. Both reductions combined, the one of the total rate and the one of the non-Poisson component, lead to a smaller total uncertainty on the measured neutrino mass. Due to these properties, the SAP setting is the operational configuration since fall 2020 and the majority of the data for neutrino mass analysis with KATRIN so far has been measured using the SAP setting.
The SAP magnetic field and the electric retardation feature relatively large inhomogeneities over the analyzing plane. SAP field simulation results therefore have to be taken with caution, as small model inaccuracies can have severe impacts on the simulated field. The goal of this chapter was to experimentally determine SAP transmission functions. The main results are:

- Measurements and analyses performed in this work show that high-precision results of the magnetic field strength and the retarding potential in the analyzing plane are possible using the e-gun. However, a comprehensive analysis of the whole SAP cross section is not possible with the e-gun in a realistic scenario as the large measurement preparation and data acquisition time would lead to significant measurement time loss for neutrino mass β scans.
- ^{83m}Kr measurements of the K line (section 6.3) as well as of the $N_{2,3}$ line doublet (section 6.4) time-efficiently allow us to completely characterize the SAP in 14 pixel segments, the so-called patches. With methods developed in the thesis at hand, the parameters describing the SAP transmission function are extracted from the integral ^{83m}Kr measurements, using the NAP configuration as reference. The ^{83m}Kr analysis of both lines lead to precise results, the systematic uncertainty contribution on the squared neutrino mass yields $\Delta m^2_{\nu,\mathrm{sys}} \approx 3 \times 10^{-3}\,\mathrm{eV}^2$ in a preliminary estimate. This fulfills the final KATRIN requirement on a single systematic uncertainty contribution of $\Delta m^2_{\nu,\mathrm{sys}} \leq 7.5 \times 10^{-3}\,\mathrm{eV}^2$. The results of the two methods agree to a neutrino mass bias of $6 \times 10^{-3}\,\mathrm{eV}^2$.

As a result of the thesis at hand, neutrino mass measurements conducted in the SAP Main Spectrometer configuration can be analyzed with one of the ^{83m}Kr-based period summaries on a systematic uncertainty level that is compatible with current uncertainties (see reference [Ake+21a]) and also compatible with the final KATRIN sensitivity goal.
Based on the results achieved in this work, measurements with a high-intensity ^{83m}Kr source have been conducted in the second half of 2021 to enable a pixel-wise measurement of the SAP magnetic field strength, the electric retardation, and the intra-pixel energy broadening. These measurements have been performed with the

$N_{2,3}$ line doublet due to its large sensitivity on the parameters of interest. In the presented measurements, the 11-hour $N_{2,3}$ line doublet measurement enables us to analyze the SAP properties with significantly better precision than the 72-hour K line measurement. To avoid sources of uncertainties in the analysis from the inner electrode ramping mode, the measurements with the high-intensity ^{83m}Kr source have been performed with the nominal vessel-ramping mode. The analysis of this measurement is still on-going, first results are expected in early 2022 [Ake+22]. The obtained transmission properties from the e-gun can be used as complementary tool to cross-check the determined transmission properties at individual pixels to avoid unaccounted energy-dependent effects in the analysis of the $N_{2,3}$ line doublet measurements.

7. The WGTS Column Density

An unbiased inference of the neutrino mass requires precise and accurate modeling of the β-decay electron energy losses. The major energy-loss process of β-decay electrons in the KATRIN experiment is the scattering of decay electrons off tritium gas molecules in the WGTS. The scattering magnitude mainly depends on the tritium gas amount in the WGTS, described by the column density as characteristic quantity. The column density is in this context defined as the gas density in the WGTS integrated along the beam axis. To accurately calculate the scattering magnitude, the column density thus needs to be known with high accuracy and precision as external input for successful neutrino mass measurements with KATRIN.
In the following, the definition of the column density, the calculation of the response function and the detailed role of the column density in neutrino mass analyses are introduced in section 7.1. In section 7.2, we summarize the work carried out in previous publications and theses concerning the simulation and calculation of the gas distribution and column density inside the WGTS. Subsequently, a direct column density measurement method with the Rear Section e-gun is presented in section 7.3. An important simulation prediction, namely the radial and azimuthal homogeneity of the WGTS gas density, is investigated by comparing the prediction to dedicated column density measurements in section 7.4. In section 7.5, we introduce two complementary approaches for the crucial column density monitoring during neutrino mass measurement campaigns based on the column density measurements by the e-gun and gas model calculations. We then close the chapter with a summary in section 7.6.

7.1. Influence of Column Density in KATRIN

All energy-loss processes of β-decay electrons reaching the FPD need to be considered for exact spectral modeling. In the typical KATRIN neutrino mass analysis, this is realized by introducing the response function R, that combines the known energy-loss models together with the MAC-E filter transmission function [Kle+19]. The expected measured spectrum is calculated by a convolution of the response function with the theoretical description of the β-decay spectrum (see also section 3.3.1).
The major energy-loss process of β-decay electrons is the inelastic scattering off tritium gas in the WGTS before entering the SDS for energy selection. The gas density rapidly decreases outside of the WGTS, thus scattering processes in the transport section or thereafter are of no concern [Kle+19]. For a proper description of the inelastic scattering process we need to introduce the term column density.

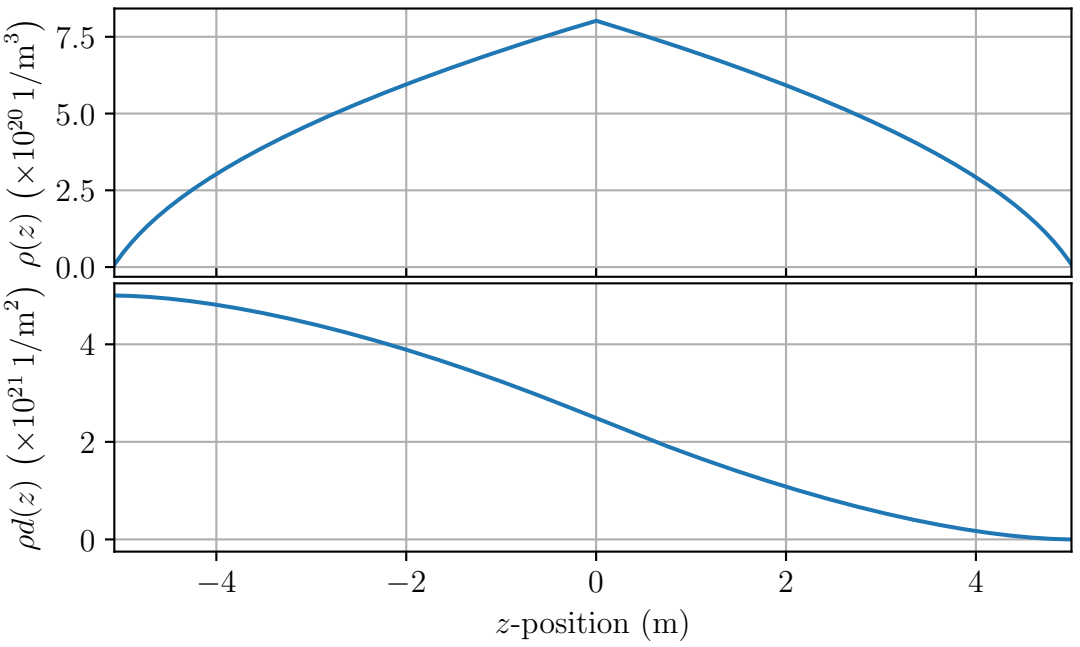

Figure 7.1.: **Relation between gas density $\rho(z)$ and column density $\rho d(z)$ over the longitudinal z-position.** The simulated tritium gas density $\rho(z)$ in the WGTS as a function of the z-position in the central beam tube is shown in the upper patch. Tritium gas is injected at the longitudinal center of the beam tube ($z = 0\,\mathrm{m}$), from where it can stream to the WGTS front ($z = 5\,\mathrm{m}$) and rear ($z = -5\,\mathrm{m}$) end. The column density $\rho d(z)$ that an electron with zero pitch angle traverses before leaving the WGTS to the front side as a function of its starting position z is shown in the lower patch.

7.1.1. Definition of Column Density

As described in section 3.2.2, the tritium gas is injected at the longitudinal center of the central WGTS beam tube. From there on it streams to the WGTS front and rear end, where it is pumped out. The steady tritium circulation by the WGTS loop system allows the gas to form a stable density profile. The gaseous tritium is mostly distributed along the central 10 m-long beam tube and eventually decays, releasing a β-decay electron. If the β-decay electron is emitted in the source in upstream direction, it is guided by the strong magnetic fields towards the rear wall. An electron emitted in downstream direction can reach the FPD and can be used for neutrino mass analysis. During its propagation towards the transport section, it needs to pass through a certain gas amount before leaving the WGTS. This gas amount, depending on the electron's place of production z in the WGTS, is given by the column density $\rho d\,(z)$ to

$$\rho d\,(z) = \int_{z'=z}^{+L/2} \rho(z')\;\mathrm{d}z', \tag{7.1}$$

if the β-decay electron leaves the WGTS on the direct path. The half length of the central WGTS beam tube, that contains 99 % of the tritium gas, is denoted as $L/2$ here. For this and following WGTS gas density calculations, the coordinate system

is chosen such, that the tritium injection is centered at $z = 0$, the rear and front end of the WGTS are thus located at $z = -L/2$ respectively at $z = +L/2$. The z-axis is aligned with the beam tube axis. The relation between gas density $\rho(z)$ and column density $\rho d(z)$ in the WGTS is visualized in figure 7.1. The total column density $\rho d = \rho d(-5\,\mathrm{m})$, assuming perfect radial homogeneity in the beam tube, is directly related to the number of tritium nuclei N_T in the WGTS

$$N_\mathrm{T} = 2\epsilon_\mathrm{T} \cdot \rho d \cdot A, \tag{7.2}$$

with A being the cross section of the WGTS beam tube. The factor 2 is necessary since ρd is defined in number of tritium molecules. The tritium purity of the WGTS gas composition is denoted as ϵ_T. The LARA system monitors in real-time the gas composition that is injected into the WGTS beam tube. An increased column density results in a larger amount of tritium atoms in the source and therefore larger activity and count rates at the detector. A lower column density consequently results in smaller count rates at the detector. [Kuc+18; Ake+21d]
The unit of the column density is molecules/m^2, the unit $1/\mathrm{m}^2$ is used synonymously in the following. Please note also that $\rho d\,(z)$ indicates the column density that a certain electron experiences at position z before leaving the WGTS through the front end, while ρd is the total column density from rear to front end. In the KATRIN terminology, the column density is regularly used to indicate the total gas amount in the source. The nominal KATRIN column density is defined as $\rho d_\mathrm{nom} = 5 \times 10^{21}\,\mathrm{molecules/m}^2$ [KAT05]. Although measurements at nominal column density are technically possible and commissioning measurements have been successful, neutrino mass measurement campaigns at nominal column density have not been conducted to date. Model uncertainties on the starting potential of β-decay electrons in the WGTS cause a preference towards lower column densities. Due to historical reasons, all column densities are referenced in relative size to the nominal column density in the KATRIN terminology. For consistency, we stick to this notation in the following. In the scope of the present thesis, the column densities of 75 % and 84 % nominal column density are of interest.

7.1.2. Calculation of Scattering Probabilities

The β-decay electrons can scatter off diatomic tritium molecules, atomic tritium, and further hydrogen isotopologues in the WGTS. Since diatomic tritium molecules constitute the overwhelming majority of source gas, the contributions from scattering off atomic tritium and further hydrogen isotopologues can be neglected. The scattering of electrons off tritium molecules is a complex process, since the molecules allow rotational and vibrational excitations, as well as for dissociation or ionization. [Ake+21c]
The scattering cross section, indicating the probability of scattering processes, summarizes contributions from elastic and inelastic scattering. Elastic scattering does not affect or change the initial tritium gas molecule state. In inelastic scattering processes, the molecule experiences excitation, ionization, or dissociation. The calculation of the scattering probabilities discussed in the following is identical for both scattering processes. [Ake+21c]

The scattering probability for an electron starting at position z depends inter alia on the column density. However, the aforementioned definition of $\rho d(z)$ in equation

7.1 implicitly assumes, that the electron leaves the WGTS on the direct path. This assumption is only valid for β-decay electrons with pitch angle $\theta_{\text{src}} \approx 0^\circ$ in the source. For larger pitch angles, the electrons follow the magnetic field lines in a cyclotron motion. This motion enlarges the effective path length through the gas density, leading to a higher effective column density $\rho d_{\text{eff}}(z, \theta_{\text{src}})$ [Kuc+18]. The effective column density can be calculated in analogy to equation 7.1 to

$$\rho d_{\text{eff}}(z, \theta_{\text{src}}) = \frac{\rho d(z)}{\cos\theta_{\text{src}}} = \frac{1}{\cos\theta_{\text{src}}} \int_{z'=z}^{+L/2} \rho(z')\, \mathrm{d}z', \tag{7.3}$$

taking into account the electron's extended path in the tritium gas [Kuc+18]. The scattering probability for the β-decay electrons depends on the term $\rho d_{\text{eff}}(z, \theta_{\text{src}}) \cdot \sigma$, where σ denotes the scattering cross section of electrons with tritium molecules for the respective investigated case of either elastic or inelastic scattering. Although the scattering cross section is considered energy dependent in the 40 eV fit window in neutrino mass analyses, we treat it as a constant for the following derivation of the scattering probabilities for ease of reading [Ake+21a; Ake+21b].
Because of the low probability for an electron to scatter off a single gas molecule in the WGTS, the probability P_i for i-times scattering can be calculated according to a Poisson distribution

$$P_i(z, \theta_{\text{src}}) = \frac{\left(\rho d_{\text{eff}}(z, \theta_{\text{src}}) \cdot \sigma\right)^i}{i!} \mathrm{e}^{-\rho d_{\text{eff}}(z, \theta_{\text{src}}) \cdot \sigma} \tag{7.4}$$

with expectation value $\rho d_{\text{eff}}(z, \theta_{\text{src}}) \cdot \sigma$ [Kle+19]. Depending on the start position of the electron, the different scattering probabilities differ significantly. The probability to leave the WGTS without scattering is $P_0(z, \theta_{\text{src}}) = \exp\left(-\rho d_{\text{eff}}(z, \theta_{\text{src}}) \cdot \sigma\right)$ and thus significantly larger for signal electrons starting near the WGTS front end compared to those starting from the rear end. The electron's pitch angle θ_{src} in the source influences the path length of the electron in the source gas, additionally altering the scattering probabilities. The probability for β-decay electrons to leave the WGTS in downstream direction without inelastic scattering is shown in figure 7.2 as a function of the axial starting position and the electron's pitch angle in the source.

The asymmetric dependence of the scattering probability on the axial starting position, as well as on the electron's pitch angle, needs to be included in the calculation of the response function, and thus also in the calculation of the scattering probabilities. In the KATRIN experiment, two approaches are being pursued.
The first one is to longitudinally subdivide the source region into individual segments along the WGTS beam tube, the scattering probability is then calculated for each segment individually. To increase the computational speed, it is useful to exploit the isotropic angular emission $\omega(\theta_{\text{src}}) = \sin\theta_{\text{src}}$ of the β-decay electrons in the WGTS. The scattering probability $P_i(z, \theta_{\text{src}})$ can then be averaged with respect to the pitch angle to

$$P_i(z) = \frac{1}{1 - \cos(\theta_{\text{max}})} \int_{\theta_{\text{src}}=0}^{\theta_{\text{max}}} \sin\theta_{\text{src}} \cdot P_i(z, \theta_{\text{src}})\, \mathrm{d}\theta_{\text{src}}, \tag{7.5}$$

with θ_{max}, describing the maximal acceptance angle due to the magnetic mirror effect in the PCH (see section 3.1.2). The averaging process assumes that the scattering probability is not significantly affected by the small angular changes resulting from

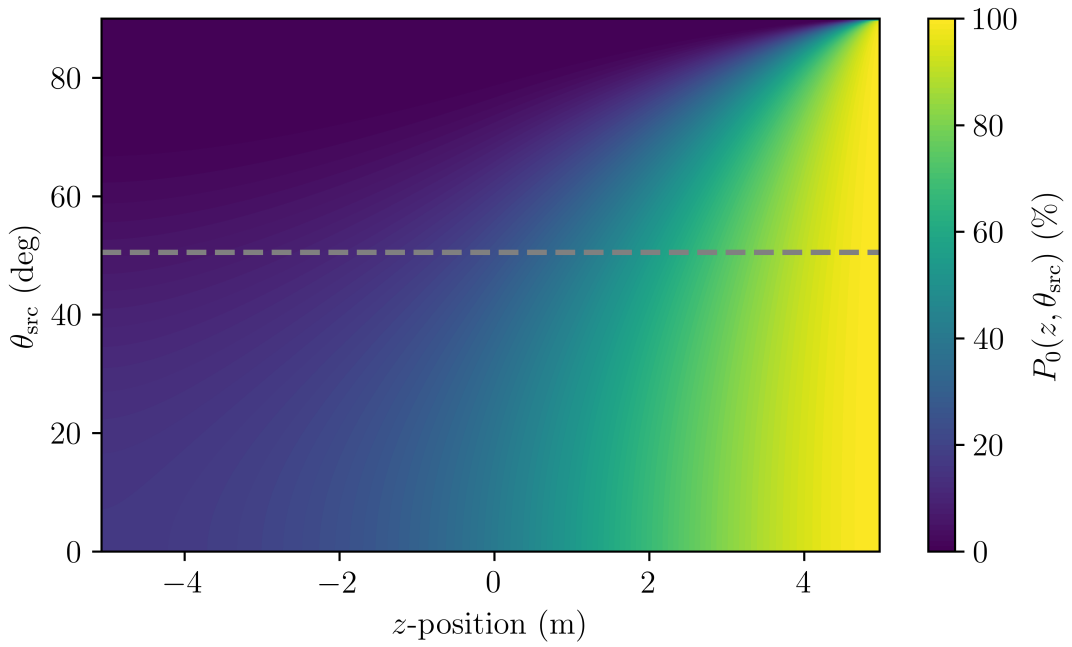

Figure 7.2.: **Probability P_0 for β-decay electrons to leave the WGTS without inelastic scattering in downstream direction as function of the axial starting position z and pitch angle θ_{src}.** Probability calculated according to equation 7.4. The dashed line represents the maximal acceptance angle $\theta_{\mathrm{max}} = 50.5°$, larger pitch angles are magnetically reflected by the PCH magnetic field.

the scattering. As shown in reference [Gro15], the angular changes due to scattering processes are indeed small and can be neglected for neutrino mass analysis in the 40 eV fit window. Based on the individual scattering probabilities that now solely depend on the z-position, the response function for every longitudinal segment is calculated. Afterwards, the individual response functions are averaged to a central response functions with weights according to tritium gas molecules inside the individual segments. This method allows not only to include the asymmetric longitudinal scattering probability, but also further longitudinal inhomogeneities along the WGTS beam tube, for example variations of the magnetic field. [Kle+19] S. Groh estimates that 50 segments along the WGTS beam tube are necessary in the calculation to meet the KATRIN sensitivity requirement [Gro15]. The major disadvantage of this method is that it is computationally expensive, as the scattering probabilities and the response function need to be evaluated for each segment individually.

An alternative approach was proposed by L. Kuckert in reference [Kuc16]. The scattering probabilities are averaged with respect to the initial pitch angle as well as with respect to their longitudinal starting position. At the same time, all physical quantities, for example the source magnetic field, are averaged in this approach. The calculation of the averaged scattering probabilities is significantly faster compared to the segmentation approach, as it can be performed with pre-calculated analytical formulas. In the following, we derive the analytical formula by example of the zero scattering probability, based on reference [Kuc16]. In a first step, the averaged effec-

tive column density is introduced. Following equation 7.3, we exploit the isotropic angular emission of β-decay electrons to average over the pitch angle. This leads to

$$\begin{aligned}\overline{\rho d(z)}_{\text{eff}} &= \frac{1}{1-\cos(\theta_{\max})}\int_{\theta_{\text{src}}=0}^{\theta_{\max}} \sin\theta_{\text{src}} \cdot \ \rho d_{\text{eff}}\left(z,\theta_{\text{src}}\right)\mathrm{d}\theta_{\text{src}},\\ &= \frac{\rho d(z)}{1-\cos(\theta_{\max})}\int_{\theta_{\text{src}}=0}^{\theta_{\max}} \frac{\sin\theta_{\text{src}}}{\cos\theta_{\text{src}}}\mathrm{d}\theta_{\text{src}},\\ &\approx 1.24\cdot\rho d(z) \end{aligned} \tag{7.6}$$

for $\theta_{\max} = 50.5°$. Inserting this relation into equation 7.4 leads to a purely z-dependent formula for the scattering probabilities, with

$$P_i(z) = \frac{\left(1.24\cdot\rho d\left(z\right)\cdot\sigma\right)^i}{i!}\mathrm{e}^{-1.24\cdot\rho d(z)\cdot\sigma}.$$

Averaging by integration over z then finally leads to the averaged zero scattering probability to

$$\begin{aligned}\overline{P}_0 &= \frac{1}{1.24\cdot\rho d\cdot\sigma}\int_{(\rho d\sigma)'=0}^{\rho d\cdot\sigma}\mathrm{e}^{-1.24\cdot(\rho d\sigma)'}\mathrm{d}(\rho d\sigma)',\\ &= \frac{1}{1.24\cdot\rho d\cdot\sigma}\left(1-\mathrm{e}^{-1.24\cdot\rho d\cdot\sigma}\right)\end{aligned} \tag{7.7}$$

that only depends on the overall WGTS column density. [Kuc+18] The derived formula yields a 40 % probability for β-decay electrons to leave the WGTS without inelastic scattering in the case of nominal column density, assuming that the electrons' energies are near the molecular tritium endpoint.
Sensitivity studies carried out with the SSC software package yield consistent results for the averaging and the segmentation approach, as long as the number of segmentations are sufficiently large. We use the averaging approach in the following analyses due to the significantly faster calculation time.

As shown in equation 7.2, the column density is proportional to the number of tritium atoms in the WGTS and thus to the overall activity. By either increasing the column density or the cut-off angle, we would increase the signal count rate at the detector, leading to an improved statistical uncertainty in neutrino mass measurements. The consequence of enlarging the column density or the cut-off angle is an enhanced scattered-to-unscattered-electrons ratio, increasing the systematic uncertainty due to energy losses in scattering processes [KAT05]. The design values of $\rho d_{\text{nom}} = 5\times10^{21}\,\text{molecules/m}^2$ and $\theta_{\max} = 50.5°$ balance the effects of statistical and systematic uncertainty [Kle+19; KAT05].

7.1.3. Energy-Loss Function and Response Function

Having derived an accurate description for the scattering probabilities, it is necessary to derive the probability density function that describes the energy loss for i-fold scattering. This function is crucial to include the energy-loss process of the β-decay electrons due to scattering off tritium molecules in the KATRIN response function. The description of the energy-loss model requires a clear separation of the elastic from the inelastic scattering process, since significantly more energy is exchanged in the inelastic process.

Elastic Scattering Process

In an elastic scattering process, only the angle of the incoming electron is changed due to Coulomb interactions with the molecule. Unlike inelastic scattering, the initial electronic state of the molecule is not changed. [Sch21]
The angular change of the incident electron leads to a momentum transfer, reducing its kinetic energy. This angular change is small for electron scattering off tritium molecules, the median scattering angle is $\overline{\theta}_{\mathrm{scat}} = 2.1^{\circ}$ [Kle+19]. The energy loss ΔE in the elastic scattering process due to the angular change is estimated as

$$\Delta E = 2\frac{m_{\mathrm{e}}}{M_{\mathrm{T}_2}} E \cdot (1 - \cos\theta_{\mathrm{scat}})$$

with M_{T_2} being the molecular mass of tritium [Kle+19]. Based on angular distribution measurements of elastic scattering of electrons off molecular hydrogen [NDS85], the energy-loss distribution is estimated to be narrow with median energy loss $\overline{\Delta E} = 4\,\mathrm{meV}$. [Kle+19]
J. Liu parametrized the cross section for elastic scattering of high-energy electrons off hydrogen in the first Born approximation in reference [Liu87]. Applying the derived formula for β-decay electrons near the tritium decay endpoint yields $\sigma_{\mathrm{el}} = 0.28 \times 10^{-22}\,\mathrm{m}^2$ [Kle+19]. The inelastic scattering cross section for this energy is $\sigma_{\mathrm{inel}} = (3.64 \pm 0.02) \times 10^{-22}\,\mathrm{m}^2$ [Ake+21b], one order of magnitude larger than the elastic scattering cross section. The probability for elastic scattering of molecular tritium by electron impact is therefore significantly suppressed with respect to the inelastic process.
Incorporating the narrow elastic scattering energy-loss distribution in the response function is computationally expensive, as it requires fine numerical binning for the convolution [Kle+19]. The small mean energy loss paired with the relatively small cross section make elastic scattering, compared to the inelastic process, a minor energy-loss process for β-decay electrons in KATRIN [Kle+19]. Neglecting this effects yields a negligible bias on the squared neutrino mass of $5 \times 10^{-5}\,\mathrm{eV}^2$ [Kle+19]. The elastic scattering of electrons with tritium gas in the WGTS is therefore neglected in KATRIN neutrino mass analyses.

Inelastic Scattering Process

The energy loss of electrons in inelastic scattering processes with tritium molecules starts at $\Delta E \approx 11\,\mathrm{eV}$ and increases up to half the incident electron's kinetic energy [Ake+21c]. The precise and accurate knowledge of the energy-loss model up to 40 eV is crucial for a proper modeling of the β-decay spectrum in the 40 eV analysis window. The systematic uncertainty contribution to the measured neutrino mass, related to uncertainties of the energy-loss model in scattering processes, was expected to be the dominant systematic contribution in the KATRIN technical design report. [KAT05; Ake+21b]
An electron scattering off a tritium molecule is much more complex than the case of scattering off a single atom, as the tritium molecule features a rich spectrum of electronic excitations in combination with rotational and vibrational states up to the ionization threshold at around 15.5 eV. Measurements of the energy-loss probability density function performed so far (see for example references [Ase+00; Abd+17])

do not meet the KATRIN requirements in accuracy and precision. Therefore the energy-loss probability density function is measured with the Rear Section e-gun. The energy-loss model is approached by complementary methods of integral (see reference [Sch21]) and time-of-flight measurements (see reference [Ake+21c]), using the laser light source of the e-gun in different modes. Combining both experimental results leads to the accurate and precise KATRIN energy-loss probability density function used in neutrino mass analysis. [Ake+21b]
The KATRIN energy-loss function $f(\Delta E)$ close to the tritium endpoint is based on a semi-empirical model. Three Gauss functions describe the three groups of tritium molecular states between 11 eV and 15 eV. The ionization continuum above 15.486 eV is described by the relativistic binary-encounter-dipole model [KSP00]. The energy-loss model is normalized to unity for the integral $\int_{\Delta E=0}^{E/2} f(\Delta E)\ \mathrm{d}\Delta E$ to represent a probability density distribution. [Ake+21c]
The energy-loss probability function for one-fold scattering $f_1(\Delta E)$ equals the general energy-loss function $f(\Delta E)$ [Ake+21c]. The energy-loss probability function for i-fold scattering is derived by $(i-1)$-times convolution of the general energy-loss function with itself [Ake+21c]. The energy loss for zero-times scattering is mathematically described by the Dirac delta function $\delta(\Delta E)$ [Ake+21c]. Summarizing, the energy-loss probability distributions for different number of scatterings are

$$\begin{aligned} f_0(\Delta E) &= \delta(\Delta E) \\ f_1(\Delta E) &= f(\Delta E) \\ f_2(\Delta E) &= f(\Delta E) \otimes f(\Delta E) \\ f_3(\Delta E) &= f(\Delta E) \otimes f(\Delta E) \otimes f(\Delta E) \\ &\dots \end{aligned} \tag{7.8}$$

The energy-loss probability distributions for one-, two- and three-fold scattering, derived from the KATRIN model, is shown in the lower plot of figure 7.3.

Calculation of the Response Function

The response function describes the probability for β-decay electrons at certain kinetic starting energy and Main Spectrometer retarding potential to reach the detector. Therefore, the profound knowledge of the energy-loss model due to scattering processes in the WGTS is merged together with the transmission function of the Main Spectrometer into the response function.
In a first step, the weighted energy-loss function needs to be defined, that describes the resulting energy-loss probability distribution for all scatterings combined, taking the individual scattering probabilities for i-fold scattering into account. For this, the individual energy-loss probability distributions $f_i(\Delta E)$ are weighted with the probability for i-fold scattering in the source $\overline{P}_i(\rho d \cdot \sigma)$, as derived in equation 7.7.

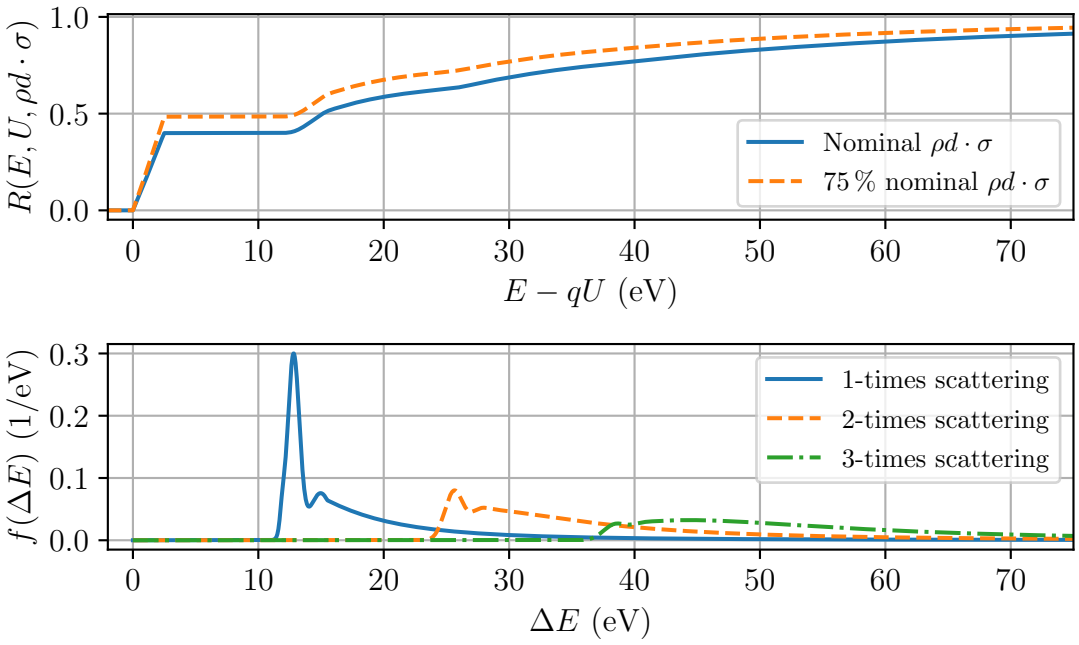

Figure 7.3.: **KATRIN response function $R(E, U, \rho d \cdot \sigma)$ (upper plot) and energy-loss probability distribution $f(\Delta E)$ for inelastic scattering (lower plot).** The KATRIN response function is the convolution of the MAC-E filter transmission function with the weighted energy loss due to inelastic scattering. The shape of the response function versus surplus energy $E - qU$ below 11 eV is defined by the transmission function and the probability for electrons to escape the WGTS without scattering. Once scattered electrons loose at least $f(\Delta E) \approx 11$ eV in inelastic scattering off molecular tritium, therefore they can only contribute for energies higher $E - qU > 11$ eV to the response function. Same holds for higher-order scattering.

The weighted energy-loss function $\mathcal{F}(\rho d \cdot \sigma, \Delta E)$ is then calculated to

$$\begin{aligned}\mathcal{F}(\rho d \cdot \sigma, \Delta E) =& \overline{P}_0(\rho d \cdot \sigma) \cdot \delta(\Delta E) \\ &+ \overline{P}_1(\rho d \cdot \sigma) \cdot f_1(\Delta E) \\ &+ \overline{P}_2(\rho d \cdot \sigma) \cdot f_2(\Delta E) \\ &+ \ldots \\ =& \sum_{i=0} \overline{P}_i(\rho d \cdot \sigma) \cdot f_i(\Delta E). \end{aligned} \tag{7.9}$$

[Sch21] Processes of eight times scattering and larger are normally neglected in the analysis because of their vanishing contribution and for faster calculation.
The response function $R(E, U, \rho d \cdot \sigma)$ is then derived by convolving $\mathcal{F}(\rho d \cdot \sigma, \Delta E)$ with the transmission function $T(E, U)$ (see equation 3.12) to [Kle+19; Sch21]

$$R(E, U, \rho d \cdot \sigma) = \int_{\Delta E=0}^{E} T(E - \Delta E, U) \cdot \mathcal{F}(\rho d \cdot \sigma, \Delta E)\, \mathrm{d}\Delta E. \tag{7.10}$$

The response functions for an isotropic source with the nominal Main Spectrometer energy resolution and two different column densities are shown in the upper graph of figure 7.3.

7.1.4. Column Density Impact on Neutrino Mass Measurements

As described in 3.3.1, the rate $\dot{N}_{\mathrm{theo}}$ of β-decay electrons arriving at the detector can be described with the response function R and the theoretical description of the β-decay spectrum $\mathrm{d}\Gamma/\mathrm{d}E$ to

$$\dot{N}_{\mathrm{theo}}(U, \rho d) = \frac{1}{2} \cdot N_{\mathrm{T}}(\rho d) \int_{qU}^{E_0} \frac{\mathrm{d}\Gamma}{\mathrm{d}E}(E_0, m_\nu^2) \cdot R(E, U, \rho d \cdot \sigma)\ \mathrm{d}E. \tag{7.11}$$

The factor 1/2 denotes that only electrons emitted in forward direction can contribute to the measured rate at the FPD. The number of tritium nuclei in the WGTS is depicted as N_{T}. The dependence of the expected count rate on the column density enters the equation in the number of tritium nuclei as well as in the response function. [Kle+19] As shown in reference [Köh19], it is necessary to include the column density as external input for neutrino mass analysis, because it cannot be treated as free fit parameter in order to reach the KATRIN sensitivity goal. Since one of the major goals of this chapter is to develop accurate and precise determination methods of the column density during neutrino mass measurements, it is necessary to investigate the column density impact on neutrino mass analysis in this thesis.

Qualitative Investigation

The number of tritium nuclei $N_{\mathrm{T}}(\rho d)$ in the WGTS acts as normalization factor in equation 7.11. It is proportional to the column density (see equation 7.2). If the calculated column density, used as input for neutrino mass analyses, differs from the unknown true column density, it will result in a discrepancy between measured and expected rates. However, the signal amplitude of the decay spectrum is treated as free fit parameter in neutrino mass analyses (see chapter 3.3.2). This fitted amplitude fully absorbs the potentially incorrect modeling of the term $N_{\mathrm{T}}(\rho d)$.
The second term depending on the column density is the response function R. The column density determines in the response function the probabilities for i-fold inelastic scattering of β-decay electrons with tritium gas in the WGTS (see equation 7.9 and 7.10). If the estimated input column density differs from the true column density, also the scattering probabilities differ. This leads to a different shape of the response function (see upper plot of figure 7.3). The shape distortion in the response function propagated into the expected decay spectrum biases the fitted neutrino mass, as the neutrino mass imprint itself on the spectrum is also a shape distortion.
The influence of a deviating column density on the expected measured β-decay spectrum is visualized in figure 7.4. The deviation is chosen to be 25 % for better visibility by eye. The expected rates for the two column densities is shown in the upper graph. The larger column density causes, as expected, higher count rates at the detector due to more tritium molecules in the WGTS. The lower graph shows the resulting shape distortion between the two spectra, using the ratio of both spectra as indicator. For decreasing retarding potential, the strength of the shape distortion increases, since more i-times scattered electrons contribute to the spectrum and therefore the scattering probabilities become more important. As the ratio is not constant versus retarding potential, it will not fully be absorbed by the fitted signal amplitude, but also by the inferred neutrino mass.

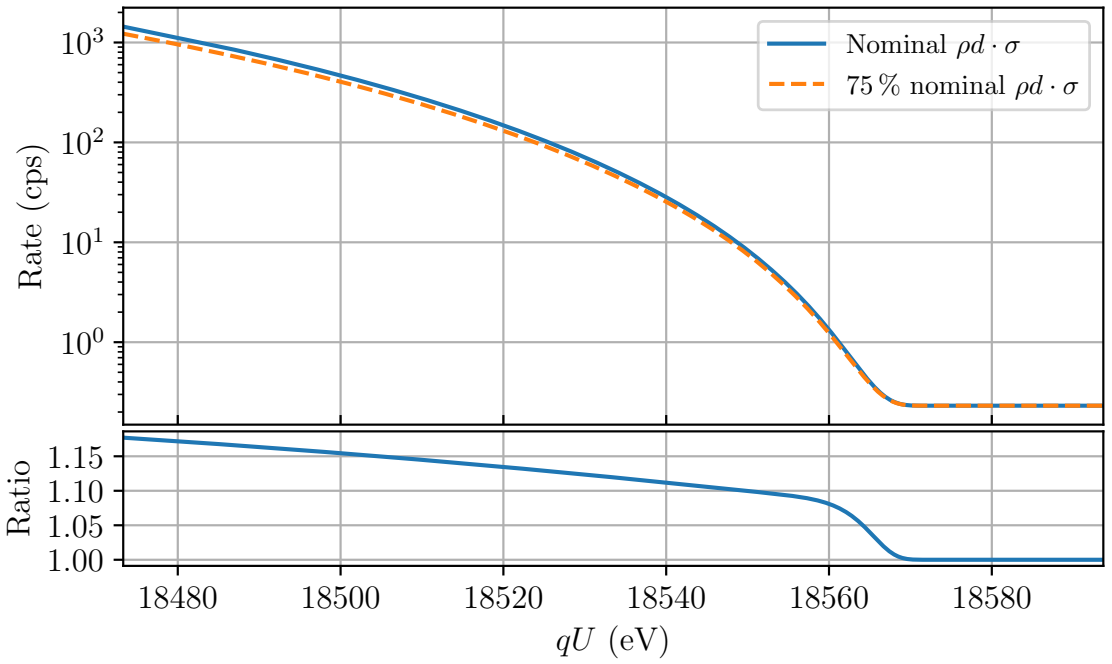

Figure 7.4.: **Influence of the column density on the expected measured β-decay rate.** The simulated β-decay rate over the applied retarding potential qU for nominal and 75 % column density is shown in the upper graph. The difference between the two spectra increases for decreasing retarding potential. The ratio of both spectra to visualize the difference in shape, that also increases with decreasing retarding potential, is presented in the lower graph.

Quantitative Investigation

After the qualitative discussion of the column density influence on the measured neutrino mass, the SSC software package and the KaFit framework are used to quantify the influence. Before discussing the procedure and results of the neutrino mass study for the necessary column density precision and accuracy, we must address the question of the exact quantity to be investigated in the sensitivity study.
As examined in the qualitative discussion, the neutrino mass bias due to wrong column density input is caused by the response function term in equation 7.11. As it comprises the scattering probabilities, it depends on the product of column density times inelastic scattering cross section $\rho d \cdot \sigma$ (see equation 7.10). Consequently, the observable for the quantification of the column density impact on the neutrino mass uncertainty is the term $\rho d \cdot \sigma$. In the following, we will focus thus on the study of the $\rho d \cdot \sigma$ impact and its uncertainties. As reference quantity, we translate the nominal column density $\rho d_{\mathrm{nom}} = 5 \times 10^{21}\,1/\mathrm{m}^2$ to column density times cross section $\rho d_{\mathrm{nom}} \cdot \sigma = 1.82 \pm 0.01$.
We investigate the column density influence on the neutrino mass with the pull-term method as described in section 3.3.5. An Asimov dataset is simulated using the SSC software package with certain column density $\langle \rho d \cdot \sigma \rangle$ and neutrino mass set to zero. Typical values are chosen for the nuisance parameters necessary for spectrum calculation, for example the magnetic fields. Instead of the nominal four-parameter fit with m_ν^2, E_0, A_s, and R_{bg}, the $(\rho d \cdot \sigma)$-term is added as fifth fit

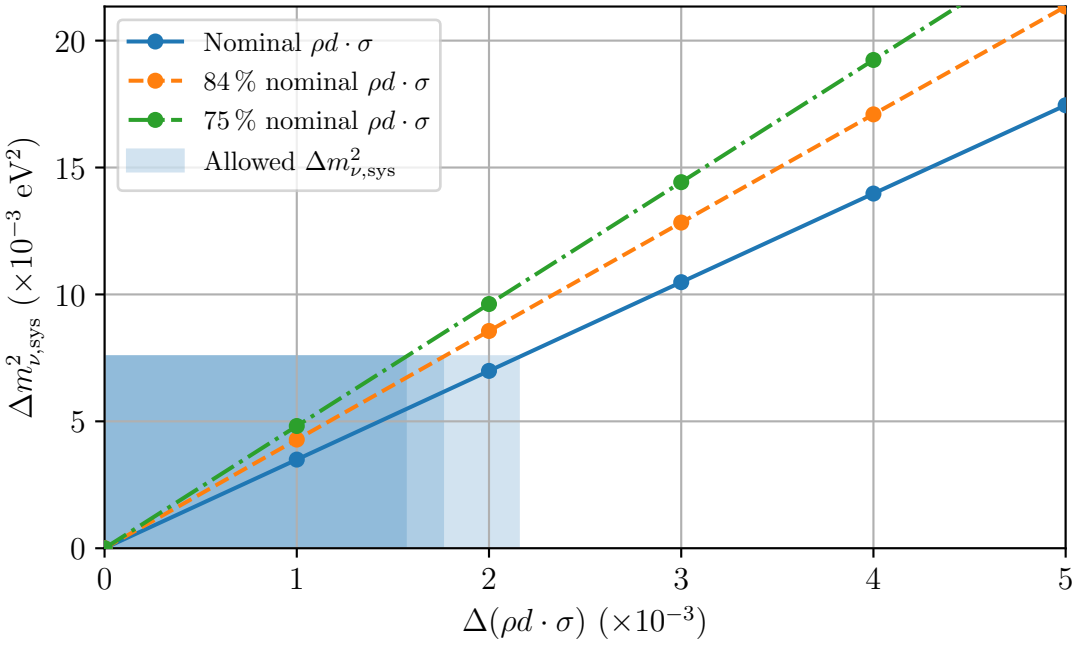

Figure 7.5.: **Impact of the column density uncertainty $\Delta(\rho d \cdot \sigma)$ on the systematic neutrino mass uncertainty $\Delta m^2_{\nu,\mathrm{sys}}$.** The influence of the column density uncertainty on the systematic neutrino mass uncertainty is shown for three different mean column densities in the nominal 40 eV analysis window. The allowed systematic uncertainty contribution to the squared neutrino mass of $\Delta m^2_{\nu,\mathrm{sys}} \leq 7.5 \times 10^{-3}\,\mathrm{eV}^2$ in order to reach the final KATRIN sensitivity goal is indicated for each column density by the blue-shaded area.

parameter, constrained by a penalty term. The penalty term in the likelihood is Gauss-shaped with mean $\langle \rho d \cdot \sigma \rangle$ and width $\Delta(\rho d \cdot \sigma)$, that is chosen accordingly to the investigated uncertainty. By comparison of the shape of the likelihood function in the four- versus the five-parameter fit, we can estimate the systematic uncertainty contribution $\Delta m^2_{\nu,\mathrm{sys}}$ due to the column density uncertainty.

The influence of the column density uncertainty at various mean column densities on the systematic neutrino mass uncertainty is calculated in the range $\Delta(\rho d \cdot \sigma) \in [0, 5] \times 10^{-3}$. We use the nominal 40 eV fit range as analysis window. This study is carried out for 100 %, 84 %, and 75 % nominal column density, as they are of interest for the subsequent sections.
The results of this study is shown in figure 7.5, the neutrino mass uncertainty increases proportionally with column density uncertainty for the investigated range. The fit does obviously not learn about the column density from the measured data at this precision, as otherwise the uncertainty would deviate from the linear behavior (see for example figure 4.6). This underlines the importance of a correctly estimated column density value as input parameter for neutrino mass analysis with KATRIN. The study also shows, that the neutrino mass uncertainty is larger for smaller mean column density at fixed absolute $\Delta(\rho d \cdot \sigma)$. Comparing the calculated neutrino mass uncertainties to the allowed $7.5 \times 10^{-3}\,\mathrm{eV}^2$ uncertainty of a single systematic contribution, it is clear that the precision and accuracy on the calculated column density

has to be on the permill-level. It needs to be better than 1.6×10^{-3} for 75 %, better than 1.8×10^{-3} for 84 %, and better than 2.1×10^{-3} for nominal column density to fulfill the final KATRIN systematic requirement. All the three boundaries translate to a maximal relative uncertainty on the column density times cross section of approximately 0.12 %.

An approach to reach the necessary precision and accuracy on the column density is the profound modeling of the gas dynamics in the STS. The following section gives an overview of achievements to model the gas dynamics in KATRIN.

7.2. Column Density Modeling

The comprehensive model of tritium gas dynamics in the WGTS, summarized below, was developed by several authors (see references [Höt12; Kuc16; Kuc+18; Hei18]). The devised model allows one to investigate characteristics of the tritium gas distribution in the framework of the KATRIN experiment. The impact of effects that can barely be measured, for example radial temperature inhomogeneity, can be tested in great detail with this model. Additionally, it can be used to predict the column density as input parameter for neutrino mass analyses. The following section summarizes the main steps in deriving the gas model, based on references [Hei18; Kuc+18] unless stated otherwise. For details we recommend the original publications to the interested reader.

7.2.1. General Approach and Challenges

The gas transport in the WGTS can be described by the kinetic Boltzmann equation [Sha15]

$$\frac{\partial f}{\partial t} + \vec{v} \cdot \nabla_r f = Q(f, \vec{v}). \tag{7.12}$$

The collision integral $Q(f, \vec{v})$ accounts for binary intermolecular collisions. Based on the collision integral, the Boltzmann equation is solved for the particle velocity distribution f of the gas molecules describing macroscopic quantities like bulk velocity of the gas. [Kuc+18]
The Boltzmann equation can only be solved numerically for simple cases or analytically with approximations to the collision integral [SS98]. Approximate model equations, used in the KATRIN model, are the S-model [Sha68] and the BKG equation [BGK54]. Complementary, direct simulation Monte Carlo approaches [Dav60; Bir63] are used to describe the complete KATRIN source section with its rich variety of pressure regimes. [Kuc+18]
Further approximations can be applied to solve equation 7.12 depending on the gas flow regime. Thereby, the rarefaction parameter δ serves as indicator for the regime [Sha15]. It is calculated to

$$\delta = \frac{a}{\lambda} = \frac{\eta v_{\mathrm{m}}}{p}, \tag{7.13}$$

with free path λ, characteristic dimension a of the gas flow, most probable speed v_m, pressure p and dynamic viscosity η [Sha15].
Typically three regimes can be distinguished, each with its own characteristics, leading to different methods to calculate the gas flow:

- Hydrodynamic regime with $\delta \gg 1$: the mean free path is so small, that collisions between gas and tube walls can be neglected compared to inter-molecular collisions. The gas flow can be described by continuum mechanics.
- Transitional regime with $\delta \approx 1$: inter-molecular collisions and collisions between gas and tube wall are equally important; neither of them can be neglected.
- Free-molecular regime with $\delta \ll 1$: probability for inter-molecular collisions is vanishingly small, since the free path length is significantly larger than the characteristic dimension.

The WGTS covers the whole range of rarefied gas flow regimes. Close to the longitudinal center of the beam tube, the tritium gas flow is in the hydrodynamic regime. This regime covers most parts of the central beam tube, namely the range from $z = -4\,\mathrm{m}$ to $z = 4\,\mathrm{m}$. Afterwards, the transitional regime starts. At the axial positions of the second DPS-1R/F pump ports, the molecules enter the free molecular regime. Due to the combination of all three rarefied gas regimes in the WGTS, different approaches must be used to describe the gas flow in the respective area to derive the gas density distribution. [Hei18; Kuc+18]

7.2.2. Individual and Combined Density Distributions

About 99 % of the tritium gas column density is situated in the central beam tube of the WGTS [Kuc+18]. Therefore, accurate gas calculations are required especially in this part. However, if we aim to fulfill the KATRIN requirement with sub-percent uncertainty on column density estimations, we need to take into account also the gas distribution in the DPS-1F/R pump ports.

Central WGTS Beam Tube

The central beam tube features a large length (10 m) to radius (0.045 m) ratio, that allows us to consider the flow fully developed for the main part of the tube. In this part, the calculation can be reduced to one dimension. Only the gas inlet region of the WGTS as well as the outlet region should be modeled in two dimensions. The connections between the regions are calculated via the assumption, that the system is in equilibrium and the flow rates are the same in all parts. [Kuc+18]
The mass flow rate is the key to solve the Boltzmann equation for the central beam tube, as it is constant in the absence of additional gas sources. The mass flow rate $\dot{M}$ is defined for a long thin tube as

$$\dot{M} = \frac{\pi R^3}{v_\mathrm{m}} \left(-G_\mathrm{P}(\delta, \alpha) \frac{\mathrm{d}p}{\mathrm{d}z} + G_\mathrm{T}(\delta, \alpha) \frac{p(z)}{T(z)} \frac{\mathrm{d}T}{\mathrm{d}z} \right) \tag{7.14}$$

with beam tube radius R, local temperature T, and local pressure p. The coefficient for the Poiseuille flow is denoted as $G_{\mathrm{P}}(\delta, \alpha)$, the one for the thermal creep as $G_{\mathrm{T}}(\delta, \alpha)$ [Sha97; Sha15]. The coefficients are dimensionless and depend on the rarefaction parameter and the accommodation coefficient α, describing gas surface interactions. Parameterizations as well as tabulated values can be found in literature, for example in references [SS98; Sha15]. For KATRIN, isothermal and non-isothermal flow need to be considered, thus both $G_{\mathrm{P}}(\delta, \alpha)$ as well as $G_{\mathrm{T}}(\delta, \alpha)$ become important. We can then derive the longitudinal pressure profile, which is equivalent to the longitudinal density profile, by solving equation 7.14 for $\mathrm{d}p/\mathrm{d}z$ via the constant mass flow rate. Important parameters for this are:

- The coefficients $G_{\mathrm{T}}(\delta, \alpha)$ and $G_{\mathrm{T}}(\delta, \alpha)$, that depend on the accommodation coefficient as well as the rarefaction parameter.
- Inlet pressure p_{in} at the centre of the WGTS, defined via the pressure controlled buffer vessel p_{b}.
- Outlet pressure p_{out} at the end of the WGTS, defined via the pumping probability of DPS-1R/F.
- Temperature profile $T(z)$ of the beam tube, defined by the cooling system. The profile is derived from temperature measurements along the beam tube.
- Tritium throughput q, defined inter alia by the pressure controlled buffer vessel. The throughput defines the mass flow rate $\dot{M}$.

Furthermore, the longitudinal rarefaction parameter evolution needs to be converted to a pressure evolution with equation 7.13. The necessary tritium viscosity at 30 K temperature is derived from measurement with hydrogen and deuterium, considering inter alia the mass ratio of the isotopologues. [Hei18; Kuc+18]
Due to a small asymmetry of the WGTS cryostat of about 7 cm in length between rear and front part relative to the tritium injection, the calculations need to be performed separately for up- and downstreaming gas, starting from the injection chamber [Hei18]. As mentioned above, the injection chamber as well as the outlet region of the beam tube should be modeled in two dimensions. However, by using an effective length for these two regions, we can still calculate the complete beam tube in one dimension [SS98; PVS14].
As shown in great detail by F. Heizmann [Hei18], the heat load from the pump ports can cause a warming of the beam tube parts, that are not in contact with the beam tube cooling. This azimuthal temperature gradient can cause radial and azimuthal gas flow, leading to radial and azimuthal column density inhomogeneity (more details given in section 7.4). Despite this gradient, the one dimensional calculation can be maintained by introducing pre-calculated azimuthal density distributions. The distributions are included with weights according to the corresponding temperature profile at a certain beam tube cross section, deriving thereby a pseudo-three-dimensional density distribution for each point in the central WGTS beam tube. [Hei18]

Pumping Section DPS-1R/F

The density distribution in the DPS-1R/F defines the outlet pressure of the WGTS, that is needed as an input parameter for the density calculation in the central WGTS

beam tube. The rarefaction parameter ranges from $\delta \approx 0.5$ (first pump port), to $\delta \approx 10^{-2}$ in the second pump port. Therefore, the flow is in the transitional regime in the first pump port and changes to the free-molecular regime towards the second pump port. In this part, the calculations need to be carried out in three dimensions due to the complex geometry, and since collisions of the gas molecules with the beam tube walls can no longer be neglected. [Hei18; Kuc+18]
The density distribution in the first pump port is solved by a direct simulation Monte Carlo. For the sake of computational costs, the geometry is simplified where possible. An overlapping region of 32 cm between the central beam tube and the first pump port is used to ensure a smooth transition. With that approach, the outlet density of the central WGTS beam tube is estimated to 2 % of the inlet density. [Hei18; Kuc+18]
The gas flow in the beam tube connecting the first and second pump port is also in the transitional regime. By using the COMSOL Multiphysics software, the Boltzmann equation is solved in an isothermal approach in two dimensions. Uncertainties in the first pump port directly propagate into the gas density uncertainty of the tube connecting the first and second pump port. [Hei18; Kuc+18]
In the second pump port, the rarefaction parameter yields $\delta \approx 10^{-2}$, we can thus assume that the gas flow is in the free-molecular regime. The Boltzmann equation for the three-dimensional model of the pump port is solved by the molecular flow interface of COMSOL. [Hei18]

Combined Density Distribution

The above discussed domains need to be smoothly connected to yield the global density distribution. Based on the gas flow in the central WGTS, the inlet and outlet regions are scaled accordingly. The uncertainties of the respective outlet pressures are propagated to the global WGTS gas outlet. [Kuc+18] The calculated combined longitudinal gas distribution in the WGTS and its uncertainty is shown in figure 7.6.

7.2.3. Gas Model for Nominal Operation

Based on the gas flow calculations derived in section 7.2.2, it is now possible to calculate the WGTS column density as function of a quantity, that can be monitored during nominal KATRIN operation. The input of choice by F. Heizmann [Hei18] is the tritium injection rate, that is equivalent to the WGTS throughput. The throughput before injection is measured by a flow meter, located between the two buffer vessels (see also figure 7.15). During nominal KATRIN operation, the inner loop is operated in a closed circle. [Hei18]
During the start-up of the circulation, tritium might be adsorbed by the walls of the tritium injection capillary causing a reduction of the mass flow rate between the buffer vessel and the injection chamber. As soon as a stable circulation is reached, there is no decrease or additional source of tritium gas between the buffer vessel and the injection chamber. In this steady state, the mass flow rate in the beam tube can be estimated by the flow meter measurement. Based on the measured throughput, we can calculate the density profile and thus get an estimate on the column density. [Hei18]

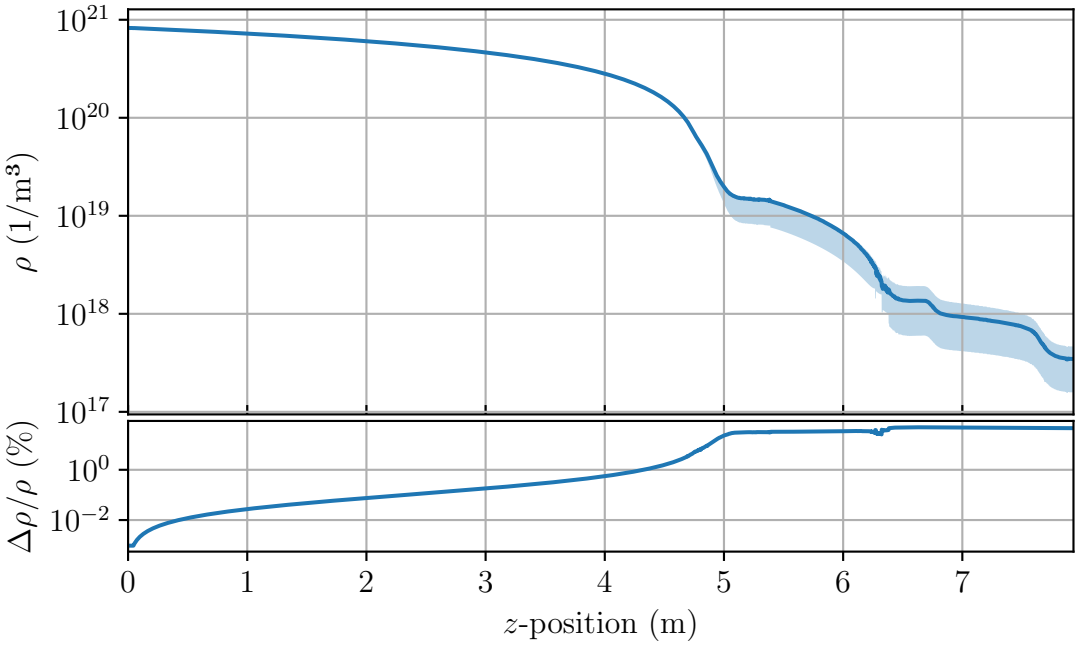

Figure 7.6.: **Calculated longitudinal gas density profile ρ and its relative precision $\Delta\rho/\rho$ from tritium injection position to the WGTS front end.** The tritium gas density is at maximum at the injection position ($z = 0\,\mathrm{m}$) and decreases towards the end of the central beam tube ($z \approx 5\,\mathrm{m}$) by nearly two orders of magnitude. The density is reduced by another magnitude by the front end pump ports ($z > 5\,\mathrm{m}$). The relative uncertainty on the gas model calculation is mostly below 1 % in the central beam tube. It increases significantly in DPS-1F, as the uncertainties of the density distributions propagate in the gas flow direction and due to the uncertainty on the sticking coefficient of the turbo-molecular pumps. Simulation data based on [Kuc+18].

F. Heizmann discusses in great detail the derivation of the estimated column density based on gas model calculations [Hei18]. We briefly summarize in the following the main steps.
The throughput, measured by the flow meter between the two buffer vessels is not exactly the injection rate, as the second buffer vessel can use its valve to stabilize its pressure. Therefore, a semi-empirical translation of pressure controlled buffer vessel to injection rate q is derived by measurements at stable gas circulation. The mass flow rate $\dot{M}$ can then be calculated to

$$\dot{M} = \frac{M_{\mathrm{T}_2}}{k_{\mathrm{B}} T} \cdot q,$$

with M_{T_2} being the mass of the tritium gas molecule and k_{B} as the Boltzmann constant. With the known mass flow rate, the pressure profile is calculated by solving equation 7.14 via a finite numerical difference scheme. The derived pressure profile is translated to a density profile via

$$pV = N k_{\mathrm{B}} T$$

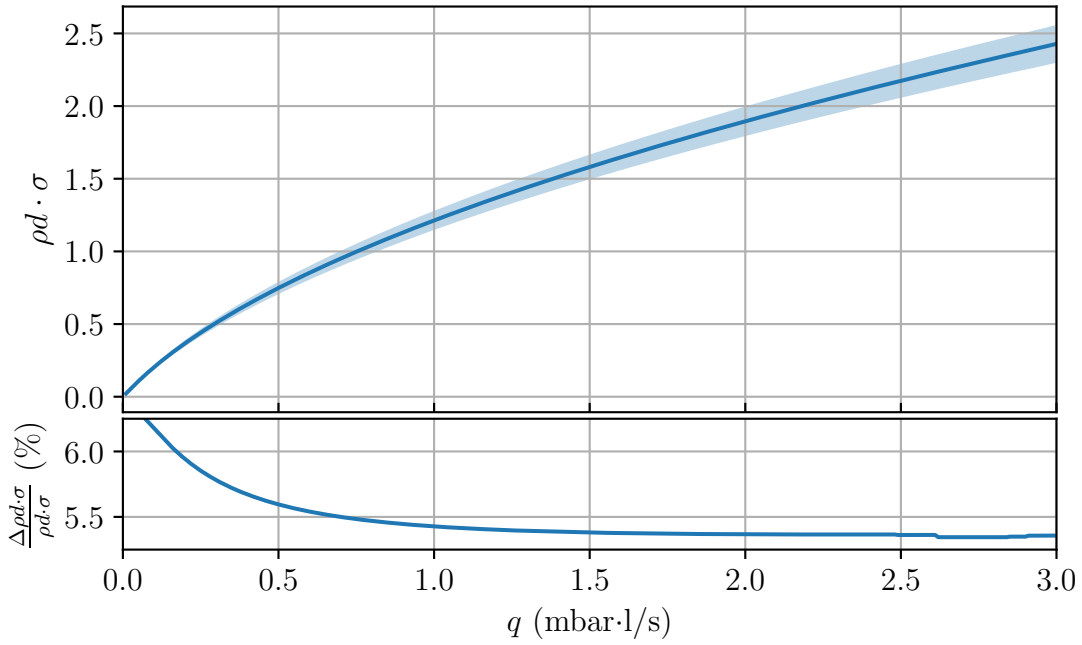

Figure 7.7.: **Simulated column density times cross section $\rho d \cdot \sigma$ and its relative precision $\Delta\rho d \cdot \sigma / (\rho d \cdot \sigma)$ as function of the measured throughput q by the flow meter.** The calculation is carried out for the measured temperature profile at 30 K WGTS beam tube temperature. The relative uncertainty on the calculated column density times cross section is dominated by the uncertainty on the measured throughput. More information given in main text, based on calculation devised in [Hei18].

with V being the volume and N the number of tritium gas molecules. Integration of the density profile yields the column density. As input for neutrino mass measurements, we are interested in the term column density times inelastic scattering cross section $\rho d \cdot \sigma$. Consequently, the calculated column density needs to be multiplied with the calculated inelastic scattering cross section $\sigma = (3.64 \pm 0.02) \times 10^{-22}\,\mathrm{m}^2$ at the tritium endpoint energy [Ake+21b]. The resulting calculated column density times cross section as function of the measured throughput is shown in figure 7.7 together with its error band. [Hei18]

The uncertainties on the calculated column density times cross section are caused by three groups of effects:

- Gas-simulation related uncertainties: Several assumptions on pressure ratios and on theoretical values, for example the accommodation coefficient α, have to be made in the calculation of the density profile [Hei18]. Uncertainties on these assumptions yield a relative uncertainty on the estimated $\rho d \cdot \sigma$ of 2.5 %.
- Uncertainty on the inelastic scattering cross section: the inelastic scattering cross section is calculated to $\sigma = 3.64 \times 10^{-22}\,\mathrm{m}^2$ with a relative uncertainty of 0.5 % [Ake+21b]. This uncertainty directly propagates into the calculated $\rho d \cdot \sigma$.
- Uncertainty on the measured throughput: the relative uncertainty on the absolute throughput, measured with the flow meter, is estimated to 2.5 % [Hei18].

This effect causes the dominant uncertainty on $\rho d \cdot \sigma$ in the range of 4.7 % to 5.8 %.

The overall relative uncertainty on the calculated absolute column density times cross section yields at least 5.3 %. Using the results obtained in section 7.1.4, we can estimate the uncertainty on the squared neutrino mass, if we would use the calculated absolute column density times cross section and its uncertainties as input for neutrino mass measurements at 84 % nominal column density and with the 40 eV fit range. The uncertainty on $\rho d \cdot \sigma$ obtained by simulations is $\Delta(\rho d \cdot \sigma) = 0.082$. This leads to an estimated uncertainty on the squared neutrino mass of $\Delta m^2_{\nu,\mathrm{sys}} = 0.22\,\mathrm{eV}^2$, surpassing the absolute KATRIN systematic uncertainty budget by a factor of twelve.

In summary, the gas model calculations are a powerful tool to describe the tritium gas density distribution in the WGTS. However, the uncertainty of the simulation on the absolute column density times cross section is more than an order of magnitude too large to be used as an input for neutrino mass analysis. Therefore, either the model needs to be calibrated by dedicated column density measurements (as proposed in [Kuc+18]) or an empirical model to estimate the absolute value of the column density times cross section has to be devised. The following sections present a method to directly measure the column density as well as a technique to estimate the absolute column density times cross section during neutrino mass measurements.

7.3. Experimental Test of Column Density Model

The Rear Section e-gun enables direct column density measurements which allows us to test the column density prediction by the gas density model. The following section 7.3.1 describes the measurement and analysis principle, section 7.3.2 gives a comparison between experimental result and expectations from gas model calculations.

7.3.1. Column Density Measurements with the E-Gun

As part of the thesis at hand, a method to directly measure the column density is derived in collaboration with Christoph Köhler [Köh19] and Alexander Marsteller [Mar20a].

We start with explaining the basic principle of column density measurements, as proposed by Kuckert et al. [Kuc+18]. Therefore we assume an ideal e-gun with perfectly stable rate and vanishing pitch angle of all emitted electrons.
The pure e-gun electron rate at full transmission and evacuated WGTS is R_{all} at the FPD. After filling the WGTS to certain column density ρd, the e-gun rate at the FPD is measured again at one surplus energy $E - qU$ in the range of $E - qU \in [1, 10]\,\mathrm{eV}$, with E being the acceleration energy at the e-gun (see section 5.3.1) and qU the applied retarding potential at the Main Spectrometer. At this surplus energy, only the rate of non-scattered e-gun electrons R_0 can overcome the retarding potential, since the minimal energy loss of inelastically scattered electrons in the WGTS filled with molecular tritium is 11 eV. By calculating the ratio R_0

over R_{all}, we derive the probability P_0 of e-gun electrons to traverse the WGTS without undergoing inelastic scattering processes. The comparison of this ratio to the theoretical description for inelastic scattering probabilities (see equation 7.4) leads to

$$\frac{R_0}{R_{\text{all}}} = \mathrm{e}^{-\rho d \cdot \sigma}.$$

In this scenario, the column density times cross section can trivially be derived. [Kuc+18] However, the KATRIN Rear Section e-gun does not feature these ideal characteristics of only emitting electrons with vanishing pitch angle and perfectly stable electron rate. Therefore, the column density measurement principle needs to be adapted accordingly.

Measurement and Analysis Principle

The minimal time difference between measurements with evacuated WGTS and filled WGTS is at least two hours, depending on the desired column density and its stability. The rate of electrons emitted by the Rear Section e-gun depends on several parameters, for example the power of the used UV light source or the status of the optical fiber. Commissioning measurements carried out in 2018 indicate that the e-gun rate cannot be assumed to be sufficiently stable to achieve sub-percent uncertainty in the measurement principle described above. Additionally, it is necessary to measure the column density in short breaks between neutrino mass measurements without evacuating and refilling the WGTS.

A solution to bypass the rate stability problem is by measuring the response function of the e-gun electrons at discrete surplus energies with high statistics, compare it to model expectations, and extract the column density information. As described in section 7.1.3, the response function comprises the transmission function $T(E, U)$, as well as the energy loss due to inelastic scattering, given by the individual energy-loss probability distributions $f_i(\Delta E)$ and the scattering probabilities $P_i(\rho d \cdot \sigma)$. Based on these components, we can derive a response function model for e-gun electrons.
The transmission function of the e-gun electrons at the FPD can be measured with an evacuated source within 40 minutes (see section 5.3.3). The mean e-gun pitch angle is chosen to be zero for the transmission function measurement, as well as for the column density measurements, as this angle can be accurately set, despite the reproducibility problems of the e-gun plate angle (see reference [Sac20]). Since the transmission function is needed for the convolution with the energy-loss distributions, we only need to describe the shape of the function and not fully characterize all its properties. Therefore, one transmission function scan per measurement campaign is completely sufficient in the context of e-gun column density measurements. The shape description of the transmission function is derived by a fit of the e-gun Peaberry model (see section 5.3.1) to the data. The amplitude of the model describing the transmission function is normalized to unity, and likewise for the e-gun response function model the same normalization is used.
The scattering probabilities P_i of an electron in the source are generally described by

$$P_i(z, \theta_{\text{src}}) = \frac{\left(\rho d_{\text{eff}}\left(z, \theta_{\text{src}}\right) \cdot \sigma\right)^i}{i!} \mathrm{e}^{-\rho d_{\text{eff}}(z, \theta_{\text{src}}) \cdot \sigma},$$

with the pitch angle θ_{src} in the WGTS (see also section 7.1.2) [Kle+19] and with the effective column density

$$\rho d_{\mathrm{eff}}\left(z, \theta_{\mathrm{src}}\right) = \frac{\rho d(z)}{\cos\theta_{\mathrm{src}}} \ .$$

E-gun electrons have to traverse the whole WGTS before eventually arriving in the spectrometer section, the scattering target for the e-gun electrons is therefore formed by all tritium molecules in the WGTS. Consequently, $\rho d_{\mathrm{eff}}\left(z, \theta_{\mathrm{src}}\right)$ simplifies for the special case of e-gun electrons to $\rho d_{\mathrm{eff}}\left(\theta_{\mathrm{src}}\right)$, similarly $P_i(z, \theta_{\mathrm{src}})$ to $P_i(\theta_{\mathrm{src}})$. The angular distribution of the e-gun electrons in the WGTS, necessary to estimate the angular-dependent scattering probabilities, is implemented as in the Peaberry model by Behrens et al. [Beh+17] with the sum of two Gauss functions (see section 5.3.1). Based on a combined analysis of several transmission function measurements, we estimate the width of the angular e-gun distribution to $\sigma_{\theta,\mathrm{pch}} = (6.3 \pm 0.3)^\circ$ in the PCH (see chapter 5.3.3). Using the magnetic adiabatic transformation of the pitch angle (see equation 3.5) allows the translation of the angular width in the PCH to the one in the WGTS to

$$\begin{aligned}\sigma_\theta &= \arcsin\left(\sqrt{\frac{B_{\mathrm{src}}}{B_{\mathrm{pch}}}} \cdot \sin\sigma_{\theta,\mathrm{pch}}\right) \\ &= (4.8 \pm 0.2)^\circ \ . \end{aligned} \tag{7.15}$$

The e-gun scattering probabilities are then obtained through

$$P_i(\rho d \cdot \sigma) = A \cdot \int_{\theta_{\mathrm{src}}=0}^{\theta_{\mathrm{max}}} \sin\theta_{\mathrm{src}} \cdot \omega\left(\theta_{\mathrm{src}}\right) \cdot P_i(\theta_{\mathrm{src}}) \ \mathrm{d}\theta_{\mathrm{src}},$$

with the e-gun angular distribution $\omega\left(\theta_{\mathrm{src}}\right)$ in the WGTS, the cut-off angle $\theta_{\mathrm{max}} = 50.5^\circ$ and the normalization $A \approx 0.072$ given by the integration over the angular distribution.
The individual energy-loss probability distributions $f_i(\Delta E)$ for electrons scattering off molecular tritium at energies around 18.6 keV are well-known due to dedicated measurements with the e-gun (see section 7.1.3) [Ake+21c]. These distributions can be adopted for the calculation of the e-gun response function without any further modifications.

We obtain the e-gun specific response function $R'(E, U, \rho d \cdot \sigma)$ by calculating the sum of the individual energy-loss distributions, weighted with the respective scattering probabilities, and convolving it with the transmission function. The resulting e-gun specific response function for nominal and 75 % column density as function of the surplus energy is shown in figure 7.8. The effect of the column density is maximal at the plateau of non-scattered electrons for surplus energies of $E - qU \in [1, 10]$ eV. At surplus energies around 200 eV and higher, the total rate becomes quasi-independent of the column density for densities of interest for KATRIN. Nearly all i-times scattered electrons surpass the Main Spectrometer retarding potential at these large surplus energies, due to vanishingly small scattering probabilities for more than eight times scattering.
Based on the derived e-gun specific response function, C. Köhler investigates possible measurement time distributions for column density measurements to optimize the sensitivity [Köh19]. Hereby, the hardware limitation of 300 eV maximal surplus

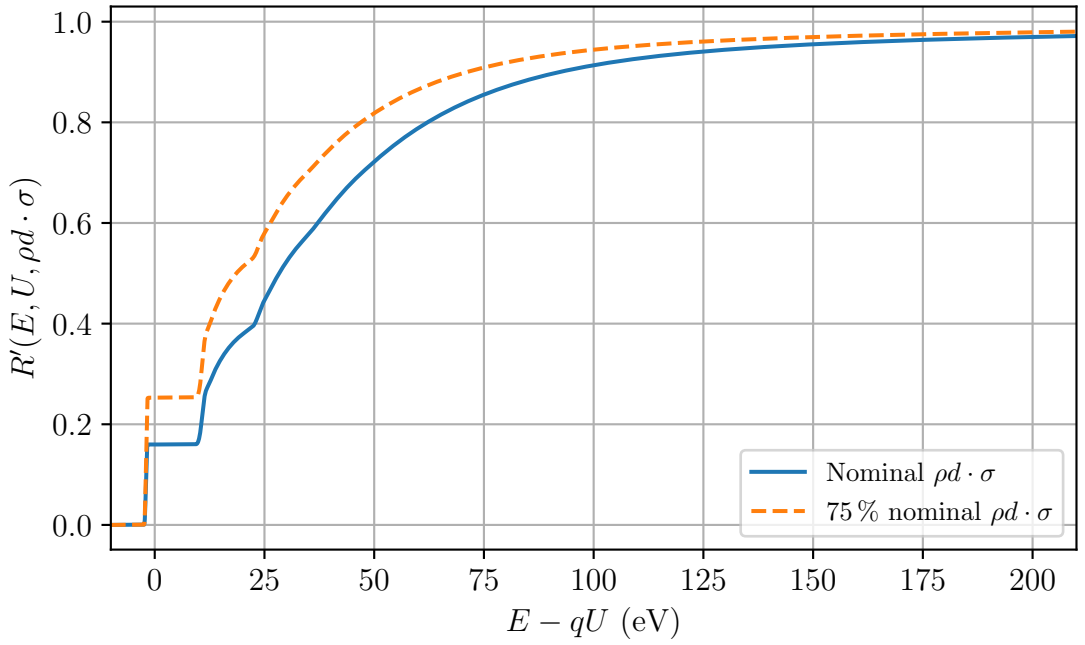

Figure 7.8.: **Response function $R'(E, U, \rho d \cdot \sigma)$ for e-gun electrons versus the surplus energy $E - qU$.** The difference for the response functions at different column densities is maximal at the plateau, indicating the zero scattering probability. The difference between the shown response functions decreases for increasing surplus energy, as electron energy loss due to i-times inelastic scattering off tritium becomes less likely.

energy of e-gun electrons (see section 5.3.1) needs to be considered. The optimal measurement time distribution yields e-gun electron rate measurements at 200 eV, 100 eV, 50 eV, and 5 eV surplus energies. The two measurements at 5 eV and 200 eV have the largest lever arm on the fitted column density times cross section. Due to the significantly smaller e-gun rate at 5 eV surplus energy at the FPD, the measurement time of 900 seconds is significantly larger compared to the other scan steps with around 200 seconds. The rate measurements at larger surplus energies are split to effectively cancel out long-term drifts, for example of the e-gun rate. The column density measurement starts with measuring the surplus energies in decreasing order, starting from 200 eV down to 5 eV. After measuring the rate at 5 eV, the higher surplus energies are again measured, but now in increasing order. The pure measurement time for one column density measurement amounts to approximately 25 minutes.

The column density measurements are performed at electron energies larger than the tritium endpoint to avoid an energy-dependent background of β-decay electrons, that would worsen the sensitivity on $\rho d \cdot \sigma$. Therefore, the measurements are performed at $E = 18.78$ keV. The retarding potential in the Main Spectrometer is set accordingly in the range from $qU = 18.58$ keV to $qU = 18.775$ keV for the measurements of the electron rates at the discrete surplus energies. Due to the chosen electron energy, the inferred column density times cross section from the measurement corresponds to an inelastic scattering cross section at 18.78 keV. It has to be scaled afterwards to the molecular tritium endpoint energy of 18.574 keV for the KATRIN neutrino

mass analysis input.

The column density measurement analysis is based on a two parameter fit to the measured e-gun rates. The model M_i, describing the measured rates, consists of the e-gun response function and a normalization A,

$$M_i\left(\rho d \cdot \sigma, A\right) = A \cdot R'(E, qU_i, \rho d \cdot \sigma). \tag{7.16}$$

The normalization is an indicator for the overall e-gun rate. With the model description, we can write the least-squares term (see also section 3.3.2) as

$$S\left(\rho d \cdot \sigma, A\right) = \vec{y}^{\,T} \cdot V^{-1} \cdot \vec{y}.$$

The residual vector $\vec{y}$ contains the difference between measured data and model prediction, the covariance matrix V summarizes the experimental and model uncertainties [BL98]. The least-squares term is minimized with respect to $\rho d \cdot \sigma$ and the nuisance parameter A, leading to the measured column density times cross section. The best-fit value of $\rho d \cdot \sigma$ does not only depend on the measured data and the model, but also on the covariance matrix V. Thus, all possible uncertainties contributing to V have to be modeled correctly for an accurate estimation of the measured column density.

Sources of Uncertainties

We need to investigate several sources of uncertainties for accurate analyses of the column density measurements. The uncertainties are grouped in experimental and model-related uncertainties in the following discussion. The size of the uncertainties are shown by the realistic example of 84 % nominal column density and total e-gun rate of 1.1 kcps by calculating the covariance matrices of the respective effects.

The group of experimental uncertainties comprises effects related to the limited measurement time as well as hardware-related instabilities during a measurement. The investigated uncertainties in this work are the statistical uncertainty, uncertainties due an unstable e-gun rate, pile-up corrections as well as high-voltage fluctuations. C. Köhler investigates further systematic effects, for example magnetic field fluctuations, and finds them to be negligibly small [Köh19].

- The statistical uncertainty on the rate is directly given by the number of measured counts at the FPD, assuming that the rate of incoming electrons is Poisson distributed. With the aforementioned measurement time distribution, the relative rate uncertainty is in the range of 0.17 % to 0.27 % with the assumed column density and e-gun rate.
- Instabilities in the e-gun rate lead to a non-Poissonian rate over-dispersion. Its influence on the rate uncertainty is quantified with the non-Poissonian factor f, as introduced in section 5.3.3. Dedicated measurements yield $f = 1.01$ (see section 5.3.3), the uncertainty on the non-Poisson factor itself can be neglected in that case.
- The e-gun rate at the FPD pixel used for the measurement can be larger than 1 kcps, depending on the scan step. We correct for the resulting electron

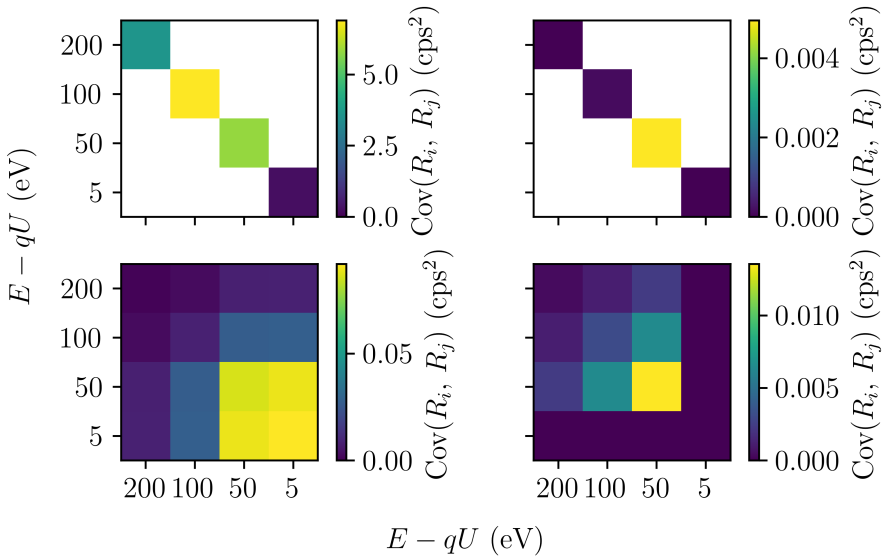

Figure 7.9.: **Covariance matrices for e-gun column density measurements, indicating the individuals sources of uncertainties in a single measurement.** The matrices are calculated for 84 % nominal column density and total e-gun rate of 1.1 kcps. The upper left matrix shows uncertainties related to the measured rate, the upper right the impact of high voltage fluctuations during the measurement. Matrix entries with exactly zero are shown in white for better visualization. The lower left matrix depicts the rate error due to uncertainties on the e-gun angular distribution in the WGTS, the lower right one shows the impact of energy-loss model uncertainties.

pile-up effects with a two-fold random coincidence model assuming incident electrons with Poissonian random time distribution [Eno19]. The pile-up correction ranges from 3 ‰ at 200 eV surplus energy to 0.7 ‰ at 5 eV. The relative uncertainty on the correction is quantified to 18 % [Eno19].

- High voltage fluctuations within a measurement at certain retarding potential result in fluctuations of the measured count rate. The mean value of the retarding potential is directly taken into account in the fit, the maximal potential fluctuation within one measurement is conservatively assumed to be less than 10 meV. This yields relative uncertainties of 8 ‰ at maximum on the measured count rates.

The first three aforementioned effects (Poisson rate uncertainty, non-Poissonian rate over-dispersion, pile-up effects) are summarized in the following in one diagonal covariance matrix, as they are all directly related to the produced and detected e-gun rate. The influence of high voltage fluctuations is also described by a diagonal covariance matrix. Both matrices are displayed in the upper row of figure 7.9.

The group of model-related uncertainties summarizes contributions to the model that are not exactly known. The following investigated contributions are the uncertainties on the energy-loss model as well as uncertainties of the angular e-gun distribution in the WGTS.

- The uncertainty on the angular distribution is given by the uncertainty on the mean angle and the angular width. The mean e-gun angle is chosen before each measurement campaign to match a pitch angle of 0°. We conservatively estimate the uncertainty on the mean angle to 1°, based on reference [Sac20]. The uncertainty on the angular width in the WGTS is given by the transformation carried out in equation 7.15 to 0.2°. The uncertainty on the angular distribution affects mainly the rate at 5 eV surplus energy and is at maximum approximately half the statistical uncertainty.
- The energy-loss model consists of nine parameters, each with its own uncertainties resulting from the e-gun measurements. The variation of the parameters within their uncertainties and according to their correlations leads to a covariance matrix with negligible small systematic effects.

Both covariance matrices are depicted in the lower row of figure 7.9. The covariance matrix describing the angular uncertainty is larger by at least one order of magnitude compared to the energy-loss model covariance matrix.

In the fit, we only take the two leading covariance matrices into account. One of the two considered covariance matrices is the matrix, that is based on the purely Poissonian statistical uncertainty, the non-Poissonian over-dispersion, and the pile-up effects, as this one reflects the total statistical uncertainty. The second one is the covariance matrix based on the e-gun angular distribution uncertainty, as this matrix is the leading model systematic uncertainty.
An additional source of uncertainty arises from the energy scaling of the cross section. As mentioned, the fit result of the e-gun column density measurement describes the column density times cross section at 18.78 keV electron energy. Thus, the fit result needs to be scaled to the energy at the molecular tritium endpoint to be used as input in neutrino mass analysis. Using the energy dependence of the cross section, as described in reference [Ake+21b], results in a scale factor of $c = 1.0092 \pm 0.0005$. The measured e-gun rates as well as the best-fit model of a single column density measurement at roughly 84 % column density is shown in figure 7.10. The result of column density times cross section at the molecular tritium endpoint is

$$\rho d \cdot \sigma = 1.532 \pm 0.003 \text{ (stat.)} \pm 0.001 \text{ (sys.)}.$$

The statistical uncertainty outweighs by factor three the systematic uncertainty. We thus focus on the computationally cheaper statistics-only analysis in the following when investigating single e-gun column density measurements.

7.3.2. Comparison of Measurement to Simulation

The results of e-gun column density measurements can be used to calibrate the column density calculations introduced in section 7.2, as proposed in reference [Kuc+18]. For this purpose, we compare all measurements taken at 30 K WGTS beam tube temperature to the simulation prediction.
We performed in total 23 column density measurements at 30 K beam tube temperature and at several column densities, ranging from 22 % nominal to 100 % nominal column density. The comparison of measurement and simulation prediction for the absolute column density is shown in figure 7.11. Overall, the gas model calculation

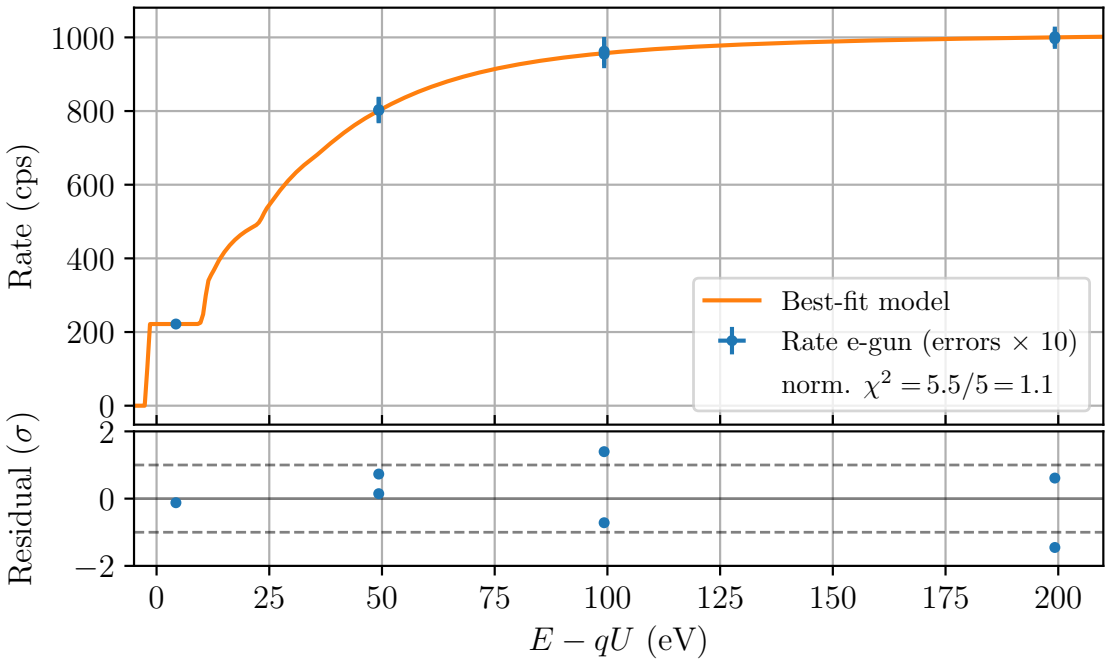

Figure 7.10.: **E-gun column density measurement at 84 % nominal column density.** The measured e-gun rates versus surplus energy (drawn in blue) as well as the best-fit model of the e-gun response function to data (drawn in orange) are shown in the upper graph. We infer from the best-fit model the measured column density $\rho d \cdot \sigma = 1.532 \pm 0.003$ and the total e-gun rate $A = (1024 \pm 2)$ cps. The normalized $\chi^2 = 1.1$ indicates good agreement of model and data. The residual of measured rates relative to the model, shown in the lower graph, do not show any structure.

agrees with the e-gun measurements within the uncertainties. However, the comparison indicates that the shape of the simulation versus the throughput measured by the flow meter does not exactly meet the e-gun results. For $\rho d \cdot \sigma \approx 0.4$, the simulation underestimates the column density with respect to the measurement. Yet, at larger column densities, the simulation predicts larger values than the measured ones.

P. Filip made an attempt to refine input parameters of the gas model from the comparison of simulation to measurement in reference [Fil20]. The gas model input parameters inlet-to-outlet pressure ratio, accommodation coefficient, and tritium viscosity were treated as free fit parameters in a χ^2-minimization of the column density model to measurement [Fil20]. However, this fit approach lead to non-conclusive results about the input parameters of the gas model, which is likely related to the uncertainty on the inelastic scattering cross section as well as the uncertainty of the absolute measured throughput.

Since the approach by P. Filip to calibrate the gas model calculation with e-gun measurements was not successful, new approaches are pursued to refine the gas model. The current approach is to investigate the properties of gaseous tritium in direct measurements, for example studies of the gas viscosity at temperatures similar to the ones in the WGTS (see reference [Wyd24]).

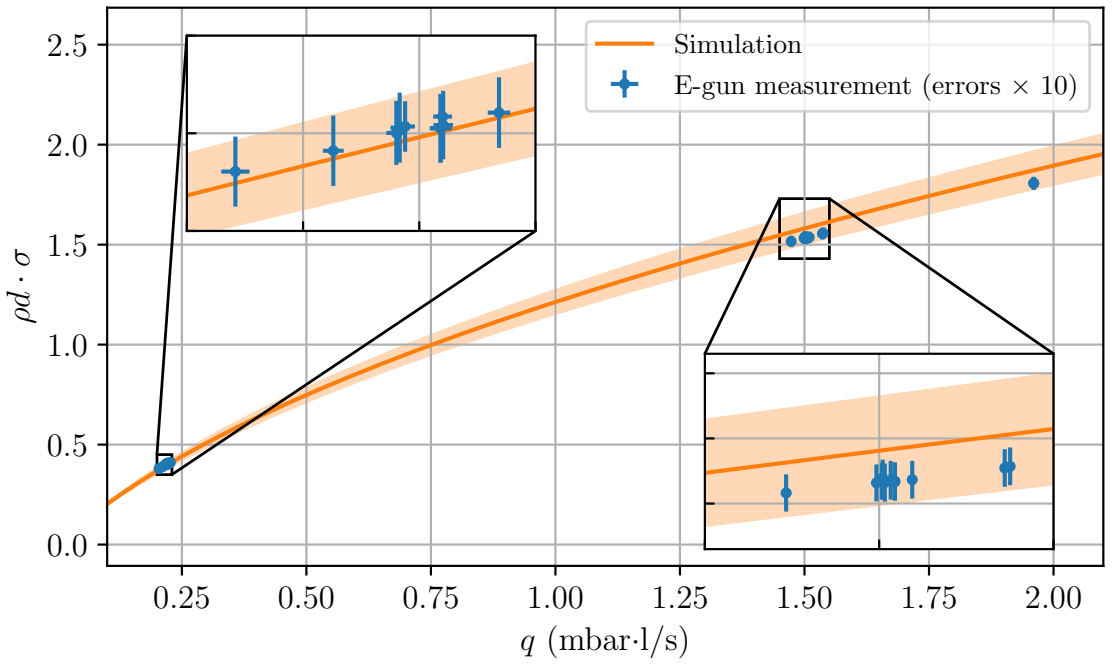

Figure 7.11.: **Comparison of e-gun column density measurements (drawn in blue) with predictions by gas model calculations (drawn in orange).** Shown is the column density times cross section $\rho d \cdot \sigma$ versus the measured throughput q by the flow meter. We perform 23 e-gun column density measurements ranging from 22 % nominal to nominal column density. The measurements and gas model calculation agree within their uncertainties. Nevertheless, the gas model can be refined as it underestimates the column density at small throughput and overestimates it at large throughput.

The gas model simulation predicts not only the absolute column density, but also properties of the gas distribution in the beam tube that are difficult to experimentally access with the spatial resolution required for neutrino mass measurements. In the following section, we experimentally investigate one of these predictions, namely the radial and azimuthal inhomogeneity of the column density, with respect to neutrino mass analyses.

7.4. Radial and Azimuthal Column Density Inhomogeneity

The two-phase neon cooling system of the central WGTS beam tube ends in axial direction about 25 cm before the DPS-1R/F pump ports. The turbo-molecular pumps in the pump ports are operated at room temperature. To mitigate the heat load from the pumps, the pump ducts are lined with thermal radiation shields cooled with liquid nitrogen. [Ake+21d] Nevertheless, the pump ports cause a heat load on the central beam tube, consequently it is expected that both ends of the WGTS central beam tube are warmer compared to its center. The cooling pipes for the beam tube cooling are brazed on both sides of the beam tube (azimuth angle $\phi = 0, \pi$).

The top and bottom side ($\phi = \pi/2, 3\pi/2$) are thus not in direct contact with the cooling. As a consequence, the heat load from the pump ports causes a warming of the top and bottom side of the beam tube, that decreases towards the longitudinal center of the WGTS cryostat. The heat load from the pump ports therefore causes longitudinal as well as azimuthal temperature inhomogeneities of the central beam tube. [Kuc16; Hei18]
According to reference [Hei18], the beam tube temperature at longitudinal position z can be written as

$$T(\phi, z) = T_0 + \Delta T(z) \cdot \sin^2 \phi, \tag{7.17}$$

with the temperature difference between side and top or bottom $\Delta T(z)$. Based on the temperature sensors mounted at the central WGTS beam tube, F. Heizmann develops a longitudinal temperature profile $\Delta T(z)$ for $T_0 = 30\,\mathrm{K}$ mean beam tube temperature. The rear end of the central beam tube yields temperature inhomogeneities of up to $\Delta T(-5\,\mathrm{m}) \approx 0.5\,\mathrm{K}$, while the front end shows significantly smaller values of only up to $\Delta T(5\,\mathrm{m}) \approx 0.1\,\mathrm{K}$. [Hei18]
The major consequence of this inhomogeneous temperature profile is a radially and azimuthally dependent gas density profile. Normally we would therefore assume that the one-dimensional gas model calculations, as described in section 7.2, are not possible anymore. However, the small pressure and temperature gradients allow to treat longitudinal and azimuthal gas flow, and thus also the gas density calculation, separately [Sha09]. This allows maintaining the approach of one-dimensional gas model calculations. Pre-calculated flow distributions [Höt12] for a certain rarefaction parameter enable corrections for given azimuthal temperature inhomogeneities [Kuc+18]. Using these pre-calculated flow distributions, the Heizmann temperature model, and the gas density calculations described in section 7.2, we can calculate the three-dimensional gas density distribution in the central WGTS beam tube. The rear end shows the largest radially and azimuthally dependent inhomogeneity, as the temperature variation is at maximum with $\Delta T(-5\,\mathrm{m}) \approx 0.5\,\mathrm{K}$. As consequence, the gas density is at both sides of the flux tube 5.3 % larger than at top and bottom at the rear end of the central WGTS beam tube. The effects of the heat loads by the pump ports decrease towards the longitudinal center of the WGTS beam tube, thus also the radial and azimuthal gas density inhomogeneity decreases. As large part of the tritium gas is located at or near the longitudinal center (see figure 7.6), the major part of the gaseous tritium is not affected by the temperature inhomogeneity. The temperature variation grows again stronger towards the WGTS front end, compared to the axial center. However, the gas density inhomogeneity is less pronounced due to the smaller temperature variation of $\Delta T(5\,\mathrm{m}) \approx 0.1\,\mathrm{K}$. The relative gas density difference between side and top or bottom is on the order of 1.5‰ at the front end. The resulting variation of column density times cross section $\delta(\rho d \cdot \sigma)$ due to the temperature variation, relative to the column density at the radial center, is visualized in figure 7.12 in the projection to the FPD. The absolute variation is rather small with at maximum 6×10^{-4}, since large parts of the tritium gas amount is in the central part of the WGTS and thus unaffected by the heat load from the pump ports.

The pseudo-three-dimensional gas density calculation is computationally expensive compared to the simple one-dimensional calculation described in section 7.2. Additionally, the temperature inhomogeneity does not allow the computationally fast

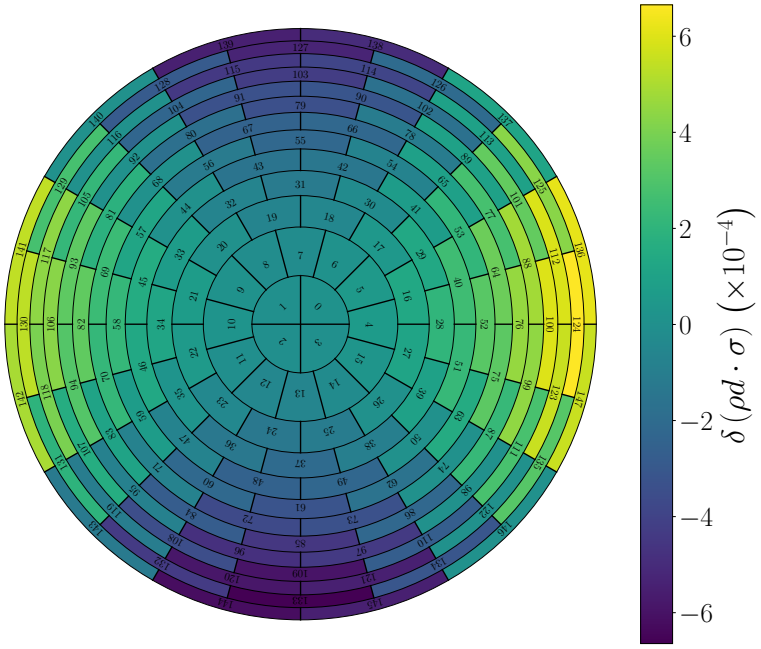

Figure 7.12.: **Expected radial and azimuthal column density variation $\delta(\rho d \cdot \sigma)$ due to WGTS beam tube temperature inhomogeneity, calculated by the pseudo-three-dimensional gas model.** The column density variations are shown as a projection to the FPD. We expect higher column density on both sides of the beam tube and lower density on top and bottom, according to the gas model calculation. The inhomogeneity amplitude is on the order of 6×10^{-4}.

averaging approach for scattering probabilities described in section 7.1.2, but requires source segmentation. In the segmentation approach, the WGTS gas density distribution needs to be calculated in each evaluation of the likelihood during neutrino mass parameter inference. Larger computation time for the gas density model and for the response function due to segmentation therefore directly enlarges the minimization time, in this case by more than a factor 20. Therefore, the preferred solution is to neglect the radial and azimuthal column density inhomogeneity in favor of faster calculation, or to correct the fitted neutrino mass for a constant bias. Thus, the investigations performed in this part of the work and presented in this chapter have to answer two questions. The first one is whether the radial and azimuthal column density inhomogeneity can be neglected in neutrino mass analysis altogether or whether we can correct for a constant neutrino mass bias. The second question is whether the simulation correctly estimates the inhomogeneity of the column density, that then gives the uncertainty on a possible bias correction.

7.4.1. Impact on Neutrino Mass Determination

The pseudo-three-dimensional gas model calculation indicates that mainly the temperature fluctuation at the WGTS rear end causes the radial and azimuthal column density inhomogeneity. Furthermore, tests with several temperature inhomogeneity

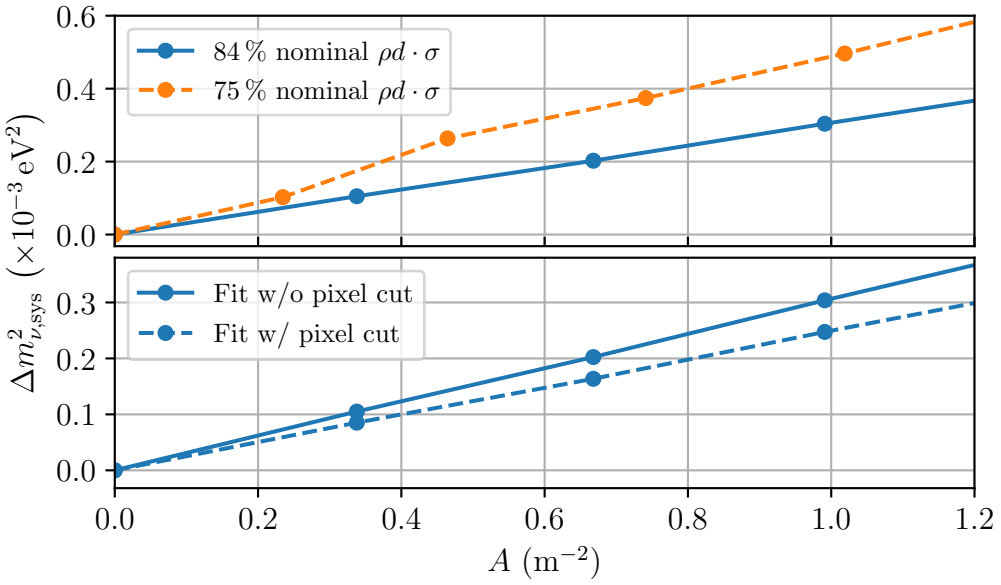

Figure 7.13.: **Neutrino mass bias $\Delta m^2_{\nu,\mathrm{sys}}$ if the radial and azimuthal column density variations are neglected in the analysis, as function of the inhomogeneity parameter A.** The neutrino mass bias for two different column densities is shown in the upper graph. The influence of the typical pixel cut on the neutrino mass bias for 84 % nominal column density is presented in the lower graph.

calculations show that the resulting column density profile is well-parametrized by

$$\rho d \cdot \sigma(r, \phi) = A \cdot r^2 \cdot \sin\left(2\phi + \frac{\pi}{2}\right) + B \tag{7.18}$$

with ϕ and r being the the polar coordinates of the column density distribution. The parameter A denotes the amplitude of the inhomogeneity, while B is the column density in the radial center of the beam tube. This empirical model has two advantages. Firstly, it allows to fit the measured column density profile in section 7.4.2 without re-calculating the three-dimensional gas distribution for each minimization step. Secondly, the parameter A directly represents the column density inhomogeneity, that is of importance for a possible neutrino mass bias.

We estimate the impact of radial and azimuthal column density inhomogeneity on the neutrino mass by simulating an Asimov dataset with the pseudo-three-dimensional column density model. The neutrino mass is fixed to zero. This dataset is then fitted with a homogeneous gas model, all other parameters are the same as for the Asimov dataset production. The best-fit result for the parameter describing the squared neutrino mass therefore directly gives the bias on the neutrino mass by neglecting the column density inhomogeneity. This procedure is repeated for a range of inhomogeneity amplitudes A to obtain a global picture.
The upper graph in figure 7.13 displays the neutrino mass bias as function of the inhomogeneity amplitude A for 84 % and 75 % nominal column density. The three-dimensional column density calculation predicts, based on the Heizmann temperature model for 30 K beam tube temperature, an inhomogeneity of $A = 0.337\,\mathrm{m}^{-2}$

for 84 % nominal column density. This corresponds to a small neutrino mass bias of $\Delta m^2_{\nu,\mathrm{sys}} = 10^{-4}\,\mathrm{eV}^2$. The application of the Heizmann temperature model to a beam tube temperature of 80 K leads to temperature inhomogeneity of $\Delta T \approx 0.1\,\mathrm{K}$ at maximum at the WGTS rear end. This translates with the three-dimensional gas model to $A = 0.08\,\mathrm{m}^{-2}$, resulting in a neutrino mass bias of $\Delta m^2_{\nu,\mathrm{sys}} = 2 \times 10^{-5}\,\mathrm{eV}^2$. It is also shown in the upper graph in figure 7.13 that the neutrino mass bias as function of the absolute inhomogeneity amplitude is larger for smaller column densities.
In the first two neutrino mass measurement campaigns KNM1 and KNM2, 31 of total 148 FPD pixels are excluded from the analysis. The excluded pixels have either a broadened energy resolution, are shadowed by beam line instrumentation, or have a decreased rate due to misalignment of the beam line with the magnetic flux tube. The excluded pixels are located in the outer-most rings of the FPD, in particular the complete outer-most FPD ring is not used for neutrino mass analysis. [Ake+21a; Ake+21b] The situation is similar for the analysis of KNM3 and KNM4, although only 25 pixels are excluded from the analysis. However, also the KNM3 pixel cut mainly affects the outer-most pixels. Since the column density inhomogeneity is more pronounced at larger flux tube radius, we expect that the neutrino mass bias is smaller if the pixel cut is applied in the study. The expectations are met, the pixel cut suppresses the neutrino bias by approximately 25 % for all amplitudes for the example of 84 % nominal column density (see lower graph in figure 7.13).

In summary, the presented study indicates that the expected neutrino mass bias for ignoring the radial and azimuthal column density inhomogeneity due to the WGTS temperature inhomogeneity in the analysis is negligibly small in neutrino mass analyses. The bias is even more reduced by the pixel cut at the FPD, that is usually applied in the analyses. However, the obtained results are only valid, if the pseudo-three-dimensional model correctly predicts the influence of the temperature inhomogeneity on the column density. Thus, it is necessary to experimentally verify the simulation prediction.

7.4.2. Measurement of Column Density Inhomogeneity

Due to operational constraints, direct measurements of the column density inhomogeneity could unfortunately not be performed at a column density now commonly used in neutrino mass measurements. Instead, it was performed at 80 K beam tube temperature and approximately 40 % nominal column density. As the temperature inhomogeneity at 80 K is rather small with $\Delta T = 0.1\,\mathrm{K}$, also the expected column density inhomogeneity predicted by the gas model calculation is small with $A = 0.002\,\mathrm{m}^{-2}$ and therefore difficult to discriminate experimentally.
Using the e-gun, we test the simulation prediction for the radial and column density inhomogeneity experimentally. Similar to the potential measurements in the analyzing plane with the e-gun (see section 5.3.3), the magnetic dipoles at the WGTS rear end are employed to steer the e-gun electron beam at different radial and azimuthal positions in the beam tube before it enters the tritium gas column on its way to the FPD. By subsequently performing the e-gun scanning procedure described in section 7.3, we can measure the column density at different radial and azimuthal positions in the beam tube. In between individual e-gun measurements, the tritium

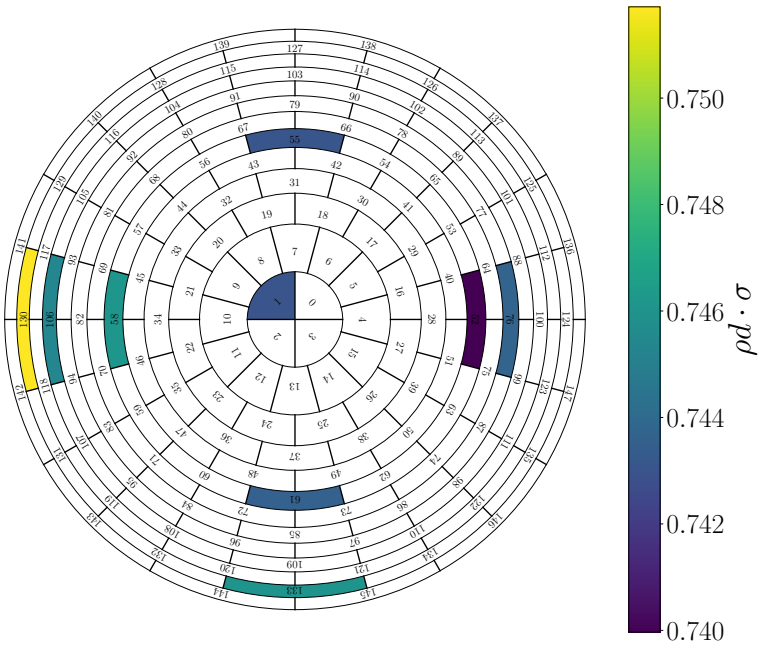

Figure 7.14.: **Column density measurements with the e-gun at several radial and azimuthal positions in the WGTS beam tube, visualized in the FPD projection.** The uncertainty on the column density times cross section of a single measurement is approximately 3×10^{-3}. The measurements at pixel 61, 76, and 133 have been performed twice, making in total twelve e-gun measurements.

β-electron rate at 300 eV below the endpoint is measured. The β-decay rate stability measurements allow one to correct for any potential column density drift during the measurement at the various positions.
As indicated in figure 7.12, the column density inhomogeneity is expected to be below 10^{-3} for the typical WGTS temperature fluctuations. The statistical and systematic uncertainty of a single e-gun column density measurement is on the order of 3×10^{-3} (see section 7.3.1). Thus, we expect to find with this measurement a result that is compatible with no inhomogeneity, if the pseudo-three-dimensional gas model calculation as well as the analysis of the measurement is accurate.

The e-gun column density is measured at nine FPD pixels (see figure 7.14), each representing a certain radial and azimuthal position in the beam tube. A total of twelve e-gun measurements are performed, with measurements conducted twice on three pixels. The FPD pixels are mapped into the WGTS beam tube to estimate the equivalent position of each pixel in the WGTS beam tube. We use equation 7.18 to effectively describe the column density inhomogeneity in the WGTS. The amplitude A as well as the mean column density times cross section B are treated as free fit parameters in the fit. The two parameters are inferred as

$$A = (0.8 \pm 0.8)\,\mathrm{m}^{-2},$$
$$B = 0.751 \pm 0.001.$$

The normalized χ^2 is 0.7, that corresponds to a p-value of roughly 77 % indicating good agreement of fit model and data. The best-fit inhomogeneity amplitude

agrees within its uncertainties with the expectation of no inhomogeneity and thus with the gas model prediction, that is motivated by the pseudo-three-dimensional column density calculation. However, the uncertainty on the measured inhomogeneity amplitude is more than a factor of 100 larger than the simulated inhomogeneity. The informative value of the study with this number of measurements is therefore limited.

Based on the measured amplitude, we can now set an upper limit on the inhomogeneity and put this in context of neutrino mass uncertainties. The 95 % C.L. upper limit of the measured amplitude yields $2.072\,\mathrm{m}^{-2}$. Similar to the uncertainty studies described in 7.4.1, we translate the upper limit on the amplitude to an upper neutrino mass bias in a neutrino mass measurement with 40 % nominal column density. The study yields that the neutrino mass bias at 95 % C.L. is smaller than $1.6 \times 10^{-3}\,\mathrm{eV}^2$. This neutrino mass bias is currently a minor systematic contribution (see reference [Ake+21a]), nevertheless, to correct the measured neutrino mass for this possible bias it is necessary to reduce the uncertainty on the measured amplitude.
We recommend to repeat the measurement of radial and azimuthal column density inhomogeneity with two modifications. The first one is to change the column density to a setting that is regularly used in neutrino mass measurements to directly investigate the set-up of interest. The second one is to increase the individual e-gun measurement time at each pixel to improve the uncertainties on the inhomogeneity amplitude. This allows to set a more reliable upper limit on the amplitude itself and therefore also on the maximal neutrino mass bias.

7.5. Monitoring during Neutrino Mass Measurements

As shown in section 7.2.3, column density simulations with the current gas model do not meet the KATRIN requirements in terms of necessary precision and accuracy on the absolute value of column density times cross section. An approach to calibrate the model input parameters with e-gun measurements of the column density to suppress the model's uncertainty leads to non-conclusive results (see section 7.3.2). Consequently, a new approach has to be pursued to monitor the column density during neutrino mass measurements.
As presented in section 7.3.1, column density measurements with the e-gun are a suitable tool to directly determine the column density times cross section with sub-percent precision. However, these measurements are not possible in parallel to nominal β-spectrum scans for neutrino mass measurements, as both require their own special Main Spectrometer setting. It is thus necessary to connect the column density measurements of a e-gun to observables that are sensitive to the column density and that can be observed in parallel to β scans. Examples for these kind of observables are measurements by gas-sensitive sensors in the WGTS loop system or by activity detectors in the beam line. In the following section 7.5.1, we are presenting and testing a semi-empirical model approach to estimate the column density during β scans based on e-gun measurements and gas-sensitive sensors. Another semi-empirical model based on e-gun and activity measurements is introduced in section 7.5.2.
The method of estimating and monitoring the column density during neutrino mass measurements, as described in the following, is devised in collaboration with Christoph

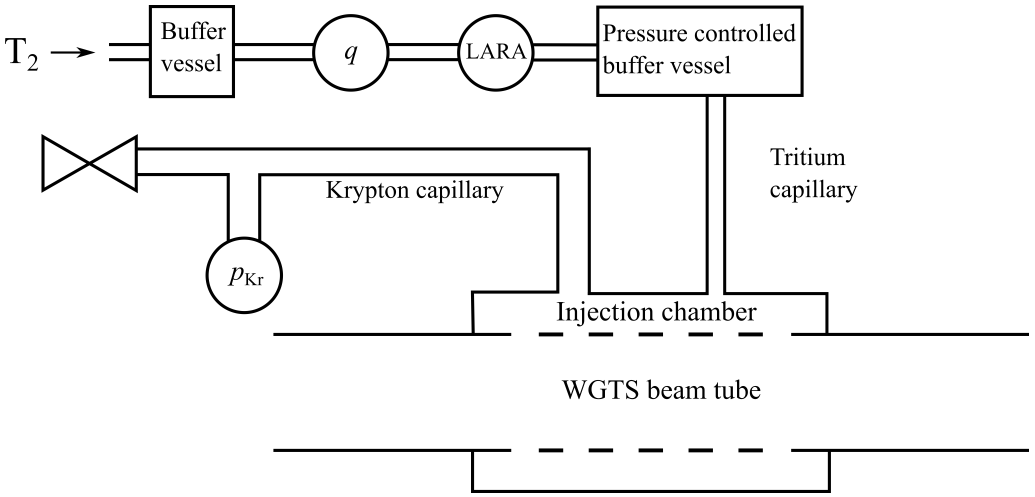

Figure 7.15.: **Schematic drawing of the tritium and krypton injection system in the nominal tritium injection mode.** The throughput q is measured between the two buffer vessels, similar to the tritium concentration measured by LARA. The valve between krypton injection chamber and outer WGTS parts is closed in nominal tritium mode, the measured pressure p_{Kr} indicates thus the pressure in the injection chamber. Geometry is not to scale, figure inspired by F. Heizmann [Hei18].

Köhler [Köh19] and Alexander Marsteller [Mar20a]. The contributions of the thesis at hand to this method are tests of models with gas-sensitive sensors, as well as the development and test of the model with activity measurements. Furthermore, the systematic uncertainties of the individual models are evaluated in this work.

7.5.1. Monitoring with Gas-Sensitive Sensors

In principle we could use any gas-sensitive sensor that is connected to the whole WGTS gas volume to empirically estimate the column density and monitor fluctuations over time. However, the sensor has to meet the demands of good time-stability as well as precise measurements. These requirements are fulfilled by two gas-sensitive sensors in the WGTS. One of these sensors is the flow meter, that enables the theoretical prediction of column density in section 7.2.3. The other sensor, used for column density estimations in the following, is the pressure gauge in the krypton injection capillary. The locations of both sensors is schematically shown in figure 7.15.
The semi-empirical column density model is constructed for each individual measurement campaign. One campaign has typically a total measurement time of around 90 days. Within this measurement time, the column density stability is significantly better than 1 %. The basic principle is to measure the column density with the e-gun in several steps around or at the planned setting for the respective measurement campaign. The sensor data is acquired in parallel to the e-gun measurement. In the analysis, the sensor data is calibrated to the column density measurement, the shape of the calibration function is given by gas model calculations. The found calibration function then enables precise and accurate translation of sensor data into an estimated column density.

An accurate calibration requires basically two inputs. Firstly, we need to know the shape of the calibration function. Secondly, reliable uncertainty estimation on the measured sensor data is required for proper error estimation on the calibration function. The following paragraph discusses the shape of the calibration functions and uncertainty estimations for the flow meter and the pressure gauge. Afterwards, the calibration is performed for 84 % nominal column density. The section then closes with the example of column density monitoring during KNM2, the resulting uncertainties on the column density estimation, and its impact on systematic neutrino mass uncertainties.

Shape of the Calibration Function and Uncertainty of the Sensor Data

The overall relation between throughput and column density is discussed in section 7.2.3. However, the total range of column density fluctuations during one measurement campaign is smaller than 1 % relative change. For the example of 84 % nominal column density, the measured throughput is $q \approx 1.5\,\mathrm{mbar \cdot l/s}$. In the range of $\Delta q = \pm 0.04\,\mathrm{mbar \cdot l/s}$, the relation between column density and throughput is well approximated by a linear model (see figure 7.11). Consequently, the shape of the calibration function for throughput translation to column density is a first-order polynomial function.
The second ingredient for an unbiased calibration of measured flow to column density is the estimated uncertainty on the measured sensor data. The flow meter, which measures the throughput between the two buffer vessels, is a mass-flow meter with 200 sccm full-scale range [MKS15]. The manufacturer estimates the accuracy to 1 % of full scale [MKS15]. Consequently, the uncertainty on the absolute measured flow yields for the used flow meter type and tritium $33\,\mathrm{\mu bar \cdot l/s}$. In the calibration, however, we describe the relation between measured throughput and column density by a first-order polynomial with slope and offset as free fit parameters. Possible systematic offsets in the measured total flow are thus absorbed in the fitted offset, provided they posses good temporal stability in the narrow flow range during one measurement campaign. The reproducibility of the sensor, that describes the agreement of results for several measurements at constant flow, is therefore the uncertainty of interest for the calibration. The reproducibility, estimated by the manufacturer, is 0.2 % of full scale [MKS15], that corresponds to $6.7\,\mathrm{\mu bar \cdot l/s}$ in the present case.
The manufacturer's estimate for the reproducibility is usually based on a longer operation time than a few weeks. For the calibration purpose in one measurement campaign, we need the flow sensor's reproducibility in the measurement time of only a few weeks, since the calibration model is constructed individually and independently for each measurement campaign. Therefore, we derive the sensor's reproducibility for KNM2 by comparing it to a reference activity measured with the FPD. The FPD is calibrated on a regular basis with electrons and γ sources, thus, it is a reliable reference tool. We use the β-decay rate measured at 300 eV below the endpoint in each β scan as reference rate and compare it with the measured flow. As motivated before, the column density has a linear dependence on the measured throughput. The rate at the FPD, corrected for fluctuations in the tritium concentration, is also linked via a linear relation to the column density in the narrow range of a measurement campaign. Therefore, the rate and the flow of each β scan in KNM2 are expected to show full correlation. This full correlation for all β scans can again be

described by a linear model, when plotting the measured flow over the rate. The spread of the fit residuals, in combination with a possible time-dependent drift of the residuals, gives the reproducibility for KNM2. Since the rate measured with the FPD is vulnerable to time-dependent drifts of the electrons' starting potential in the source, this study is only performed with constant rear wall voltages and on short time scales, assuming that the starting potential changes slowly and steadily, if at all. Afterwards, the reproducibility results of the individual periods are summarized in one mean reproducibility. With this method, we estimate the flow meter's reproducibility for KNM2 to $\Delta q = 3.7\,\mu\text{bar}\cdot\text{l/s}$. An interesting cross-check is to repeat the same procedure, but using now e-gun column density measurements instead of the FPD rate as reference. This way, we can cross-check the FPD based estimation of the reproducibility. We obtain with the e-gun method $\Delta q = 2.3\,\mu\text{bar}\cdot\text{l/s}$, that is in good agreement to the result above. However, due to low statistics of only 11 e-gun column density measurements and to avoid circular arguments, we proceed with the reproducibility of $\Delta q = 3.7\,\mu\text{bar}\cdot\text{l/s}$, that is roughly a factor of two smaller compared to the conservative estimation by the manufacturer.

The krypton capillary is the counterpart of the tritium capillary, it is used to inject krypton into the WGTS at high temperatures. Krypton is not injected into the WGTS in nominal tritium mode during neutrino mass measurements, therefore the valve in the krypton capillary between the tritium injection chamber and the outer parts of the WGTS is closed. The pressure sensor in the krypton capillary is located between the valve and the injection chamber (see figure 7.15). Consequently, the measured pressure by the gauge is an indicator for the tritium gas pressure in the injection chamber, that again defines the column density in the beam tube. However, we need to take into account that the injection chamber has a temperature of 30 K, while the 7 m-distant pressure gauge in the krypton capillary is at room temperature. The relation between the pressure in the injection chamber p_{ch} and the pressure measured by the krypton pressure gauge p_{Kr} is found to

$$\frac{p_{\text{Kr}}}{p_{\text{ch}}} = \left(\frac{T_{\text{Kr}}}{T_{\text{ch}}}\right)^{\gamma},$$

with $T_{\text{ch}} = 30\,\text{K}$, $T_{\text{Kr}} = 295\,\text{K}$ and $\gamma = 0.32$. By using the injection chamber geometry, F. Heizmann proved that one can obtain the tritium injection pressure into the beam tube and derive the column density. [Hei18] A. Marsteller showed, that the relation between the pressure measured by the pressure sensor in the krypton capillary and the column density can well be approximated by a linear model for a narrow column density range [Mar20a]. Consequently, also the calibration function shape of the measured pressure in the krypton capillary to the column density is a first-order polynomial function.
The pressure gauge in the krypton capillary is a heated baratron capacitance manometer. According to the manufacturer, the pressure gauge features an excellent long-term stability and a gas-composition independent pressure measurement. The manufacturer estimates the overall accuracy to 0.25 % of the measured pressure, a concrete value for the reproducibility is not stated. [MKS19] With the methods explained above, we estimate the relative reproducibility for the pressure sensor to Δp =0.18 % during KNM2.

Calibration to Column Density

All eleven e-gun column density measurements performed in the course of KNM2 are combined in one calibration model in the following. The throughput as well as the pressure in the krypton capillary are measured in parallel to the e-gun column density measurement and can thus directly be used for the calibration.
The uncertainty on the measured flow is given by two components. The first component is the standard deviation of the measured data in the roughly 25 minutes-long column density measurement. The second part is the reproducibility of the flow meter Δq, as derived in the section above. The total uncertainty on the measured flow is then both uncertainty components added in square. The total uncertainty on the measured pressure Δp is calculated the same way.

The e-gun measurements used for the calibration of the slow-control sensors to the column density for one measurement campaign are split up in two parts. The first part are measurements at elevated and decreased column density with respect to the mean density in the measurement campaign. The mean column density in KNM2 is 84 % nominal column density, we therefore measure at roughly 85 % and 83 % nominal column density with the e-gun after KNM2. These measurements at elevated and decreased column density give a necessary lever arm on the slope of the first-order polynomial, leading to higher precision of the calibration model. In total, three e-gun column density measurements are successfully carried out at non-mean column density. The second part of column density measurements consists of weekly calibration measurements. The β scans are interrupted once to twice per week for two hours for calibration measurements, inter alia the column density measurement. These measurements are then taken at the column density that is momentarily used in neutrino mass measurements. The purpose of these measurements is to increase the precision close to the column density of interest. In KNM2, eight e-gun measurements are performed at mean KNM2 column density.

As outlined in section 7.3.1, the statistical uncertainty dominates a single column density measurement. Since we now combine 11 e-gun column density measurements in one calibration model, we also need to consider the leading systematic uncertainty arising from uncertainties on the e-gun angular distribution and the resulting correlations among the measurements. All uncertainties and correlations among the e-gun column density measurements are again summarized in a covariance matrix. The size of the covariance matrix's diagonal elements is of the order of 10^{-5}, while the off-diagonal elements are of size 10^{-6} with positive sign.
As explained in the previous section, a first-order polynomial is sufficient as calibration function for the measured flow as well as for the measured pressure in the krypton capillary to the column density. The first-order polynomial is fitted to the e-gun column density measurement by considering the covariance matrix as well as the uncertainty on the measured flow, respectively the pressure, in a χ^2-minimization. The calibration of the measured pressure in the krypton capillary to the column density times cross section is shown in figure 7.16. The calibration for the measured throughput is not shown here, however it is similar to figure 7.16.

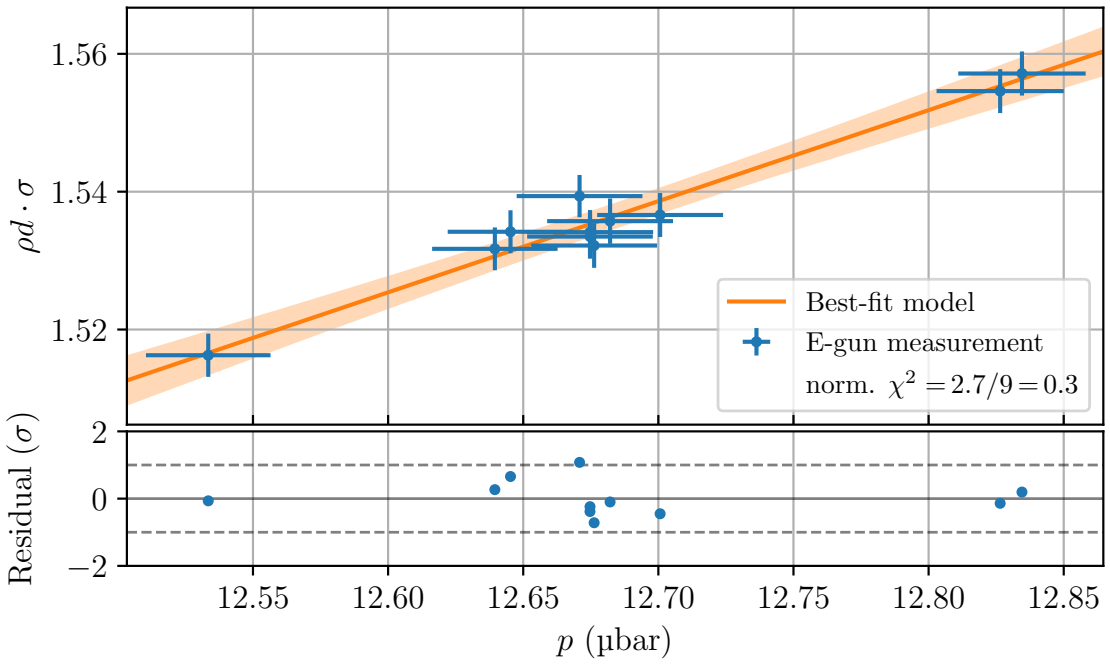

Figure 7.16.: **Calibration of the measured pressure p in the krypton capillary to the column density $\rho d \cdot \sigma$.** The blue data points represent the individual e-gun column density measurements, performed in the course of KNM2. The orange line represents the best-fit calibration function, the orange error band is the uncertainty on the calibration. The pressure in the krypton capillary during the KNM2 neutrino mass measurements is normally around $p \approx 12.67\,\mu\text{bar}$. We artificially increase and decrease the column density for measurements at $p \approx 12.54\,\mu\text{bar}$ and $p \approx 12.83\,\mu\text{bar}$ to improve the accuracy of the calibration. The normalized $\chi^2 = 0.3$ indicates that the assumed uncertainties on the individual measurement are slightly overestimated.

The fit of the first-order polynomial to the measured calibration data results in the parameter set

$$m = (0.13 \pm 0.02)\,\mu\text{bar}^{-1}$$
$$b = -0.1 \pm 0.2$$

where m denotes the slope and b the offset. This calibration allows to translate any measured pressure in the krypton capillary in the range from $[12.5, 12.9]\,\mu\text{bar}$ and at 30 K beam tube temperature to column density times cross section. The uncertainty on the translation (depicted by the shaded error band in figure 7.16) is near the KNM2 mean column density on the order of $\Delta(\rho d \cdot \sigma) = 2 \times 10^{-3}$, that corresponds to roughly 0.13 % relative uncertainty. The uncertainty is dominated by the statistical uncertainty with 1.6×10^{-3}, while the systematic contribution yields 1.2×10^{-3}. Consequently, the overall uncertainty on the calibration model can be improved by increasing the number of e-gun column density measurements during neutrino mass measurement campaigns. Starting with KNM4, the total number of column density measurements is therefore increased to 14 measurements, also distributed over the whole campaign.

Similarly, we retrieve the parameter set for the translation of measured flow to column density with

$$m = (0.62 \pm 0.07)\,\mathrm{s/(mbar \cdot l)}$$
$$b = 0.6 \pm 0.1,$$

for the flow range $[1.47, 1.54]$ mbar $\cdot$ l/s. The overall uncertainty is slightly smaller compared to the pressure translation, namely $\Delta(\rho d \cdot \sigma) = 1.8 \times 10^{-3}$.
These translations of the measured flow and pressure in the krypton capillary allow to estimate the column density times cross section during KNM2, as long as a measurement of the pressure in the krypton capillary or of the throughput is available. Normally, both sensors are read out at time intervals of a few seconds, allowing monitoring with excellent time resolution.

Column Density Estimation for KNM2

During each β scan, the pressure in the krypton capillary as well as the throughput is measured and stored into ADEI. By combining these measurements with the previously derived translation functions, we can calculate the column density for a specific β scan.

Figure 7.17 presents in the upper two plots the time evolution of the column density for each β scan estimated with the translation based on the measured pressure and the one based on the measured throughput. The uncertainty on the individual scan-wise estimation is shown as a shaded area.
Both estimations show abrupt column density fluctuations on small time-scales in the first 500 hours of measurement time in KNM2. Towards the end of the measurement campaign (measurement time larger than 900 hours), the column density seems to continuously increase. A. Marsteller shows that both features, the steady increase as well as the short-term fluctuations, are mainly caused by temperature fluctuations and drifts in the WGTS liquid nitrogen shield [Mar20a]. As the WGTS liquid nitrogen shield is thermally coupled to the tritium injection capillary, temperature fluctuations on the shield propagate onto the injection capillary, changing its conductance [Mar20a]. Since the tritium injection pressure is kept constant by the buffer vessels, the tritium flow changes with changing conductance, leading to unstable column density in the WGTS over time [Mar20a]. The impact of these column density fluctuations on neutrino mass measurements will be part of the discussion towards the end of this section.

The difference in column density estimation by the pressure sensor and the throughput over the measurement time is shown in the lower left graph of figure 7.17. At the beginning of the measurement campaign, the difference between the two column density estimations is on the order of 2×10^{-3}, about half the size of the column density uncertainty on a single scan. The difference decreases towards the end of the measurement campaign. Although the individual difference is smaller than the uncertainty on the scan, the trend of all scans together yields a significant drift. The most likely explanation for the time-dependent difference between the two methods is a time-dependent drift of one sensor with respect to the other. To avoid a biased column density input for neutrino mass measurements, it is necessary to find a

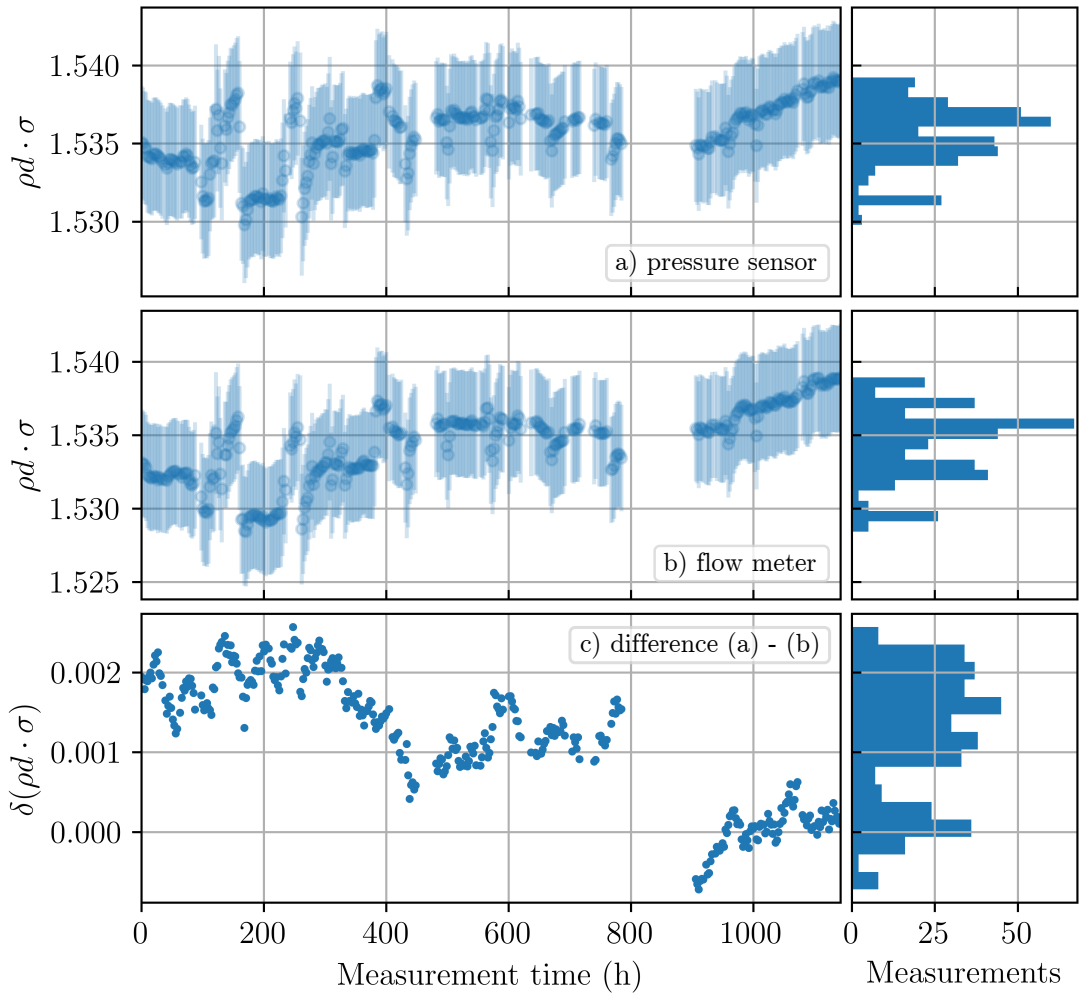

Figure 7.17.: **Column density evolution based on the estimation by the measured pressure and by the throughput during KNM2.** a) Column density time evolution $\rho d \cdot \sigma$ over measurement time based on the pressure in the krypton capillary. b) Evolution as estimated by the measured throughput by the flow meter between the two buffer vessels. c) Difference between the two estimations over time. The graphs in the right-hand panels show the resulting distributions of the data shown in the left column's plots. The gap in the data is a break in the KNM2 β scans for calibration measurements.

method to identify the more time-stable sensor for column density estimation over measurement time.

An approach to identify the more time-stable sensor is based on e-gun column density measurements. In case of a drifting sensor reading with time, we should also see a time-dependent drift on the x-axis in the calibration plot (see figure 7.16) at constant column density on the y-axis. Unfortunately, individual measurements at mean KNM2 column density do not feature enough sensitivity to resolve this behavior. Alternatively, we could use the e-gun measurements performed at elevated and decreased column density. These measurements posses a large lever arm on the calibration function, as described in the preceding section. By performing this mea-

surement not only after the measurement campaign (as in KNM2), but before and after the campaign, we could exclude or find drifts in the sensor reading, since the time difference between the two measurements is also maximized. Time-dependent sensor drifts would then result in different calibration functions between the pre- and the post-KNMX measurements. Consequently, we recommend to perform the measurements at in- and decreased column density before and after campaigns for the upcoming neutrino mass measurements.
However, we only have one measurement at in- an decreased column density in KNM2, and can thus not clearly decide which of the two sensors is more trustworthy for column density estimation. We know from experience that the offset at zero throughput of the flow meter is time dependent[1]. Additionally, the manufacturer attests the pressure sensor located in the krypton capillary an "excellent long-term stability" [MKS19]. Therefore we decide to use the column density estimation based on the pressure sensor in the krypton capillary for further analysis in KNM2.

The total uncertainty on a single β scan is on the order of $\Delta(\rho d \cdot \sigma) = 3.6 \times 10^{-3}$, that corresponds to a relative uncertainty of 0.24 %. The uncertainty on the calibration contributes with 2×10^{-3} to this overall uncertainty. The dominating fraction of 3×10^{-3} in the total uncertainty is given by the error on the measured pressure in the krypton capillary, that again is dominated by the sensor's reproducibility. Using the column density uncertainty on a single β scan, we can estimate the impact on the systematic neutrino mass uncertainty, based on the relation derived in section 7.1.4. The uncertainty of $\Delta(\rho d \cdot \sigma) = 3.6 \times 10^{-3}$ leads to $\Delta m^2_{\nu,\mathrm{sys}} = 1.5 \times 10^{-2}\,\mathrm{eV}^2$, and thus to a significant improvement compared to the simulation uncertainty of $\Delta m^2_{\nu,\mathrm{sys}} = 0.22\,\mathrm{eV}^2$ (see section 7.2.3). Although the column density with this uncertainty is only a minor systematic uncertainty contribution on the neutrino mass in KNM2 (see reference [Ake+21a]), we still need to improve to achieve the final KATRIN sensitivity goal. The column density is only allowed to contribute with an uncertainty of $\Delta m^2_{\nu,\mathrm{sys}} \leq 7.5 \times 10^{-3}\,\mathrm{eV}^2$. That translates to an allowed column density uncertainty of $\Delta(\rho d \cdot \sigma) \leq 1.8 \times 10^{-3}$ at 84 % nominal column density. First steps to improve the uncertainty require a better description of the sensor's reproducibility together with dedicated sensor calibrations also during measurement campaigns, for example high-statistic measurements with the e-gun.

To derive the impact of column density fluctuations on the neutrino mass, we need to discuss the KATRIN neutrino mass analysis approach of an individual measurement campaign. Since a single β scan does not possess enough statistical sensitivity to significantly constrain the neutrino mass, the method of choice for KNM2 is to combine the accumulated statistics in the 361 KNM2 β scans via the stacking procedure (see section 3.3.6). In this procedure, the data of all scans is merged into one high-statistics scan. Thereby all measured electrons at the same scan step are added, the corresponding high-voltage retarding-potential values are averaged over all scans. Similarly, all slow-control parameters, for example the column density, are also averaged. As the averaging of the slow-control parameters can introduce a bias on the neutrino mass, the procedure relies on sufficiently good time stability. Slow-control parameter fluctuations are analyzed with respect to their potential to bias the measured neutrino mass and if necessary, a correction is applied. [Ake+21a; Ake+21b] Consequently, the neutrino mass analysis requires as input the mean abso-

[1] Indicated by several calibration entries in the KATRIN data base KDB.

lute column density times cross section, the uncertainty on the mean column density as well as its temporal evolution.
We calculate the mean estimated column density by averaging over all used β scans in neutrino mass analysis to $\langle \rho d \cdot \sigma \rangle = 1.535$. As absolute uncertainty on the mean value, we use the above-discussed uncertainty $\Delta(\rho d \cdot \sigma) = 3.6 \times 10^{-3}$ on a single β scan. Although it might be a conservative uncertainty on the absolute mean value, we will use it in the following analysis, as it already compensates for another uncertainty, as discussed further below.
A measure for the time stability Δ_t during a measurement campaign is the calculated standard deviation of the column density distribution, that is shown in the right column of figure 7.17. In KNM2, this quantity yields $\Delta_\mathrm{t}(\rho d \cdot \sigma) = 2 \times 10^{-3}$. The systematic impact on the neutrino mass determination of this fluctuating and drifting column density is investigated for KNM2 with Asimov data. We simulate 361 Asimov β scans with the scan-wise estimated column density, all other slow-control parameters are constant for all runs. As usual, the neutrino mass is set to zero in these studies. Afterwards, the Asimov β scans are stacked and fitted with the mean column density, similar to the analysis procedure of one neutrino mass measurement campaign (see for example reference [Ake+21b]). The best-fit result of the neutrino mass parameter of the stacked dataset yields $m_\nu^2 = 3 \times 10^{-6}\,\mathrm{eV}^2$. The fit result for an Asimov dataset with constant mean column density and same measurement time is $m_\nu^2 = 2 \times 10^{-7}\,\mathrm{eV}^2$. Fluctuations of the column density during KNM2 consequently result in a negligible bias on the determined neutrino mass as consequence of the stacking procedure. The uncertainty on the bias is difficult to quantify, since the estimated column density trend is influenced by unknown sensor drifts or the sensor's reproducibility. However, we already account for these effects in the uncertainty on the absolute value, therefore we can neglect the uncertainty on the bias. The uncertainty on the inferred neutrino mass is, within the numerical noise, the same for the study with fluctuated column density and with constant column density. Thus, the stacking procedure does not broaden the likelihood function and therefore also does not introduce additional uncertainties in the analysis.

The above-described procedure to monitor relative changes in the column density times cross section and to estimate its absolute value during neutrino mass measurements can be carried out for different temperature and column density settings. The prerequisites to apply the procedure are only a sufficient number of e-gun column density measurements and that the WGTS loop mode, and especially the tritium injection procedure, stay as described in section 3.2.2. In the third neutrino mass measurement campaign, for example, we applied the procedure for 40 % and 75 % column density at 80 K WGTS beam tube temperature. Since the procedure for KNM3 is as stated above, we do not go into detail here on the achieved precision. An overview of achieved precision on the column density times cross section in the individual neutrino mass measurement campaigns is given in table 7.1.

7.5.2. Monitoring with Activity Detectors

Uncertainties in the description of source potential variations lead to systematic uncertainties on the measured squared neutrino mass on the order of $0.08\,\mathrm{eV}^2$ [Ake+21a]. Decay electrons from $^{83\mathrm{m}}$Kr are an appropriate tool to investigate the source potential

due to nearly mono-energetic decay lines [Mac21]. However, ^{83m}Kr measurements in combination with tritium in the WGTS can only be performed at 80 K WGTS beam tube temperature or higher to avoid freezing of krypton gas in the beam tube [Ake+21d]. Extrapolations or assumptions, for example regarding the temperature dependence of the source potential, are undesired in source potential measurements [KAT20], since it is necessary to replicate the conditions during neutrino mass measurements as closely as possible. This requires to directly inject krypton into the WGTS without changing operational parameters of the loop system. Therefore, the WGTS operation mode in neutrino mass measurements is adapted to allow direct krypton injection. The first major adaption is the change of beam tube temperature from 30 K to 80 K. The higher temperature limits the maximal column density to 75 % nominal column density due to a limitation of maximum pressure in the DPS-1R/F pumps. The second major adaption is that the gas stream pumped by the DPS-1R/F is split into two parts. One part is sent to the inner loop system for purification, reducing the fraction of non-hydrogen isotopologues in the gas [Mar20a]. The other part is directly circulated back into the WGTS injection chamber via the krypton capillary [Mar20a]. In addition, purified gas is fed to the beam tube via the tritium capillary [Mar20a]. Gas is therefore injected into the central beam tube by both capillaries, the tritium as well as the krypton injection capillary [Mar20a], and not only through the tritium capillary as in the nominal mode. In that WGTS mode, krypton can be added to the source gas without major modifications. This adapted tritium operation mode is firstly applied in KNM4.

The new WGTS mode presents us with new challenges regarding column density estimation. A. Marsteller outlined an approach to extend the gas model calculations, described in section 7.2, for the novel operation mode [Mar20a]. However, the model calculations did not fulfill the uncertainty requirement for the final KATRIN sensitivity [Mar20a]. A semi-empirical column density model based on e-gun measurements and gas sensors as presented in section 7.5.1 can also not be applied due to intrinsic properties of the new loops mode. The flow meter measurement is not representative anymore, as it only monitors the injection flow through the tritium capillary and misses the flow through the krypton injection capillary. The pressure in the krypton capillary exceeds in the new WGTS mode the measurement range of the pressure sensor, therefore it can not be used to quantify the gas flow through the krypton capillary. In summary, there are currently no gas sensors describing accurately the total injection flow into the WGTS beam tube. We therefore have to rely on activity detector measurements to describe the mean column density and column density fluctuations during neutrino mass measurements.

The KATRIN beam line comprises three activity-sensitive detectors, namely BIXS, FBM and FPD. Unfortunately, BIXS and FBM feature time-dependent drifts in the detector efficiency [Köh19; Ake22]. Consequently, neither BIXS nor FBM can be used for accurate column density monitoring on the permill-level in neutrino measurement campaigns over several weeks. The last remaining activity-sensitive detector, the FPD, features great time stability and is calibrated on a regular basis. We present in the following a method to estimate the column density using rate measurements performed with the FPD, based on ideas by F. Glück, M. Klein, C. Weinheimer, and A. Lokhov. The method is explained by example of a selected KNM4 dataset.

Estimation of Activity and Source-Potential Evolution

The FPD measures in each β scan the activity with high statistics at 300 eV below the endpoint. The measured activity can in principle be calibrated with e-gun column density measurements, leading to a translation function of rate to column density, similar to the approach described in section 7.5.1. Fluctuations in the tritium purity can be corrected based on the measured LARA data. Yet, this approach has one key assumption, namely that the electron starting potential in the WGTS does not change over the course of the measurement campaign. However, this assumption does not hold in general. Neglecting possible fluctuations in the electron starting potential can lead to a biased column density estimation with this method, as an increasing source potential with time results in higher count rates at the FPD at constant column density. With the approach solely based on the measured rate at 300 eV below the endpoint, we would interpret the increased rate as increased column density and vice versa. Therefore, we need a method that can distinguish changes in column density from changes in the WGTS starting potential.

As first step towards robust column density estimation, we try to disentangle the effects of column density and potential drifts by including the scan step at 90 eV below the endpoint in the analysis. The rates in the 300 eV and 90 eV scan steps below the endpoint are measured in every β scan and both feature high statistics compared to other scan steps. Additionally, both scan steps are not used for neutrino mass analysis, circular arguments are therefore avoided by using the column density input based on these two scan steps. A time-dependent source potential drift causes in first-order approximation a shift of the β decay electron's energy scale relative to the Main Spectrometer retarding potential. As outlined in section 2.5.3, the β-decay rate in the differential β-decay spectrum is approximately proportional to $(E - E_0)^2$. The FPD measures the integrated spectrum due to the MAC-E filter system, therefore the measured rate R is proportional to $(E - E_0)^3$. The time-dependent source potential $\Delta qU(t)$ would therefore affect the rate measured at 300 eV below the endpoint in first-order approximation to

$$R_{300}(t) \propto (-300\,\mathrm{eV} + \Delta qU(t))^3\,, \tag{7.19}$$

while the 90 eV scan step would yield

$$R_{90}(t) \propto (-90\,\mathrm{eV} + \Delta qU(t))^3\,. \tag{7.20}$$

The time evolution of the rate would therefore not be the same for both scan steps in case of drifts in the source potential and would allow to draw conclusions on the source potential stability. Column density drifts would affect both measured rates the same way, neglecting electron tritium scattering in the WGTS. F. Glück and M. Klein therefore propose to calculate the ratio of $R_{90}(t)/R_{300}(t)$ versus time to receive a first impression of possible drifts. Constant ratio over time indicates constant source potential during the measurement and the column density could be estimated with the 300 eV point. Non-constant ratio points towards time-dependent source potentials. This ratio approach, however, contains among others the assumption that column density changes correspond exactly to activity changes, which does not hold in the presence of inelastic scattering in the source. Therefore we need to improve this approach.

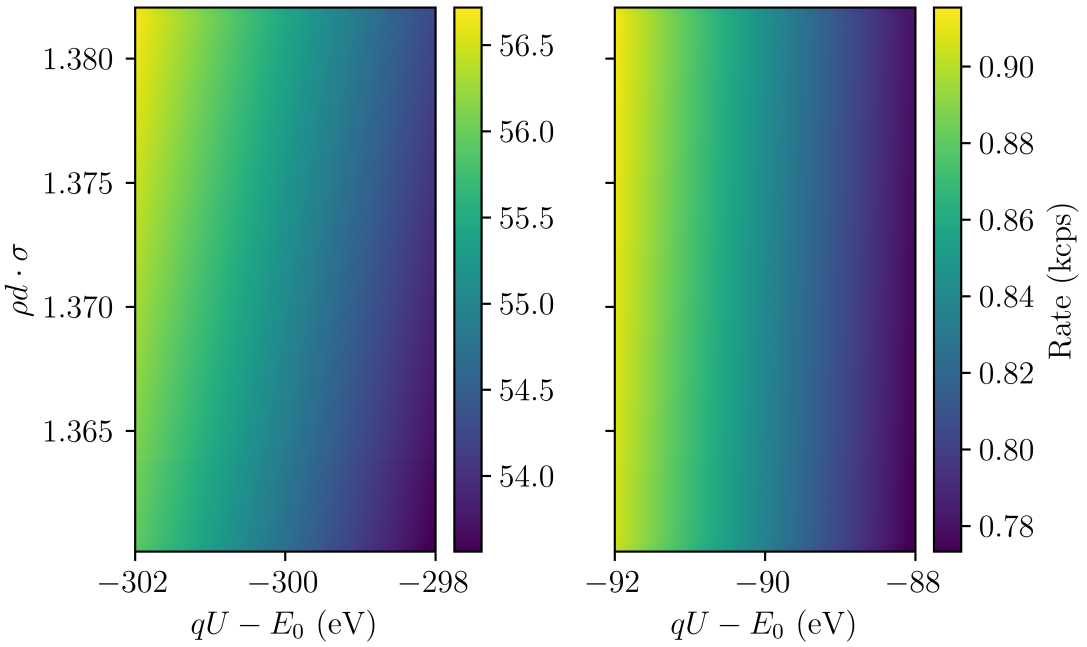

Figure 7.18.: **Expected integrated β-decay rates as function of the column density and Main Spectrometer retarding potential.** The rate dependence in the range of 300 eV below the molecular tritium endpoint E_0 is shown in the left plot, the one for 90 eV below the endpoint in the right plot. The expected rate change for potential variations (x-axis) and column density fluctuations (y-axis) is different for 300 and 90 eV below the endpoint. We make use of this difference to disentangle source potential fluctuations from column density fluctuations.

The refined approach uses the full β-decay model as implemented in the SSC software package, that is also used for neutrino mass analysis. Parameters that are necessary for the spectrum calculation are set to typical KATRIN values. The tritium endpoint is chosen to be at 18573.5 eV, the neutrino mass is fixed at zero. Although the SSC β-decay model is an effective model to describe count rates in the last 40 eV below the molecular tritium endpoint, it cannot accurately predict absolute count rates at 300 eV below the endpoint due to the lack of accurate final state distributions at these large surplus energies. Nevertheless, we assume that relative rate changes are correctly predicted by the model around 300 eV and 90 eV below the endpoint and we just need to experimentally determine the normalization.
C. Weinheimer and A. Lokhov propose to bypass the problem of absolute count rates by using a dedicated coordinate system. Therefore the relative rate change

$$\delta R(300) = 1 - \frac{R_\mathrm{i}(300)}{R_\mathrm{r}(300)} \tag{7.21}$$

is defined. The rate measured at retarding potential 300 eV below the tritium endpoint in the β scan of interest is denoted as $R_\mathrm{i}(300)$, and $R_\mathrm{r}(300)$ is the rate of an arbitrarily chosen reference measurement. The definition for $\delta R(90)$ is accordingly. The two observables $\delta R(90)$ and $\delta R(300)$ form the basis of the coordinate system, that is needed for the disentanglement of source potential and column density drift.

We can then calculate the predicted count rates at 300 eV and 90 eV below the endpoint for several column densities around the expectation value, in the following we use the KNM4 expectation value of 75 % nominal column density. Additionally, the count rate is calculated at small potential variations of up to 2 eV around 300 eV and 90 eV surplus energy. The count rates predicted by the β-decay model are shown in figure 7.18. The two graphs indicate a slightly different rate dependence on potential and column density variations at 300 eV and 90 eV surplus energy, as expected from equations 7.19 and 7.20. The information gained from these model calculations allows one to describe expectations for potential and column density drifts in the $\delta R(300)$-$\delta R(90)$ coordinate system.

The calculations carried out for figure 7.18 yield that potential drifts result in an first-order polynomial with zero offset and slope $m_{\Delta qU} = 3.585$ in the dedicated coordinate system for potential variations smaller than 4 eV (see figure 7.19). This relation is independent of the exact column density in the model in the narrow range from 74 % to 76 % nominal column density. Similarly, column density drifts also follow a first-order polynomial with slope $m_{\rho d\sigma} = 0.723$. This relation is also independent of the initial potential in the narrow 4 eV range.
As the two relations should later on be used for column density and potential drift analysis, an experimental test was carried out to validate the relations. Firstly, the relation describing the source potential drift is cross-checked. A mean starting potential shift of 1 eV in the source changes in first-order approximation the energy scale of the β-decay electrons by 1 eV. The same effect can be imitated in KATRIN by changing the Main Spectrometer retarding potential by 1 eV. Therefore, rate measurements were carried out at 301, 300, and 299 eV, as well as at 91, 90, and 89 eV below the endpoint. These measurements were taken in a short period of time to avoid significant column density drifts during the measurement time, as the pure potential drift effect shall be cross-checked. The analysis of the measured data yields good agreement with the expected slope of 3.585, namely 3.59 ± 0.07. Measurements with artificially elevated and decreased column densities allow to test the relation for column density drifts. The measured slope also meets the simulation expectation with 0.75 ± 0.05.
The rates, measured during the β scans relative to the reference scan, are located at the coordinates $(x_\mathrm{i}, y_\mathrm{i})$ in the $\delta R(300)$-$\delta R(90)$ coordinate system. With the above derived relations, the data point can be written as linear combination of potential and column density drift to

$$\begin{pmatrix} x_\mathrm{i} \\ y_\mathrm{i} \end{pmatrix} = c_{\Delta qU} \cdot \begin{pmatrix} 1 \\ m_{\Delta qU} \end{pmatrix} + c_{\rho d\sigma} \cdot \begin{pmatrix} 1 \\ m_{\rho d\sigma} \end{pmatrix} \tag{7.22}$$

with c being the coefficients that describe the potential, respectively the column density drift, relative to the reference. By using a normalization stemming from the spectrum calculations, we can translate the calculated coefficients to physical units.

Pre-Processing of Measured Data

The rates measured at the 300 eV and 90 eV scan step need to be pre-processed before entering the analysis to achieve accurate and robust results. Time-dependent

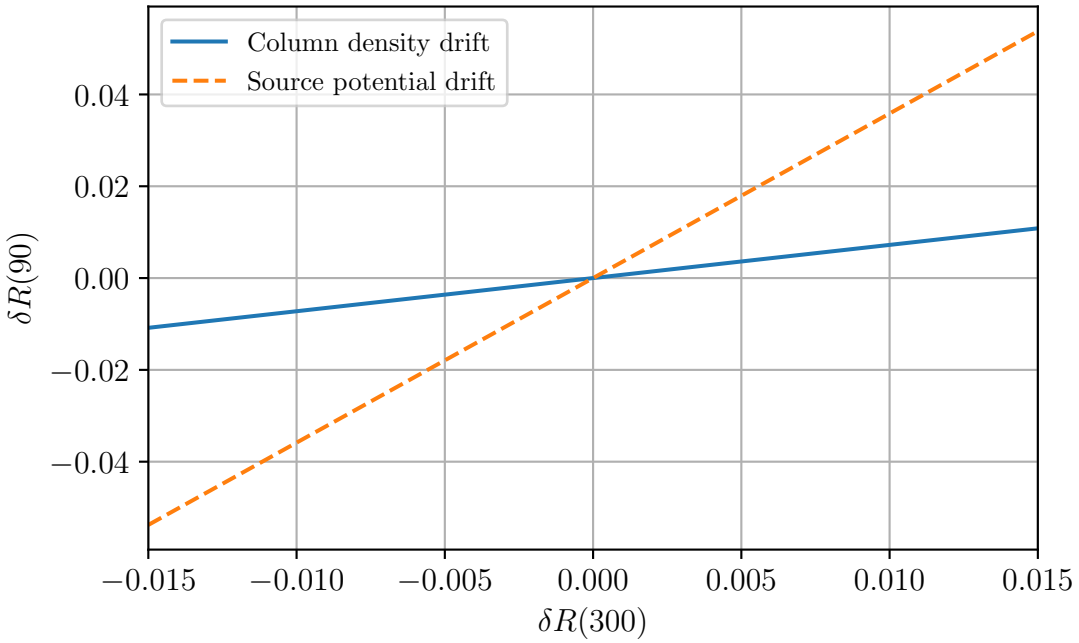

Figure 7.19.: **Column density and source potential drift in the coordinate system given by the relative rate change at 300 eV below the endpoint $\delta R(300)$ and the relative change 90 eV below the endpoint $\delta R(90)$.** Column density drifts in a narrow range follow a first-order polynomial with slope $m_{\rho d\sigma} = 0.723$ in this coordinate system. Source potential variations also follow a first-order polynomial, but with slope $m_{\Delta qU} = 3.585$.

effects, for example a drift in tritium concentration, do in general have a different slope than the potential or column density change in the relative rate coordinate system. Neglecting these effects would therefore bias the source potential and column density coefficient calculation. We thus have to correct for known effects, that influence the measured rate. In the following considerations, the effects of changing tritium gas composition, high voltage, tritium activity accumulation at the rear wall, and FPD efficiency drifts are discussed and correction methods are presented.

The tritium gas concentration in the WGTS changes continuously during a measurement phase. New tritium batches are inserted several times in the loop system during one campaign and the existing tritium gas is continuously purified, leading to a time dependency of the gas composition. A change of gas composition with time follows a first-order polynomial with slope 1 in the relative rate coordinate system, as it affects the 300 eV rate and the 90 eV rate exactly the same way. Neglecting gas concentration changes result in a biased estimation of the source potential drift as well as the column density drift, as both coefficients absorb the slope-1 effects from concentration drifts. The concentration monitoring by LARA enables a straightforward correction of the measured count rates for gas composition changes. The uncertainty on the correction also needs to be taken into account as additional uncertainty on the measured rate.

The applied retarding voltage on the Main Spectrometer is measured during the β-scan steps with a high-precision voltage divider [TMW09; Bau+13; Res+19]. The

applied retarding voltage deviates up to 40 mV for individual β scans from the set point at 300 eV and 90 eV below the molecular tritium endpoint. Although this deviation affects the measured rate mostly below the 0.1 ‰ level, a correction is applied based on simulations for deviating retarding potential. The uncertainty on the correction is negligibly small and thus not considered in the following analysis.
A fraction of tritium molecules and ions streaming upwards in the WGTS can collide with the rear wall and gets implanted in the gold-coated surface in the process, leading to β-decay electron emission from the rear wall. The increasing activity with time does not contribute as tritium gas to the WGTS column density, but causes an increasing rate at both analyzed retarding potentials and thus needs to be corrected. Since the accumulation process cannot trivially be described in simulations, we rely here on rear wall activity measurements with evacuated WGTS performed before and after the measurement campaign. Assuming 75 % mean column density in KNM4, we can translate the measured rates with empty WGTS to rates at 90 eV and 300 eV retarding potential with filled WGTS [Her21; Köh21]. F. Hermann and C. Köhler estimate the rate contributions to (276 ± 4) cps at the 300 eV scan step and (3.3 ± 0.1) cps for 90 eV at the end of the KNM4 measurement campaign [Her21; Köh21]. The time-dependent activity accumulation at the rear wall during KNM4 is described by a linear model, with relative activity increase of (0.5 ± 0.1) %/day in nominal measurement mode [Ake21]. The uncertainties on the model for the time-dependent accumulation as well as the one predicting the absolute count rates from the rear wall are propagated into the uncertainties of the corrected count rates.
FPD efficiency drifts affect all measured rates with the same relative size and would therefore consequently also bias the column density estimation. A model by S. Enomoto corrects for FPD efficiency drifts due to for example temperature fluctuations. In total, possible FPD efficiency drifts are estimated to be on the order of less than 2 ‰ during KNM4. [Eno21a; Eno21b] Based on the efficiency drift model, we apply a rate correction on the measured rates and also propagate the uncertainties.

Analysis of KNM4 Data

The procedure of estimating the column density based on the rate measurements at 300 eV and 90 eV below the endpoint is shown by example of a selected time range in KNM4. The measured rates are processed as described above. We combine the statistics from the last four β scans in the measurement campaign with the stacking approach and use this as reference measurement. Based on this choice, the relative rate changes $\delta R(300)$ and $\delta R(90)$ for each scan are calculated. Subsequently, equation 7.22 allows the derivation of the coefficients describing potential and column density drift for each scan relative to the reference measurement.
The resulting estimations for source potential, as well as column density drifts relative to the reference measurements in a selected time range of KNM4 is shown in figure 7.20. The uncertainties on the derived drifts per β scan are mostly dominated by statistical uncertainty. The systematic uncertainty on the drifts caused by model uncertainties on the β-decay spectrum shape near 300 eV and 90 eV surplus energy is more than one order of magnitude smaller compared to the statistical uncertainty.

The potential drift relative to the reference measurement in KNM4 is well described by a first-order polynomial. The derived slope yields a significant source potential

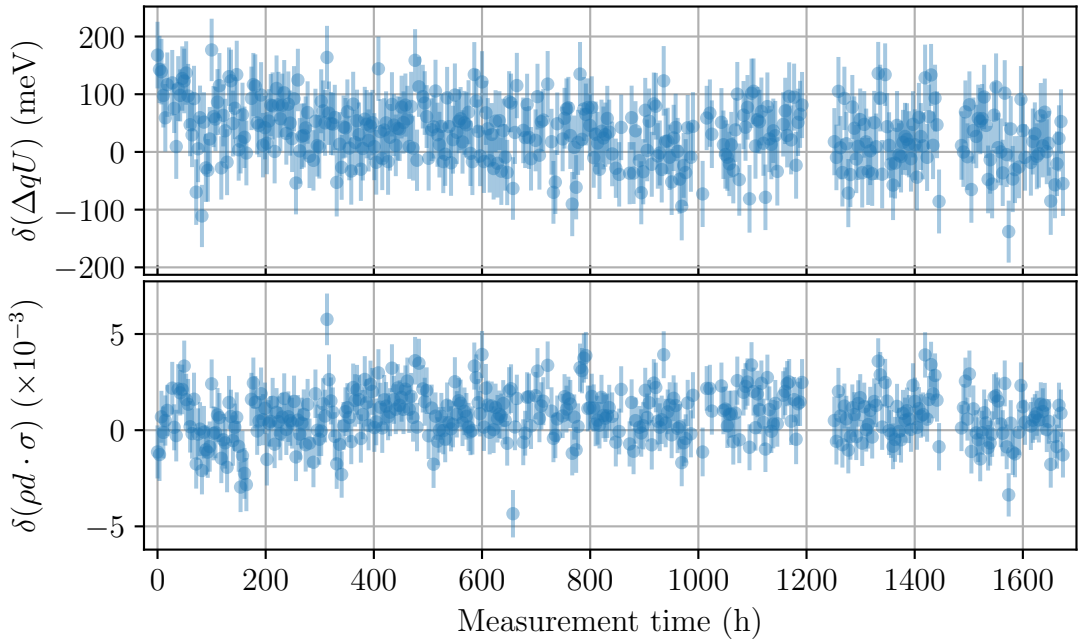

Figure 7.20.: **Estimated source potential drift $\delta(\Delta qU)$ during a selected time range in KNM4 (upper plot) and column density drift $\delta(\rho d \cdot \sigma)$ (lower plot) over the measurement time.** The drifts are relative to the stacked data of the last four β scans in KNM4.

drift of (-0.7 ± 0.1) meV/day. The physical interpretation of the negative sign depends on the definition of the relative rate changes $\delta R(90)$ and $\delta R(300)$. For the definition chosen here, a negative potential slope with time indicates an increase in the absolute source potential. The β-decay electrons start at higher absolute potential with time, leading to a larger electron rate measured at the FPD at constant Main Spectrometer retarding potential and constant WGTS column density. This time-dependent potential drift should be taken into account in the KNM4 neutrino mass analysis as it modifies the measured spectral shape.

The column density time evolution relative to the reference measurement is shown in the lower plot of figure 7.20. However, the neutrino mass analysis requires its absolute value, the uncertainty, and the time evolution as input. Therefore, the drifts need to be translated to absolute column densities. The column density is measured regularly with the e-gun during KNM4. By comparing the estimated column density drifts in the neighboring β scans with the result of the e-gun measurement, we fit a constant offset to the drifts for translation into absolute values. The covariance matrix, used in the χ^2 minimization, summarizes the uncertainties on the individual measurements as well as the correlations among the column densities measured with the e-gun. The minimization gives a total offset of (1.368 ± 0.001), that is added to the drift values to translate them in absolute column densities (see figure 7.21).
The obtained column density values are measured once per β scan and thus every four hours, given by the length of the scan. This method is thus blind to column density changes in between the scan steps at 90 and 300 eV surplus energy. However, some analyses in KATRIN require the column density estimation as input in individual scan steps. An interpolation method, based on FBM activity measurements,

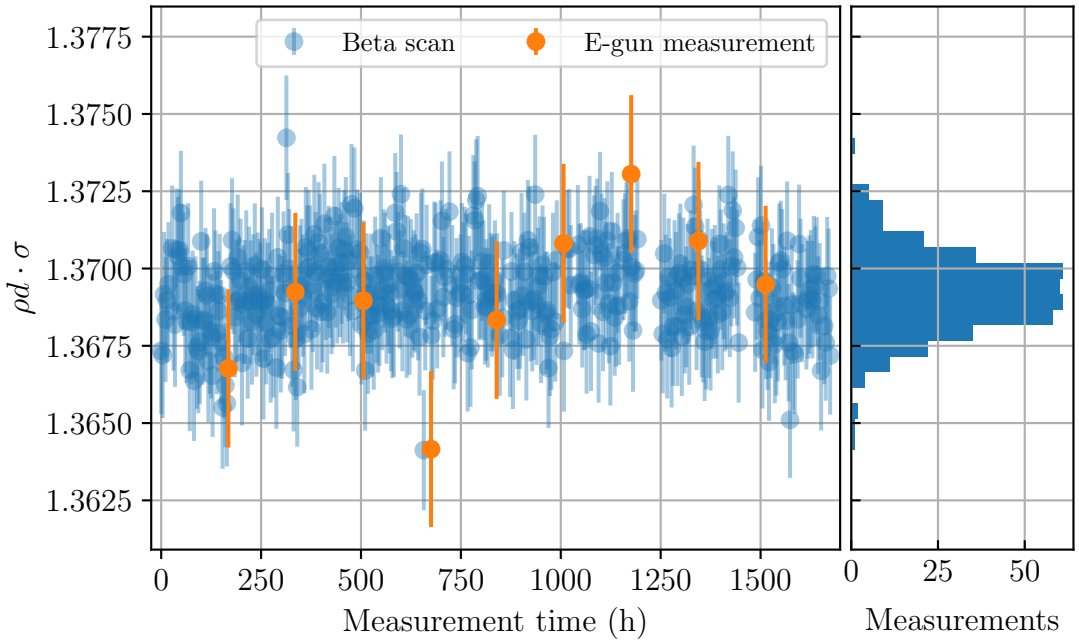

Figure 7.21.: **Absolute column density estimation for a selected time range in KNM4.** The obtained column density fluctuations, relative to the reference measurement, are translated to absolute column density estimations for the β scans, drawn in blue. We therefore make use of the regular e-gun column density measurements, drawn in orange.

enables an estimation of the column density evolution in specific β scans. Therefore, the measured FBM rate in the individual scan step r_i is compared to the one measured in scan steps r_0 at 90 and 300 eV surplus energy, leading to an interpolation factor $f = r_i/r_0$. The column density for the individual scan step is then estimated by applying the obtained interpolation factor to the known column density $(\rho d \cdot \sigma)_0$, based on the 90 and 300 eV scan step

$$(\rho d \cdot \sigma)_i = f \cdot (\rho d \cdot \sigma)_0.$$

The multi-week-scale FBM efficiency drift can be neglected on the time scale of four hours for the interpolation.

Overall, the mean KNM4 column density in the shown time range is calculated to $\langle \rho d \cdot \sigma \rangle = 1.369$. The total column density uncertainty on a single β scan with the presented method is $\Delta(\rho d \cdot \sigma) = 2 \times 10^{-3}$. The major contribution to the overall uncertainty is given by the statistical uncertainty on the measured rate at the 300 eV and 90 eV scan step with approximately 1.3×10^{-3}. The model uncertainty on the angular distribution of the e-gun electrons in the WGTS, as well as the uncertainty due to a limited number of column density measurements with the e-gun during KNM4 contribute with 10^{-3} each. Minor contributions to the total uncertainty are the time evolution of the rear wall rate during KNM4 or the model uncertainties on the coefficients in equation 7.22. The overall uncertainty on the estimated column density transforms for the KNM4 setting to a systematic neutrino mass uncertainty of $\Delta m_\nu^2 = 9 \times 10^{-3}\,\mathrm{eV}^2$. To reach the final KATRIN sensitivity goal of $\Delta m_\nu^2 \leq 7.5 \times 10^{-3}\,\mathrm{eV}^2$, we need to further optimize the column density estimation based

on this method. We therefore recommend to increase the measurement time at the 90 eV scan step and to conduct dedicated e-gun characterization measurements to get a better knowledge on the e-gun angular distribution in the WGTS. An approach to precisely determine the e-gun angular distribution with the current KATRIN hardware setup is presented in appendix A.
The time stability of the column density in the presented KNM4 time range is quantified by calculating the standard deviation of the distribution, as shown in the right graph in figure 7.21. The standard deviation calculation yields $\Delta_T(\rho d \cdot \sigma) = 1.3 \times 10^{-3}$. We cannot make any clear statement about possible column density fluctuations, as the statistical uncertainty on the estimated column density on a single β scan is on the same order of magnitude as the calculated standard deviation. Similar to chapter 7.5.1, we calculate a neutrino mass bias resulting from the stacking procedure of scans with different column densities for the selected KNM4 time range. The study, based on stacking of Asimov datasets, results in a small bias of $\delta m_\nu^2 = 10^{-4}\,\mathrm{eV}^2$ on the squared neutrino mass.

7.6. Summary

The inelastic scattering of β-decay electrons off molecular tritium in the WGTS is one of the major electron energy losses in the KATRIN experiment and thus needs to be modeled accurately for correct spectrum calculation for neutrino mass analysis. The probability for a β-decay electron to scatter inelastically off tritium gas depends on the gas column density in the WGTS, as shown in section 7.1.2. In neutrino mass analysis, the energy loss due to scattering is then included in the response function, by weighting the i-fold scattering probability with the respective energy-loss model (see section 7.1.3).

Based on this implementation, the necessary accuracy and precision on the product $\rho d \cdot \sigma$ of column density and inelastic scattering cross section for neutrino mass measurements with KATRIN is quantified in this work (see section 7.1.4). The study is performed for several column density set points that are used so far in neutrino mass measurement campaigns. It is necessary to achieve a relative precision on the absolute column density times cross section of better than 0.12 % during β scans to satisfy the KATRIN systematic uncertainty requirement on a single effect of $\Delta m^2_{\nu,\mathrm{sys}} \leq 7.5 \times 10^{-3}\,\mathrm{eV}^2$ in the 40 eV analysis window.
In the course of several previous works, a gas simulation was developed to describe the distribution of tritium gas in the WGTS beam tube (see for example references [Höt12; Kuc16; Kuc+18; Hei18]). The findings of the simulation are summarized in section 7.2. The simulation is suitable to determine the spatial distribution of the gaseous tritium in the WGTS and to monitor relative changes in the column density. Due to its properties, it can also be used to estimate the absolute column density in the WGTS, however, it does not feature the necessary precision on the absolute column density times cross section to be used as input for neutrino mass analysis.
Section 7.3 introduces the approach to measure the tritium gas column density with the e-gun. As shown in the present thesis, the precision of the measurements is limited by the statistical uncertainty, given by the e-gun rate and measurement time, as well as the uncertainty on the e-gun angular distribution in the WGTS as major systematic error. In total, this leads to a relative precision on the order of 0.2 % on

the column density times cross section in a single e-gun measurement. These column density measurements allow one to test the gas model prediction, which shows that e-gun measurements and model calculations agree within their uncertainties.

The simulation of the WGTS gas model predicts a deviation from radial and azimuthal WGTS homogeneity due to heat loads from the DPS-1 pump ports. The resulting radial and azimuthal inhomogeneity of the column density is normally not taken into account in neutrino mass analyses due to computational costs and can thus cause a bias, as studied in section 7.4. We have shown that the expected neutrino mass bias, based on the inhomogeneity calculated by the gas model, is on the order or below $\Delta m^2_{\nu,\mathrm{sys}} = 10^{-4}\,\mathrm{eV}^2$. Consequently, it is valid to neglect the radial and azimuthal inhomogeneity of the column density in neutrino mass analysis, if the simulation correctly predicts the magnitude of the inhomogeneity.
We therefore test the gas model prediction with twelve e-gun column density measurements at several radial and azimuthal positions in the WGTS. Due to operational constraints, the presented measurement took place with 40 % nominal column density instead of the 84 % or 75 % that are normally used in neutrino mass measurement campaigns. Within the experimental uncertainty, the measured column density inhomogeneity agrees with the prediction by simulation.
In summary, we have shown in this work that it is a valid approximation to neglect the predicted column density inhomogeneity in neutrino mass analysis, and that the simulated inhomogeneity is consistent with experimental findings. Nevertheless, we recommend to repeat the inhomogeneity measurement with the e-gun at a column density setting, e.g. 75 % nominal column density, that is regularly used in neutrino mass measurements.

Column density determination with e-gun measurements cannot take place in parallel to neutrino mass measurements as they require different Main Spectrometer settings. We therefore present in section 7.5 two approaches to use the e-gun column density measurements to construct models to describe the mean column density times cross section and its time evolution during neutrino mass measurements. The two approaches are based on

- Gas-sensitive sensors: This approach is introduced by example of the second neutrino mass measurement campaign KNM2. It utilizes the flow meter of the tritium injection pipe as well as the pressure sensor in the krypton capillary to calibrate the respective measured quantity versus the results from the e-gun measurements. The detailed evaluation of the systematic uncertainties of this methods, performed in the present thesis, leads to an uncertainty on the estimated absolute column density in an individual β scan to $\Delta(\rho d{\cdot}\sigma) = 3.6{\times}10^{-3}$. This corresponds to a relative precision of approximately 0.24 %, resulting in a systematic neutrino mass uncertainty of $\Delta m^2_{\nu,\mathrm{sys}} = 1.5 \times 10^{-2}\,\mathrm{eV}^2$ in KNM2. That is approximately a factor of two larger than the allowed systematic uncertainty contribution for the final KATRIN goal. To improve the uncertainty of this method to eventually satisfy the KATRIN requirement, it is necessary to increase the number of column density measurements with the e-gun as well as to refine the reproducibility estimation of the used sensor. This approach, based on gas-sensitive sensors, is also applied to determine the absolute column density, and to monitor relative changes, in the analysis of the third neutrino mass measurement campaign (see table 7.1).

Table 7.1.: **Overview of applied methods to determine the absolute column density times cross section, and the achieved relative precision, in the individual neutrino mass measurement campaigns.** The relative precision on the absolute column density times cross section, using gas-sensitive sensors, steadily increases from KNM1 to KNM3. Due to the novel WGTS loop mode, the absolute column density must be estimated using activity measurements from KNM4 onwards.

Method	Relative precision (%)	Applied in m_ν^2 campaign
Gas sensor (flow meter)	0.85	KNM1
Gas sensor (pressure sensor)	0.24	KNM2
Gas sensor (pressure sensor)	0.13	KNM3a
Gas sensor (flow meter)	0.15	KNM3b
Activity detector	0.15	KNM4

- FPD rate measurements at 300 eV and 90 eV below the endpoint: To enable column density monitoring in a novel WGTS loop mode, an approach based on β-decay rate measurements with the FPD is devised in this thesis. We use the different relative rate changes of the two measurement points at 300 eV and 90 eV below the endpoint for a changing energy scale to disentangle column density variations from source potential drifts utilizing the theoretical description of the β-decay spectrum. This method is shown by example of a dataset taken during the KNM4 measurement campaign. The resulting uncertainty on the column density yields $\Delta(\rho d \cdot \sigma) = 2 \times 10^{-3}$, corresponding to a relative precision of 0.15 %. This translates to a systematic neutrino mass uncertainty contribution of $\Delta m^2_{\nu,\mathrm{sys}} = 9 \times 10^{-3}\,\mathrm{eV}^2$, close to the KATRIN requirement. The uncertainty of this approach is dominated by the limited measurement time at the 90 eV scan step below the endpoint, limited amount of e-gun column density measurements within one campaign, and systematic uncertainty contributions from the e-gun model parameters.

An improved precision and accuracy in the determination of the absolute column density times cross section in the WGTS beam tube during β-decay scans, and the monitoring of relative changes, is achieved in the thesis at hand. The relative uncertainty on the absolute value is close to satisfy the KATRIN systematic uncertainty requirement on a single effect.
To further enhance the precision of the presented approaches, it is inter alia necessary to reduce systematic uncertainty contributions from the e-gun. We present in appendix A a method to determine the e-gun angular parameters in the WGTS with larger precision.

8. Summary and Outlook

Since its postulation by Pauli in 1930 [PKW64], the neutrino as the most-elusive particle of the Standard Model of particle physics has been studied in detail. The observation of neutrino flavor oscillation provided the proof of a non-zero neutrino mass [Zyl+20]. However, the absolute mass scale of the neutrino as lightest massive particle of the Standard Model could not yet be determined despite several experiments and complementary approaches [Zyl+20].
The KATRIN experiment aims to model-independently probe the effective electron neutrino mass with an unprecedented sensitivity of 200 meV at 90 % confidence level by high-resolution spectroscopy of the β-decay spectrum close to the endpoint region. Since the measurement principle is based on the Fermi theory of β decay, the observable for KATRIN is the squared effective electron neutrino mass $m_\nu^2 = \sum_{i=1}^{3} \left|U_{e,i}\right|^2 m_i^2$, where $U_{e,i}$ are the elements of the PMNS matrix and m_i are masses of the neutrino mass eigenstates. To reach the sensitivity goal, the experimental setup of KATRIN combines a high-luminosity Windowless Gaseous Tritium Source (WGTS) and a high-resolution MAC-E filter, called Main Spectrometer. Modifications of the intrinsic β-decay spectrum by the experimental apparatus are modeled via the KATRIN response function which comprises the Main Spectrometer transmission function and energy losses of β-decay electrons. The response function is thus a crucial input for the calculation of the integral β spectrum that is used to determine the neutrino mass. To achieve the final KATRIN sensitivity, strict requirements must be met on the uncertainty of the response function. The systematic uncertainty contribution on the squared neutrino mass due to a single effect has to be below $\Delta m^2_{\nu,\mathrm{sys}} \leq 7.5 \times 10^{-3}\,\mathrm{eV}^2$, and all systematic uncertainties combined below $\Delta m^2_{\nu,\mathrm{sys}} \leq 17 \times 10^{-3}\,\mathrm{eV}^2$. [KAT05]
The main objectives of the thesis at hand are concerned with the characterization of contributions to the KATRIN response function, and their impact on the neutrino mass analysis. The findings on the contributions by the Pinch (PCH) and WGTS magnetic fields, by the electromagnetic fields in the Main Spectrometer, and by the column density in the WGTS are summarized in the following.

Characterization of PCH and WGTS Magnetic Field

The tasks of the PCH and WGTS magnetic fields go beyond the mere transport of β-decay electrons from the source to the FPD. The WGTS magnetic field strength defines together with the PCH field strength the fraction of reflected β-decay electrons by the magnetic mirror in the PCH, impacting the Main Spectrometer transmissions function. Thus, both field strengths must be determined accurately and precisely for accurate modeling of the Main Spectrometer transmission function.
A comparison of high-precision field measurements inside the PCH's warm bore hole in a standalone mode [Sch15] with simulations shows good agreement. Taking

into account additional uncertainties from small unknown misalignments of the coil orientation inside the cryostat results in a relative precision on the PCH magnetic field strength of 0.1 %. This translates to a systematic uncertainty contribution of $\Delta m^2_{\nu,\mathrm{sys}} = 3 \times 10^{-3}\,\mathrm{eV}^2$, meeting the KATRIN requirements. To improve the understanding of the flux tube evolution between the analyzing plane of the Main Spectrometer and the FPD, it is furthermore necessary to investigate the alignment of the PCH and DET coils inside the cryostats as they mostly define the flux tube orientation. In the present thesis, a precise measurement technique is developed and conducted to investigate this alignment by measuring the magnetic stray fields of both solenoids at well-defined locations. The coil alignment is then determined by the comparison to simulations leading to an improved understanding of the flux tube evolution between analyzing plane and FPD which is used in the characterization of the nominal analyzing plane.
The systematic uncertainty estimation on the model of the source magnetic field strength was formerly based on stray field measurements outside the WGTS cryostat, which are vulnerable to background magnetic fields. A novel measurement method is devised in the thesis at hand to determine the maximal magnetic field in the central beam tube of the WGTS. Therefore, β-decay electrons from the rear wall are used as field probes inside the beam tube and the well-known PCH magnetic field as reference. The measurement and prediction by simulation show a good agreement of 5.5 mT. Taking into account statistical uncertainties of the novel method in addition to the small offset of 5.5 mT leads to a systematic uncertainty estimation on the simulation input of the source magnetic field for neutrino mass measurements of 5.8 mT. This yields a systematic uncertainty contribution on the squared neutrino mass of $\Delta m^2_{\nu,\mathrm{sys}} = 4 \times 10^{-3}\,\mathrm{eV}^2$, fulfilling the final KATRIN requirement. Compared to the former uncertainty estimation on the source magnetic field strength, a reduction of the uncertainty contribution on the squared neutrino mass by more than a factor six is achieved in this thesis. Based on the comparison of WGTS magnetic field and gas density distribution in the WGTS, an effective central value for the source magnetic field is derived in the present work to account for inhomogeneities of the source magnetic field. This value of $B_{\mathrm{src}} = (2.510 \pm 0.006)\,\mathrm{T}$ shall be used in future neutrino mass analysis, as it reduces the bias on the measured squared neutrino mass to the $10^{-4}\,\mathrm{eV}^2$ level.
Consequently, a detailed determination of the PCH and WGTS magnetic field strength was achieved in this thesis, with the uncertainties on the field strengths meeting the final KATRIN requirement for individual systematic uncertainty contributions.

Characterization of the Nominal Analyzing Plane

The analyzing plane is one of the KATRIN key features as it ensures optimal energy analysis by defining the transmission function of the Main Spectrometer together with the PCH and source fields. In chapter 5, the absolute electromagnetic field strength and the radial homogeneity of the nominal analyzing plane is characterized via simulations, e-gun, and $^{83\mathrm{m}}$Kr measurements. In the analysis of the first two neutrino mass measurement campaigns, and also partially in the third one (see table C.4), the electric and magnetic field in the analyzing plane are simulated for the calculation of the transmission function.
We test the prediction of the simulated electric field in the analyzing plane with

e-gun and ^{83m}Kr K line position measurements. Both measurement methods indicate deviations to the simulation, that form a dipole-like structure on the FPD. As found in the present thesis, the dipole-like structure can for the most part be resolved by introducing a shift of the simulated position in the analyzing plane perpendicular to the beam axis. From this, we infer that the alignment of at least one of the subsystems between analyzing plane and FPD is not accurately incorporated in the Kassiopeia geometry model. Taking into account the new information on the PCH and DET coil alignment, we conclude that the most-likely source for the deviation between simulation and measurement is an inaccurate FPD position by a few millimeter in the simulation. This leads to an improved understanding of the experimental misalignment in KATRIN. Although the deviation between electrostatic field simulation and measurement does not introduce a measurement bias on the neutrino mass relevant for the final KATRIN sensitivity, this dipole structure has to be resolved for further systematic studies (see for example reference [Mac21]). Similar to the electric field, the simulated magnetic field is also tested with measurements. Magnetic field measurements with the e-gun in the nominal analyzing plane are not possible in the current experimental setup, since the stepper motor to tilt the e-gun capacitor plates sometimes misses steps, leading to an non-reproducible tilt position [Sac20]. The simulated magnetic field strength can therefore only be cross-checked via field sensor measurements close to the analyzing plane and ^{83m}Kr $N_{2,3}$ line doublet measurements. As found in this work, the comparison of Kassiopeia field simulation and magnetic field sensors outside the Main Spectrometer vessel yields a deviation of 6 µT in the nominal 6 G configuration ($B_{\text{mean}} = 630\,\mu\text{T}$) for neutrino mass measurements. If the difference between simulation and real magnetic field in the analyzing plane is the same, this would introduce a measurement bias on the neutrino mass on the order of $2.6 \times 10^{-2}\,\text{eV}^2$, surpassing the overall systematic uncertainty budget for the long-term data-taking. However, the magnitude of the systematic uncertainty stemming from the uncertainty on the simulated analyzing plane magnetic field is acceptable for the analysis of KNM1 and KNM2 due to the vast magnitude of statistical uncertainty in these campaigns. A single source for the difference between magnetic field simulation and measurement cannot be identified. A great precision on the magnetic field strength in the analyzing plane in the 2.7 G and 1 G Main Spectrometer configuration is achieved in the thesis at hand by measurements with ^{83m}Kr conversion electrons stemming from the $N_{2,3}$ line doublet. The analysis results of these ^{83m}Kr measurements confirm the result from the comparison of simulation to sensor measurements of the magnetic field outside the Main Spectrometer vessel. As a result of the findings in the present thesis, high-statistics $N_{2,3}$ line doublet measurements in the 6 G neutrino mass measurement configuration were performed in the second half of 2021 to receive a more accurate magnetic field model for the analyzing plane for future measurements in this configuration. Additionally, the high-statistics measurement results could give a hint on the reason causing the deviation between simulation and measurement.

Characterization of the Shifted Analyzing Plane

The Shifted Analyzing Plane (SAP) configuration reduces the spectrometer-induced background rate, which is the dominating background in neutrino mass measurements, by approximately a factor of two. The SAP setting is the operational config-

uration since fall 2020. To date, the majority of the data for neutrino mass analysis with KATRIN has been measured using the SAP setting, future campaigns are also expected to be performed in this configuration. In contrast to the nominal analyzing plane that is located in the center of the Main Spectrometer, the SAP is close to the exit of the spectrometer. This location in the area of the conical spectrometer segments introduces comparably strong inner-plane field inhomogeneities.
Similar to the nominal analyzing plane, the SAP can in principle be characterized via simulations, e-gun, and ^{83m}Kr measurements. However, small inaccuracies in the Kassiopeia geometry model, as found in the characterization of the nominal analyzing plane, can lead to a significant bias between electromagnetic field simulation and reality in the SAP setting, resulting in a severe neutrino mass measurement bias. The focus of the studies performed in the present thesis, summarized in the following, is therefore on the experimental determination of the SAP transmission function.
Using the e-gun, high-precision measurements of the electric field are conducted at 28 FPD pixels. The comparison to simulation shows a dipole-like structure, similar to the one found in the characterization of the nominal analyzing plane. Using the nominal analyzing plane as reference allows us to use the e-gun in the current experimental setup for magnetic field measurements. The comparison of the measured SAP magnetic field at ten FPD pixels shows an offset on the order of 16 µT in comparison to the simulation. Although the e-gun gives high-precision results on the SAP fields, a characterization of the whole analyzing is not possible as the necessary measurement time is too large for a commissioning measurement in between neutrino mass campaigns.
In contrast to pin-pointed e-gun measurements, ^{83m}Kr conversion electrons allow a characterization of the whole SAP cross section in one measurement. Using the nominal analyzing plane as reference, the transmission function parameters of the SAP configuration are determined via a relative approach. To test for energy-dependent effects, we characterize the SAP with conversion electrons from the ^{83m}Kr K line at 17.8 keV, close to the tritium endpoint, and electrons from the $N_{2,3}$ line doublet at 32 keV kinetic energy in two independent analyses. Due to limited statistics, a pixel-wise analysis is not possible. Instead, we derive the transmission function parameters for a group of pixels, a so-called patch. The analysis of the ^{83m}Kr K line as well as the one of the $N_{2,3}$ line doublet result in a similar uncertainty on the measured transmission function, that can be translated to a systematic uncertainty contribution on the squared neutrino mass of $\Delta m^2_{\nu,\mathrm{sys}} \approx 3 \times 10^{-3}\,\mathrm{eV}^2$. The central values slightly differ for the two derived parameter sets describing the transmission function. This can potentially lead to a neutrino-mass bias based on the chosen parameter set in the analysis. To suppress the possible bias, we recommend the use of electromagnetic field values based on the $N_{2,3}$ line doublet measurement due to the more robust derivation.
The e-gun electrostatic field measurement shows results consistent with both estimations by the ^{83m}Kr K and $N_{2,3}$ line measurements. A simulation-independent comparison of e-gun magnetic field measurements with ^{83m}Kr measurements is not possible. The experimental result from the ^{83m}Kr measurement represents the mean magnetic field in the analyzing plane over eight to nine pixels in one patch, while the result from the point-like e-gun measurement is the magnetic field at a certain location at one pixel. Due to the large inhomogeneity of the magnetic field strength within one patch, the experimental results of the patch-wise ^{83m}Kr measurement is

not comparable without simulations to the e-gun results.
To summarize, the measurements with ^{83m}Kr conversion electrons enable a patch-wise characterization of the SAP electromagnetic fields with a precision that satisfies the final KATRIN requirements on a single systematic effect. The neutrino mass data, gathered in the SAP configuration, can therefore be analyzed with period summaries derived in the course of the thesis at hand. Based on the methods developed and tested in this work, high-statistics ^{83m}Kr measurements were performed in the SAP configuration in the second half of 2021, and their analysis is expected to be completed until early 2022 [Ake+22]. These measurements enable the pixel-wise derivation of the SAP transmission function parameters which then also allows the simulation-independent comparison to the e-gun results.

The WGTS Column Density

The inelastic scattering of β-decay electrons off molecular gaseous tritium in the WGTS is one of the dominating energy losses for electrons in the KATRIN setup. The energy-loss model for this scattering has been derived in previous works (see for example references [Ake+21c; Sch21]). To apply this model in the response function calculation, it is necessary to determine the probabilities for i-fold scattering which depend on the total amount of tritium gas in the WGTS, quantified by the column density. Sensitivity studies performed in the present work show that it is necessary to achieve a relative precision on the estimated column density times cross section of better than 0.12 % in order to fulfill the systematic uncertainty requirement on the squared neutrino mass of $\Delta m^2_{\nu,\mathrm{sys}} \leq 7.5 \times 10^{-3}\,\mathrm{eV}^2$.
A method to measure the absolute column density times cross section with the e-gun is presented in this thesis, devised in corporation with C. Köhler [Köh19] and A. Marsteller [Mar20a]. The measurement approach exploits the good knowledge of the energy-loss model to measure the e-gun-specific response function at four discrete surplus energies, leading to a relative precision of better than 0.2 %. However, this type of measurement cannot be performed in parallel to neutrino mass measurements.
Using the e-gun column density measurements, we present two approaches to construct models that monitor the absolute column density times cross section during neutrino mass measurement campaigns. Gas sensitive sensors, like the pressure gauge in the krypton injection capillary, are employed in the first approach. A detailed systematic uncertainty evaluation of this approach is performed in the thesis at hand, leading to a systematic uncertainty contribution on the squared neutrino mass of $1.5 \times 10^{-2}\,\mathrm{eV}^2$ in the second neutrino mass measurement campaign. The uncertainty of this method is dominated by the uncertainty on the reproducibility of the gas-sensitive sensor. The second approach, devised in this work, is based on rate measurements with the FPD at 300 eV and 90 eV below the tritium endpoint to monitor changes of the column density. The uncertainty of this approach translates to an improved systematic uncertainty on the neutrino mass of $9 \times 10^{-3}\,\mathrm{eV}^2$ in the fourth neutrino mass measurement campaign. For a further improvement of the rate-based approach it is necessary to elongate the measurement time at the 90 eV scan step below the endpoint and to gain a better understanding on the e-gun angular distribution in the WGTS.
Sophisticated gas simulations derived in former works (see references [Kuc+18;

Hei18; Kuc16; Höt12]) predict a radial and azimuthal WGTS column density inhomogeneity due to temperature inhomogeneities of the central WGTS beam tube [Hei18]. This column density inhomogeneity is normally not taken into account in the neutrino mass analysis. In this work, we show that neglecting this effect causes a negligible bias on the measured neutrino mass on the order of $10^{-4}\,\mathrm{eV}^2$, as long as the magnitude of the inhomogeneity is correctly predicted by the simulation. By performing a dedicated e-gun measurement, we could show that the magnitude of the measured column density inhomogeneity is consistent with the prediction by the simulation.

Conclusion and Outlook

The main objectives within this thesis are to characterize contributions to the KATRIN response function. The major results are as follows:

- The PCH and WGTS magnetic fields are sufficiently well understood and characterized for neutrino mass measurements.
- The electromagnetic field strength in the nominal analyzing plane can be characterized to a precision that is sufficient for the analysis of the first two neutrino mass measurement campaigns. However, the understanding of the magnetic field strength in the analyzing plane needs to be improved to meet the final KATRIN requirements. $^{83\mathrm{m}}$Kr conversion electrons of the $N_{2,3}$ line are a suitable tool to probe the magnetic field, as shown in measurements of the 2.7 G and 1 G settings.
- The patch-wise characterization of the SAP electromagnetic field strengths with $^{83\mathrm{m}}$Kr conversion electrons via a relative method is successful. The uncertainties on the obtained transmission function parameters meet the final KATRIN requirements.
- The monitoring of the column density based on the FPD rate measurement gives precise results leading to systematic uncertainties on the measured neutrino mass close to the final KATRIN requirement.

To achieve the final systematic uncertainty budget of $\Delta m^2_{\nu,\mathrm{sys}} \leq 17 \times 10^{-3}\,\mathrm{eV}^2$, five major systematic uncertainties are allowed, each with an uncertainty of $7.5 \times 10^{-3}\,\mathrm{eV}^2$ on the squared neutrino mass [KAT05].
The magnetic field strengths in the WGTS and the PCH, and the electromagnetic fields in the SAP define the transmission function of the Main Spectrometer in the SAP configuration which is a central element in the energy analysis of KATRIN. A sensitivity study based on Monte Carlo shows that these three effects combined lead to a systematic uncertainty of $\Delta m^2_{\nu,\mathrm{sys}} = 5 \times 10^{-3}\,\mathrm{eV}^2$. Consequently, the models characterizing these electromagnetic fields, derived in the present thesis, have sufficient accuracy and precision to describe the transmission function of the Main Spectrometer with an uncertainty fulfilling the KATRIN sensitivity requirement as one of the major systematic uncertainties.
The column density is an input parameter for the calculation of the i-fold inelastic scattering probability of β-decay electrons off gaseous tritium in the WGTS. It thus quantifies, in combination with the energy-loss model, the dominating energy losses for the signal electrons. Using the parameters and uncertainties of the energy-loss

model stated in reference [Ake+21c], the combined systematic uncertainty contribution on the squared neutrino mass due to uncertainties on the inelastic scattering process is $\Delta m^2_{\nu,\mathrm{sys}} = 10 \times 10^{-3}\,\mathrm{eV}^2$. The uncertainty due to inelastic scattering of β-decay electrons off tritium molecules in the WGTS is consequently another one of the five major systematic uncertainties.

As an outlook, we would like to highlight two measurements that will be performed in the near future or have recently been performed to further refine the results of this thesis:

- Using the methods developed in this work, a high-statistics $^{83\mathrm{m}}$Kr measurement campaign with the nominal analyzing plane as well as with the SAP configuration was conducted in the second half of 2021, with the analysis still on-going. This data will enables us direct access to the transmission function parameters of both analyzing plane modes with sufficient precision and accuracy to meet the KATRIN systematic uncertainty requirements with pixel-wise resolution.
- In early 2022, e-gun characterization measurements will be performed (see appendix A) that shall lead to a deeper understanding on the e-gun angular distribution in the WGTS, reducing the systematic uncertainty on the column density estimation.

The KATRIN experiment impressively demonstrated its sensitivity on the neutrino mass with the results of the first two measurement campaigns leading to the first sub-eV direct upper limit on the effective electron neutrino mass [Ake+21a; Ake+21b]. This thesis has laid important foundations for an improved understanding of the KATRIN response function, leading to reduced systematic uncertainty contributions and to full sensitivity on the neutrino mass after three years of net measurement time.

Appendix

A. Measurements of the E-Gun Angular Distribution

The parameters of the e-gun angular distribution have to be precisely and accurately known for column density measurements with the e-gun, as they define the effective path length of the electrons in the WGTS and thus their scattering probability. The mean zero pitch angle of the e-gun electrons can be set with 0.5° accuracy (see reference [Sac20]). The e-gun angular width cannot directly be set, it therefore needs to be precisely measured for a correct model implementation leading to accurate column density measurements. We are able to estimate the e-gun angular width to $\sigma_{\theta,\mathrm{pch}} = (6.3 \pm 0.3)^\circ$ in the PCH magnetic field by combining the measurements of ten e-gun transmission functions (see section 5.3.3). The uncertainty on the angular width causes an error on the measured column density times cross-section of $\Delta(\rho d \cdot \sigma) \approx 10^{-3}$ (see sections 7.3.1 and 7.5.2). Since this is a non-negligible contribution to the overall determination uncertainty of 2×10^{-3} during neutrino mass measurement campaigns, it needs to be reduced to reach the KATRIN sensitivity requirement (see section 7.5.2).
In the following, we present a method to measure the e-gun angular distribution. The idea is based on a measurement by M. Erhard (see reference [Erh16]), but adapted to the current KATRIN experimental environment. Additionally, a first proof-of-principle measurement is analyzed.

A.1. Measurement Procedure

To extract the angular width from a measured e-gun transmission function, we have to disentangle the effects stemming from the initial electron energy and the angular distribution. M. Erhard proposes to measure the effects from the distribution of the initial electron energy with high-resolution measurements at low electron energy [Erh16]. The filter width ΔE of the MAC-E filter is proportional to the electron energy for an isotropic source, according to

$$\Delta E = \frac{B_{\mathrm{ana}}}{B_{\mathrm{pch}}} \cdot E \,.$$

A measurement with a retarding potential of $qU_{\mathrm{ret}} = 1\,\mathrm{keV}$ has thus a factor 18.6 better energy resolution than a measurement with $qU_{\mathrm{ret}} = 18.6\,\mathrm{keV}$. The same principle holds for the magnetic field strength B_{ana} in the analyzing plane that can be adjusted with the eLFCS. Using a 1 G measurement configuration leads to a factor 6 better energy resolution compared to the nominal 6 G setting at a fixed electron energy E.

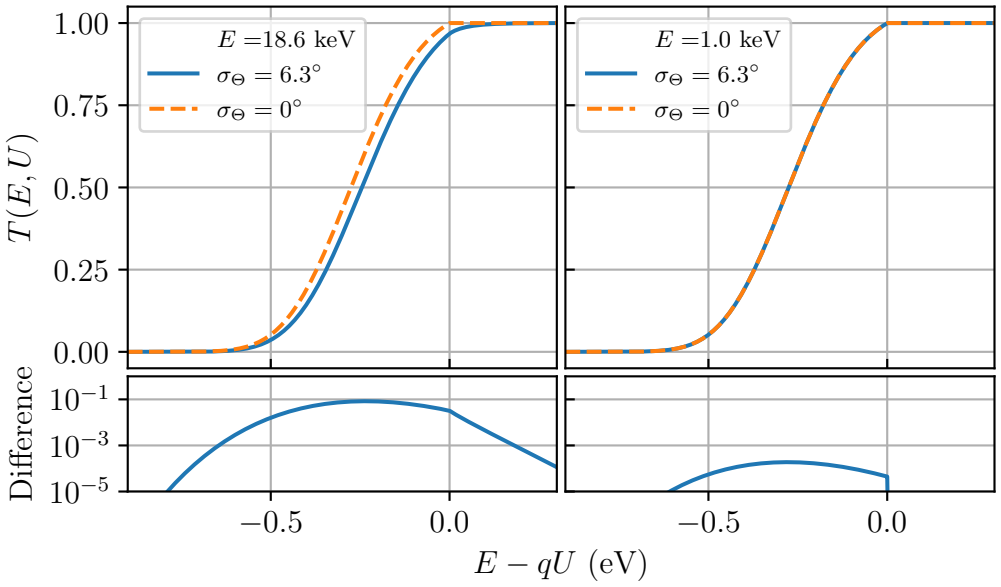

Figure A.1.: **Simulated impact of a non-vanishing e-gun angular distribution on the measured transmission function at 18.6 keV and 1 keV electron energy.** An e-gun angular width of $\sigma_\Theta = 6.3°$ in the PCH field has a shape impact on the measured transmission function at $E = 18.6\,\text{keV}$ and $B_\text{ana} = 6\,\text{G}$, leading to differences of up to 0.08 relative to an e-gun transmission function with vanishing width ($\sigma_\Theta = 0°$, left plot). As the Main Spectrometer resolution improves with decreasing electron energy and decreasing magnetic field strength in the analyzing plane, the effect of the angular width on the measured transmission function is suppressed by two orders of magnitude at $E = 1\,\text{keV}$ and $B_\text{ana} = 1\,\text{G}$ (right column).

However, the e-gun is not an isotropic source. The difference between a 6 G measurement at 18.6 keV electron energy and the one in a 1 G setting at 1 keV is therefore numerically calculated with the Peaberry e-gun model (see section 5.3.1) and visualized in figure A.1. The parameters defining the energy and angular distribution for this simulation are chosen according to the knowledge gained by analyzing several measurements of the e-gun transmission function in the course of the present thesis. As indicated in the left graph of figure A.1, the impact of an angular width of 6.3° causes a difference of up to 0.08 to a transmission function with the same energy distribution but vanishing angular width at electron energies of 18.6 keV due to the finite Main Spectrometer resolution. This difference reduces by more than two orders of magnitude to a difference of up to 2×10^{-4} for a 1 G measurement at 1 keV electron energy. A difference on the 10^{-4} level is negligible for typical measurements of the e-gun transmission function, since the relative statistical uncertainty on each scan step is on the order of 5×10^{-3} or larger. Consequently, if we measure in the low-energetic, high-resolution Main Spectrometer setup, we are mostly sensitive to the parameters of the initial electron energy distribution of the e-gun. The analysis results can be used afterwards for the measurement of the angular width.

To estimate the angular width, we again use the properties shown in figure A.1. The effect of a non-vanishing angular width on the measured transmission function depends mostly on the Main Spectrometer setting and increases with larger filter width of the Main Spectrometer. Consequently, if we perform a 6 G transmission function measurement at 18.6 keV electron energy, we measure the mixed impact of electron energy and angular distribution. Introducing the results of the initial electron energy distribution from the reference measurement in the low-energy, high-resolution setting in the analysis of the high-energy measurement allows us to determine the angular width.

In theory, the procedure is a straight-forward measurement. Nevertheless, for putting the measurement into practice we have to consider the KATRIN experimental environment. The low-energy, high-resolution measurement to extract the energy distribution of the e-gun is a challenging measurement. Setting the Main Spectrometer retarding potential to small potentials, for example −1 kV, causes residual tritium β-decay electrons, mostly from the rear wall, to overcome the potential barrier and to produce large count rates at the detector. In the measurement of the source magnetic field (see section 4.2.4), the count rate at the detector due to residual tritium β-decay electrons after KNM4 is 3.1 kcps at one FPD bulls-eye pixel with a Main Spectrometer retarding potential of −16 kV. The e-gun LDLS signal rate in full transmission is on the order of 1 kcps. Measurements with only −1 kV retarding potential in the Main Spectrometer are thus non-conclusive in this experimental environment due to the dominating background from residual tritium on the rear wall. Consequently, the low-energy measurement with the e-gun can only be conducted if we find ways to reduce the rear wall signal on the FPD.
Several approaches are pursued simultaneously to reduce the rear wall signal rate at the FPD. The low-energy measurement is performed after a 2 month-long maintenance break without tritium in the source, leading to a decrease of β-decay electrons from the rear wall in that time. Additionally, the tritium implanted in the rear wall is reduced by cleaning the rear wall surface with a dedicated procedure of ultraviolet irradiation, purging with gas, and heating up to 165 °C [Sac21b]. The β-decay electrons from the rear wall are produced in the rear wall and at its surface, the e-gun electrons enter the WGTS through the rear wall hole. By reducing the DET magnetic field strength from its nominal 2.5 T to only 0.4 T, we enlarge the cross section of the flux tube on the FPD and thus also the mapping of the 5 mm-wide rear wall hole on the FPD. With the decreased DET current, the rear wall hole projection completely covers one FPD pixel. The electron rate on this pixel is therefore dominated by e-gun electrons in full transmission. In addition, the rear wall rate on the FPD is reduced in the data analysis by applying a stringent pixel and energy cut on the measured data.
The high-energy measurement in which we measure the combined impact of electron energy and angular distribution on the e-gun transmission function is a normal 6 G measurement at 18.6 keV, similar to the ones performed for example in section 5.3.3. This measurement is conducted directly after the low-energy measurement to avoid time-dependent effects like a change of the e-gun work function that would cause a bias on the measured e-gun angular width. In principle, stronger magnetic fields in the analyzing plane are preferred for the measurement goal as the effect of the non-vanishing angular width becomes more pronounced due to the larger filter width of the Main Spectrometer. However, the simulation accuracy significantly decreases

towards magnetic fields stronger than 6 G, likely due to a inaccurate eLFCS simulation, leading to possible biases on the determined angular width. We therefore decide to use the 6 G setting.

A.2. Proof-Of-Principle Measurement

The measurements are conducted in February 2021, before the start of the fifth neutrino mass measurement campaign. As motivated above, the low-energy, high-resolution measurement is performed with a 1 G setting at electron energies of 1 keV, as opposed to the high-energy measurement with a 6 G setting and energies of 18.6 keV. Both measurements are analyzed with the e-gun Peaberry model as implemented in Kasper. The measurement comprises in total only two e-gun scans, the statistical uncertainty is thus huge. Therefore, the results obtained in the following should be more understood as a test of principle for this measurement technique.

The Peaberry model for the low-energy measurement comprises the electron energy distribution, a normalization factor for the e-gun rate, and a constant background offset as free parameters. The parameters of the angular distribution are fixed here at reasonable values of $\hat{\theta} = 0^\circ$ and $\sigma_\theta = 10^\circ$, since the fit does not significantly depend on these angular input parameters in the low-energy, high-resolution setting, as indicated by the right graph in figure A.1. The field uncertainties on the 1 G eLFCS configuration is introduced in the fit with the pull-term method. Since the measurement is performed with 1 keV electron energy, the e-gun front plate cannot be set to the nominal, 4 kV more positive, voltage (see section 5.3.1), but only to 0.5 kV. This can lead to a worse collimination of the electrons in the capacitor, resulting in a larger angular width. The larger width itself is not a problem for the energy analysis in the Main Spectrometer, however, the electrons at larger widths are more likely to loose energy due to for example cyclotron radiation during the transport towards the spectrometers. Additionally, energy-loss effects could appear that are not well understood at the unfamiliar $E = 1\,\mathrm{keV}$ energy scale in the KATRIN experiment. High-frequency fluctuations of the Main Spectrometer vessel, that are vanishingly small at $-18.6\,\mathrm{kV}$ but are not well known at $-1\,\mathrm{kV}$ retarding potential, could for example lead to a broadening of the measured transmission function. We therefore introduce an energy broadening parameter in the transmission function model to account for possible effects.
The measured e-gun rates as well as the best-fit model of the low-energy, high-resolution measurement are shown in figure A.2. The normalized $\chi^2 = 0.82$ indicates good agreement of model to data, that is confirmed by the randomly distributed residuals. The constant background in the region of interest is estimated by the fit of the model to the data to approximately 20 cps. This indicates that the efforts to reduce the background stemming from the β-decay electrons of the rear wall on the FPD are successful. The best-fit result for the energy broadening is $(68 \pm 12)\,\mathrm{meV}$ and thus larger than expected. We therefore recommend detailed simulations and further studies as a cross-check. However, the parameters of interest are the ones of the energy distribution (see section 5.3). Their best-fit estimates are

$$\begin{aligned} \hat{E} &= (168 \pm 73)\,\mathrm{meV}, \\ \sigma_E &= (223 \pm 62)\,\mathrm{meV}, \\ \kappa &= 0.4 \pm 0.2\,. \end{aligned} \tag{8.1}$$

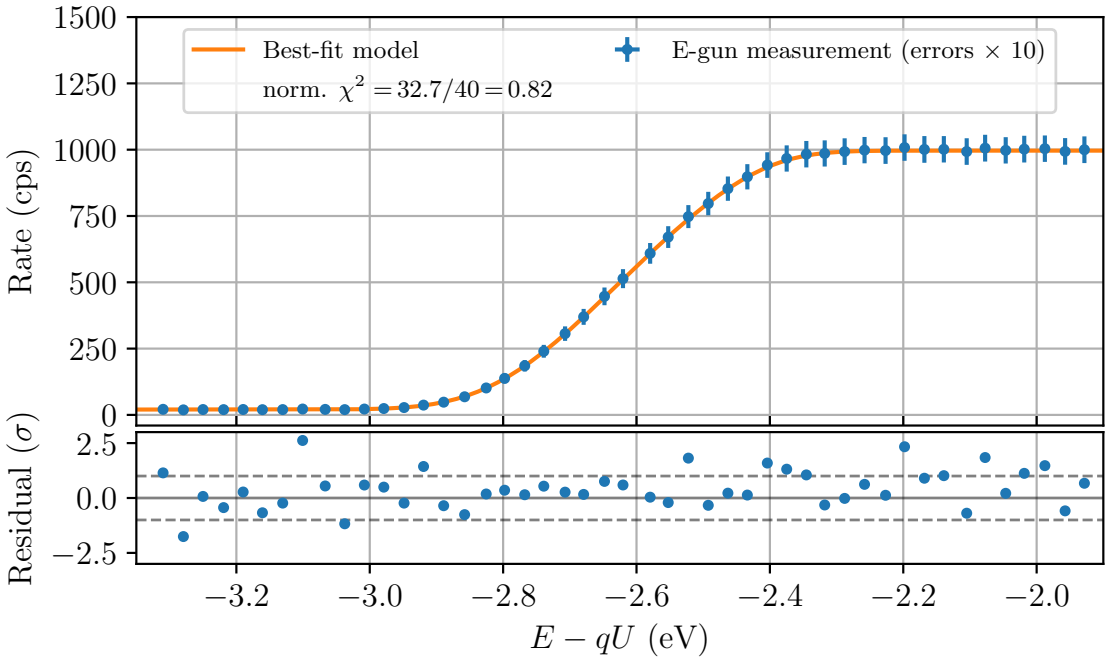

Figure A.2.: **E-gun transmission function measurement with low electron energies of $E = 1$ keV.** The measured e-gun rate (blue data points) and the best-fit model (orange curve) are shown in the upper graph. The best-fit residuals are presented in the lower graph.

These parameters are not as precise, i.e. they have a larger statistical uncertainty, as the ones obtained from the combination of several transmission function measurements (see section 5.3.3) since they are obtained only from a single measurement. Nevertheless, we expect them to be accurate. The obtained central values and their uncertainties are used in the following analysis of the high-energy measurement to determine the angular distribution parameters.

The high-energy measurement is sensitive to the impact of non-vanishing e-gun initial energy and angular distribution. To disentangle these two effects, we introduce penalty terms on the parameters of the electron energy distribution, based on the best-fit results from the low-energy reference measurement (see equation 8.1). Similar to the low-energy measurement, we choose as reference magnetic field the PCH field. The uncertainties on the PCH and the magnetic field in the analyzing plane are again included with the pull-term method.
The measured e-gun rates are shown together with the best-fit model in figure A.3. The normalized $\chi^2 = 1.15$ of the best-fit model is in agreement with model deviations caused by statistical fluctuations. The angular width is estimated by the best-fit model to

$$\sigma_\Theta = (6.8 \pm 0.4)^\circ$$

in the PCH field of 4.23 T. This measurement result is consistent with the obtained angular width by either combining several transmission functions at zero mean pitch angle (see section 5.3.3) or at several angles and several analyzing plane magnetic fields (see section 6.2.2).

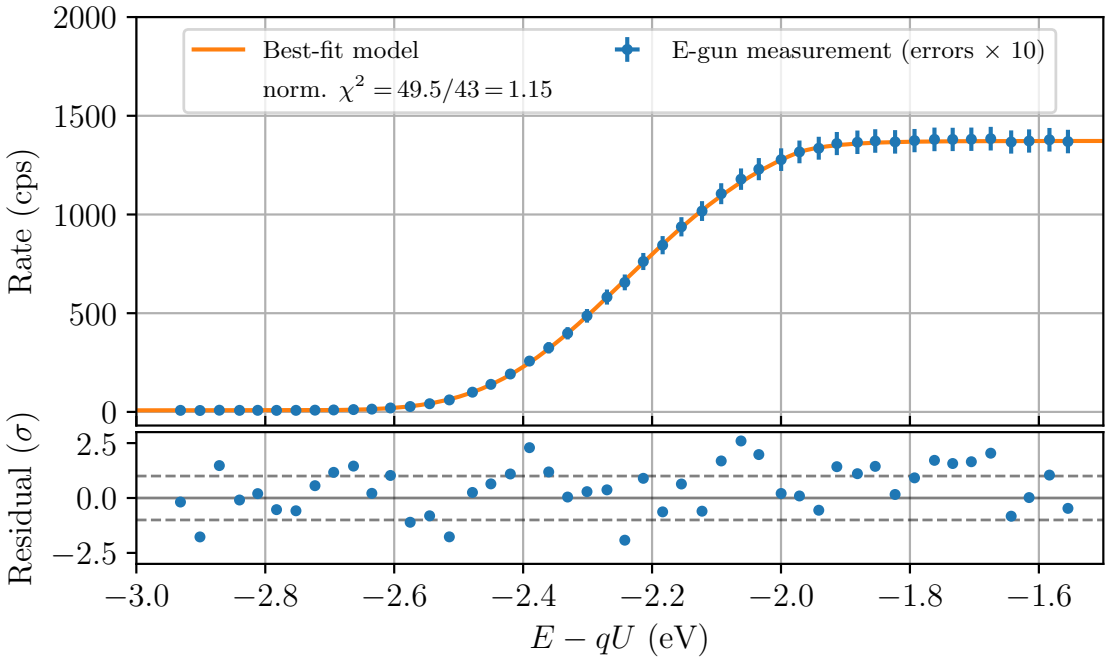

Figure A.3.: **E-gun transmission function measurement at 18.6 keV electron energy.** The measured e-gun rate (blue data points) is well-described by the best-fit model (orange curve), as shown in the upper graph. The best-fit residuals do not show any structure, as expected from statistical fluctuations (lower graph).

The proof-of-principle measurement is successful: we are able to determine the e-gun angular width by combining a single low-energy, high-resolution transmission function measurement with a normal one at 18.6 keV electron energy. It is planned to increase the precision of this analysis by conducting repeated measurements of the e-gun transmission function at both settings, leading to an improvement in precision and accuracy in the determination of the e-gun angular width compared to former determination methods. This value can then be used as input parameter for other analyses, for example column density measurements.

B. KATRIN Operational Parameters for Electric and Magnetic Field

Table B.1.: **Overview of the set currents for the KATRIN beamline solenoids as used in β scans.** Deviations on the order of 0.1 A are possible in individual neutrino mass measurement campaigns.

Solenoid	Current (A)
Rear section	57.0
WGTS M1M4M5	216.9
WGTS M2M3	216.2
WGTS M6M7	146.2
DPS M1	56.8
DPS M2	56.7
DPS M3	56.7
DPS M4	56.7
DPS M5	56.9
CPS	140.0
PS1	109.5
PS2	108.8
PCH	60.9
DET	39.3

Table B.2.: **eLFCS set currents *I* for the investigated magnetic field settings in the analyzing plane of the Main Spectrometer.**

eLFCS	I (A) for 1 G	I (A) for 2.7 G	I (A) for 6 G	I (A) for SAP
1	-24.4	0.0	50.8	120.0
2	0.0	0.0	0.0	-4.0
3	-19.0	5.0	44.6	116.0
4	-12.2	0.0	45.4	70.0
5	-4.7	0.0	24.6	70.0
6	-1.0	5.7	37.0	70.0
7	3.5	9.7	14.7	70.0
8	21.5	27.0	52.8	110.0
9	9.1	30.0	34.9	110.0
10	11.5	3.0	38.7	110.0
11	6.5	9.0	9.2	-60.0
12	4.4	5.3	35.9	-28.0
13	-15.9	10.7	92.7	58.0
14	-25.0	-22.0	13.2	5.0
15	0.0	0.0	0.0	120.0
16	25.6	0.0	0.0	120.0
17	25.6	0.0	0.0	-120.0
18	0.0	0.0	0.0	-119.0
19	0.0	0.0	0.0	-120.0
20	0.0	0.0	0.0	-120.0
EMCS-Vertical	45.0	45.0	45.0	45.0
EMCS-Horizontal	0.0	0.0	0.0	0.0

Table B.3.: **Set voltages U on the inner electrode system for measurement configurations in the NAP and SAP.** The steep cones are close to the entrance (ring 2, 3) or to the exit (ring 15, 16) of the Main Spectrometer. The flat cones (ring 4-6, 12-14) are located between the steep cones and the electrodes in the central part (ring 7-11, see figure 3.9).

Ring	U (V) for NAP β scans	U (V) for NAP ^{83m}Kr scans	U (V) for SAP β and ^{83m}Kr scans
2	-160	-70	-80
3	-160	-70	-80
4	-200	-200	-180
5	-200	-200	-180
6	-200	-200	-180
7	-200	-200	-195
8	-200	-200	-195
9	-200	-200	-195
10	-200	-200	-195
11	-200	-200	-195
12	-200	-200	-203
13	-200	-200	-205
14	-200	-200	-203
15	-160	-70	-160
16	-160	-70	-100

C. Overview of KATRIN Neutrino Mass Measurement Campaigns (2019-2021)

Table C.4.: **Overview of conducted neutrino mass measurement campaigns with their individual settings, relevant for the present thesis.** Five measurement campaigns are performed within 2.5 years. The measurement campaigns are either carried out with a symmetric Main Spectrometer configuration (NAP at 6 G) or with the asymmetric Shifted Analyzing Plane (SAP). The loop mode "Tr+Kr" stands for the novel mode that allows to add krypton to the source gas without significant changes in operational configuration (see section 7.5.2).

Neutrino mass campaign	KNM1	KNM2	KNM3 a	KNM3 b	KNM4	KNM5
WGTS beam tube temperature (K)	30	30	80	80	80	80
Approximate column density (% nominal)	22	84	42	75	75	75
Loop configuration	Nominal	Nominal	Nominal	Nominal	Tr+Kr	Tr+Kr
Main Spectrometer configuration	NAP	NAP	SAP	NAP	SAP	SAP
Year	2019	2019	2020	2020	2020	2021

List of Figures

List of Tables

Bibliography

[Aar+89] P. Aarnio et al. "Measurement of the mass and width of the Z0-particle from multihadronic final states produced in e+e− annihilations". In: *Physics Letters B* 231.4 (1989), pp. 539–547. DOI: 10.1016/0370-2693(89)90706-5.

[Aba+19] K. Abazajian et al. *CMB-S4 Decadal Survey APC White Paper*. 2019. arXiv: 1908.01062 [astro-ph.IM].

[Abd+17] D. N. Abdurashitov et al. "Electron scattering on hydrogen and deuterium molecules at 14–25 keV by the "Troitsk nu-mass" experiment". In: *Physics of Particles and Nuclei Letters* 14.6 (2017), pp. 892–899. DOI: 10.1134/S1547477117060024.

[Abd+96] J. N. Abdurashitov et al. "The Russian-American Gallium Experiment (SAGE) Cr Neutrino Source Measurement". In: *Phys. Rev. Lett.* 77 (1996), pp. 4708–4711. DOI: 10.1103/PhysRevLett.77.4708.

[Abe+17] K. Abe et al. "Combined Analysis of Neutrino and Antineutrino Oscillations at T2K". In: *Phys. Rev. Lett.* 118 (2017), p. 151801. DOI: 10.1103/PhysRevLett.118.151801.

[Ada+17] P. Adamson et al. "Constraints on Oscillation Parameters from ν_e Appearance and ν_μ Disappearance in NOvA". In: *Phys. Rev. Lett.* 118 (2017), p. 231801. DOI: 10.1103/PhysRevLett.118.231801.

[Ada15] B. Adams. "Untersuchung magnetischer Materialien und Inbetriebnahme der Magnetfeldüberwachung am KATRIN-Hauptspektrometer". Master Thesis. Karlsruher Institut für Technologie (KIT), 2015. URL: https://fuzzy.fzk.de/bscw/bscw.cgi/d975195/mth-adams_birgit.pdf.

[Ada16] B. Adams. "Demagnetization of steel". 27th KATRIN Collaboration Meeting. 2016. URL: https://fuzzy.fzk.de/bscw/bscw.cgi/935843?op=preview&back_url=935697%3fclient_size%3d1344x726.

[Ade+89] B. Adeva et al. "A determination of the properties of the neutral intermediate vector boson Z0". In: *Physics Letters B* 231.4 (1989), pp. 509–518. DOI: 10.1016/0370-2693(89)90703-X.

[Aha+05] B. Aharmim et al. "Electron energy spectra, fluxes, and day-night asymmetries of ^{8}B solar neutrinos from measurements with NaCl dissolved in the heavy-water detector at the Sudbury Neutrino Observatory". In: *Phys. Rev. C* 72 (2005), p. 055502. DOI: 10.1103/PhysRevC.72.055502.

[Ahm+01] Q. R. Ahmad et al. "Measurement of the Rate of $\nu_e + d \rightarrow p + p + e^-$ Interactions Produced by ^8B Solar Neutrinos at the Sudbury Neutrino Observatory". In: *Phys. Rev. Lett.* 87 (2001), p. 071301. DOI: 10.1103/PhysRevLett.87.071301.

[Ahm+02] Q. R. Ahmad et al. "Direct Evidence for Neutrino Flavor Transformation from Neutral-Current Interactions in the Sudbury Neutrino Observatory". In: *Phys. Rev. Lett.* 89 (2002), p. 011301. DOI: 10.1103/PhysRevLett.89.011301.

[Ake+21a] M. Aker et al. *First direct neutrino-mass measurement with sub-eV sensitivity*. 2021. arXiv: 2105.08533 [hep-ex].

[Ake+21b] M. Aker et al. "Analysis methods for the first KATRIN neutrino-mass measurement". In: *Phys. Rev. D* 104 (2021), p. 012005. DOI: 10.1103/PhysRevD.104.012005.

[Ake+21c] M. Aker et al. "Precision measurement of the electron energy-loss function in tritium and deuterium gas for the KATRIN experiment". In: *The European Physical Journal C - Particles and Fields* 81.7 (2021), p. 579. DOI: 10.1140/epjc/s10052-021-09325-z.

[Ake+21d] M. Aker et al. "The design, construction, and commissioning of the KATRIN experiment". In: *Journal of Instrumentation* 16.08 (2021), T08015. DOI: 10.1088/1748-0221/16/08/t08015.

[Ake+22] M. Aker et al. "Calibration of the electromagnetic fields in the analysing plane of the KATRIN main spectrometer". to be published in 2022.

[Ake20] M. Aker. "Status Update Residual Tritium Activity". Internal report. 2020. URL: https://ikp-katrin-wiki.ikp.kit.edu/katrin/images/f/f0/201201_RW-Activity.pdf.

[Ake21] M. Aker. *Personal correspondence*. 2021.

[Ake22] M. Aker. "Thesis in preparation". PhD thesis. Karlsruher Institut für Technologie (KIT), to be published in 2022.

[Aks+77] H. Aksela et al. "$N_{6,7}O_{4,5}O_{4,5}$ Auger electron spectrum of atomic mercury". In: *Phys. Rev. A* 15 (1977), pp. 985–989. DOI: 10.1103/PhysRevA.15.985.

[Ala+20] S. Alam et al. *The completed SDSS-IV extended baryon oscillation spectroscopic survey: cosmological implications from two decades of spectroscopic surveys at the apache point observatory*. 2020. arXiv: 2007.08991 [astro-ph.CO].

[Alt+20] K. Altenmüller et al. "High-resolution spectroscopy of gaseous ^{83m}Kr conversion electrons with the KATRIN experiment". In: *Journal of Physics G: Nuclear and Particle Physics* 47.6 (2020), p. 065002. DOI: 10.1088/1361-6471/ab8480.

[Ams+12] J. Amsbaugh et al. "Prototype focal-plane detector system for the KATRIN experiment". Internal report. 2012. URL: https://fuzzy.fzk.de/bscw/bscw.cgi/d722700/FPD_System_Prototype_Jan2012.pdf.

[Ams+15] J. Amsbaugh et al. "Focal-plane detector system for the KATRIN experiment". In: *Nuclear Instruments and Methods in Physics Research Section A: Accelerators, Spectrometers, Detectors and Associated Equipment* 778 (2015), pp. 40–60. DOI: 10.1016/j.nima.2014.12.116.

[Ant13] M. Antoni. "Entwicklung eines Sensornetzes zur kontinuierlichen Magnetfeldüberwachung am KATRIN Hauptspektrometer". Diploma Thesis. Karlsruher Institut für Technologie (KIT), 2013. URL: https://fuzzy.fzk.de/bscw/bscw.cgi/d875150/dth-antoni_marco.pdf.

[Are+16] M. Arenz et al. "Commissioning of the vacuum system of the KATRIN Main Spectrometer". In: *Journal of Instrumentation* 11 (2016), P04011. DOI: 10.1088/1748-0221/11/04/P04011.

[Are+18a] M. Arenz et al. "First transmission of electrons and ions through the KATRIN beamline". In: *Journal of Instrumentation* 13.04 (2018), P04020. DOI: 10.1088/1748-0221/13/04/P04020.

[Are+18b] M. Arenz et al. "The KATRIN Superconducting Magnets: Overview and First Performance Results". In: *Journal of Instrumentation* 13.08 (2018), T08005. DOI: 10.1088/1748-0221/13/08/T08005.

[Ase+00] V. N. Aseev et al. "Energy loss of 18 keV electrons in gaseous T_2 and quench condensed D_2 films". In: *Eur. Phys. J. D* 10 (2000), pp. 39–52. DOI: 10.1007/s100530050525.

[Ase+11] V. N. Aseev et al. "Upper limit on the electron antineutrino mass from the Troitsk experiment". In: *Phys. Rev. D* 84 (2011), p. 112003. DOI: 10.1103/PhysRevD.84.112003.

[Bab14] M. Babutzka. "Design and development for the Rearsection of the KATRIN experiment". PhD thesis. Karlsruher Institut für Technologie (KIT), 2014. DOI: 10.5445/IR/1000045598.

[Bar+14] J. Barrett et al. *Results of the first KATRIN SDS measurement phase*. Internal report. 2014. URL: https://fuzzy.fzk.de/bscw/bscw.cgi/d875500/SDSPhase1Report.pdf.

[Bar11] Bartington® Instruments. *Mag-03® - Three-Axis Magnetic Field Sensor*. 2011. URL: https://www.bartington.com/mag-03.html.

[Bar17] J. P. Barrett. "A spatially resolved study of the KATRIN main spectrometer using a novel fast multipole method". PhD thesis. Massachusetts Institute of Technology, 2017. URL: https://dspace.mit.edu/bitstream/handle/1721.1/114314/1028736454-MIT.pdf.

[Bau+13] S. Bauer et al. "Next generation KATRIN high precision voltage divider for voltages up to 65kV". In: *Journal of Instrumentation* 8.10 (2013), P10026–P10026. DOI: 10.1088/1748-0221/8/10/p10026.

[BB20] J. Behrens and F. Block. "Magnetic field measurement and optimization at the KATRIN main spectrometer". Poster presentation at the XXIX International Conference on Neutrino Physics and Astrophysics. 2020.

[BBG18] J. Behrens, F. Block, and F. Glück. "LFCS Field Deviation in STS-IIIa". Internal report. 2018. URL: https://ikp-katrin-wiki.ikp.kit.edu/katrin/images/d/d0/LFCS_Field_Deviation_STS3a.pdf.

[BBM21] F. Block, J. Behrens, and M. Machatschek. "Alignment from eGun and Simulation applied to KNM5 Krypton". Internal presentation. 2021. URL: https://ikp-katrin-wiki.ikp.kit.edu/katrin/images/4/42/AnaCall_20210720_merged.pdf.

[BC38] H. A. Bethe and C. L. Critchfield. "The Formation of Deuterons by Proton Combination". In: *Phys. Rev.* 54 (1938), pp. 248–254. DOI: 10.1103/PhysRev.54.248.

[Bec+19] D. Becker et al. "Working principle and demonstrator of microwave-multiplexing for the HOLMES experiment microcalorimeters". In: *Journal of Instrumentation* 14.10 (2019), P10035–P10035. DOI: 10.1088/1748-0221/14/10/p10035.

[Bec96] A. H. Becquerel. "Sur les radiations invisibles émises par les corps phosphorescents". In: *CR Acad. Sci. Paris* 122 (1896), p. 501.

[Beg+21] A. Beglarian et al. *Forward Beam Monitor for the KATRIN experiment*. 2021. arXiv: 2101.11495 [physics.ins-det].

[Beh+17] J. Behrens et al. "A pulsed, mono-energetic and angular-selective UV photo-electron source for the commissioning of the KATRIN experiment". In: *The European Physical Journal C* 77.6 (2017), p. 410. DOI: 10.1140/epjc/s10052-017-4972-9.

[Beh16] J. D. Behrens. "Design and commissioning of a mono-energetic photoelectron source and active background reduction by magnetic pulse at the KATRIN spectrometers". PhD thesis. Westfälische Wilhelms-Universität Münster, 2016. URL: http://www.katrin.kit.edu/publikationen/phd%5C_behrens.pdf.

[Beh21] J. Behrens. *Personal correspondence*. 2021.

[Bel+08] A. Belesev et al. "Investigation of space-charge effects in gaseous tritium as a source of distortions of the beta spectrum observed in the Troitsk neutrino-mass experiment". In: *Physics of Atomic Nuclei* 71 (2008), pp. 427–436. DOI: 10.1134/S1063778808030046.

[BGK54] P. L. Bhatnagar, E. P. Gross, and M. Krook. "A Model for Collision Processes in Gases. I. Small Amplitude Processes in Charged and Neutral One-Component Systems". In: *Phys. Rev.* 94 (1954), pp. 511–525. DOI: 10.1103/PhysRev.94.511.

[Bie20] B. Bieringer. "Shifted Analyzing Plane: Field optimization for background reduction of the KATRIN experiment". Master Thesis. Westfälische Wilhelms-Universität Münster, 2020.

[Bil10] S. Bilenky. *Introduction to the Physics of Massive and Mixed Neutrinos*. Lecture Notes in Physics. Springer, Berlin, Heidelberg, 2010. ISBN: 978-3-642-14043-3. DOI: 10.1007/978-3-642-14043-3.

[Bir63] G. Bird. "Approach to translational equilibrium in a rigid sphere gas". In: *The Physics of Fluids* 6.10 (1963), pp. 1518–1519. DOI: 10.1063/1.1710976.

[BL98] V. Blobel and E. Lohrmann. *Statistische und numerische Methoden der Datenanalyse*. 1615-3766. Vieweg+Teubner Verlag, 1998. ISBN: 978-3-519-03243-4. DOI: 10.1007/978-3-663-05690-4.

[Bou19] H. Bouquet. *Personal correspondence*. 2019.

[BP34] H. Bethe and R. Peierls. "The "Neutrino"". In: *Nature* 133.3362 (1934), p. 532. DOI: 10.1038/133532a0.

[BPT80] G. Beamson, H. Q. Porter, and D. W. Turner. "The collimating and magnifying properties of a superconducting field photoelectron spectrometer". In: *Journal of Physics E: Scientific Instruments* 13.1 (1980), p. 64. DOI: 10.1088/0022-3735/13/1/018.

[Bra04] W. H. Bragg. "LXXIII. On the absorption of α rays, and on the classification of the α rays from radium". In: *The London, Edinburgh, and Dublin Philosophical Magazine and Journal of Science* 8.48 (1904), pp. 719–725. DOI: 10.1080/14786440409463245.

[Bra16] M. Branchesi. "Multi-messenger astronomy: gravitational waves, neutrinos, photons, and cosmic rays". In: *Journal of Physics: Conference Series* 718 (2016), p. 022004. DOI: 10.1088/1742-6596/718/2/022004.

[CAC48] S. C. Curran, J. Angus, and A. L. Cockcroft. "Beta Spectrum of Tritium". In: *Nature* 162.4112 (1948), pp. 302–303. DOI: 10.1038/162302a0.

[Cap+18] F. Capozzi et al. "Current unknowns in the three-neutrino framework". In: *Progress in Particle and Nuclear Physics* 102 (2018), pp. 48–72. DOI: 10.1016/j.ppnp.2018.05.005.

[CEC98] O. Chubar, P. Elleaume, and J. Chavanne. "A three-dimensional magnetostatics computer code for insertion devices". In: *Journal of Synchrotron Radiation* 5.3 (1998), pp. 481–484. DOI: 10.1107/S0909049597013502.

[Cha14] J. Chadwick. "Intensitätsverteilung im magnetischen Spectrum der β-Strahlen von radium B+ C". In: *Verhandl. Dtsc. Phys. Ges.* 16 (1914), p. 383.

[Cha32] J. Chadwick. "Possible Existence of a Neutron". In: *Nature* 129.3252 (1932), p. 312. DOI: 10.1038/129312a0.

[Chi+10] S. Chilingaryan et al. "Advanced data extraction infrastructure: Web based system for management of time series data". In: *Journal of Physics: Conference Series* 219.4 (2010), p. 042034. DOI: 10.1088/1742-6596/219/4/042034.

[Cle+98] B. T. Cleveland et al. "Measurement of the Solar Electron Neutrino Flux with the Homestake Chlorine Detector". In: *The Astrophysical Journal* 496.1 (1998), p. 505. DOI: 10.1086/305343.

[Cor14] T. Corona. "Methodology and Application of High Performance Electrostatic Field Simulation in the KATRIN Experiment". PhD thesis. University of North Carolina at Chapel Hill, 2014. URL: https://cdr.lib.unc.edu/record/uuid:6f44a9c2-f053-404a-b726-b960d5772619.

[Cow+11] G. Cowan et al. "Asymptotic formulae for likelihood-based tests of new physics". In: *The European Physical Journal C - Particles and Fields* 71.2 (2011), p. 1554. DOI: 10.1140/epjc/s10052-011-1554-0.

[Cow+56] C. L. Cowan et al. "Detection of the Free Neutrino: a Confirmation". In: *Science* 124.3212 (1956), pp. 103–104. ISSN: 0036-8075. DOI: 10.1126/science.124.3212.103.

[Cro+16] M. P. Croce et al. "Development of Holmium-163 Electron-Capture Spectroscopy with Transition-Edge Sensors". In: *Journal of Low Temperature Physics* 184.3 (2016), pp. 958–968. DOI: 10.1007/s10909-015-1451-2.

[Cur10] M. Curie. *Traité de radioactivité*. Vol. 2. Gauthier-Villars, 1910.

[Dan+62] G. Danby et al. "Observation of High-Energy Neutrino Reactions and the Existence of Two Kinds of Neutrinos". In: *Phys. Rev. Lett.* 9 (1962), pp. 36–44. DOI: 10.1103/PhysRevLett.9.36.

[Dav60] D. Davis. "Monte Carlo calculation of molecular flow rates through a cylindrical elbow and pipes of other shapes". In: *Journal of Applied Physics* 31.7 (1960), pp. 1169–1176. DOI: 10.1063/1.1735797.

[Dec+90a] D. Decamp et al. "A precise determination of the number of families with light neutrinos and of the Z boson partial widths". In: *Physics Letters B* 235.3 (1990), pp. 399–411. DOI: 10.1016/0370-2693(90)91984-J.

[Dec+90b] D. Decamp et al. "A precise determination of the number of families with light neutrinos and of the Z boson partial widths". In: *Physics Letters B* 235.3 (1990), pp. 399–411. DOI: 10.1016/0370-2693(90)91984-J.

[Dec+90c] D. Decamp et al. "ALEPH: A detector for electron-positron annihilations at LEP". In: *Nuclear Instruments and Methods in Physics Research Section A: Accelerators, Spectrometers, Detectors and Associated Equipment* 294.1 (1990), pp. 121–178. DOI: 10.1016/0168-9002(90)91831-U.

[Def17] M. Deffert. "Simulation of the global beam line alignment of the KATRIN experiment". Master Thesis. Karlsruher Institut für Technologie (KIT), 2017. URL: https://www.katrin.kit.edu/publikationen/mth_Marco_Deffert.pdf.

[DHH68] R. Davis, D. S. Harmer, and K. C. Hoffman. "Search for Neutrinos from the Sun". In: *Phys. Rev. Lett.* 20 (1968), pp. 1205–1209. DOI: 10.1103/PhysRevLett.20.1205.

[Dör+05] L. Dörr et al. "The Closed Tritium Cycle of the Tritium Laboratory Karlsruhe". In: *Fusion Science and Technology* 48.1 (2005), pp. 262–267. DOI: 10.13182/FST05-A924.

[DPR19] M. J. Dolinski, A. W. Poon, and W. Rodejohann. "Neutrinoless Double-Beta Decay: Status and Prospects". In: *Annual Review of Nuclear and Particle Science* 69.1 (2019), pp. 219–251. DOI: 10.1146/annurev-nucl-101918-023407.

[Dyb19] S. Dyba. "Background reduction by the inner wire electrode and set-up of the condensed krypton source at the neutrino mass experiment KATRIN". PhD thesis. Westfälische Wilhelms-Universität Münster, 2019.

[ECC97] P. Elleaume, O. Chubar, and J. Chavanne. "Computing 3D magnetic fields from insertion devices". In: *Proceedings of the 1997 Particle Accelerator Conference (Cat. No.97CH36167)*. Vol. 3. 1997, pp. 3509–3511. DOI: 10.1109/PAC.1997.753258.

[EHM87] S. R. Elliott, A. A. Hahn, and M. K. Moe. "Direct evidence for two-neutrino double-beta decay in ^{82}Se". In: *Phys. Rev. Lett.* 59 (1987), pp. 2020–2023. DOI: 10.1103/PhysRevLett.59.2020.

[Eno19] S. Enomoto. "Detector Count Corrections for First Tritium". Internal report. 2019. URL: https://ikp-katrin-wiki.ikp.kit.edu/katrin/images/d/d2/FirstTritiumDetectorSystematics_20190203.pdf.

[Eno21a] S. Enomoto. "FPD Systematics Model for KNM4". Internal presentation. 2021. URL: https://ikp-katrin-wiki.ikp.kit.edu/katrin/images/f/fa/FPD_Systematics_KNM4-210713.pdf.

[Eno21b] S. Enomoto. *Personal correspondence*. 2021.

[Erh+18] M. Erhard et al. "Technical design and commissioning of the KATRIN large-volume air coil system". In: *Journal of Instrumentation* 13.02 (2018), P02003. DOI: 10.1088/1748-0221/13/02/P02003.

[Erh16] M. G. Erhard. "Influence of the magnetic field on the transmission characteristics and neutrino mass systematic of the KATRIN experiment". PhD thesis. Karlsruher Institut für Technologie (KIT), 2016. DOI: 10.5445/IR/1000065003.

[Esc+20] M. Escudero et al. "Relaxing cosmological neutrino mass bounds with unstable neutrinos". In: *Journal of High Energy Physics* 2020.12 (2020), p. 119. DOI: 10.1007/JHEP12(2020)119.

[Esf+17] A. A. Esfahani et al. "Determining the neutrino mass with cyclotron radiation emission spectroscopy—Project 8". In: *Journal of Physics G: Nuclear and Particle Physics* 44.5 (2017), p. 054004. DOI: 10.1088/1361-6471/aa5b4f.

[FdR21] J. A. Formaggio, A. L. C. de Gouvêa, and R. H. Robertson. "Direct measurements of neutrino mass". In: *Physics Reports* (2021). DOI: 10.1016/j.physrep.2021.02.002.

[Fen21] C. Fengler. "Investigation of systematic effects in ^{83m}Kr $N_{2,3}$ line measurements". 40th KATRIN Collaboration Meeting. 2021. URL: https://indico.scc.kit.edu/event/2061/contributions/8323/contribution.pdf.

[Fer34] E. Fermi. "Versuch einer Theorie der β-Strahlen." In: *Zeitschrift für Physik* 88.3–4 (1934), pp. 161–177. DOI: 10.1007/BF01351864.

[Fil20] P. Filip. "Measurements of source column density during KATRIN neutrino mass measurements". Bachelor Thesis. Karlsruher Institut für Technologie (KIT), 2020. URL: https://fuzzy.fzk.de/bscw/bscw.cgi/1311935.

[Fis+11] S. Fischer et al. "Monitoring of tritium purity during long-term circulation in the KATRIN test experiment LOOPINO using laser Raman spectroscopy". In: *Fusion Science and Technology* 60.3 (2011), pp. 925–930. URL: http://www.ans.org/pubs/journals/fst/a_12567.

[FLS00] M. Fukugita, G.-C. Liu, and N. Sugiyama. "Limits on Neutrino Mass from Cosmic Structure Formation". In: *Phys. Rev. Lett.* 84 (2000), pp. 1082–1085. DOI: 10.1103/PhysRevLett.84.1082.

[Fog+02] G. L. Fogli et al. "Getting the most from the statistical analysis of solar neutrino oscillations". In: *Phys. Rev. D* 66 (2002), p. 053010. DOI: 10.1103/PhysRevD.66.053010.

[For+11] J. A. Formaggio et al. *Solving for Micro- and Macro- Scale Electrostatic Configurations Using the Robin Hood Algorithm*. 2011. arXiv: 1111.5035 [physics.comp-ph].

[For+13] D. Foreman-Mackey et al. "emcee: The MCMC Hammer". In: *Publications of the Astronomical Society of the Pacific* 125.925 (2013), pp. 306–312. DOI: 10.1086/670067.

[Frä+11] F. Fränkle et al. "Radon induced background processes in the KATRIN pre-spectrometer". In: *Astroparticle Physics* 35.3 (2011), pp. 128–134. DOI: 10.1016/j.astropartphys.2011.06.009.

[Frä+20] F. Fränkle et al. *KATRIN background due to surface radioimpurities*. 2020. arXiv: 2011.05107 [physics.ins-det].

[Frä21] F. Fränkle. *Personal correspondence*. 2021.

[Fri+19] F. Friedel et al. "Time-dependent simulation of the flow reduction of D_2 and T_2 in the KATRIN experiment". In: *Vacuum* 159 (2019), pp. 161–172. ISSN: 0042-207X. DOI: 10.1016/j.vacuum.2018.10.002.

[Fri20] F. Friedel. "Ion and plasma systematics during the first KATRIN neutrino mass measurements". PhD thesis. Karlsruher Institut für Technologie (KIT), 2020. DOI: 10.5445/IR/1000126837.

[Fuk+98] Y. Fukuda et al. "Evidence for Oscillation of Atmospheric Neutrinos". In: *Phys. Rev. Lett.* 81 (1998), pp. 1562–1567. DOI: 10.1103/PhysRevLett.81.1562.

[Fuk+99] Y. Fukuda et al. "Measurement of the Flux and Zenith-Angle Distribution of Upward Throughgoing Muons by Super-Kamiokande". In: *Phys. Rev. Lett.* 82 (1999), pp. 2644–2648. DOI: 10.1103/PhysRevLett.82.2644.

[Ful20] A. Fulst. "A Novel Quasi-Differential Method for MAC-E Filters and Determination and Control of the Electric Potentials of the KATRIN Experiment with a Stabilized Condensed Krypton Source and a UV Illumination System". PhD thesis. Westfälische Wilhelms-Universität Münster, 2020.

[Fur+17] D. Furse et al. "Kassiopeia: a modern, extensible C++ particle tracking package". In: *New Journal of Physics* 19.5 (2017), p. 053012. DOI: 10.1088/1367-2630/aa6950.

[Gar17] J. Garbe. "Positionsbestimmung von Magnetfeldsensoren am KATRIN-Experiment". Bachelor Thesis. Hochschule Fulda, 2017.

[Gar51] M. W. Garrett. "Axially Symmetric Systems for Generating and Measuring Magnetic Fields. Part I". In: *Journal of Applied Physics* 22.9 (1951), pp. 1091–1107. DOI: 10.1063/1.1700115.

[GGS58] M. Goldhaber, L. Grodzins, and A. W. Sunyar. "Helicity of Neutrinos". In: *Phys. Rev.* 109 (1958), pp. 1015–1017. DOI: 10.1103/PhysRev.109.1015.

[Gil20a] W. Gil. *Personal correspondence*. 2020.

[Gil20b] W. Gil. "Study of the Magnetic Field of the KATRIN-WGTS Main Solenoids". Internal report. 2020. URL: https://ikp-katrin-wiki.ikp.kit.edu/katrin/images/9/9b/Report_WGTS-Magnetic-Field_20200313.pdf.

[GL13] R. Gumbsheimer and J. Lichter. "Prüfung Luftspuleninnenradius". KATRIN Collaboration Meeting. 2013. URL: https://fuzzy.fzk.de/bscw/bscw.cgi/d898608/Kontrollvermessung_Luftspule.pdf.

[Glü+13] F. Glück et al. "Electromagnetic design of the large-volume air coil system of the KATRIN experiment". In: *New Journal of Physics* 15.8 (2013), p. 083025. DOI: 10.1088/1367-2630/15/8/083025.

[Glü11] F. Glück. "Axisymmetric Electric Field Calculation with Zonal Harmonic Expansion". In: *Progress In Electromagnetics Research B* 32 (2011), pp. 319–350. DOI: 10.2528/PIERB11042106.

[GPM12] A. Giuliani, A. Poves, and A. B. McDonald. "Neutrinoless Double-Beta Decay". In: *Advances in High Energy Physics* 2012 (2012), p. 857016. DOI: 10.1155/2012/857016.

[Gri14] D. J. Griffiths. *Introduction to electrodynamics*. 4th Edition. Pearson custom library. Harlow, Essex: Pearson, 2014. ISBN: 129202142X.

[Gro+08] S. Grohmann et al. "Cryogenic Design of the KATRIN Source Cryostat". In: *AIP Conference Proceedings* 985 (2008), pp. 1277–1284. DOI: 10.1063/1.2908483.

[Gro+11] S. Grohmann et al. "Precise temperature measurement at 30 K in the KATRIN source cryostat". In: *Cryogenics* 51.8 (2011), pp. 438–445. DOI: 10.1016/j.cryogenics.2011.05.001.

[Gro09] S. Grohmann. "Stability analyses of the beam tube cooling system in the KATRIN source cryostat". In: *Cryogenics* 49.8 (2009), pp. 413–420. DOI: 10.1016/j.cryogenics.2009.06.001.

[Gro15] S. Groh. "Modeling of the response function and measurement of transmission properties of the KATRIN experiment". PhD thesis. Karlsruher Institut für Technologie (KIT), 2015. DOI: 10.5445/IR/1000046546.

[Har15] F. Harms. "Characterization and Minimization of Background Processes in the KATRIN Main Spectrometer". PhD thesis. Karlsruher Institut für Technologie (KIT), 2015. DOI: 10.5445/IR/1000050027.

[Hei18] F. Heizmann. "Analysis tools and methods for tritium data taking with the KATRIN experiment". PhD thesis. Karlsruher Institut für Technologie (KIT), 2018. DOI: 10.5445/IR/1000093536.

[Her21] F. Hermann. *Personal correspondence*. 2021.

[Hig64] P. W. Higgs. "Broken Symmetries and the Masses of Gauge Bosons". In: *Phys. Rev. Lett.* 13 (1964), pp. 508–509. DOI: 10.1103/PhysRevLett.13.508.

[Hil16] D. F. R. Hilk. "Electric field simulations and electric dipole investigations at the KATRIN main spectrometer". PhD thesis. Karlsruher Institut für Technologie (KIT), 2016. DOI: 10.5445/IR/1000065869.

[Hin22] D. Hinz. "Thesis in preparation". PhD thesis. Karlsruher Institut für Technologie (KIT), to be published in 2022.

[HK21] S. Hickford and L. Köllenberger. "Neutrino mass analysis in KATRIN". Poster presentation at the ISAPP 2021 Valencia Summer School. 2021. URL: https://isapp2020vlc.astroparticles.es/posters/pdf/posterPDF-14.pdf.

[Höt12] M. Hötzel. "Simulation and analysis of source-related effects for KATRIN". PhD thesis. Karlsruher Institut für Technologie (KIT), 2012. DOI: 10.5445/IR/1000031259.

[How+04] M. Howe et al. "Sudbury neutrino observatory neutral current detector acquisition software overview". In: *IEEE Transactions on Nuclear Science* 51.3 (2004), pp. 878–883. DOI: 10.1109/TNS.2004.829527.

[HS17] F. Heizmann and H. Seitz-Moskaliuk. "The Windowless Gaseous Tritium Source (WGTS) of the KATRIN experiment". In: *Journal of Physics: Conference Series* 888.1 (2017), p. 012071. DOI: 10.1088/1742-6596/888/1/012071.

[Jam+13] T. M. James et al. "Automated Quantitative Spectroscopic Analysis Combining Background Subtraction, Cosmic Ray Removal, and Peak Fitting". In: *Applied Spectroscopy* 67.8 (2013). PMID: 23876734, pp. 949–959. DOI: 10.1366/12-06766.

[Jar89] C. Jarlskog. *CP Violation*. Singapur: World Scientific, 1989. ISBN: 978-9971-5-0561-5. DOI: 10.1142/0496.

[Kaš+04] J. Kašpar et al. "Effect of energy scale imperfections on results of neutrino mass measurements from β-decay". In: *Nuclear Instruments and Methods in Physics Research Section A: Accelerators, Spectrometers, Detectors and Associated Equipment* 527.3 (2004), pp. 423–431. DOI: 10.1016/j.nima.2004.03.201.

[Kas+09] L. W. Kastens et al. "Calibration of a liquid xenon detector with $^{83}Kr^{m}$". In: *Phys. Rev. C* 80 (2009), p. 045809. DOI: 10.1103/PhysRevC.80.045809.

[KAT05] KATRIN collaboration. *KATRIN Design Report*. FZKA scientific report 7090. 2005. URL: http://bibliothek.fzk.de/zb/berichte/FZKA7090.pdf.

[KAT20] KATRIN analysis team. "Plasma in KNM2". Internal report. 2020. URL: https://ikp-katrin-wiki.ikp.kit.edu/katrin/images/9/94/Plasma_Report_for_KNM2_2020_09_12.pdf.

[KAT21] KATRIN Wiki. *Run Summary — KATRIN Wiki*. 2021. URL: http://ikp-katrin-wiki.ikp.kit.edu/katrin/index.php?title=Run_Summary&oldid=37114 (visited on 09/10/2021).

[Kir+99] T. Kirsten et al. "GALLEX solar neutrino results and status of GNO". In: *Nuclear Physics B - Proceedings Supplements* 77.1 (1999), pp. 26–34. DOI: 10.1016/S0920-5632(99)00389-8.

[Kir20] R. Kirchgässner. "Simulations and characteristics of radon-induced background in the KATRIN main spectrometer". Bachelor Thesis. Karlsruher Institut für Technologie (KIT), 2020. URL: https://fuzzy.fzk.de/bscw/bscw.cgi/d1312650/BA2020_Kirchgaessner.pdf.

[Kle+19] M. Kleesiek et al. "β-Decay spectrum, response function and statistical model for neutrino mass measurements with the KATRIN experiment". In: *The European Physical Journal C* 79.3 (2019), p. 204. DOI: 10.1140/epjc/s10052-019-6686-7.

[Kle14] M. Kleesiek. "A Data-Analysis and Sensitivity-Optimization Framework for the KATRIN Experiment". PhD thesis. Karlsruher Institut für Technologie (KIT), 2014. DOI: 10.5445/IR/1000043301.

[Kod+01] K. Kodama et al. "Observation of tau neutrino interactions". In: *Physics Letters B* 504.3 (2001), pp. 218–224. DOI: 10.1016/S0370-2693(01)00307-0.

[Köh19] C. Köhler. "Determination of the Column Density in the KATRIN Beamline with Electrons from the Photo-Electric Source". Master Thesis. Technical University of Munich, 2019. URL: https://publications.mppmu.mpg.de/2019/MPP-2019-357/FullText.pdf.

[Köh21] C. Köhler. *Personal correspondence*. 2021.

[Kra+05] C. Kraus et al. "Final results from phase II of the Mainz neutrino mass search in tritium β decay". In: *The European Physical Journal C - Particles and Fields* 40.4 (2005), pp. 447–468. DOI: 10.1140/epjc/s2005-02139-7.

[KSP00] Y.-K. Kim, J. P. Santos, and F. Parente. "Extension of the binary-encounter-dipole model to relativistic incident electrons". In: *Phys. Rev. A* 62 (2000), p. 052710. DOI: 10.1103/PhysRevA.62.052710.

[Kuc+18] L. Kuckert et al. "Modelling of gas dynamical properties of the KATRIN tritium source and implications for the neutrino mass measurement". In: *Vacuum* 158 (2018), pp. 195–205. DOI: 10.1016/j.vacuum.2018.09.036.

[Kuc16] L. Kuckert. "The Windowless Gaseous Tritium Source of the KATRIN Experiment – Characterisation of Gas Dynamical and Plasma Properties". PhD thesis. Karlsruher Institut für Technologie (KIT), 2016. DOI: 10.5445/IR/1000065077.

[LB20] A. Lokhov and J. Behrens. "Reduction of KATRIN background with the shifted analyzing plane configuration in KNM4". Internal report. 2020. URL: https://ikp-katrin-wiki.ikp.kit.edu/katrin/images/8/88/2020-08-17_SAP_KNM4_Proposal_v10.pdf.

[Let+18] J. Letnev et al. "Technical design and commissioning of a sensor net for fine-meshed measuring of the magnetic field at the KATRIN spectrometer". In: *Journal of Instrumentation* 13.08 (2018), T08010. DOI: 10.1088/1748-0221/13/08/T08010.

[Let19] J. Letnev. "Ein Sensornetz zur Vermessung des Magnetfeldes am KATRIN Hauptspektrometer". PhD thesis. Kassel, Universität Kassel, Fachbereich Elektrotechnik / Informatik, 2019. DOI: 10.17170/kobra-20190226207.

[Liu87] J. W. Liu. "Total cross sections for high-energy electron scattering by H_2 ($^1\Sigma_g^+$), N_2 ($^1\Sigma_g^+$), and O_2 ($^3\Sigma_g^-$)". In: *Phys. Rev. A* 35 (1987), pp. 591–597. DOI: 10.1103/PhysRevA.35.591.

[LW20] A. Lokhov and C. Weinheimer. "Transmission function for pixels and patches in SAP configuration". Internal presentation. 2020. URL: https://ikp-katrin-wiki.ikp.kit.edu/katrin/images/1/15/2020-06-30_sap_transmission.pdf.

[Mac16] M. Machatschek. "Simulation of the ^{83m}Kr Mode of the Tritium Source of the KATRIN Experiment". Master Thesis. Karlsruher Institut für Technologie (KIT), 2016. URL: https://www.katrin.kit.edu/publikationen/mth-machatschek.pdf.

[Mac21] M. Machatschek. "A Phenomenological Theory of KATRIN Source Potential Systematics and its Application in Krypton-83m Calibration Measurements." PhD thesis. Karlsruher Institut für Technologie (KIT), 2021. DOI: 10.5445/IR/1000132391.

[Mar+21] A. Marsteller et al. "Neutral tritium gas reduction in the KATRIN differential pumping sections". In: *Vacuum* 184 (2021), p. 109979. DOI: 10.1016/j.vacuum.2020.109979.

[Mar20a] A. Marsteller. "Characterization and optimization of the KATRIN tritium source". PhD thesis. Karlsruher Institut für Technologie (KIT), 2020. DOI: 10.5445/IR/1000127553.

[Mar20b] A. Marsteller. *Personal correspondence*. 2020.

[Mer+13] S. Mertens et al. "Background due to stored electrons following nuclear decays in the KATRIN spectrometers and its impact on the neutrino mass sensitivity". In: *Astroparticle Physics* 41 (2013), pp. 52–62. DOI: 10.1016/j.astropartphys.2012.10.005.

[Met20] Metrolab. *THM1176 and TFM1186 Key Specifications*. 2020. URL: https://www.metrolab.com/wp-content/uploads/2020/11/THM1176-TFM1186-Key-specifications.pdf.

[MKS15] MKS Instruments. *Type 179A All-Metal Mass-Flo® Meter*. Andover, United States of America, 2015. URL: http://www.mhzelectronics.com/ebay/manuals/mks_179a-series_mass_flow_meter_datasheet.pdf.

[MKS19] MKS Instruments. *627F Heated (45 °C) Absolute Baratron® Capacitance Manometer*. Andover, United States of America, 2019. URL: https://www.mksinst.com/mam/celum/celum_assets/resources/627F-DS.pdf?1.

[MNS62] Z. Maki, M. Nakagawa, and S. Sakata. "Remarks on the Unified Model of Elementary Particles". In: *Progress of Theoretical Physics* 28.5 (1962), pp. 870–880. DOI: 10.1143/PTP.28.870.

[MS85] S. P. Mikheyev and A. Y. Smirnov. "Resonance enhancement of oscillations in matter and solar neutrino spectroscopy". In: *Yadernaya Fizika* 42 (1985), pp. 1441–1448.

[Mül14] A. Müller. "Field Alignment Studies at the KATRIN Pinch Magnet". Bachelor Thesis. Karlsruher Institut für Technologie (KIT), 2014. URL: https://fuzzy.fzk.de/bscw/bscw.cgi/977642?op=preview&back_url=831858.

[Mül21] K. Müller. *Personal correspondence*. 2021.

[NDS85] H. Nishimura, A. Danjo, and H. Sugahara. "Differential Cross Sections of Electron Scattering from Molecular Hydrogen I. Elastic Scattering and Vibrational Excitation ($X^1\Sigma_g^+$, $v = 0 \rightarrow 1$)". In: *Journal of the Physical Society of Japan* 54.5 (1985), pp. 1757–1768. DOI: 10.1143/JPSJ.54.1757.

[New+14] M. Newville et al. *LMFIT: Non-Linear Least-Square Minimization and Curve-Fitting for Python*. Version 0.8.0. 2014. DOI: 10.5281/zenodo.11813.

[OW08] E. W. Otten and C. Weinheimer. "Neutrino mass limit from tritium β decay". In: *Reports on Progress in Physics* 71.8 (2008), p. 086201. DOI: 10.1088/0034-4885/71/8/086201.

[Per+75] M. L. Perl et al. "Evidence for Anomalous Lepton Production in $e^+ - e^-$ Annihilation". In: *Phys. Rev. Lett.* 35 (1975), pp. 1489–1492. DOI: 10.1103/PhysRevLett.35.1489.

[PKW64] W. E. F. Pauli, R. Kronig, and V. F. Weisskopf. *Collected scientific papers*. Offener Brief an die Gruppe der Radioaktiven bei der Gauvereinstagung zu Tübingen (datiert 4. Dez. 1930). New York, NY: Interscience, 1964.

[Pla+20] Planck Collaboration et al. "Planck 2018 results - VI. Cosmological parameters". In: *A&A* 641 (2020), A6. DOI: 10.1051/0004-6361/201833910.

[Pla83] R. L. Plackett. "Karl Pearson and the Chi-Squared Test". In: *International Statistical Review / Revue Internationale de Statistique* 51.1 (1983), pp. 59–72. URL: http://www.jstor.org/stable/1402731.

[Pon57] B. Pontecorvo. "Mesonium and anti-mesonium". In: *Sov. Phys. JETP* 6 (1957), p. 429.

[Pon58] B. Pontecorvo. "Inverse beta processes and nonconservation of lepton charge". In: *Zh. Eksp. Teor. Fiz.* 34 (1958), p. 247.

[Pon68] B. Pontecorvo. "Neutrino experiments and the problem of conservation of leptonic charge". In: *Sov. Phys. JETP* 26.984-988 (1968), p. 165.

[Pov+15] B. Povh et al. *Particles and Nuclei : An Introduction to the Physical Concepts*. 7th ed. 2015. Berlin, Heidelberg: Springer, 2015. DOI: 10.1007/978-3-662-46321-5.

[PVS14] S. Pantazis, D. Valougeorgis, and F. Sharipov. "End corrections for rarefied gas flows through circular tubes of finite length". In: *Vacuum* 101 (2014). Including rapid communications, original articles and a special section: Measurement Characteristics and Use of Quadrupole Mass Spectrometers for Vacuum Applications, pp. 306–312. DOI: 10.1016/j.vacuum.2013.09.015.

[Rat09] B. Ratner. "The correlation coefficient: Its values range between +1/−1, or do they?" In: *Journal of Targeting, Measurement and Analysis for Marketing* 17.2 (2009), pp. 139–142. DOI: 10.1057/jt.2009.5.

[RC59] F. Reines and C. L. Cowan. "Free Antineutrino Absorption Cross Section. I. Measurement of the Free Antineutrino Absorption Cross Section by Protons". In: *Phys. Rev.* 113 (1959), pp. 273–279. DOI: 10.1103/PhysRev.113.273.

[Rei13] J. Reich. "Magnetic Field Inhomogeneities and Their Influence on Transmission and Background at the KATRIN Main Spectrometer". PhD thesis. Karlsruher Institut für Technologie (KIT), 2013. DOI: 10.5445/IR/1000033076.

[Res+19] O. Rest et al. "A novel ppm-precise absolute calibration method for precision high-voltage dividers". In: *Metrologia* 56.4 (2019), p. 045007. DOI: 10.1088/1681-7575/ab2997.

[RK88] R. G. H. Robertson and D. A. Knapp. "Direct Measurements of Neutrino Mass". In: *Annual Review of Nuclear and Particle Science* 38.1 (1988), pp. 185–215. DOI: 10.1146/annurev.ns.38.120188.001153.

[Rod20] C. Rodenbeck. "Energy Loss at Impurities in the Krypton mode". Internal presentation. 2020. URL: https://ikp-katrin-wiki.ikp.kit.edu/katrin/images/0/03/2020-09-01_ElossAtImpurities.pdf.

[Rod21a] C. Rodenbeck. "High Voltage in KNM2". Internal report. 2021. URL: https://ikp-katrin-wiki.ikp.kit.edu/katrin/images/6/64/HV_KNM2_Summary.pdf.

[Rod21b] C. Rodenbeck. *Personal correspondence*. 2021.

[Rod21c] C. Rodenbeck. "Update on recent K35 calibration results". Internal report. 2021. URL: https://ikp-katrin-wiki.ikp.kit.edu/katrin/images/6/6a/2020_06_18_K35_Calibration_Results.pdf.

[Rod22] C. Rodenbeck. "Investigation of inelastic scattering of beta electrons in KATRIN's gaseous tritium source using time of flight methods to determine the neutrino mass". Thesis in preparation. PhD thesis. Westfälische Wilhelms-Universität Münster, to be published in 2022.

[Röt17] C. Röttele. "Results of the first Cool-down of the KATRIN Cryogenic Pumping Section". In: *Journal of Physics: Conference Series* 888.1 (2017), p. 012228. DOI: 10.1088/1742-6596/888/1/012228.

[Röt19] C. Röttele. "Tritium suppression factor of the KATRIN transport section". PhD thesis. Karlsruher Institut für Technologie (KIT), 2019. DOI: 10.5445/IR/1000096733.

[Rut05] E. Rutherford. *Radio-activity*. Cambridge: University Press, 1905.

[Sac20] R. Sack. “Measurement of the energy loss of 18.6 keV electrons on deuterium gas and determination of the tritium Q-value at the KATRIN experiment”. PhD thesis. Westfälische Wilhelms-Universität Münster, 2020.

[Sac21a] R. Sack. *Personal correspondence*. 2021.

[Sac21b] R. Sack. “Rear Wall Status”. 40th KATRIN Collaboration Meeting. 2021. URL: https://fuzzy.fzk.de/bscw/bscw.cgi/1337941?op=preview&back_url=15294.

[Sak91] A. D. Sakharov. “Violation of CP-invariance, C-asymmetry, and baryon asymmetry of the universe”. In: *Soviet Physics Uspekhi* 34.5 (1991), pp. 392–393. DOI: 10.1070/pu1991v034n05abeh002497.

[Sal+18] P. F. de Salas et al. “Neutrino Mass Ordering from Oscillations and Beyond: 2018 Status and Future Prospects”. In: *Frontiers in Astronomy and Space Sciences* 5 (2018), p. 36. DOI: 10.3389/fspas.2018.00036.

[Sch+06] S. Schael et al. “Precision electroweak measurements on the Z resonance”. In: *Physics Reports* 427.5 (2006), pp. 257–454. DOI: 10.1016/j.physrep.2005.12.006.

[Sch+13] M. Schlösser et al. “Accurate calibration of the laser Raman system for the Karlsruhe Tritium Neutrino Experiment”. In: *Journal of Molecular Structure* 1044.0 (2013), pp. 61–66. DOI: 10.1016/j.molstruc.2012.11.022.

[Sch06] P. Schneider. *Einführung in die Extragalaktische Astronomie und Kosmologie*. 1st ed. Berlin, Heidelberg: Springer, 2006. DOI: 10.1007/3-540-30589-0.

[Sch15] C. Schönfeld. “Commissioning of the KATRIN Pinch Magnet”. Bachelor Thesis. Karlsruher Institut für Technologie (KIT), 2015. URL: https://fuzzy.fzk.de/bscw/bscw.cgi/d1236629/BA2015-Sch%c3%b6nfeld.pdf.

[Sch19] L. Schlüter. “Development of New Methods to Include Systematic Effects in the First Tritium Data Analysis and Sensitivity Studies of the KATRIN Experiment”. Master Thesis. Technical University of Munich, 2019. URL: http://www.katrin.kit.edu/publikationen/SchlueterLisaMSc19%5C%20(1).pdf.

[Sch20a] A. K. Schaller. “Characterization and mitigation of the background in KATRIN”. PhD thesis. Technical University of Munich, 2020. URL: http://nbn-resolving.de/urn/resolver.pl?urn:nbn:de:bvb:91-diss-20200828-1553598-1-6.

[Sch20b] A. Schwemmer. “Time-correlated Background and Background Mitigation Strategies in the KATRIN Experiment”. Master Thesis. Ludwig-Maximilians-Universität München, 2020. URL: https://publications.mppmu.mpg.de/2020/MPP-2020-260/FullText.pdf.

[Sch20c] T. Schwetz-Mangold. “Neutrino physics”. Lecture notes: KSETA topical courses. 2020.

[Sch21] L. Schimpf. "Characterisation of energy loss processes of 18.6 keV electrons inside the windowless tritium source of KATRIN". PhD thesis. Karlsruher Institut für Technologie (KIT), 2021.

[Sch23] S. Schneidewind. "Improvement of the neutrino mass sensitivity and background reduction of the KATRIN experiment". Thesis in preparation. PhD thesis. Westfälische Wilhelms-Universität Münster, to be published in 2023.

[Sei19] H. Seitz-Moskaliuk. "Characterisation of the KATRIN tritium source and evaluation of systematic effects". PhD thesis. Karlsruher Institut für Technologie (KIT), 2019. DOI: 10.5445/IR/1000090748.

[SEN20] SENSYS Sensorik & Systemtechnologie GmbH. *SENSYS FGM3D Matrix of Technical Parameters*. 2020. URL: https://my.hidrive.com/lnk/98MxIqf4#file.

[SEN21] SENIS. *SENIS 3MH3A Magnetic Field Digital Teslametrer*. 2021. URL: http://c1940652.r52.cf0.rackcdn.com/5a7090adb8d39a6f2d00212a/Magnetic-Teslameter-3MH3A-Datasheet-r3.pdf.

[Sha09] F. Sharipov. "Gas Circulation Due an Azimuthal Temperature Distribution Over a Micro-Tube Wall". In: *International Conference on Nanochannels, Microchannels, and Minichannels*. Vol. ASME 2009 7th International Conference on Nanochannels, Microchannels and Minichannels. 2009, pp. 373–381. DOI: 10.1115/ICNMM2009-82028.

[Sha15] F. Sharipov. *Rarefied gas dynamics: fundamentals for research and practice*. John Wiley & Sons, 2015.

[Sha68] E. M. Shakhov. "Generalization of the Krook kinetic relaxation equation". In: *Fluid Dynamics* 3.5 (1968), pp. 95–96. DOI: 10.1007/BF01029546.

[Sha97] F. Sharipov. "Rarefied gas flow through a long tube at arbitrary pressure and temperature drops". In: *Journal of Vacuum Science & Technology A: Vacuum, Surfaces, and Films* 15.4 (1997), pp. 2434–2436. DOI: 10.1116/1.580904.

[SS98] F. Sharipov and V. Seleznev. "Data on internal rarefied gas flows". In: *Journal of Physical and Chemical Reference Data* 27.3 (1998), pp. 657–706. DOI: 10.1063/1.556019.

[Thé+15] E. Thébault et al. "International Geomagnetic Reference Field: the 12th generation". In: *Earth, Planets and Space* 67.1 (2015), p. 79. DOI: 10.1186/s40623-015-0228-9.

[The02] The Royal Swedish Academy of Sciences. *The Nobel Prize in Physics 2002*. Oct. 8, 2002. URL: https://www.nobelprize.org/prizes/physics/2002/summary/ (visited on 03/13/2021).

[The15] The Royal Swedish Academy of Sciences. *The Nobel Prize in Physics 2015*. Oct. 6, 2015. URL: https://www.nobelprize.org/prizes/physics/2015/press-release/ (visited on 03/13/2021).

[The80] The Royal Swedish Academy of Sciences. *The Nobel Prize in Physics 1980*. Oct. 12, 1980. URL: https://www.nobelprize.org/prizes/physics/1980/press-release/ (visited on 03/15/2021).

[The95] The Royal Swedish Academy of Sciences. *The Nobel Prize in Physics 1995*. Oct. 11, 1995. URL: https://www.nobelprize.org/prizes/physics/1995/summary/ (visited on 03/04/2021).

[Thü20] T. Thümmler. "Spectrometer and Detector System Status Update". 38th KATRIN Collaboration Meeting. 2020. URL: https://fuzzy.fzk.de/bscw/bscw.cgi/1318629?op=preview&back_url=1318494.

[TMW09] T. Thümmler, R. Marx, and C. Weinheimer. "Precision high voltage divider for the KATRIN experiment". In: *New Journal of Physics* 11.10 (2009), p. 103007. DOI: 10.1088/1367-2630/11/10/103007.

[Tro19] N. R.-M. Trost. "Modeling and measurement of Rydberg-State mediated Background at the KATRIN Main Spectrometer". PhD thesis. Karlsruher Institut für Technologie (KIT), 2019. DOI: 10.5445/IR/1000090450.

[TZ02] V. I. Tretyak and Y. G. Zdesenko. "Tables of Double Beta Decay Data - an Update". In: *Atomic Data and Nuclear Data Tables* 80.1 (2002), pp. 83–116. ISSN: 0092-640X. DOI: 10.1006/adnd.2001.0873.

[Urb19] K. Urban. "Application of a TRISTAN Silicon Drift Detector as Forward Beam Monitor in KATRIN". Master Thesis. Technical University of Munich, 2019. URL: https://publications.mppmu.mpg.de/2019/MPP-2019-356/FullText.pdf.

[Val09] K. Valerius. "Spectrometer-related background processes and their suppression in the KATRIN experiment". PhD thesis. Westfälische Wilhelms-Universität Münster, 2009. URL: http://nbn-resolving.de/urn:nbn:de:hbz:6-28479494638.

[Vel+19] C. Velte et al. "High-resolution and low-background ^{163}Ho spectrum: interpretation of the resonance tails". In: *The European Physical Journal C - Particles and Fields* 79.12 (2019), p. 1026. DOI: 10.1140/epjc/s10052-019-7513-x.

[Vén+18a] D. Vénos et al. "Properties of ^{83m}Kr conversion electrons and their use in the KATRIN experiment". In: *Journal of Instrumentation* 13.02 (2018), T02012–T02012. DOI: 10.1088/1748-0221/13/02/t02012.

[Vén+18b] D. Vénos et al. "Properties of ^{83m}Kr conversion electrons and their use in the KATRIN experiment". In: *Journal of Instrumentation* 13.02 (2018), T02012. DOI: 10.1088/1748-0221/13/02/T02012.

[Wan13] N. Wandkowsky. "Study of background and transmission properties of the KATRIN spectrometers". PhD thesis. Karlsruher Institut für Technologie (KIT), 2013. DOI: 10.5445/IR/1000036631.

[Wil+87] J. F. Wilkerson et al. "Limit on $\overline{\nu}_e$ Mass from Free-Molecular-Tritium Beta Decay". In: *Phys. Rev. Lett.* 58 (1987), pp. 2023–2026. DOI: 10.1103/PhysRevLett.58.2023.

[Wol16] J. Wolf. "De-Magnetization of the Spectrometer Building". 27th KATRIN Collaboration Meeting. 2016. URL: https://fuzzy.fzk.de/bscw/bscw.cgi/d936561/95-TRP-5760-S5-JWolf.pdf.

[Wol78] L. Wolfenstein. "Neutrino oscillations in matter". In: *Phys. Rev. D* 17 (1978), pp. 2369–2374. DOI: 10.1103/PhysRevD.17.2369.

[Wol79] L. Wolfenstein. "Neutrino oscillations and stellar collapse". In: *Phys. Rev. D* 20 (1979), pp. 2634–2635. DOI: 10.1103/PhysRevD.20.2634.

[Wu+57] C. S. Wu et al. "Experimental Test of Parity Conservation in Beta Decay". In: *Phys. Rev.* 105 (1957), pp. 1413–1415. DOI: 10.1103/PhysRev.105.1413.

[Wyd24] J. Wydra. "Investigation of Systematic Effects of the Tritium Loop System and the WGTS of KATRIN". Thesis in preparation. PhD thesis. Karlsruher Institut für Technologie (KIT), to be published in 2024.

[Zub12] K. Zuber. *Neutrino physics*. 2nd ed. 2012. Boca Raton, London, New York: CRC Press, Taylor & Francis Group, 2012. ISBN: 978-1-283-30928-8.

[Zyl+20] P. Zyla et al. "Review of Particle Physics". In: *PTEP* 2020.8 (2020), p. 083C01. DOI: 10.1093/ptep/ptaa104.

List of acronyms

ADEI	Advanced Data Extraction Infrastructure
BEANS	Building Elements for ANalysis Sequence
BIXS	Beta Induced X-ray Spectroscopy
CPS	Cryogenic Pumping System
DET	DETector magnet
DPS	Differential Pumping System
e-gun	Photoelectron source (electron gun)
eLFCS	extended Low-Field Correction System
emcee	Affine-invariant ensemble sampler for Markov Chain Monte Carlo
EMCS	Earth Magnetic field Compensation System
FBM	Forward Beam Monitor
FPD	Focal Plane Detector
KaFit	Fit environment for KATRIN-spectra
Kasper	KATRIN C++ software package
Kassiopeia	Particle tracking framework
KATRIN	KArlsruhe TRItium Neutrino (experiment)
KDB	KATRIN DataBase
KNM1	First KATRIN Neutrino Mass measurement campaign
KNM2	Second KATRIN Neutrino Mass measurement campaign
KNM3	Third KATRIN Neutrino Mass measurement campaign
KNM4	Fourth KATRIN Neutrino Mass measurement campaign
KNM5	Fifth KATRIN Neutrino Mass measurement campaign
LARA	LAser RAman spectroscopy system
LDLS	Laser-Driven Light Source of the e-gun
LFCS	Low-Field Correction System
LMFIT	Non-Linear Least-Square Minimization Package
MAC-E	Magnetic Adiabatic Collimation with Electrostatic filtering
MCMC	Markov Chain Monte Carlo
MobSU	Mobile Sensor Unit
NAP	Nominal Analyzing Plane of the Main Spectrometer
PCH	Pinch magnet
Peaberry	KATRIN Python post-analysis framework
PS1	Upstream Pre-Spectrometer Magnet
PS2	Downstream Pre-Spectrometer Magnet
RMMS	Radial Magnetic Monitoring System
SAP	Shifted Analyzing Plane of the Main Spectrometer
SDS	Spectrometers and Detector Section
SSC	Source and Spectrum Calculation package of Kasper
STS	Source and Transport Section
TLK	Tritium Laboratory Karlsruhe

VMMS	Vertical Magnetic Monitoring System
WGTS	Windowless Gaseous Tritium Source

Danksagungen

Zum Abschluss dieser Arbeit möchte ich mich noch herzlich bei allen bedanken, die mich während der Promotion unterstützt und zum Gelingen dieser Arbeit beigetragen haben:

- Prof. Dr. Kathrin Valerius für die erstklassige Betreuung während der Promotion, die zahlreichen Gruppentreffen, das Ermöglichen der Teilnahme an verschiedenen Konferenzen und die tolle Atmosphäre sowohl während der Arbeit als auch bei außerdienstlichen Unternehmungen.
- Prof. Dr. Guido Drexlin für das Begleiten der Arbeit als Korreferent und das Fördern meiner Neugierde an der Neutrinophysik in der ATP-Vorlesung.
- dem GRK 1694 sowie KSETA für die finanzielle Unterstützung während der Promotion.
- den Korrekturlesern dieser Arbeit, insbesondere Jan, Stephanie, Ferenc, Alexander, Leonard, Moritz, Christoph und Caroline.
- der Magnetfeldarbeitsgruppe rund um Dr. Jan Behrens, Heiko Bouquet, Marco Deffert, Dr. Woosik Gil, Dr. Ferenc Glück und Prof. Dr. Alexander Osipowicz für die Planung und Durchführung von zahlreichen Messungen.
- der "Column Density"-Arbeitsgruppe mit den Mitgliedern Christoph Köhler und Dr. Alexander Marsteller für die gemeinsame Erarbeitung der Säulendichtemessungen und Methoden zur Überwachung dieser während β-Scans.
- der SAP-Arbeitsgruppe mit Dr. Alexey Lokhov und Alessandro Schwemmer für die ertragreichen Diskussionen der Kryptonmessungen und die Interpretation der Messresultate.
- dem KaFit-Team bestehend aus Dr. Won-Qook Choi, Dr. Stephanie Hickford, Leonard Köllenberger und Dr. Moritz Machatschek, die bei Problemen jeglicher Art stets schnell und unkompliziert helfen konnten, sowie dem Enthusiasmus mit dem gemeinsam neue Algorithmen implementiert und getestet wurden.
- den E-Gun Experten Caroline Rodenbeck, Dr. Rudolf Sack und Dr. Lutz Schimpf für die gemeinsame Planung und Durchführung von Messungen, sowie die Diskussion der Messresultate.
- Dr. Jan Behrens für seine unermüdliche Geduld bei diversen Softwarefragen und der schnellen Hilfe bei der Beseitigung von Bugs und sonstigen Softwareproblemen.
- allen KATRIN Kollegen für die tolle Atmosphäre vor Ort, am Experiment, im Kontrollraum und auf Dienstreisen, die die letzten 4,5 Jahre bei KATRIN für mich zu einer unvergesslichen Zeit werden ließen.

- meinen Freunden und meiner Familie, die mich während der Schreibphase dieser Thesis immer wieder auf andere Gedanken gebracht haben.

Außerdem möchte ich mich bei meinen Eltern Ellen und Thomas Block bedanken, die mich stets unterstützt, motiviert und mir das Physikstudium ermöglicht haben. Zu guter Letzt möchte ich mich noch bei meiner Verlobten Nadine Kloss für die bedingungslose moralische Unterstützung bedanken und dass du mir während der Schreibphase stets den Rücken freigehalten hast.